

THE UNIVERSITY OF HULL

The Preparation and Characterisation of Mixed-Anion and
Non-Oxide Materials

being a Thesis submitted for the Degree of PhD

in the University of Hull

by

David Andrew Headspith MChem (Hons)

December 2009

Abstract

Traditionally, research in solid-state chemistry has focused largely on the chemistry of oxides and on chemical tailoring of the structure and physical properties via cationic substitutions. Consequentially, the chemistry of non-oxide compounds and other means of chemical tailoring, such as anionic substitutions, have been comparatively overlooked by the scientific community. Non-oxides offer a wide diversity of chemistry, most noticeable in unusual oxidation states and coordination geometries found for metals in these compounds. Furthermore, the development of anionic substitutions could open up an alternative avenue for the modification of the structure and properties in solids and the preparation of novel compounds.

The work reported here covers: (1) the preparation of non-oxide compounds (Ba_2CoS_3 , Ba_2MnS_3 , Ce_2MnN_3 , $\text{Ce}_{2-x}\text{La}_x\text{MnN}_3$) and mixed-anion compounds ($\text{Ce}_2\text{MnN}_3\text{F}_{2-\delta}$, apatite oxide-nitrides) via direct synthesis and/or cationic and anionic substitutions; (2) the characterisation of their structure and (3) the characterisation of selected physical properties.

The three-dimensional magnetic cell of Ba_2CoS_3 , which undergoes a transition to long-range order at 46 K, was found to be double the size of the crystallographic unit cell, along the *c*-axis. A conclusive representation of the magnetic cell of Ba_2MnS_3 , with similar structure to Ba_2CoS_3 , could not be achieved and two possible models are proposed.

A one-step synthetic route for Ce_2MnN_3 , more convenient than the route reported in the literature, was developed in this work. Cationic substitutions led to the preparation of the solid solution $\text{Ce}_{2-x}\text{La}_x\text{MnN}_3$ and anionic manipulation of the lattice, via fluorination, led to the preparation of the first example of a quaternary nitride-fluoride $\text{Ce}_2\text{MnN}_3\text{F}_{2-\delta}$. The structure of $\text{Ce}_2\text{MnN}_3\text{F}_{2-\delta}$ showed layers of distorted MnN_3F octahedra and staged fluorine occupancy of the interstitial sites.

A range of novel oxide-nitrides were prepared via reaction of the apatite-type oxides $\text{La}_{9.33}\text{Si}_6\text{O}_{26}$, $\text{La}_{8+x}\text{Sr}_{2-x}\text{M}_6\text{O}_{26+x/2}$ ($\text{M} = \text{Si}, \text{Ge}; 0 \leq x \leq 2$), $\text{La}_{9.67}\text{Si}_5\text{CoO}_{26}$ and $\text{La}_{10}\text{M}_5\text{CoO}_{26.5}$ ($\text{M} = \text{Si}, \text{Ge}$) with gaseous ammonia at temperatures above 700 °C, most retaining the apatite structure with nitrogen located in interstitial sites.

Acknowledgements

I would first like to thank my supervisor, Dr M. Grazia Francesconi, for all of her help and support throughout my PhD.

I wish to acknowledge the collaborators Prof. Peter Battle in Oxford, for his assistance with the magnetic neutron diffraction, Dr Emma Kendrick in Surrey and, in Birmingham, Dr Peter Slater, Dr Alodia Orera for the work on oxide nitride apatites, Dr David Apperley for NMR data collection and Prof. Colin Greaves and his group, including Erin Sullivan and Hany El Shinawi for use of the fluorine line, assistance with fluorination reactions and collection and analysis of the magnetic data. In addition, I would like to thank Dr Nigel Young, of the University of Hull for his assistance with XAFS data collection and analysis and Emmanuelle Suard and Ludovic Gendrin at the Instiut Laue-Langevin, Grenoble for their assistance with collection of neutron diffraction data. I would also like to thank all of the people I have worked with at the University of Hull, especially Tom, Andy, Chris, Becky, Mark, Phil, Tim, Vincent, Steve, Amanda, Ryan, Graeme, Antony and Aaron. I would like to thank all of the technical staff in the chemistry department for their help over the last three years, particularly Anthony Sinclair for the EDX spectroscopy measurements, Mark and Joe, the porters and Carol Kennedy for miscellaneous laboratory equipment.

The author would also like to thank the Leverhulme trust for financial support. I also wish to acknowledge the use of the EPSRC's Chemical Database Service at Daresbury.¹

Finally, I would like to thank my Mum, Dad, Chris, Nanna and Granddad for putting up with me.

Abbreviations

AFC	Alkaline Fuel Cell
EDX	Energy Dispersive X-ray
EXAFS	Extended X-ray Absorption Fine Structure
FT	Fourier Transform
LMTO	Linear Muffin-tin Orbital
Ln	Lanthanide
MAS	Magic Angle Spinning
MCFC	Molten Carbonate Fuel Cell
ND	Neutron Diffraction
NMR	Nuclear Magnetic Resonance
PAFC	Phosphoric Acid Fuel Cell
PEMFC	Polymeric Electrolyte Membrane Fuel Cell
PND	Powder Neutron Diffraction
PSD	Position Sensitive Detector
PVDF	Polyvinylidene fluoride
PXRD	Powder X-ray Diffraction
RP	Ruddlesden-Popper
RT	Room Temperature
SEM	Scanning Electron Microscope
SOFC	Solid Oxide Fuel Cell
SQUID	Superconducting Quantum Interference Device
TB	Thermal Bomb
TGA	Thermogravimetric Analysis
TM	Transition Metal
XAFS	X-ray Absorption Fine Structure
XANES	X-ray Absorption Near-Edge Structure
XAS	X-ray Absorption Spectroscopy
XPS	X-ray Photoemission Spectroscopy
XRD	X-ray Diffraction

Contents

1	Introduction	5
1.1	Perovskite and Related Structures	5
1.1.1	Perovskites	5
1.1.2	Ruddlesden-Popper Phases	7
1.1.2.1	<i>T Structure</i>	8
1.1.2.2	<i>T' Structure</i>	9
1.1.2.3	<i>T* Structure</i>	9
1.1.2.4	<i>Anion Deficient Structures</i>	10
1.1.3	Fluorination of Perovskite-Like Materials	11
1.2	Low Dimensional Ternary Chalcogenides	17
1.3	Low-Dimensional Nitrides	22
1.3.1	Nitrides Containing Infinite Chains of Octahedra	24
1.3.2	Nitrides Containing Infinite Chains of Tetrahedra	25
1.3.3	Nitrides Containing Infinite Chains of Square Planar Units	32
1.3.4	Nitrides Containing Infinite Chains of Triangular Units	33
1.3.5	Nitrides Containing Infinite Linear Chains	34
1.3.6	Synthesis of Nitrides	39
1.4	Binary, Ternary and Quaternary Nitride-Halides	41
1.4.1	Binary and Ternary Nitride-Halides	42
1.4.1.1	Nitride-Halides of Elements in Group 3	43
1.4.1.1.1	<i>Compounds Showing Three-Dimensional Structural Features</i>	43
1.4.1.1.2	<i>Compounds Showing Two-Dimensional Structural Features</i>	44
1.4.1.1.3	<i>Compounds Showing One-Dimensional Structural Features</i>	46
1.4.1.2	Nitride-Halides of Elements in Group 4	50
1.4.1.2.1	<i>Compounds Showing Three-Dimensional Structural Features</i>	50
1.4.1.2.2	<i>Compounds Showing Two-Dimensional Structural Features</i>	53
1.4.1.3	Nitride-Halides of Elements in Group 5	59
1.4.1.3.1	<i>Compounds Showing One-Dimensional Structural Features</i>	59
1.4.1.4	Nitride-Halides of Elements in Group 6	60
1.4.1.4.1	<i>Compounds Showing Two-Dimensional Structural Features</i>	60
1.4.1.4.2	<i>Compounds Showing One-Dimensional Structural Features</i>	61
1.4.1.4.3	<i>Compounds Showing Isolated Coordination Polyhedra</i>	64
1.4.1.5	Nitride-Halides of Elements in Group 7	65
1.4.1.5.1	<i>Compounds Showing One-Dimensional Structural Features</i>	65
1.4.1.5.2	<i>Compounds Showing Isolated Coordination Polyhedra</i>	66
1.4.1.6	Nitride-Halides of the Lanthanides	67
1.4.1.6.1	<i>Compounds Showing Three Dimensional Structural Features</i>	67
1.4.2	Quaternary Nitride-Halides	67
1.5	Properties of Solids	73
1.5.1	Magnetism	73
1.5.1.1	<i>Bulk Magnetism</i>	73
1.5.1.2	<i>Low Dimensional Magnetism</i>	78
2	Experimental Techniques	80
2.1	Synthetic Methods	80
2.1.1	“Hard” Chemistry	80
2.1.2	“Soft” Chemistry	81
2.2	Equipment	83
2.2.1	Glove Boxes	83
2.2.2	Furnaces	84
2.2.2.1	Box Furnace	84
2.2.2.2	Tubular Furnaces	86
2.2.2.2.1	<i>Reactions Under N₂ Gas</i>	87
2.2.2.2.2	<i>Reactions in NH₃ Gas</i>	90
2.2.2.2.3	<i>Reactions with CS₂ Vapour</i>	90
2.2.2.2.4	<i>Reactions with F₂/N₂ Gas</i>	91

2.3	Structural Determination.....	92
2.3.1	Crystallography	92
2.3.1.1	Symmetry	92
2.3.1.2	Crystal Systems	94
2.3.1.3	Lattices	95
2.3.1.4	Space Groups and Notation	98
2.3.2	Diffraction	101
2.3.2.1	Theory of Diffraction	101
2.3.2.2	Powder X-ray Diffraction (PXRD)	103
2.3.2.2.1	Generation of X-rays	104
2.3.2.2.2	Equipment for Powder X-ray Diffraction	109
2.3.2.2.3	X-ray Detection	111
2.3.2.3	Powder Neutron Diffraction (PND)	111
2.3.2.3.1	Generation of Neutrons	115
2.3.2.3.2	Equipment for Neutron Diffraction	117
2.3.2.3.3	Neutron Detection	118
2.3.3	Rietveld Refinement	118
2.3.3.1	Lorentz, Polarisation and Multiplicity Factors, L_K	119
2.3.3.2	Reflection Profile Function, ϕ	120
2.3.3.3	Preferred Orientation Function, P_K	121
2.3.3.4	Absorption Factor, A	121
2.3.3.5	Structure Factor, F_K	122
2.3.3.6	Background, y_{bi}	123
2.3.3.7	Quality of Fit Criteria	123
2.3.4	Le Bail Extraction	124
2.3.5	X-ray Absorption Spectroscopy (XAS)	124
2.3.6	Thermogravimetric Analysis (TGA)	131
2.3.7	Energy Dispersive X-ray Analysis (EDX)	132
2.3.8	Magnetic Measurements	133
2.3.9	Nuclear Magnetic Resonance Spectroscopy (NMR)	134
3	Low Temperature Magnetic Structures of Ba_2MS_3 (M = Co, Mn)	136
3.1	Ba_2MS_3 (M = Co, Mn)	136
3.2	Structural Description of Ba_2MS_3 (M = Co, Mn)	141
3.2.1	Experimental	141
3.2.1.1	Preparation	141
3.2.1.2	Characterisation	141
3.2.2	Results and Discussion	142
3.2.2.1	Structural Characterisation of Ba_2CoS_3	142
3.2.2.1.1	Powder X-ray Diffraction (PXRD) – Room Temperature	142
3.2.2.1.2	Powder Neutron Diffraction (PND) – 200 K	144
3.2.2.1.3	Powder Neutron Diffraction (PND) – 1.5 K	148
3.2.2.2	Structural Characterisation of Ba_2MnS_3	155
3.2.2.2.1	Powder X-ray Diffraction (PXRD) – Room Temperature	155
3.2.2.2.2	Powder Neutron Diffraction (PND) – 200 K	157
3.2.2.2.3	Powder Neutron Diffraction (PND) – 4 K and Powder X-ray Diffraction (PXRD) – 77 K	159
3.2.3	Conclusions	166
4	Preparation of Ce_2MnN_3 and Low-Dimensional Nitrides	168
4.1	Ce_2MnN_3	168
4.1.1	Experimental	171
4.1.1.1	Preparation of Cerium Nitride, CeN	172
4.1.1.1.1	Method 1 – Ammoniation of Cerium Carbide, CeC_2	173
4.1.1.1.2	Method 2 – Ammoniation of Cerium Metal	173
4.1.1.1.3	Method 3 – Nitrogenation of Cerium in Molten Zinc	174
4.1.1.1.4	Method 4 – Nitrogenation of Cerium Metal	174
4.1.1.2	Preparation of Ce_2MnN_3	174
4.1.1.2.1	Method 1 – Reaction of Cerium Nitride, Manganese and Nitrogen	174

4.1.1.2.2 Method 2 – Reaction of Cerium, Manganese and Nitrogen	175
4.1.1.3 Characterisation.....	175
4.1.2 Results and Discussion	176
4.1.2.1 Structural Characterisation of CeN	176
4.1.2.1.1 Powder X-ray Diffraction (PXRD).....	176
4.1.2.2 Structural Characterisation of Ce ₂ MnN ₃	179
4.1.2.2.1 Powder X-ray Diffraction (PXRD).....	179
4.1.2.2.2 Energy Dispersive X-ray (EDX) Spectroscopy.....	184
4.1.2.2.3 Powder Neutron Diffraction (PND)	185
4.1.2.2.4 Magnetic Susceptibility	188
4.1.3 Conclusions	188
4.2 Cationic Substitution in Ce₂MnN₃.....	189
4.2.1 Substitution on the Cerium Site of Ce ₂ MnN ₃	189
4.2.1.1 Experimental	190
4.2.1.1.1 Preparation of Ce _{1-x} A _x N (A = Y, La, Pr, Dy, Tb).....	190
4.2.1.1.1.1 Method 1 – Ammoniation of the Metals	190
4.2.1.1.1.2 Method 2 – Nitrogenation in Molten Zinc.....	191
4.2.1.1.2 Preparation of Ce _{2-x} A _x MnN ₃ (A = Tb, Dy, Zr, La)	191
4.2.1.1.2.1 Method 1– Reaction of Metals and Nitrogen	191
4.2.1.1.2.2 Method 2– Reaction of Cerium Lanthanum Nitride, Manganese and Nitrogen.....	191
4.2.1.1.3 Characterisation.....	192
4.2.1.1 Results and Discussion.....	192
4.2.1.1.1 Structural Characterisation of Ce _{1-x} A _x N (A = Y, La, Pr, Tb, Dy).....	192
4.2.1.1.1.1 Powder X-ray Diffraction (PXRD).....	192
4.2.1.1.2 Structural Characterisation of Ce _{2-x} A _x MnN ₃ (A = Zr, La, Tb, Dy).....	196
4.2.1.1.2.1 Powder X-ray Diffraction (PXRD).....	196
4.2.1.1.2.2 Powder Neutron Diffraction (PND).....	198
4.2.1.1.2.3 Magnetic Susceptibility	202
4.2.1.2 Conclusions	204
4.2.2 Substitution on the Manganese Site of Ce ₂ MnN ₃	204
4.2.2.1 Experimental	205
4.2.2.1.2 Preparation of Cr _x N _y	205
4.2.2.1.2.1 Method 1 – Reaction of Chromium Metal with Nitrogen	206
4.2.2.1.2.2 Method 2 – Reduction of Cr _x N _y in Argon.....	206
4.2.2.2 Results and Discussion.....	206
4.2.2.2.1 Structural Characterisation of Cr _x N _y	206
4.2.2.2.1.1 Powder X-ray Diffraction (PXRD).....	206
4.2.2.2.1 Structural Characterisation of Ce ₂ Mn _{1-x} M _x N ₃ (M = Cr, Co, Ni, Cu).....	210
4.2.2.2.1.1 Powder X-ray Diffraction (PXRD).....	210
4.2.2.3 Conclusions	212
5 Ce₂MnN₃F_{2-δ}, the First Quaternary Nitride-Fluorides	213
5.1 Synthesis of Ce₂MnN₃F_{2-δ}.....	214
5.1.1 Experimental	215
5.1.1.1 Preparation of Ce ₂ MnN ₃ F _{2-δ}	216
5.1.1.1.1 Method 1 – Reaction of Ce ₂ MnN ₃ with Polyvinylidene fluoride (PVDF).....	216
5.1.1.1.2 Method 2 – Reaction of Ce ₂ MnN ₃ with XeF ₂	218
5.1.1.1.3 Method 3 – Reactions of Ce ₂ MnN ₃ with MF ₂ (M = Cu, Zn).....	218
5.1.1.1.4 Method 4 – Reactions with Fluorine Gas.....	219
5.1.1.1.5 Method 5 - Reaction of Cerium Nitride-Fluoride, Manganese and Nitrogen	220
5.1.1.2 Preparation of CeN _x F _{3-3x}	220
5.1.1.3 Characterisation.....	221
5.1.2 Results and Discussion	221
5.1.2.1 Structural Characterisation of CeN _x F _{3-3x}	222
5.1.2.1.1 Powder X-ray Diffraction (PXRD).....	222
5.1.2.2 Structural Characterisation of Ce ₂ MnN ₃ F _{2-δ}	223
5.1.2.2.1 Reaction of Cerium Nitride-Fluoride, Manganese and Nitrogen.....	223
5.1.2.2.1.1 Powder X-ray Diffraction (PXRD).....	223
5.1.2.2.2 Reaction of Ce ₂ MnN ₃ with Polyvinylidene fluoride (PVDF).....	224
5.1.2.2.2.1 Powder X-ray Diffraction (PXRD).....	224

5.1.2.2.3	Reaction of Ce_2MnN_3 with XeF_2	226
5.1.2.2.3.1	Powder X-ray Diffraction (PXRD).....	226
5.1.2.2.4	Reactions of Ce_2MnN_3 with MF_2 ($M = Cu, Zn$).....	227
5.1.2.2.4.1	Powder X-ray Diffraction (PXRD).....	227
5.1.2.2.5	Reactions of Ce_2MnN_3 with Fluorine Gas.....	238
5.1.2.2.5.1	Powder X-ray Diffraction (PXRD).....	238
5.1.2.2.5.2	Powder Neutron Diffraction (PND).....	244
5.1.2.2.5.3	Magnetic Susceptibility Measurements.....	255
5.1.3	Conclusions.....	256
6	Ammonolysis of Apatites.....	258
6.1	Ammonolysis of $La_{9.33}Si_6O_{26}$.....	266
6.1.1	Experimental.....	266
6.1.1.1	Preparation.....	266
6.1.1.2	Characterisation.....	267
6.1.2	Results and Discussion.....	269
6.1.2.1	Powder X-ray Diffraction (PXRD).....	269
6.1.2.2	Thermogravimetric Analysis (TGA).....	273
6.1.2.3	Powder Neutron Diffraction (PND).....	274
6.1.2.4	^{29}Si Nuclear Magnetic Resonance (NMR).....	277
6.2	Ammonolysis of $La_{8+x}Sr_{2-x}M_6O_{26+x/2}$ ($M = Si, Ge; 0 \leq x \leq 2$).....	279
6.2.1	Experimental.....	279
6.2.1.1	Preparation.....	279
6.2.1.2	Characterisation.....	279
6.2.2	Results and Discussion.....	280
6.2.2.1	Powder X-ray Diffraction (PXRD).....	280
6.2.2.2	Thermogravimetric Analysis (TGA).....	282
6.2.2.3	^{29}Si Nuclear Magnetic Resonance (NMR).....	285
6.3	Ammonolysis of $La_{9.67}Si_5CoO_{26}$, $La_{10}M_5CoO_{26.5}$ ($M = Si, Ge$).....	286
6.3.1	Experimental.....	286
6.3.1.1	Preparation.....	286
6.3.1.2	Characterisation.....	286
6.3.2	Results and Discussion.....	287
6.3.2.1	Powder X-ray Diffraction (PXRD).....	287
6.3.2.2	X-ray Absorption Spectroscopy.....	289
6.3.2.2.1	Co-K-edge XANES of $La_{9.67}Si_5CoO_{26}$, $La_{10}M_5CoO_{26.5}$ ($M = Si, Ge$).....	290
6.3.2.2.2	Co-K-edge XANES of Ammoniated $La_{9.67}Si_5CoO_{26}$, $La_{10}M_5CoO_{26.5}$ ($M = Si, Ge$).....	293
6.3.2.2.3	Co-K-edge EXAFS of $La_{9.67}Si_5CoO_{26}$, $La_{10}M_5CoO_{26.5}$ ($M = Si, Ge$).....	297
6.3.2.2.4	Co-K-edge EXAFS of Ammoniated $La_{9.67}Si_5CoO_{26}$, $La_{10}M_5CoO_{26.5}$ ($M = Si, Ge$).....	302
6.3.2.2.5	Thermogravimetric Analysis of Ammoniated $La_{9.67}Si_5CoO_{26}$, $La_{10}M_5CoO_{26.5}$ ($M = Si, Ge$).....	308
6.4	Conclusions.....	311
7	Overall Conclusions.....	313
8	References.....	317

1 Introduction

1.1 Perovskite and Related Structures

1.1.1 Perovskites

Perovskite, CaTiO_3 was discovered by Gustav Rose in 1839 and is named after a Russian mineralogist Count Lev Aleksevich von Perovski.² The name now applies to compounds, of the general formula ABX_3 , in which A is an electropositive metal (alkali or alkaline-earth metal or lanthanide), B a transition metal (smaller in size than A) and X the anion.²

The ideal perovskite lattice is cubic with B cations located in the centre of the unit cell, in octahedral coordination with X anions. The BX_6 octahedra are connected via their vertices to six other octahedra, giving the characteristic three-dimensional structure. In addition, each octahedron resides within a cube of eight A cations which sit on the corners of the unit cell, as shown in Figure 1-1. An alternative unit cell can be chosen where A is considered central in the unit cell (Figure 1-1).

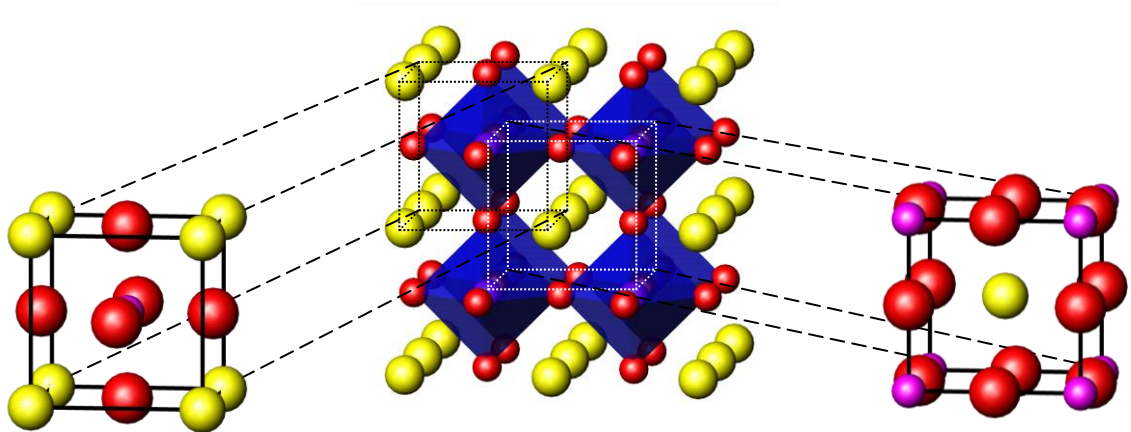


Figure 1-1. The ideal perovskite structure. The yellow, purple and red spheres represent A, B and X ions respectively. The blue octahedra represent the corner linked BX_6 units.

There are a number of conditions under which distortion from the ideal perovskite structure will occur; in the event, for example, of oxygen non-stoichiometry, Jahn-Teller

distortion, or a large size mismatch between the A and B cations.² A common distortion consists of a tilting of the octahedra from the ideal positions accompanied by a shifting of the A cations. In this way the cubic symmetry of the perovskite is lost.³

As an aid to predict the stability range of the perovskite structure, Goldschmidt suggested a tolerance factor, t_R , for the ABX_3 phases:

$$t_R = (r_A + r_X) / \sqrt{2}(r_B + r_X) \quad (1-1)$$

with r_A , r_B and r_X corresponding with the ionic radii of A, B and X respectively. The tolerance factor, gives an indication of distortion based simply on the ionic radii of the elements present.⁴

Experiments by Goldschmidt on existing perovskites indicate an ideal structure in the range of $0.8 \leq t_R \leq 0.9$.^{4,5}

The tolerance factor continues to be used in the description of perovskite stability and as additional structures are discovered improved knowledge of the tolerance factor limits is gained. Currently, oxide perovskites are known to exist in the range $0.75 \leq t_R \leq 1.0$ of which those in the $0.815 \leq t_R \leq 0.964$ region are cubic (based on around 223 oxide compounds).⁶⁻¹⁰ There are, however, a number of problems with the tolerance factor. Firstly, these values give an indication of the stability of perovskites, but there are exceptions, with a number of distorted perovskites with tolerance factors within the ideal cubic range.¹⁰ Secondly, values obtained are highly dependent on the ionic radii used, which vary from source to source. Furthermore, the tolerance factor relies on the suitability of the “rigid-sphere” model, which is not always applicable.

Another complementary approach to the tolerance factor is the octahedral factor (r_B/r_X), an extension of the radius ratio rules.^{9, 10} The stable range over which the B cations are found in an octahedral coordination is $0.414 \leq r_B/r_X \leq 0.732$.¹¹ Work by C. H. Li and co-workers has indicated that cubic oxide perovskites will most likely occur in the

$0.414 \leq r_B/r_X \leq 0.6785$ range.¹⁰ Using the two factors in conjunction will act to improve the accuracy of the prediction.

In general, any structure which consists of an ordered array of BX_6 octahedra, or related anion deficient polyhedra, can be classified as distorted perovskites or perovskite-like structures. This diversity of perovskites allows for a wide range of possible applications. Examples include ferroelectric and piezoelectric devices ($BaTiO_3$),^{2, 12} catalysts ($LaFeO_3$),¹³ photocatalysts ($SrTiO_3$),^{14, 15} ion conductors ($LaGaO_3$),¹⁶ optical switches ($LiNbO_3$),^{17, 18} superconductors ($YBa_2Cu_3O_{7-x}$),¹⁹ pigments ($YCrO_3$) and colossal magnetoresistive materials ($La_{0.85}Ca_{0.15}MnO_3$).^{5, 20, 21}

Several examples of perovskite-like materials, relevant to this work, are discussed in the following sections.

1.1.2 Ruddlesden-Popper Phases

The most recognizable characteristic of the perovskite structure is the corner sharing BX_6 octahedra. Compounds, which show structures made up of stacking sequences of perovskite-type slabs separated by layers of simpler units such as rock salt or fluorite are often referred to as perovskite-like compounds.²²

Well known examples are the Ruddlesden-Popper (RP) phases. These phases are named from their first investigators who, in the 1950s, investigated the Sr-Ti-O system and reported Sr_2TiO_4 , $Sr_3Ti_2O_7$ and $Sr_4Ti_3O_{10}$.^{23, 24} These phases have the general formula $A_{n+1}B_nO_{3n+1}$, where n is an integer.

RP phases consist of perovskite slabs, n octahedra in height, stacked on top of each other along the c -axis and separated by rock salt-type layers (AX) (Figure 1-2). This structural arrangement is emphasised if the general formula of the RP phase is given as $AX(ABX_3)_n$.

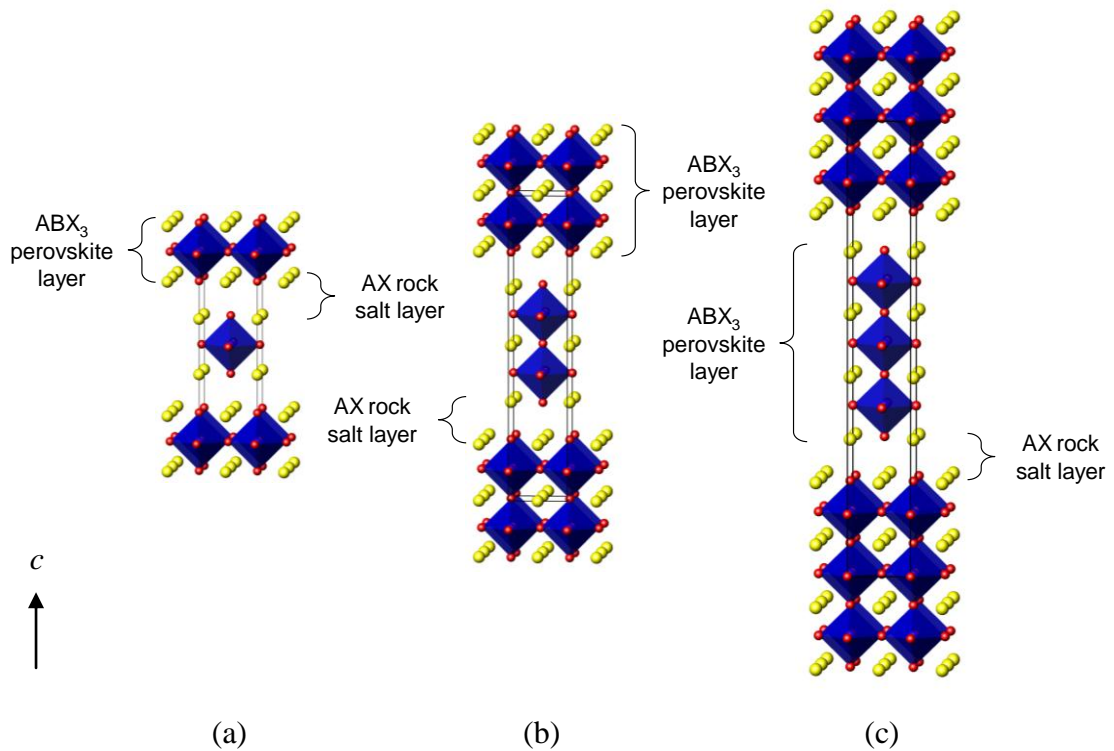


Figure 1-2. The structures of the RP phases (a) A_2BX_4 ($n = 1$), (b) $A_3B_2X_7$ ($n = 2$) and (c) $A_4B_3X_{10}$ ($n = 3$). The yellow, purple and red spheres represent A, B and X ions respectively. The blue octahedra represent the corner linked BX_6 units.

A large part of this thesis contains research based on A_2BX_4 -type compounds, which include the RP type phase ($n = 1$), but also a number of related phases that share the overall cationic arrangement. The structures in question are the T , T' and T^* structures.^{25, 26}

1.1.2.1 T Structure

The $n = 1$ RP phase, shown in Figure 1-2 (a) and Figure 1-3 (a), is also referred to as the K_2NiF_4 -type structure or the T structure.²⁷ The T structure consists of two-dimensional layers of corner sharing BX_6 octahedra stacked long the c -axis and separated by an AX rock salt layer. The coordination of the A cation drops from 12 coordinate in the perovskite structure to 9 coordinate in the T structure. When all four equatorial B-X bonds are equivalent in length the symmetry is tetragonal. If these bonds are different lengths the symmetry adopted is orthorhombic.

1.1.2.2 T' Structure

The T' structure is shown in Figure 1-3 (b). Also referred to as the Nd_2CuO_4 -type structure, the T' structure is made up of two-dimensional sheets of corner connected BX_4 square planar units separated by fluorite layers.²⁷ These fluorite layers consist of a cubic close packed arrangement of A with X in tetrahedral holes. The A cations are in 8 coordination with X.

The structure may also be described as a T -type structure with the apical anion sites of the octahedra vacant. Instead the anions reside within the A layers generating the fluorite like arrangement.

1.1.2.3 T^* Structure

The T^* structure (Figure 1-3 (c)), can be regarded as half way between the T and T' structures.²⁷ The metal on the B site shows coordination number five. The polyhedra show corner connectivity, forming two-dimensional layers, separated by alternating layers of fluorite and rock salt regions. The T^* structure can be described as the T -type with only half the octahedral apical anions vacant. These anions reside in the interstitial tetrahedral sites of half the A layers to generate the fluorite 'spacer' units. The A cations show both 8 and 9 coordination with X.

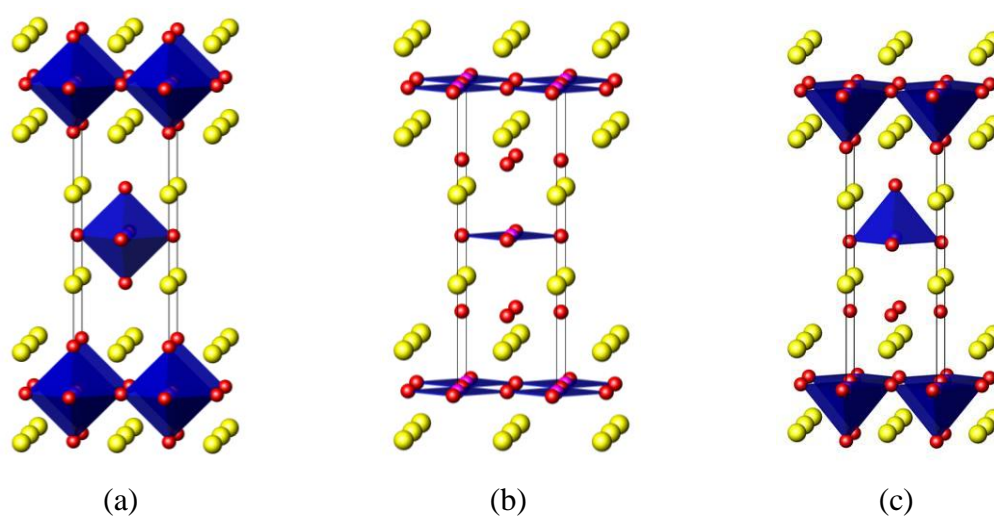


Figure 1-3. Representation of the (a) T , (b) T' and (c) T^* structures. The yellow, purple and red spheres correspond with A, B and X respectively. The blue polyhedra highlight the coordination of B with X.

The similarities between these phases and the perovskite structure have led to an extension of the tolerance factor, equation (1-1) to include the ‘ T ’ phases. It has been found that, in general the tetragonal T phase exists in the range $0.88 \leq t_R \leq 0.99$, the orthorhombic T phase in the $0.87 \leq t_R \leq 0.88$ range and $0.83 < t_R \leq 0.865$ gives the T' phase, while T^* is intermediate between the two.^{25, 26, 28}

A tolerance factor tailored more directly for the ‘ T ’ phases was suggested by Chen:

$$t_f = [3\sqrt{2}r_X + 2\sqrt{6}(r_A + r_X)] / 9(r_B + r_X) \quad (1-2)$$

where r_A , r_B and r_X are the ionic radii of A, B and X respectively.²⁸ Using the tolerance factor and the ionic radii from Shannon, it was found that the T' phase occurs for $1.00 > t_f > 0.96$ and T for $1.00 < t_f < 1.14$.^{28, 29} T^* occurs between these two boundaries.²⁸

1.1.2.4 Anion Deficient Structures

Although the T , T' and T^* phases show the same stoichiometry, the transition metal (B) coordination falls from the perovskite coordination of six to five (T^*) and four (T'). Structures which can be related to the perovskite or RP phases by removal of the anions in the transition metal (B) coordination sphere can be described as anion-deficient structures. For example, removal of two equatorial anions, in an ordered manner, to generate chains of corner connected square planar arrangements gives an anion-deficient K_2NiF_4 structure with a 213 stoichiometry e.g. Sr_2CuO_3 .

A number of possible transition metal coordinations that can be present in anion-deficient perovskite-like phases are shown in Figure 1-4. Removal of the two apical anions from an octahedron gives the square planar arrangement. Connectivity between square planes may be either one- or two-dimensional giving rise to either chains or sheets of polyhedra. In Figure 1-4, the image at the top right shows

connectivity through only one corner of the square. These are linked with additional square planes in a linear manner (one-dimensionality).²²

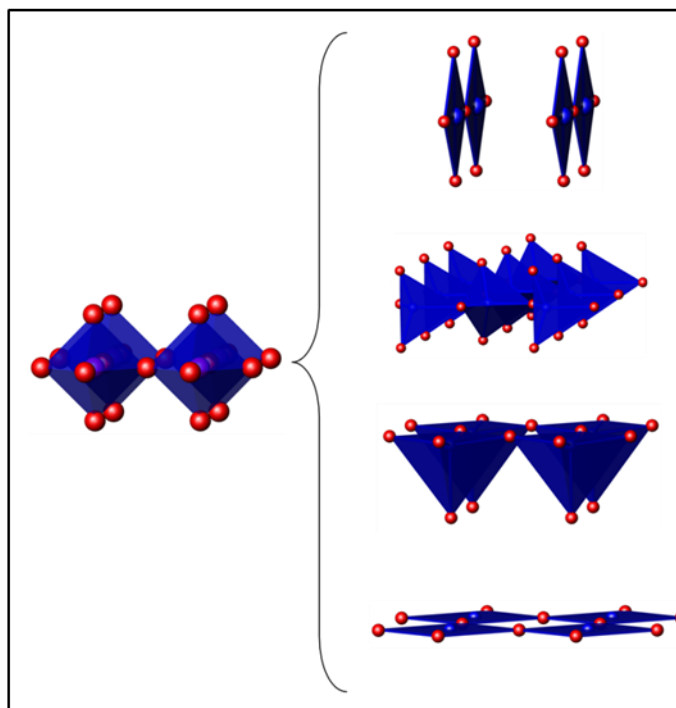


Figure 1-4. Representation of the corner linked polyhedra in perovskite-like compounds. The red and blue spheres represent the anions and cations respectively.²²

The significance of these anion-deficient compounds is that additional anions can potentially be inserted onto these vacant sites. Most relevant to this work, is the substitution and insertion of fluoride anions in A_2MO_3 compounds ($A = \text{Sr, Ca}$; $M = \text{Cu, Pd}$).

1.1.3 Fluorination of Perovskite-Like Materials

In 1994, high temperature superconductivity was discovered in the oxide-fluoride $\text{Sr}_2\text{CuO}_2\text{F}_{2+\delta}$, prepared via the fluorination of Sr_2CuO_3 .³⁰ Superconductors are materials, which show zero electrical resistance below a critical temperature, T_c .^{11, 31} The discovery of $\text{Sr}_2\text{CuO}_2\text{F}_{2+\delta}$ started worldwide research on fluorination techniques and ternary/quaternary mixed-anion compounds. Many oxide-fluorides were prepared in subsequent years.

The ionic radius of the fluoride anion is smaller, but comparable to the ionic radius of oxide anions ($r_{\text{O}^{2-}} = 1.26 \text{ \AA}$, $r_{\text{F}^-} = 1.19 \text{ \AA}$) allowing F^- to fit into anion vacancies in oxides and also to substitute for O^{2-} .³² F^- has a greater electronegativity than O^{2-} and this affects the bond strengths, while the difference in charge between O^{2-} and F^- anions may affect metal oxidation states and electronic configuration.³³

There are several possible processes that are known to take place in the fluorination of perovskite-like (RP) oxide materials:

- the insertion of fluorine into interstitial sites,
- the substitution of two fluorine for each oxygen,
- the substitution of one fluorine for one oxygen.³⁴

These fluorination processes are usually performed at low temperatures to favour these relatively minor structural changes. “Metastable” oxide-fluorides are usually formed and tend to decompose at relatively low temperatures ($T < 400 \text{ }^\circ\text{C}$). This section aims to describe the fluorination of anion-deficient K_2NiF_4 -type oxides and the structures of oxide-fluorides closely related to T and T' type structures.

In the fluorination process involving the substitution of two F^- for one O^{2-} and the insertion of interstitial F^- , the structure is required to adjust in such a way as to permit the insertion of additional anions. When one F^- substitutes for one O^{2-} , and in the case of F^- insertion, electronic changes must take place, usually within the outer electronic configuration of the transition metal. In the case of F^-/O^{2-} substitution, the transition metal is reduced, while in the case of F^- insertion oxidation must take place.

Initially the oxide-fluorides derived from fluorination of stoichiometric T - and T' -type oxides will be discussed. La_2CuO_4 shows a distorted K_2NiF_4 -type (T -type) structure. Reactions in F_2 gas at $T < 200 \text{ }^\circ\text{C}$ result in fluoride insertion and the formation of $\text{La}_2\text{CuO}_4\text{F}_\delta$ ($Fmmm$, $a = 5.4328 \text{ \AA}$, $c = 13.187 \text{ \AA}$, with no errors given).^{35, 36} The F^- inserts into the rock salt layers of the RP phase, at $(\sim 1/4, \sim 1/4, \sim 1/4)$ and copper is partially oxidised from $2+$ to $3+$ (Figure 1-5). When this results in an optimum fluoride content superconductivity is induced ($T_c \sim 38.5 \text{ K}$, $\delta \sim 0.17$).³⁵

The K_2NiF_4 -type oxide $LaSrMnO_4$ also shows F^- insertion when heated in 10% F_2/N_2 gas at 200 °C.³⁷ After two hours, an approximate stoichiometry of $LaSrMnO_4F_{1.7}$ is obtained, corresponding with partial filling of interstitial anion positions. Reaction between $LaSrMnO_4F_{1.7}$ and $LaSrMnO_4$ at 300 °C for 12 hours yields $LaSrMnO_4F$ ($P4/nmm$, $a = 3.7749(1)$ Å, $c = 14.1049(3)$ Å). $LaSrMnO_4F$ is the first example of a K_2NiF_4 -type material showing staged F^- insertion i.e. the fluorine is inserted in alternate rock salt layers giving filled and empty interstitial regions (Figure 1-5 (a)).³⁷

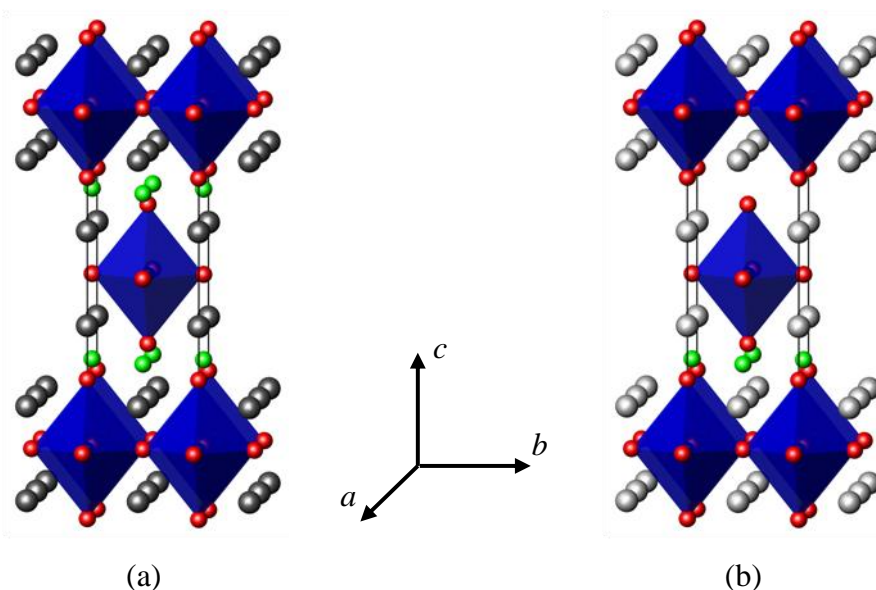


Figure 1-5. Structures of (a) La_2CuO_4F and (b) $LaSrMnO_4F$. The dark and light grey spheres are lanthanum and lanthanum/strontium respectively. The red and green spheres are oxygen and fluorine respectively. The blue octahedra are centred on copper/manganese.

The staged fluorine insertion has subsequently been observed in $Sr_2TiO_3F_2$ ($P4/nmm$, $a = 3.8017(1)$ Å, $c = 15.536(1)$ Å).³⁸ $Sr_2TiO_3F_2$ was prepared by Slater *et al.* from the reaction of Sr_2TiO_4 and NH_4F or CuF_2 at 250 °C for 15 hours.³⁸ In addition to the staged F^- insertion, fluorination of Sr_2TiO_4 also leads to F^-/O^{2-} substitution. The overall fluorination process can be considered a substitution of one O^{2-} for two F^- , where one F^- replaces the O^{2-} at the apical position of the octahedra and the second F^- inserts at the interstitial site in a staged manner. The exact anion distribution across the apical anion positions, which is shared by O^{2-} and F^- , could not be obtained owing to the similar neutron scattering lengths of the anions (5.803×10^{-15} m and 5.654×10^{-15} m for oxygen and fluorine respectively).^{38, 39} It is suggested by Slater *et al.* that the

apical sites may be split with F^- on one site and O^{2-} occupying the opposite apical position in an ordered fashion.³⁸

The ordering of apical anions is observed in other oxide-fluoride materials, e.g. Ba_2InO_3F .⁴⁰ Ba_2InO_3F ($P4/nmm$, $a = 4.1640(2)$, $c = 13.9439(8)$ Å) and Ba_2ScO_3F ($I4/mmm$, $a = 4.1480(2)$ Å, $c = 13.5441(8)$ Å) are not formed from the fluorination of the ternary oxides, however, these compounds are included in this discussion for their relevant structures. Ba_2InO_3F and Ba_2ScO_3F were prepared by Needs *et al.* via heating of $BaCO_3$, BaF_2 , In_2O_3 or Sc_2O_3 at 850 °C for 24 hours and subsequently at 1025-1075 °C for 48 hours.⁴⁰ Ba_2InO_3F may be viewed as a K_2NiF_4 -type structure where the equatorial oxide anions and one apical anion are O^{2-} and F^- in an ordered arrangement (Figure 1-6 (a)). Ba_2ScO_3F shows a similar K_2NiF_4 -type structure, however, the apical ordering is absent and O^{2-} and F^- are distributed in a random fashion over these sites (Figure 1-6 (b)). This difference between Ba_2InO_3F and Ba_2ScO_3F was attributed, by Needs *et al.*, to the different electronegativities of scandium and indium, 1.36 and 1.78 respectively.⁴⁰ The more electropositive scandium favours large coordination environments, more ionic in nature, while indium shows a more covalent behaviour and coordination with five oxide anions in an essentially square based pyramidal arrangement.⁴⁰ The rock salt regions are alternating BaF and BaO layers.

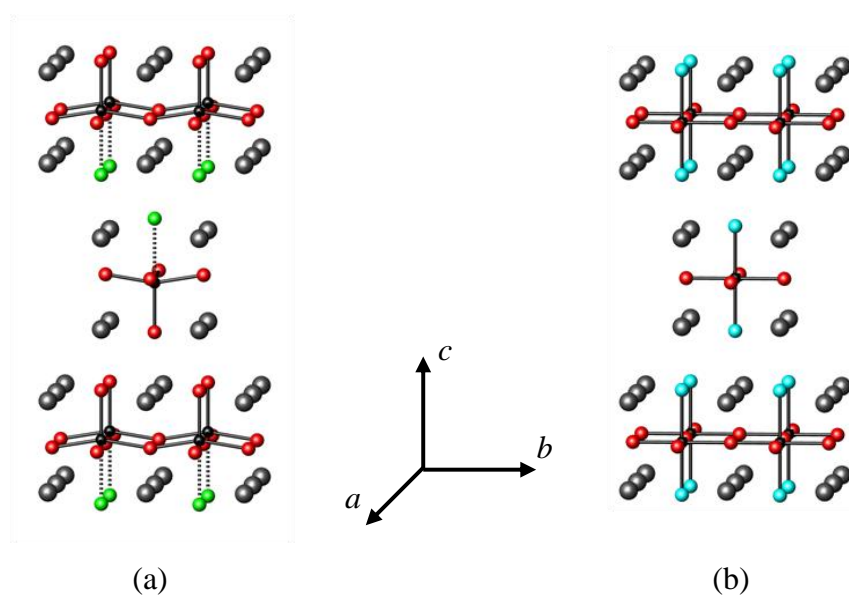


Figure 1-6. Structures of (a) Ba_2InO_3F and (b) Ba_2ScO_3F . The grey spheres are barium, the red and green spheres are oxygen and fluorine respectively. The turquoise spheres are oxygen and fluorine randomly distributed on the same site.

The Nd_2CuO_4 -type oxides (T' -type) behave slightly differently under fluorination conditions. The fluorination of Nd_2CuO_4 with XeF_2 gas, at temperatures below $300\text{ }^\circ\text{C}$, shows F^- insertion giving an oxide-fluoride of formula $\text{Nd}_2\text{CuO}_4\text{F}_x$. The site of the extra F^- was suggested by Hadermann *et al.* to be the ‘apical’ position above the CuO_4 square planar sheets.⁴¹ At higher temperatures, $T > 300\text{ }^\circ\text{C}$, fluorination occurs via an anion exchange process to give $\text{Nd}_2\text{CuO}_{4-x}\text{F}_x$.⁴¹ The substituted O^{2-} is removed from the fluorite layers of Nd_2CuO_4 , leaving the CuO_2 sheets intact.^{42, 43} $\text{Nd}_2\text{CuO}_{4-x}\text{F}_x$ may also be prepared via solid state reaction of CuO , Nd_2O_3 and NdF_3 at $900\text{ }^\circ\text{C}$ for 14 hours. The resulting oxide-fluoride can be optimised to give superconductivity from the partial reduction of copper.⁴⁴

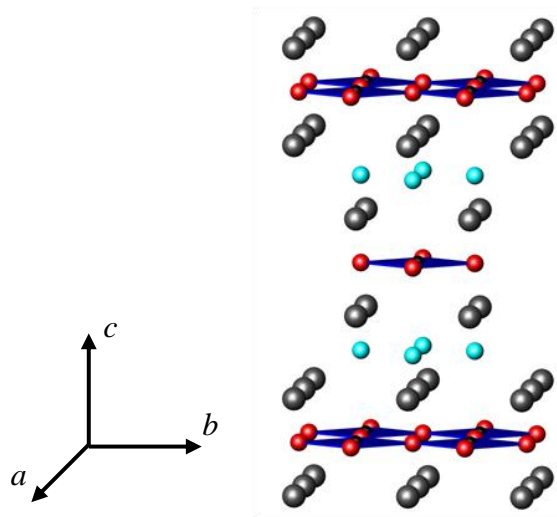


Figure 1-7. Structure of $\text{Nd}_2\text{CuO}_{4-x}\text{F}_x$. The grey and red spheres represent neodymium and oxygen respectively. The turquoise spheres represent oxygen and fluorine randomly distributed on the same site.

A number of interesting oxide-fluorides, including $\text{Sr}_2\text{CuO}_2\text{F}_{2+\delta}$, are prepared from anion-deficient K_2NiF_4 -type materials. Fluorination of Sr_2CuO_3 to give $\text{Sr}_2\text{CuO}_2\text{F}_{2+\delta}$ ($Fmmm$, $a = 5.394(1)\text{ \AA}$, $b = 5.513(1)\text{ \AA}$, $c = 13.468(3)\text{ \AA}$) involves a number of structural modifications. Sr_2CuO_3 consists of one-dimensional chains of CuO_4 square planar units, corner connected along the b -axis. Upon treatment in F_2 gas one O^{2-} anion is substituted by two F^- anions, with additional F^- insertion (δ) (Figure 1-9).³⁰ This extra fluorine results in partial oxidation of the copper cation and for optimum fluorine content superconductivity ($\delta \sim 0.2\text{-}0.3$).³⁰

The structural re-arrangement taking place involves the transformation of the CuO_4 square planes from one-dimensional chains to two-dimensional sheets of corner connected polyhedra with the elimination of one O^{2-} anion.³⁴ The two substituting fluoride anions insert at the apical positions to generate a K_2NiF_4 -type arrangement of CuO_4F_2 octahedra (Figure 1-8). This preference of F^- for the apical position has been confirmed through Madelung calculations, X-ray emission, photoelectron spectroscopy (XPS) and electronic structure calculations.^{30, 45, 46} The excess F^- (δ) partially occupies the interstitial positions within the rock salt layers. Computer simulations by D'Arco *et al.* support this location of the interstitial fluoride site.⁴⁷

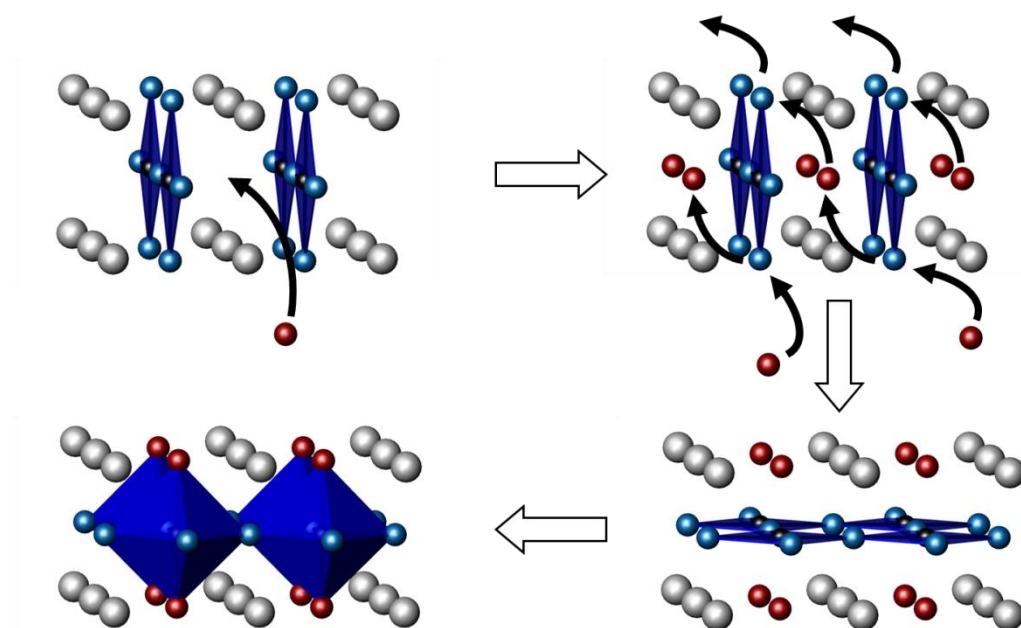


Figure 1-8. The structural re-arrangement occurring during the fluorination of Sr_2CuO_3 to form $\text{Sr}_2\text{CuO}_2\text{F}_{2+\delta}$. The red and blue spheres represent fluorine and oxygen respectively.

Ca_2CuO_3 and Ba_2PdO_3 are isostructural with Sr_2CuO_3 .^{48, 49} Fluorination of these materials, however, differs from Sr_2CuO_3 yielding $\text{Ca}_2\text{CuO}_2\text{F}_{2+\delta}$ ($I4/mmm$, $a = 3.850(1) \text{ \AA}$, $c = 11.842(3) \text{ \AA}$) and $\text{Ba}_2\text{PdO}_2\text{F}_2$ ($I4/mmm$, $a = 4.1398(3) \text{ \AA}$, $c = 14.0459(13) \text{ \AA}$).⁴⁸⁻⁵⁰ Both $\text{Ca}_2\text{CuO}_2\text{F}_{2+\delta}$ and $\text{Ba}_2\text{PdO}_2\text{F}_2$ also show substitution of one O^{2-} anion by two F^- anions, with structural re-arrangement of the MO_4 square planes ($M = \text{Cu, Pd}$) to give corner sharing two-dimensional sheets of MO_4 square planes. However, unlike in the fluorination of Sr_2CuO_3 , the substituting F^- inserts into the interstitial anion position to give the Nd_2CuO_4 -type structure (Figure 1-9 (c)).^{46, 48, 50}

Although the possible addition of F^- at the apical sites is considered in the work by Al-Mamouri *et al.*, these materials are not high temperature superconductors.⁴⁸

The Nd_2CuO_4 -type analogue of the strontium containing copper oxide-fluoride, $Sr_2CuO_2F_2$ can also be prepared. Kissick *et al.* found that reduction of $Sr_2CuO_2F_{2+\delta}$ in 10% H_2 / 90% N_2 between 250 °C and 450 °C yields $Sr_2CuO_2F_2$ ($I4/mmm$, $a = 3.967(1)$ Å, $c = 12.816(2)$ Å).⁵¹ The structure was confirmed through Madelung energy calculations, bond valence sum calculations and XPS.

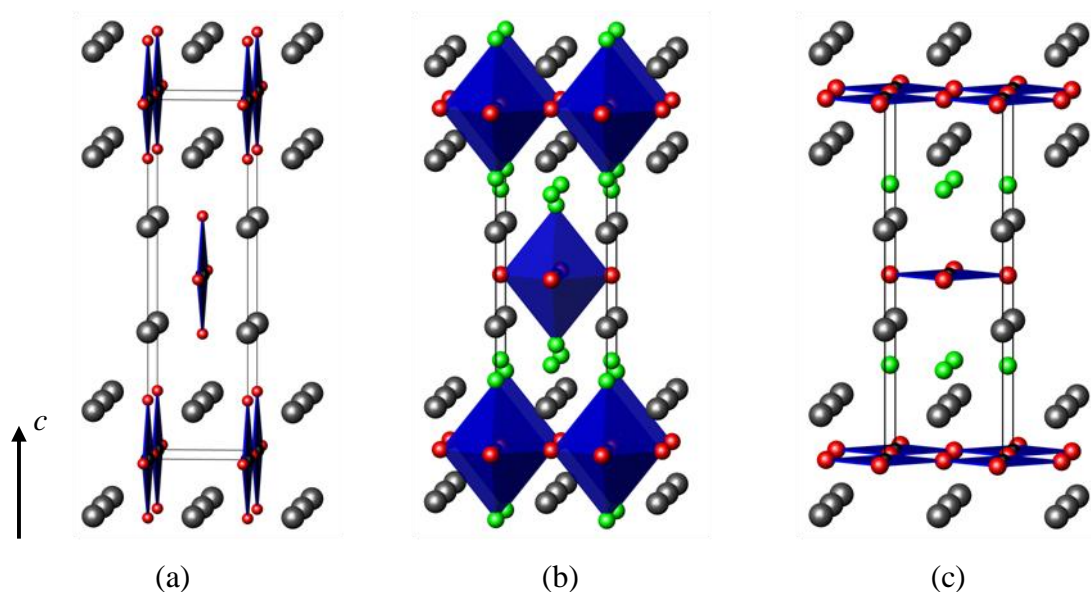


Figure 1-9. Structure of (a) A_2CuO_3 ($A = Sr, Ca$) and Ba_2PdO_3 , (b) $Sr_2CuO_2F_{2+\delta}$ and (c) $Ca_2CuO_2F_2$ and $Ba_2PdO_2F_2$. The grey, black, red and green spheres represent A/Ba, Cu/Pd, oxygen and fluorine respectively.

1.2 Low Dimensional Ternary Chalcogenides

Sulfides have been relatively under explored compared to oxides. This is due, in part, to the greater experimental requirements of sulfide synthesis. While oxides may simply be prepared in air, non-oxides often require a slightly more complex approach such as alternative atmospheres or sealed reaction systems. However, with progress in preparation methods, the investigation of non-oxide materials has gained pace, fuelled by the interesting and often unique physical properties they reveal.

Sulfides, for example, have shown a number of useful properties such as superconductivity,⁵² photovoltaics,⁵³ magnetoresistance,^{54, 55} ferromagnetism and antiferromagnetism and catalytic activity.⁵⁶⁻⁵⁸

The relatively high polarisability of the sulfide ion, relative to the oxide ion, ensures that sulfides are in general less ionic than oxides, and therefore low-dimensional structures occur more frequently in sulfides. In fact these materials can make an important contribution to the study of magnetic interactions in solids due to this low dimensionality. The characterisation of one-dimensional materials is particularly welcome, as these systems are rarer than two-dimensional materials.⁵⁹

In “ionic” solids metals, often transition metals, are coordinated by anions and the coordination polyhedra are connected via either corners, edges or faces. If transition metals with unpaired electrons are present then below a certain critical temperature phenomena of collective magnetism, such as ferromagnetism or antiferromagnetism may take place. In the case of corner connected coordination polyhedra the anions often mediate the magnetic coupling between transition metal cations. One-dimensional magnetic interactions take place between localised unpaired electrons along a chain of cations (section 1.5.1.2). Understanding these interactions along a chain, in the absence of higher order magnetism (two or three-dimensional interaction) is of particular benefit when investigating the influence of factors such as atom type and bonding on magnetic interactions,⁶⁰ or in the development of theoretical models of magnetism, which may then be applied to more complex systems.

These studies are traditionally carried out on oxides, however, the preparation and characterisation of one-dimensional sulfides can make a significant contribution to the understanding of low-dimensional magnetism, in particular where considering the influence of the anion on the magnetic interactions.

One group of compounds, investigated for their quasi-one-dimensional magnetic structures, is the Ba_2MS_3 ($\text{M} = \text{Mn, Fe, Co, Zn, Cd, Hg}$) type compounds.

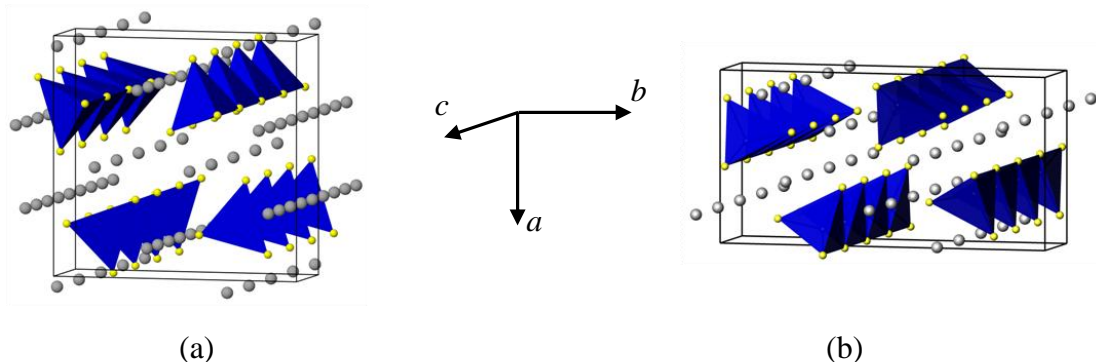


Figure 1-10. Structure of (a) Ba_2MS_3 ($M = \text{Zn, Co, Fe}$) and (b) Ba_2MS_3 ($M = \text{Mn, Hg, Cd}$). The grey and yellow spheres represent the barium and sulfur respectively. The blue polyhedra are transition metal centred.

The sulfides Ba_2MS_3 ($M = \text{Mn, Fe, Co, Zn, Cd, Hg}$) show a number of structural similarities, in that they all contain one-dimensional chains of corner linked ${}^1_{\infty}[\text{MX}_2\text{X}_{2/2}^{4-}]$ interleaved by Ba^{2+} cations (Figure 1-10). In order to facilitate direct comparison between the compounds, Ba_2MS_3 ($M = \text{Mn, Fe, Hg, Cd}$) have been redefined, in this section, in the space group $Pnam$, rather than $Pnma$, in which they were originally classified. The cell parameters are given in Table 1-1.

Compound	a (Å)	b (Å)	c (Å)
Ba_2MnS_3	8.814(5)	17.0480(80)	4.302(2)
Ba_2FeS_3	12.087(5)	12.359(5)	4.246(2)
Ba_2CoS_3	12.000(1)	12.470(1)	4.205(2)
Ba_2ZnS_3	12.054(2)	12.647(2)	4.21(1)
Ba_2CdS_3	8.9145(6)	17.2439(9)	4.3356(2)
Ba_2HgS_3	8.931(4)	17.257(7)	4.357(2)

Table 1-1. Unit cell parameters of Ba_2MS_3 ($M = \text{Mn, Fe, Co, Zn, Cd, Hg}$).^{54, 58, 61-64}

These compounds can be split into two groups of isostructural materials. Ba_2MS_3 ($M = \text{Zn, Co, Fe}$) show the K_2CuCl_3 -type structure, while Ba_2MS_3 ($M = \text{Mn, Hg, Cd}$) show the K_2AgI_3 -type structure. In both cases the corner sharing tetrahedra run along the shortest axis and both structures show two crystallographically independent barium sites with the barium coordinated to seven anions. These barium cations show mono-capped trigonal prismatic coordination with the chalcogens, with the capping anion lying above the centre of one of the rectangular faces of the prism. Shoemaker

reported that the differences between the K_2CuCl_3 and K_2AgI_3 structures lie in the connectivity of the K-(Cl/I) polyhedra (or the Ba-S polyhedra of Ba_2MS_3).⁶⁵ Here the main points outlined by this paper are reiterated, using Ba_2CoS_3 and Ba_2MnS_3 as examples of the K_2CuCl_3 and K_2AgI_3 structures respectively.

In both structure types, the mono-capped trigonal prisms, centred on Ba(1), form chains of triangular face-sharing polyhedra running along the short axis, c . In the description by Shoemaker the Ba(1) coordination was extended to include an eighth anion.⁶⁵ This eighth anion can be taken as capping a second rectangular face of the prism, shown by the dashed lines in Figure 1-11 (a). It is these square based pyramids that separate the MX_4 tetrahedra of the ${}^1_{\infty}[MX_2X_{2/2}^{4-}]$ chains ($M = Mn, Fe, Co, Zn, Cd, Hg$). The square based pyramids formed by the original capping anion, to the right hand side of the trigonal prismatic chains of Figure 1-11 (a), also form tetrahedra of sulfide anions. These tetrahedra are corner connected into one-dimensional chains, but remain unoccupied.

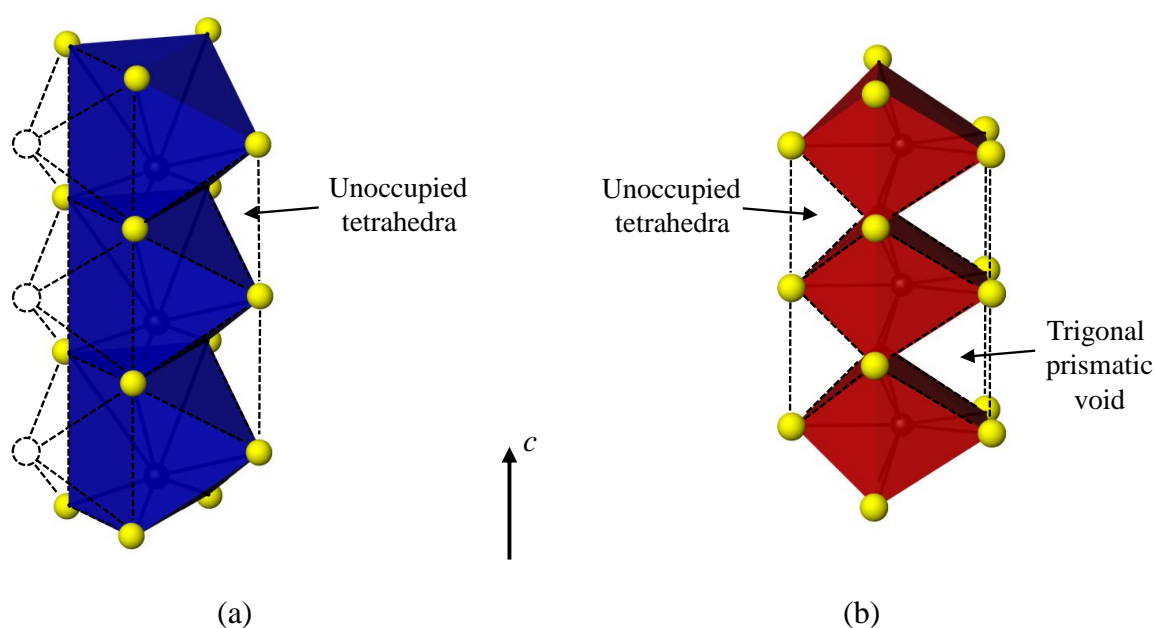


Figure 1-11. Representation of (a) the face sharing chains of Ba(1) centred polyhedra and (b) the edge sharing chains of Ba(2) centred polyhedra.

The Ba(2) polyhedra form chains of edge sharing mono-capped trigonal prisms along c , with the prism axis perpendicular to the c -axis. To the right of these chains of mono-capped trigonal prisms, as represented in Figure 1-11 (b), is a trigonal prismatic

void that also shares a face with the ${}_{\infty}^1[\text{MX}_2\text{X}_{2/2}^{4-}]$ chains. On the opposite side of this polyhedral chain, the capping anions give rise to another, corner-sharing, chain of unoccupied tetrahedra.

The difference between the two structure types is the manner in which these Ba-S chains are arranged with respect to one another. The Ba-S prisms of the Ba_2CoS_3 -type structure share anions from three nearest neighbour chains of transition metal centred tetrahedra. In the Ba_2MnS_3 -type structure these differ, with Ba(1) coordinated to the S^{2-} anions of two neighbouring chains and Ba(2) coordinated to the anions from four adjacent chains.⁶⁵ The differences between the two structures can be seen more clearly when observing projections down the structures down the [001] as shown in Figure 1-12.

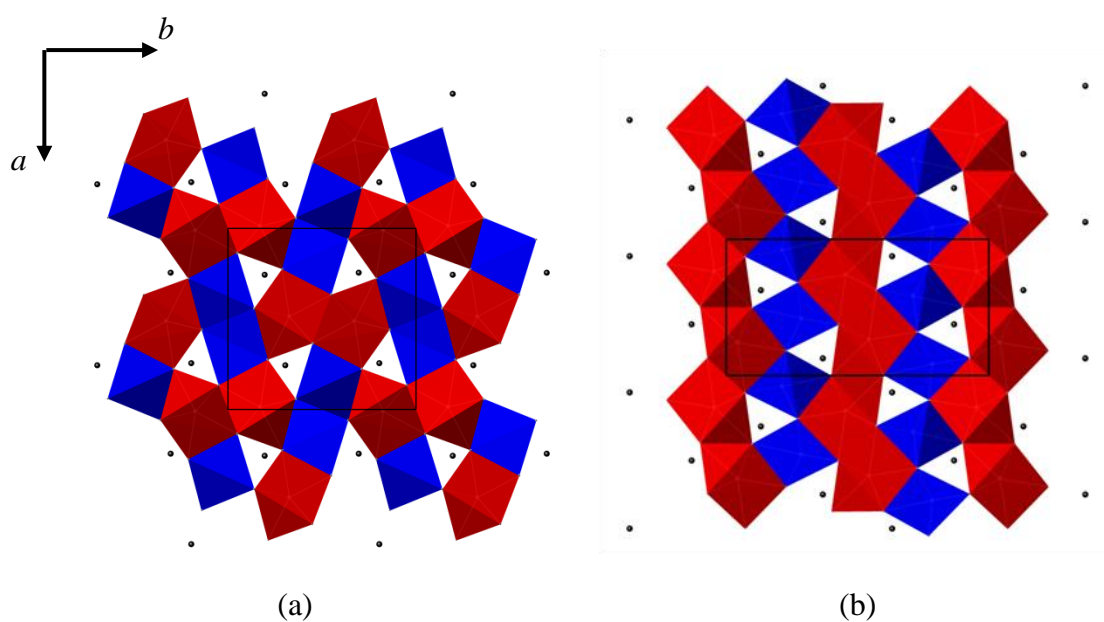


Figure 1-12. Representation of the (a) Ba_2CoS_3 -type and (b) Ba_2MnS_3 -type structures. The two crystallographically independent barium positions are represented at the centre of the mono-capped trigonal prisms in red and blue. The black spheres correspond with the transition metal site. The black lines represent the unit cell edges.

In the Ba_2CoS_3 -type structure the chains of mono-capped Ba-S trigonal prisms are in pairs. Each pair of chains share edges so as to displace one chain by half a prism length along the short cell edge, Figure 1-13. The Ba(1)-S and Ba(2)-S polyhedra also share edges with each other.

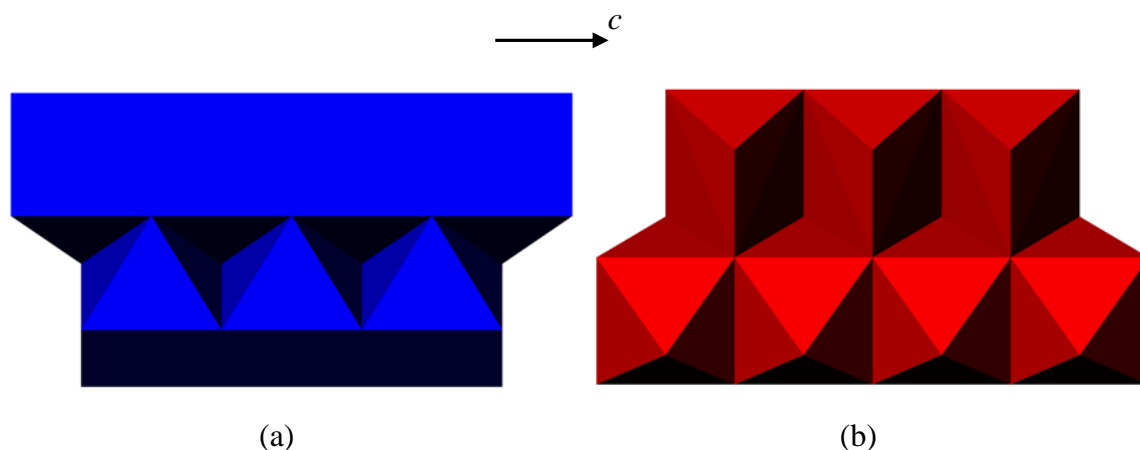


Figure 1-13. Representation of the chains of mono-capped trigonal prisms in the BaCoS_3 -type structure with (a) the face sharing chains of Ba(1) centred polyhedra and (b) the edge sharing chains of Ba(2) centred polyhedra.

In the Ba_2MnS_3 -type structure the Ba(1) centred mono-capped trigonal prisms are connected via a single edge along a to give two-dimensional sheets in the (010) plane. The Ba(2)-S polyhedra also form planes parallel to (010), formed by the sharing of two edges along a and a single edge along c . These Ba(1)-S and Ba(2)-S planes are edge connected as shown in Figure 1-12. The Mn centred chains of tetrahedra fill voids between the two planes.

1.3 Low-Dimensional Nitrides

Non-oxide materials have been, until recently, relatively under-explored. One such family of compounds is the nitrides. Binary nitrides have been investigated for a long time as tough, refractory materials, but it is the ternary and higher order nitride materials which are receiving a great deal of attention.⁶⁶ Ternary nitrides are defined as “ionic” solids containing two different cations, on different crystallographic sites, and nitride anions. Ternary and higher order nitrides show cations in unusual oxidation states and yield structures not seen in oxide chemistry.

A contributing factor to the slow development of nitrides has been the difficulty in the preparation of samples. When reacted in air, a mixture of reagents will, in the majority of cases, give oxides. In order to prepare nitrides from nitrogen gas it is necessary to break the strong triple bond of N_2 , a process that is thermodynamically unfavourable.

In fact, the N₂ triple bond has a bond energy of 941 kJmol⁻¹, which is far stronger than the corresponding double bond of O₂ at 500 kJmol⁻¹.⁶⁶ The necessity to input large amounts of energy into breaking the triple bond increases the energies of formation of nitrides over oxides and results in a low standard free energy of formation. The high temperatures required to form the nitrides tend to favour decomposition due to the entropy gain in forming N₂ gas. The energy of formation of N³⁻ from N, 2300 kJmol⁻¹ is also particularly high when compared to the energies of formation of O²⁻ and S²⁻ which are 700 kJmol⁻¹ and 331 kJmol⁻¹ respectively.⁶⁶ This has the further disadvantage of reducing the effect of ionic bonding on the stability of nitrides. In fact, in ternary nitrides the presence of an electropositive metal adds stability to the system via inductive effects.⁶⁷ A further problem for many of the ternary nitrides is the presence of oxygen or moisture, which leads to decomposition to hydroxides/oxides and ammonia. This is the reason why ternary nitrides often require inert atmospheres and therefore specialised equipment for handling and synthesis. This has not facilitated a speedy and widespread development of the chemistry of nitrides. However, as the search for new materials has led to the development of more complex synthetic techniques, work in nitride materials has gathered pace. Section 1.3.6 describes the common methods employed in the preparation of nitride materials.

The primary focus of this thesis is the description, analysis, preparation and modification of the ternary nitride Ce₂MnN₃, first prepared by Niewa *et al.*⁶⁸ Ce₂MnN₃ can be described as a one-dimensional anion-deficient K₂NiF₄-type nitride. The structure of Ce₂MnN₃ and other one-dimensional nitrides are outlined here.

Ternary nitrides are defined here as compounds containing two different metals and nitrogen. In general, these nitrides contain an electropositive atom that stabilises the system via inductive effects, usually an alkali, alkaline earth or lanthanide metal and a second metal commonly a transition metal (TM). The transition metal tends to form nitridometalate anions, MN_xⁿ⁻, with the metal, M, in a variety of coordination geometries.⁶⁹ The coordination and connectivity of the nitridometalate anions dictates the main structural characteristics of the nitrides and influences the physical properties. In general, the early transition metals, in ternary nitrides, show relatively high oxidation states and high coordination numbers, while the late transition metals show lower oxidation states, and lower coordination.⁶⁹ Compounds that show arrangement of the

nitridometalate anions, or similar structural units, into chains or sheets can be classified as low dimensional materials showing one- or two-dimensionality respectively.

Below, several known nitride systems are described. These have been subdivided into groups showing similar, one-dimensional, structural features. Although every effort has been made not to exclude any structurally significant compounds some may have been unintentionally omitted.

1.3.1 Nitrides Containing Infinite Chains of Octahedra

In general, the ternary nitrides, in which the transition metal shows high coordination numbers (5 or 6) with nitrogen, tend to form rock salt, perovskite or layered structures and are commonly considered to contain TM-N polyhedra.⁶⁹ However, many subnitrides, containing a high metal to nitrogen ratio, are commonly described in terms of the nitrogen coordination. This description is also used often for mixed-anion compounds (section 1.4). Many subnitrides are ternary, *s*-block, nitrides. NaBa₃N (*P6₃/mmc*, *a* = 8.4414(6) Å, *c* = 6.9817(8) Å) and Na₅Ba₃N (*Pnma*, *a* = 11.897(3) Å, *b* = 7.056(2) Å, *c* = 17.801(3) Å) are subnitrides showing nitrogen centred octahedra of barium cations forming Ba₃N chains.⁷⁰⁻⁷² NaBa₃N consists of elongated nitrogen centred barium octahedra (trigonal anti-prisms), face connected in one-dimensional chains, running along [001]. These chains are hexagonally stacked and separated by sodium atoms at the centre of triangular channels formed by the chains (Figure 1-14). As a result the sodium atoms are coordinated to twelve barium atoms from the three nearest chains.

Na₅Ba₃N is very similar to NaBa₃N and shows face-sharing Ba₃N octahedra in chains running along the *b*-axis and arranged in slightly distorted hexagonal stacking. The additional sodium increases the chain separation from 8.44 Å in NaBa₃N to 10.70 Å in Na₅Ba₃N.⁷¹

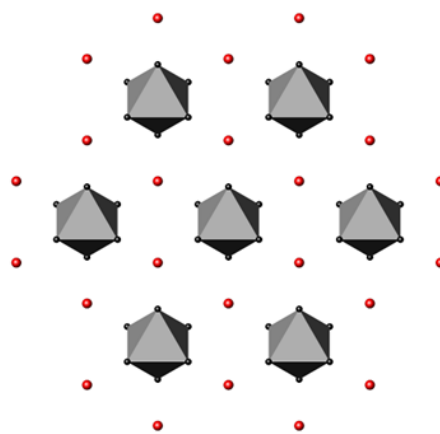


Figure 1-14. Structure of NaBa_3N viewed along $[001]$. The red and black spheres represent sodium and barium respectively and the grey polyhedra are Ba_6N octahedra.

1.3.2 Nitrides Containing Infinite Chains of Tetrahedra

Tetrahedral coordination of metals in nitrides is particularly common. Compounds with a range of structural features, from isolated tetrahedra to complex three-dimensional networks are known to occur.⁶⁹ The following structures show chains of metal centred nitrogen tetrahedra, showing either edge or corner connectivity.

Nitrides containing first row transition metal and lithium can be classified in two structural groups, depending on whether they show the anti-fluorite type structure or the Li_3N type structure.⁷³ In general, the transition metal elements adopting higher oxidation states have a preference for the anti-fluorite-type structure, while the elements of lower oxidation state tend towards a Li_3N related structure. The ratio between the cation sizes also plays a role, with anti-fluorite related structures prevalent when the ratio is $r_{\text{Li}^+}/r_{\text{M}^{n+}} \geq 1$.⁷⁴ In the Li-Fe-N system, solid solutions of compositions $\text{Li}_{1-x}\text{Fe}_x[\text{Li}_2\text{N}]$ ($0 \leq x \leq 1$), $\text{Li}_{1-3x}\text{Fe}_x[\text{Li}_2\text{N}]$ ($0 \leq x \leq 1/3$), $\text{Fe}_{1.04}[\text{Li}_2\text{N}]_2$ and $\text{Fe}[\text{Li}_2\text{N}]_2$ show three-dimensional arrays based on Li_3N .⁷³

Li_3FeN_2 , however, belongs to the anti-fluorite-like superstructural group of compounds with $r_{\text{Li}^+}/r_{\text{Fe}^{3+}} \approx 1.2$.^{29, 75} The Li_3FeN_2 (*Ibam*, $a = 4.872(1) \text{ \AA}$, $b = 9.641(3) \text{ \AA}$, $c = 4.792(1) \text{ \AA}$) structure consists of a distorted cubic close packed array of nitrogen anions with the tetrahedral holes occupied by lithium and iron in a 3:1 ratio

respectively.⁷³ The FeN_4 tetrahedra are ordered in such a way as to result in chains of edge-sharing ${}^1_{\infty}[\text{FeN}_{4/2}^{3-}]$ tetrahedra connected along [001]. These tetrahedral chains are in a similar arrangement to those found in SiS_2 .⁷⁶ In SiS_2 , edge-sharing ${}^1_{\infty}[\text{SiS}_{4/2}]$ units are hexagonally packed and held together by van der Waals interactions.^{76, 77} The chains in Li_3FeN_2 are also arranged with hexagonal rod packing, but are separated by lithium centred tetrahedra (Figure 1-15).

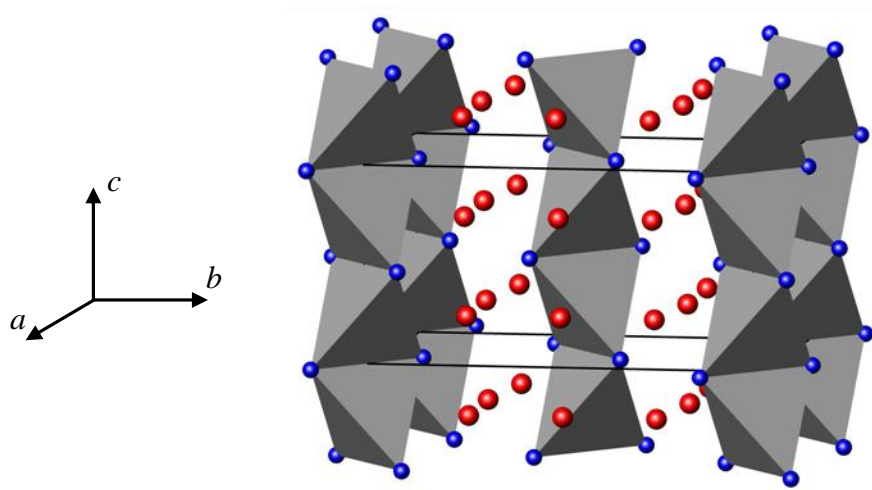


Figure 1-15. Structure of Li_3FeN_2 . The red and blue spheres represent lithium and nitrogen respectively. The chains of grey tetrahedra represent the ${}^1_{\infty}[\text{FeN}_{4/2}^{3-}]$ chains.

The nitrogen anions are eight coordinate, surrounded by six lithium and two iron cations to give a distorted cube.

$\text{A}_3\text{M}_2\text{N}_4$ ($\text{A} = \text{Sr}, \text{Ba}$; $\text{M} = \text{Al}, \text{Ga}$), (space group $Pnna$) also show SiS_2 -like chains of tetrahedra.⁷⁸⁻⁸¹ In $\text{A}_3\text{M}_2\text{N}_4$ the nitrogen atoms are in a distorted cubic close packed arrangement, with a quarter of the tetrahedral holes occupied by $\text{Ga}^{3+}/\text{Al}^{3+}$, generating the ${}^1_{\infty}[\text{GaN}_{4/2}^{3-}]/{}^1_{\infty}[\text{AlN}_{4/2}^{3-}]$ chains in a similar way to Li_3FeN_2 . Due in part to the larger size of Ba^{2+} and Sr^{2+} over Li^+ , barium and strontium cations rest in three quarters of the octahedral holes, rather than the smaller tetrahedral holes. The result is that the chains have a slight undulation of four tetrahedra, which run along [010] (Figure 1-16).

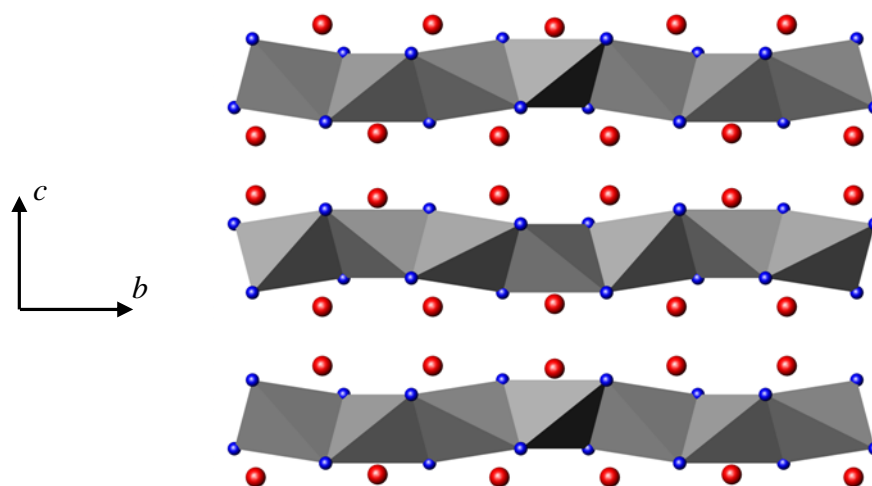


Figure 1-16. Structure of $\text{Ba}_3\text{Ga}_2\text{N}_4$. The red and blue spheres represent barium and nitrogen respectively. The grey tetrahedra represent the ${}^1_{\infty}[\text{GaN}_{4/2}^{3-}]$ chains.

Table 1-2 gives the unit cell parameters for $\text{A}_3\text{M}_2\text{N}_4$ ($\text{A} = \text{Sr}, \text{Ba}$; $\text{M} = \text{Al}, \text{Ga}$). As expected, the incorporation of a larger alkaline earth cation into the structure results in increased unit cell dimensions.

Compound	a (Å)	b (Å)	c (Å)
$\text{Sr}_3\text{Al}_2\text{N}_4$	5.901(3)	10.005(5)	9.580(4)
$\text{Sr}_2\text{Ga}_2\text{N}_4$	5.9552(6)	10.2753(8)	9.5595(9)
$\text{Ba}_2\text{Al}_2\text{N}_4$	6.179(2)	10.052(4)	10.230(4)
$\text{Ba}_2\text{Ga}_2\text{N}_4$	6.2010(12)	10.511(2)	10.070(2)

Table 1-2. Unit cell parameters for $\text{A}_3\text{M}_2\text{N}_4$ ($\text{A} = \text{Sr}, \text{Ba}$; $\text{M} = \text{Al}, \text{Ga}$).

Another lithium compound showing an anti-fluorite like structure, with an $r_{\text{Li}^+}/r_{\text{Ta}^{5+}} \approx 1.2$ is $\text{Li}_4[\text{Ta}_2\text{N}_3]$ (*Ibca*, $a = 4.9185(5)$ Å, $b = 9.7359(6)$ Å, $c = 14.150(1)$ Å).^{29, 75, 82} The nitrogen anions form a distorted cubic close packed array, with lithium and tantalum occupying the tetrahedral holes in an ordered way. The Ta_2N_3 tetrahedra are linked via the corners into ${}^1_{\infty}[\text{Ta}_2\text{N}_{2/2}^{4-}]$ chains running along [100]. These chains have a repeating unit of two tetrahedra, giving a zigzag like pattern along the chain. The site at the centre of the tetrahedron, formed by the nitrogen atoms from three adjacent Ta_2N_3 -units, remains vacant. The lithium occupies the remaining tetrahedral holes, surrounding the chains within an array of edge and vertex-sharing

LiN₄ tetrahedra. The result is a 1 × 2 × 3 supercell with the Li₂O structure and the composition Li₄□[TaN₃] (□ represents the cation vacancy). The Li-Ta-N system is not limited to the Li₄[TaN₃] composition and structure, there is in fact a range of structures available, many of which do not show one-dimensional structures. Li₇[TaN₄], for example, shows isolated [TaN₄]⁷⁻ tetrahedra within a cubic close packed array of nitrogen atoms and Li_{2-x}Ta_{2+x}N₄ (~0.2 < x < ~1) has a disordered rock salt structure.^{82, 83}

The following sodium nitrides contain one-dimensional chains of tetrahedra, connected via shared vertices. Na₃WN₃ shows the *Cc* space group with *a* = 13.810(8) Å, *b* = 10.983(1) Å, *c* = 6.395(1), β = 117.48(3)° and Na₃MoN₃ also shows the *Cc* space group with *a* = 13.854(5) Å, *b* = 10.889(2) Å, *c* = 6.366(2) Å, β = 117.23(3)°.^{84, 85} The MN₄ tetrahedra are corner connected to give distorted ¹_∞[MN₂N_{2/2}³⁻] chains. These chains run between the *a*- and *c*-axes in a sinusoidal manner, with a repeat unit of four tetrahedra (Figure 1-17).

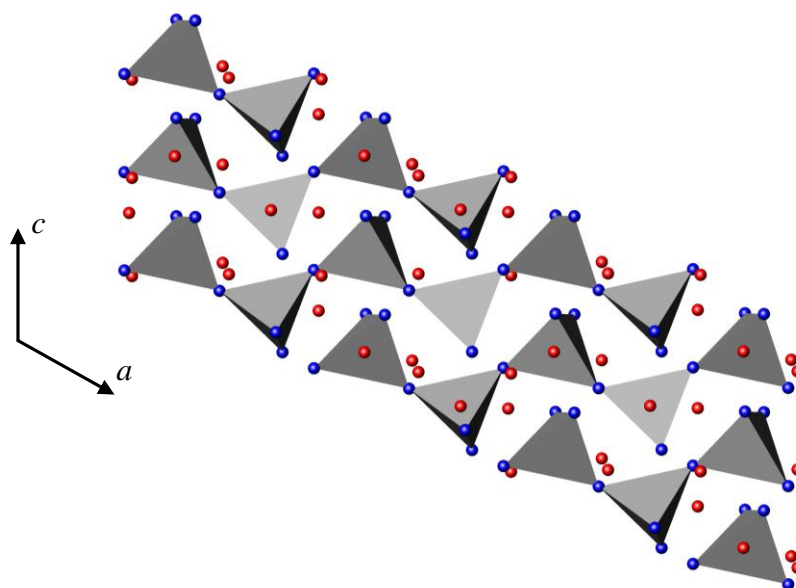


Figure 1-17. Structure of Na₃MN₃ M = W, Mo. The red and blue spheres represent sodium and nitrogen respectively. The chains of grey tetrahedra represent the ¹_∞[MN₂N_{2/2}³⁻] chains.

The chains show hexagonal rod packing, with sodium sitting within the void between the chains.⁸⁵

The introduction of a larger electropositive metal onto the sodium site has the effect of altering the orientation of the WN_4 tetrahedra and, thus, the overall appearance of the chains. The other known alkali metal nitridotungstate(VI) compounds, showing infinite chains are $\text{Na}_2\text{K}[\text{WN}_3]$, $\text{Na}_5\text{Rb}[(\text{WN}_3)_2]$, $\text{Na}_{11}\text{Rb}[(\text{WN}_3)_4]$ and $\text{Na}_5\text{Cs}[(\text{WN}_3)_2]$.^{86, 87} The arrangement of tetrahedra in the chains of $\text{Na}_2\text{K}[\text{WN}_3]$ (*Pbcm*, $a = 6.3948(9)$ Å, $b = 11.924(3)$ Å, $c = 12.292(3)$ Å) and $\text{Na}_{11}\text{Rb}[(\text{WN}_3)_4]$ (*Pbca*, $a = 11.701(3)$ Å, $b = 12.140(3)$ Å, $c = 12.502(2)$ Å) are quite similar, both being examples of unbranched *vierer* single chain compounds, i.e. chains with a repeat unit of four tetrahedra. The chains in each compound connect along the *c*- and *a*-axes respectively.

As stated above, a contributing factor to the structural variation is the larger size of the alkali metal cations. In $\text{Na}_2\text{K}[\text{WN}_3]$ there are two crystallographically independent potassium positions. The first potassium is coordinated to four nitrogen atoms in a distorted tetrahedral manner, in a similar way to $\text{Na}_3[\text{WN}_3]$, in which the sodium predominantly shows tetrahedral coordination. The second potassium rests in a larger hole, surrounded by twelve nitrogen atoms. It is this larger hole, which is partially occupied by rubidium in the $\text{Na}_{11}\text{Rb}[(\text{WN}_3)_4]$ structure. The site is shared between rubidium and sodium in an ordered way, which is the cause of the increased unit cell volume when compared to $\text{Na}_3[\text{WN}_3]$. The WN_4 tetrahedra are then twisted round towards the sodium positions and away from the larger potassium and rubidium positions to give the winding chains shown in Figure 1-18.^{86, 87} These broader chains show tetragonal rod packing.

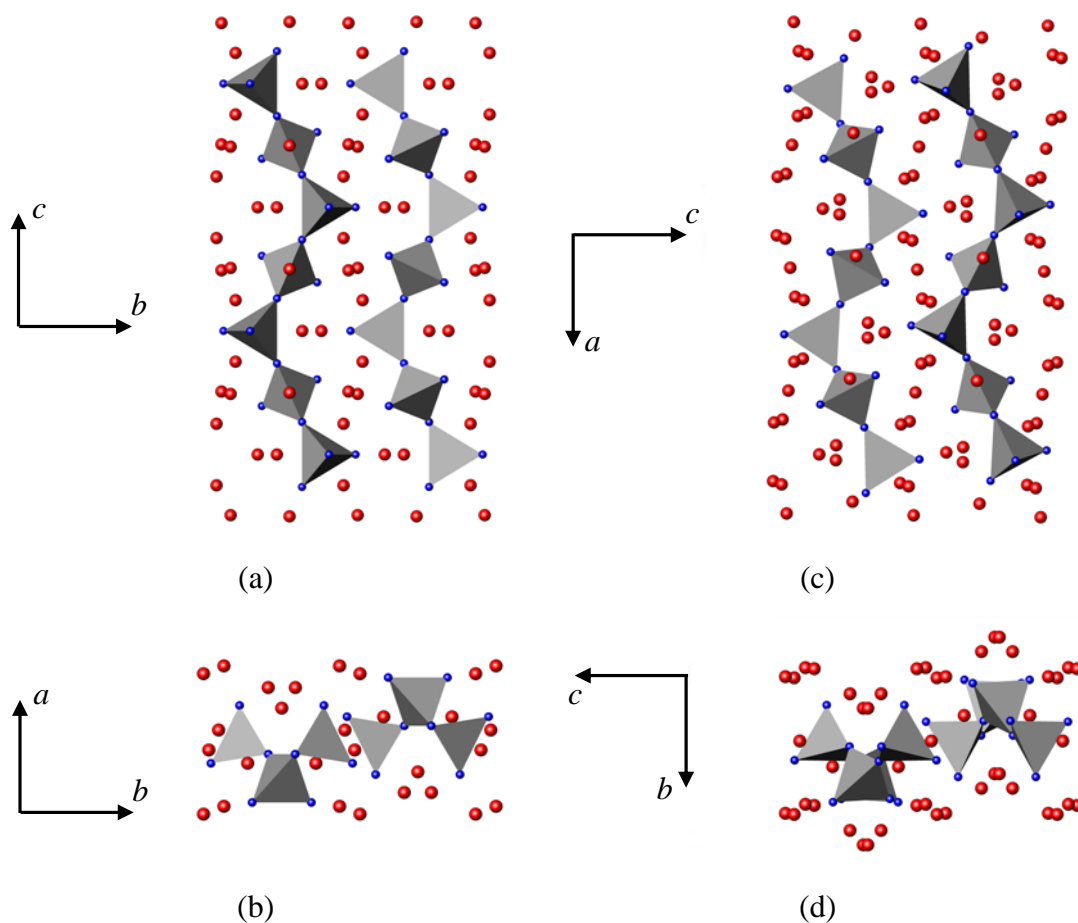


Figure 1-18. Structure of (a, b) $\text{Na}_2\text{K}[\text{WN}_3]$ and (c, d) $\text{Na}_{11}\text{Rb}[(\text{WN}_3)_4]$. The red and blue spheres represent sodium/rubidium and nitrogen respectively. The chains of grey tetrahedra represent the ${}^1_{\infty}[\text{MN}_2\text{N}_{2/2}^{3-}]$ chains.

Increasing the rubidium content further gives $\text{Na}_5\text{Rb}[(\text{WN}_3)_2]$ ($P2_1/c$, $a = 9.355(2) \text{ \AA}$, $b = 10.277(3) \text{ \AA}$, $c = 19.165(3) \text{ \AA}$, $\beta = 90.12(2)^\circ$).⁸⁶ $\text{Na}_5\text{Rb}[(\text{WN}_3)_2]$ is isostructural to $\text{Na}_5\text{Cs}[(\text{WN}_3)_2]$ ($P2_1/c$, $a = 9.403(3) \text{ \AA}$, $b = 10.236(2) \text{ \AA}$, $c = 19.501(4) \text{ \AA}$, $\beta = 90.01(2)^\circ$) and both show *vierer* chains of ${}^1_{\infty}[\text{WN}_2\text{N}_{2/2}^{3-}]$ running along $[100]$.⁸⁶ In these examples the chains oscillate in the (010) plane with far less “twisting” when compared to Na_2WN_3 (Figure 1-19).

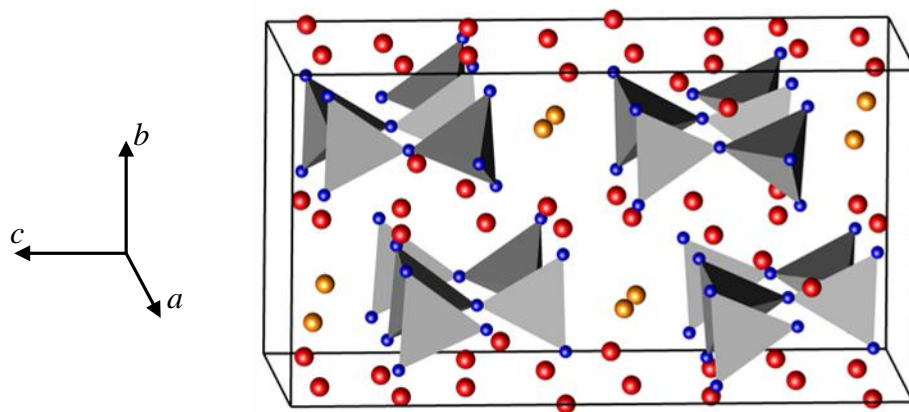


Figure 1-19. Structure of $\text{Na}_5\text{Rb}[(\text{WN}_3)_2]$. The red, orange and blue spheres represent sodium, rubidium and nitrogen respectively. The grey polyhedra represent the ${}^1_{\infty}[\text{WN}_2\text{N}_{2/2}^{3-}]$ chains.

The larger alkali metal (Rb or Cs) rests in distorted prismatic coordination, bound to nitrogen, forming layers parallel to the (010) plane. In compensating for the cation size the chains are diverted around these sites. The sodium rests within the loops of the chains and also to the sides, separating them along [010]. Hence, the sodium remains either in approximately tetrahedral or 4+1 coordination.

The family of A_2MN_3 nitrides (A = Sr, Ba; M = V, Nb, Ta) all show chains of edge-sharing MN_4 tetrahedra. The unit cell parameters are given in Table 1-3. A_2MN_3 (A = Sr, Ba; M = Nb, Ta), Sr_2VN_3 and Ca_2VN_3 are isostructural with Ba_2ZnO_3 .^{88, 89} These are examples of *zweier* single chain compounds i.e. containing a repeat unit of two tetrahedra. These chains run parallel to [100]. The Ba^{2+} , Sr^{2+} and Ca^{2+} cations lie on two crystallographically independent sites, both seven coordinate, A(1) is in distorted pentagonal bipyramidal coordination and A(2) shows monocapped trigonal prismatic coordination.⁹⁰

Compound	Space Group	<i>a</i> (Å)	<i>b</i> (Å)	<i>c</i> (Å)	β (°)	Mean A-X distance (Å)	Mean M-X distance (Å)
Ca_2VN_3	<i>C2/c</i>	5.59538(5)	10.41027(1)	11.62243(1)	92.342(1)	2.65	1.82
Sr_2VN_3	<i>C2/c</i>	5.71036(9)	10.9521(2)	12.2881(2)	90.986(1)	2.80	1.81
Sr_2NbN_3	<i>C2/c</i>	5.9864(2)	11.2271(3)	12.5465(4)	92.587(2)	2.88	1.96
Sr_2Ta_3	<i>C2/c</i>	5.9832(2)	11.2832(2)	12.5814(2)	92.26(1)	2.88	1.91
Ba_2VN_3	<i>Cmca</i>	5.8614(4)	11.4682(7)	12.9121(9)	90	2.90	1.84
Ba_2NbN_3	<i>C2/c</i>	6.132(3)	11.768(3)	13.229(4)	91.65(2)	3.00	1.94
Ba_2Ta_3	<i>C2/c</i>	6.130(3)	11.815(4)	13.263(5)	91.2(1)	3.01	1.96

Table 1-3. Selected structural properties of A_2MN_3 (A = Sr, Ba; M = V, Nb, Ta) and Ca_2VN_3 .⁸⁸⁻⁹⁰

Increasing the size of the A cation results in straighter chains and therefore a reduction in the monoclinic distortion, in a similar way to the Na-Rb-Cs-W-N systems mentioned previously.

1.3.3 Nitrides Containing Infinite Chains of Square Planar Units

Ternary nitrides containing transition metal centres in low oxidation states show some unusual coordination. A_2MN_3 (A = Th, U, Ce; M = Cr, Mn) are believed to contain M^+ cations, which form one-dimensional chains of planar MN_4 .^{68, 91-94} Ce_2MnN_3 , as one of the compounds relevant to this thesis, is discussed further in section 4.1 and a brief summary of the determination of the cation oxidation states, achieved by Niewa and co-workers is given.^{68, 93, 94}

A_2MN_3 (A = Th, U, Ce; M = Cr, Mn) are isostructural with Sr_2CuO_3 showing an orthorhombic anion deficient *T*-type structure (section 1.1.2). In 1970, Benz *et al.* reported the crystal structure of A_2MN_3 (A = Th, U; M = Cr, Mn), with space group *Immm* (unit cell parameters are given in Table 1-4), as consisting of corner linked chains of MN_4 , which are in approximately square planar geometry.⁹¹ These ${}^1_{\infty}[MN_2N_{2/2}^{8-}]$ chains are linked along the *a*-axis and show hexagonal rod packing. The square planar units are all orientated to lie parallel to the (010) plane and each MN_4 unit sits within a cuboid of eight A^{4+} cations (Figure 1-20).

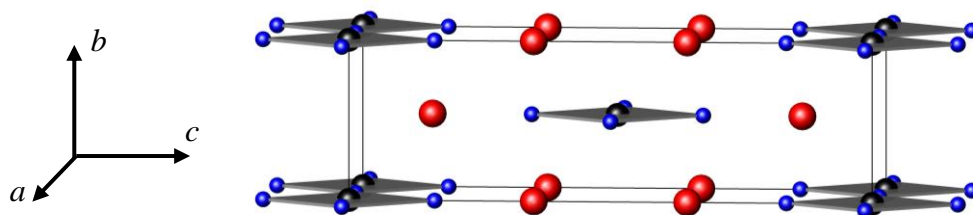


Figure 1-20. Structure of A_2MN_3 (A = Th, U, Ce; M = Cr, Mn). The red, black and blue spheres represent A, M and nitrogen respectively.

The nitrogen atoms show two crystallographically independent positions and a near octahedral coordination. N(1) bridges two transition metal centres and is surrounded by

four A atoms, while N(2) is the terminal nitrogen position and therefore is bound to a single transition metal and five A atoms. Each A is located roughly at the centre of a monocapped trigonal prism of nitrogen anions.

Compound	a (Å)	b (Å)	c (Å)
Th ₂ CrN ₃	3.8654(5)	3.5154(2)	12.8446(19)
U ₂ CrN ₃	3.7397(3)	3.3082(3)	12.3335(7)
Ce ₂ CrN ₃	3.7900(10)	3.4040(10)	12.5170(2)
Th ₂ MnN ₃	3.7919(3)	3.5482(2)	12.8321(4)
U ₂ MnN ₃	3.7216(6)	3.3274(2)	12.2137(8)
Ce ₂ MnN ₃	3.74994(6)	3.44450(6)	12.4601(2)

Table 1-4. Unit cell parameters for A₂MN₃ (A = Th, U, Ce; M = Cr, Mn).^{68, 91-94}

1.3.4 Nitrides Containing Infinite Chains of Triangular Units

LiCaN (*Pnma*, $a = 8.471(3)$ Å, $b = 3.676(2)$ Å, $c = 5.537(3)$ Å) is another example of a lithium compound adopting the anti-fluorite type structure.^{74, 95} In this case calcium occupies half the tetrahedral holes and lithium occupies the other half. The lithium is shifted from the centre of the tetrahedral hole towards a face. These distortions are ordered in such a way as to give planes of edge-sharing LiN₃ triangular units, as shown in Figure 1-21.

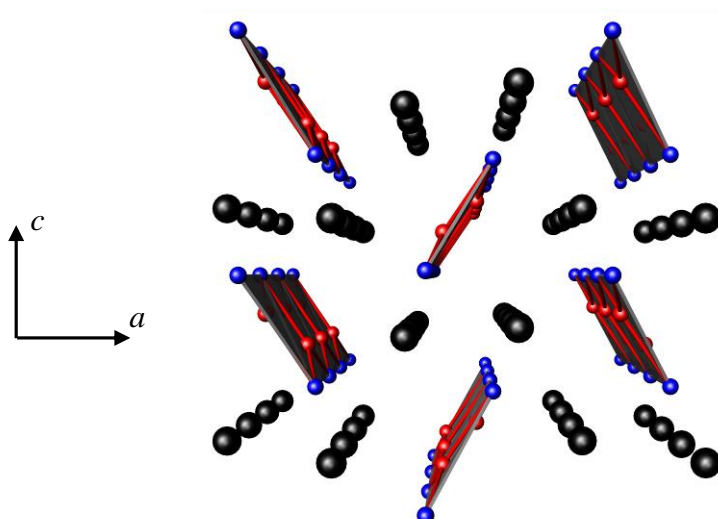


Figure 1-21. Representation of LiCaN, viewed along [010]. The red, blue and black spheres indicate lithium, nitrogen and calcium respectively.

$\text{Sr}_2\text{Li}[\text{Fe}_2\text{N}_3]$ ($C2/c$, $a = 6.559(1) \text{ \AA}$, $b = 11.414(2) \text{ \AA}$, $c = 6.593(1) \text{ \AA}$) and $\text{Ba}_2\text{Li}[\text{Fe}_2\text{N}_3]$ ($C2/c$, $a = 6.875(2) \text{ \AA}$, $b = 11.781(4) \text{ \AA}$, $c = 6.809(2) \text{ \AA}$) contain ${}^1_2[\text{FeN}_{3/2}]_2^{5-}$ chains as shown in Figure 1-22.⁹⁶ Each iron is in distorted trigonal-planar coordination to nitrogen forming FeN_3 units, which are linked via two shared nitrogen anions and form ${}^1_2[\text{FeN}_{3/2}]_2^{5-}$ units linked via the remaining nitrogen. The chains are separated along [101] by lithium atoms. These layers are surrounded by the strontium/barium atoms in distorted trigonal-bipyramidal coordination to nitrogen.

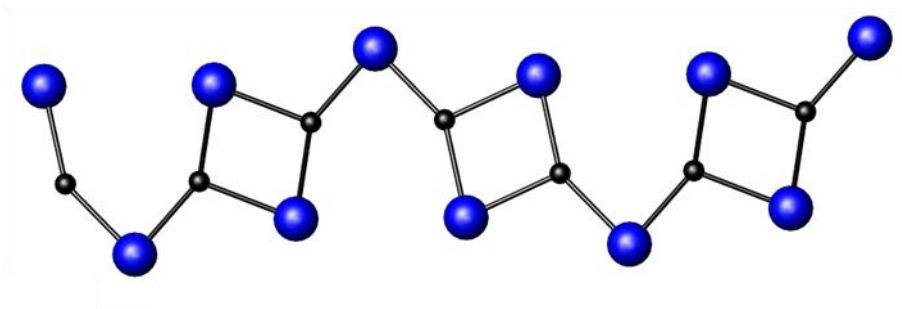


Figure 1-22. Structure of the ${}^1_2[\text{FeN}_{3/2}]_2^{5-}$ chains of $\text{Sr}_2\text{Li}[\text{Fe}_2\text{N}_3]$. The blue and black spheres are nitrogen and iron respectively.

1.3.5 Nitrides Containing Infinite Linear Chains

A coordination of two for a transition metal, is a less common coordination in ternary nitrides. Linear coordination occurs for several of the late transition metals in low oxidation states, +1 and +2.⁹⁷ Those nitrides with transition metals in +1 oxidation state tend to form infinite linear metal nitride chains. These chains can take straight, zigzagged or helical orientations.

Cationic substitution of the lithium in LiCaN yields $\text{Ca}[(\text{Ni}_{1-x}\text{Li}_x)\text{N}]$ ($0 \leq x \leq 0.58$). This solid solution has a different structure from the parent compound, with ${}^1_2[\text{Ni}_{1-x}\text{Li}_{1-x}\text{N}_{2/2}]$ linear chains, and the YCoC -type structure.⁹⁸

CaNiN ($P4_2/mmc$, $a = 3.5809(2) \text{ \AA}$, $c = 7.0096(3) \text{ \AA}$) was discovered in 1990 by DiSalvo *et al.* and found to contain ${}^1_2[\text{NiN}_{2/2}]$ linear chains.⁹⁹ These chains are arranged into planes of parallel chains, which are stacked along the c -axis. The chains alternate

between running along [100] and [010] moving along [001] (Figure 1-23). The calcium sits in tetrahedral coordination with four nitrogen atoms.

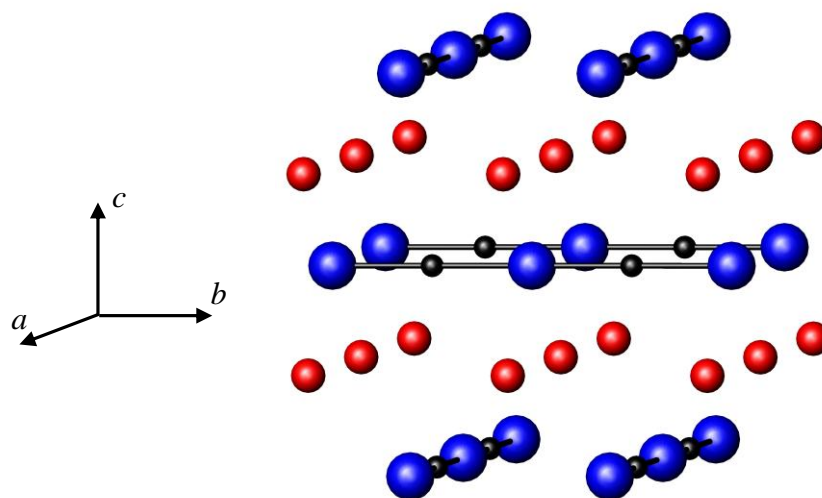


Figure 1-23. Structure of CaNiN. The red, black and blue spheres represent calcium, nickel and nitrogen respectively.

Partial substitution of Sr^{2+} for Ca^{2+} gives the $\text{Ca}_{1-x}\text{Sr}_x\text{NiN}_3$ solid solution, up to $x \approx 0.5$. The unit cell dimensions of CaNiN increase due to the insertion of the larger Sr^{2+} , but the overall structure remains the same.^{100, 101} The increase in unit cell dimensions is more significant in the c -axis as it is easier for the structure to accommodate the larger cations by increasing the perpendicular interchain separation along c , while the criss-crossing of the chains along a and b restricts expansion due to the limiting Ni-N bond distances.

The nitride LiSrN ($I4_2/mmc$, $a = 3.924(3) \text{ \AA}$, $c = 7.085(4) \text{ \AA}$), unlike LiCaN, adopts the CaNiN structure.¹⁰² Substitution of the lithium cation with nickel gives $\text{SrLi}_x\text{Ni}_{1-x}\text{N}$ ($0 \leq x \leq 0.52$) and induces a structural transformation to the SrNiN structure ($Pnma$, $a = 9.0859(4) \text{ \AA}$, $b = 13.230(93) \text{ \AA}$, $c = 5.2473(3) \text{ \AA}$), which contains zigzagging ${}^1_{\infty}[\text{NiN}_{2/2}]$ chains.^{95, 101} The chains run along [010] and alternate directions, by 78° , on every third nitrogen down the chain producing the zigzag. The chains are slightly distorted and tilted with respect to the a -axis by $\pm 62^\circ$. The chains are stacked along [100] with alternating orientation of the chains to produce a herringbone pattern (Figure 1-24).

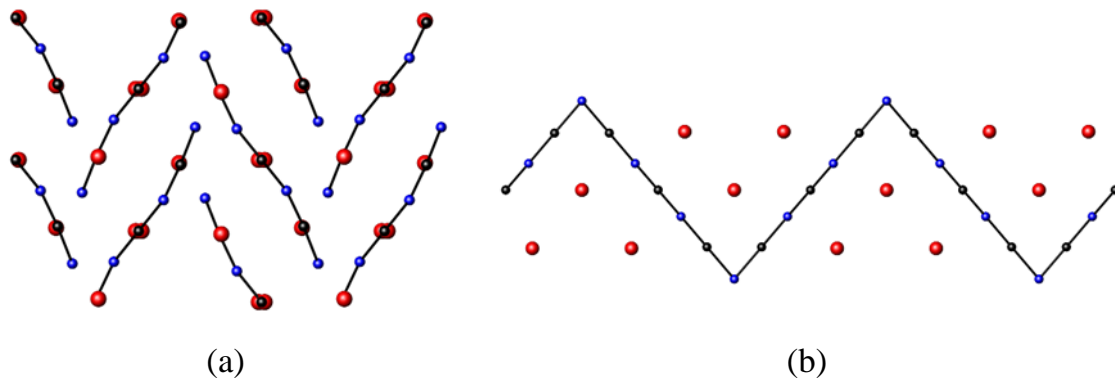


Figure 1-24. Structure of SrNiN showing (a) the herringbone stacking, viewed along [010] and (b) the zigzagging chains, viewed along [100]. The red, blue and black spheres represent strontium, nitrogen and nickel atoms respectively.

The two strontium positions are four coordinate, bound to nitrogen anions in distorted tetrahedral coordination. Yamamoto *et al.* proposed that the strontium centred tetrahedra play an important role in determining the overall structure of the system in $\text{Ca}_{1-x}\text{Sr}_x\text{NiN}$.¹⁰⁰ As the strontium content increases from $x = 0$ to $x = 0.5$ the c -axis expands more than the other two axes. The result is a greater increase in two of the Sr-N distances, those along c , compared to the Sr-N distances within a or b , and hence a greater deviation from the ideal tetrahedral symmetry. At $x = 1$, SrNiN, the structure adopted has a more favourable tetrahedral environment for strontium.¹⁰⁰

Increasing the size of the alkaline earth metal further, i.e. considering the Ba-Ni-N system, also results in a SrNiN-like structure.¹⁰³ BaNiN ($Pnma$, $a = 9.639(3) \text{ \AA}$, $b = 13.674(2) \text{ \AA}$, $c = 5.432(1) \text{ \AA}$) shows less distorted ${}^1_0[\text{NiN}_{2/2}]$ chains, with the same repeating zigzag unit altering direction every third nitrogen.

Replacing the transition metal in these linear structures also has an interesting effect on the arrangement of the chain. SrCuN and $\text{Sr}(\text{Li}_{1-x}\text{Cu}_x)\text{N}$, $0.33 \leq x \leq 0.53$, are isostructural with SrNiN,^{95, 104} however, barium containing compounds show variation in the structure of the chains.

BaCoN ($Pnma$, $a = 9.599(2) \text{ \AA}$, $b = 23.510(3) \text{ \AA}$, $c = 5.476(2) \text{ \AA}$) and BaCuN ($C2_1/c$, $a = 14.462(2) \text{ \AA}$, $b = 5.5700(8) \text{ \AA}$, $c = 9.478(1) \text{ \AA}$, $\beta = 102.960(2)^\circ$) still show a

herringbone stacking of transition metal nitride, ${}^1_{\infty}[\text{NiN}_{2/2}]$ chains, but these chains differ from SrNiN showing a more complex alternating pattern, shown in Figure 1-25.^{97, 105}

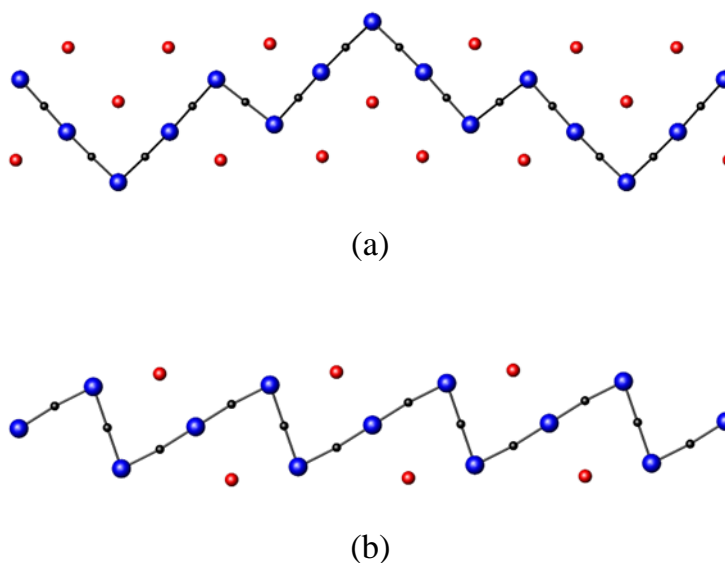


Figure 1-25. Representations of the chains in (a) BaCoN and (b) BaCuN. The red, black and blue spheres represent barium, cobalt/copper and nitrogen respectively.

Reducing the transition metal content gives rise to $\text{Ba}_8[(\text{NiN})_6]\text{N}$ ($C2_1/c$, $a = 9.487(4)$ Å, $b = 16.578(6)$ Å, $c = 12.137(7)$ Å, $\beta = 107.05(5)^\circ$) and $\text{Ba}_{16}[(\text{CuN})_8][\text{Cu}_2\text{N}_3][\text{Cu}_3\text{N}_4]$ ($P2_1/c$, $a = 9.5611(4)$ Å, $b = 7.2731(2)$ Å, $c = 13.5225(5)$ Å, $\beta = 93.115(2)^\circ$).^{97, 106}

$\text{Ba}_8[(\text{NiN})_6]\text{N}$ contains ${}^1_{\infty}[\text{NiN}_{2/2}]$ chains that form distorted, zigzagging helical arrangements. These chains intertwine to give an array of interconnected crosses when viewed along [001], as shown in Figure 1-26 (a). The barium cation sits in the voids between the chains in both trigonal planar and distorted tetrahedral coordination with nitrogen. The trigonal planar units are corner connected into layers of six-cornered star arrangements. The tetrahedra show both edge and corner connectivity, forming chains along the c -axis.

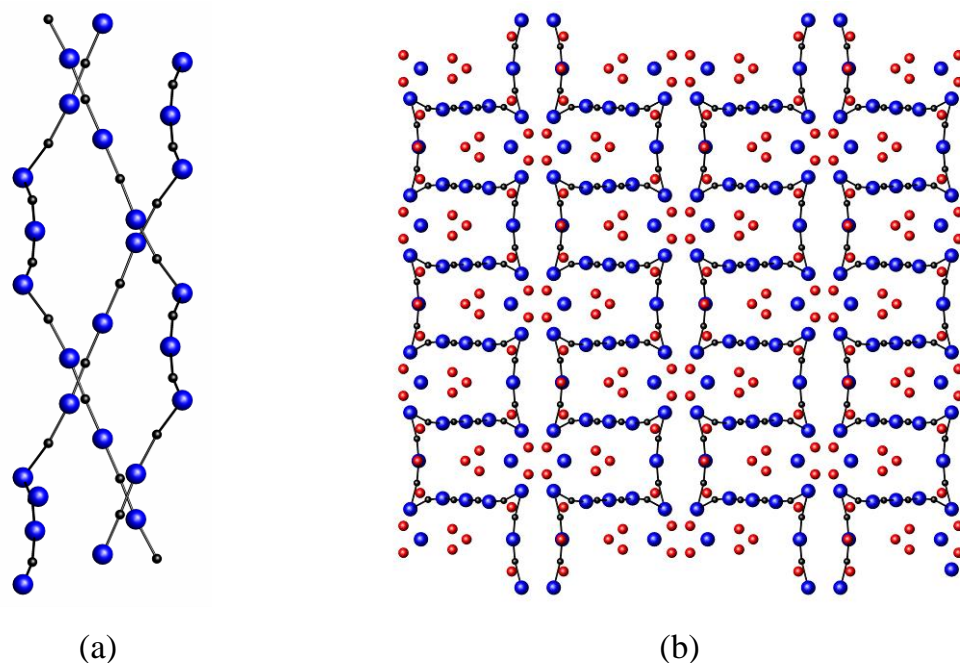


Figure 1-26. Representation of $\text{Ba}_8[(\text{NiN})_6]\text{N}$. (a) shows the intertwining ${}^1_{\infty}[\text{NiN}_{2/2}^{2-}]$ chains (for clarity barium has been omitted) and (b) shows $\text{Ba}_8[(\text{NiN})_6]\text{N}$, viewed along $[001]$. The red, blue and black spheres represent barium, nitrogen and nickel respectively.

$\text{Ba}_{16}[(\text{CuN})_8][\text{Cu}_2\text{N}_3][\text{Cu}_3\text{N}_4]$ contains isolated $[\text{Cu}_2\text{N}_3]^{7-}$ and $[\text{Cu}_3\text{N}_4]^{9-}$ units and ${}^1_{\infty}[\text{CuN}_{2/2}^{2-}]$ chains, which form helical patterns. The ${}^1_{\infty}[\text{CuN}_{2/2}^{2-}]$ chains are bent at every nitrogen, giving the distinct shape shown in Figure 1-27. These chains traverse along $[010]$ and are approximately stacked into layers along $[001]$. The direction of rotation of these helices alternates along these chains.

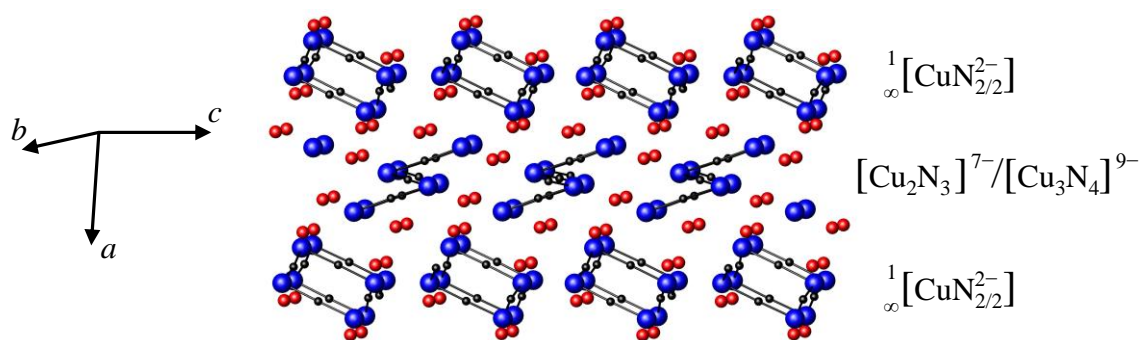


Figure 1-27. Representation of $\text{Ba}_{16}[(\text{CuN})_8][\text{Cu}_2\text{N}_3][\text{Cu}_3\text{N}_4]$. The red, blue and black spheres represent barium, nitrogen and copper respectively.

The layers are then separated by the isolated $[\text{Cu}_2\text{N}_3]^{7-}$ and $[\text{Cu}_3\text{N}_4]^{9-}$ units, which are distributed over the same site in a random manner. Both $[\text{Cu}_2\text{N}_3]^{7-}$ and $[\text{Cu}_3\text{N}_4]^{9-}$ are near linear units. $[\text{Cu}_2\text{N}_3]^{7-}$ is a near linear chain of five atoms, while $[\text{Cu}_3\text{N}_4]^{9-}$ forms a zigzag chain, which bends at every nitrogen atom. The barium atoms interpenetrate these Cu_xN_y units and separate them.

1.3.6 Synthesis of Nitrides

Despite experimental challenges, there has been a great deal of progress in the synthetic approaches to nitrides in the last century. In the last few decades there have been a number of excellent reviews on nitrides and their synthesis.^{66, 95, 107-113} Several of the more common preparative techniques are summarised here.

In spite of the difficulties in breaking the $\text{N} \equiv \text{N}$ bond, it is still possible to synthesise a number of nitrides using nitrogen gas, at elevated temperatures, through traditional solid-state ceramic approaches. Ternary nitrides can be prepared by either the reaction of two metal powders under a nitrogen atmosphere or via reaction of metal nitrides with metals/metal nitrides.¹⁰⁹ Such approaches are simple but limited by the low number of metals which readily form binary and higher nitrides in nitrogen.

Lithium is the only alkali metal to readily form a nitride, Li_3N , from the reaction of lithium metal with nitrogen gas at 400 °C.¹¹⁰ Li_3N can act as both the nitrogen source and reaction medium. Li_3N fluxes have been a common synthetic approach to lithium containing metal nitrides.¹¹⁴ The low melting point of Li_3N (840-850 °C in N_2) facilitates intimate mixing of the reagents and favours crystal growth and consequently a vast number of ternary nitrides contain lithium.^{109, 115} Juza *et al.* initially investigated lithium metal nitrides in 1940.¹¹⁴

Sodium does not react readily with nitrogen to give a nitride but has found use as a solvent in nitride preparation.¹⁰⁸ Metals are dissolved/dispersed in molten sodium and nitrogen gas is absorbed into the mixture. By dissolving the metals an increased surface area is generated, favouring a higher and more homogeneous diffusion of nitrogen into the solid. The non-reactivity of sodium towards nitrogen and its low boiling point are

exploited as the unreacted sodium can be removed by vacuum distillation or by washing with liquid ammonia to yield the metal nitride.

The preparation of alkaline earth containing nitrides can be achieved from direct reactions of the metals with nitrogen gas or in sodium fluxes and this family of materials makes up the second largest group of ternary nitrides.^{109, 116}

A number of metals tend to favour sub-nitride formation, with only partial absorption of nitrogen, resulting in non stoichiometric products or materials with low overall nitrogen content.^{66, 108} For example the alkaline-earth metals, strontium, barium, tend to produce the subnitrides Sr_2N and Ba_2N when reacted with N_2 , while many of the transition metals form interstitial compounds, with metallic-like arrays and nitrogen residing at available interstitial sites, e.g. Cr_2N .^{108, 117-120}

The subnitrides and interstitial compounds exhibit interesting bonding, structural and metallic properties. However, they present disadvantages when used as reagents to prepare ternary or more complex nitrides, via solid-state reaction, due to their low nitrogen stoichiometry. The low nitrogen content necessitates additional nitrogen sources to produce more complex nitrides. Various more reactive sources of nitrogen have been employed to prepare a range of nitrides in recent years.

One alternative to nitrogen is the solid nitrogen source sodium azide, NaN_3 . Upon decomposition NaN_3 , releases N_2 , which can be used in the reaction. The drawback is the presence, in the product, of sodium. NaN_3 may also be coupled with sodium fluxes, optimising the mixing of the reagents to produce crystalline nitrides with only additional sodium as a by-product.¹⁰⁸

The most common alternative to nitrogen, however, is ammonia, which has been known to react with metals for some time.¹²¹ Refinement of ammonolysis techniques has shown that ammonia has several advantages over nitrogen gas. Firstly, ammoniation reactions take place at a lower temperature than reactions in nitrogen. Secondly, the process can be performed on a wider range of starting materials, such as oxides, carbides, halides and sulfides.¹⁰⁸

Mixed transition metal nitrides, like $\text{Fe}_3\text{Mo}_3\text{N}$, FeWN_2 , $\text{Ni}_2\text{Mo}_3\text{N}$ and Ti_3AlN , may also be prepared via ammonolysis of metallorganic/complex precursors.^{111, 122, 123} Organic compounds, such as urea and melamine, can be used as an ammonia/nitrogen source.^{124, 125} Heating pellets of ternary metal oxide and urea, for example, has resulted in $\text{M}_3\text{Mo}_3\text{N}$ ($\text{M} = \text{Fe}, \text{Co}$).¹²⁴ Unfortunately, these methods can give samples of poor crystallinity or favour the presence of unwanted secondary compounds.¹⁰⁸

Reduction-nitridation of oxides under dilute hydrogen in nitrogen has also been successful for the preparation of mixed transition metal nitrides. Starting materials are ternary or binary oxides, as for the synthesis of $\text{Ni}_{2-x}\text{M}'_x\text{Mo}_3\text{N}$ ($\text{M}' = \text{Co}, 0 \leq x \leq 1$; $\text{M}' = \text{Pd}, 0 \leq x \leq 1.5$), $\text{Fe}_{2-x}\text{M}_x\text{Mo}_3\text{N}$ ($\text{M} = \text{Ni}, \text{Pd}, \text{Pt}$) and $\text{Fe}_{3-x}\text{Co}_x\text{Mo}_3\text{N}$.¹²⁶⁻¹²⁹ This procedure represents a relatively quick synthesis of high purity phases from simple oxide precursors.

Lately more complex methods have been explored in order to improve the reactivity of nitrogen. These include plasma synthesis and high-pressure techniques. Plasma nitridation has been used to extend the use of dilute hydrogen in nitrogen to less reactive oxides. In this approach metal oxides are reacted under a stream of microwave induced H_2/N_2 plasma.¹³⁰

Through the use of high temperature and pressure synthetic approaches, compounds unreactive under normal conditions, are reacted to give novel compounds. In addition the application of pressure to known samples can induce structural transformation to yield new structural features. Equipment for high pressure synthesis range from simple autoclaves to more complex diamond anvil cells, which can apply up to 500 GPa of pressure.¹³¹ This method is, however, limited by the availability of suitable equipment.

1.4 Binary, Ternary and Quaternary Nitride-Halides

It has been shown, in section 1.1.3, that compounds containing another anion, together with oxygen, have acquired a certain importance, displaying useful properties such as superconductivity. Conversely, research on non-oxide mixed-anion compounds (nitride-halides, chalcogenides-halides, pnictide-chalcogenides etc.) has always been

less pursued in solid state chemistry and only a limited number of compounds are known.

This section concentrates on binary, ternary and quaternary nitride-halide compounds and provides a description of a number of compounds known to date. Pnictide-halides are growing in importance, as they have also been found to show attractive properties such as superconductivity. The first part of this section focuses on binary and ternary nitride-halides, which are here defined as compounds containing a single type of cation and two or more anions, occupying the same crystallographic sites (binary) or different sites (ternary). Groups to which the cations belong are used to categorise the ternary nitride-halides. Only compounds containing transition metals are included as well as a selection of lanthanide containing materials. Transition metals are defined in the IUPAC Nomenclature of Inorganic Chemistry as elements whose atom has an incomplete *d* sub-shell, or which can give rise to cations with an incomplete *d* sub-shell i.e. group 3 to 11.¹³² Within each group, the nitride-halides will be subdivided on the basis of the dimensionality of their structure (one-, two- and three-dimensional).

The second part of this section is dedicated to a small number of quaternary nitride-halides known to date, which are defined here as compounds containing two cations occupying two distinct crystallographic sites and two or more anions occupying distinct crystallographic sites. Synthetic methodologies are reported for all the compounds described, in order to show not only the challenges but also the “experimental imagination” sometimes needed to prepare nitride-halides and, in general, non-oxide compounds.

1.4.1 Binary and Ternary Nitride-Halides

Structural characterisation of pnictide-halides has proven difficult, with recent papers questioning initial structural assignments. One of the challenges is the difficulty in determining pnictide/halide ordering through powder X-ray diffraction, due to the similar X-ray scattering factors of anions with similar electronic configurations. In addition, minor modifications to the preparation method, such as altering the cooling rates, can give slightly different structural conformations.

Nitride-halides, which have shown promising properties, include β -ZrNCl and β -HfNCl, which show superconductivity, following electron doping via intercalation of alkali metals, with T_c values, for example, of 13 K and 25.5 K, for $\text{Li}_{0.16}\text{ZrNCl}$ and $\text{Li}_{0.48}(\text{THF})_y\text{HfNCl}$ respectively.¹³³

Generally, the only pnictide present in the large majority of the compounds is nitrogen. This could be linked to the fact that in recent years nitride materials have grown in importance and more synthetic routes have become available. The elements in groups from 3 to 5 form pnictide-halides that can be related to known structures, even well known oxide structures like TiO_2 anatase, whereas pnictide-halides formed by elements in groups from 6 to 11 show unique structures.

1.4.1.1 Nitride-Halides of Elements in Group 3

There are several examples of nitride-halide compounds of group 3 elements and it is worth noting that they tend to favour metal cluster formation, centred on the pnictide.

1.4.1.1.1 Compounds Showing Three-Dimensional Structural Features

$\text{Sc}_7\text{Cl}_{12}\text{N}$ ($R\bar{3}$, $a = 12.990(2)$ Å, $b = 12.990(2)$ Å, $c = 8.835(1)$ Å $\gamma = 120^\circ$), prepared from the metal trichloride and nitrogen at 850-950 °C, consists of both discrete clusters of scandium and isolated metal (III) ions.¹³⁴ The clusters are based around N-centred scandium octahedra. The octahedra are then encapsulated within an array of chloride ions, to give the cluster shown in Figure 1-28 (b). Each cluster is connected to six other cluster units via the chlorine atoms.

The remaining scandium is located between the cluster units, forming linear arrays along [001], as shown in Figure 1-28 (a).

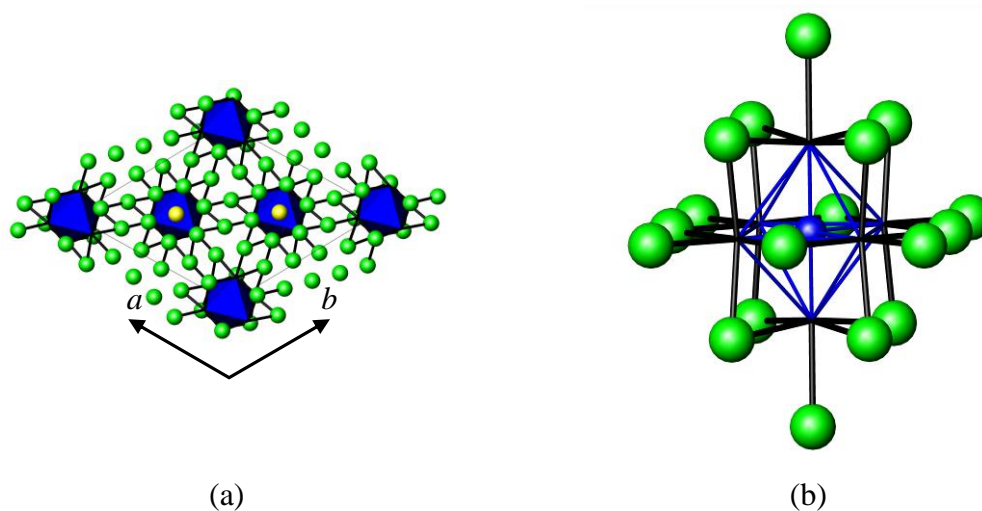


Figure 1-28. (a) The structure of $\text{Sc}_7\text{Cl}_{12}\text{N}$ and (b) a nitrogen centred scandium cluster unit of $\text{Sc}_7\text{Cl}_{12}\text{N}$. The green and yellow spheres represent chlorine and scandium respectively. The blue polyhedra are nitrogen centred scandium octahedra, with scandium located on each vertex.

1.4.1.1.2 Compounds Showing Two-Dimensional Structural Features

$\text{Sc}_2\text{Cl}_2\text{N}$ was shown by Hwu *et al.* to have a layered structure ($P\bar{3}m1$ $a = 3.517(7)$ Å, $c = 8.813(2)$ Å) with several structural similarities with the binary monochloride ScCl (or reported as ScClH_x , with the limits of x extending from 0.3 to 1, even though the determination was complicated by possible sample decomposition). Hwu *et al.* synthesised $\text{Sc}_2\text{Cl}_2\text{N}$ by heating a mixture of ScCl_3 , Sc and NaN_3 , at 735-860 °C in a sealed vessel, for five weeks.¹³⁵

The structure of ScCl is shown in Figure 1-29 (a) and consists of four cubic-close packed layers of closely bound ions in Cl-Sc-Sc-Cl slabs, which are stacked |AbcA|CabC|BcaB|, where the capital letters represent the anions and the lower case letters the cations.¹³⁶ This stacking results in antiprismatic coordination of scandium and prismatic coordination of chlorine. More recent work by Meyer *et al.* has suggested that the monochloride may in fact be stabilised by hydride anions positioned between the scandium bilayer in the tetrahedral holes.¹³⁷ The resulting scandium monochloride hydride shows the same Cl-Sc-Sc-Cl layer arrangement, but the slab stacking is dependent on hydrogen content. Below $x = \sim 0.7$, in ScClH_x , the primary component

stacks with an ACB stacking sequence. Above $x = \sim 0.7$ the phase alters to stack with an ABC sequence as seen in ZrCl and shown in Figure 1-29 (b).¹³⁷

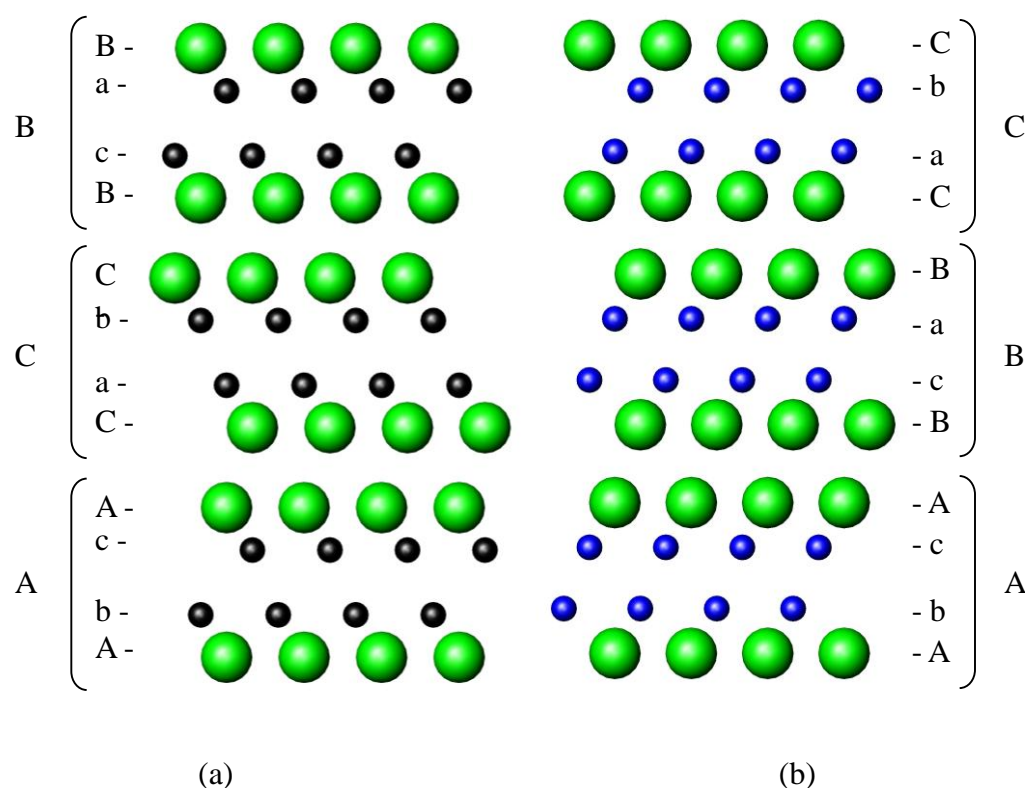


Figure 1-29. Projection in the (100) plane, showing a comparison between the stacking sequences of (a) ScCl and (b) ZrCl. The black, blue and green spheres represent scandium, zirconium and chlorine respectively. The lower case letters show the packing of the layers along [001] and the capital letters show the packing of the four-layered slabs.

Another polymorph, $\text{Sc}_2\text{Cl}_2\text{N}$ also shows a layered structure (Figure 1-30), with planes of close packed atoms. The nitrogens are inserted between the Sc-Sc layers, in a similar way to hydrogen in ScClH_x , however, the N^{3-} anions have a preference for the larger trigonal-antiprismatic holes. There is also a deviation from the AbcA packing within the Cl-Sc-Sc-Cl slabs of ScClH_x to AbaB. The weak van der Waals interaction between the slabs means the layered structure often contains stacking defects. An overall stacking order of the slabs was, therefore, not given.¹³⁵

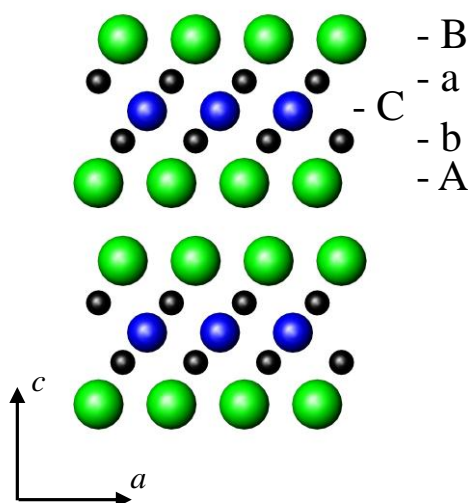


Figure 1-30. The structure of $\text{Sc}_2\text{Cl}_2\text{N}$ projected in the (010) plane, the black, blue and green spheres represent scandium, nitrogen and chlorine respectively.¹³⁵

1.4.1.1.3 Compounds Showing One-Dimensional Structural Features

As in the case of the binary monochloride, ScCl , it has been suggested by Hwu *et al.* that pentascandium octachloride, Sc_5Cl_8 , is in fact stabilised by the inclusion of other anions as $\text{Sc}_5\text{Cl}_8\text{Z}$ ($\text{Z} = \text{C}, \text{N}$).^{138, 139} Single crystals of $\text{Sc}_5\text{Cl}_8\text{N}$ can be prepared via the reaction of ScCl and NaN_3 , in the presence of excess scandium, at 900-950 °C over four weeks.¹³⁹

The $\text{Sc}_5\text{Cl}_8\text{N}$ structure ($C2/m$, $a = 17.85(1) \text{ \AA}$, $b = 3.5505(7) \text{ \AA}$, $c = 12.090(8) \text{ \AA}$, $\beta = 130.13(4)^\circ$), shown in Figure 1-31, consists of one-dimensional chains of edge-sharing octahedra separated by chloride ions.¹³⁹

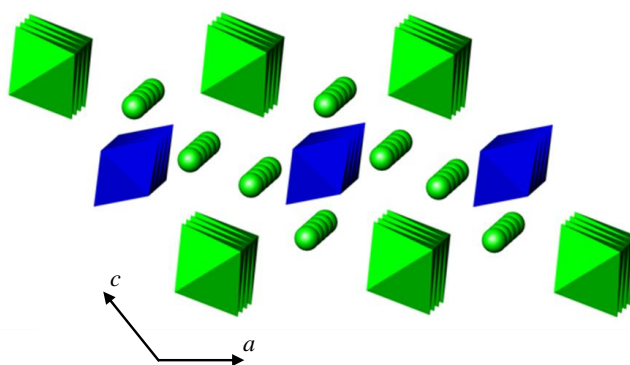


Figure 1-31. The structure of $\text{Sc}_5\text{Cl}_8\text{N}$, the green and blue octahedra are ScCl_6 and NSc_6 respectively and the green spheres represent chlorine.

There are two types of octahedra present, the first is made up of ScCl_6 , bridged through the equatorial chlorine along the b -axis, and the second are clusters of metal atoms. The clusters of scandium form distorted octahedra, which sit within a rectangular prism of chloride ions. These scandium octahedra are also edge linked along the b -axis, but have a displacement of $b/2$ from the ScCl_6 units. In addition, the scandium octahedra are tilted by approximately 78° , in the (010) plane, with respect to the ScCl_6 octahedra. The nitrogen was found to sit in the void at the centre of the scandium clusters.¹³⁹

$\text{Sc}_4\text{Cl}_6\text{N}$ (*Pbam*, $a = 11.625(4) \text{ \AA}$, $b = 12.118(3) \text{ \AA}$, $c = 3.5447(7) \text{ \AA}$) is an example of a nitrogen centred $\text{Sc}_6\text{Cl}_{12}$ cluster compound, with several structural features related to NaMo_4O_6 .^{134, 140} Prepared through the reaction of scandium and scandium chloride, in nitrogen at $850\text{-}950 \text{ }^\circ\text{C}$, $\text{Sc}_4\text{Cl}_6\text{N}$ is made-up of scandium octahedra, which connect through opposite edges to form linear chains parallel to the c -axis, as shown in Figure 1-32. The centre of the scandium octahedra is occupied by a nitride anion.

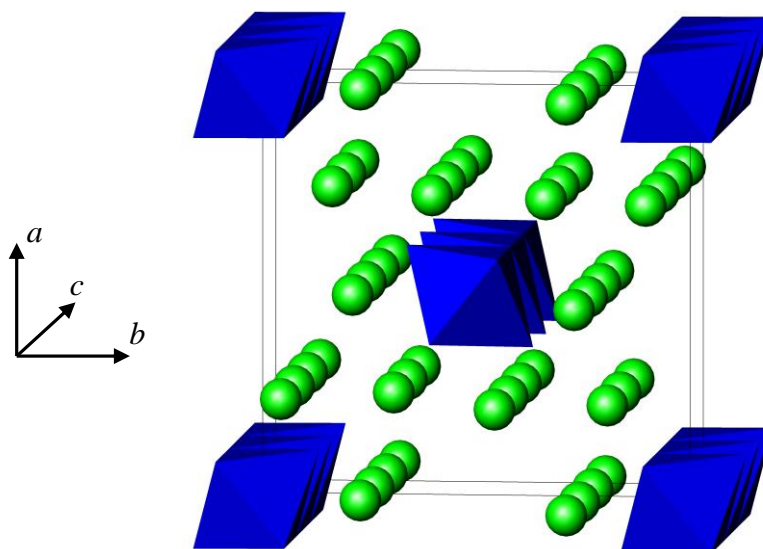


Figure 1-32. The structure of $\text{Sc}_4\text{Cl}_6\text{N}$, the blue octahedra are NSc_6 and the green spheres represent chlorine.

These octahedra rest within a rectangular prism of chloride ions and are then interconnected by the remaining chloride ions, as shown in Figure 1-33.

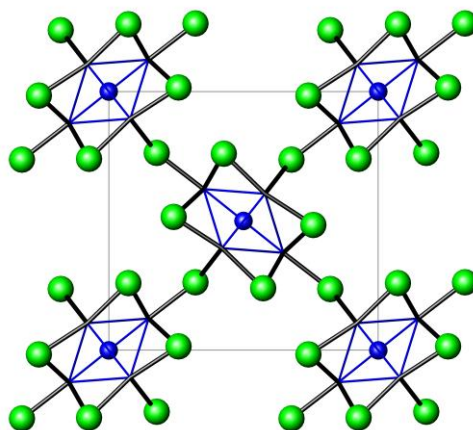


Figure 1-33. The structure of $\text{Sc}_4\text{Cl}_6\text{N}$ projected in the (001) plane, highlighting the connectivity of the clusters. The blue and green spheres represent nitrogen and chlorine respectively and the scandium octahedra are indicated by the blue lines.

$\alpha\text{-Y}_2\text{Cl}_3\text{N}$ ($Pbcn$, $a = 12.761(1) \text{ \AA}$, $b = 6.676(2) \text{ \AA}$, $c = 6.1000(7) \text{ \AA}$), forms from the reaction of YCl_3 and YN in the temperature range $750\text{-}1000 \text{ }^\circ\text{C}$ in around ten days and shows the $\text{Gd}_2\text{Cl}_3\text{N}$ type structure.¹⁴¹ The $\text{Gd}_2\text{Cl}_3\text{N}$ structure is made up of one-dimensional chains of nitrogen-centred tetrahedra edge-connected along the c -axis. The chains can be said to lay in layers, parallel to (100), separated, along [010], by linear arrays of chloride anions. These layers are stacked, along [100], with a displacement of $b/2$ (Figure 1-34).¹⁴²

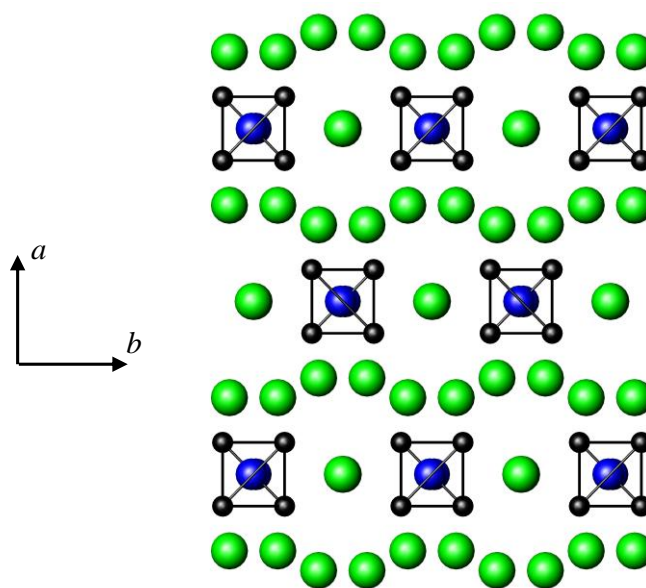


Figure 1-34. The structure of $\text{Gd}_2\text{Cl}_3\text{N}$ projected in the (001) plane. The black, blue and green spheres represent gadolinium, nitrogen and chlorine respectively. The gadolinium tetrahedra are highlighted via the thick black lines.

The remaining chloride ions rest above and below these layers capping each face of the gadolinium tetrahedra, as shown in Figure 1-35.

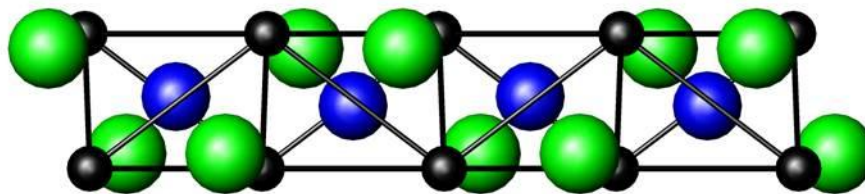


Figure 1-35. The structure of a NGd_4 chain in $\text{Gd}_2\text{Cl}_3\text{N}$ projected in the (100) plane. The black, blue and green spheres represent gadolinium, nitrogen and chlorine respectively. The tetrahedra are highlighted via the thick black lines.

$\beta\text{-Y}_2\text{Cl}_3\text{N}$ is another example of an “impurity-stabilised” cluster compound.¹⁴¹ Single crystals of $\beta\text{-Y}_2\text{Cl}_3\text{N}$ can be made through the reaction of YCl_3 , YN and yttrium metal in a 6:6:1 to 6:9:1 range. Initially, this mixture is heated at 900 °C for two days followed by fourteen days at 800 °C. Structurally $\beta\text{-Y}_2\text{Cl}_3\text{N}$ ($C2/m$, $a = 15.248(2)$ Å, $b = 3.8520(4)$ Å, $c = 10.157(2)$ Å, $\beta = 118.41(1)^\circ$) is very similar to Y_2Cl_3 ($C2/m$, $a = 15.144(3)$ Å, $b = 3.825(1)$ Å, $c = 10.077(2)$ Å, $\beta = 118.24(2)^\circ$).¹⁴³ Both show one-dimensional chains of edge-sharing yttrium octahedra, connected along the b -axis. These yttrium polyhedra are stabilised by chloride ions, which cap the exterior surfaces of the chains, as shown in Figure 1-36, the remaining chloride anions separate the chains in the c -axis.¹⁴³

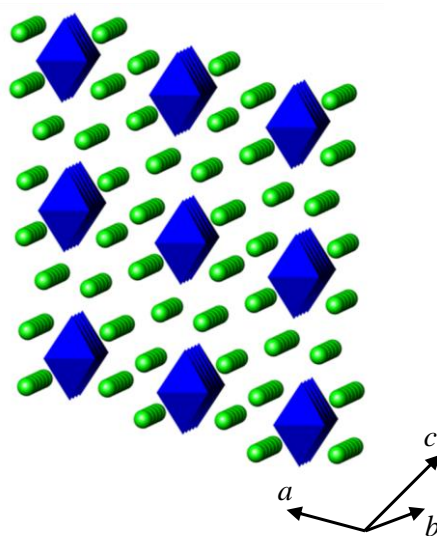


Figure 1-36. The structure of Y_2Cl_3 along the b -axis. The blue octahedra represent Y_6 polyhedra and the green spheres are the chloride anions.

Mattausch *et al.* described the Y_2Cl_3N structure as chains of $Y_{4/2}Y_2Cl_4$ close packed into layers separated by a layer of bridging chlorine atoms.¹⁴³ Nitride anions, in this description, do not occupy the centre of the metal octahedra as in the previous examples of cluster compounds, but rest in tetrahedral holes formed from adjacent yttrium octahedra.

1.4.1.2 Nitride-Halides of Elements in Group 4

1.4.1.2.1 Compounds Showing Three-Dimensional Structural Features

The synthesis of TiNF proposed by Wüstefeld *et al.* involved the reaction of $(NH_4)_2TiF_6$ with equimolar amounts of NH_4Cl at 400 °C, under an inert atmosphere, for 12 hours. The resulting $(NH_4)_2TiF_2 \cdot NH_4Cl$ was then thermally decomposed at 280 °C, under an inert gas, before ammonolysis to yield a light green powder identified as TiNF.¹⁴⁴ The structure of TiNF was determined via X-ray diffraction using Synchrotron radiation. Refinement was performed in the space group $I4_1/amd$ and TiNF was found to show the TiO_2 , anatase, structure.¹⁴⁴ In the case of TiNF, the 8e (O^{2-}) site of TiO_2 is occupied, equally, by N^{3-} and F^- anions. The similarities in the ionic radii between O^{2-} , N^{3-} and F^- allow these anions to share the 8e site without significant deviation between the anatase structure, TiO_2 ($I4_1/amd$, $a = 3.796(1)$ Å, $c = 9.444(3)$ Å), and the “pseudooxide” TiNF ($I4_1/amd$, $a = 3.7891(4)$ Å, $c = 9.4863(9)$ Å).^{29, 75, 144} Within the TiNF structure the Ti^{4+} cation shows a distorted octahedral coordination to N^{3-}/F^- anions. These octahedra are connected along four edges as shown in Figure 1-37. The work of Wüstefeld *et al.* did not give any indication of order within the anion lattice, but it was indicated that neutron diffraction studies would be required to confirm this.¹⁴⁴

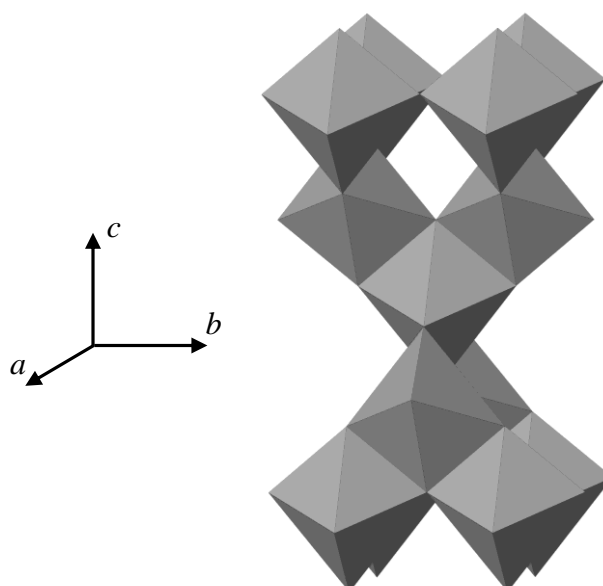


Figure 1-37. Polyhedral representation of the anatase structure.

More recently, work performed by Nukumizu *et al.* indicated that the anion site may in fact show a large oxygen occupancy.¹⁴⁵ The synthesis performed by Nukumizu *et al.*, suggested the olive green powder, showing anatase structure, could only be prepared when an oxygen source was present. They therefore included SiO₂ in the reaction mixture. The resulting compound was TiN_xO_yF_z, where $y \geq 1.64$.¹⁴⁵

Jung *et al.* and Schlichenmaier *et al.*, reported the synthesis of ZrN_xF_y, via ammonolysis of ZrF₄ at ~ 580 °C.^{146, 147} A range of non-stoichiometric solid solution ZrN_xF_{4-3x} ($0.906 < x < 0.936$) were reported by Jung *et al.* and are based on the CaF₂, fluorite, type structure, with a range of superstructures. ZrN_{0.906}F_{1.28} (*Cm2a*, $a = 145.098$ Å, $b = 5.368$ Å, $c = 5.186$ Å, no structural derivation was given), for example, shows a 27-fold *a*-axis.¹⁴⁶ More recently, Schlichenmaier *et al.* have indicated that these solid solutions are actually nitride oxide fluorides, Zr(N,O,F)_x ($2.12 < x < 2.25$) and that only the ZrNF form is produced as an oxygen-free nitride-fluoride. In this case the compound was described as isotopic to the monoclinic, room temperature, form of ZrO₂, baddeleyite, with substitution of O²⁻ with N³⁻ and F⁻.¹⁴⁷ The baddeleyite structure, shown in Figure 1-38, contains seven coordinate zirconium and two crystallographically independent anion sites. The first form a square planar arrangement, resembling half the cubic arrangement found in the fluorite structure, with

the oxygen showing tetrahedral coordination. Almost parallel to these planes are the other anions, which form triangular planes.¹⁴⁸

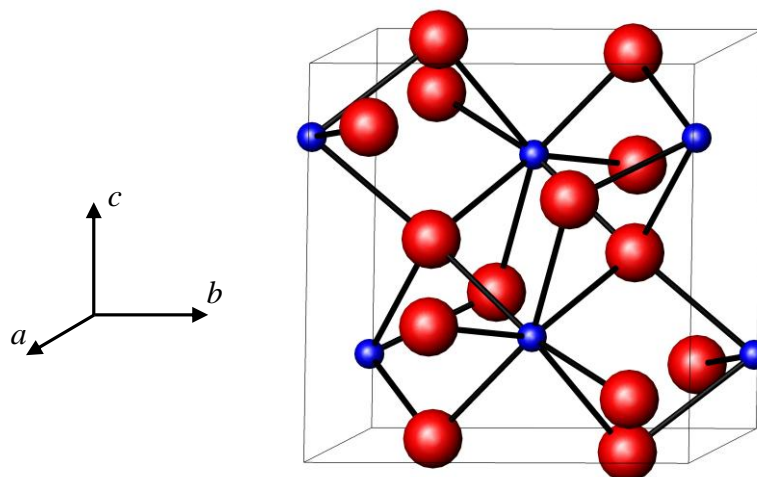


Figure 1-38. The structure of baddeleyite. The blue and red spheres represent the cations and anions respectively.

There is no preference suggested, between either of the two crystallographically independent O^{2-} sites, for N^{3-}/F^- anions in $ZrNF$ ($P2_1/c$, $a = 5.227(3) \text{ \AA}$, $b = 5.026(2) \text{ \AA}$, $c = 5.191(3) \text{ \AA}$, $\beta = 98.98(7)^\circ$).¹⁴⁷

The most recent report on $ZrNF$ synthesis was made by Zhu *et al.*¹⁴⁹ Zhu *et al.*, used a high temperature (1000 °C) and pressure (3 GPa) method to synthesis $ZrNF$, using NH_4F flux.¹⁴⁹ Although their completed structure is yet to be published, $ZrNF$ showed a 5-fold a -axis superstructure, with similar XRD patterns to those of $ZrN_{0.906}F_{1.28}$, published by Jung *et al.*^{146, 149}

Another compound that consists of octahedral nitrogen centred metal clusters is $Zr_6Cl_{15}N$ ($Ia\bar{3}d$, $a = 21.171(1) \text{ \AA}$). Formed from the reaction of zirconium, $ZrCl_4$, $ZrNCl$, NaN_3 and NH_4Cl at 700 °C, $Zr_6Cl_{15}N$ adopts a Ta_6Cl_{15} -type structure.¹⁵⁰ The structure consists of isolated NZr_6 octahedra, which are separated by chlorine atoms (Figure 1-39). The chlorine atoms form square-based pyramids around each of the zirconium atoms. The square-based pyramids are connected, via shared equatorial vertices, around the NZr_6 octahedron. The apical chlorine in the square-based pyramidal unit is shared between the clusters to generate a three-dimensional array.

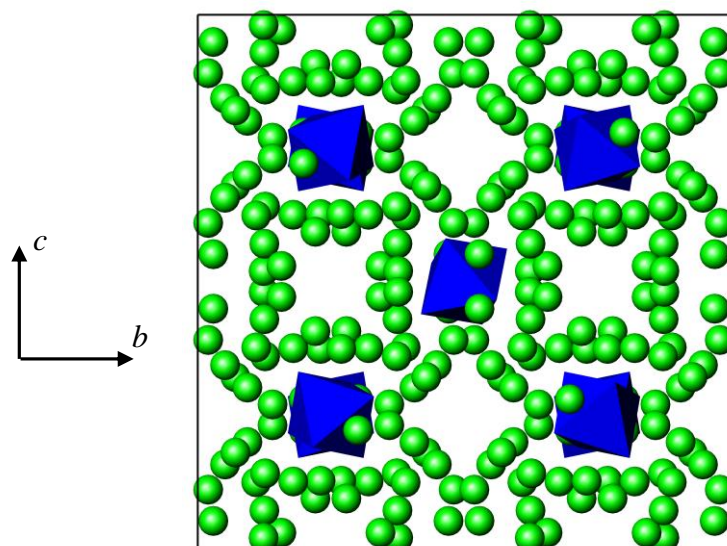


Figure 1-39. The structure of $Zr_6Cl_{15}N$. The green spheres and blue polyhedra represent the chlorine and NZr_6 units respectively.

1.4.1.2.2 Compounds Showing Two-Dimensional Structural Features

One family of compounds showing intercalation properties are MNX (M = Ti, Zr, Hf; X = Cl, Br, I). MNX are known to show different layered structures. These are the α - and β -forms, which resemble the FeOCl, SmSI or YOF (polytype of SmSI) type structures.¹⁵¹ These structures show similar structural features, both containing metal nitride sheets sandwiched between layers of chloride anions. In the case of MNCI (M = Zr, Hf) and β -ZrNBr structural transformation from the α - and β -forms is also possible, with some evidence that the α -form is the low temperature polymorph and that heating α -ZrNCl above 600 °C results in the β -form.¹³³ Alternatively, β -MNX (M = Zr, Hf; X = Cl) and β -ZrNBr can be prepared by applying high pressure to the α -form, with the β -form showing a higher density. β -ZrNI, β -HfNBr and β -HfNI can only be prepared under high-pressure conditions.¹⁵² Yamanaka *et al.* first synthesised β -ZrNI, β -HfNBr and β -HfNI from the α -forms using a pressure of 3-5 GPa at 900 °C.¹⁵³

α -MNX (M = Ti, Zr, Hf; X = Cl, Br, I) are examples of pseudooxidechlorides, showing the same structure as FeOCl.¹⁵¹ The FeOCl structure, given in Figure 1-40, consists of distorted *cis*-(FeCl₂O₄)⁷⁻ octahedra, which form layers, stacked along the *b*-axis.¹⁵⁴ The

stacking order can be described as |AaBAbB|, where the capital letters refer to the anion positions and the lower-case letters the cation sites.

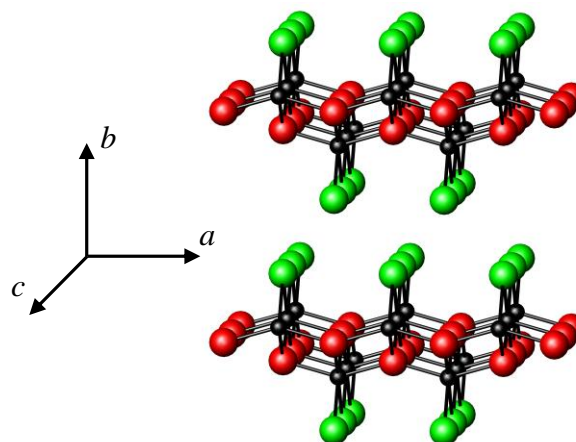


Figure 1-40. The structure of the layered structure FeOCl. The black, red and green spheres represent iron, oxygen and chlorine respectively.

The *cis*-(FeCl₂O₄)⁷⁻ octahedra are joined through a shared chloride and oxide ion along the *c*-axis and shared oxide ions in the *a*-axis. The result is a central (FeO)_n sheet sandwiched between chloride layers.¹⁵⁴

The FeOCl-type structure appears to show a reasonable degree of flexibility with respect to substituents. This is, in part, due to the similarity in ionic radii of the cations ($r_{\text{Fe}^{3+}} \approx 0.645 \text{ \AA}$, $r_{\text{Ti}^{4+}} \approx 0.605$, $r_{\text{Zr}^{4+}} \approx 0.720 \text{ \AA}$ and $r_{\text{Hf}^{4+}} \approx 0.760 \text{ \AA}$) and between oxide and nitride anions, as well as to the stable (*d*⁰) cations, which compensate for the additional negative charge introduced by N³⁻ anions.^{29, 75}

Table 1-5 shows the cell parameters for α -MNX (M = Ti, Zr, Hf; X = Cl, Br, I). It can be seen that, in general, as the sizes of the ions increases the overall size of the unit cell increases. Due to the orientation of the octahedra, with the halide anion shared along the *c*-axis and only connectivity through nitrogen along *a*, increasing the size of the halide anion greatly affects the size of the *c* axis, while the *a* axis is relatively unaffected. The interlayer spacing is also dictated by the extent of repulsion between the halide layers along *b*.

Compound	a (Å)	b (Å)	c (Å)	V (Å ³)
FeOCl	3.773	7.9096	3.3010	98.51
TiNCl	3.937	3.258	7.803	100.09
TiNBr	3.927	3.349	8.332	109.58
TiNI	3.941	3.515	8.955	124.05
ZrNCl	4.08	3.52	8.57	123.08
ZrNBr	4.116	3.581	8.701	128.25
ZrNI	4.114	3.724	9.431	144.49
HfNCl	4.130	3.497	8.070	116.55
HfNBr	4.1165	3.5609	8.6440	126.708
HfNI	4.106	3.694	9.382	142.30

Table 1-5. Cell parameters for α -MNX (M = Ti, Zr, Hf; X = Cl, Br, I).^{155, 156} Cell parameters of FeOCl are included for comparison.

Due to the structural similarities between β -MnCl (M = Zr, Hf) and β -ZrNBr, the main structural features of these compounds will be illustrated through a description of the ZrNCl structure. The structure and properties of β -ZrNCl are reviewed in a paper by Yamanaka, and some of the more important structural developments are reiterated here.¹³³

Several structures have been proposed for β -ZrNCl since its discovery in 1964.¹⁵⁶ The structure of β -ZrNCl was first developed by Juza and Friedrichsen in 1964 and described as consisting of Cl-Zr-N-N-Zr-Cl slabs, stacked |AbCAbC|, where the capital letters refer to the anion positions and the lower-case letters the cation sites.¹⁵⁷ The stacking of the ZrNCl structure proposed by Juza *et al.* is shown in Figure 1-41. Within the Cl-Zr-N-N-Zr-Cl slabs the zirconium and nitrogen form a bilayer, which is sandwiched between close-packed layers of chloride ions. The result is a hexagonally packed array of anions with zirconium in an anti-prismatic hole, surrounded by three nitride and three chloride anions. The layers themselves were considered, by Juza *et al.*, to show a random stacking of the chloride layers between the cubic close packed, CdCl₂-type, and hexagonal close packed, CdI₂-type, stacking.

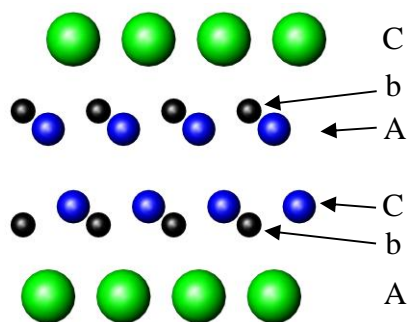


Figure 1-41. The structure of the structure of β -ZrNCl proposed by Juza and Friedrichsen, illustrating the stacking sequence. The blue, black and green spheres represent nitrogen, zirconium and chlorine respectively.

This structure was developed further after a new synthetic route, which allowed the preparation of a highly crystalline powder, was developed by Ohashi *et al.* Ohashi *et al.* proposed a rhombohedral unit cell with an ordered stacking sequence for the Cl-Zr-N-N-Zr-Cl slabs.^{158, 159} The stacking sequence, shown in Figure 1-42, is an ordered CdCl₂-type |AbCAbC|BcABcA|CaBCaB|. A true structural description proved difficult due to the layered nature of the samples giving rise to preferred orientation, which complicates analysis by X-ray diffraction.

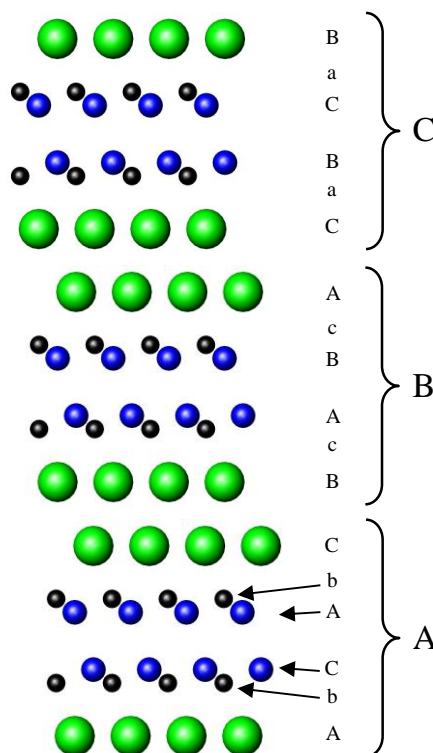


Figure 1-42. The structure of the structure of β -ZrNCl proposed by Ohashi *et al.*, illustrating the stacking sequence. The blue, black and green spheres represent nitrogen, zirconium and chlorine respectively.

Neutron diffraction, performed by Shamoto *et al.*, supported by several X-ray diffraction studies and provided the currently accepted crystal structure of β -ZrNCl.¹⁶⁰⁻¹⁶⁴ The space group was identified as $R\bar{3}m$ ($a = 3.5974(2)$ Å, $c = 27.5480(20)$ Å, $\gamma = 120^\circ$). The β -ZrNCl structure shows several similarities to ZrCl, mentioned in section 1.4.1.1.2. ZrCl consists of close-packed layers of ions in Cl-Zr-Zr-Cl slabs and the stacking sequence of zirconium and chlorine in ZrCl and ZrNCl are identical; |AbcA|BcaB|CabC|. ¹⁶⁵ The result is approximately anti-prismatic, nearest neighbour, coordination of zirconium and chlorine. The nitrogen of β -ZrNCl can be said to sit in tetrahedral sites formed by zirconium, within the metal bilayer of ZrCl, forming parallel sheets in the (001) plane. ¹³³ It should be noted that there is a shift of the sheets relative to the model given by Ohashi *et al.* to produce interlayer bonds between zirconium and nitrogen (Figure 1-43). The overall result is a stacking sequence of |AbCBcA|BcACaB|CaBAbC| along the c -axis, with each zirconium ion resting in monocapped octahedral coordination, bound to three chloride and four nitride anions. ¹⁶⁰

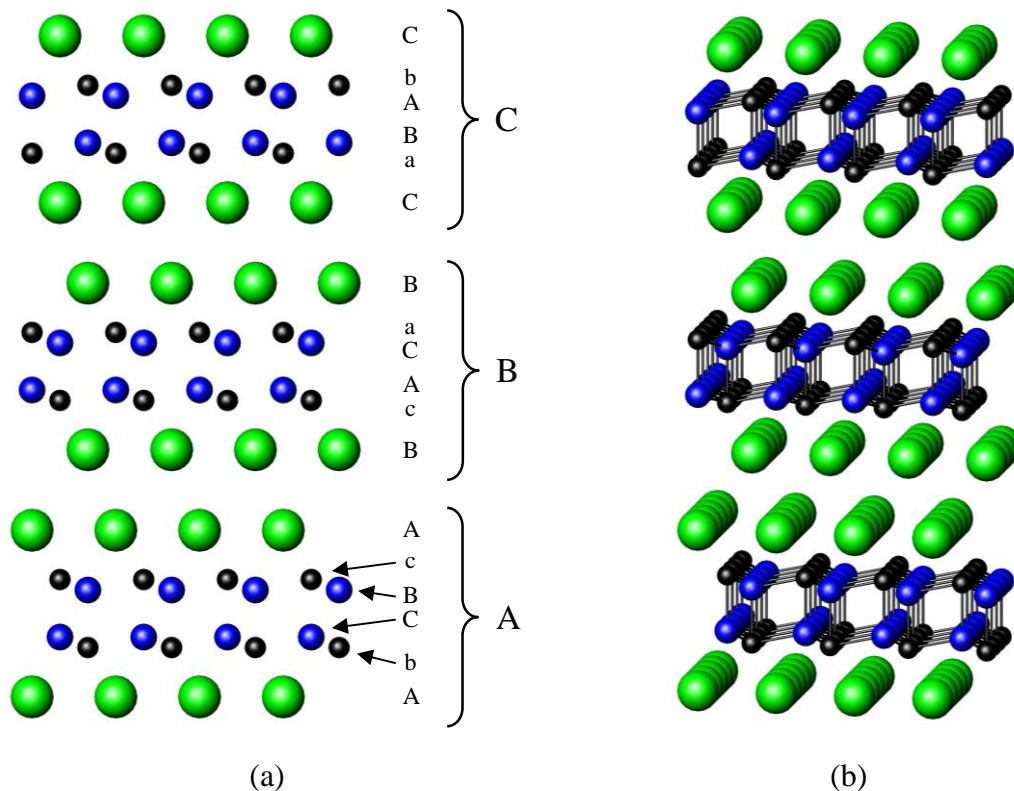


Figure 1-43. The structure of the structure of β -ZrNCl, illustrating (a) the stacking sequence and (b) the interlayer bonding between zirconium and nitrogen. The blue, black and green spheres represent nitrogen, zirconium and chlorine respectively.

In general, β -MNX has shown less flexibility in terms of the atoms that can be present, while maintaining the SmSI-type structure. Only β -ZrNCl, β -HfNCl and β -ZrNBr are known. The unit cell parameters are given in Table 1-6. Once again it can be seen that increasing the size of the anion results in an increase in the cell dimensions, particularly in the stacking direction, along c .

Compound	a (Å)	b (Å)	c (Å)	V (Å ³)
SmSI	4.54(1)	4.54(1)	32.69(2)	583.52
ZrNCl	3.6031(6)	3.6031(6)	27.672(2)	311.12
ZrNBr	3.6379(5)	3.6379(5)	29.263(2)	335.39
HfNCl	3.5744(3)	3.5744(3)	27.70749(90)	306.57

Table 1-6. Cell parameters for β -MNX (M = Zr, Hf; X = Cl) and β -ZrNBr.^{133, 166} The cell parameters of SmSI are included for comparison.

Initially β -ZrNI, β -HfNBr and β -HfNI were thought to adopt the β -ZrNCl structure, however, further investigation by Yamanaka *et al.* identified the structure as YOF-type.^{152, 153} The YOF-type structure is a very similar polytype of SmSI, showing a similar layered structure, made up of X-M-N-N-M-X slabs, but with a different stacking sequence. The β -ZrNCl structure consists of ZrCl-type stacking, ABC, with nitrogen in the corresponding tetrahedral holes, within the metal layer. β -ZrNI, β -HfNBr and β -HfNI, instead, show a ZrBr stacking, ACB, with nitrogen resting in the resultant tetrahedral holes. Maintaining the stacking notation used previously, the stacking of β -ZrNI, β -HfNBr and β -HfNI can be described as |AcBCbA|BaCAcB|CbABaC| compared to the |AbCBcA|BcACaB|CaBAbC| stacking of β -ZrNCl.¹⁵² The stacking sequence of β -ZrNI, β -HfNBr and β -HfNI are shown in Figure 1-44. There is also the effect that both chlorine and nitrogen show cubic close packed arrangements, with regard to the other anions, in β -ZrNI, β -HfNBr and β -HfNI ($C_{Cl}A_NB_NC_{Cl}B_{Cl}C_NA_NB_{Cl}A_{Cl}B_NC_NA_{Cl}$), while in β -ZrNCl the chloride anions are hexagonally close packed and the nitride anions are cubic close packed ($A_{Cl}B_NC_NA_{Cl}B_{Cl}C_NA_NB_{Cl}C_{Cl}A_NB_NC_{Cl}$).

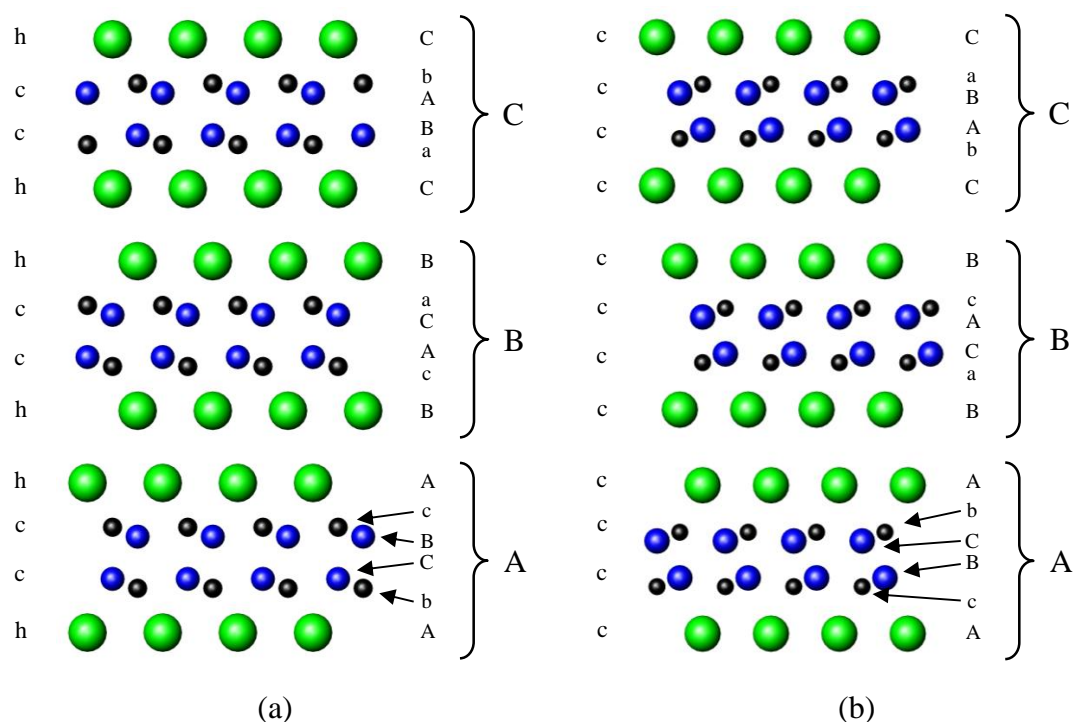


Figure 1-44. The structure of the stacking in (a) β -ZrNCl (SmSI-type) and (b) β -ZrNI (YOF-type) structures. The blue, black and green spheres represent nitrogen, zirconium and chlorine/iodine respectively.

A comparison of the unit cell parameters for a selection of these layered compounds is shown in Table 1-7.

Compound	a (Å)	b (Å)	c (Å)	V (Å ³)
YOF	3.797(1)	3.797(1)	18.89(1)	235.85
ZrNI	3.718(2)	3.718(2)	31.381(9)	375.7(3)
HfNBr	3.610(1)	3.610(1)	29.294(6)	330.6(2)
HfNI	3.689(1)	3.689(1)	31.329(6)	369.2(2)

Table 1-7. Cell parameters for β -ZrNI, β -HfNBr and β -HfNI.^{133, 167} Cell parameters of YOF are also included for comparison.

1.4.1.3 Nitride-Halides of Elements in Group 5

1.4.1.3.1 Compounds Showing One-Dimensional Structural Features

Cl_3VNCl was prepared via the reaction of VN in a stream of chlorine gas, at approximately 130 °C, and the crystal structure was determined by Strähle *et al.* in

1968.¹⁶⁸ The unit cell is triclinic, ($P\bar{1}$, $a = 7.64 \text{ \AA}$, $b = 7.14 \text{ \AA}$, $c = 5.91 \text{ \AA}$, $\alpha = 94.9^\circ$, $\beta = 112.4^\circ$, $\gamma = 107.8^\circ$) and is made up of Cl_3VNCl molecular units. Within these units vanadium is coordinated to four chlorine atoms, which form the base of a tetragonal-pyramid, and a nitrogen atom at the apex. This apical nitrogen is bound to the remaining chlorine forming near linear V-N-Cl bonds (Figure 1-45).

The tetragonal-pyramids form edge sharing dimers, with a centre of inversion on the shared edge. The connectivity of the polyhedra can be emphasised if the vanadium coordination sphere is extended to include the next nearest chlorine atom. The result is distorted octahedra forming zigzagging chains along $[001]$, Figure 1-45 (b).

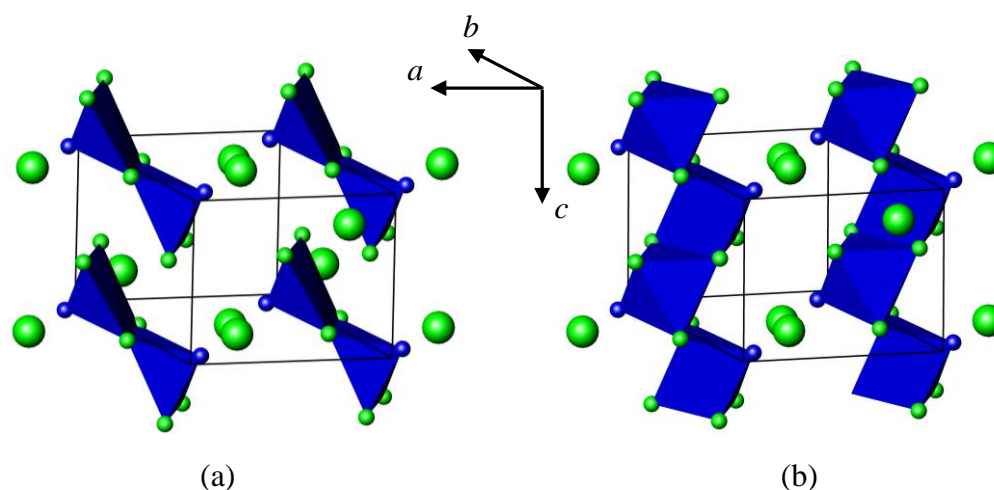


Figure 1-45. The structure of Cl_3VNCl showing both (a) tetragonal-pyramidal and octahedral coordination of vanadium. The green and blue spheres represent chlorine and nitrogen respectively.

1.4.1.4 Nitride-Halides of Elements in Group 6

1.4.1.4.1 Compounds Showing Two-Dimensional Structural Features

MnCl_3 ($M = \text{Mo}, \text{W}$) were prepared by Dehnicke and Strähle in 1965 via the reaction of MCl_6 and chlorine azide in carbon tetrachloride at 30°C .^{169, 170} Alternatively the reaction between trimethylsilyl azide and molybdenum chloride or tris(trimethylsilyl)amine and tungsten chloride can be used.¹⁷⁰ MoNCl_3 and WNCl_3 show the $P\bar{1}$ space group ($a = 9.14(1) \text{ \AA}$, $b = 7.67(1) \text{ \AA}$, $c = 8.15(1) \text{ \AA}$, $\alpha = 108.8(3)^\circ$, $\beta = 99.3(3)^\circ$, $\gamma = 108.6(3)^\circ$; $a = 7.752(2) \text{ \AA}$, $b = 8.143(2) \text{ \AA}$, $c = 9.114(2) \text{ \AA}$,

$\alpha = 98.71(3)^\circ$, $\beta = 107.52(3)^\circ$, $\gamma = 110.40(3)^\circ$ respectively).^{170, 171} MoNCl_3 , for example, consists of MoNCl_3 molecular units, which form tetramers via the nitrogen atoms. The result is heavily distorted Mo centred octahedra, made up of four chlorine and two nitrogen atoms (Figure 1-46).¹⁷² Each octahedron can be described as being bound to two others via the nitrogen atoms and a third octahedron, showing edge-sharing connectivity via two chlorine atoms. The result is an array of layers parallel to (010).

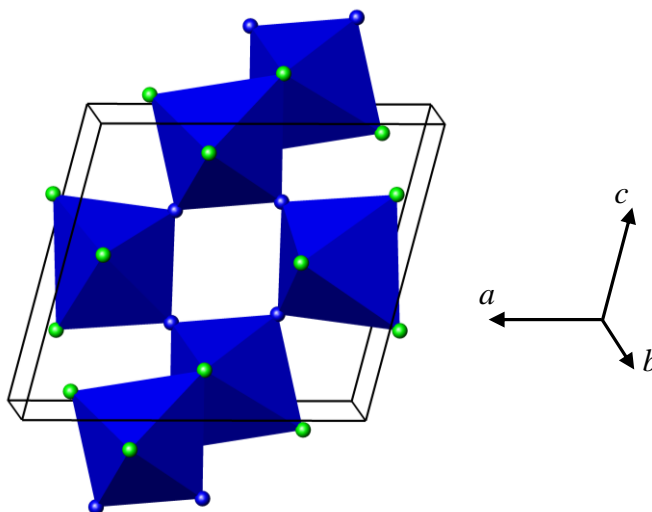


Figure 1-46. The structure of MoNCl_3 . The blue and green spheres represent nitrogen and chlorine respectively. The blue polyhedra are molybdenum centred octahedra.

1.4.1.4.2 Compounds Showing One-Dimensional Structural Features

Single crystals of Mo_2NCl_7 can be prepared via the reaction of VN with MoCl_5 , in a sealed vessel, at 175°C and shows a triclinic space group ($P\bar{1}$, $a = 9.057(8) \text{ \AA}$, $b = 9.754(6) \text{ \AA}$, $c = 12.834(8) \text{ \AA}$, $\alpha = 103.13(4)^\circ$, $\beta = 109.83(5)^\circ$, $\gamma = 98.58(5)^\circ$).¹⁷³ The structure was described by Dinh *et al.* as consisting of dinuclear units $[\text{Mo}_2\text{N}_2\text{Cl}_7]^{3-}$ and $[\text{Mo}_2\text{Cl}_7]^{3+}$ connected via the nitrogen atom into chains. Three of the chloride ions within each dinuclear unit are bridged between the metal centres, $[\text{Cl}_2(\text{N}\equiv)\text{Mo}(\mu_2\text{-Cl})_3\text{Mo}(\equiv\text{N})\text{Cl}_2]^{3-}$ and $[\text{Cl}_2\text{Mo}(\mu_2\text{-Cl})_3\text{MoCl}_2]^{3+}$.¹⁷³ In order to make comparisons, the overall structure may also be described in terms of distorted octahedra. In this way the Mo atom is said to be surrounded by five chlorine atoms and one

nitrogen atom. These octahedra are then connected into pairs which are linked through the nitrogen atom into approximately linear chains traversing along [110] (Figure 1-47).

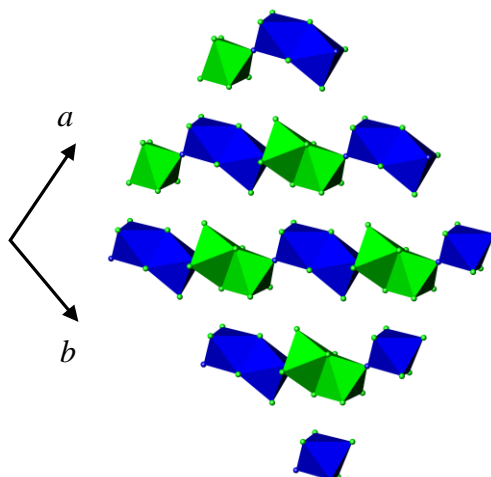


Figure 1-47. The structure of Mo_2NCl_7 . The blue polyhedra represent the $[\text{Cl}_2(\text{N}\equiv)\text{Mo}(\mu_2\text{-Cl})_3\text{Mo}(\equiv\text{N})\text{Cl}_2]^-$ based units and the green polyhedra the $[\text{Cl}_2\text{Mo}(\mu_2\text{-Cl})_3\text{MoCl}_2]^{3+}$ based units, including the nitride bridges. The blue and green spheres represent nitrogen and chlorine respectively.

The reaction of MoCl_5 and Cl_3VNCI_8 in a sealed vessel at 140°C results in single crystals of Mo_2NCl_8 .¹⁷⁴ Mo_2NCl_8 has the monoclinic space group $P2/c$ ($a = 9.961(1) \text{ \AA}$, $b = 6.294(1) \text{ \AA}$, $c = 17.808(3) \text{ \AA}$, $\beta = 101.82(2)^\circ$).¹⁷⁴ In a similar way to Mo_2NCl_7 , the description of the structure given by Dinh *et al.* shows two dinuclear units $[\text{Mo}_2\text{N}_2\text{Cl}_7]^-$ and $[\text{Mo}_2\text{Cl}_9]^+$ connected via the nitrogen atom into chains. The $[\text{Mo}_2\text{N}_2\text{Cl}_7]^-$ unit resemble the $[\text{Mo}_2\text{N}_2\text{Cl}_7]^{3-}$ units of Mo_2NCl_7 , with three chlorine atoms bridging the metal centres, $[\text{Cl}_2(\text{N}\equiv)\text{Mo}(\mu_2\text{-Cl})_3\text{Mo}(\equiv\text{N})\text{Cl}_2]^-$, while the $[\text{Mo}_2\text{Cl}_9]^+$ units show only a single bridging chlorine, $[\text{Cl}_4\text{Mo}(\mu_2\text{-Cl})\text{MoCl}_4]^+$.¹⁷⁴ The resulting structure may also be viewed as an array of distorted Mo centred octahedra, made up of five chlorine atoms and one nitrogen atom. In this way, Mo_2NCl_8 can be described as consisting of, one dimensional, undulating chains of octahedra, traversing along [100] and stacked in (010) (Figure 1-48).

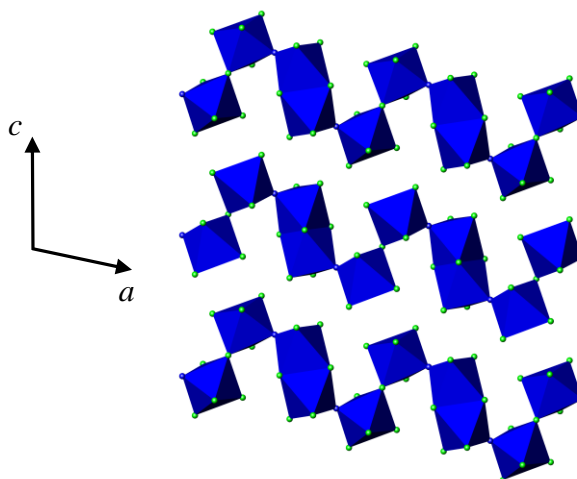


Figure 1-48. The structure of Mo_2NCl_8 . The green and blue spheres represent chlorine and nitrogen respectively. The blue polyhedra are molybdenum centred octahedra.

Alternatively, the reaction of MoCl_3 and Cl_3VNCl in a sealed vessel at $140\text{ }^\circ\text{C}$ can also yield $\text{Mo}_3\text{N}_2\text{Cl}_{11}$ ($Pca2_1$, $a = 12.561(1)\text{ \AA}$, $b = 10.019(1)\text{ \AA}$, $c = 13.3010(5)\text{ \AA}$).¹⁷⁴ The $\text{Mo}_3\text{N}_2\text{Cl}_{11}$ structure also shows $[\text{Cl}_2(\text{N}\equiv)\text{Mo}(\mu_2\text{-Cl})_3\text{Mo}(\equiv\text{N})\text{Cl}_2]^-$ dinuclear units, however these are connected to MoCl_4^+ units, via the nitrogen atoms. Once again, these form chains of distorted octahedra, although in this case there are both MoNCl_5 and MoN_2Cl_4 polyhedra present. The chains themselves form a wave-like patterns propagating along $[100]$ (Figure 1-49). These chains are stacked on top of each other in (010) , but due to the two-fold screw axis the chains alternate in orientation by 180° .

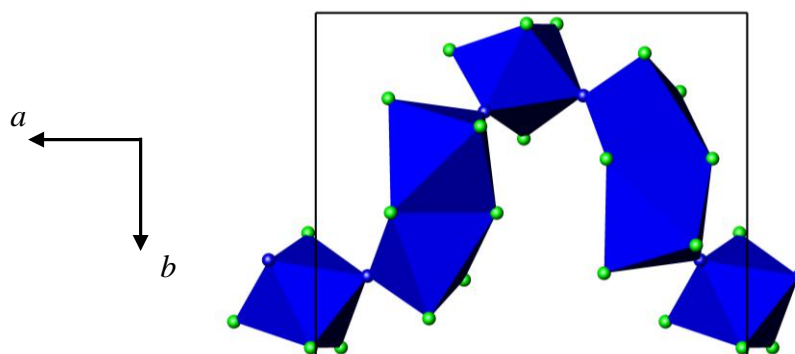


Figure 1-49. The structure of a chain of distorted octahedra in $\text{Mo}_3\text{N}_2\text{Cl}_{11}$, viewed along $[001]$. The blue and green spheres represent nitrogen and chlorine respectively.

The solid state reaction of WCl_6 and CN_2H_2 was found by Weisser *et al.* to yield two tungsten nitride-chloride compounds, W_2NCl_8 and W_2NCl_9 , which both also show

arrays of dinuclear units.¹⁷⁵ W_2NCl_8 shows linear chains while W_2NCl_9 shows isolated dimers.

W_2NCl_8 ($P\bar{1}$, $a = 6.2423(11)$ Å, $b = 6.3094(12)$ Å, $c = 6.9311(12)$ Å, $\alpha = 89.76(2)^\circ$, $\beta = 81.51(2)^\circ$, $\gamma = 82.68(2)^\circ$) is made up of $[Cl_{2/2}Cl_3WNWCl_3Cl_{2/2}]$ -units, which can be described in terms of tungsten centred, WCl_5N , octahedra that are connected into chains via nitrogen vertices and chlorine edges in a regularly alternating manner along $[001]$ (Figure 1-50).¹⁷⁵ These chains form planes in (100) and (010) .

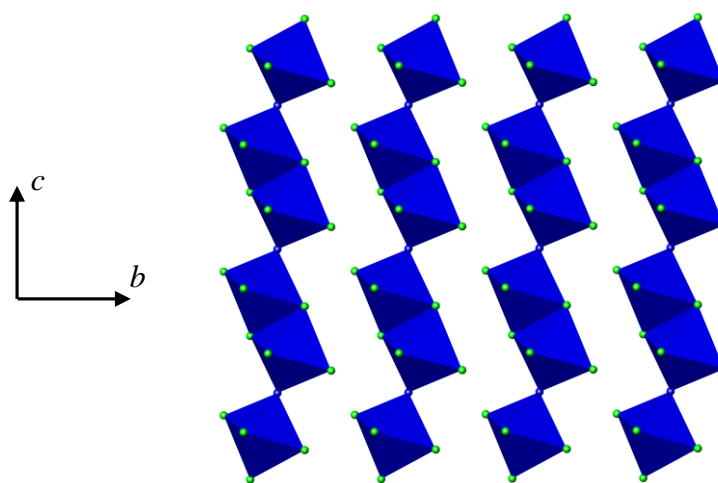


Figure 1-50. Representation of W_2NCl_8 . The green and blue spheres represent chlorine and nitrogen respectively. The blue polyhedra are tungsten centred octahedra.

1.4.1.4.3 Compounds Showing Isolated Coordination Polyhedra

W_2NCl_9 ($P2_1/c$, $a = 8.4213(14)$ Å, $b = 16.786(3)$ Å, $c = 11.9301(19)$ Å, $\beta = 134.735(13)^\circ$) shows $[Cl_5WNWCl_3Cl_{2/2}]_2$ units which are stacked into layers parallel to $[100]$, within these planes the $[Cl_5WNWCl_3Cl_{2/2}]_2$ units are staggered to be approximately close packed. Once again the basic building block is a WCl_5N octahedron. In this case, these units are connected as a pair of octahedra sharing an edge of two chlorine atoms, with the other two octahedra sharing nitrogen vertices (Figure 1-51).

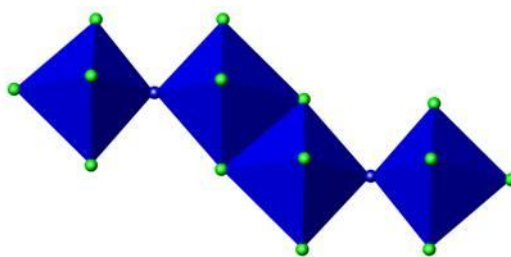


Figure 1-51. Representation of the $[\text{Cl}_5\text{WNWCl}_3\text{Cl}_{2/2}]_2$ units of W_2NCl_9 . The green and blue spheres represent chlorine and nitrogen respectively.

1.4.1.5 Nitride-Halides of Elements in Group 7

1.4.1.5.1 Compounds Showing One-Dimensional Structural Features

ReNCl_4 ($I4$, $a = 8.267(4)$ Å, $c = 4.051(2)$ Å) forms in the reaction of ReCl_5 with Cl_3VNCl at 140 °C, in an evacuated ampoule.¹⁷⁶ Structurally ReNCl_4 consists of isolated rhenium square pyramidal units, made up of a square plane of four chloride anions capped with nitrogen. These square pyramidal units all point along the c -axis. If the rhenium coordination is extended to octahedral, including the nitrogen from the adjacent square based pyramid, then the structure consists of, nitrogen-corner sharing, one-dimensional chains of octahedra along $[001]$ (Figure 1-52).

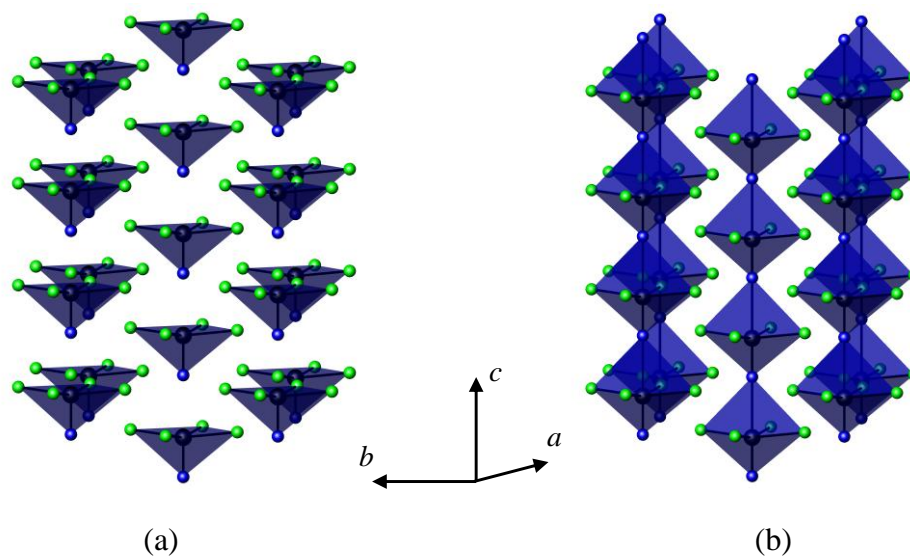


Figure 1-52. Structure of ReNCl_4 showing (a) square pyramidal and (b) octahedral coordination of rhenium. The blue, green and black spheres represent nitrogen, chlorine and rhenium respectively.

ReF_4N ($a = 5.64 \text{ \AA}$, $b = 14.76 \text{ \AA}$, $c = 4.26 \text{ \AA}$, the errors are not published) has also been reported, although to the best of our knowledge no structural determination has been achieved to date.^{177, 178}

Synthesised by Fawcett *et al.* in 1982, ReF_4N was formed in an intermediate step in the preparation of ReF_5NF , described in the following subsection.

1.4.1.5.2 Compounds Showing Isolated Coordination Polyhedra

ReF_5NF ($P2_1/c$, $a = 2.298(2) \text{ \AA}$, $b = 9.286(3) \text{ \AA}$, $c = 9.979(6) \text{ \AA}$, $\beta = 109.4(2)^\circ$) can be prepared via the route outlined in Figure 1-53.

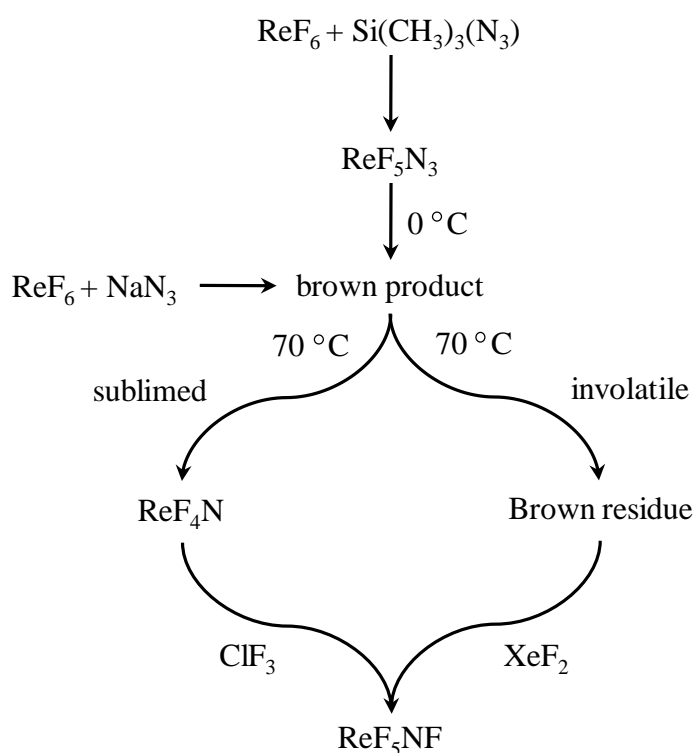


Figure 1-53. Scheme showing the preparation of ReF_5NF .^{177, 178}

Structurally ReF_5NF consists of isolated molecular units made up of rhenium centred octahedra of five fluoride and one nitride anion, which is linked in a near linear fashion to an additional fluoride anion.^{177, 178} These units are then arranged in an approximately close packed way.

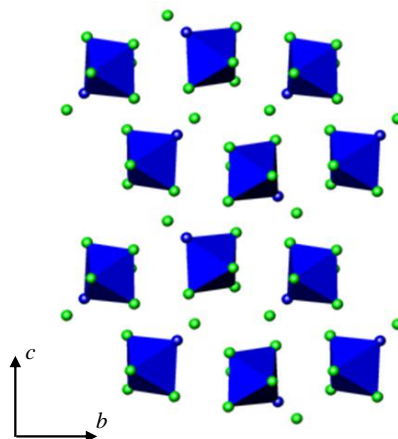


Figure 1-54. The structure of ReF_5NF . The green and blue spheres represent fluorine and nitrogen respectively. The blue polyhedral are centred on rhenium.

1.4.1.6 Nitride-Halides of the Lanthanides

1.4.1.6.1 Compounds Showing Three Dimensional Structural Features

The lanthanide nitride-fluorides $\text{LnN}_x\text{F}_{3-3x}$ ($0.33 \leq x \leq 0.54$); La, Ce, Pr) and Gd_3NF_6 have all been prepared through the reaction of LnN and LnF_3 in a 1:2 ratio in approximately one week at 870°C , or via ammoniation of the fluoride.¹⁷⁹⁻¹⁸² These compounds show an anion-excess-fluorite-type structure. Powder neutron diffraction experiments on the cerium and praseodymium analogues, by Vogt *et al.*, showed a fluorite structure, with nitrogen and fluorine occupying the tetrahedral sites, with additional interstitial fluorine on the 32f site, (x, x, x), where $x = 0.416$.¹⁸²

1.4.2 Quaternary Nitride-Halides

The quaternary nitride-halide selected for this chapter are compounds containing an electropositive metal, such as an alkali and/or an alkaline earth metal, a transition metal and two anions. However, other interesting Nitride-halides, which do not fall into this category, have been reported, including the Li_xMNCl ($\text{M} = \text{Zr}, \text{Hf}$) series, for example, deriving from the intercalation of Li^+ between the layers of the two-dimensional structure of the binary nitride-chlorides MNCl . Superconductivity was discovered by

Yamanaka *et al.* in the materials doped with electrons by means of Li intercalation.¹⁸³ The preparation of ternary and multinary pnictide–halide compounds is experimentally difficult. The synthetic routes of the compounds known to date are reported here and it is easy to notice the challenges involved in synthesis and characterisation, which, among other experimental details, involve that all operations are carried out in air-free atmosphere. The only pnictide-halides containing electropositive metals and transition metals known to date are the nitride-chlorides: $\text{Ba}_{25}\text{Nb}_5\text{N}_{19}\text{Cl}_{18}$,¹⁸⁴ $\text{Ba}_4[\text{WN}_4]\text{Cl}_2$,¹⁸⁵ $\text{LiBa}_4[\text{Mo}_2\text{N}_7]\text{BaCl}_2$,¹⁸⁶ $\text{Ba}_3\text{Ta}_3\text{N}_6\text{Cl}$ and $\text{Ba}_{15}\text{Ta}_{15}\text{N}_{33}\text{Cl}_4$,¹⁸⁷ K_2OsNCl_5 .¹⁸⁸ All of these compounds show three-dimensional structures that are not easily related to that of any other known compounds, with the exception of $\text{Ba}_3\text{Ta}_3\text{N}_6\text{Cl}$ and $\text{Ba}_{15}\text{Ta}_{15}\text{N}_{33}\text{Cl}_4$, which show a zeolitic framework predicted for SiO_2 . Curiously, all the known quaternary nitride-chlorides have been prepared in the form of single crystals and have not been “translated” yet into a polycrystalline form.

Single crystals of $\text{Ba}_{25}\text{Nb}_5\text{N}_{19}\text{Cl}_{18}$, $\text{Ba}_3\text{Ta}_3\text{N}_6\text{Cl}$ and $\text{Ba}_{15}\text{Ta}_{15}\text{N}_{33}\text{Cl}_4$ were prepared using a technique originally employed for ternary nitrides and subsequently adapted to more complicated systems.¹⁸⁹ Single crystals were grown on niobium and tantalum foils by reaction of the foil with molten Ba_2N and BaCl_2 in flowing nitrogen at 1000 °C followed by slow-cooling to room temperature. This is a productive route to new mixed-anion compounds but tends to yield small single crystals within an amorphous matrix and chemical analysis of products is therefore unreliable.

In $\text{Ba}_{25}\text{Nb}_5\text{N}_{19}\text{Cl}_{18}$, Nb^{5+} is tetrahedrally coordinated by nitrogen and forms isolated monomeric and corner-linked dimeric Nb-N tetrahedral units. The structure of $\text{Ba}_{25}\text{Nb}_5\text{N}_{19}\text{Cl}_{18}$ is illustrated in Figure 1-55.

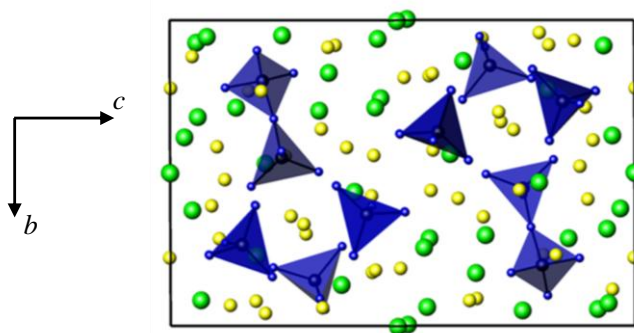


Figure 1-55. The structure of $\text{Ba}_{25}\text{Nb}_5\text{N}_{19}\text{Cl}_{18}$. The green, blue and yellow spheres represent chlorine, nitrogen and barium respectively. The blue polyhedra are Nb-N tetrahedra.

Tetrahedral units constitute an unusual situation for Nb, which tends to form edge-sharing polyhedra in ternary and quaternary nitrides and oxynitrides such as Li_7NbN_4 ,¹⁹⁰ $\text{Li}_3\text{Ba}_2\text{NbN}_4$ and $\text{Li}_{16}(\text{NbN}_4)_2\text{O}$.^{191, 192} The only example of monomeric $(\text{NbN}_4)^{7-}$ units is found in $\text{Ba}_9(\text{NbN}_4)_2\text{N}(\text{N}_3)$, which contains nitride and azide ions.¹⁹³ The presence of both monomeric $(\text{NbN}_4)^{7-}$ and dimeric $(\text{Nb}_2\text{N}_7)^{11-}$ isolated tetrahedral units in the same structural context constitutes a peculiar feature of $\text{Ba}_{25}\text{Nb}_5\text{N}_{19}\text{Cl}_{18}$. Nb^{5+} cations form almost regular tetrahedra with N^{3-} anions, whereas Ba^{2+} cations form heavily distorted polyhedra with both nitrogen and chlorine anions in this compound.

Crystals of $\text{Ba}_3\text{Ta}_3\text{N}_6\text{Cl}$ and $\text{Ba}_{15}\text{Ta}_{15}\text{N}_{33}\text{Cl}_4$ were found in the same batch. However, crystal structure analysis showed both nitride-chlorides crystallise in $P\bar{6}2c$ with topologically equivalent frameworks formed from TaN_4 tetrahedra (Figure 1-56) but differing in the number and position of chloride ions within the unit cells and the number of interstitial nitrogen ions.¹⁸⁷

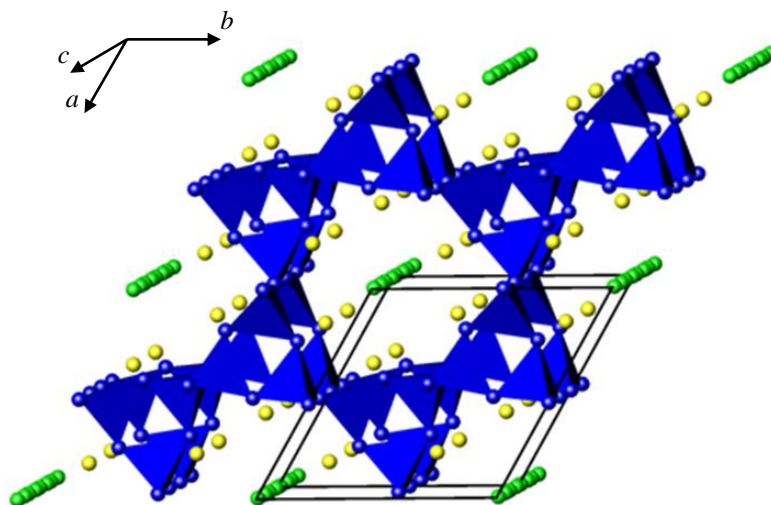


Figure 1-56. Framework common to $\text{Ba}_3\text{Ta}_3\text{N}_6\text{Cl}$ and $\text{Ba}_{15}\text{Ta}_{15}\text{N}_{33}\text{Cl}_4$. The green, blue and yellow spheres represent chlorine, nitrogen and barium respectively. The blue polyhedra are Ta-N.

Tetrahedra assemble into triangular clusters in the ab plane by corner sharing. The remaining vertices of each tetrahedron each link to another triangular cluster displaced along c (Figure 1-56). The chloride anions are located at the centre of the the channels centred along $[001]$ and are coordinated by six Ba^{2+} cations. In $\text{Ba}_3\text{Ta}_3\text{N}_6\text{Cl}$ the single chloride anion resides on the $4e$ position $(0, 0, z)$, and is half occupied. The fivefold

expansion along c in $\text{Ba}_{15}\text{Ta}_{15}\text{N}_{33}\text{Cl}_4$ conserves the framework but differences arise in the positions of the extra-framework species. There are three chloride positions in $\text{Ba}_{15}\text{Ta}_{15}\text{N}_{33}\text{Cl}_4$, each $(0, 0, z)$, two of which are fully occupied while the third is disordered over two symmetry equivalent sites $1.63(6)$ Å apart. The changes in chloride content and positions are accompanied by small changes in the positions adopted by the barium cations, giving rise to the fivefold expansion in $\text{Ba}_{15}\text{Ta}_{15}\text{N}_{33}\text{Cl}_4$. Final difference Fourier maps for $\text{Ba}_{15}\text{Ta}_{15}\text{N}_{33}\text{Cl}_4$ suggested the presence of some further nitrogen within the structure. Additional nitride, not involved in framework formation, was added to the model in octahedral holes formed from three Ta and three Ba ions, subject to the constraint that the Ta oxidation state could not exceed +5. The formula for $\text{Ba}_{15}\text{Ta}_{15}\text{N}_{33}\text{Cl}_4$ is best written $\text{Ba}_{15}\text{Ta}_{15}\text{N}_{30}\text{Cl}_4[\text{N}_3]$, where the distinction between framework and interstitial nitrogen is clear.

Charge balancing constraints in $\text{Ba}_3\text{Ta}_3\text{N}_6\text{Cl}$ imply that the formal oxidation state for tantalum is +4.333, implying the presence of Ta^{5+} and Ta^{3+} . In $\text{Ba}_3\text{Ta}_3\text{N}_6\text{Cl}$ the Ta-N distances are $1.96(4)$ and $1.962(5)$ Å. These are in good agreement with other Ta/N phases where the tantalum oxidation state is +5 such as Li_4TaN_3 ,⁸² Sr_2TaN_3 ,⁸⁸ Ba_2TaN_3 .¹⁹⁴

$\text{Ba}_2(\text{WN})_4\text{Cl}_2$ was prepared by the reaction of $\text{Ba}(\text{NH}_2)_2$ and W (molar ratio 4.5:1) mixed together in a tungsten crucible with an excess of KCl. The system was heated to 850°C for forty eight hours, under flowing nitrogen. $\text{Ba}(\text{NH}_2)_2$ was prepared by reaction of Ba with ammonia in an autoclave at 125°C for seven days.

The structure of $\text{Ba}_2(\text{WN})_4\text{Cl}_2$ can be described as a stacking of Re_3B and distorted NaCl type layers (Figure 1-57). Isolated $[\text{WN}_4]^{6-}$ tetrahedra are located on the position of the boron atom and barium is located on the rhenium position. The sodium and chlorine positions are occupied by the barium and chlorine respectively. The W-N distances are 1.85 Å and 3×1.88 Å, comparable to those found in tungsten ternary nitrides like $\text{Li}_6[\text{WN}_4]$ and $\text{Li}_2\text{Sr}_5[\text{WN}_4]_2$.^{195, 196}

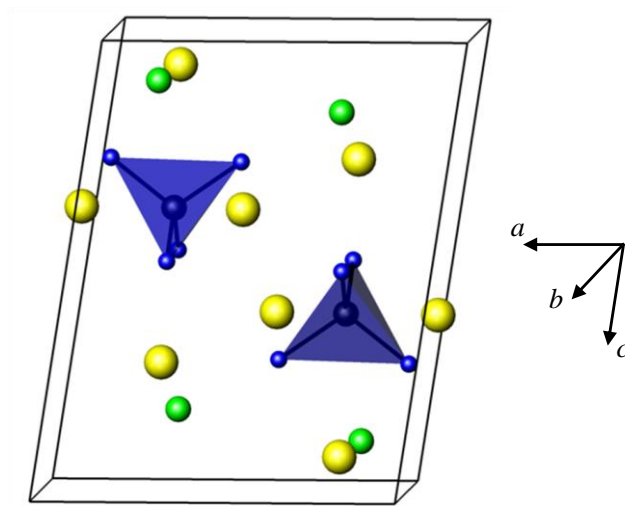


Figure 1-57. Structure of $\text{Ba}_2(\text{WN})_4\text{Cl}_2$. The green, blue and yellow spheres represent chlorine, nitrogen and barium respectively. The blue polyhedra are W-N tetrahedra.

Single crystals of $\text{LiBa}_4[\text{Mo}_2\text{N}_7]\text{BaCl}_2$ were prepared by reacting LiCl with Ba_3MoN_4 in the molar ratio 3:1.¹⁸⁶ The reagents were placed in a molybdenum crucible and heated in argon up to 1050 °C. After five hours the mixture was cooled down to room temperature at 5 °C/hour. The structure contains layers of $[\text{Mo}_2\text{N}_7]^{9-}$ dimers composed by two Mo-N tetrahedra joined via one corner. Ba shows coordination numbers in the range from six to eight and all the baria are coordinated by both nitrogen and chlorine except one, which is only coordinated by nitrogen. Lithium is coordinated by four nitrogen anions and one chlorine anion. The structure of $\text{LiBa}_4[\text{Mo}_2\text{N}_7]\text{BaCl}_2$ is shown in Figure 1-58.

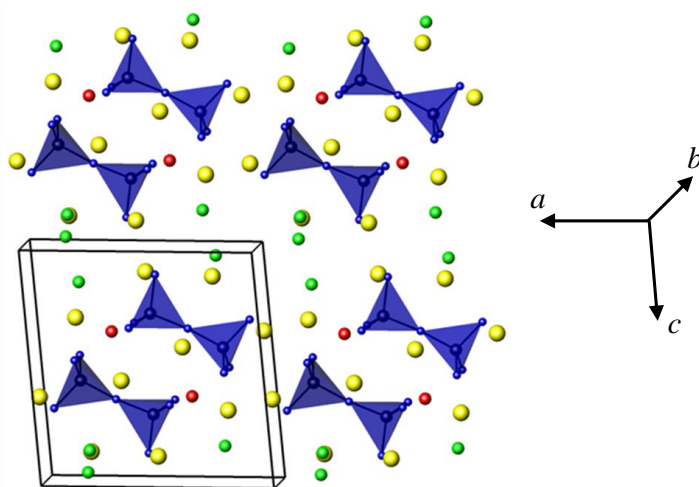


Figure 1-58. Structure of $\text{LiBa}_4[\text{Mo}_2\text{N}_7]\text{BaCl}_2$. The yellow, blue, green and red spheres represent barium, nitrogen, chlorine and Li respectively. The blue pairs of tetrahedra are the Mo-N dimers.

Not a great deal of detail is provided for the preparation of K_2OsNCl_5 except that the method of Clifford and Kobayashi was used and single crystals were grown by slow evaporation of diluted solutions of HCl .¹⁹⁷ The unit cell of K_2OsNCl_5 is orthorhombic ($Pnma$) with unit cell parameters $a = 13.27(2) \text{ \AA}$, $b = 9.85(1) \text{ \AA}$ and $c = 6.84 \text{ \AA}$. The structure is described as consisting of layers of $(\text{OsNCl}_5)^{2-}$ units alternating with layers of K^+ cations along the b -axis (Figure 1-59). In the $(\text{OsNCl}_5)^{2-}$ units, Os^{6+} is said to be coordinated by five chloride and one nitride anions in a distorted octahedral fashion. The distortion derives from the chloride anions moving away from the nitride anion to minimise electrostatic interaction.

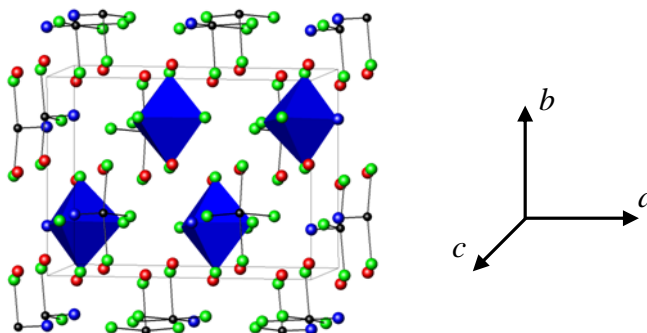


Figure 1-59. Structure of K_2OsNCl_5 . The red, blue, green and red spheres represent potassium, nitrogen and chlorine respectively. The blue octahedra are the $[\text{OsNCl}_5]^{2-}$ units.

Interestingly, the crystallographic data for all nitride-chlorides indicate that the transition metal is only co-ordinated by nitrogen, whereas chlorine only coordinates the more electropositive metal, as Cl^- is more electronegative than N^{3-} .

The only exception is K_2OsNCl_5 in which Os^{6+} is coordinated by both N^{3-} and Cl^- , perhaps due to the low amount of nitride present in the chemical formula. No details are reported on the coordination of K^+ in K_2OsNCl_5 .

Progress beyond binary systems has always been hindered by synthetic difficulties and, sometimes, limitations of analytical methods. General classifications based on composition–structure–property relationships are not yet possible in such an unexplored

area, but with the increased information available from synthetic chemists and physicists this situation may change in the not-too-distant future.

A goal of this work was to prepare a quaternary nitride-fluoride material. As seen in the previous section, currently only nitride-chloride materials are known. In the preparation of oxy-fluoride materials, higher order mixed-anion compounds can be prepared via the structural modification of existing complex oxides. Such an approach has not, to-date, been successfully applied to nitride-fluoride synthesis.

1.5 Properties of Solids

1.5.1 Magnetism

1.5.1.1 Bulk Magnetism

Magnetism is generally associated with the presence of unpaired electrons on an atom. These unpaired electrons give rise to a magnetic dipole moment, the behaviour of which results in the different forms of magnetism.

In compounds where these magnetic moments do not interact there are two types of behaviour prevalent; diamagnetism and paramagnetism.

Diamagnetism is associated with electron pairs, which under an applied magnetic field circulate/precess in such a way as to generate their own magnetic field to oppose the external one. The result is that diamagnetic materials will be repelled by applied fields. Diamagnetism is generally only a small effect (Table 1-8), present in most materials to some degree. The effect is temperature independent and for most magnetic measurements a diamagnetic correction, using Pascal's constants, is performed to remove this contribution from the data.¹⁹⁸

Behaviour	Typical χ values
Diamagnetism	-1×10^{-6}
Paramagnetism	0 to 10^{-2}
Ferromagnetism	10^{-2} to 10^{-6}
Antiferromagnetism	0 to 10^{-2}

Table 1-8. Typical values for magnetic susceptibilities associated with different magnetic behaviour. The susceptibility, χ , is defined later in the text.

Paramagnetism is associated with unpaired electrons. Unpaired electrons generate a moment by spinning around their own axis. In the absence of a magnetic field these spins are randomly orientated (Figure 1-60 (a)). When an external magnetic field is applied the dipoles attempt to align with the applied magnetic field, enhancing it. Thermal interactions act against this alignment and paramagnetism is therefore dependent on temperature.

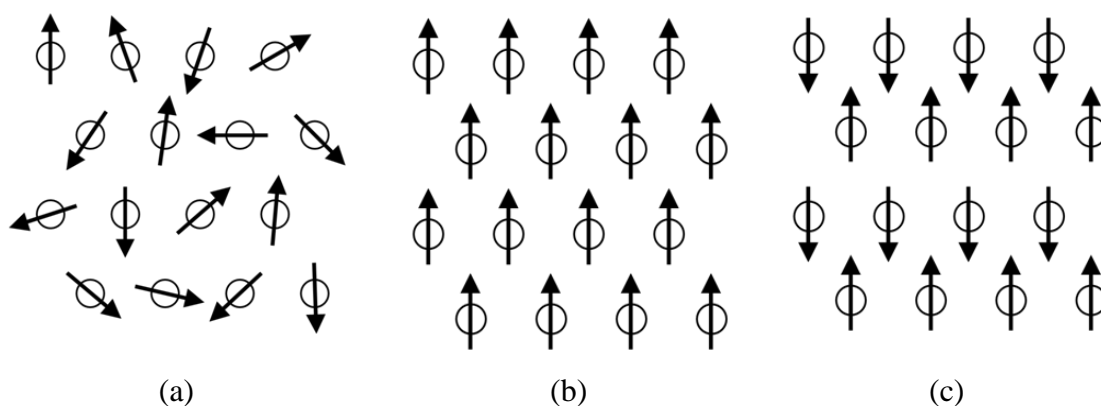


Figure 1-60. Two-dimensional representations of (a) random paramagnetic arrangement of magnetic dipoles, (b) ferromagnetic ordering and (c) antiferromagnetic ordering.

The modification to the applied magnetic field is given by:

$$H = (1 + \chi)H_0 \tag{1-3}$$

where H is the field inside the compound, H_0 is the applied field and χ is the magnetic susceptibility, a measure of the ease of which a substance is influenced by a magnetic

field. When $1 + \chi < 1$ the field is reduced and the material is diamagnetic and when $1 + \chi > 1$ the field is enhanced.

The temperature dependence of paramagnetism is generally defined in terms of χ and, in the case of ideal paramagnetism, obeys the Curie law:

$$\chi = C/T \tag{1-4}$$

where χ is the susceptibility, C is the Curie constant, specific to the compound under analysis, and T is the temperature. A plot of χ versus T is shown in Figure 1-61.

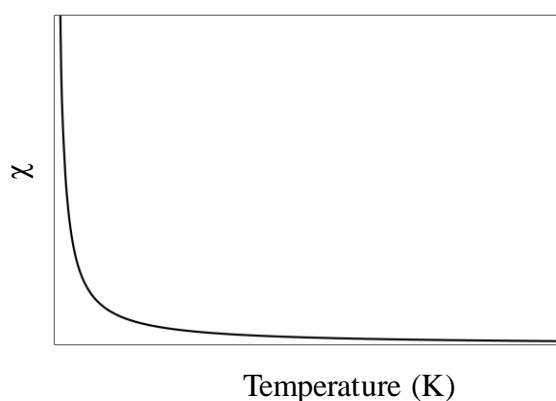


Figure 1-61. Schematic diagram of the susceptibility versus temperature plot for a paramagnetic material.

Another weaker form of paramagnetism, Pauli paramagnetism, is also known. Commonly associated with metals this property arises from electrons in partially filled conduction bands. Electrons obey the Pauli exclusion principle and are paired up with opposite spins. With the application of a magnetic field there is a small polarisation of the electrons. Those electrons whose spins are reinforced by the magnetic field will show a lower energy than those whose spins oppose the magnetic field. Electrons at the Fermi surface may re-orientate in the applied field to the lower energy state. The higher population of one state over the other gives rise to the weak magnetisation.

When magnetic centres interact, either directly or via the electron density of a bridging atom, two of the most common forms of magnetic behaviour observed are ferromagnetism and antiferromagnetism.

Ferromagnetic materials show parallel alignment of the spins on adjacent atoms (Figure 1-60 (b)). The material itself may not show any overall magnetic behaviour as these parallel spins can exist in domains. Each domain consists of parallel alignment of the spins, but the domains themselves are orientated antiparallel to one another. Upon application of a magnetic field these parallel spins re-orientate and act to reinforce the field. If the domains all remain aligned after the magnetic field has been removed the material is said to have been magnetised.

As in the case of paramagnetism, ferromagnetism is also influenced by thermal motions, acting to reduce and randomise the spin alignment. A standard χ versus temperature plot for a ferromagnet is given in Figure 1-62.

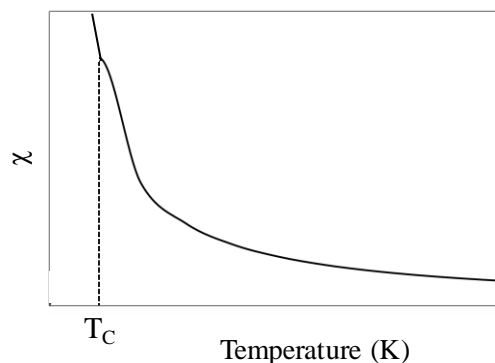


Figure 1-62. Schematic diagram of the susceptibility versus temperature trends for a ferromagnetic materials.

As the temperature is increased χ reduces with increased thermal randomisation of the spins and at a critical temperature, the Curie temperature, T_c , the spin alignment is destroyed and the sample becomes paramagnetic. Above the T_c the susceptibility data obeys a modified version of the Curie-Weiss law:

$$\chi = \frac{C}{T - \theta}$$

(1-5)

where C is the Curie constant, T is the temperature and θ is the Weiss temperature. θ is positive for ferromagnets.

Antiferromagnetic materials show antiparallel alignment of the magnetic spins (Figure 1-60 (c)). The interactions in antiferromagnetism are mediated through a bridging atom as direct spin interaction favour ferromagnetism. One mechanism giving rise to antiferromagnetic interaction, mediated through a bridging atom, is superexchange. An illustration of superexchange is shown in Figure 1-63, with only a single unpaired electron on each metal centre given. The two d -block metals shown are separated by a p -block anion in a 180° M-L-M arrangement. The filled p -orbital of the bridging anion donates part of its electron density to the metals. If the spin on the first metal centre is taken to be “up” then, by the Pauli exclusion principle, the donated electron of the p -orbital must be spin “down”. Electron density is also transferred from the p -orbital to the second metal centre. This shows a spin “up” alignment yielding a spin “down” orientation for the second metal. The alignment between the two metal centres is therefore antiparallel i.e. antiferromagnetic.¹⁹⁹

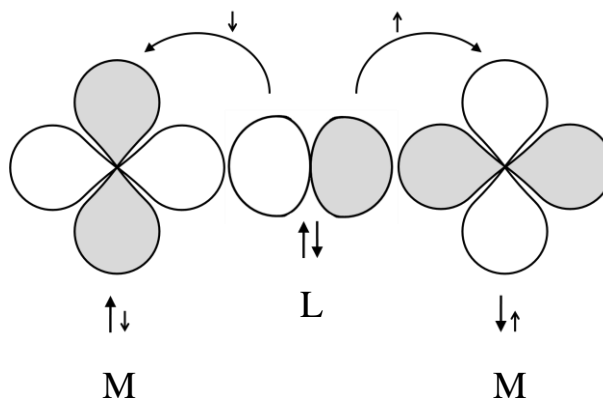


Figure 1-63. A simple representation of superexchange in a linear M-L-M (Two d -block metals bridged by a p -block anion). Reproduced from the literature.¹⁹⁹

Antiferromagnetic materials do not act to enhance the applied magnetic field. The antiparallel alignment of the spins is increasingly disrupted by thermal motion and like ferromagnetic materials these will undergo a transition to paramagnetism at a critical temperature, the Néel temperature, T_N (Figure 1-64). Above T_N the susceptibility data obeys the Curie-Weiss law and θ is negative.

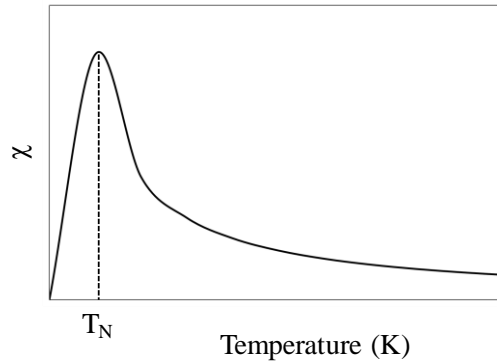


Figure 1-64. Schematic diagram of the susceptibility versus temperature trends for antiferromagnetic materials.

By recording the variation in χ with temperature the magnetic behaviour of a sample can be obtained.

Magnetic materials are also commonly described in terms of their magnetic moment, μ_{eff} , which may be derived from the χ measurements and used to calculate the number of electrons per magnetic centre.

$$\mu_{eff} = \left(\frac{3k}{N_a \beta^2} \right)^{1/2} (\chi T)^{1/2} \quad (1-6)$$

where k is the Boltzmann's constant, N_a is Avogadro's constant β is the Bohr magneton, χ is the susceptibility and T the temperature.

1.5.1.2 Low Dimensional Magnetism

Low-dimensional or short-range magnetic order can be described as consisting of interactions between nearest neighbour magnetic ions, occurring in less than three spatial dimensions. These interactions can occur via directly or via an intervening ligand between the metal centres (superexchange).²⁰⁰

When the interactions are between adjacent linear sites the spin Hamiltonian energy term for two magnetic ions is:

$$H = -2J\Sigma S_i \cdot S_j \quad (1-7)$$

where J is the exchange constant and S_i and S_j are the spin operators of the interacting ions i and j .²⁰⁰ This Hamiltonian can be expanded to:

$$H = -2J\Sigma[\alpha S_{zi} \cdot S_{zj} + \beta(S_{xi} \cdot S_{xj} + S_{yi} \cdot S_{yj})] \quad (1-8)$$

When $\alpha = 1$ and $\beta = 0$ the system is said to consist of linear chains with no interaction between them i.e. a one-dimensional system. This is known as the Ising model.²⁰⁰

When $\alpha = 0$ and $\beta \neq 0$ the spins are interacting in two dimensions, this is known as an XY Hamiltonian model. Finally, when $\alpha = \beta = 1$ the system has spin interactions in all three dimensions and the system is isotropic and follows the Heisenberg model.²⁰⁰ In general, it is only the highly anisotropic systems that are characterised as Ising materials. For those materials where the anisotropy is less pronounced the Heisenberg model is more representative of the magnetic interactions involved.²⁰¹

One of the main techniques, which can provide data about magnetic interactions, is neutron diffraction. This was used in the analysis of Ba_2MS_3 ($M = Co, Mn$) compounds in chapter 3.

2 Experimental Techniques

Solid state chemistry calls for the use of a wide range of synthetic and characterisation techniques. The following section aims to provide a brief introduction to the important techniques and apparatus used throughout this work.

2.1 Synthetic Methods

There are a number of synthetic approaches used to prepare crystalline materials and these are often specific to the type of materials being prepared. According to the reaction conditions used, synthetic methodology can be classified into two main groups: the “hard” and “soft” chemistry methods. “Hard” chemistry is often considered to include the more traditional solid state reactions i.e. direct reaction of solid state reagents at high temperatures, but generally refers to reactions under relatively harsh environments with high temperatures, pressures etc. “Soft” chemistry usually applies to reactions carried out under milder reaction conditions, i.e. at lower temperatures, and can often provide a degree of control over the structure of the final product. A brief description of each of these preparative methods in the context of this work is shown in the following subsections.

2.1.1 “Hard” Chemistry

The best known solid state synthetic method is the ceramic method, also known as the “shake ‘n’ bake” method. Solid precursors are intimately ground together before heating in a furnace for an extended period (often several days). High temperatures are commonly used in these reactions ($T > 700\text{ }^{\circ}\text{C}$) and therefore solid state reactions can be included in the group of ‘hard’ chemistry methods. The high temperatures are required to aid diffusion of atoms within the highly ordered solids. This is an essential process in the production of new phases. The ceramic method is favoured for its simplicity, but the high temperatures of reaction give rise to a number of disadvantages. The poor surface contact between the grains and low rates of diffusion, despite the high

temperatures, often means that the reaction mixture requires several re-grinding and heating steps. The large amount of energy provided by these temperatures ensures the final product of the reaction will be the most thermodynamically stable outcome. This may show no structural relation to the original reagents. There is, therefore, no overall structural control over the outcome of the reaction.

High temperature reactions of this general type are used in several of the preparations outlined here, in particular the formation of the ternary sulfide, Ba_2CoS_3 (chapter 3), the Ce_2MnN_3 type nitrides, $\text{Ce}_{2-x}\text{A}_x\text{MnN}_3$ and $\text{Ce}_2\text{Mn}_{1-x}\text{M}_x\text{N}_3$ (chapter 4).

2.1.2 “Soft” Chemistry

“Soft” chemistry, also referred to as “chimie douce”, is commonly performed at low temperatures of less than 600 °C. There are a number of advantages of ‘soft’ over ‘hard’ chemistry. One such advantage of lower temperatures is it allows for the use of solvents allowing co-precipitation and sol-gel reactions. Co-precipitation and sol-gel syntheses both optimise the mixing of reagents via either precipitation of a suitable intermediate or, in the case of the sol-gel method, the formation of solvated mixed metal polymers. These intermediate products are then heated in a furnace. By maximising the mixing of these reagents, and reducing the diffusion distances a lower temperature can be used.

While high temperature conditions provide a large amount of energy, enough to activate the transition to the thermodynamically stable product (Figure 2-1), the lower temperature of “soft” chemistry can be sufficient to yield kinetically stable phases.

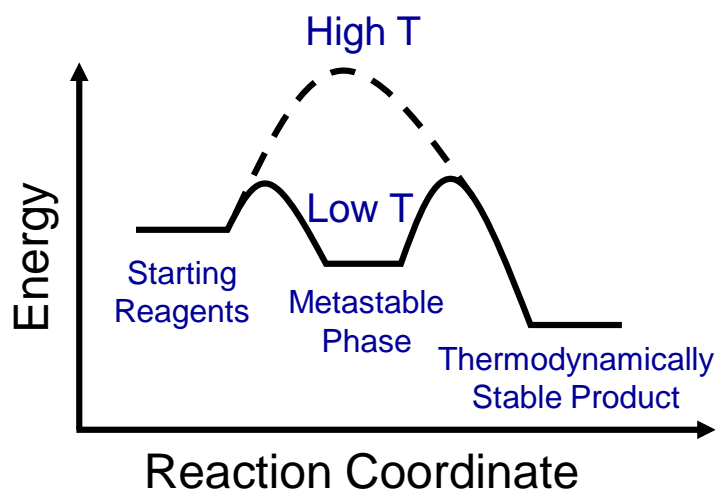


Figure 2-1. Schematic diagram showing the reaction to the thermodynamically stable and metastable products.

The metastable phase will result when enough energy is provided to activate the transition to the “potential well”, but is insufficient to allow the formation of the thermodynamically stable phase. Such a transition is often only possible within a very narrow range of reaction conditions and can be very difficult to optimise.

An advantage of “soft” chemistry is that the lower temperatures used reduce the extent of structural modification in the reaction. The result of which is that the structure of the final product may show similarities to the structure of the initial reagents. Reagents can potentially be selected based on their structure and subtle modifications made, providing some degree of control over the reaction outcome. Unfortunately, this requires a structurally desirable precursor, which may not be available.

Examples of these types of structural modifications include the fluorination of ternary oxides (section 1.1.3), where a structural modification to the anion network occurs while leaving the cation distribution relatively unaltered, and intercalation reactions. Intercalation reactions, the insertion of additional ions into an existing structure, often occur under particularly mild reaction conditions and have been used in the preparation of Li-ion batteries (e.g. LiCoO_2) and in the preparation of superconductors (e.g. $\text{Li}_{0.16}\text{ZrNCl}$).^{133, 202}

The low temperature approach of structural modification is exploited in the fluorination of Ce_2MnN_3 , which shows an anion-deficient K_2NiF_4 -type structure before fluorination, and transforms into a K_2NiF_4 -type material, with additional staged fluorine insertion upon reaction with fluorine gas (chapter 5).

2.2 Equipment

2.2.1 Glove Boxes

For the majority of the work shown here, the reagents and products of reaction are air- or moisture-sensitive. These materials, therefore, were handled under an inert atmosphere. This was achieved through the use of glove boxes, shown in Figure 2-2 and Figure 2-3.



Figure 2-2. A Braun MB 150B-G glove box.

The glove boxes operate with a permanent argon atmosphere. This atmosphere is circulated, passing over molecular sieves and copper based catalysts, to remove moisture and oxygen. The glove boxes contain oxygen and moisture sensors and levels are maintained at $\text{O}_2 \leq 0.1$ ppm and $\text{H}_2\text{O} \leq 0.1$ ppm. Access into and out of the glove

boxes is achieved via transfer ports on the side of the instruments. These ports have two doors, one external and one internal, so that air from outside can be replaced with argon prior to entering the glove box chamber. The ports are evacuated using a rotary pump and refilled with argon gas. This evacuation procedure is repeated several times to minimise the amount of air entering the system.



Figure 2-3. A M-Braun Lab-Star glove box.

2.2.2 Furnaces

Generally speaking, two types of furnaces were used in the preparation of the materials reported here: box furnaces and tubular furnaces.

2.2.2.1 Box Furnace

Box furnaces (muffle or chamber furnaces) commonly consist of a cuboidal chamber with heating elements located in the walls. The box furnace used was a Carbolite CWF 1200, shown in Figure 2-4 and has an operational range of 25-1200 °C.



Figure 2-4. The Carbolite CWF 1200 box furnace.

The box furnace alone does not support the reaction of air or moisture sensitive materials. When an oxygen-free atmosphere was required, reactions were performed within a sealed vessel. A representation of the Parr acid digestion bomb, referred to here as a thermal bomb, used in these reactions is shown in Figure 2-5.

This thermal bomb consists of a cylindrical (45 cm³) Teflon inner chamber encompassed by a stainless steel, screw top, outer shell.

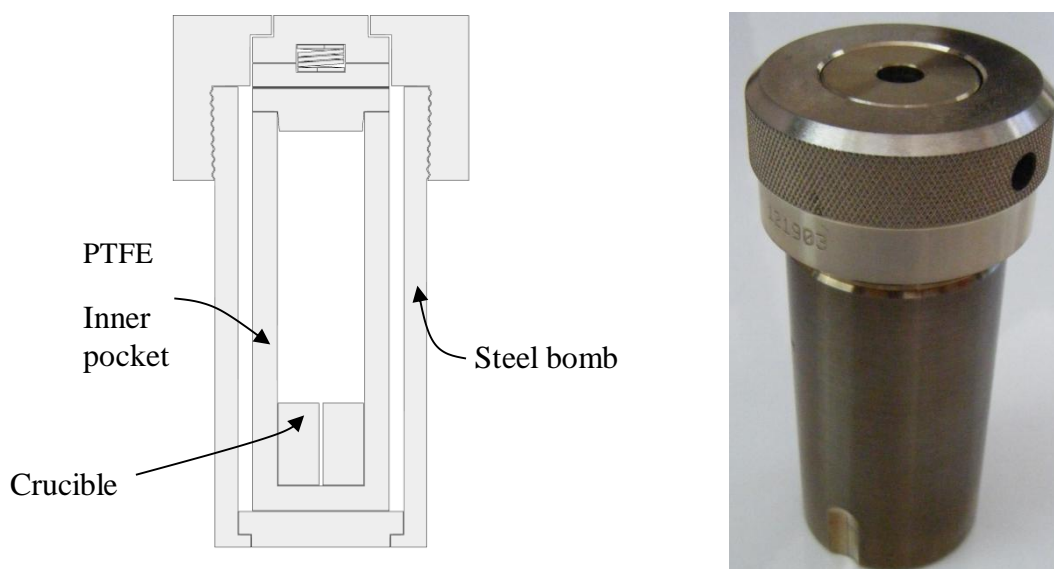


Figure 2-5. Schematic of (a) the Parr acid digestion bomb and (b) a photo of the digestion bomb.

The thermal bomb can be heated up to a temperature of 250 °C. This vessel has a spring loaded pressure release mechanism located on the screw top to prevent explosions in the event of internal pressure build up. The small size of the vessel ensures insertion and removal in and out of the glove box and ensures that all reactions are performed under an argon atmosphere (i.e. the atmosphere of the glove box).

The interior of the thermal bomb is made of Teflon (polytetrafluoroethylene ((CF₂CF₂)_n)) which is stable to fluorine gas as opposed to quartz, which is prone to fluorine absorption and corrosion. This was fundamental for carrying out fluorination reactions in this work (chapter 5).

2.2.2.2 Tubular Furnaces

As the name suggests, a tubular furnace consists of a cylindrical (tubular) heating region surrounded by the heating elements and thermal insulation (Figure 2-6). An inner reaction tube is commonly inserted into these furnaces, in order to contain reagents, protect the delicate inner workings of the furnace from chemical emissions and to allow control over the reaction atmosphere used.



Figure 2-6. An example of a tubular furnace.

A number of different tubular furnaces were employed to best suit the requirements of each reaction. The maximum operating temperature of these furnaces is 1200 °C.

Tubular furnaces were used for reactions carried out under N_2 , NH_3 , CS_2 and F_2/N_2 atmospheres in the preparation of nitrides, sulfides and nitride-fluorides.

2.2.2.2.1 Reactions Under N_2 Gas

Where the reactions of solid precursors took place under a nitrogen atmosphere the experimental set-up shown in Figure 2-7 was used. This consists of a quartz reaction vessel, which contains the reagents and can be sealed from air via a lid with two taps. In this way the reagents can be inserted in the tube inside the glove box, under an argon atmosphere, sealed and transferred to the tubular furnace. Once outside of the glove box, the sealed quartz tube is placed in a tubular furnace and attached to the nitrogen supply. The gas is directed through the 'by-pass' tube on the top of the reaction vessel. When the system has been purged of air, the gas stream is re-directed through the reaction vessel. This ensures there is no air present in the system.

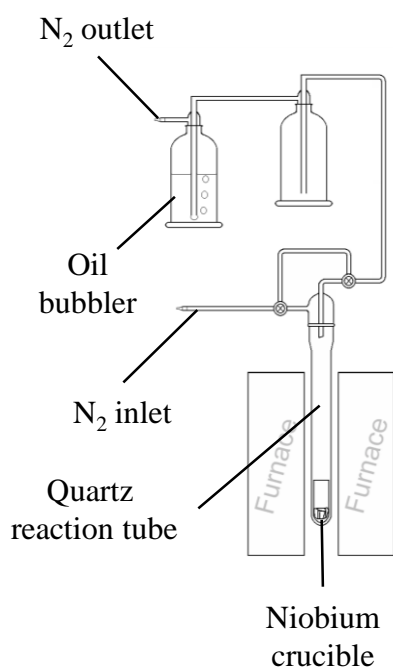
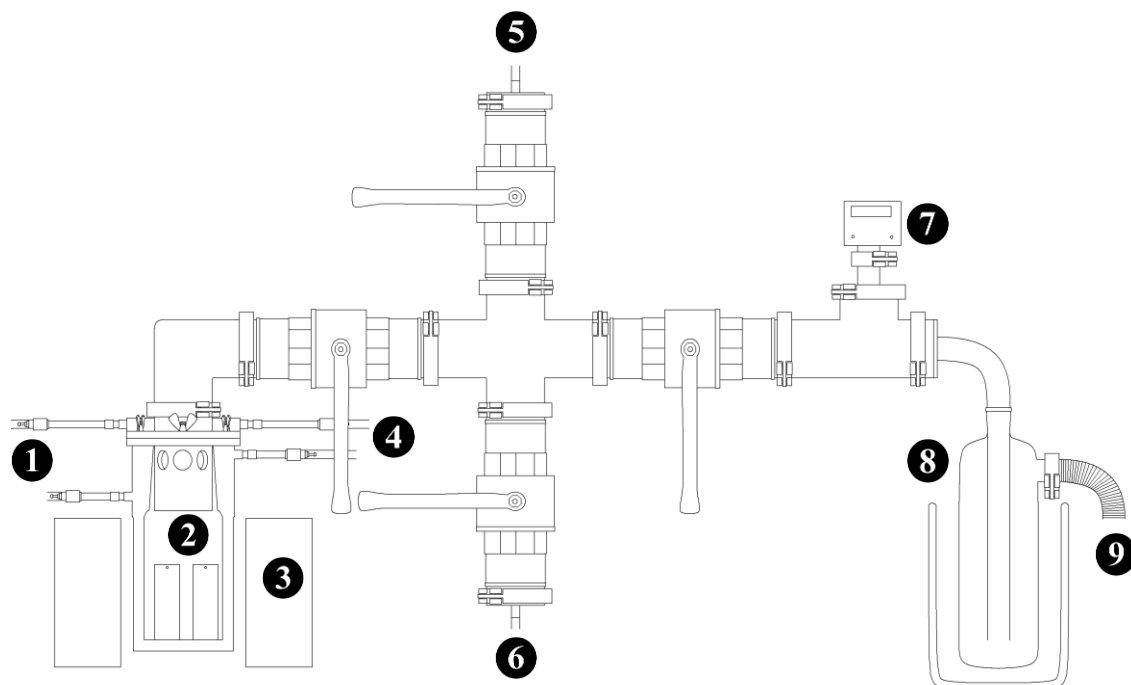


Figure 2-7. Representation of the apparatus used in the reactions under N_2 gas.

A more complex reaction set-up, for reactions under nitrogen, was also used. This was specifically for the reaction of materials using molten metals as solvents. The reaction of air sensitive materials in molten metals requires a reaction vessel capable of being

transferred to the glove box, permitting a dynamic nitrogen atmosphere and a system capable of removing unreacted metals via vacuum distillation. The system used here is shown in Figure 2-8.



Key

- ① Water inlet to cooling jackets of reaction pot.
- ② Reaction vessel, containing the steel crucible in which the compounds are placed.
- ③ Tubular furnace
- ④ Water outlet, to waste.
- ⑤ Nitrogen gas inlet.
- ⑥ Nitrogen gas outlet, to oil bubbler.
- ⑦ Pressure meter.
- ⑧ Condenser, liquid nitrogen cooled to trap remaining metal vapour before vacuum pump.
- ⑨ Outlet to vacuum and turbo vacuum pumps.

Figure 2-8. Representation of the experimental set-up used with the reactions in molten metals and distillation process.

The reaction vessel itself is made up of a cylindrical steel chamber, which can be inserted into a large, vertical, tubular furnace. In the top of the reaction vessel is a water cooled cold finger (Figure 2-9), which rests just beyond the heating zone of the furnace. This acts to protect the seal of the vessel from the heat and, when removing the metal 'solvent' via evaporation, provides a cool surface to condense the metal vapour. Above this point the vessel can be sealed from the system (Figure 2-8) and placed into a glove box. For reaction in nitrogen gas, the argon is removed from the system using a vacuum pump prior to the reaction. When performing the vacuum distillation step the system is evacuated using a Leybold PT 50 turbo vacuum pump, which can achieve pressures of around 1×10^{-7} mbar. The system is generally not used for temperatures above 850 °C.

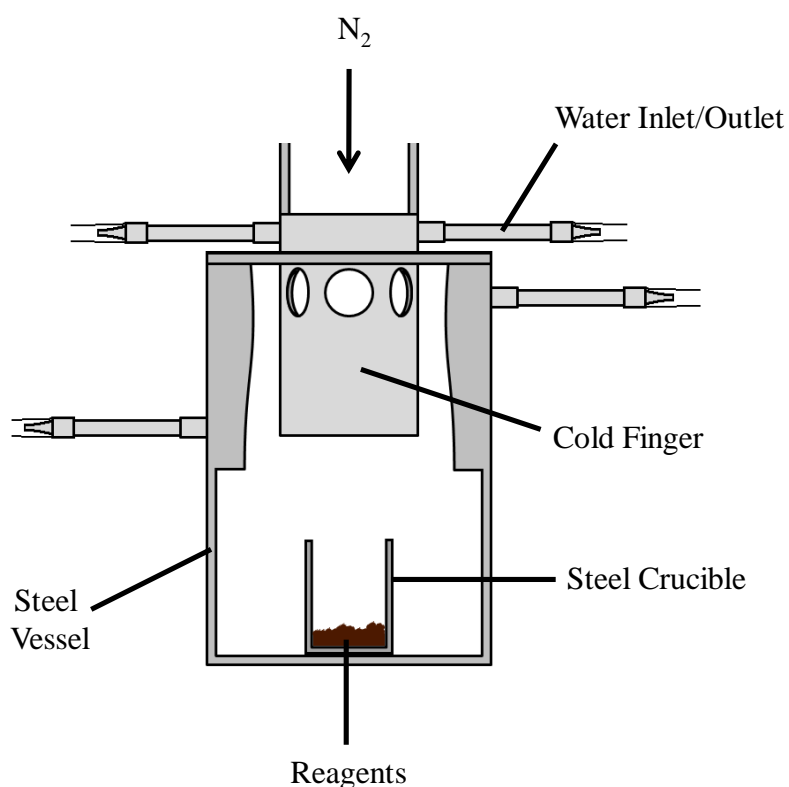


Figure 2-9. Expanded view of the interior of the reaction vessel used with reactions in molten metals.

The reactions in NH₃, CS₂ and F₂/N₂, show a similar equipment set-up, utilizing horizontal tubular furnaces with cylindrical reaction tubes.

2.2.2.2.2 Reactions in NH_3 Gas

Where the reaction with flowing ammonia gas was required, the apparatus shown in Figure 2-10 was used. This consists of a quartz reaction vessel, which can be sealed from the atmosphere via two taps. In this case, due to the dimensions of the reaction vessel a split-hinge furnace (a furnace which may be opened along the central axis) was used.

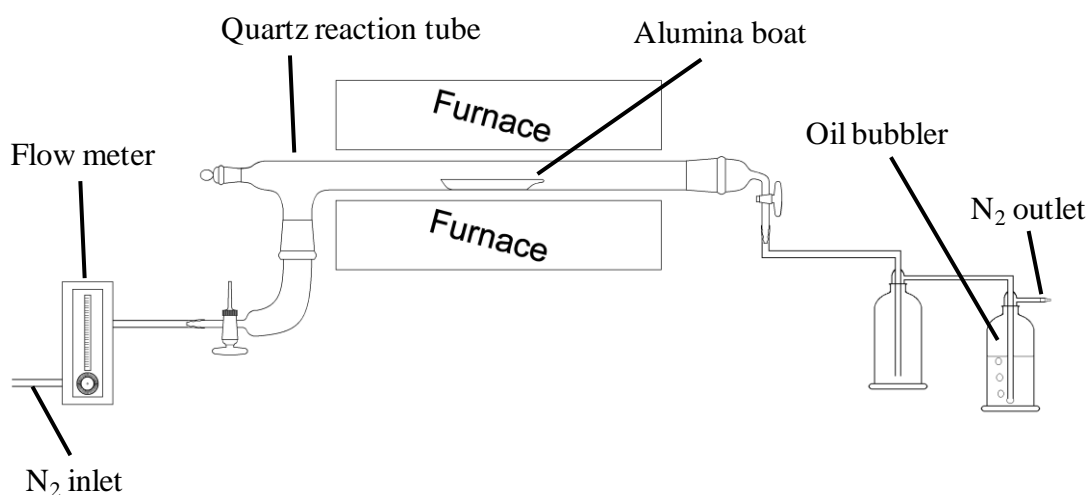


Figure 2-10. Representation of the apparatus used in the reactions under NH_3 gas.

2.2.2.2.3 Reactions with CS_2 Vapour

For reactions with CS_2 , a nitrogen gas cylinder is connected to the reaction tube via plastic pipes and a Dreschel bottle containing concentrated H_2SO_4 , which acts to remove moisture from the carrier gas. This Dreschel bottle is connected to a second Dreschel bottle containing liquid CS_2 (Figure 2-11). CS_2 has a low vapour pressure, which can be exploited by using N_2 as a carrier gas to vaporise the CS_2 and carry it through the system. The CS_2/N_2 vapour passes into the quartz reaction tube and over the sample. The gas stream leaving the quartz reaction tube was treated by passing it through a Dreschel bottle containing paraffin oil. This seals the system from air and acts to reduce the release of any residual CS_2 . The materials prepared via this method, Ba_2MS_3 ($\text{M} = \text{Co}, \text{Mn}$), are not significantly air or moisture sensitive and therefore did not require transfer to the glove box.

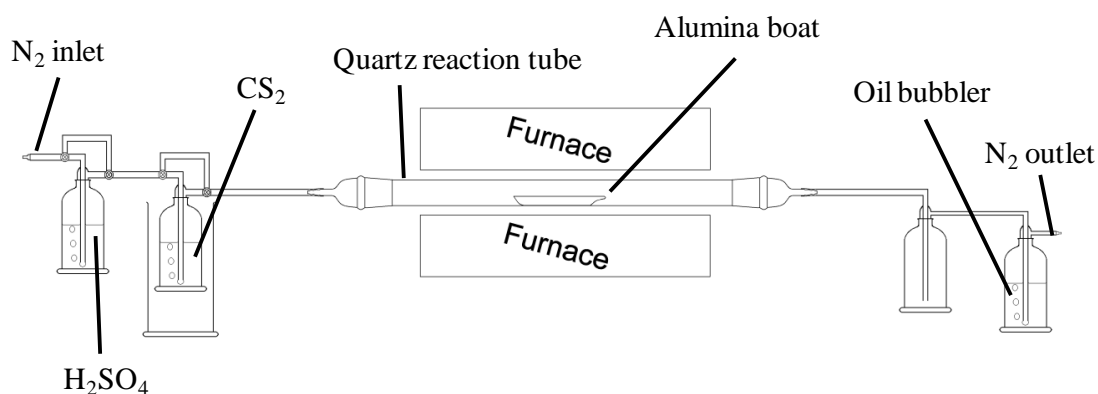


Figure 2-11. Representation of the apparatus used in reactions with CS_2 .

2.2.2.2.4 Reactions with F_2/N_2 Gas

The reaction set-up used in the fluorination reactions is similar to that used in reactions with NH_3 gas. However, due to the high reactivity of F_2 gas towards quartz, a nickel (or steel) reaction tube was used in the fluorinations (Figure 2-12). Before use the tube was passivated with fluorine gas to prevent significant absorption of fluorine upon reaction. The system itself is connected to two gas lines: F_2/N_2 for the reaction and N_2 to allow the system to be purged with N_2 before and after reaction. The fluorine gas was passed over NaF pellets to remove any HF prior to entering the reaction vessel.

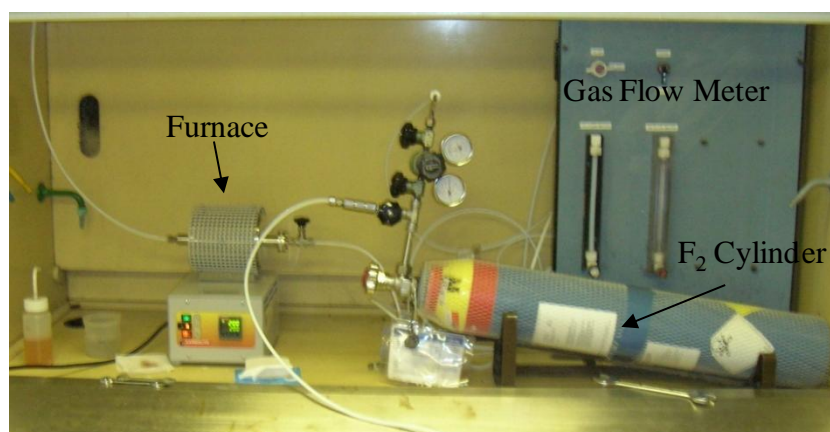


Figure 2-12. Apparatus used in the fluorination of Ce_2MnN_3 by F_2 gas.*

* Provided and used in collaboration with Colin Greaves at Birmingham University.

2.3 Structural Determination

2.3.1 Crystallography

Crystals of solid compounds possess a highly ordered array of atoms propagating in all three spacial dimensions. Crystals, therefore, show a high degree of symmetry, which can be used to simplify and describe the crystal structure.

2.3.1.1 Symmetry

Symmetry in crystals can be studied by means of symmetry operations. The symmetry operations that are important in solid state chemistry can be split into two: the point symmetry, applying to the symmetry of isolated shapes in which at least one point will remain unaltered after application of a symmetry operation, and translational symmetry operations. A shape is said to possess one or more of the symmetry elements when, upon application of the symmetry operation, the resulting configuration is indistinguishable from the initial form.

The point symmetry operations and the Hermann-Mauguin symbols used to describe them are as follows:

Rotation – The rotation of a shape around an axis in an anti-clockwise manner by $360^\circ/n$, where n is an integer. The symbol used to describe the rotation, n , can take the value of 1, 2, 3, 4 or 6 in crystal structures.

Reflection – The reflection of an object in a mirror plane. Here every point is recreated at a position on the opposite side of a mirror plane at a distance equal to that between the initial object and the plane. A vector connecting these points must be normal to the mirror plane. The reflection operation takes the symbol m .

Inversion – Given by the symbol ($\bar{1}$), this operation involves the inversion of each point through an inversion centre so that a point at (x, y) , with the inversion centre at the

origin, will generate an equivalent point at (\bar{x}, \bar{y}) , where the bar denotes a negative value.

Rotoinversion – A combination of rotation anticlockwise by $360^\circ/n$ followed by inversion through an inversion centre located on the axis of rotation. The symbol used to describe this symmetry operation is therefore a combination of the constituent elements, \bar{n} e.g. $\bar{3}$ a three fold rotoinversion. The rotoinversion is also referred to as an improper rotation axis.

Rotoreflexion – This involves a rotation anticlockwise of $360^\circ/n$ anti-clockwise followed by a reflection in a mirror plane perpendicular to the axis of rotation. This is given the symbol \tilde{n} . Due to the similarity with rotoinversion, rotoreflexion is generally not used to describe structures. The relation between rotoreflexion and rotoinversion is shown in Table 2-1.

Axis of rotoreflexion	Axis of rotoinversion
$\tilde{1}$	$\bar{2} (m)$
$\tilde{2}$	$\bar{1}$
$\tilde{3}$	$\bar{6}$
$\tilde{4}$	$\bar{4}$
$\tilde{6}$	$\bar{3}$

Table 2-1. Comparison between rotoreflexion and rotoinversion.²⁰³

When the symmetry is extended into three-dimensional crystal structures further symmetry operations are possible and these include a translational component:

Rototranslation – A combination of a rotation of $360^\circ/n$ followed by a translation parallel to the axis of rotation for distance of t . The operation is given a symbol n_m , where m is an integer and $t = m/n$. An example is a 4_1 rototranslation, which involves a rotation anti-clockwise by 90° followed by a translation of $\frac{1}{4}$ of the cell edge parallel to the rotational symmetry element. The rototranslation element is commonly referred to as a screw axis.

Reflectotranslation – A combination of a reflection in a mirror plane followed by a translation parallel to this plane. This element is commonly referred to as a glide plane.

The magnitude of the translation and the corresponding Hermann-Mauguin symbols are dependent on the orientation of the glide planes, but generally glide planes along a , b and c contain translational components along $\mathbf{a}/2$, $\mathbf{b}/2$ and $\mathbf{c}/2$ respectively. n corresponds with diagonal glides i.e. possessing either translations diagonally along a cell face or body diagonal by $\frac{1}{2}$ e.g. $\frac{1}{2}(\mathbf{a}+\mathbf{b})$. Finally are the diamond glide planes, d , which are similar to n , however involve a translation of only $\frac{1}{4}$ of the specified vector e.g. $\frac{1}{4}(\mathbf{a}+\mathbf{b})$.

2.3.1.2 Crystal Systems

The unit cell is a three dimensional section of a structure, which when translated a distance equal to its dimensions, parallel to its edge and without re-orientation, will yield the crystal structure. In essence the crystal structure is a three-dimensional tessellation pattern of unit cells. The unit cell is usually chosen to highlight the symmetry of the system. The cell is defined in terms of the length of the cell edges, a , b and c and the angles that separate them α , β and γ . α is defined as the angle between \mathbf{b} and \mathbf{c} , β is the angle between \mathbf{a} and \mathbf{c} and γ between \mathbf{a} and \mathbf{b} . These are shown in Figure 2-13.

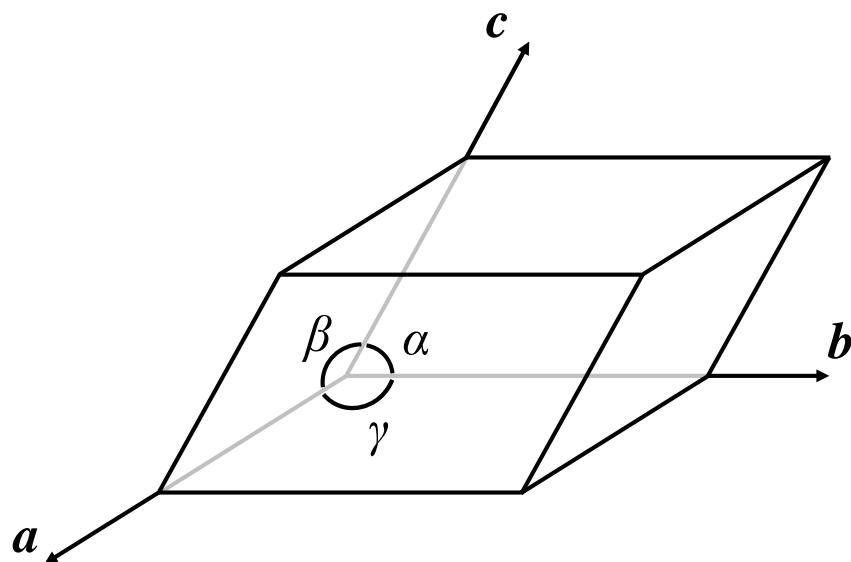


Figure 2-13. The unit vectors and angles defining the unit cell.

In crystallography the unit cell of any possible ordered crystalline materials can be classified within one of the seven crystal systems depending on its symmetry. The relationship between each of the cell dimensions are preordained by the symmetry of the system. The general relationships between the lattice parameters are outlined in Table 2-2 and the symmetry requirements of each system in Table 2-3.

System	Unit cell
Triclinic	$\alpha \neq \beta \neq \gamma \neq 90^\circ$ $a \neq b \neq c$
Monoclinic	$\alpha = \gamma = 90^\circ$ $\beta \neq 90^\circ$ $a \neq b \neq c$
Orthorhombic	$\alpha = \beta = \gamma = 90$ $a \neq b \neq c$
Trigonal/rhombohedral	$\alpha = \beta = \gamma \neq 90^\circ$ $a = b = c$
Hexagonal	$\alpha = \beta = 90^\circ$ $\gamma = 120^\circ$ $a = b \neq c$
Tetragonal	$\alpha = \beta = \gamma = 90^\circ$ $a = b \neq c$
Cubic	$\alpha = \beta = \gamma = 90^\circ$ $a = b = c$

Table 2-2. The seven crystal systems.²⁰³

2.3.1.3 Lattices

Lattices are mathematical concepts used in the description of crystalline materials. Lattices are made up of infinite ordered arrays of points, each of which show identical surroundings. Placing atoms or groups of atoms, referred to as the basis or motif, on each of these points generates the crystal structure.

The four lattice types are the primitive, P, the body centred, I, the face-centred (all face-centred), F, and the face-centred (A-centred, B-centred, C-centred), A, B or C. A representation of these lattice types is given in Figure 2-14, where the lattices are defined with the origin set on a lattice point. In this way lattice points at the corners of the unit cell are shared by eight adjacent cells, and those on faces are shared by two unit cells. The A, B and C lattices can be viewed as the primitive unit cell with an additional

pair of lattice points in the centre of opposite cell faces on the bc , ac and ab faces respectively.

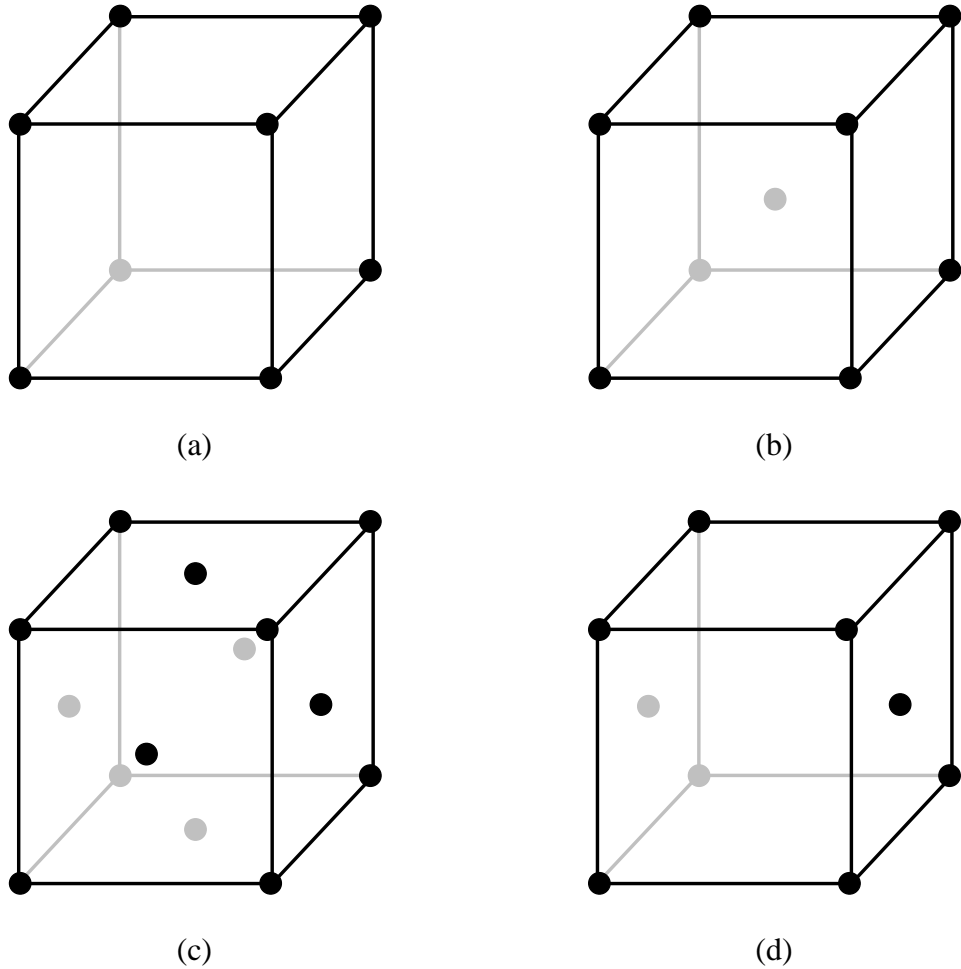


Figure 2-14. Representations of the (a) primitive (P), (b) body-centred (I), (c) face-centred (F) and (d) C-centred lattices.²⁰⁴ The cubic shape is used for simplicity.

When the four lattice types are considered in combination with the seven crystal systems, the constraints imposed by the minimum symmetry requirements of the crystal systems give rise to fourteen lattices, known as Bravais lattices.

Crystal system	Lattice symbol	Minimum symmetry requirements
Triclinic	aP	None
Monoclinic primitive	mP	One two-fold axis or one symmetry plane
Monoclinic centred	mC	
Orthorhombic primitive	oP	Any combination of three mutually perpendicular two-fold axes or planes of symmetry
Orthorhombic C-face-centred	oC	
Orthorhombic body-centred	oI	
Orthorhombic face-centred	oF	
Tetragonal primitive	tP	One four-fold axis or one four-fold improper axis
Tetragonal body-centred	tI	
Trigonal (Rhombohedral)	hR	One three-fold axis
Hexagonal primitive	hP	One six-fold axis or one six-fold improper axis
Cubic primitive	cP	Four three-fold axes along the body diagonals
Cubic body-centred	cI	
Cubic face-centred	cF	

Table 2-3. The 14 Bravais lattices.²⁰³⁻²⁰⁵

A three-dimensional shape can possess any number of symmetry elements giving rise to an unlimited number of point groups. A point group is simply a classification used to describe an isolated shape based on the point symmetry it possesses. In a similar way to the point symmetry elements, these groups will include at least one point that remains unaltered.

The crystal systems introduce the restriction of interconnecting polygons/unit cells with no voids between them, reducing the possible number of point groups. For example an interconnecting network of unit cells cannot show a five-fold rotation axis without destroying the tessellation of the polygons.

In the same way, a description of an array of points fails to account for the limitations introduced when a motif is placed upon each of these points. If the motif does not

possess the symmetry of the lattice the overall symmetry of the array is reduced. The possible structural arrangements based on the point symmetry elements, when associating a three-dimensional shape with the crystal systems, are the 32 point groups.

Finally, if the translational symmetry elements are combined with the 14 Bravais lattices and the 32 point groups a set of 230 space groups result. These space groups provide a description of all the possible three-dimensional repeating patterns available for crystalline materials.

A more in depth description of the crystallographic concepts, touched upon here, can be found in a large number of solid state text books and literature reviews.²⁰³⁻²⁰⁷

2.3.1.4 Space Groups and Notation

The 230 space groups are usually defined in terms of the symmetry elements they possess. The space groups are numbered and also given a unique symbol, which shows the most significant symmetry elements of the group. The symbol can be split into two parts, the first corresponding with the lattice i.e. P, F, I, A, B, C, R (Primitive Rhombohedral), and the second a set of symmetry elements as defined by the Hermann-Mauguin symbols. For example space group 71, *Immm*, is made up of a body centred cell with three mutually perpendicular mirror planes. There are also a number of other symmetry elements present as a consequence of these three planes, including inversion centres, two-fold rotation axes and two-fold screw axes.

In order to describe a crystal structure it becomes necessary to identify the position of each of the atoms present within the unit cell. This is usually defined as a fraction of the unit cell edge with the coordinates (x, y, z). Alternatively, any position can be defined as a vector **r**:

$$\mathbf{r} = x\mathbf{a} + y\mathbf{b} + z\mathbf{c} \tag{2-1}$$

where x, y and z are integers or rational numbers.

In cases where there are only a few atoms present in a unit cell this is a relatively simple task. However as the structures become more complex the number of atoms present grows quite rapidly. It is here that the symmetry of the systems becomes useful as a structure can be defined by a small number of atoms from which the whole cell can be reproduced when the relevant symmetry elements are applied. This group of atoms is known as the asymmetric unit.

The relatively simple case of NaCl is considered here. NaCl consists of two interconnected face centred cubic lattices, one of sodium atoms and one of Cl atoms, displaced by $\frac{1}{2}a$, $\frac{1}{2}b$, $\frac{1}{2}c$, in which the sodium is in octahedral coordination with six chloride anions. If we describe each of the atomic positions in the unit cell of NaCl independently it requires 27 sets of coordinates. With the aid of the symmetry NaCl can be defined simply via one sodium position, one chloride position and the space group.

If a lattice point is taken as the origin, any other point will be given by the vector $\mathbf{P}(uvw)$, where:

$$\mathbf{P}(uvw) = u\mathbf{a} + v\mathbf{b} + w\mathbf{c} \tag{2-2}$$

u , v and w are taken as integers or rational numbers. As shown in Figure 2-15, each point can therefore be described in terms of the u , v and w values e.g. 001, a point one unit along c from the origin, 120 a point one unit cell along a and two along b . In cases where u , v or w take negative values they are represented as \bar{u} , \bar{v} and \bar{w} e.g. $\bar{1}00$ is a point one unit cell along $-a$.

These values can also be used to describe direction. In this case the direction is given by $[uvw]$, where u , v and w are the simplest set of integers necessary to define the vector e.g. $[884]$ is represented as $[221]$. It is possible for directions to be equivalent by the symmetry of the lattice. These families of directions take the notation $\langle uvw \rangle$.

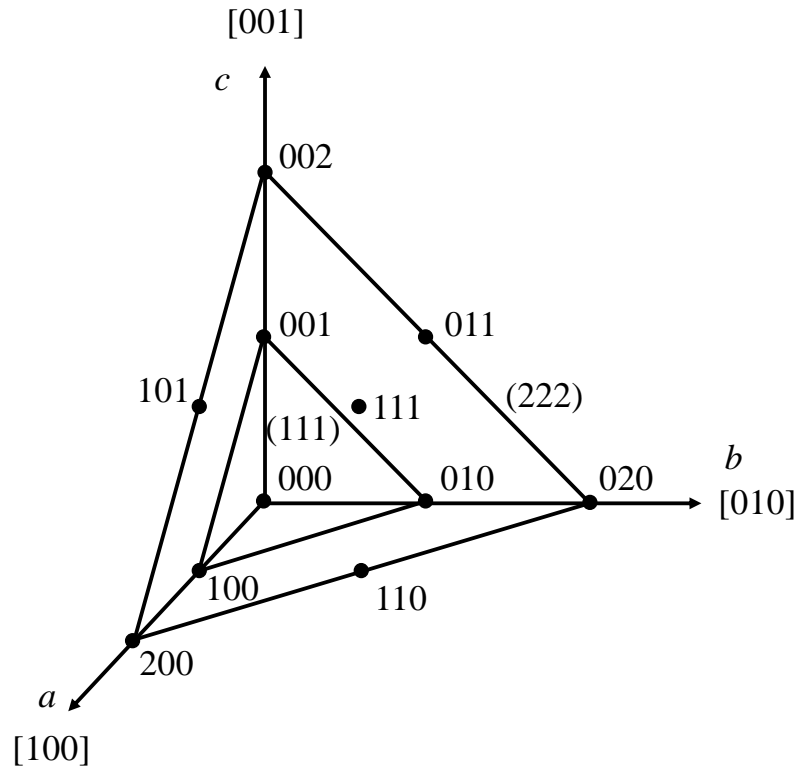


Figure 2-15. Illustration showing the notation of lattice points, directions and lattice planes.

Lattice planes can also be described in a similar way, through the use of Miller indices h , k and l corresponding with the reciprocal of the fractional intercept along each of the unit cell edges. The planes are represented in round brackets as (hkl) and are commonly simplified to the lowest set of integers to identify all identical parallel planes. If the plane fails to intercept with a cell edge then the corresponding h , k or l value will be 0. So for example the plane (222) will cross the cell edges at $\frac{1}{2}a$, $\frac{1}{2}b$ and $\frac{1}{2}c$. Once again the negative intercepts are given as \bar{h} , \bar{k} and \bar{l} . These planes may be related by symmetry. When this is the case the family of equivalent planes is represented by $\{hkl\}$. For example the $\{100\}$ family of planes in a cubic system corresponds with (100) , (010) and (001) .

These planes are of particular relevance when looking at the theory of X-ray diffraction.

2.3.2 Diffraction

2.3.2.1 Theory of Diffraction

The most common techniques for structural determination utilise the diffraction of photons, neutrons and electrons, exploiting the wave-like behaviour of these “particles”. Diffraction is the interaction of waves to give interference patterns. While waves of a large wavelength (e.g. 4000-7000 Å), scattered elastically (i.e. without change in energy), are refracted by atoms, those showing a wavelength of similar size or smaller than the atomic spacing of a crystalline material can interact with the crystal and are diffracted. The waves scattered from an ordered array of atoms can interact either constructively (in phase) or destructively (out of phase) (Figure 2-16). The phase of each wave with respect to one another is dependent on the atoms and crystal structure and diffract in a unique manner.

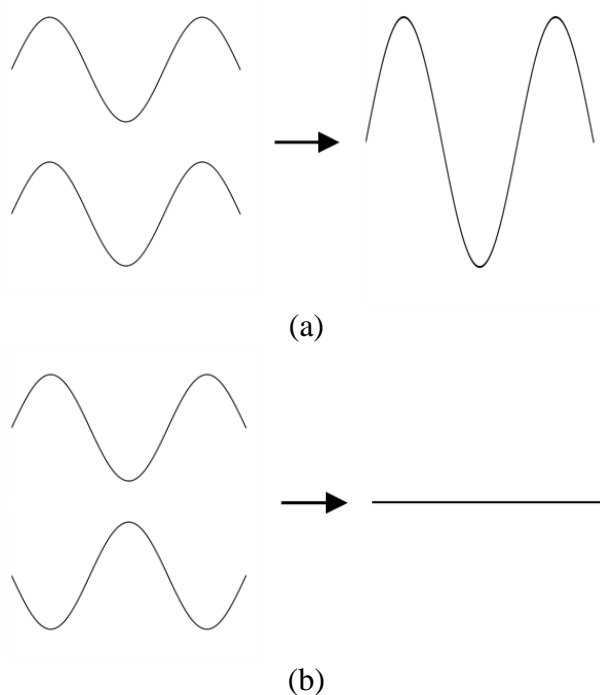


Figure 2-16. Representation of (a) constructive interference of two waves in phase with each other and (b) destructive interference of two waves out of phase with each other.

A frequently used and simple explanation of the diffraction from a crystal was provided by W. L. Bragg.²⁰⁸ This description assumes partial specular reflection of incident

radiation upon a series of parallel layers of atoms (Figure 2-17). The resulting reflected beams interact in a constructive or destructive manner. Due to the ordered nature of a crystalline material thousands of planes of atoms reflect a small fraction of the incident radiation. Only when the phase difference between the reflected waves is an integer number of wavelengths will constructive interference occur. In all other cases the overall interference between the waves is destructive. The conditions under which constructive interference occur are therefore given by:

$$n\lambda = 2d\sin\theta \tag{2-3}$$

where n is an integer, λ the wavelength, d the spacing between lattice planes and θ the angle between the incident radiation and the planes of atoms. This equation is known as the Bragg equation, or Bragg's law. The law is only obeyed when $\lambda \leq 2d$.

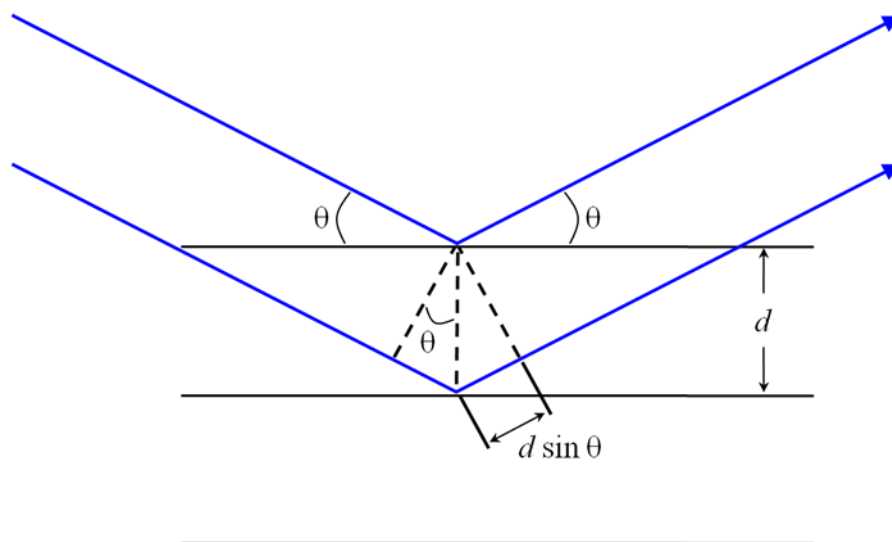


Figure 2-17. Derivation of the Bragg equation. d is the spacing between parallel atomic planes and θ the angle between these planes and the incident radiation.

Each crystal is made up of multiple families of planes separated by different d spacing. These are referred to by their Miller indices i.e. d_{hkl} . As the crystal planes vary with atom size and crystal structure, collection of the diffracted radiation for each of these planes produces a unique pattern. Structural information is also present in the intensity of the constructive waves, from which relative atomic positions can be derived. Methods for extraction of this structural information are briefly discussed below.

2.3.2.2 Powder X-ray Diffraction (PXRD)

In order to characterise a material it is necessary to detect the diffracted intensity from all or as many planes as possible so as to meet the Bragg conditions of each of these planes either the angle or the wavelength of incident radiation must be varied. The most common diffraction experiments involve a fixed wavelength of X-rays and rotation of the crystal so that each lattice plane is passed through the required Bragg angle. It is also, therefore, necessary to place a suitable X-ray detector at all the possible diffraction angles. By knowing the wavelength of radiation used and the 2θ angle that gives rise to each diffraction, the d spacing of the lattice planes can be calculated. Collecting a full set of diffraction data for a crystal can, via this route, be a time consuming process particularly if the crystal under investigation has little symmetry. One way to improve collection times is to use polycrystalline material. PXRD is the most common diffraction technique used in solid state laboratories and plays a large part in this work. The powdered material is made up of a very large number of small crystals in random orientation to one another. Therefore, in an X-ray beam the crystals will be orientated to meet the Bragg conditions of each plane and produce a series of cones of diffracted X-rays (Figure 2-18). By passing a detector through these cones at known 2θ angles a diffraction pattern for the sample is generated. The next step is to identify which planes have resulted in each diffraction peak and to assign the relevant Miller indices. This process is referred to as indexing and is used to derive crystal symmetry and cell dimensions. Indexing is commonly done using computer programs, e.g. DICVOL or Chekcell.^{209, 210}

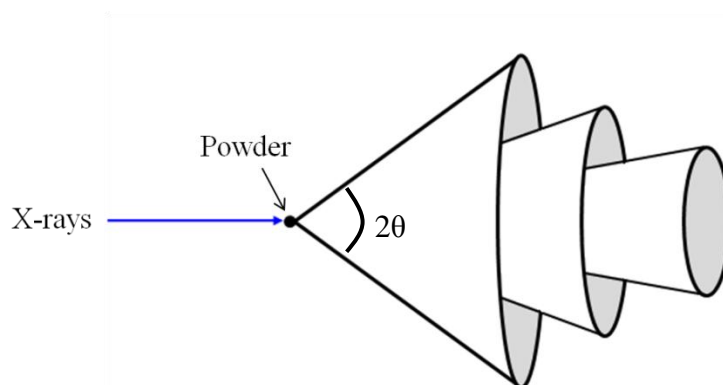


Figure 2-18. Representation of the cones produced in PXRD.

2.3.2.2.1 Generation of X-rays

In general, there are a number of ways to generate X-radiation. In the standard laboratory X-ray diffractometer an X-ray tube, similar to the one shown in Figure 2-19 is used.

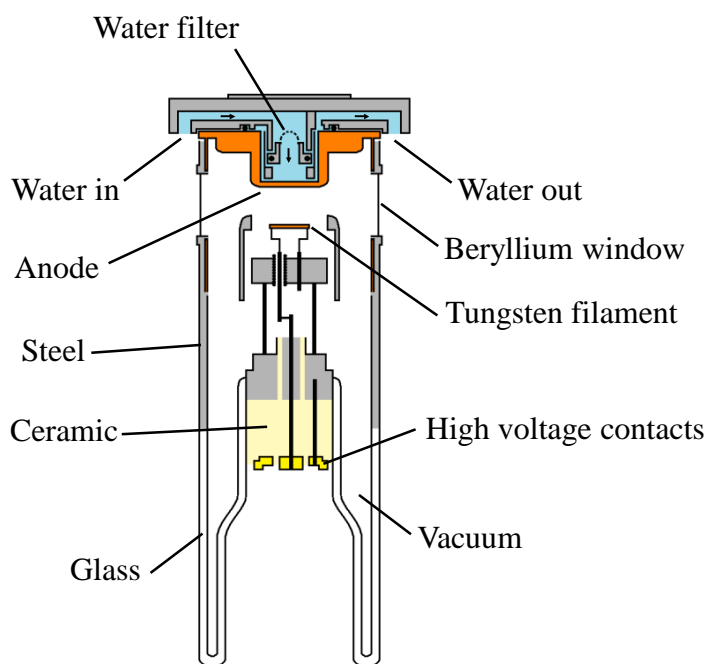


Figure 2-19. Schematic diagram of a laboratory X-ray tube. Recreated from the literature.²¹¹

X-rays are generated by acceleration of electrons from a metal filament towards a metal anion target. X-radiation is generated via the rapid deceleration of electrons as they hit the metal target. This form of radiation is referred to as Bremsstrahlung radiation. Additionally, electrons from the filament can knock electrons, in the target, from the inner shells of the atoms e.g. K ($n = 1$) shell. This vacancy is filled when an electron from a higher shell falls into it, releasing electromagnetic radiation (Figure 2-20).

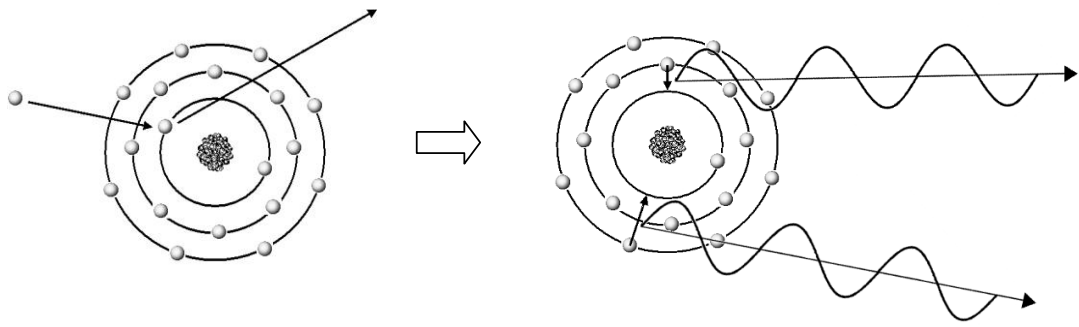


Figure 2-20. Illustration of X-ray generation. The grey spheres represent electrons.

This electromagnetic radiation emitted by an X-ray tube takes the form of a broad background of Bremsstrahlung radiation and intense X-ray emission maxima, the frequency of which is specific to the metal used in the target. Figure 2-21 shows an X-ray emission spectrum. The $K\alpha$ and $K\beta$ peaks are those used in XRD (commonly only one is used, the $K\beta$ is filtered out) and correspond with electrons falling from the L ($n = 2$) and M ($n = 3$) shells respectively (Figure 2-22). These peaks are actually made up of doublets corresponding with slightly different energies from the spin multiplicity in the p shell, giving $K\alpha_1$, $K\alpha_2$ and $K\beta_1$ and $K\beta_2$.²⁰⁴

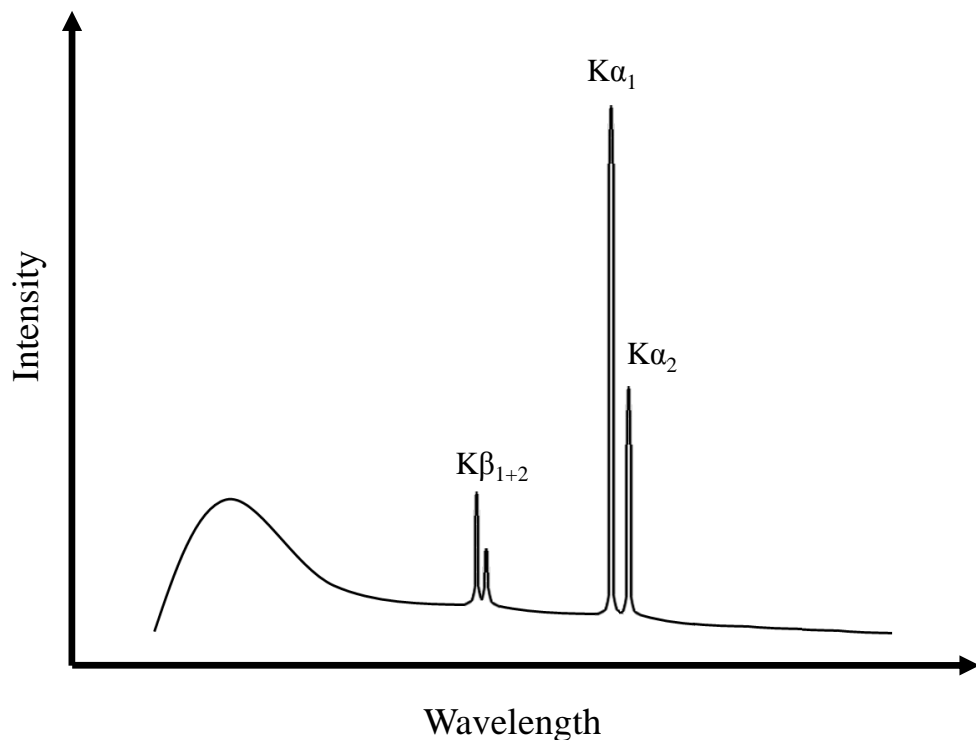


Figure 2-21. Representation of an X-ray spectrum.²⁰⁴

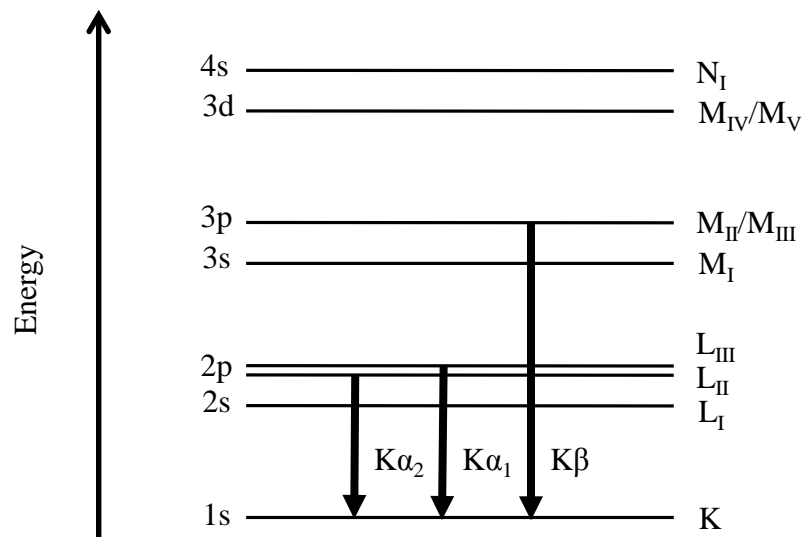


Figure 2-22. Energy level diagram for copper metal. Reproduced from the literature.²¹¹

The second common X-ray source is the synchrotron. In a synchrotron electromagnetic radiation is emitted from rapidly moving electrons, close to the speed of light, when powerful magnets redirect them. This electromagnetic radiation often covers a broad range of energies from infrared to X-rays.

The electrons originate from an electron gun. This consists of a metal cathode, which emits electrons via thermionic emission, initially accelerated towards an anode. The stream of electrons is then passed into a linear accelerator known as the “linac”. Just prior to the linac the electron stream is separated into short packets or bunches. In the linac these bunches of electrons are accelerated into a booster synchrotron. The booster synchrotron is a ring shaped channel made up of two straight sections connected via two semicircular curves. The electrons are accelerated via the application of radio frequency radiation in the straight sections and redirected using dipole bending magnets around the curves. Once the required speed is achieved the electrons are injected into the final storage ring. The storage ring is made up of multiple straight regions connected by curved sections with large dipole bending magnets attached to arc the electrons around the system (Figure 2-23).

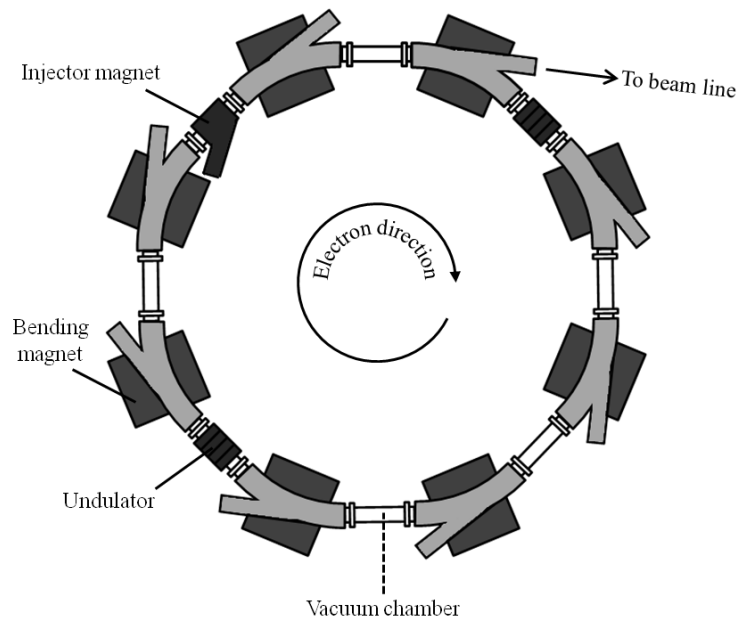


Figure 2-23. Representation of the synchrotron storage ring. Reproduced from the literature.²¹¹

As the electrons are re-directed around these bends they emit an intense beam of electromagnetic radiation as a cone of light at a tangent to the electron direction (Figure 2-24).

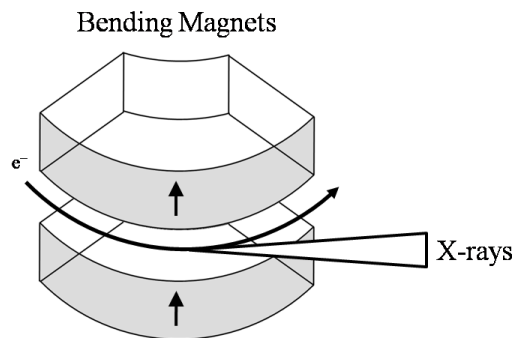


Figure 2-24. Emission of X-ray radiation by electrons redirected in bending magnets. Reproduced from the literature.²¹¹

It is along these tangents that the beam stations are placed, positioned to make use of this electromagnetic radiation. Additional radiation can be produced through the use of insertion devices. These are devices inserted into the linear sections of the storage ring. Two commonly used devices are wigglers and undulators. Wigglers consist of a series of magnets designed to deflect (wobble) the circulating electrons back and forth producing X-rays in a similar manner to a bending magnet (Figure 2-25). Wigglers

produce a broad band of electromagnetic radiation with a higher intensity than bending magnets due to multiple “wiggles”. If deflection is less pronounced, and the radiation emitted interferes to give a central narrow band, then the device is known as an undulator and gives a very high flux density.

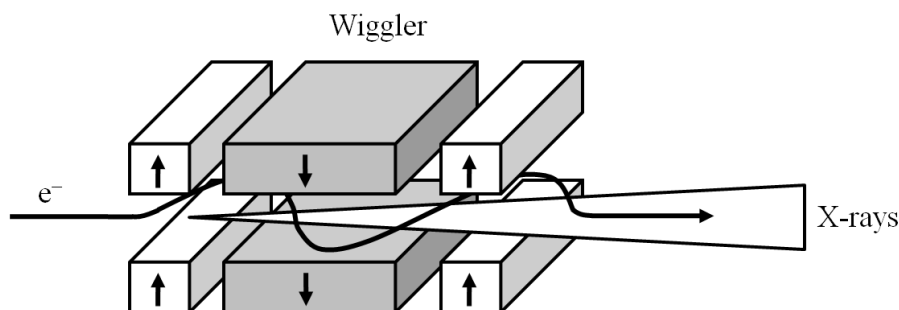


Figure 2-25. Representation of X-ray emission from a wiggler. Recreated from the literature.²¹¹

In order to select a specific wavelength from the broad spectrum of radiation it is common to insert monochromators along the radiation path. Monochromators are usually single crystals, cut along a specific plane, designed to select a wavelength of radiation in accordance with Bragg’s law. Monochromator materials include silicon, germanium, quartz and graphite. Silicon 111 is a frequently used material due to its high crystallinity. If it is necessary to maintain the beam direction a double monochromator may be used, consisting of two monochromators positioned in such a way as to deflect the beam back to its original direction while selecting the desired wavelength (λ) of radiation (Figure 2-26).

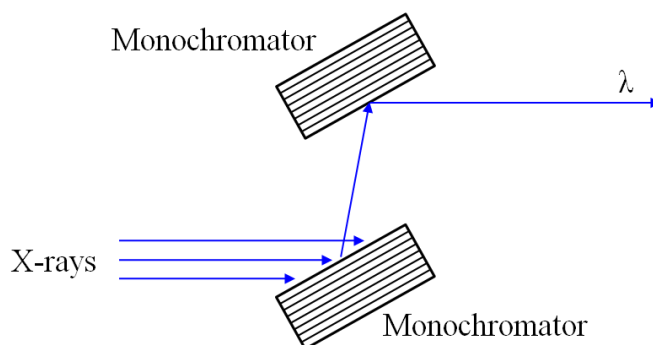


Figure 2-26. Representation of a double monochromator arrangement.

2.3.2.2.2 Equipment for Powder X-ray Diffraction

There are a large number of approaches to the collection of PXRD data and several possible geometries available for the diffractometer configuration. In this work two geometries were used: reflection and transmission.

The reflection geometry adopted was the Bragg-Brentano geometry, as shown in Figure 2-27.

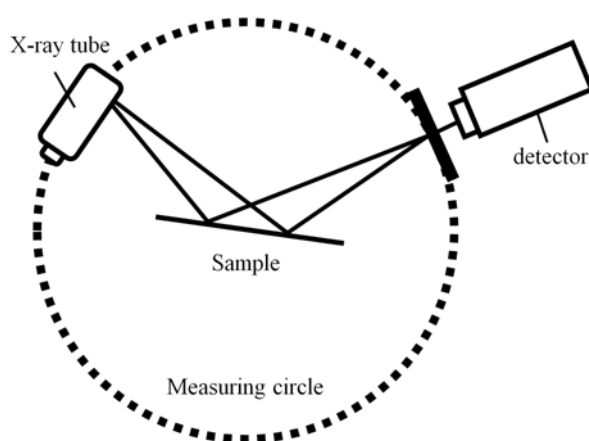


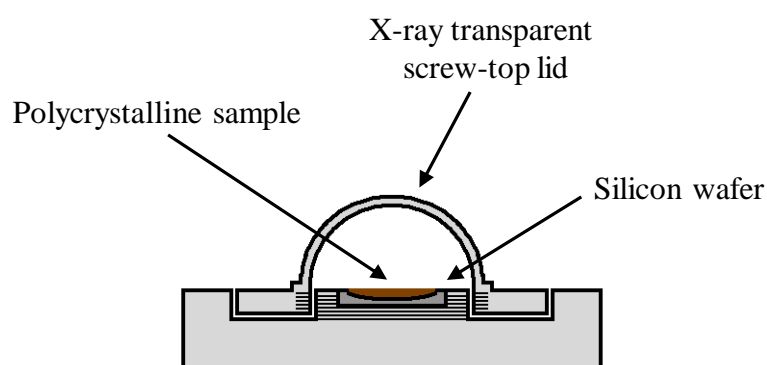
Figure 2-27. Representation of the Bragg-Brentano geometry. The dotted circle shows the measuring circle about which the detector moves.

For the experiments performed here, the generated X-rays were first passed through a Söller slit to collimate the radiation and slits used to narrow the beam to minimise overspill beyond the sample and onto the sample holder at low angles. The sample itself was placed upon a flat plate, with suitable size circular well, at the centre of the goniometer. The sample could then be rotated about its normal to give a good average crystallite orientation.

As the materials under analysis were often air or moisture sensitive they required a suitable sealed vessel for PXRD data collection. Figure 2-28 shows the Bruker air-tight sample holder used, consisting of a cylindrical plastic base with silicon wafer, cut along (510), with a 1 cm diameter well into which the sample was placed. The samples were then encompassed by an X-ray transparent screw top dome.



(a)



(b)

Figure 2-28. Photo (a) and schematic diagram (b) of the Bruker air-sensitive sample holder for use in sample characterisation by PXRD.

After the sample holder was an anti-scatter slit and a second Söller slit to minimise unwanted background scattering and to refocus the radiation as it is passed into the detector.

The second geometry used was the transmission geometry. This diffractometer configuration was very similar to that given above, however, the X-rays are directed through the sample. The samples were sealed within capillaries or between X-ray transparent adhesive strips prior to insertion in the beam. This method also required a beam stop to prevent the original, undiffracted beam from overloading the detector.

2.3.2.2.3 X-ray Detection

There are three types of detector used in PXRD. These are a point detector, linear detector and area detector and collect data in one-, two- and three-dimensions respectively. All of these types of detectors were used in this work. A scintillation counter is a point detector, which operates in two steps. First, an X-ray photon is absorbed by a phosphor screen emitting a photon in the visible region. This photon is detected by a photomultiplier tube generating an electrical impulse, which can be recorded.²¹¹ Such a detector gives a relatively high peak resolution, but can be slow as it must be passed through the entire scan range, collecting at regular intervals. The use of linear detectors can reduce this collection time, taking a larger fragment of the 2θ range at any one time. These detectors must still be translated around a measuring circle, but as multiple diffraction angles are measured at once higher overall peak intensities can also be obtained. Linear position sensitive detectors (PSD) work through the ionisation of an inert gas, such as argon or xenon, by X-rays. This generates electrons which can be guided towards a metal anode. Although generally of poorer resolution, linear detectors are a popular choice offering a compromise between resolution and collection time. Area detectors are large single plates which can be used to collect a whole diffraction pattern at once. Despite this, area detectors are not commonly used in modern PXRD experiments, often giving poorer resolution, detection limits and difficulties in determining relative peak intensities. For an area detector such as an image plate, the diffracted X-rays result in a two-dimensional image of multiple different size rings, which must be read once the collection is complete.

2.3.2.3 Powder Neutron Diffraction (PND)

Neutron diffraction shows a lot of similarities to X-ray diffraction as neutrons also show wave-like properties with a range of wavelengths small enough to satisfy the Bragg law ($\lambda \leq 2d$), making neutron diffraction a good complementary technique in structural determination.

Neutron diffraction has a number of advantages over X-ray diffraction. Firstly, while X-rays are diffracted by the electron cloud around an atom, neutrons are diffracted by the nucleus of the atom. This provides a far more accurate representation of where the atoms are located (the nucleus has a radius around 10^{-15} m, while the atom, due to the electron orbit, is around 10^5 times larger than this).²¹² Also, the 2θ dependence of the intensity seen in X-ray diffraction is not present in neutron diffraction. In addition, as the scattering of neutrons is not primarily dependent on the electron cloud, the scattering power of atoms with similar electronic configurations can be quite different.³⁹ Some small anions may have larger neutron scattering lengths than other large cations (e.g. oxygen has a coherent scattering length of 5.803×10^{-15} m, while cerium has a scattering length of only 4.84×10^{-15} m).³⁹ Neutrons therefore provide a useful tool for determining the location of smaller atoms or alternatively in discriminating between similar atoms such as N^{3-} and F^- , which show different neutron scattering lengths (9.36×10^{-15} m and 5.654×10^{-15} m respectively), but identical electronic configurations.³⁹

As neutrons are not diffracted by the electron clouds of the atoms they also penetrate further into the sample than X-rays. Neutrons can penetrate several centimetres into a sample, whereas X-rays commonly only penetrate a few millimetres.²¹³ A result of this and the relatively low flux available from neutron diffraction sources is that far more sample is required for neutron diffraction (up to several grams are necessary).²¹³

A further useful property of neutrons is that they possess a magnetic moment of 1.9132 nuclear magnetons.²¹³ Hence, they will interact via dipole-dipole interactions with magnetic moments of unpaired electrons, generating a set of magnetic peaks in accordance with the Bragg equation.^{213, 214} This effect is on a similar scale to the diffraction arising from the nuclear (crystallographic) structure. Therefore, neutrons can be used to determine the magnetic structure of materials with open electron shells. In order for magnetic peaks to arise in the diffraction patterns it is necessary for constructive interference to occur with the diffracted waves. The magnetic dipoles within the structure must therefore show an ordered array of spins.

The overall diffraction pattern is a result of both the nuclear and magnetic scattering. In the case of ferromagnetic materials the magnetic unit cell will be the same size as the nuclear unit cell (Figure 2-29).

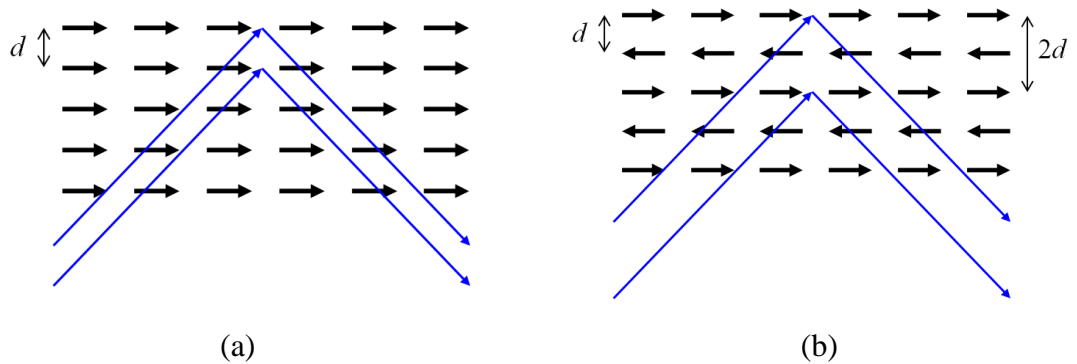
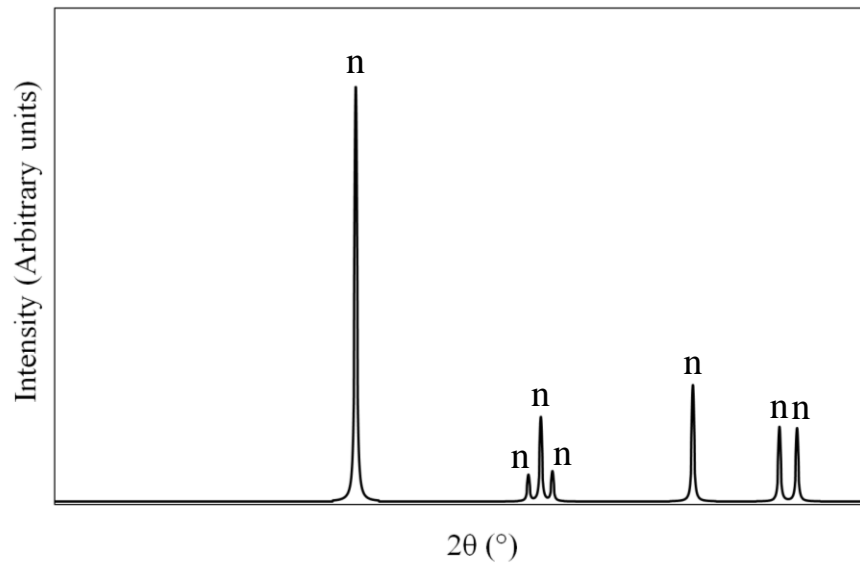


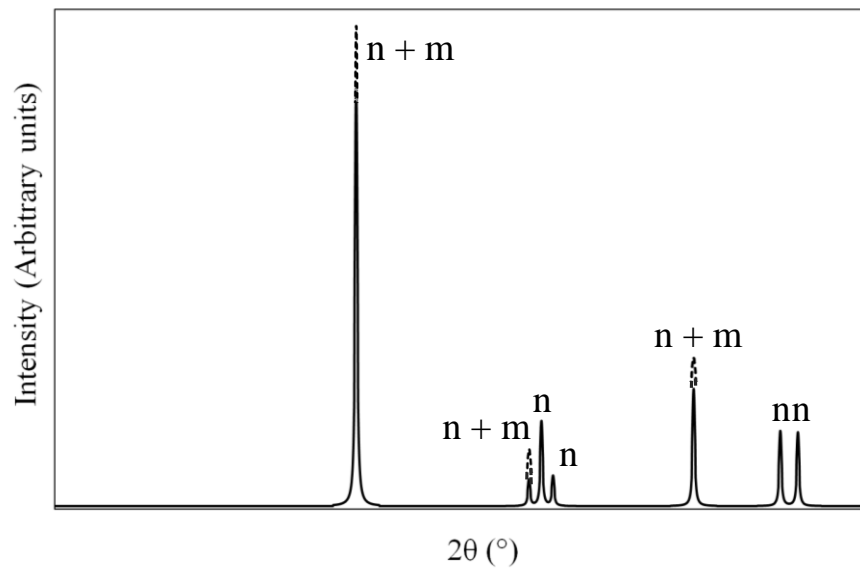
Figure 2-29. Representation of neutron diffraction in (a) ferromagnetic and (b) antiferromagnetic materials. The black arrows show the magnetic spin alignment of the atoms and blue arrows show the neutron paths which will successfully give constructive interference.²¹⁴

The result is that the separation between the planes of aligned spins, and hence the d spacing, is identical to existing crystallographic planes. Hence, the additional diffraction arising from the magnetic contribution will add to a number of existing peaks from the nuclear (crystallographic) unit cell (Figure 2-30). The magnetic peaks will show the same 2θ positions as the peaks from the nuclear cell.

Magnetic scattering from antiferromagnetic compounds results from a change in the neutron's potential energy, $\gamma S_n B$ (S_n and γ are the spin and gyromagnetic ratio of the neutron and B is the magnetic induction due to the atoms).²¹⁴ This energy varies in sign between two planes of oppositely aligned spins and so constructive interference no longer occurs between these two neighbouring planes of atoms, but between every other plane of equal spin direction i.e. constructive interference occurs when $n\lambda = 4d\sin\theta$.²¹⁴ This gives rise to a magnetic unit cell which is larger than the crystallographic unit cell (Figure 2-29).²¹⁴ The resulting diffraction pattern will then show additional magnetic peaks at positions not observed in the crystallographic pattern (Figure 2-31).

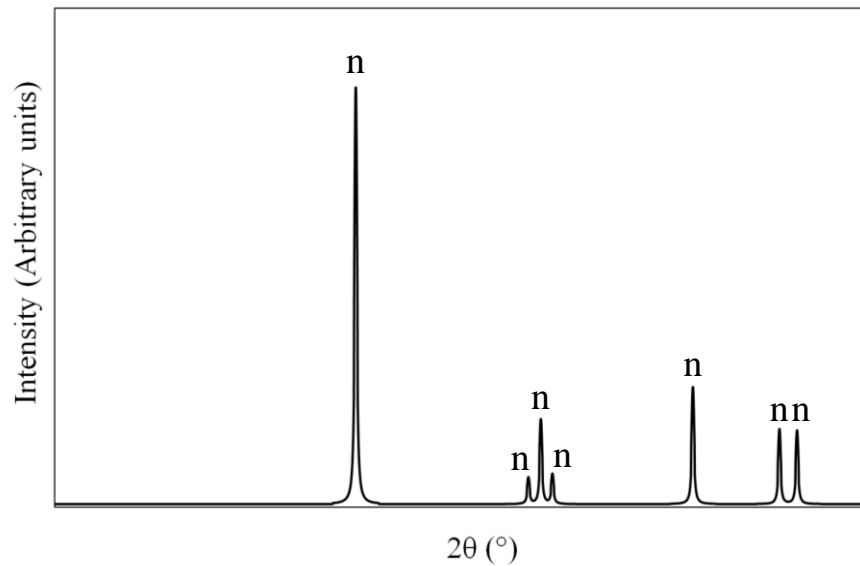


(a)

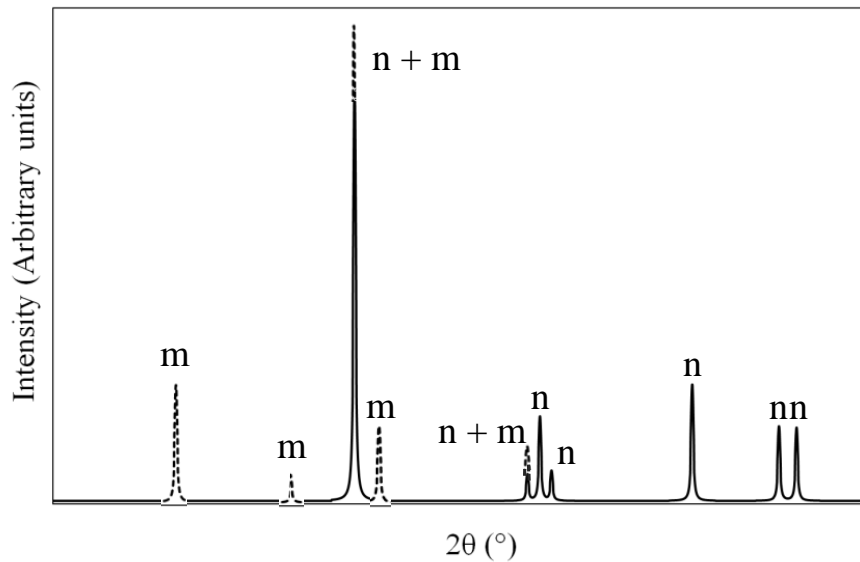


(b)

Figure 2-30. Powder neutron diffraction patterns, from a ferromagnetic material, showing (a) the diffraction from a nuclear, n , unit cell and (b) a magnetic, m , and nuclear, n , cell.



(a)



(b)

Figure 2-31. Powder neutron diffraction patterns, from an antiferromagnetic material, showing (a) the diffraction from a nuclear, n , unit cell and (b) a magnetic, m , and nuclear, n , cell.

2.3.2.3.1 Generation of Neutrons

There are two methods conventionally used for the preparation of neutrons employed in neutron diffraction. These are the controlled fission of ^{235}U and spallation. Fission is commonly used for constant-wavelength diffractometers. Here the ^{235}U is combined with a neutron inducing fission, where the atom splits into lighter elements with the

expulsion of further neutrons and energy. The neutrons released can either initiate further fission of ^{235}U or be emitted from the reactor. The neutrons are at too high an energy ($\sim 5\text{MeV}$) to be used for structural determination.²¹³ In order to reduce the energy they are passed through a moderator, commonly H_2O or D_2O , which reduces the energy of the neutrons via inelastic scattering with the protons or deuterium. The resulting neutrons have a broad distribution of wavelengths so a monochromator is used to select the desired wavelength for use in the structural analysis. The monochromator is commonly a single crystal of germanium or silicon, although other materials may also be used. Often, the neutrons are passed through a collimator prior to hitting the monochromator to ensure a parallel beam of neutrons is diffracted, improving the resolution of the instrument.

This type of neutron source is used at the Institut Laue-Langevin (ILL), Grenoble, France, which has a very high neutron flux of 1.5×10^{15} neutrons $\text{cm}^{-2}\text{s}^{-1}$.²¹⁵ A high flux is particularly important to compensate for the poor diffraction efficiency of neutrons and to allow a reasonable data acquisition in a suitable period of time. The ILL facility was used for the neutron diffraction experiments presented in the following sections. A graphical representation of the diffractometer set-up is shown in Figure 2-32.

The second neutron generation technique is spallation, commonly applied in time-of-flight experiments.²¹³ The neutrons are produced when a metal target (uranium, lead or tungsten are common) is bombarded with fast moving particles such as protons. The resulting neutrons are passed through a moderator producing a distribution of wavelengths. Rather than select a specific wavelength this whole range is used and passed through a chopper. The chopper is a rotating disk of neutron absorbing material with apertures to allow neutrons of a selected speed to pass through in pulses. As a range of wavelengths are used the measurements are collected at a fixed diffraction angle. The wavelength of diffracted radiation is then determined by the time taken by the neutrons to reach the detector after leaving the sample:

$$\lambda = h/mv = ht/mL = 2d\sin\theta \quad (2-4)$$

where t is the time of flight, L is the length of the flight path and m the mass of a neutron.²¹¹ An advantage of time-of-flight diffraction, therefore, is that the whole beam of radiation is used giving a greater overall intensity.

This type of experimental procedure is used at the ISIS Rutherford laboratory, UK.

2.3.2.3.2 Equipment for Neutron Diffraction

For the neutron diffraction experiments performed in this thesis (chapters 3, 4 and 5), the data were collected at the D2B high-resolution powder diffractometer at the ILL, France. The constant wavelength diffractometer set-up of the D2B is shown in Figure 2-32 and is similar to the experimental arrangement used for constant wavelength X-ray diffraction, although with neutron diffraction a number of detectors are used spanning the whole diffraction range in order to minimise collection times.

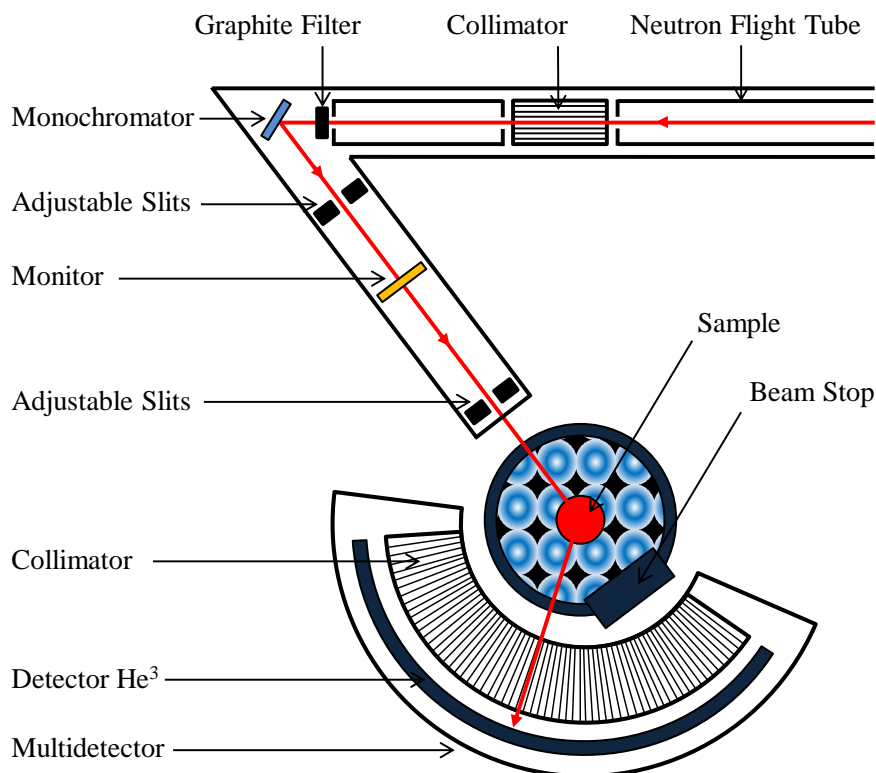


Figure 2-32. Schematic of the D2B powder neutron diffractometer at the ILL, France.²¹⁶

2.3.2.3.3 Neutron Detection

Unlike X-rays, neutrons do not ionise materials for detection. Instead neutron detection exploits the absorption of neutrons by atomic nuclei with the emission of γ -radiation.²¹¹

A common choice of detection material is ^3He gas:



The ^3He can therefore be used in a PSD much like those used in X-ray detection. For the D2B diffractometer multiple (65) PSD detectors are positioned around the sample 2.5° apart. By passing the neutrons through a collimator just after diffraction and prior to these detectors, the resolution of the instrument is improved.²¹¹

2.3.3 Rietveld Refinement

Rietveld refinement is the most common method used for the determination of crystal structures from PXRD or PND data. A theoretical diffraction pattern is calculated based on a proposed model and compared to the experimental data. Modifications are made to the model in an attempt to minimise the difference between the two patterns. This is usually performed using a computer software package such as GSAS.²¹⁷ The value to be minimised, S_y , is:

$$S_y = \sum_i w_i (y_i - y_{ci})^2 \quad (2-6)$$

where w_i is $1/y_i$, y_i is the observed intensity at the i th step and y_{ci} is the calculated intensity at the i th step.²¹⁸ This type of minimisation is known as a least-squares refinement.

The calculated intensity at any point in the diffraction pattern is dependent on a number of variables:

$$y_{ci} = s \sum_K L_K |F_K|^2 \phi(2\theta_i - 2\theta_K) P_K A + y_{bi} \quad (2-7)$$

where

s is the scale factor,

K represents the Miller indices for a Bragg reflection,

L_K contains the Lorentz, polarisation and multiplicity factors,

ϕ is the reflection profile function,

P_K is the preferred orientation function,

A is an absorption factor,

F_K is the structure factor for the Kth Bragg reflection and

y_{bi} is the background intensity at the ith step.²¹⁸

The significance of these variables is discussed below.

2.3.3.1 Lorentz, Polarisation and Multiplicity Factors, L_K

In general, in X-ray diffraction the beam produced is unpolarised. The random orientation of the crystallites under analysis can result in the partial polarisation of this beam upon diffraction and give rise to a reduction in the overall peak intensity of the diffraction pattern.²¹¹ The variation in an unpolarised beam is given by:

$$P = \frac{1}{2}(1 + \cos^2 2\theta) \quad (2-8)$$

It is also found that the Bragg angle for a reflection, θ , will occur over a very narrow range, rather than the idealised exact θ value. The extent of this range also shows a 2θ dependence. This is known as the Lorentz factor.²⁰³ This is usually added to the polarisation term to give an overall correction of:

$$(1 + \cos^2 2\theta) / (\sin^2 2\theta \cos \theta) \quad (2-9)$$

An additional consequence is that the diffraction pattern resulting from a powdered sample is made up of rings (corresponding with the diffraction cones, Figure 2-18) rather than spots, as in single crystal X-ray diffraction. These rings overlap with those of equivalent diffraction planes, e.g. (002) and (00 $\bar{2}$), which would in single crystal X-ray diffraction give rise to two distinct spots. The resulting ring intensity is a composite of all equivalent planes. The rings are said to have a multiplicity equal to the number of planes contributing to the overall intensity. The multiplicity is dependent on the cell symmetry (Table 2-4) and must be taken into account when fitting the data.

Crystal Class		Diffracting plane and multiplicity					
Triclinic	all, 2						
Monoclinic	0k0, 2	h0l, 2	hkl, 4				
Orthorhombic	h00, 2	0k0, 2	00l, 2	hk0, 4	0kl, 4	h0l, 4	hkl, 8
Tetragonal	00l, 2	h00, 4	hh0, 4	hk0, 8	0kl, 8	hhl, 8	hkl, 16
Triclinic	00l, 2	h00, 6	hh0, 6	hk0, 12	0kl, 12	hhl, 12	hkl, 24
Hexagonal	00l, 2	h00, 6	hh0, 6	hk0, 12	0kl, 12	hhl, 12	hkl, 24
Cubic	h00, 6	hh0, 12	hk0, 24	hhh, 8	hkl, 24	hkl, 48	

Table 2-4. Multiplicity of equivalent reflections in powder diffraction.²⁰³

2.3.3.2 Reflection Profile Function, ϕ

Although the Bragg law implies that a diffraction pattern from a polycrystalline material will consist of a flat background with perfectly defined lines corresponding with each Bragg reflection, this is not the case. A number of factors, such as instrumental contributions, crystal defects, particle size and microstrain broadening result in diffraction peaks of various shapes. This must be accounted for when fitting the diffraction data.

A number of different profile functions can be employed to model these peaks. The most common are the Gaussian ('G') (2-10), Lorentzian ('L') (2-11) and pseudo-Voigt profile functions (2-12) (or modifications of these):

$$\frac{C_0^{1/2}}{H_K \pi^{1/2}} \exp(-C_0(2\theta_i - 2\theta_K)^2/H_K^2) \quad (2-10)$$

$$\frac{C_1^{1/2}}{\pi H_K} 1/\left[1 + C_1 \frac{(2\theta_i - 2\theta_K)^2}{H_K^2}\right] \quad (2-11)$$

$$\eta L + (1 - \eta)G \quad (2-12)$$

where $C_0 = 4\ln 2$, $C_1 = 4$, the mixing parameter $\eta = NA + NB*(2\theta)$ and NA and NB are refinable.²¹⁸ The peak width, H , is taken as the full-width-at-half-maximum (FWHM) and is defined as:

$$H^2 = U \tan^2 \theta + V \tan \theta + W \quad (2-13)$$

where U , V and W are refinable parameters.

2.3.3.3 Preferred Orientation Function, P_K

Preferred orientation is a particular issue for those crystallites, which show rod or plate-like structures, for example, as these have a tendency to favour a certain orientation when distributed over the specimen holder. The result is a greater number of certain families of planes being exposed to the beam, giving rise to an increased peak intensity for these reflections. A number of correction techniques are available in analysis software packages, but were not required in this work.

2.3.3.4 Absorption Factor, A

Absorption has the overall effect of removing beam intensity and reducing the intensity of the diffraction peaks. In an ideal Bragg-Brentano diffractometer the effect of absorption is uniform across the whole 2θ range and does not require a correction.

However, in cases where highly absorbing materials show a lower packing density at the surface than in the bulk material, a 2θ dependence, particularly at low angles, may result giving rise to reduced thermal parameters in the refinement. A number of corrections are available.

2.3.3.5 Structure Factor, F_K

The total diffraction intensity of a unit cell can be calculated by combining the waves scattered from each plane of atoms. This is referred to as the structure factor, F_K , where K indicates each set of (hkl) planes and is given by:

$$F_K = \sum_j N_j f_j \exp[2\pi i(hx_j + ky_j + lz_j)] \exp[-M_j] \quad (2-14)$$

where

hkl are Miller indices,

x_j, y_j, z_j are the atomic positions of the j th atom,

N_j is the site occupancy multiplier for the j th atom site (the site occupancy/site multiplicity),

$$M_j = 8\pi^2 u_s^2 \sin^2 \theta / \lambda^2,$$

u_s^2 is the root-mean-square thermal displacement of the j th term parallel to the diffraction vector,

f_j is the atomic scattering factor.

The f_j values are quite different in X-ray and neutron diffraction. For X-rays f_j are dependent on the number of electrons possessed by the atom in the sample, increasing with atomic number (Z), while in neutron diffraction the diffracted neutrons, often described in terms of the scattering length, b , do not show a linear increase in scattering length with Z .^{39, 203} The scattering factor in X-ray diffraction shows a 2θ dependence:

$$f_j = \sum_{j=1}^4 a_j \exp[-b_j(\sin^2 \theta / \lambda^2)] + c \quad (2-15)$$

where a_j , b_j and c are Cromer-Mann coefficients, specific to each atom and are either experimentally derived or obtained via quantum mechanical calculations. The intensity of the diffraction peaks decreases with increasing values of θ . This type of dependence is not seen in neutron diffraction. However, due to the dependence of magnetic neutron diffraction on the electron clouds the magnetic peak intensity will show similar behaviour to X-ray diffraction.

2.3.3.6 Background, y_{bi}

The background of a diffraction pattern may show unwanted contributions from a number of causes such as the presence of amorphous materials, scattering from the sample holder, adhesive used in sample placement and inelastic scattering. To account for these contributions and to prevent modelling of this intensity as crystallographic contributions, this background must be accounted for. There are several ways to achieve this: tables of known instrumental background, linear interpolation between user defined points and modelling to background functions.²¹⁸ Most refinement software packages provide a wide range of possible background functions, which can be selected to describe the specific background characteristics of each pattern in the best way.

2.3.3.7 Quality of Fit Criteria

In addition to a difference profile plot between the experimental and calculated patterns, numerical representations of the fit quality are also used.^{218, 219}

The fit values of R_{wp} , R_p and χ^2 will be used here and are defined as:

$$R_{wp} = (\sum_i w_i [y_i(\text{obs}) - y_i(\text{calc})]^2 / \sum_i w_i [y_i(\text{obs})]^2)^{1/2} \quad (2-16)$$

$$R_p = \sum_i |y_i(\text{obs}) - y_i(\text{calc})| / \sum_i y_i(\text{obs}) \quad (2-17)$$

$$\chi^2 = R_{wp}/R_{exp} \quad (2-18)$$

$$R_{exp} = [(N - P) / \sum_i^N w_i y_i(\text{obs})^2]^{1/2} \quad (2-19)$$

where w_i is a weighting factor, $y_i(\text{obs})$ and $y_i(\text{calc})$ are the observed and calculated intensity, N is the number of observations and P is the number of parameters.

In general the values of R_{wp} and R_p should be minimised and χ^2 approach a value of 1.

2.3.4 Le Bail Extraction

While Rietveld refinement is used to determine the structure of solid compounds based on an initial structural model, Le Bail extraction attempts to fit the observed intensity, without this structural model and is instead based on profile fitting alone. The structure factor contributions to the calculated peak intensity, $F_K^2(\text{calc})$, are arbitrarily set as equal for all points and used to derive the observed peak intensities. These observed intensities are re-injected as $F_K^2(\text{calc})$ values for the next iteration of the refinement.²²⁰ Le Bail Extraction is used to determine accurate cell dimensions, prior to full refinement.

2.3.5 X-ray Absorption Spectroscopy (XAS)

Structural details may also be obtained from the absorption of X-rays. X-rays lie in the energy range of around 500 eV to 500 keV (25 Å-0.25 Å), sufficient for materials to absorb X-rays with the promotion of an electron from a core level out of the atom, i.e. to ionise the atom. This is the photo-electric effect and requires that the binding energy of the electron is lower than the energy of the X-rays. The additional energy constitutes the kinetic energy of the emitted photoelectron.²²¹ Each element has its own unique absorption energies, corresponding with the energy required to excite electrons from each atomic level into the continuum.

It is common to describe the absorption of electromagnetic radiation in terms of the absorption coefficient, μ , determined from the decay in intensity as X-rays pass through a sample:

$$I = I_0 e^{-\mu x} \quad (2-20)$$

where x is the sample thickness, I_0 the intensity of the incident radiation and I the intensity of the transmitted light exiting the sample.^{221, 222} Plotting μ against the X-ray energy gives the characteristic absorption spectrum shown in Figure 2-33. The large increases in absorption are commonly referred to as absorption edges and correspond with the ionisation of atoms. The spectrum is generally separated into two regions, the area at the edge is known as the XANES (X-ray Absorption Near-Edge Structure) and the region ~ 20 -30 eV beyond the edge is known as the EXAFS (Extended X-ray Absorption Fine Structure). The whole spectrum is referred to as the XAFS (X-ray Absorption Fine Structure).²²³

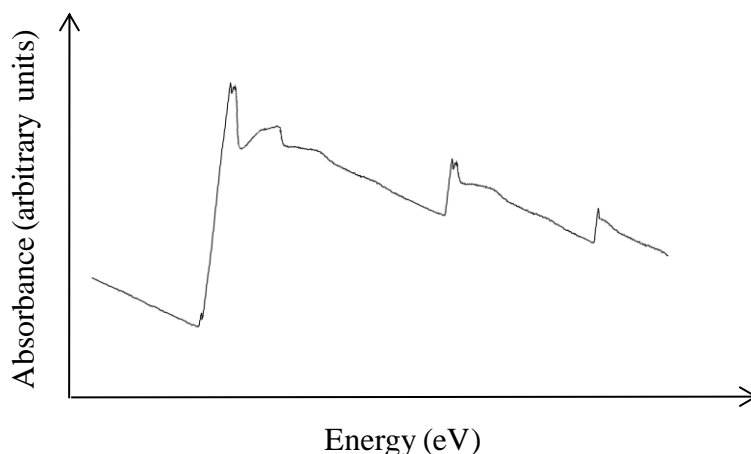


Figure 2-33. Absorbance of several elements over an X-ray range.

Upon absorption of a photon and emission of an electron, the atom is in an excited state with a core electron hole. The levels from which each electron has been lost is referred to by the letter corresponding to the principal quantum number (K, L, M, N for $n = 1, 2, 3, 4$) with the angular momentum state of the level described in subscript (1, 2, 3, 4 for $s, p_{1/2}, p_{3/2}, d_{3/2}$).²¹³ For example the L_3 edge would correspond with the loss of an electron from the $2p_{3/2}$ state. The excited state of the ion will then decay via a number of possible routes. The first is via X-ray fluorescence (Figure 2-34 (a)). An electron

from a higher energy level falls into the electron hole with the emission of X-rays. As seen in the generation of X-rays (section 2.3.2.2.1) this emitted light has a characteristic energy. The second decay route is via the Auger effect. In Auger emission an electron falls from a higher energy level and a second electron is emitted from the atom (Figure 2-34 (b)).²²²

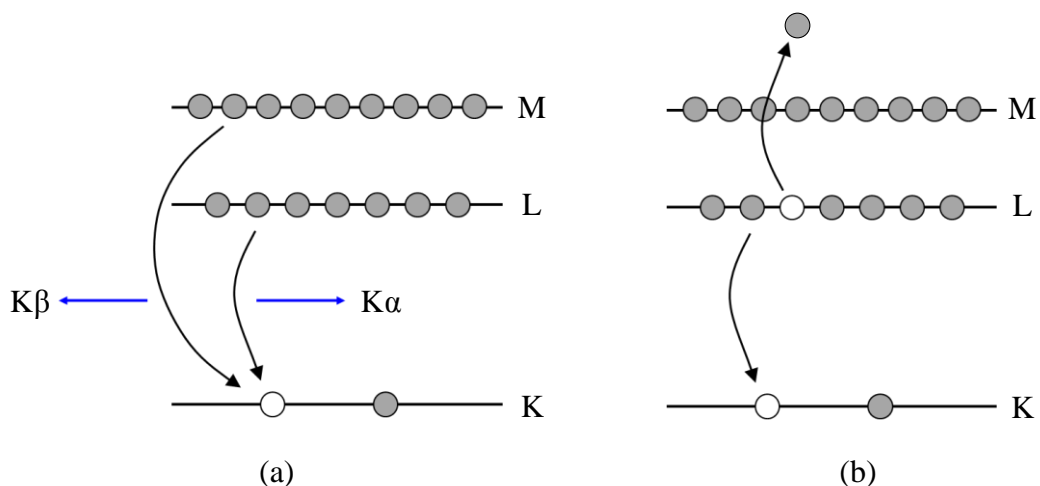


Figure 2-34. Decay of the excited state via (a) X-ray fluorescence and (b) the Auger effect. The grey and white circles correspond with electrons and electron holes respectively. The blue arrows represent the X-rays.²²²

The absorption spectrum is generally collected in one of two ways: transmission or fluorescence mode (Figure 2-35).

In transmission mode the beam is first passed through a detector, to determine the intensity of the incident radiation, through the sample and straight to a second detector where the transmitted light is recorded. In fluorescence mode the sample is angled at 45° to the incident radiation and the primary detector positioned normal to the beam. In this way only the emitted radiation is detected. With both experimental geometries a metal foil may also be placed along the beam line, after the sample, with an additional detector positioned beyond. This foil may then be used as an internal standard, with known absorption edges to which the data can be calibrated. This provides an accurate determination of the absorption edge position. The detectors used operate on a similar principle to those used in X-ray diffraction. When it is necessary to record the intensity of radiation while maintaining the beam for subsequent absorption by the sample, an Ar

or He filled ion chamber is used. Ionisation of the gas is detected by the migration of electrons towards an anode, generating an electrical signal proportional to the beam intensity.²¹³

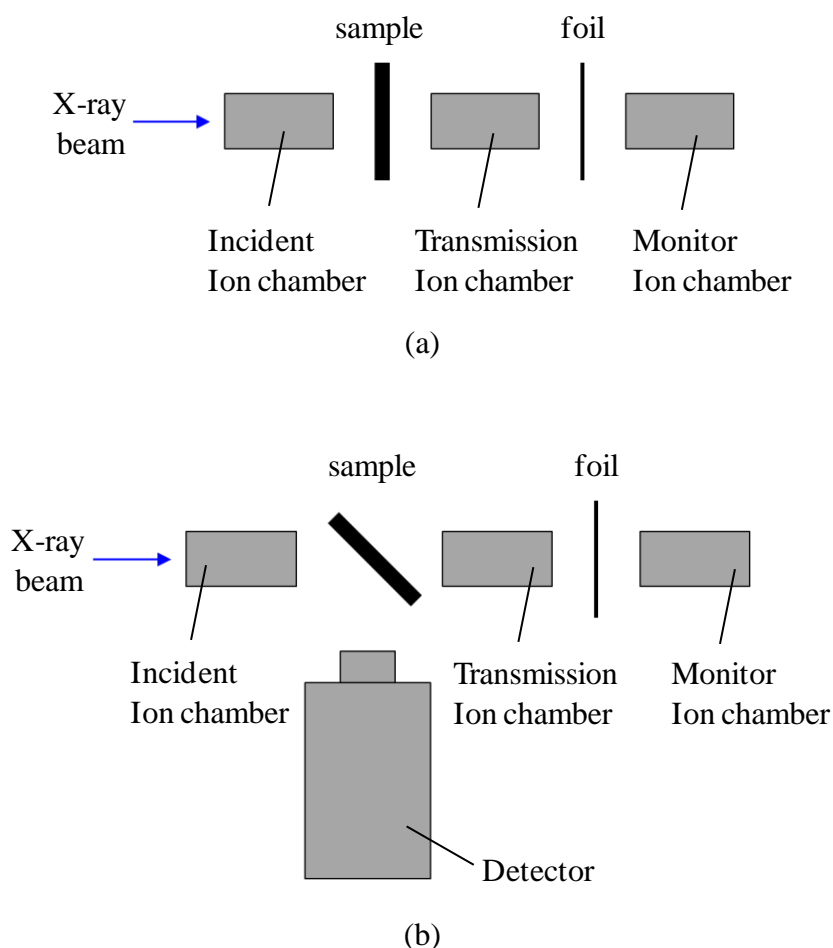


Figure 2-35. XAS apparatus for (a) transmission and (b) fluorescence modes.

The value of the absorption coefficient is then related by $\mu(E) = \log(I_0/I)$ and $\mu(E) \propto I_f/I_0$ for transmission and fluorescence mode respectively (I_f is the monitored intensity of a fluorescence line).²²²

The resulting XAFS can be used to provide structural information about the material under analysis. The position of the absorption edge is specific to the atom or ion under analysis and the shape of the XANES is dependent on the allowed electronic transitions and selection rules, which are dictated by an atom's coordination environment and geometry. The EXAFS consists of a number of oscillations beyond the absorption edge

and contains useful information about the type of atoms around the atom under investigation, their number and also their distance. The EXAFS, $\chi(E)$, is given by:

$$\chi(E) = \frac{\mu(E) - \mu_0(E)}{\Delta\mu_0(E)} \quad (2-21)$$

where $\mu(E)$ is the measured absorption coefficient, $\mu_0(E)$ is a smooth background function representing the absorption of an isolated atom and $\Delta\mu_0(E)$ is the measured jump in absorption.²¹³ In the analysis of EXAFS data modelling of $\Delta\mu_0(E)$ must be performed prior to use.

As stated, the absorption of the X-rays results in the formation of a photoelectron. This photoelectron can be described in terms of a photoelectron wave, propagating outward from the central atom. This wave is then scattered by the neighbouring atoms (Figure 2-36). The backscattering waves then interfere with the forward waves. The result is a modification in the transition probability of X-ray absorption. This alters the absorption coefficient and gives rise to oscillations in the EXAFS.

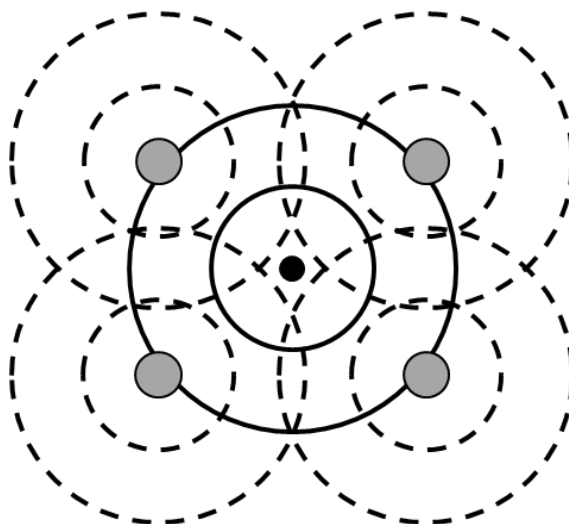


Figure 2-36. Two-dimensional representation of the scattering process. The photoelectron waves (black line) originate from the central atom and are scattered back (dotted lines) from the four neighbouring atoms. The lines indicate the wave maxima.²¹³

The constructive and destructive interference between the photoelectron waves will vary with the position, number and thermal motion of the surrounding atoms. These can be derived from the oscillations in the EXAFS. The EXAFS, $\chi(k)$, is usually defined in wave numbers, k , and given by:

$$\chi(k) = \sum_j \frac{N_j f_j(k) e^{-2k^2 \sigma_j^2}}{k R_j^2} \sin[2kR_j + \delta_j(k)] \quad (2-22)$$

where $f_j(k)$ and $\delta_j(k)$ are overall amplitude and phase factors of the scattering, sensitive to the type of neighbouring atom, N is the number of neighbouring atoms, R is the distance to the neighbouring atoms and σ^2 the disorder in the neighbouring atom distances.^{213, 222}

Once the XAFS data has been collected it is necessary to process the data to remove unwanted background, instrumental contributions and to isolate the XANES and EXAFS data. For the XAFS analysis reported here the following steps were performed to process the data prior to analysis, using the computer programs PAXAS (steps 1-4), PySpline (steps 5) and EXCURV98 (steps 6-7).²²⁴⁻²²⁶

1. **Data summation.** Several scans were performed on each sample and then summed, reducing background noise.
2. **Edge correction.** During the data collection process a standard with a known edge position was also analysed. For this work a cobalt foil was used. The shift in the edge position of this standard relative to the literature value (7709.0 eV) was then removed in all the apatite and germanate sample spectra using appropriate software.²²⁷
3. **Subtraction of pre-edge background.** The instrumental background and absorption from other edges were removed by fitting the pre-edge region to a simple polynomial (Figure 2-37).

- Normalisation of intensity.** The spectra were normalised to between 0 and 1 to ensure all spectra are on the same scale for comparison of XANES.

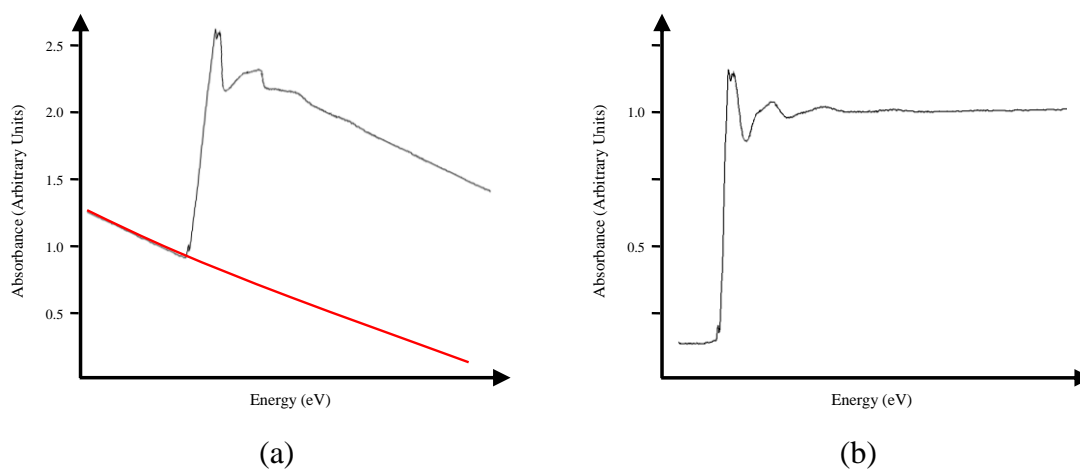


Figure 2-37. XAFS pre-edge subtraction and normalisation (a) XAFS spectrum and pre-edge background polynomial in black and red respectively and (b) the resulting background subtracted and normalised XAFS spectrum.

- Fine edge correction.** In order to ensure minor shifts in each spectra were accounted for independently calibrations were applied. These calibrations were based on an internal standard, positioned after the sample, in the spectrometer, as shown in Figure 2-35. In each case a cobalt foil was used as the internal standard and each pattern was shifted to match the cobalt edge position reported in the literature.²²⁷ This is of particular relevance for the analysis of XANES data. In XANES spectra subtle deviations in absorption edge arise from the difference in cation oxidation state and it is therefore important to minimise any instrumental shift.
- Subtraction of post-edge background.** A particular problem in the EXAFS is low frequency background modulations and absorption contributions attributed to the absorbing atom. This is the contribution expected from the absorbing atom in the absence of neighbouring atoms. These components are approximated by splines and subtracted from the spectra.

At this stage XANES data may be extracted to a graphical image program such as Excel or Origin. Further data manipulation is required in the treatment of the EXAFS data.

7. **Weighting of EXAFS data.** The EXAFS data show a rapid drop in the data intensity at high k and this implies a loss of structural information. The data, therefore, is weighted by k^3 amplifying the high k data to ensure it may be fitted satisfactorily and not overlooked, see Figure 2-38.

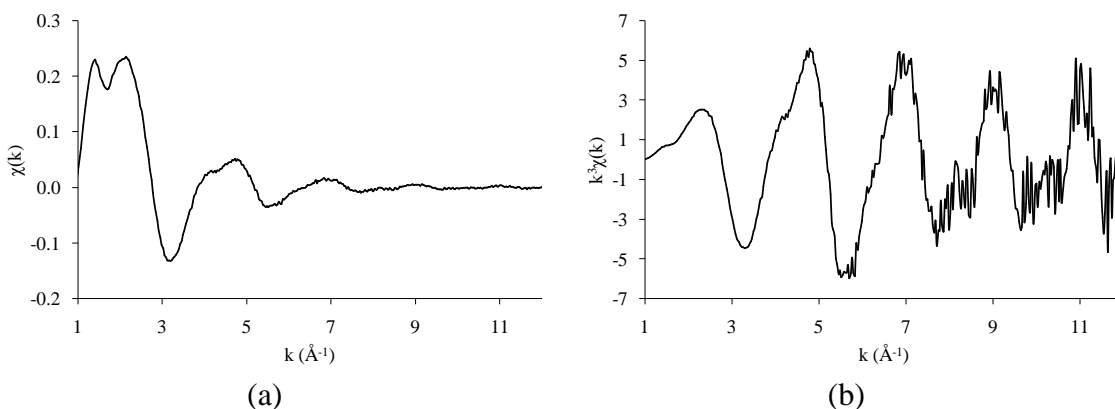


Figure 2-38. Representation of (a) EXAFS in $\chi(k)$ and (b) weighted by k^3 .

8. **Fourier transform.** Fourier transform of the EXAFS data provides an additional representation of intensity against interatomic distance. Such a representation is a useful visual guide to the quality of the fit.

2.3.6 Thermogravimetric Analysis (TGA)

Thermogravimetric analysis is the measurement of the change in a sample's weight with temperature. TGA can be performed under a number of different atmospheres and the resulting mass changes can be used as an indication of a number of features such as chemical composition, reactivity or thermal stability.

The apparatus used is simple and consists of a balance, with the sample stage positioned within a small furnace, under a flowing stream of gas Figure 2-39.

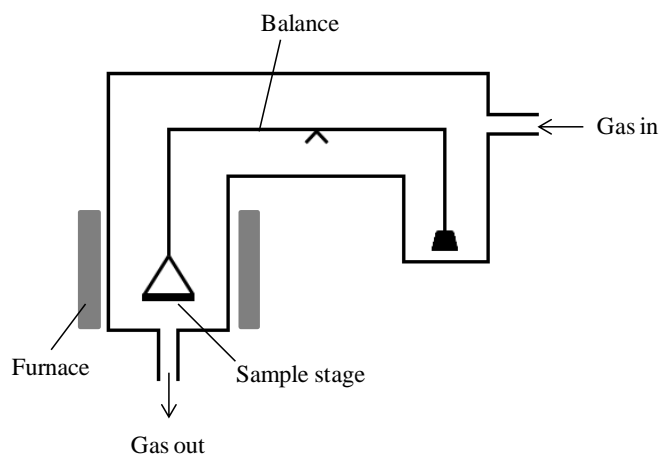


Figure 2-39. Representation of a TGA instrument.

TGA was used in this work (chapter 6) to determine the nitrogen content of oxide-nitrides. The TGA data were collected by Slater and co-workers at the University of Birmingham.

2.3.7 Energy Dispersive X-ray Analysis (EDX)

As specified in section 2.3.2.2.1, when a material is bombarded with electrons the result is the emission of X-rays specific to the atoms being targeted. A similar result is observed when a material is bombarded by electrons in a scanning electron microscope (Figure 2-40). By collecting the emitted radiation a unique fingerprint of the compound is produced as a plot of intensity versus X-ray energy. The relative peak position and intensity may be used to derive the elemental content of the sample.

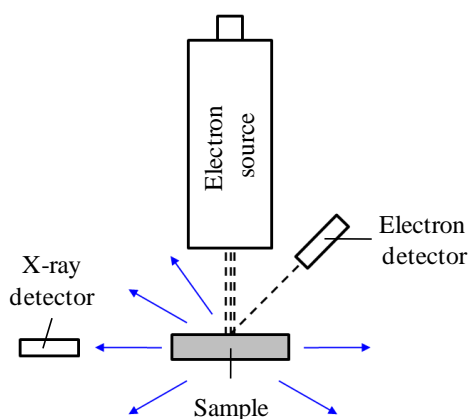


Figure 2-40. Representation of an SEM with EDX attachment. The black dotted lines and blue arrows represent electrons and X-rays respectively.

2.3.8 Magnetic Measurements

Magnetic measurements were performed on a Quantum Design MPMS SQUID magnetometer at the University of Birmingham.

The Superconducting Quantum Interference Device (SQUID) is a highly sensitive technique used for the measurement of magnetic properties of materials, allowing detection of a mass susceptibility of below $10^{-12} \text{ emu g}^{-1}$.²²⁸

A SQUID utilises a Josephson junction, which can be described as a weak link between two superconducting regions. An example would be a thin layer of insulator separating two superconducting regions (Figure 2-41).

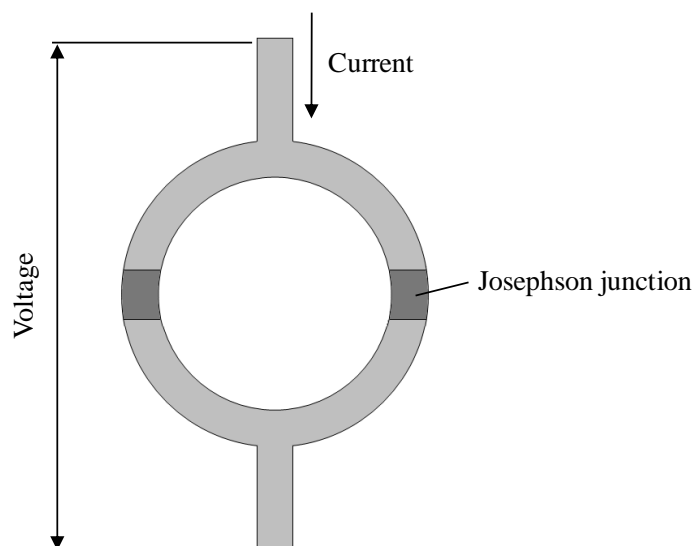


Figure 2-41. DC superconducting quantum interferometer with two Josephson junctions.

Below a critical current I_c the Cooper pairs of the superconducting material can tunnel across this insulating layer without destroying their coupling or the superconductivity.^{206, 228} The maximum critical current, i_{cmax} , that can flow across the device is given by:

$$i_{cmax} = 2I_j \cos\left(\frac{\pi\Phi}{\Phi_0}\right) \tag{2-23}$$

where I_j is a constant dependent on the junction geometry, Φ is the enclosed magnetic flux and Φ_0 is the flux quantum.²⁰⁶

For a loop of superconducting material the magnetic flux within it is trapped and may only exist in discrete levels i.e. it is quantised to take on multiples of the flux, Φ_0 . In a SQUID, introduction of a magnetic material into the system produces changes in the voltage passing through the superconducting loop which is proportional to the flux.²²⁹ Hence the SQUID is used to determine small changes in the magnetic flux arising from an externally applied field. From this the magnetic properties of the material may be determined.

2.3.9 Nuclear Magnetic Resonance Spectroscopy (NMR)

NMR spectroscopy works on the principle that atoms showing a non-zero spin angular momentum, i.e. a dipole moment will, under an applied magnetic field, align themselves either with the field or opposite to it. In general the energy difference between these two states will be sufficient for a slightly higher population of the lower energy state i.e. alignment with the field. The difference between these two states is sufficiently small to allow transitions between the two levels under irradiation with electromagnetic radiation, specifically radio waves, i.e. a pulse of radio frequency radiation. This will result in a change in spin direction. The excited nuclei then relax to the lower energy state with the emission of a characteristic decay frequency, which is dependent on the atom in question and is influenced by its coordination environment. The resulting data is represented as a series of peaks, corresponding with each magnetic centre in different coordination environments, shifted relative to a known internal standard. The integrated intensity of these peaks is proportional to the number of magnetic centres which gave rise to it.

Solid state NMR generally consists of very broad peaks due to anisotropic chemical shifts and dipole-dipole interactions.²³⁰ The chemical shift anisotropy is a modification in the applied magnetic field observed by the magnetic centre due to the surrounding electrons. This is different in each of the three spatial dimensions (anisotropic). As the

sample consists of a powder in a near infinite number of orientations the resulting NMR pattern shows contribution from all of these different states and the peak breadth is large.²³⁰

In samples showing magnetically dilute spin systems, i.e. those showing a relatively low quantity of the magnetic atom well separated throughout the structure, the dipole-dipole contribution to the peak broadening is lower than ‘concentrated’ spin systems. These, along with the chemical shift anisotropy, can be reduced further through the use of magic angle spinning (MAS) techniques.²¹³ By spinning the sample at speeds higher than several kHz, the shift anisotropy is altered by a factor of $(3\cos^2\theta - 1)$.²³⁰ Hence a value of $\theta = 54.74^\circ$ (the magic angle) will remove the anisotropy leaving an isotropic chemical shift and a well defined set of peaks in the NMR spectrum.

In this work (chapter 6), ²⁹Si NMR was carried out by the Solid-State NMR Service at Durham University to determine the different Si environments in silicon oxide apatites. The peak positions are taken relative to tetramethylsilane, to allow comparison between the patterns.

3 Low Temperature Magnetic Structures of Ba₂MS₃ (M = Co, Mn)

3.1 Ba₂MS₃ (M = Co, Mn)

Ba₂MS₃ (M = Co, Mn) are classed as one-dimensional structures, both showing corner connected chains of MX₄ tetrahedra (section 1.2). These compounds have been investigated for their magnetic properties as the one-dimensional MX₄ chains can be considered independent, with sufficient spacing between the chains, from interleaved Ba²⁺ layers, preventing interchain interaction.⁶⁰ In addition, the transition metal ions at the centres of the tetrahedra, within the chains, are considered to be sufficiently separated (> 4 Å) to negate direct interaction of these magnetic centres. This implies that any magnetic interaction is mediated by the bridging anions. Such systems allow investigation into superexchange interactions.

Magnetic susceptibility measurements were carried out on Ba₂MnX₃ (X = S, Se, Te) by Greaney *et al.*⁶⁰ The susceptibility data on these materials exhibited a broad maximum at 100 K, which was attributed to one-dimensional magnetic order. To quantify the exchange constant, J, and find the extent of the coupling interactions Grey *et al.* fitted the inverse susceptibility data to a modified version of the Heisenberg model of linear chain antiferromagnetism.⁵⁸ The values obtained for J/k are given in Table 3-1.

Material	J/k (/K)	Mn-Mn (Å)
Ba ₂ MnS ₃	-12.3	4.31
Ba ₂ MnSe ₃	-9.8	4.47
Ba ₂ MnTe ₃	-7.6	4.73

Table 3-1. Exchange constant, J/k, and metal-metal distances for the Ba₂MnX₃ (X = S, Se, Te) series.⁶⁰

The magnetic interaction was predicted to increase with the increasing polarisability of the chalcogenide anions S²⁻ → Se²⁻ → Te²⁻. However, the increasing size of the anion results in increased Mn-Mn separation and reduced efficiency in orbital overlap. The extent of magnetic interaction therefore reduces with increased Mn-Mn distance.⁶⁰ Another contributing factor is the reduction in orbital overlap from a decrease in

Mn-X-Mn bridging angle; 119.8° for $X = S^{2-}$, 118.5° for $X = Se^{2-}$ and 116.3° for $X = Te^{2-}$.

The susceptibility data showed no other transitions upon cooling, however, it was suggested by Greaney *et al.* that, at very low temperatures, there could be an onset of three-dimensional order, with interactions between the chains.⁶⁰ Susceptibility measurements, by Baikie *et al.*, are shown in Figure 3-1.^{231, 232}

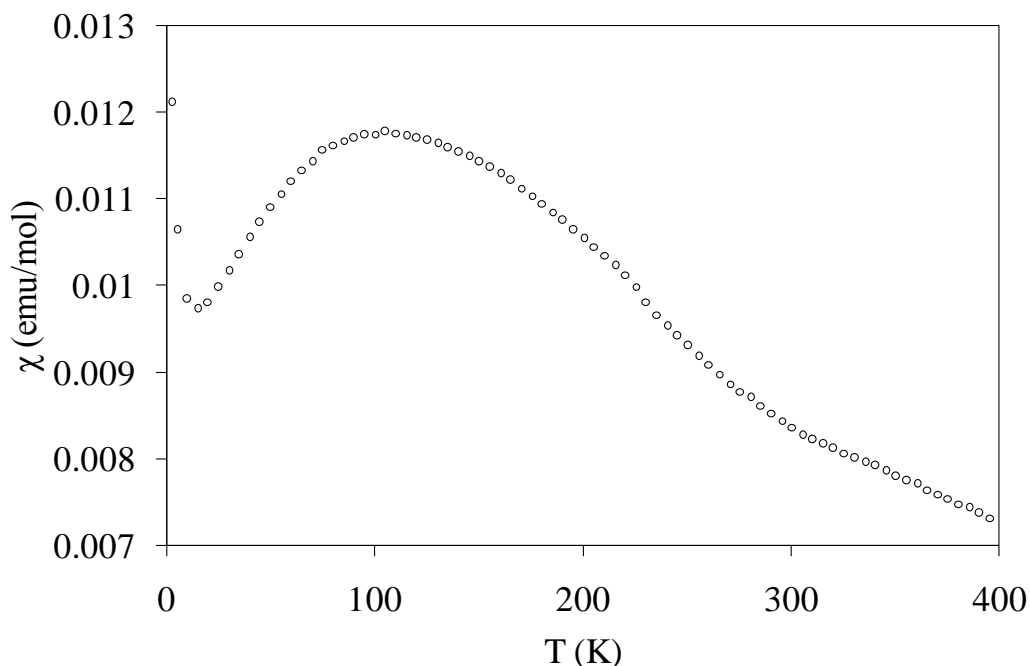


Figure 3-1. Magnetic susceptibility versus temperature, Ba_2MnS_3 (ZFC 500 Oe). Recreated from reference.²³²

Magnetic susceptibility studies into the related Ba_2MS_3 ($M = Fe, Co$) have also indicated one-dimensional antiferromagnetism with similar rounded maxima in the data (130 K and 125 K for Fe and Co) as those observed in Ba_2MnX_3 .^{54, 56, 58, 60, 233} The behaviour of Ba_2CoS_3 in a magnetic field has been of particular interest as Ba_2CoS_3 shows negative magnetoresistance (MR). Magnetoresistance is the change in conductivity of a material upon the application of a magnetic field. Magnetoresistance was discovered in 1856 by Lord Kelvin, who, while investigating iron, found an increase in resistivity of 0.2% when applying a magnetic field parallel to the current direction and a 0.4% decrease when the magnetic field is applied normal to the current.^{234, 235} At 10 K, the application of 7 T to Ba_2CoS_3 results in a -1.7% change in

resistance.⁵⁴ This negative MR is relatively unusual in one-dimensional sulfides. The previous highest negative MR seen in one-dimensional sulfides was a change of -0.8% , in 7 T at 80 K in $\text{BaV}_{0.8}\text{Ti}_{0.2}\text{S}_3$.⁵⁵ Currently, the origin of the negative MR in Ba_2CoS_3 is unknown. Cationic substitution of Co^{2+} with the non-magnetic Zn^{2+} has shown an increase in negative MR to -9% , in $\text{Ba}_2\text{Co}_{0.5}\text{Zn}_{0.5}\text{S}_3$, with the destruction of the one-dimensional antiferromagnetic ordering.²³⁶ This implies the magnetic structure of these sulfides plays a significant role in their physical properties and understanding these will aid in the understanding negative MR behaviour. The susceptibility versus temperature curve for Ba_2CoS_3 is given in Figure 3-2.

Nakayama *et al.* modelled the magnetic susceptibility using a ‘reduced spin’ approximation, based on the Ising model. Varying the J and g values resulted in J/k of -20.5 K and -15 K for Ba_2FeS_3 and Ba_2CoS_3 respectively.²³³ A study of ^{57}Fe Mössbauer spectroscopy on Ba_2FeS_3 also indicating that at low temperatures (~ 4.2 K) there is peak splitting associated with the onset of three-dimensional magnetic order.

A more recent study, by Barnes *et al.*, involved the analysis of susceptibility measurements, taken on Ba_2CoS_3 , and suggested an alternative model for the data.²²⁷ The susceptibility data (Figure 3-2) is in agreement with the data collected by Nakayama *et al.* showing the smooth curve in the susceptibility versus temperature plot, expected for one-dimensional antiferromagnetism. This broad maximum is attributed to the competition between pure paramagnetism (favoured when thermal energies are significant) and antiferromagnetic interactions along the chains. Susceptibility measurements over the 20 - 400 K range were analysed by splitting the data into a high temperature range ($T > 200$ K) and an intermediate range (110 - 380 K), fitting suitable models to the reciprocal susceptibility data and averaging the resulting coupling constants.

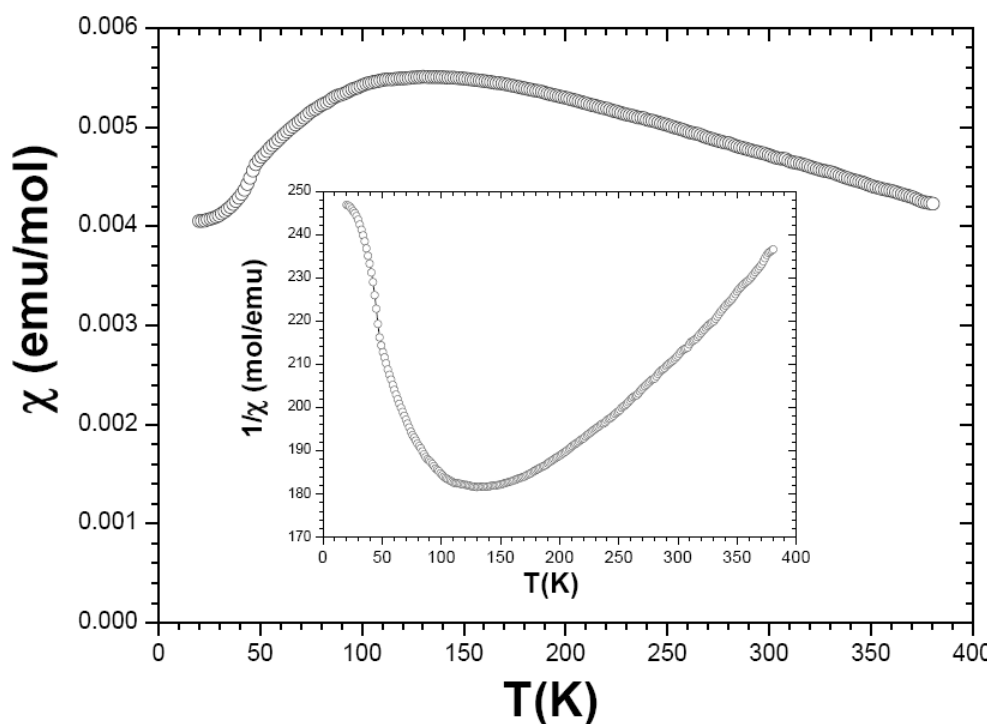


Figure 3-2. Main panel: temperature dependence of the magnetic susceptibility χ for Ba_2CoS_3 . Inset: temperature dependence of the reciprocal susceptibility $1/\chi$. Reproduced from the literature, with permission.²²⁷

High temperature data in the $1/\chi$ curve are usually modelled using the Curie-Weiss law to obtain numerical values for the exchange constants. However, a linear regime is necessary for the Curie-Weiss model to give reliable results. A linear regime was not found in the $1/\chi$ data for Ba_2CoS_3 and therefore more complex models needed to be used. The models considered need to take into account the magnetic anisotropy of the compound or, in other words, the compound should be treated in the Heisenberg-like or Ising-like limit.

The high temperature range of the $1/\chi$ curve was fitted using series expansions for both the Heisenberg and Ising models to ascertain which best describe Ba_2CoS_3 .²²⁷ The best fit to the data was found to be the Heisenberg model. The values of J and g derived from the series expansion were -35.1 K and 2.35 respectively.²²⁷ The fitting to the experimental data deviated from the calculated model at low temperatures.

The intermediate temperature range (110 - 380 K) was fit with the Wagner Friedberg model, which is a modification of the Heisenberg model to account for S values not equal to $1/2$ or ∞ . Values of J and g were -38.6 K and 2.37 respectively.²²⁷

Overall values of $J = -37 \pm 2$ K and $g = 2.36 \pm 0.01$ were derived from these two models.

Furthermore, there is some evidence of three dimensional long-range order at low temperatures for Ba_2CoS_3 . Magnetic susceptibility, collected in a 1 T field, and specific heat capacity (taken over 2 - 80 K) measurements have both shown a feature at 46 K (Figure 3-3). The shape of the susceptibility curve below this feature was noted to be similar to three-dimensional transitions in other spin chain systems showing a Néel temperature, T_N . The presence of a feature in the specific heat capacity measurements (Figure 3-3 (b)) is also significant as it is theoretically predicted for antiferromagnetic long range order, confirming the suggestion that the peak in the susceptibility curve, at 46 K, is the Néel temperature.²³⁷

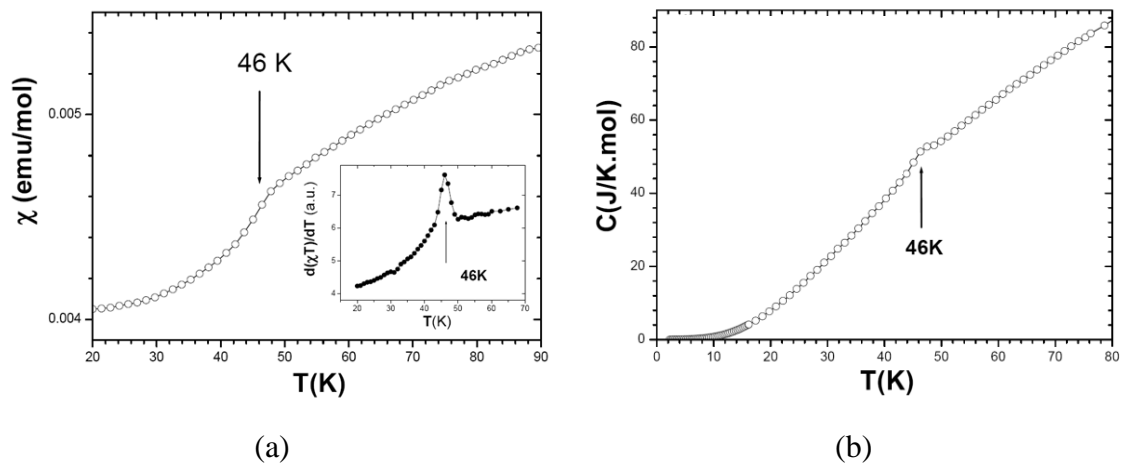


Figure 3-3. (a) Main panel: magnetic susceptibility, Inset: derivative of χT and (b) total heat capacity measurements on Ba_2CoS_3 (arrows indicate the Néel temperature at 46 K).

The interchain coupling constant was shown to be ≈ -0.9 K. This is consistent with the introduction of long-range antiferromagnetism.²²⁷

In summary, the Ba_2MX_3 ($M = \text{Co}, \text{Mn}, \text{Fe}, X = \text{S}, \text{Se}, \text{Te}$) type compounds are one-dimensional Heisenberg antiferromagnetic materials, with intrachain coupling of the magnetic centres occurring along the ${}^1_{\infty}[\text{MX}_2\text{X}_{2/2}^{4-}]$ chains. Analysis of the low temperature susceptibility data implies the presence of three-dimensional magnetic order. Susceptibility and specific heat capacity data by Barnes *et al.* on Ba_2CoS_3 shows

that below 46 K there is a transition to long-range antiferromagnetic order. Section 3.2 includes the preparation of and analysis of low temperature neutron diffraction data collected for two sulfides, Ba_2CoS_3 and Ba_2MnS_3 , to characterise the three-dimensional magnetic structures.

3.2 Structural Description of Ba_2MS_3 (M = Co, Mn)

In this work, the structure of Ba_2CoS_3 and Ba_2MnS_3 were investigated, in collaboration with Prof. Peter Battle, with particular focus on the confirmation and determination of three-dimensional magnetic ordering through low temperature PND.²³⁸

3.2.1 Experimental

3.2.1.1 Preparation

The synthesis of the ternary sulfides was achieved via a solid-gas reaction between stoichiometric mixtures of barium carbonate (Alfa Aesar, 99%) and transition metal powders, Mn (Aldrich, 99.99%), Co (Fluka, > 99.8%) or transition metal carbonates, CoCO_3 (Sigma-Aldrich, 99.998%), MnCO_3 (Sigma-Aldrich, > 99.9 % with carbon disulfide, CS_2 (Fisher Scientific, > 99%). Carbon disulfide is a liquid with low vapour pressure. If nitrogen gas is bubbled through liquid CS_2 , the gas acts as a carrier allowing a vapour of CS_2/N_2 to flow through the tubular furnace. The reaction set-up is shown in section 2.2.2.2.

Stoichiometric mixtures of the relevant reagents were loaded into a carbon boat and the reactions were performed under a CS_2/N_2 flow at 1000 °C for 48 hours with intermittent re-grinding. The samples were then slow cooled to room temperature.

3.2.1.2 Characterisation

Powder X-ray diffraction (PXRD) was carried out on all samples using a Siemens D5000 powder diffractometer with $\text{Cu K}\alpha$ radiation. Low temperature PXRD was also

performed on Ba₂MnS₃ by Professor G. Calestani at the University of Parma (Italy) down to the temperature of liquid nitrogen (~ 77 K). In addition to PXRD, high-resolution neutron diffraction data were collected, in collaboration with Prof. Peter Battle, at $\lambda = 2.3975 \text{ \AA}$ and $\lambda = 1.5943 \text{ \AA}$ for Ba₂CoS₃ and Ba₂MnS₃ respectively, over an angle range of $4 \leq 2\theta/^\circ \leq 157.45$, $\Delta 2\theta = 0.05^\circ$, on the D2B diffractometer at the Institute Laue-Langevin (ILL), Grenoble. The samples were contained in a vanadium can of internal diameter 8 mm, and the temperature was regulated using an ILL orange cryostat; data were collected at 200 K for both sulfides and low temperature data were collected at 4 K for Ba₂MnS₃ and at 1.5 K for Ba₂CoS₃. Data were collected for 8 hours at both 200 and 1.5 K; the relatively long collection times were a consequence of the weakness of the observed scattering. The powder diffraction data were analysed by profile analysis²³⁹ as implemented in the GSAS suite of programs.^{217, 240}

3.2.2 Results and Discussion

3.2.2.1 Structural Characterisation of Ba₂CoS₃

3.2.2.1.1 Powder X-ray Diffraction (PXRD) – Room Temperature

Reactions of a stoichiometric mixture of BaCO₃ and Co, under CS₂/N₂, resulted in the successful preparation of black polycrystalline Ba₂CoS₃. PXRD indicated a near single phase sample of Ba₂CoS₃ with a small quantity of BaS impurity also present. No corresponding crystalline Co-containing impurity could be identified, although the use of a stoichiometric mixture of reactants requires that one must be present.

A two phase Rietveld refinement using X-ray diffraction data was performed. A structural model by Baikie was used for the first phase, Ba₂CoS₃.²³² The model published by Rad and Hoppe, was used for the second phase, BaS.^{64, 232} The background was modelled using the reciprocal interpolation function with fourteen terms and the peak shape by a multi-term Simpson's rule integration of the pseudo-Voigt.^{241, 242} No absorption correction was applied. The parameters refined were: the cell parameters (a , b , c) for the two phases, one zero point, one scale factor,

one phase fraction, twelve atomic coordinates, six isotropic thermal parameters, seven profile parameters and fourteen background parameters. To ensure reasonable values, the isotropic thermal parameters, U_{iso} , were constrained to be equal for the sulfur positions. The refinement parameters are summarised in Table 3-2 and the refinement profile given in Figure 3-4.

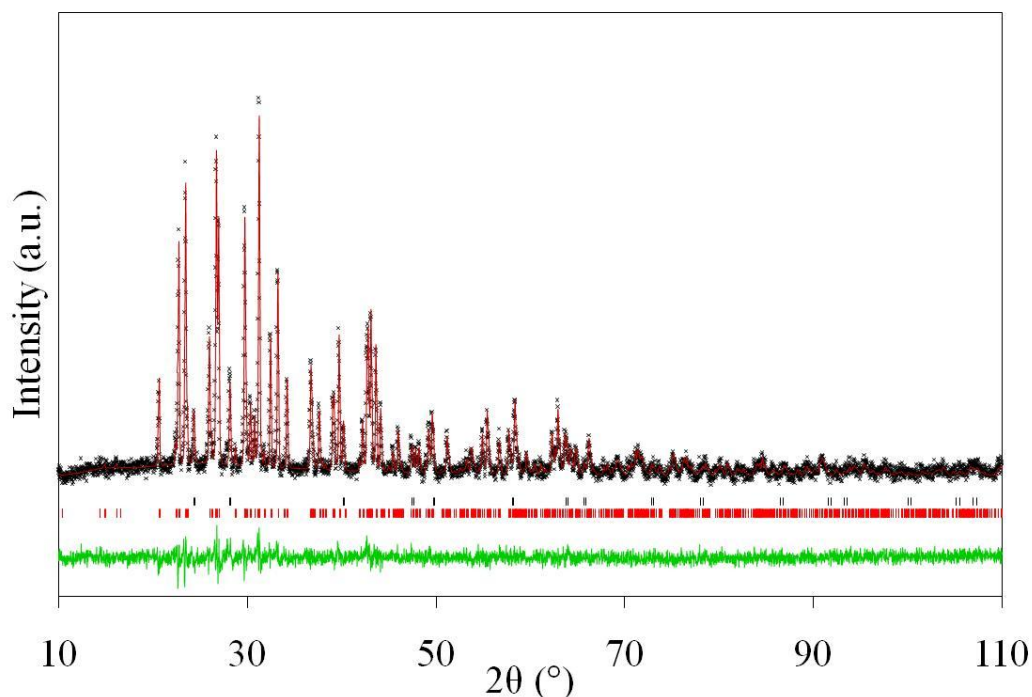


Figure 3-4. PXRD profiles for Ba_2CoS_3 at room temperature, showing observed (+), calculated (red line) and difference pattern (green line). Tick marks indicate reflection positions for BaS (upper) and Ba_2CoS_3 (lower) phases.

Formula	Ba_2CoS_3	
Space Group	$Pn\bar{m}$ (no. 62)	
	PXRD data	Baikie ²³²
a (Å)	12.0058(4)	12.000(1)
b (Å)	12.4769(5)	12.470(1)
c (Å)	4.2074(1)	4.205(2)
V (Å ³)	630.24(6)	629.236(2)
Z	4	
Calculated density (g cm ⁻³)	4.529	
No. of profile points	5250	
No. of parameters refined	44	
R_{wp}	0.0437	
R_{p}	0.0345	
χ_{red}^2	1.363	

Table 3-2. Summary of refinement data and lattice parameters for Ba_2CoS_3 at room temperature.

Ba₂CoS₃ has the space group *Pnam* and cell parameters $a = 12.0058(4)$ Å, $b = 12.4768(5)$ Å and $c = 4.2074(1)$ Å, which is consistent with known unit cell dimensions for Ba₂CoS₃ (Table 3-2).²³² Quantitative determination of the BaS content indicated 5.9(1) %, weight percentage, of this secondary phase. The structural parameters for Ba₂CoS₃ are given in Table 3-3.

Atom	Site	x	y	z	100 × U _{iso}	Occ.
Ba(1)	4c	0.3274(3)	0.0201(2)	¼	2.0(1)	1.0
Ba(2)	4c	0.9877(3)	0.8274(2)	¼	2.1(1)	1.0
Co	4c	0.2438(6)	0.3043(6)	¼	2.5(3)	1.0
S(1)	4c	0.3649(8)	0.4475(8)	¼	0.4(2)	1.0
S(2)	4c	0.0615(8)	0.3590(9)	¼	0.4(2)	1.0
S(3)	4c	0.7244(8)	0.7887(9)	¼	0.4(2)	1.0

Table 3-3. Structural parameters for Ba₂CoS₃ derived from PXRD collected at room temperature.

3.2.2.1.2 Powder Neutron Diffraction (PND) – 200 K

Powder neutron diffraction was performed at 200 K and 1.5 K. A comparison between the two sets of data was performed to confirm further the occurrence of three-dimensional magnetic ordering at 46 K and to determine the three-dimensional magnetic structure.²²⁷ A two phase Rietveld refinement was performed using the neutron data collected at 200 K.^{217, 239, 240} Structural models, for Ba₂CoS₃ and BaS, obtained from X-ray diffraction at room temperature were used for the refinement.

Despite the extended data collection time the signal-to-noise ratio was relatively poor, but the Bragg peaks were not unusually broad. The relatively poor signal-to-noise ratio could be due, in part, to the relatively poor scattering interactions of the elements involved. The interaction of neutrons with the nuclei is proportional to the scattering length. Table 3-4 gives some examples of the coherent scattering lengths, b_c , of the atoms in question and atoms nearby in the periodic table are also included for comparison. It can be seen that the scattering lengths of Ba, Co and S are relatively low, compared to those of other elements.

Element	$b_c/1 \times 10^{-15}$ m	Element	$b_c/1 \times 10^{-15}$ m	Element	$b_c/1 \times 10^{-15}$ m
Rb	7.09	C	6.646	Mn	-3.73
Sr	7.02	N	9.36	Fe	9.45
Y	7.75	O	5.803	Co	2.49
Zr	7.16	F	5.654	Ni	10.3
Cs	5.42	Si	4.1491	Tc	6.80
Ba	5.07	P	5.13	Ru	7.03
La	8.24	S	2.847	Rh	5.88
Ce	4.84	Cl	9.577	Pd	5.91

Table 3-4. Table of selected neutron coherent scattering lengths.³⁹

The presence of a high background level observed in the neutron diffraction data may be a result of an amorphous or poorly-crystalline Co-containing impurity phase. This phase has not been identified to date. The broad peak in the difference profile at $2\theta \sim 45^\circ$ may also be attributable to this Co-containing impurity. The presence of a Co-containing impurity is also supported by the presence of BaS and full occupancies of all sites (Table 3-6), which indicates that no anion or cation vacancies are present. The poor fit to the profile below $2\theta < 45^\circ$ is attributable to the presence of modulations in the diffuse background scattering consistent with the presence of one-dimensional magnetic order. This interpretation is in agreement with the susceptibility and heat capacity data, which suggest that one-dimensional ordering is developing close to room temperature with long-range ordering only observed below $T_N = 46$ K.²²⁷ However, it is important to emphasise the speculative nature of this hypothesis. It can be seen in the following section (Figure 3-8) that this background scattering is reduced in the 1.5 K data. The background was modelled using the linear interpolation function, with 36 terms to account for this modulating background. The peak shape was fit using a multi-term Simpson's rule integration of the pseudo-Voigt.^{241, 242} No absorption correction was applied. The parameters refined were: the cell parameters (a , b , c) for the two phases, one zero point, one scale factor, one phase fractions, twelve atomic coordinates, six isotropic thermal parameters, five profile parameters and thirty-six background parameters. To ensure reasonable values, all isotropic thermal parameters, U_{iso} , were constrained to be equal in Ba_2CoS_3 . The residual fit parameters are $R_{wp} = 0.0395$, $\chi^2_{red} = 3.002$. The refinement parameters are summarised in Table 3-5 and the refinement profile is shown in Figure 3-5.

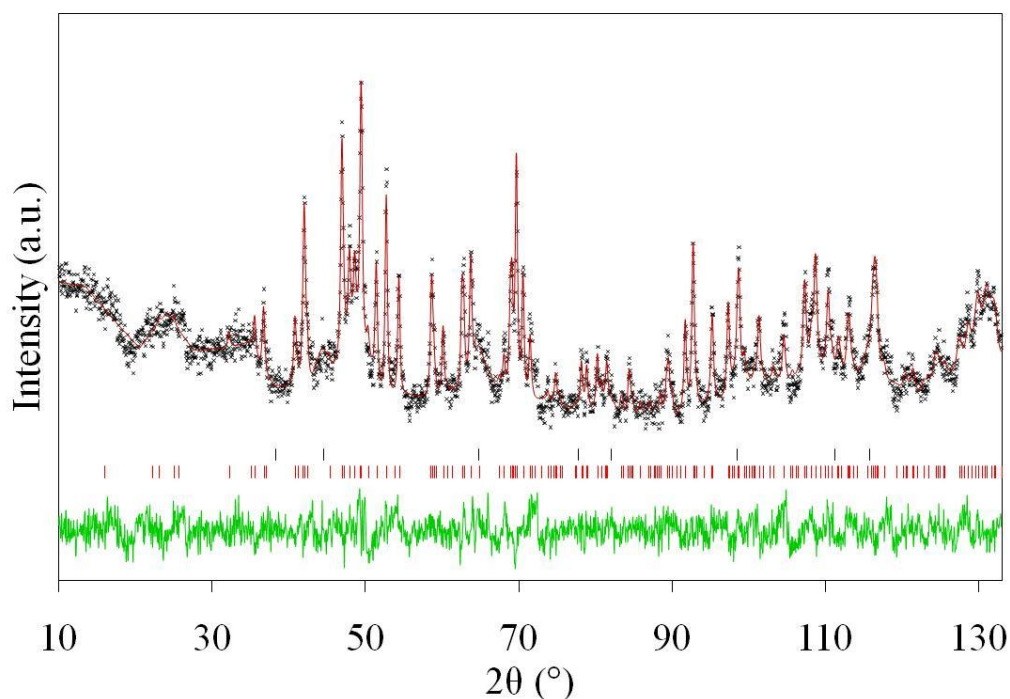


Figure 3-5. PND profiles for Ba_2CoS_3 at 200 K, showing observed (+), calculated (red line) and difference pattern (green line). Tick marks indicate reflection positions for BaS (upper) and Ba_2CoS_3 (lower) phases.

Formula	Ba_2CoS_3	
Space Group	$Pnam$ (no. 62)	
	This work	PXRD data
a (Å)	11.9780(10)	12.0058(4)
b (Å)	12.4519(10)	12.4769(5)
c (Å)	4.1947(3)	4.2074(1)
V (Å ³)	625.6(1)	630.24(6)
Z	4	
Calculated density (g cm ⁻³)	4.563	
Profile function	Pseudo-Voigt	
No. of profile points	2459	
No. of parameters refined	61	
R_{wp}	0.0395	
R_{p}	0.0311	
χ_{red}^2	3.002	

Table 3-5. Summary of refinement data and lattice parameters for Ba_2CoS_3 at 200 K.

Quantitative determination of the BaS content indicated 12(1) %, weight percentage, of the secondary phase. The higher BaS content observed with the neutron diffraction data compared to the X-ray diffraction data (12% versus 5.9% respectively) may be a result

of the greater penetration depth of neutrons over X-rays into the sample.²¹³ In fact, the data obtained from the refinement using neutron diffraction are in good agreement with both the literature values and those determined from X-ray diffraction data in the previous section.²³² As may be expected, the lower temperature at which the neutron diffraction data were collected resulted in a small reduction in the unit cell dimension. The cell parameters are given in Table 3-6.

Atom	Site	x	y	z	$100 \times U_{\text{iso}}$	Occ.
Ba(1)	4c	0.3291(7)	0.0158(7)	$\frac{1}{4}$	0.3(3)	1.0
Ba(2)	4c	0.9877(8)	0.8265(7)	$\frac{1}{4}$	0.3(3)	1.0
Co	4c	0.2469(16)	0.3022(14)	$\frac{1}{4}$	0.3(3)	1.0
S(1)	4c	0.3644(12)	0.4504(11)	$\frac{1}{4}$	0.3(3)	1.0
S(2)	4c	0.0593(12)	0.3587(13)	$\frac{1}{4}$	0.3(3)	1.0
S(3)	4c	0.7274(11)	0.7923(12)	$\frac{1}{4}$	0.3(3)	1.0

Table 3-6. Structural parameters for Ba_2CoS_3 derived from PND collected at 200 K.

The Co-S bond lengths and angles, shown in Table 3-7, confirm that Co^{2+} is in a highly distorted tetrahedral environment.

Bond lengths (Å)			
Ba(1)-Co	$3.51(2) \times 2$	Co-S(1)	2.32(2)
	3.70(2)		
Ba(1)-S(1)	3.23(1)	Co-S(2)	2.35(2)
Ba(1)-S(2)	$3.16(2) \times 2$	Co-S(3)	$2.43(1) \times 2$
	3.17(2)		
Ba(1)-S(3)	$3.25(1) \times 2$		
Ba(2)-Co	$3.82(2) \times 2$		
	$3.86(2) \times 2$		
Ba(2)-S(1)	$3.15(1) \times 2$	Co-Co (intrachain)	4.1947(3)
	3.15(2)		
Ba(2)-S(2)	$3.17(1) \times 2$		6.128(7)
Ba(2)-S(3)	3.23(2)	(interchain)	6.5702(6)
Angles (°)			
S(1)-Co-S(2)	110.0(9)	S(2)-Co-S(3)	105.5(5)
S(1)-Co-S(3)	108.0(5)	S(3)-Co-S(3)	119.8(9)

Table 3-7. Selected bond lengths and angles in Ba_2CoS_3 from neutron data collected at 200 K.

3.2.2.1.3 Powder Neutron Diffraction (PND) – 1.5 K

In general the 1.5 K data resembles the 200 K data, with the intensities of the peaks marginally increased. However, in the low angle range ($2\theta < \sim 30^\circ$) of the pattern of data collected at 1.5 K there are a number of peaks, which do not appear in the 200 K data. These peaks could not be accounted for using the orthorhombic unit cell of Ba_2CoS_3 and were attributed to magnetic Bragg scattering associated with the onset of long-range antiferromagnetic order developing in this angular region on cooling below the T_N temperature. These additional peaks are highlighted in Figure 3-6. This interpretation is consistent with the susceptibility and heat capacity data which suggest that one-dimensional ordering is developing at 200 K, and that long-range ordering is observed below $T_N \sim 46$ K.

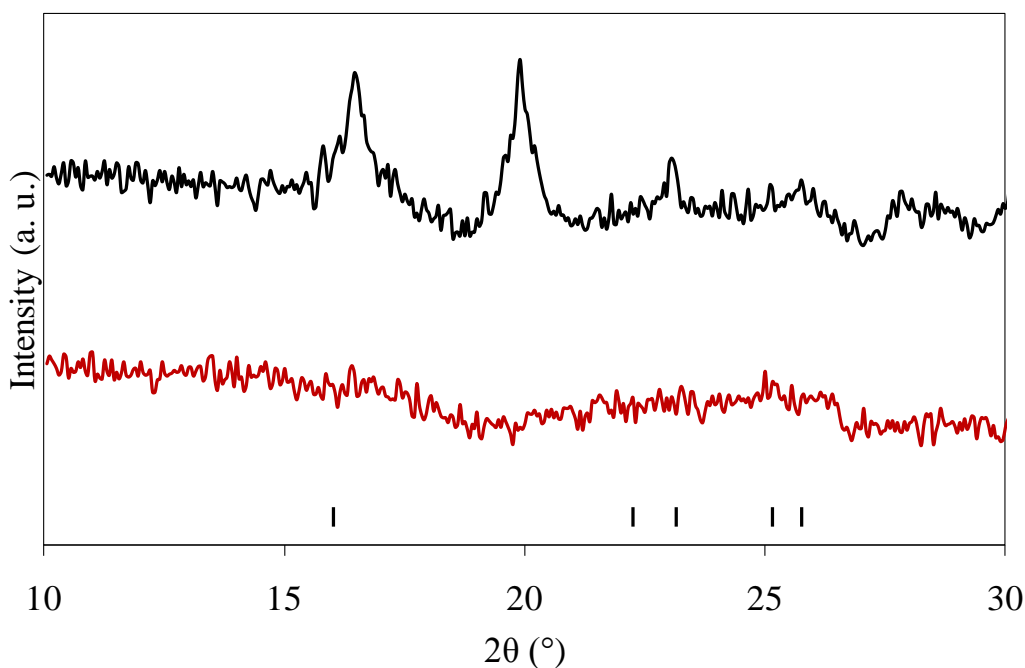


Figure 3-6. A selected low-angle range of neutron diffraction data collected on Ba_2CoS_3 at 1.5 K (black) showing the additional peaks not present in the data collected at 200 K (red). The tick marks indicate the reflection positions for the Ba_2CoS_3 crystallographic phase.

The magnetic scattering is a result of the interaction between the magnetic moment of the neutrons and those of unpaired electrons. Ba_2CoS_3 consists of Ba^{2+} , Co^{2+} and S^{2-} with electronic configurations $[\text{Xe}].6s^0$, $[\text{Ar}].3d^7$ and $[\text{Ne}].3s^2.3p^6$ respectively. Among these only Co^{2+} has an unclosed electron shell. The distorted tetrahedral coordination of the $[\text{Co}^{2+} - \text{S}^{2-}]$ polyhedra gives rise to the orbital splitting shown in Figure 3-7, which

consists of three unpaired electrons and a total spin angular momentum quantum number, S , of $3/2$.²²⁷ These Co^{2+} centres are therefore responsible for the magnetic scattering in Ba_2CoS_3 .

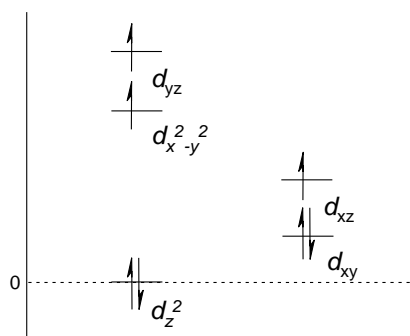


Figure 3-7. Orbital splitting of the Co^{2+} ground state.²²⁷

In the case of ferromagnetic and some antiferromagnetic materials, the ordered array of moments can be represented by a magnetic unit cell of equal dimensions to the crystallographic unit cell, $a_{\text{mag}} = a_{\text{cryst}}$, $b_{\text{mag}} = b_{\text{cryst}}$ and $c_{\text{mag}} = c_{\text{cryst}}$, where subscript “mag” and “cryst” correspond with the magnetic and crystallographic unit cells respectively. In these cases, the resulting neutron diffraction patterns resemble those arising from crystallographic scattering alone with subtle changes in the relative intensities of the peaks due to the contribution from magnetic scattering. If, however, the antiferromagnetic array of moments extends beyond the crystallographic unit cell the magnetic unit cell may be described as a multiple of the unit cell, along one, two or all three cell axes. This extended unit cell gives rise to additional peaks within the neutron diffraction pattern. To determine the dimensions of the magnetic unit cell several Le Bail extractions were performed, using the GSAS suite of programs, based on model unit cells derived from doubling axes along the a , b and c directions, along two of the three directions and along all three crystallographic unit cell directions.^{217, 240} Table 3-8 shows the residual fit parameters for these extractions.

Model	Magnetic unit cell dimensions			R_{wp}	R_p	χ_{red}^2
	a_{mag}	b_{mag}	c_{mag}			
1	a_{cryst}	b_{cryst}	c_{cryst}	0.0536	0.0375	6.418
2	$2a_{cryst}$	b_{cryst}	c_{cryst}	0.0483	0.0336	5.210
3	a_{cryst}	$2b_{cryst}$	c_{cryst}	0.0402	0.0298	3.623
4	a_{cryst}	b_{cryst}	$2c_{cryst}$	0.0358	0.0276	2.873
5	$2a_{cryst}$	$2b_{cryst}$	c_{cryst}	0.0379	0.0276	3.210
6	$2a_{cryst}$	b_{cryst}	$2c_{cryst}$	0.0337	0.0262	2.535
7	a_{cryst}	$2b_{cryst}$	$2c_{cryst}$	0.0333	0.0259	2.479
8	$2a_{cryst}$	$2b_{cryst}$	$2c_{cryst}$	0.0322	0.0247	2.312

Table 3-8. Residual fit parameters for possible magnetic unit cell dimensions for Ba_2CoS_3 derived from Le Bail extractions performed using the powder neutron diffraction data obtained at 1.5 K.

The four best fits, between the experimental data and proposed models are:

4	$a_{mag} = a_{cryst}$	$b_{mag} = b_{cryst}$	$c_{mag} = 2c_{cryst}$
6	$a_{mag} = 2a_{cryst}$	$b_{mag} = b_{cryst}$	$c_{mag} = 2c_{cryst}$
7	$a_{mag} = a_{cryst}$	$b_{mag} = 2b_{cryst}$	$c_{mag} = 2c_{cryst}$
8	$a_{mag} = 2a_{cryst}$	$b_{mag} = 2b_{cryst}$	$c_{mag} = 2c_{cryst}$

The common factor between these models is a doubling in the c axis. The residual fit parameters for these four models are very similar. Consequently the unit cell $a_{mag} = a_{cryst}$, $b_{mag} = b_{cryst}$ and $c_{mag} = 2c_{cryst}$ was chosen for the refinement with the neutron diffraction data, as the simplest model that accounts for the magnetic peaks.

A three phase Rietveld refinement was implemented to determine the magnetic unit cell.^{217, 240} The first two phases were Ba_2CoS_3 and BaS , taken from the refinement using the neutron diffraction data collected at 200 K data. These phases account for the crystallographic scattering of the diffraction pattern. The magnetic phase was introduced as the third phase to model the magnetic scattering component of Ba_2CoS_3 .

The symmetry of the crystallographic phase does not allow for all the possible orientations of magnetic moments to be considered. It was therefore necessary, and more practical, to set the magnetic unit cell to $P1$, with symmetry constraints to maintain a link to the nuclear phase. In this way each of the magnetic moments could, theoretically, be treated separately. The Co^{2+} cations in the magnetic phase and those in the nuclear phase were constrained to ensure the atomic coordinates and thermal

parameters were equivalent. The Co^{2+} x and y coordinates were constrained to move in unison between the two phases, while the z coordinates, being special positions ($z = 1/4$), were not refined. The U_{iso} values for isoatomic sites were constrained to be equal between the crystallographic and magnetic phases. The three angles, α , β and γ , of the magnetic phase were set equal to 90° and fixed. The cell parameters were also constrained between the two phases i.e. $a_{\text{cryst}} = a_{\text{mag}}$ and $b_{\text{cryst}} = b_{\text{mag}}$ and $2c_{\text{cryst}} = c_{\text{mag}}$. Consequentially the phase fraction of the magnetic phase was constrained to be half that of the nuclear phase. Only Co^{2+} cations were included in the magnetic unit cell. The crystal unit cell of Ba_2CoS_3 contains four Co^{2+} cations and therefore the magnetic unit cell contains eight Co^{2+} cations. The positions of the Co^{2+} ions in the magnetic unit cell were determined using the symmetry operation of the *Pnam* space group, i.e. the space group describing the crystallographic unit cell of Ba_2CoS_3 . These equivalent positions are listed below:

x	y	z
-x	-y	$z + 1/2$
$x + 1/2$	$-y + 1/2$	$-z + 1/2$
$-x + 1/2$	$y + 1/2$	-z

In the magnetic cell the coordinates for all the Co^{2+} must be defined individually. The doubling of the unit cell along *c* gives rise to the following set of coordinates for the eight Co^{2+} cations:

x	y	$(z)/2$
-x	-y	$(z + 1/2)/2$
$x + 1/2$	$-y + 1/2$	$(-z + 1/2)/2$
$-x + 1/2$	$y + 1/2$	$(1-z)/2$
x	y	$((z)/2) + 1/2$
-x	-y	$((z + 1/2)/2) + 1/2$
$x + 1/2$	$-y + 1/2$	$((-z + 1/2)/2) + 1/2$
$-x + 1/2$	$y + 1/2$	$((1-z)/2) + 1/2$

where x, y and z are the Cartesian coordinates of the Co^{2+} cations in the nuclear phase.

Finally, the direction and magnitude of the magnetic moments had to be defined. The spins were constrained to lie parallel, the opposed directions being represented by

opposite signs on the moments i.e. + or -. The magnitude of the spins were refined freely.

Several combinations of spin direction along a , b and c were performed in the refinement to pinpoint the direction that modelled the magnetic peaks best.

To prevent the refinement from diverging, due to the data quality, the spin directions were constrained to be along only one of the unit cell axes at any one time. For example, if the spins were set along the a axis then MY and MZ (magnetic moment in b and c respectively) were constrained to be zero.

The best agreement between model and experimental data was achieved when the atomic magnetic moments were constrained to lie along [100].

The magnitude of the magnetic moment refined to a value of 1.97(4) μ_B per Co^{2+} . The final values calculated for structural parameters and bond lengths at 1.5 K are shown in Tables B-1 and B-2 of Appendix B. Table 3-10 shows the atomic coordinates and magnetic moments for the magnetic phase. The refinement profile is shown in Figure 3-8.

Formula	Ba_2CoS_3	
Space Group	$Pnam$ (no. 62)	
	1.5 K	200 K data
a (Å)	11.971(1)	11.9780(10)
b (Å)	12.443(1)	12.4519(10)
c (Å)	4.1890(4)	4.1947(3)
V (Å ³)	624.0(2)	625.6(1)
Z	4	
Calculated density (g cm ⁻³)	4.575	
Profile function	Pseudo-Voigt	
No. of profile points	2599	
No. of parameters refined	44	
R_{wp}	0.0467	
R_p	0.0364	
χ^2_{red}	4.931	

Table 3-9. Summary of refinement data and lattice parameters for Ba_2CoS_3 at 1.5 K.

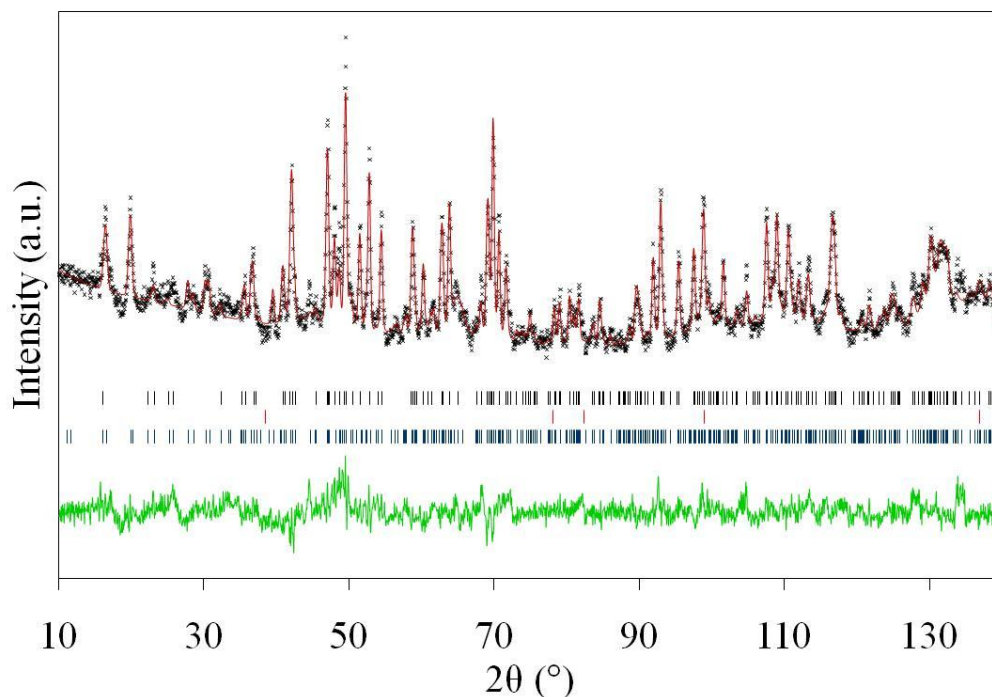


Figure 3-8. PND profiles for Ba_2CoS_3 at 1.5 K, showing observed (+), calculated (red line) and difference pattern (green line). Tick marks indicate reflection positions for Ba_2CoS_3 – crystallographic (upper), BaS (middle) and Ba_2CoS_3 – magnetic (lower) phases.

A comparison between the structure at 200 and 1.5 K shows only minor alterations, suggesting the crystallographic structure is indeed maintained.

Atom	x	y	z	m_x (μ_B)
Co(1)	0.246(1)	0.307(1)	0.1250	+1.97(4)
Co(2)	0.254(1)	0.807(1)	0.3750	+1.97(4)
Co(3)	-0.246(1)	-0.307(1)	0.3750	+1.97(4)
Co(4)	0.746(1)	0.193(1)	0.1250	+1.97(4)
Co(5)	0.246(1)	0.307(1)	0.6250	-1.97(4)
Co(6)	0.246(1)	0.807(1)	0.8750	-1.97(4)
Co(7)	-0.246(1)	-0.307(1)	0.8750	-1.97(4)
Co(8)	0.786(1)	0.193(1)	0.6250	-1.97(4)

Table 3-10. Structural parameters and magnetic moments (highlighting opposite directions) for the magnetic unit cell of Ba_2CoS_3 .

The magnetic unit cell contains 8 Co^{2+} cations, each with two nearest neighbours antiferromagnetically coupled, and the six next-nearest Co^{2+} neighbours are more than 6 Å distant (less than 6.75 Å). Ferromagnetic alignment occurs with four of these

next-nearest neighbours, and antiferromagnetic with the remaining two (Figure 3-9). The direction of the spins on Co^{2+} in the magnetic unit cell is shown in Figure 3-9 (a).

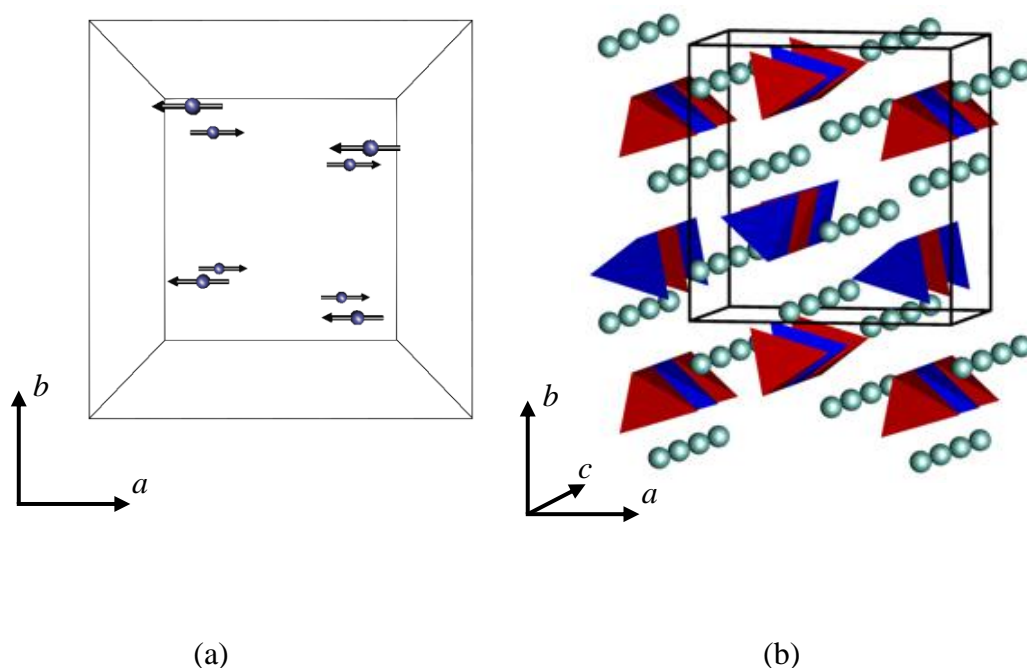


Figure 3-9. Representation of Ba_2CoS_3 magnetic unit cell along the *c* axis. In (a) the spin direction of the Co centres are shown. (b) Illustration showing the CoS_4 tetrahedra and the Ba^{2+} cations (green spheres); the different colours of the tetrahedra highlight the different spin directions of the Co^{2+} cations.

The ordered magnetic moment of the Co^{2+} cations is significantly lower than the spin-only value ($3 \mu_{\text{B}}$). This suggests that the distortion of the tetrahedral site is sufficient to quench any orbital contribution to the ordered moment, and that the value is further reduced as a consequence of covalency in the Co-S bonds. By way of comparison, the ordered moment in the spinel Co_3O_4 , in which Co^{2+} -O bonds form a regular tetrahedron has been reported to be $2.70(1) \mu_{\text{B}}$ per Co^{2+} cation.²⁴³

The relatively high Néel temperature of Ba_2CoS_3 shows that the next-nearest-neighbour interactions are still significant.²²⁷ Consequently the interchain interactions are too strong for Ba_2CoS_3 compound to be regarded as a model one-dimensional magnetic system, despite the presence of isolated chains of transition metal polyhedra in the crystal structure.

In conclusion, Ba_2CoS_3 shows three-dimensional antiferromagnetic ordering at 1.5 K, with the dominant superexchange interaction being that between Co^{2+} cations in the chains of vertex-linked CoS_4 tetrahedra that lie parallel to [001].

3.2.2.2 Structural Characterisation of Ba_2MnS_3

3.2.2.2.1 Powder X-ray Diffraction (PXRD) – Room Temperature

Reactions of stoichiometric mixtures of BaCO_3 and Mn resulted in the preparation of a near pure sample of Ba_2MnS_3 , with a small BaS impurity. In a similar way to Ba_2CoS_3 , no transition metal containing impurity could be identified.

Rietveld refinements using X-ray diffraction data were performed on a structural model by Grey and Steinfink for the first phase, Ba_2MnS_3 , and the model of BaS was taken from the refinement of Ba_2CoS_3 in the previous section.⁵⁸ The background was modelled using a cosine Fourier series and the peak shape by a multi-term Simpson's rule integration of the pseudo-Voigt.^{241, 242} No absorption correction was applied. The parameters refined were: the cell parameters (a , b , c) for the two phases, one zero point, one scale factor, one phase fractions, twelve atomic coordinates, six isotropic thermal parameters, seven profile parameters and ten background parameters. To ensure reasonable values, the isotropic thermal parameters, U_{iso} , were constrained to be equal for the sulfur positions. The refinement parameters are summarised in Table 3-11 and the refinement profile is shown in Figure 3-10.

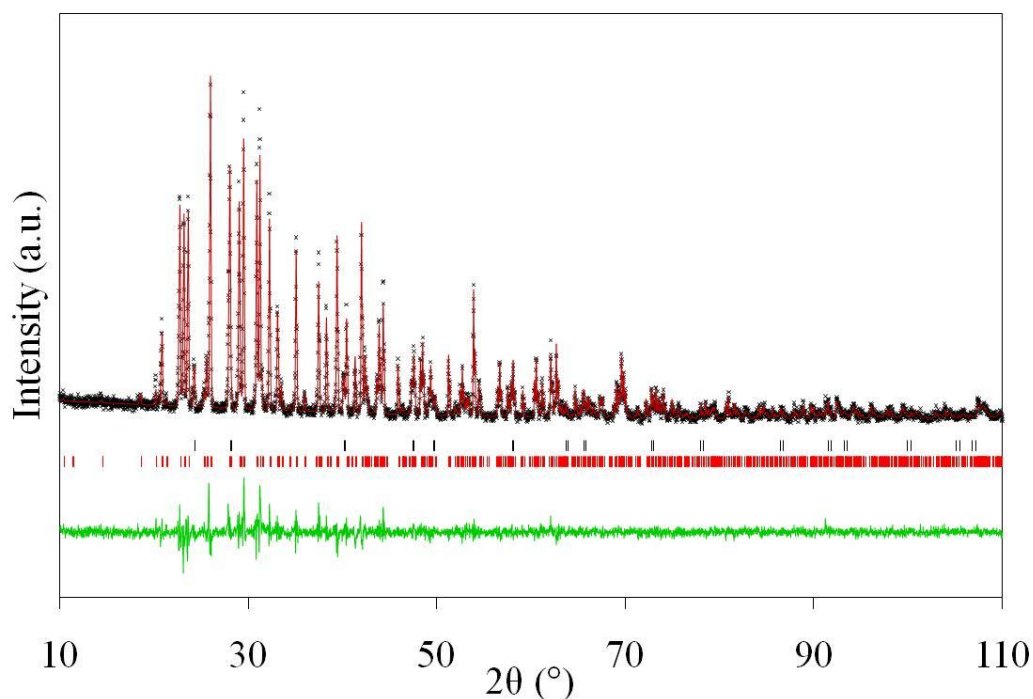


Figure 3-10. PXRD profiles for Ba_2MnS_3 at room temperature, showing observed (+), calculated (red line) and difference pattern (green line). Tick marks indicate reflection positions for BaS (upper) and Ba_2MnS_3 (lower) phases.

Formula	Ba_2MnS_3	
Space Group	$Pnma$ (no. 62)	
	PXRD data	Grey and Steinfink ⁵⁸
a (Å)	8.8231(2)	8.814(5)
b (Å)	4.3073(1)	4.302(2)
c (Å)	17.1001(3)	17.0480(80)
V (Å ³)	649.87(3)	
Z	4	
Calculated density (g cm ⁻³)	4.352	
Profile function	Pseudo-Voigt	
No. of profile points	4999	
No. of parameters refined	42	
R_{wp}	0.0818	
R_{p}	0.0639	
χ_{red}^2	1.805	

Table 3-11. Summary of refinement data and lattice parameters for Ba_2MnS_3 at room temperature.

Ba_2MnS_3 has the space group $Pnma$ and cell parameters $a = 8.8231(2)$ Å, $b = 4.3073(1)$ Å and $c = 17.1001(3)$ Å, which is consistent with known unit cell dimensions for Ba_2MnS_3 (Table 3-11). The atomic coordinates are shown in Table 3-12.

Atom	Site	x	y	z	$100 \times U_{\text{iso}}$	Occ.
Ba(1)	4c	0.4188(3)	¼	0.7129(2)	2.1(1)	1.0
Ba(2)	4c	0.2616(3)	¼	0.4564(2)	2.4(1)	1.0
Mn	4c	0.3767(7)	¼	0.1338(4)	1.9(2)	1.0
S(1)	4c	0.3112(10)	¼	0.2749(6)	0.8(2)	1.0
S(2)	4c	0.1203(11)	¼	0.0717(6)	0.8(2)	1.0
S(3)	4c	1.0024(10)	¼	0.5964(6)	0.8(2)	1.0

Table 3-12. Structural parameters for Ba₂MnS₃ derived from PXRD collected at room temperature.

3.2.2.2.2 Powder Neutron Diffraction (PND) – 200 K

The neutron diffraction data for Ba₂MnS₃ also gives a poor signal-to-noise ratio, but shows a marked improvement over the Ba₂CoS₃ data. In addition the high degree of modulation seen in the low angle $2\theta < 45^\circ$, attributed to low-dimensional magnetic ordering, is not present. This may be attributed to improved signal quality or possibly greater magnetic interactions between the magnetic centres in Ba₂CoS₃ compared to Ba₂MnS₃.

A single phase refinement was also carried out on the neutron data collected at 200 K, over the data range $10 \leq 2\theta/^\circ \leq 133$, based on the structural model derived from PXRD. Inclusion of a second phase, BaS, in the refinement failed to show an improvement to the fit and was, therefore, omitted. The background was modelled using a Cosine Fourier series with twenty-five terms and the peak shape by a multi-term Simpson's rule integration of the pseudo-Voigt.²⁴¹ No absorption correction was applied. The refinement involved the cell parameters for the Ba₂MnS₃ (*a*, *b*, *c*), one zero point, one scale factor, twelve atomic coordinates, six isotropic thermal parameters, five profile parameters and twenty-five background parameters. To ensure reasonable values, the isotropic thermal parameters, U_{iso} , were constrained to be equal for isoatomic sites. The refinement parameters are summarised in Table 3-13 and the refinement profile is shown in Figure 3-11.

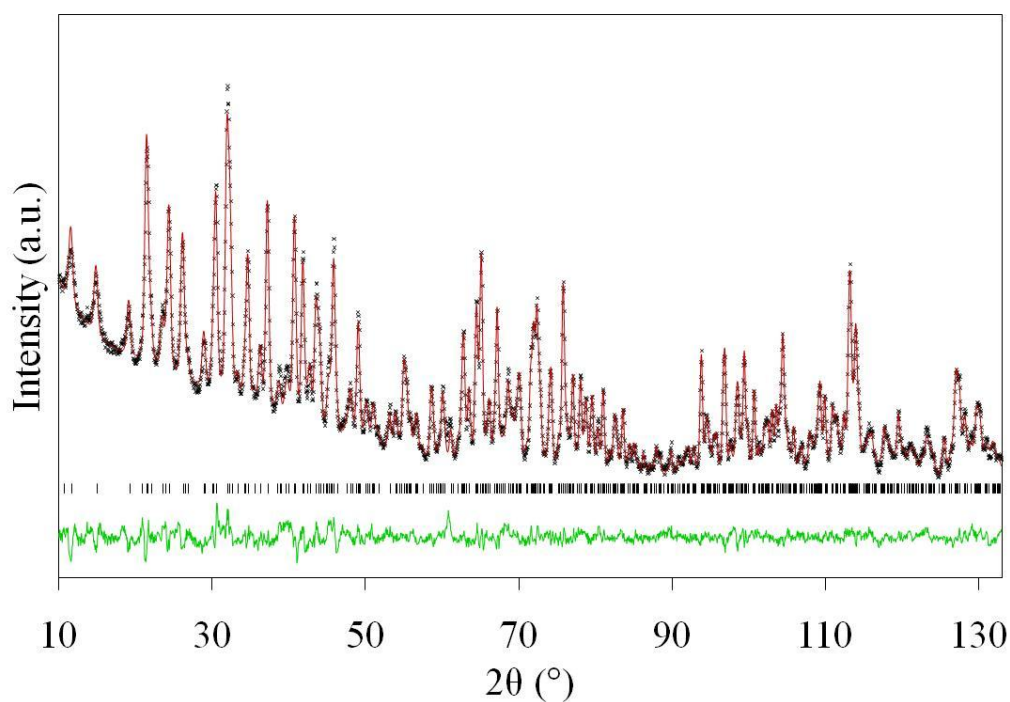


Figure 3-11. PND profiles for Ba_2MnS_3 at 200 K, showing observed (+), calculated (red line) and difference pattern (green line). Tick marks indicate reflection positions for Ba_2MnS_3 .

Formula	Ba_2MnS_3	
Space Group	$Pnma$ (no. 62)	
	200 K	PXRD data
a (Å)	8.8113(3)	8.8231(2)
b (Å)	4.2973(1)	4.3073(1)
c (Å)	17.0767(4)	17.1001(3)
V (Å ³)	646.61(3)	649.87(3)
Z	4	
Calculated density (g cm ⁻³)	4.374	
Profile function	Pseudo-Voigt	
No. of profile points	2459	
No. of parameters refined	50	
R_{wp}	0.0295	
R_{p}	0.0232	
χ_{red}^2	1.059	

Table 3-13. Summary of refinement data and lattice parameters for Ba_2MnS_3 at 200 K.

The data obtained from the refinement using the neutron diffraction data are in good agreement with the literature values and those derived from the PXRD data in the

previous section. The lower temperature neutron diffraction data shows a small reduction in unit cell dimensions. The atomic coordinates are given in Table 3-14.

Atom	Site	x	y	z	$100 \times U_{\text{iso}}$	Occ.
Ba(1)	4c	0.4183(3)	¼	0.7142(2)	0.66(4)	1.0
Ba(2)	4c	0.2627(3)	¼	0.4558(1)	0.66(4)	1.0
Mn	4c	0.3740(4)	¼	0.1308(2)	0.96(8)	1.0
S(1)	4c	0.3193(5)	¼	0.2723(3)	0.67(5)	1.0
S(2)	4c	0.1315(5)	¼	0.0729(2)	0.67(5)	1.0
S(3)	4c	0.9993(5)	¼	0.6006(3)	0.67(5)	1.0

Table 3-14. Structural parameters for Ba₂MnS₃ derived from PND collected at 200 K.

The Mn-S bond lengths and angles, shown in Table 3-15, are consistent with manganese in highly distorted tetrahedral coordination.

Bond lengths (Å)			
Ba(1)-Mn	3.644(4) × 2	Mn-S(1)	2.464(6)
	3.869(3)		
Ba(1)-S(1)	3.160(4)	Mn-S(2)	2.355(6)
Ba(1)-S(2)	3.261(4) × 2	Mn-S(3)	2.476(3) × 2
Ba(1)-S(3)	3.241(5)		
Ba(2)-Mn	3.731(5)		
	3.872(4) × 2		
Ba(2)-S(1)	3.174(6) × 2	Mn-Mn (intrachain)	4.2974(1)
Ba(2)-S(2)	3.079(4) × 2		
	3.286(5)		5.432(7)
Ba(2)-S(3)	3.298(4) × 2	(interchain)	5.998(5)
	3.391(5)		
Angles (°)			
S(1)-Mn-S(2)	96.7(9)	S(2)-Mn-S(3)	108.8(1)
S(1)-Mn-S(3)	119.7(1)	S(3)-Mn-S(3)	120.4(2)

Table 3-15. Selected bond lengths and angles in Ba₂MnS₃ from neutron diffraction collected at 200 K.

3.2.2.2.3 Powder Neutron Diffraction (PND) – 4 K and Powder X-ray Diffraction (PXRD) – 77 K

In general, the 4 K data resembles the data collected at 200 K with the intensities marginally increased. However, once again, the low angle range ($2\theta < \sim 30^\circ$) of the 4 K neutron diffraction pattern shows a number of peaks, which do not appear in the 200 K

data (Figure 3-12). The assignment of such peaks to three-dimensional magnetic ordering was much more tentative as susceptibility data for Ba_2MnS_3 do not show evidence of a transition to three-dimensional magnetic ordering. The possibility of such ordering is considered by Greaney *et al.*, but only at temperatures below 2 K.⁶⁰ A possible explanation for the lack of features in the susceptibility data, consistent with the onset of three-dimensional ordering, is poor resolution at low temperatures. For example, Figure 3-1 does not show the resolution necessary to detect such a subtle feature as the one seen at 46 K for Ba_2CoS_3 , Figure 3-2.

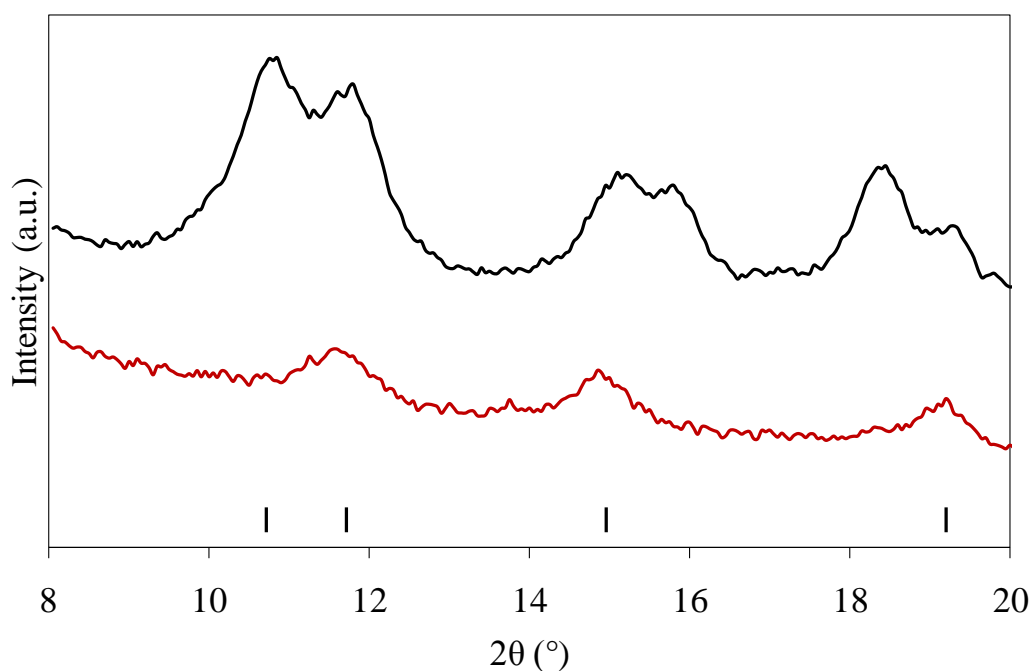


Figure 3-12. Selected low-angle range of neutron diffraction data collected on Ba_2MnS_3 at 4 K showing the additional peaks (black) not present at 200 K (red). The tick marks indicate the reflection positions for the Ba_2MnS_3 crystallographic phase.

In an attempt to rule out possible structural transitions, occurring upon cooling, that may give rise to additional diffraction peaks, PXRd was performed at ~ 77 K. Unfortunately, it was not possible to achieve lower temperatures (i.e. 4 K) with the apparatus available. However, Figure 3-13 shows the PXRd patterns for Ba_2MnS_3 at 77 K and room temperature. It can be seen that, with the exception of marginally improved signal-to-noise-ratio, there is no significant difference between the two patterns implying no structural transitions occur upon cooling to 77 K.

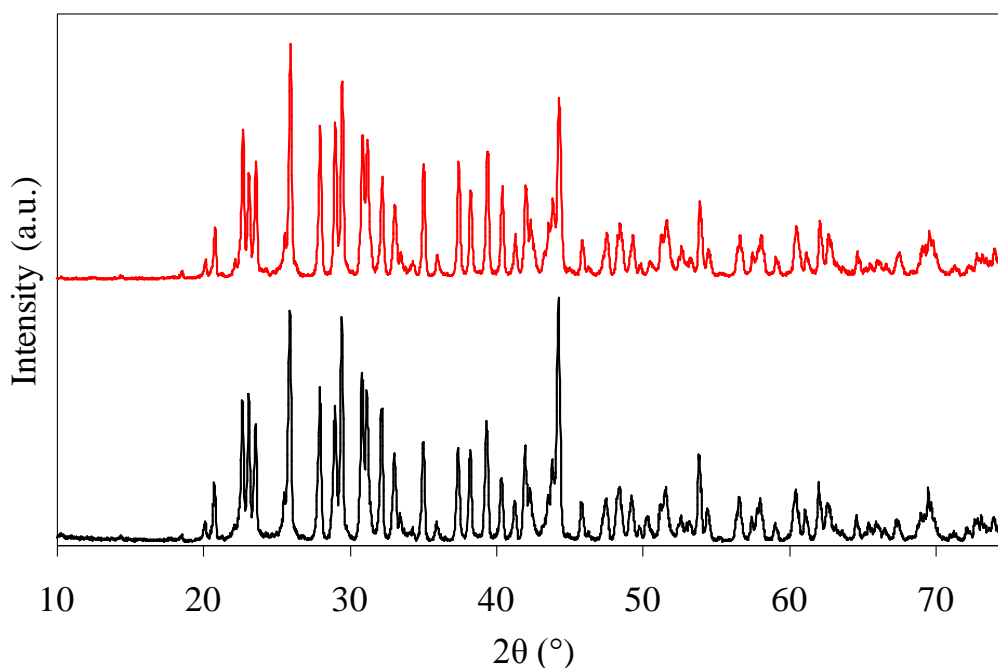


Figure 3-13. PXRD pattern of Ba_2MnS_3 collected at 77 K (red) and room temperature (black).

In addition, refinements using the neutron diffraction data collected at 4 K with a model based on the Ba_2MnS_3 crystal structure, by Grey and Steinfink,⁵⁸ satisfactorily modelled all but the new low angle peaks, supporting the hypothesis that the crystal structure is maintained at 4 K. It was, therefore, decided to proceed under the assumption that these low angle peaks were in fact the result of magnetic Bragg scattering associated with the onset of long-range magnetic ordering.

Ba_2MnS_3 consists of Ba^{2+} , Mn^{2+} and S^{2-} with electronic configurations $[\text{Xe}].6s^0$, $[\text{Ar}].3d^5$ and $[\text{Ne}].3s^2.3p^6$ respectively. Of these, only Mn^{2+} has an unclosed electron shell and unpaired electrons with which the neutrons may interact. The exact orbital splitting for the Mn^{2+} case has not been described in the literature. Calculations by Greaney *et al.* are based on a $S = 5/2$ system and hence five unpaired electrons.⁶⁰ The Mn^{2+} centres are therefore responsible for the magnetic scattering in Ba_2MnS_3 .

To determine the dimensions of the magnetic unit cell several Le Bail extractions were performed, using the GSAS suite of programs, based on model unit cells derived from doubling axes along a , b and c directions, along two of the three directions and along all three crystallographic unit cell directions.^{217, 240} Table 3-16 shows the residual fit parameters for these extractions.

Model	Magnetic unit cell dimensions			R_{wp}	R_p	χ_{red}^2
	a_{mag}	b_{mag}	c_{mag}			
1	a_{cryst}	b_{cryst}	c_{cryst}	0.0807	0.0505	8.081
2	$2a_{cryst}$	b_{cryst}	c_{cryst}	0.0696	0.0412	6.014
3	a_{cryst}	$2b_{cryst}$	c_{cryst}	0.0493	0.0336	3.016
4	a_{cryst}	b_{cryst}	$2c_{cryst}$	0.0701	0.0444	6.105
5	$2a_{cryst}$	$2b_{cryst}$	c_{cryst}	0.0465	0.0299	2.686
6	$2a_{cryst}$	b_{cryst}	$2c_{cryst}$	0.0580	0.0345	4.178
7	a_{cryst}	$2b_{cryst}$	$2c_{cryst}$	0.0388	0.0265	1.870
8	$2a_{cryst}$	$2b_{cryst}$	$2c_{cryst}$	0.0292	0.0199	1.056

Table 3-16. Residual fit parameters for possible magnetic unit cell dimensions for Ba_2MnS_3 derived from Le Bail extractions performed using neutron diffraction data obtained at 4 K.

Based on these residual fit parameters and the similarity in structure between Ba_2MnS_3 and Ba_2CoS_3 , with respect to the linear chains of M-S (M = Co, Mn) tetrahedra, the four best fits contain a doubling in the b axis (the chains are linked along b in Ba_2MnS_3 and c in Ba_2CoS_3):

4	$a_{mag} = a_{cryst}$	$b_{mag} = 2b_{cryst}$	$c_{mag} = c_{cryst}$
6	$a_{mag} = 2a_{cryst}$	$b_{mag} = 2b_{cryst}$	$c_{mag} = c_{cryst}$
7	$a_{mag} = a_{cryst}$	$b_{mag} = 2b_{cryst}$	$c_{mag} = 2c_{cryst}$
8	$a_{mag} = 2a_{cryst}$	$b_{mag} = 2b_{cryst}$	$c_{mag} = 2c_{cryst}$

The fit can be described by the simplest of these four, with magnetic unit cell dimensions of $a_{mag} = a_{cryst}$, $b_{mag} = 2b_{cryst}$ and $c_{mag} = c_{cryst}$.

A two phase refinement was performed to determine a model of the magnetic phase.^{217, 240} The Ba_2MnS_3 parameters were taken from the neutron data collected at 200 K to account for the crystallographic scattering. A second phase was introduced to account for the magnetic contributions of Ba_2MnS_3 .

The space group $P1$ was used for the magnetic phase, with constraints in place to maintain a link to the nuclear phase. The special positions, on which the Mn^{2+} lie, are constrained with respect to the y coordinate. The x and z coordinates for Mn^{2+} of the magnetic phase were set to refine in unison with the crystallographic phase. The U_{iso} values for the isoatomic sites were constrained to be equal between the magnetic phase and the crystallographic phase. The three angles, α , β and γ for the magnetic phase,

were set equal to 90° and fixed. The cell parameters were also constrained between the two phases i.e. $a_{\text{cryst}} = a_{\text{mag}}$, $2b_{\text{cryst}} = b_{\text{mag}}$ and $c_{\text{cryst}} = c_{\text{mag}}$. The phase fraction of the magnetic phase was constrained to be half that of the nuclear phase. The four Mn^{2+} positions in the crystallographic unit cell have the following equivalent positions:

x	y	z
$-x + \frac{1}{2}$	$-y$	$z + \frac{1}{2}$
$x + \frac{1}{2}$	$-y + \frac{1}{2}$	$-z + \frac{1}{2}$
$-x$	$y + \frac{1}{2}$	$-z$

The magnetic phase, with double the crystallographic cell volume, has 8 Mn^{2+} cations at the following coordinates:

x	$y/2$	z
$-x + \frac{1}{2}$	$(1-y)/2$	$z + \frac{1}{2}$
$x + \frac{1}{2}$	$(-y + \frac{1}{2})/2$	$-z + \frac{1}{2}$
$-x$	$(y + \frac{1}{2})/2$	$-z$
x	$(y/2) + \frac{1}{2}$	z
$-x + \frac{1}{2}$	$(1-y)/2 + \frac{1}{2}$	$z + \frac{1}{2}$
$x + \frac{1}{2}$	$(-y + \frac{1}{2})/2 + \frac{1}{2}$	$-z + \frac{1}{2}$
$-x$	$(y + \frac{1}{2})/2 + \frac{1}{2}$	$-z$

where x , y and z are the Cartesian coordinates of the Mn^{2+} cations in the nuclear phase.

Finally, the direction and magnitude of the magnetic moments had to be defined. The spin vectors were constrained to lie in opposed directions along the b axis, to maintain antiferromagnetic interaction along the chains. No other constraints were placed on the magnitude and direction of the spin vectors. Refinements in which the directions of the spin vectors were constrained to be parallel to one of the axes failed to provide a satisfactory fit. Due to the slightly higher quality of the data over the Ba_2CoS_3 , the spins were allowed to refine away from the cell axes, however, it was not possible to refine these vectors freely and the constrain of antiferromagnetic interactions along the chains was strictly maintained.

In this case the refinement is also hampered by the overlapping of the magnetic Bragg peaks and those of the crystallographic phase. The result of this was that a single “best fit” and hence a conclusive magnetic structure could not be obtained. Here a number of satisfactory fits to the neutron diffraction data are presented.

The first model for the magnetic phase, referred to hereafter as Model A, showed residual fit parameters of $R_{wp} = 0.0372$, $R_p = 0.0288$ and $\chi^2_{red} = 1.717$. The refinement profile is shown in Figure 3-14. The moment, of Model A, refined to a value of around $4.00 \mu_B$ per Mn^{2+} . The cell parameters, atomic coordinates and magnetic moment contribution along each cell axis for the magnetic unit cell are shown in Table 3-17.

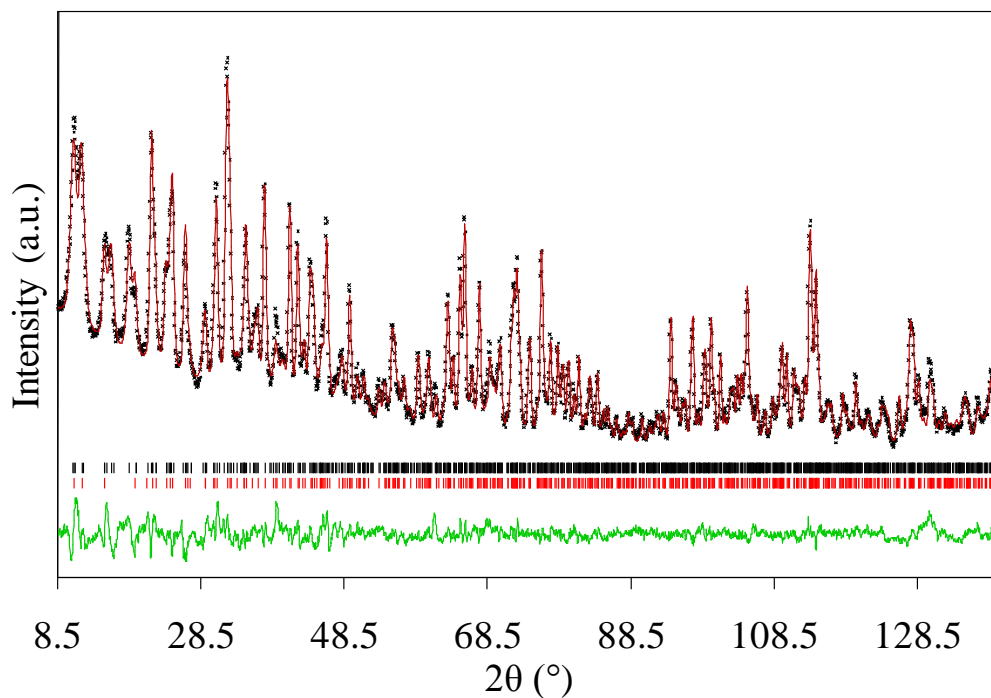


Figure 3-14. PND profiles for Ba_2MnS_3 at 4 K, showing observed (+), calculated (red line) and difference pattern (green line). Tick marks indicate reflection positions for Ba_2MnS_3 ; the crystallographic cell (lower) and the magnetic cell (upper), based on Model A.

atom	x	y	z	m_x/μ_B	m_y/μ_B	m_z/μ_B
Mn(1)	0.3735(4)	0.125	0.1314(2)	+1.86(9)	+1.43(4)	+3.24(6)
Mn(2)	0.1265(4)	0.375	0.6314(2)	+1.86(9)	+1.43(4)	+3.24(6)
Mn(3)	0.6265(4)	0.375	0.8686(2)	+1.86(9)	-1.43(4)	+3.24(6)
Mn(4)	0.8735(4)	0.125	0.3686(2)	-1.86(9)	-1.43(4)	+3.24(6)
Mn(5)	0.3735(4)	0.625	0.1314(2)	-1.86(9)	+1.43(4)	-3.24(6)
Mn(6)	0.1265(4)	0.875	0.6314(2)	-1.86(9)	+1.43(4)	-3.24(6)
Mn(7)	0.6265(4)	0.875	0.8686(2)	-1.86(9)	-1.43(4)	-3.24(6)
Mn(8)	0.8735(4)	0.625	0.3686(2)	1.86(9)	-1.43(4)	-3.24(6)

Space group PI : $a = 8.7941(4) \text{ \AA}$, $b = 8.5763(4) \text{ \AA}$, $c = 17.0471(8) \text{ \AA}$, $V = 1285.7(1) \text{ \AA}^3$

Table 3-17. Structural parameters, atomic coordinates and magnetic moments for the magnetic phase of Ba_2MnS_3 , using Model A and neutron data collected at 4 K.

The second model for the magnetic unit cell of Ba₂MnS₃, Model B, gave residual fit parameters of $R_{wp} = 0.0382$, $R_p = 0.0290$ and $\chi^2_{red} = 1.814$. The refinement profile is shown in Figure 3-15. The moment, of Model B, refined to a value of around 3.73 μ_B per Mn²⁺. The cell parameters, atomic coordinates and magnetic moment contribution along each cell axes for the magnetic unit cell are shown in Table 3-18.

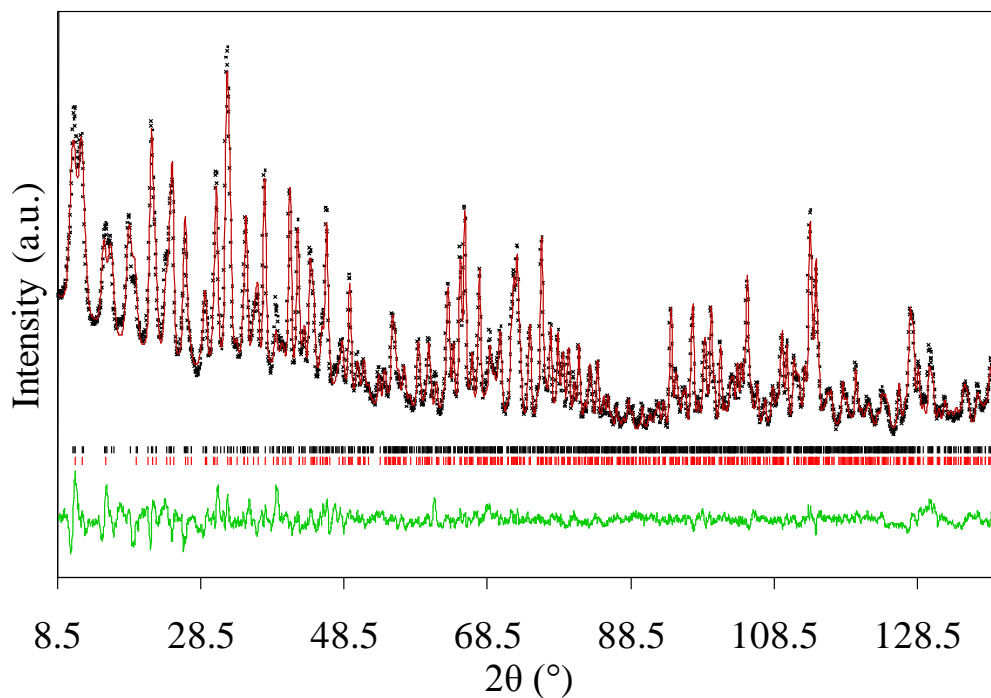


Figure 3-15. PND profiles for Ba₂MnS₃ at 4 K, showing observed (+), calculated (red line) and difference pattern (green line). Tick marks indicate reflection positions for Ba₂MnS₃; the crystallographic cell (lower) and the magnetic cell (upper), based on Model B.

atom	x	y	z	m_x/μ_B	m_y/μ_B	m_z/μ_B
Mn(1)	0.3735(4)	0.125	0.1310(2)	3.04(4)	1.09(5)	1.86(6)
Mn(2)	0.1265(4)	0.375	0.6310(2)	3.04(4)	1.09(5)	1.86(6)
Mn(3)	0.6265(4)	0.375	0.8690(2)	3.04(4)	-1.09(5)	1.86(6)
Mn(4)	0.8735(4)	0.125	0.3690(2)	3.04(4)	-1.09(5)	-1.86(6)
Mn(5)	0.3735(4)	0.625	0.1310(2)	-3.04(4)	1.09(5)	-1.86(6)
Mn(6)	0.1265(4)	0.875	0.6310(2)	-3.04(4)	1.09(5)	-1.86(6)
Mn(7)	0.6265(4)	0.875	0.8690(2)	-3.04(4)	-1.09(5)	-1.86(6)
Mn(8)	0.8735(4)	0.625	0.3690(2)	-3.04(4)	-1.09(5)	1.86(6)

Space group PI : $a = 8.7982(3) \text{ \AA}$, $b = 8.5807(4) \text{ \AA}$, $c = 17.0560(7) \text{ \AA}$, $V = 1287.7(1) \text{ \AA}^3$

Table 3-18. Structural parameters, atomic coordinates and magnetic moments for the magnetic phase of Ba₂MnS₃, using Model B and neutron data collected at 4 K.

Structural representations of the magnetic spin alignments are shown in Figure 3-16.

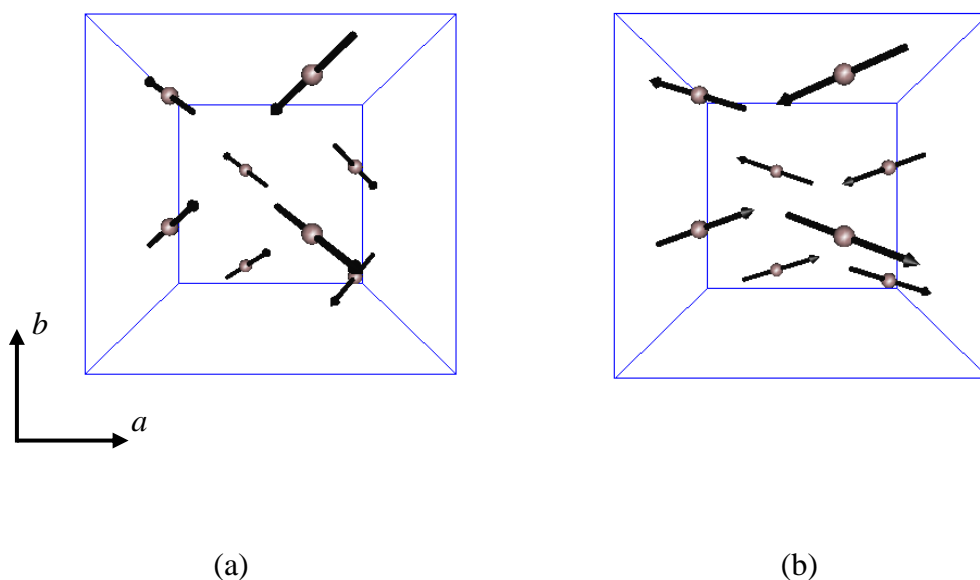


Figure 3-16. Representation of possible magnetic spin alignments in Ba₂MnS₃. (a) Model A (b) Model B.

In both cases the magnetic moment is around $4 \mu_B$ per Mn²⁺, which, as in the case of Co²⁺ in Ba₂CoS₃, is a little lower than expected. The value could be reduced, in part, by the distortion of the tetrahedral site and by the covalency in the Mn - S bonds. By way of comparison, the ordered moment in the Mn₃O₄, in which Mn²⁺ - O bonds form a regular tetrahedron has been reported to be $4.34 \mu_B$ per Mn²⁺ cation.²⁴⁴

Generally, both models show a good fit to the experimental data, with calculated intensity at each of the magnetic peak positions. However, based on this data alone it is difficult to draw a conclusion as to which, if any, of these models give the best representation of the magnetic unit cell.

3.2.3 Conclusions

In conclusion, the low temperature magnetic structures of two ternary sulfides, with one-dimensional chains of transition metal centred sulfur tetrahedra, have been investigated.

Exploration of Ba_2CoS_3 has demonstrated that the material does in fact show three-dimensional antiferromagnetic ordering at 1.5 K, consistent with the earlier interpretations of susceptibility and heat capacity data, proving the interpretations by Barnes *et al.*²²⁷ Here a magnetic structure is proposed showing antiferromagnetically aligned moments. Each Co^{2+} cation shows a moment of $1.97(4) \mu_{\text{B}}$, aligned along [100] and is ferromagnetically aligned with four cations from neighbouring chains and antiferromagnetically aligned with two others. The previously identified strong superexchange interaction, between Co^{2+} cations in the chains of vertex-linked CoS_4 tetrahedra that lie parallel to [001], dictates the long-range ordered magnetic structure adopted.

In addition, investigation of Ba_2MnS_3 implied the presence of three-dimensional ordering at low temperatures (4 K), with the appearance of additional diffraction peaks in the neutron diffraction pattern. Due to peak convolution and the relatively low peak intensity, arising from the poor neutron scattering powers of the constituent atoms, a conclusive description of the magnetic structure of Ba_2MnS_3 could not be reached, however, two possible models have been proposed. Further analysis to confirm the presence of three-dimensional magnetic ordering, through additional susceptibility data, specific heat measurements and additional neutron diffraction data at 1.5 K would be beneficial in determining if indeed these peaks are the result of long-range magnetic ordering in Ba_2MnS_3 .

4 Preparation of Ce_2MnN_3 and Low-Dimensional Nitrides

4.1 Ce_2MnN_3

As stated in section 1.3.3, Ce_2MnN_3 shows an anion deficient K_2NiF_4 -type structure with one-dimensional chains of corner sharing MnN_4 square planar units running along the a -axis. In actual fact these MnN_4 units are not in an ideal square planar arrangement as the $\text{Mn-N}_{\text{bridging}}$ bonds, 1.88 Å, are shorter than the $\text{Mn-N}_{\text{terminal}}$ bonds, 2.04 Å.⁶⁸ Structural details were investigated by Niewa *et al.*⁶⁸ Figure 4-1 shows the orbital interaction diagram proposed for the hypothetical isolated square planar MnN_4 units, as derived by Niewa *et al.*⁶⁸

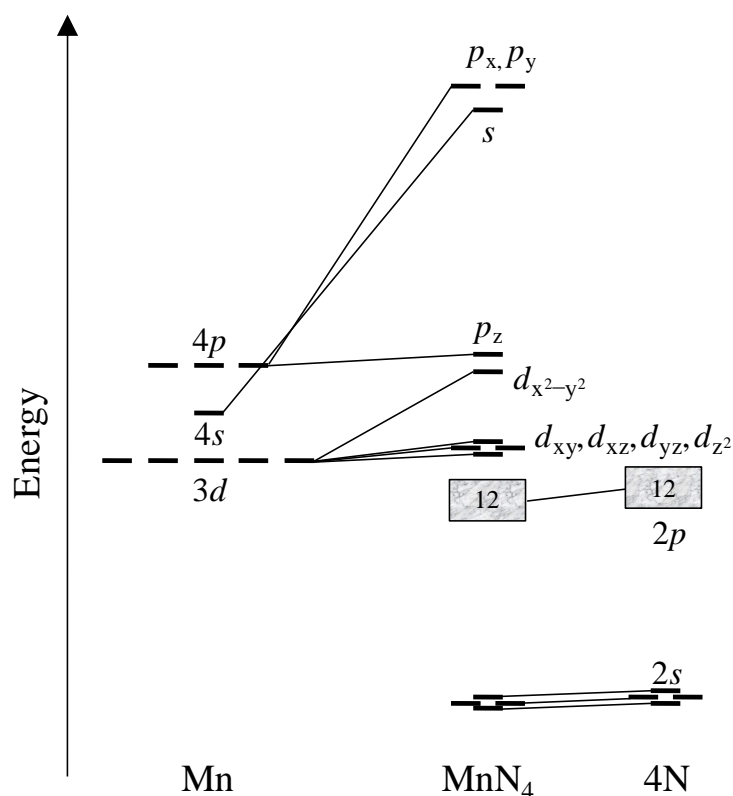


Figure 4-1. Orbital interaction diagram for a hypothetical isolated square planar MnN_4 unit. Recreated from the literature.⁶⁸

Figure 4-1 shows the expected orbital splitting pattern for square planar symmetry. The bonding orbitals consist of four Mn-N σ -bonding and four π -bonding orbitals. These

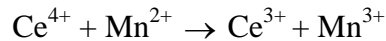
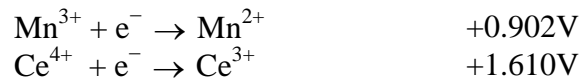
orbitals are primarily nitrogen in character. The bonding orbitals are filled with 32 electrons from the four N^{3-} anions occupying the N $2s$ and $2p$ states. The antibonding orbitals are associated with manganese and made up of five σ -antibonding orbitals (d_{z^2} , $d_{x^2-y^2}$, s , p_x , p_y) and four π -antibonding orbitals (d_{xy} , d_{xz} , d_{yz} , p_z). The remaining electrons must, therefore, fill the σ - and π -antibonding orbitals and it is the filling of these orbitals which dictates the strength of the Mn-N bonds i.e. the oxidation state of the manganese dictates the relative lengths of the Mn-N_{bridging} and Mn-N_{terminal} bonds.

Cerium can adopt 3+ or 4+ oxidation states. Assuming an oxidation state of 3- for the nitride anion, the possible oxidation states of the cations in Ce_2MnN_3 are $\text{Ce}_2^{4+}\text{Mn}^+\text{N}_3$, $\text{Ce}_2^{3+}\text{Mn}^{3+}\text{N}_3$ and $\text{Ce}^{3+}\text{Ce}^{4+}\text{Mn}^{2+}\text{N}_3$.⁶⁸ Only a small number of Mn^+ containing compounds are known, including $\text{Li}_2[(\text{Li}_{1-x}\text{Mn}_x)\text{N}]$ and $\text{Ca}(\text{Li}_2[\text{MnN}]_2)$.^{245, 246} Considering all possible cations, determination of the oxidation states in Ce_2MnN_3 is not straightforward and a number of techniques were employed.^{68, 93, 94} Electrical resistivity measurements indicated metallic like behaviour and magnetic susceptibility measurements show that Ce_2MnN_3 is Pauli paramagnetic, with a very small $\mu_{eff} = 0.53 \mu_B$.⁶⁸ Table 4-1 shows the μ_{eff} values for various cation oxidation states in square planar coordination.

Cation	μ_{eff} (μ_B)
Ce^{3+} (f^1)	2.5
Ce^{4+} (f^0)	0.0
Mn^+ (hs)	4.9
Mn^+ (ls)	0.0
Mn^{2+} (hs)	5.9
Mn^{2+} (ls)	1.7
Mn^{3+} (hs)	4.9
Mn^{3+} (ls)	0.0

Table 4-1. Calculated moments for selected cation oxidation states.

The experimentally obtained value of $\mu_{eff} = 0.53 \mu_B$ is too low to correspond with Mn^{2+} or Mn^{3+} (which also require the presence of Ce^{3+}), indicating strongly that the cations in Ce_2MnN_3 are $\text{Ce}_2^{4+}\text{Mn}^+\text{N}_3$. In solution chemistry the co-existence of such oxidation states is unlikely, with Ce^{4+} known to readily oxidise Mn^{2+} to Mn^{3+} :



$$\begin{aligned} E_{\text{cell}}^{\circ} &= 1.610 - 0.902 \\ &= 0.708\text{V} \end{aligned}$$

If Mn^{+} is assumed to be as good a reducing agent as Mn^{2+} this too will be readily oxidised in the presence of Ce^{4+} .⁶⁸

Investigating the band structure and crystal overlap populations, Niewa *et al.*, showed that the largest observed difference for Mn-N bond strengths is for Mn^{+} , in which the $\text{Mn-N}_{\text{terminal}}$ π -antibonding states are filled, but the $\text{Mn-N}_{\text{bridging}}$ π -antibonding states are unoccupied.⁶⁸ This essentially results in $\text{Mn-N}_{\text{terminal}}$ single bonds and $\text{Mn-N}_{\text{bridging}}$ double bonds, which was indicated by neutron diffraction experiments.⁶⁸ The $\text{Mn-N}_{\text{terminal}}$ bond length of 2.01 Å, in Ce_2MnN_3 , is similar to Mn-N single bonds observed in organometallic compounds, 2.01 Å.⁶⁸ The Ce_2MnN_3 $\text{Mn-N}_{\text{bridging}}$ bond length of 1.88 Å is too long to correspond with a triple bond, ~ 1.51 Å, but shows a length similar to those observed for double bonds ~ 1.74 - 1.80 Å.⁶⁸

The absence of a magnetic moment and the metallic-like behaviour of Ce_2MnN_3 does not conclusively indicate the oxidation state $\text{Ce}_2^{4+}\text{Mn}^+\text{N}_3$. In fact CeN, in which cerium has an oxidation state of 3+, is essentially non-magnetic.^{247, 248} The non-magnetic behaviour of CeN has been attributed to mixed valency of the cerium and the 4f electrons becoming involved in Ce-Ce interactions.^{247, 249} Theoretical studies of the electronic structure, by Landrum *et al.*, also suggest that it is partial occupation of the cerium 5d orbitals that gives rise to localisation of the electrons in the Ce-Ce bond rather than on the isolated ions.⁹³ This results in no overall magnetic moment. In the same study, Ce_2MnN_3 was investigated and failed to show a similarly large cerium 5d occupation and no evidence of Ce-Ce interactions.⁹³ In addition, the cerium 4f states lie primarily above the fermi level, as in CeO_2 . Linear Muffin-Tin Orbital (LMTO) calculations imply a partial occupation of the cerium 4f band by approximately 0.2 electrons per cerium, indicating an oxidation state of $\text{Ce}_2^{3.9+}\text{Mn}^{1.2+}\text{N}_3$.⁶⁸ Landrum *et al.*

suggests that the interactions between cerium and the adjacent nitride anions may act to stabilise the Ce⁴⁺ oxidation state.⁹³

Finally, XAS was performed by Niewa *et al.*⁹⁴ XAS spectroscopy is a powerful tool for the determination of ion oxidation states and coordination geometry. Mn-L_{2,3} spectra suggested a similar manganese oxidation state to that found in η-Mn₃N₂ and MnO. One particular problem with this assignment was the absence of a standard, containing Mn⁺, for comparison. Therefore, Ce-M_{4,5} and Ce-L₃ spectra were also investigated.⁹⁴ The Ce-M_{4,5} spectra show more similarity to CeO₂ than CeN or CeF₃. The Ce-L₃ spectra show only a single peak for Ce³⁺ standards and two peaks for Ce⁴⁺. It was found that, the spectra for Ce₂MnN₃ shows two peaks in a similar fashion to CeO₂, implying a Ce⁴⁺ oxidation state.⁹⁴ In addition, the presence of multiple peaks in the Ce-L₃ spectra is an indication of covalent mixing between the cerium 4*f* and nitrogen 2*p* state, as suggested by Landrum *et al.*^{93, 94} By simulating the Ce-L₃ spectra Niewa *et al.* calculated a 4*f* occupancy of 0.52, which compares to 0.49 for CeO₂.⁹⁴ In conclusions the experimental evidence and calculations indicate that the oxidation state for cerium in Ce₂MnN₃ is 4+ implying an oxidation state of 1+ for manganese.

The significance of the oxidation states in Ce₂MnN₃, when performing fluorination reactions, will be addressed in chapter 5.

4.1.1 Experimental

The original preparation of Ce₂MnN₃ performed by Niewa *et al.* involved a two step synthetic route.⁶⁸ The first step involves the preparation of the binary nitride, CeN, via reaction of cerium metal with ammonia gas. The second step is the reaction of a stoichiometric ratio of CeN with manganese metal, under a nitrogen gas stream, via a conventional solid state reaction.⁶⁸ The largely negative thermodynamics suggest that unlike other nitrides the formation of Ce₂MnN₃ is a favourable process.²⁵⁰ A comparison of enthalpies of formation for selected ternary nitrides from the elements (ΔH_f°) is shown in Table 4-2.²⁵⁰

Compound	ΔH_f° (kJ mol ⁻¹)
LiCaN	-216.8 ± 10.8
Ca ₂ ZnN ₂	-378.9 ± 8.6
Ce ₂ MnN ₃	-928.2 ± 9.5
Sr ₂ ZnN ₂	-385.6 ± 14.3
CaTaN ₂	-643.8 ± 9.6

Table 4-2. Enthalpies of formation from the elements (ΔH_f°), for selected nitrides.²⁵⁰

In addition to the synthetic route used by Niewa *et al.*,⁶⁸ a simpler method to Ce₂MnN₃ is reported here and involves the reaction of metallic precursors and N₂ gas.

4.1.1.1 Preparation of Cerium Nitride, CeN

Cerium nitride is not a commercially available compound, but several methods are available for the preparation in a synthetic laboratory. Four synthetic methods were adopted in this work; the reaction of cerium carbide (Method 1) or cerium metal (Method 2) with NH₃ (g).^{68, 251} In the case of CeC₂, either an ammonia or N₂/H₂ atmosphere can be used as reaction gas.²⁵¹ The hydrogen present, in ammonia or N₂/H₂, removes the amorphous carbon and the equilibrium is shifted in favour of CeN. Method 3 involves the reaction of cerium metal, in molten zinc, with N₂ (g) and Method 4 the reaction of cerium metal with N₂ (g). It has been reported, by Muthman and Kraft in 1903, that cerium metal melts at temperatures T > 800 °C and in its molten state reacts with N₂ gas to give CeN.^{252, 253}

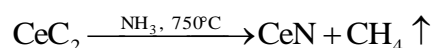
All methods involve the reaction of a solid with a gas and therefore a large surface area and small particle size are important parameters for successful reactions. In fact, some materials show a high tendency for surface nitridation, which generate a nitride surface of a few microns, which hinders any further solid gas reaction.

By dissolving the metals in molten zinc an increased surface area is generated and in the remaining three experiments, finely powdered starting material was required to ensure the surface area was as large as possible. Although cerium powder is commonly used small spheres can be produced from metal pieces. This can be achieved by dripping the molten metal through a small hole in an un-reactive container and cooling. This

procedure has the advantage that it separates the cerium metal from oxide impurities, which accompany cerium metal.⁶⁸ In practice, this can be difficult to achieve while maintaining an inert atmosphere throughout.

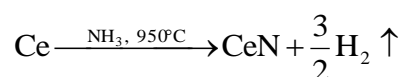
The solid reagents, and cerium nitride, are air sensitive therefore all manipulations were performed under an inert atmosphere in a glove box ($O_2 \leq 0.1$ ppm, $H_2O \leq 0.1$ ppm).

4.1.1.1.1 Method 1 – Ammoniation of Cerium Carbide, CeC_2



In a glove box, a finely ground cerium carbide powder (Avocado, 99%) was placed in an alumina boat. This was positioned centrally in a quartz tube, which was then transferred to a split-hinge tubular furnace. Nitrogen was passed through the tube for 30 minutes to ensure air was purged from the system. The sample was then heated under flowing ammonia gas ($14 \text{ dm}^3 \text{ min}^{-1}$) to $750^\circ C$. This temperature was maintained for 12 hours, followed by cooling to room temperature at $1^\circ C \text{ min}^{-1}$. The system was flushed with nitrogen to remove any residual ammonia.

4.1.1.1.2 Method 2 – Ammoniation of Cerium Metal



Two forms of cerium metal were used in these reactions, cerium powder (40 mesh, ESPI, 99.9%) and cerium rod (Alfa Aesar, 99.9%). The exterior layer of oxide was removed from cerium rods through surface abrasion and the rod was then cut into smaller pieces. The cerium was placed in a niobium crucible and inserted into a quartz reaction tube. The cerium was heated to $950^\circ C$ in flowing ammonia gas ($14 \text{ dm}^3 \text{ min}^{-1}$) for 12 hours. The system was then cooled to room temperature and flushed with nitrogen to remove residual ammonia.

4.1.1.1.3 Method 3 – Nitrogenation of Cerium in Molten Zinc

Cerium pellets were placed into stainless-steel crucibles and ten molar equivalents of zinc shot (Sigma-Aldrich, 99.99%) was added. The crucibles were sealed in a stainless-steel reaction vessel, which was connected to a nitrogen line, as shown in Figure 2-8. The argon was purged from the reaction vessel and a stream of flowing nitrogen gas introduced. The sample was gently heated to 750 °C over 9 hours. After 4.5 days the furnace was cooled to room temperature. The zinc was removed via vacuum distillation. To achieve this, the nitrogen flow was terminated and the system was evacuated. Under vacuum, the temperature was raised to 800 °C and the zinc vapour was condensed on to a water cooled cold finger (Figure 2-9). After 19 hours the reaction was allowed to cool to room temperature. The reaction vessel was then isolated from air and transferred to a glove box to be opened.

4.1.1.1.4 Method 4 – Nitrogenation of Cerium Metal

In a glove box, the exterior layer of oxide was removed from a cerium rod (Alfa Aesar, 99.9%) through surface abrasion and the rod was then cut into smaller pieces. These were placed in a niobium crucible and inserted into a quartz reaction tube. The reaction tube was placed in a tubular furnace and the cerium was heated to 1050 °C in flowing nitrogen gas. The nitrogen gas was passed through Varian gas clean filters, prior to reaction, to remove any oxygen and moisture present. Cerium metal was reacted in nitrogen for 12 hours then the system was cooled to room temperature. The quartz tube was then returned to the glove box.

4.1.1.2 Preparation of Ce_2MnN_3

4.1.1.2.1 Method 1 – Reaction of Cerium Nitride, Manganese and Nitrogen

In a glove box, previously prepared cerium nitride and manganese metal powder (Aldrich, 99.99%) were ground separately to fine powders before mixing in the required stoichiometric ratio. The mixture was hand pressed into pellets, placed into a niobium crucible and inserted into a quartz tube. The quartz tube was placed in a tubular

furnace. Under flowing nitrogen (purified), the pellets were heated to 900 °C. After 36 hours the resulting mixture was ground re-pelletised and the heating step was repeated to ensure complete conversion to Ce₂MnN₃.

4.1.1.2.2 Method 2 – Reaction of Cerium, Manganese and Nitrogen

A stoichiometric ratio of cerium (ESPI, 99.9%) and manganese (Aldrich, 99.99%) powder were mixed and placed in a niobium crucible. This was inserted into a quartz tube, which was sealed and then taken out of the glove box, put in an upright tubular furnace and connected to a nitrogen supply. The system was flushed for 30 minutes with nitrogen gas (filtered). The system was then heated to 900 °C for 36 hours, before cooling to room temperature. The resulting mixture was ground re-pelletised and the heating step was repeated to ensure complete conversion to the desired product.

4.1.1.3 Characterisation

Powder X-ray diffraction (PXRD) was carried out on all samples using a Siemens D5000 powder diffractometer with Cu K α radiation.

High-resolution powder neutron diffraction (PND) data were collected on the D2B diffractometer at the Institut Laue-Langevin (ILL), Grenoble, using a wavelength $\lambda = 1.59432 \text{ \AA}$ and covering the angular range $10 \leq 2\theta/^\circ \leq 157$ with $\Delta 2\theta = 0.05^\circ$. The samples were contained in a vanadium can of internal diameter 6.8 mm.

Magnetic susceptibility measurements were collected on a Quantum Design MPMS SQUID magnetometer with a field of 2 T at the University of Birmingham.

4.1.2 Results and Discussion

4.1.2.1 Structural Characterisation of CeN

4.1.2.1.1 Powder X-ray Diffraction (PXRD)

All the synthetic approaches to CeN, described in Section 4.1.1.1, resulted in the successful preparation of a golden yellow polycrystalline material, which was identified through PXRD as CeN. A representative example is presented here.

Rietveld refinement was performed using the data obtained from a CeN sample derived from reaction of cerium rod with ammonia gas at 1050 °C. The CeN model was based on that by Olcese, showing a rock salt structure.²⁴⁷ The background was initially modelled manually by a shifted Chebyshev function with twelve terms and was later refined freely, once an adequate representation of the peak shape had been reached. The peak shape was modelled by a multi-term Simpson's rule integration of the pseudo-Voigt.^{241, 242} The parameters refined were: the cell parameters (a , b , c), one zero point, one scale factor, two isotropic thermal parameters, five profile parameters. Due to possible absorption of X-ray radiation by cerium and from surface roughness effects (section 2.3.3.4), an absorption correction was applied, using the surface roughness correction by Suortti.²⁵⁴ The refinement parameters are summarised in Table 4-3 and the refinement profile is shown in Figure 4-2.

CeN has the space group $Fm\bar{3}m$ and cell parameter $a = 5.0242(1)$ Å, which is consistent with known unit cell dimensions for CeN.²⁴⁷ A particular problem in obtaining high quality X-ray diffraction data was the air sensitivity of CeN. Despite the use of the air sensitive sample holder, long collection times often resulted in reduced intensity and an increase in oxide content. It was therefore necessary to reach a compromise between the sample and data quality.

The synthesis of CeN via ammoniation of CeC₂ and cerium powder had the unfortunate tendency to result in a small amount of cerium oxide being present in the final product. This was due, in part, to the presence of a small oxide impurity, always present in the

starting material. There are a number of approaches to tackle this problem, such as reduction of the oxide at high temperatures or the drip separation technique, mentioned previously and used by Niewa *et al.*⁶⁸ In this work, the oxide impurity was minimised through the use of cerium rod, where the oxide could be removed prior to reaction, through surface abrasion. This method was used to prepare CeN for the subsequent reactions.

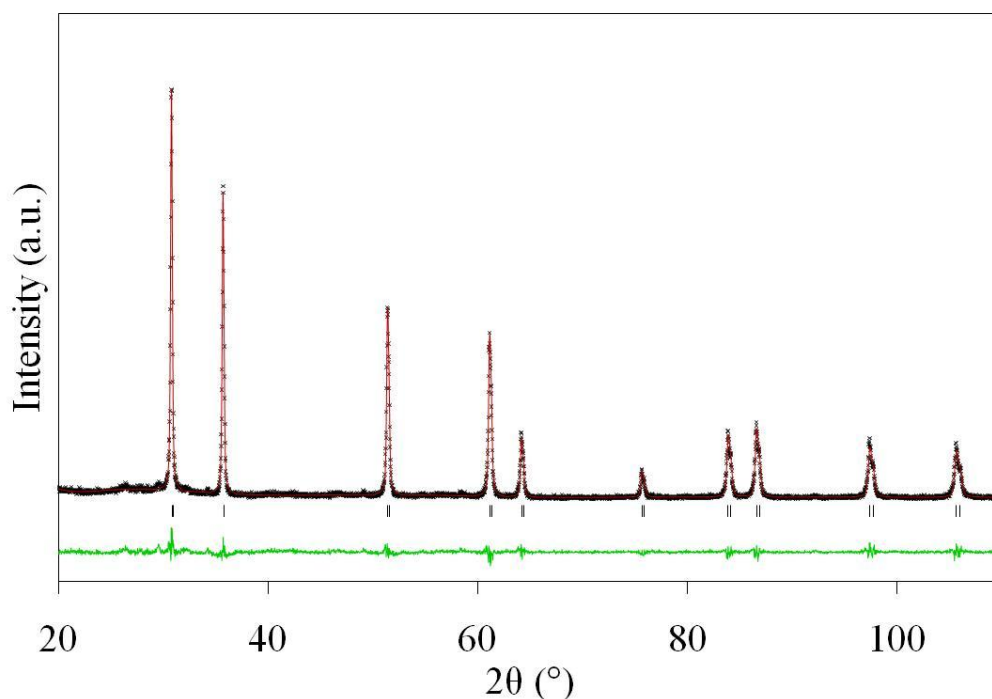


Figure 4-2. PXRD profiles for CeN at room temperature, showing observed (+), calculated (red line) and difference pattern (green line). Tick marks indicate reflection positions for CeN.

Formula	CeN	
Space Group	$Fm\bar{3}m$ (no. 225)	
	PXRD data	Olcese ²⁴⁷
a (Å)	5.0242(1)	5.020(2)
V (Å ³)	126.82(1)	126.51(1)
Z	4	
Calculated density (g cm ⁻³)	8.072	
Profile function	Pseudo-Voigt	
Absorption coefficients	0.44518, 0.70000	
No. of profile points	4499	
No. of parameters refined	22	
R_{wp}	0.1555	
R_p	0.1081	
χ_{red}^2	1.586	

Table 4-3. Summary of refinement data and lattice parameters for CeN at room temperature.

An interesting “side-reaction” observed while perfecting the preparation of CeN from CeC₂ was the formation of Ce₂O₂CN₂. Ce₂O₂CN₂ ($P\bar{3}m1$, $a = 3.9441(7)$ Å, $c = 8.361(2)$ Å[†]) was originally prepared by Hashimoto *et al.* when heating Ce₂(CO₃)₃·H₂O, in a graphite boat, under flowing ammonia at 1000 °C.²⁵⁵ In the work by Hashimoto *et al.* the graphite boat, or subsequently charcoal, acts as the carbon source and ammonia as the nitrogen source.²⁵⁵ The authors state that the carbon reacts with the ammonia gas, vaporises, and then reacts with the rare-earth phases.²⁵⁵ In the case of the reaction between CeC₂ and NH₃ a small oxygen presence may result in the formation of Ce₂O₃, which coupled with CeC₂ and NH₃ gives Ce₂O₂CN₂. The result is similar to the synthesis of lanthanide dioxymonocyanamide, which results from the reaction of Ln₂O₃, graphite and ammonia gas at elevated temperatures.²⁵⁵⁻²⁵⁷ A diffraction pattern obtained after the reaction of CeC₂ with ammonia at 900 °C is shown in Figure 4-3 and indicates the peaks corresponding to Ce₂O₂CN₂, amidst a number of other phases.

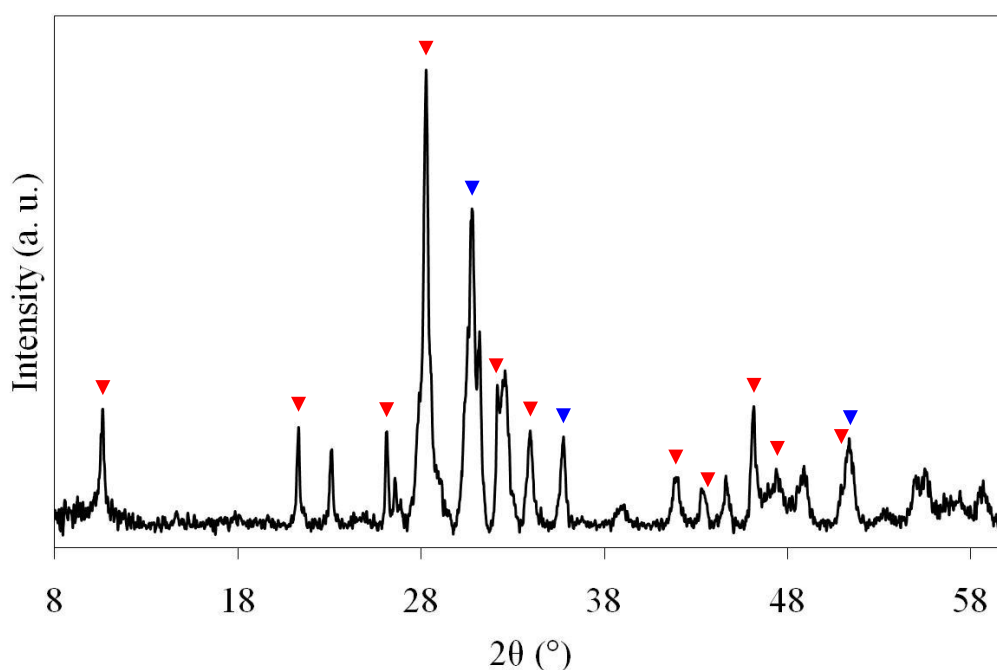


Figure 4-3. PXRD pattern for the sample after reaction of CeC₂ and NH₃ at 900 °C. The red and blue triangles highlight the peaks of Ce₂O₂CN₂ and CeN respectively. To aid clarity the pattern has been smoothed.

[†] To the best of our knowledge, a full structural description of Ce₂O₂CN₂ has not been obtained.

4.1.2.2 Structural Characterisation of Ce₂MnN₃

4.1.2.2.1 Powder X-ray Diffraction (PXRD)

Both the synthetic approaches to Ce₂MnN₃ resulted in a black/grey polycrystalline material which was identified through PXRD as Ce₂MnN₃.

Rietveld refinements using X-ray diffraction data were performed on samples derived through the reaction of CeN and Mn under nitrogen gas. The structural model by Niewa *et al.* was used for the first phase, Ce₂MnN₃.⁶⁸ Two additional phases were used to account for any minor impurities. A model by Zachariasen was used for Ce₂O₃ and a model by Olcese was used as the starting material CeN.^{247, 258}

The background was initially modelled manually by a Cosine Fourier series with twelve terms. The peak shape was modelled by a multi-term Simpson's rule integration of the pseudo-Voigt.^{241, 242} The parameters refined were: the cell parameters (*a*, *b*, *c*) for the three phases, one zero point, two scale factors, four isotropic thermal parameters, six profile parameters. The refinement parameters are summarised in Table 4-4 and the refinement profile is shown in Figure 4-4.

The cell parameters obtained are consistent with those obtained by Niewa *et al.*⁶⁸ Quantitative determination of the CeN and Ce₂O₃ content indicated 1.0(4)% and 3.0(3)%, weight percentage, of these secondary phases respectively. The structural parameters of Ce₂MnN₃ are given in Table 4-5.

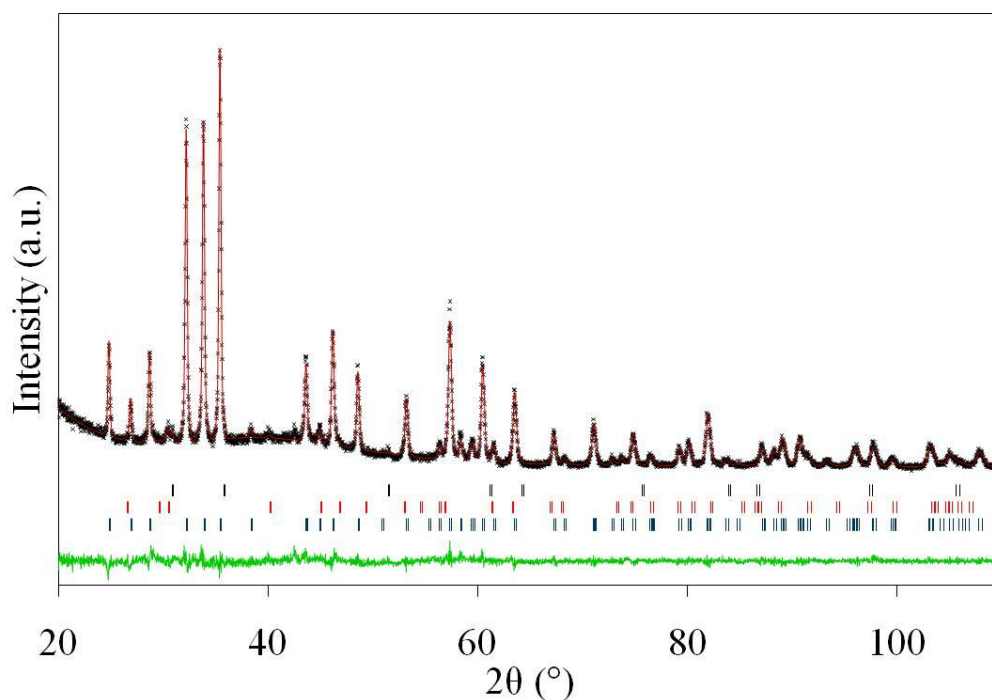


Figure 4-4. PXRD profiles for Ce_2MnN_3 at room temperature, showing observed (+), calculated (red line) and difference pattern (green line). Tick marks indicate reflection positions for CeN (upper), Ce_2O_3 (middle) and Ce_2MnN_3 (lower) phases.

Formula	Ce_2MnN_3	
Space Group	<i>Immm</i> (no. 71)	
	PXRD data	Niewa <i>et al.</i> ⁶⁸
a (Å)	3.7549(2)	3.74994(6)
b (Å)	3.4487(1)	3.444450(6)
c (Å)	12.4734(6)	12.4601(2)
V (Å ³)	161.52(2)	160.943(3)
Z	2	
Calculated density (g cm ⁻³)	7.756	
Profile function	Pseudo-Voigt	
No. of profile points	4499	
No. of parameters refined	22	
R_{wp}	0.0817	
R_{p}	0.0619	
χ_{red}^2	1.379	

Table 4-4. Summary of refinement data and lattice parameters for Ce_2MnN_3 at room temperature, derived from PXRD data.

Atom	Site	x	y	z	$100 \times U_{\text{iso}}$	Occ.
Ce	4i	0	0	0.3528(1)	0.1(3)	1.0
Mn	2a	0	0	0	0.3(1)	1.0
N(1)	2b	0	$\frac{1}{2}$	$\frac{1}{2}$	0.2(6)	1.0
N(2)	4i	0	0	0.1599(12)	0.6(3)	1.0

Table 4-5. Structural parameters for Ce_2MnN_3 derived from PXRD collected at room temperature.

Selected bond lengths are given in Table 4-6.

Distances (Å)			
Ce-N(1)	$2.5192(9) \times 2$	Mn-N(1)	$1.87744(8) \times 2$
Ce-N(2)	$2.405(8)$ $2.5540(9) \times 4$	Mn-N(2)	$1.995(15) \times 2$
Ce-Mn	$3.1418(7) \times 4$	Mn-Ce	$3.1418(7) \times 8$
Ce-Ce	$\geq 3.4487(2)$	Mn-Mn (intrachain)	$3.75489(16) \times 2$
		Mn-Mn (interchain)	$3.44865(15) \times 2$
N(1)-Mn	$1.87744(8) \times 2$	N(2)-Mn	$1.995(15)$
N(1)-Ce	$2.5192(9) \times 2$	N(2)-Ce	$2.405(8)$ $2.5540(9) \times 4$
Angles (°)			
N(1)-Mn-N(1)	180	N(2)-Mn-N(2)	180
N(1)-Mn-N(2)	90	Mn-N(1)-Mn	180

Table 4-6. Selected bond lengths and angles in Ce_2MnN_3 from PXRD collected at room temperature.

One particular problem that had to be addressed was the presence of cerium oxide, Ce_2O_3 , within the final product. As mentioned in the previous section, the use of cerium rod acts to reduce the amount of cerium oxide present in the reaction. Figure 4-5 gives a comparison between two Ce_2MnN_3 samples, prepared from cerium powder and cerium rod.

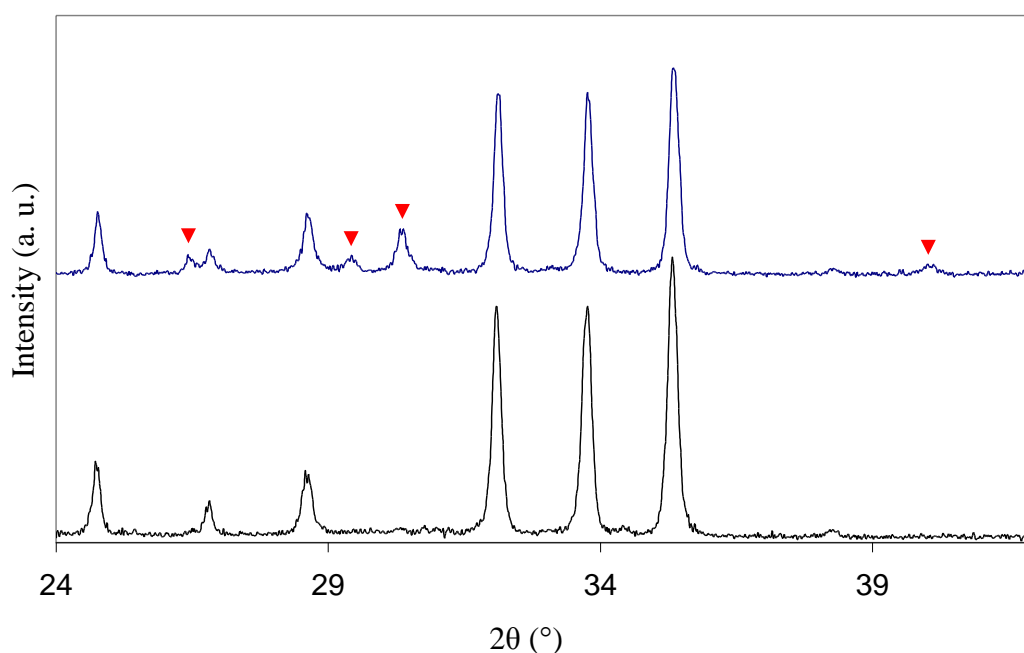


Figure 4-5. PXRD patterns of Ce_2MnN_3 prepared using cerium powder (blue) or cerium rod (black) as a starting reagent. The peaks highlighted by the red triangles correspond with Ce_2O_3 .

Through the removal of the oxide from the surface of the rod the overall cerium oxide content of the final phase was reduced to less than $\sim 3\%$. Therefore, cerium rod was used in all subsequent Ce_2MnN_3 preparations.

The second route to Ce_2MnN_3 reported here, was derived by combining the second step of the route reported by Niewa *et al.*, i.e. the reaction of CeN and Mn in nitrogen, and the synthesis of CeN in nitrogen gas. More specifically, Ce_2MnN_3 could be prepared in a one-step reaction, with CeN produced *in situ*.

The reaction of a 2:1 stoichiometric mixture of Ce and Mn metals in nitrogen gas at 900°C was shown, through PXRD, to yield Ce_2MnN_3 . As previously observed, preparation of ternary nitrides prepared by reaction of the metals with gaseous nitrogen is less common and therefore an understanding of this process was required. In order to achieve this, the progress of the reaction was checked at 12 hour intervals by PXRD. The PXRD traces are shown in Figure 4-6.

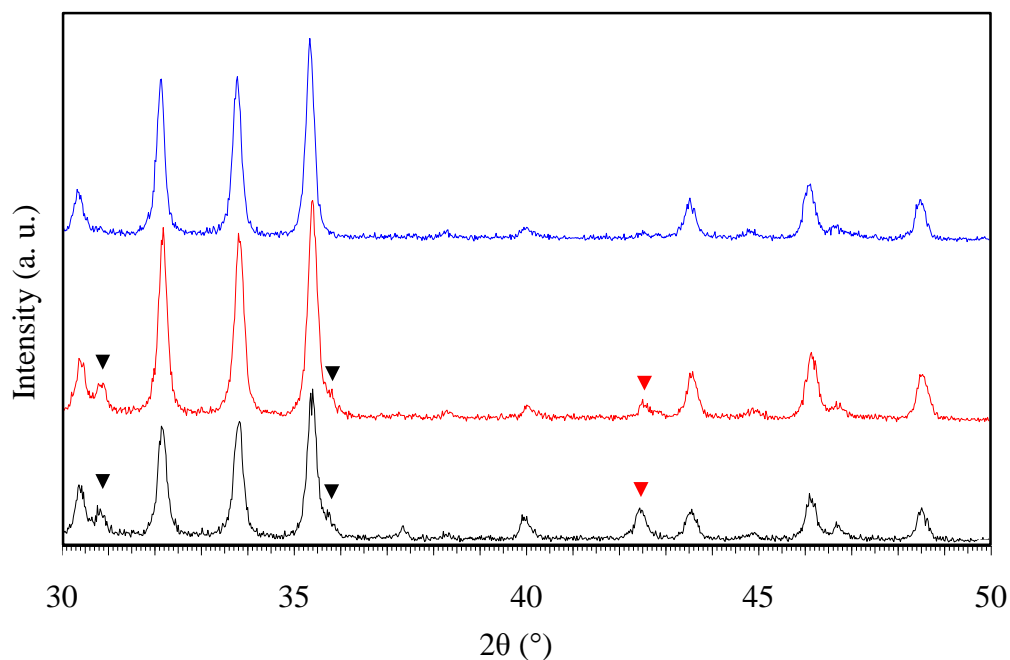


Figure 4-6. Selected 2θ range in PXRD patterns showing the progress of the reaction between Ce and Mn metal, at intervals of 12 (black), 24 (red) and 36 hours (blue). The black and red triangles indicate representative peak for CeN and Mn respectively.

The comparison of the PXRD patterns, for the reaction of the elements, after 12, 24 and 36 hours shows that Ce metal reacts readily with nitrogen gas forming CeN, whereas there is no apparent reaction between Mn metal and nitrogen gas. In fact, Figure 4-6 shows that, after only 12 hours of reaction, the main compound is Ce_2MnN_3 but CeN has formed and there is also un-reacted Mn metal. This indicates that the first reaction to occur is the formation of CeN via direct combination of Ce metal with nitrogen gas and that Ce_2MnN_3 subsequently results from the reaction of CeN with metallic Mn. Interestingly, the presence of Ce_2MnN_3 as the main phase after only 12 hours indicates that its formation requires short reaction times. PXRD patterns also show the progress of the reaction, which is visible by the disappearing of the peaks belonging to CeN and Mn.

The air sensitivity of this sample was also investigated through PXRD. Figure 4-7 shows the PXRD patterns of Ce_2MnN_3 at increments of 8.75 hours, for 35 hours. These patterns were collected using the air sensitive sample holder shown in Figure 2-28. It is apparent that even under these conditions, the patterns show a decrease in peak intensity and increase in breadth consistent with reduced crystallinity.

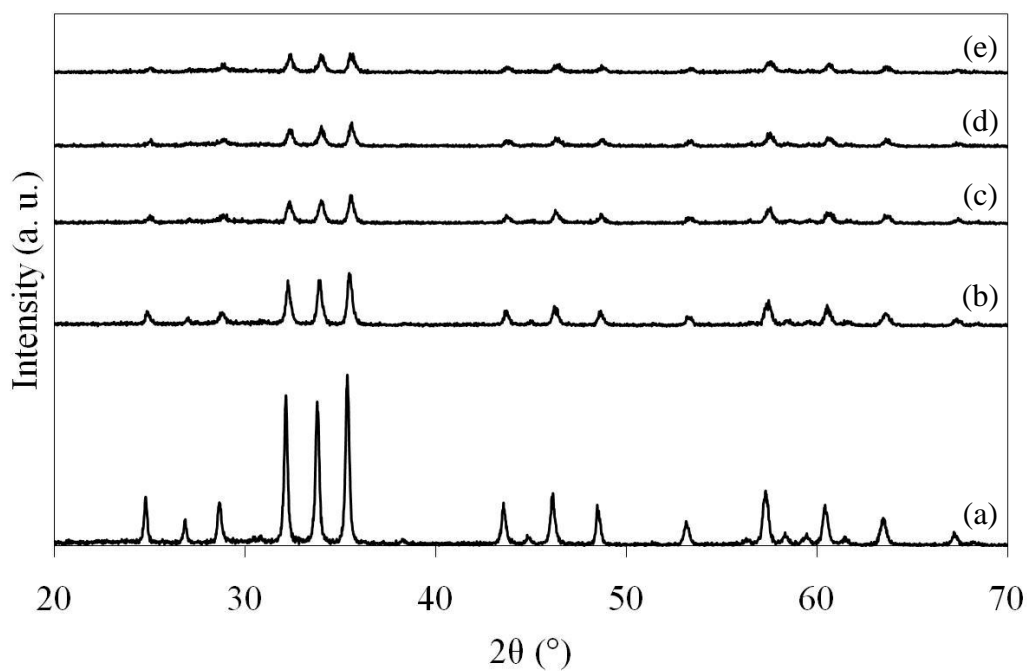


Figure 4-7. PXR D patterns of Ce_2MnN_3 after collected after approximately (a) 0, (b) 8.75, (c) 17.5, (d) 26.25 and (e) 35 hours within the air sensitive sample dome.

4.1.2.2.2 Energy Dispersive X-ray (EDX) Spectroscopy

The EDX pattern for Ce_2MnN_3 , prepared from cerium and manganese metals, is shown in Figure 4-8.

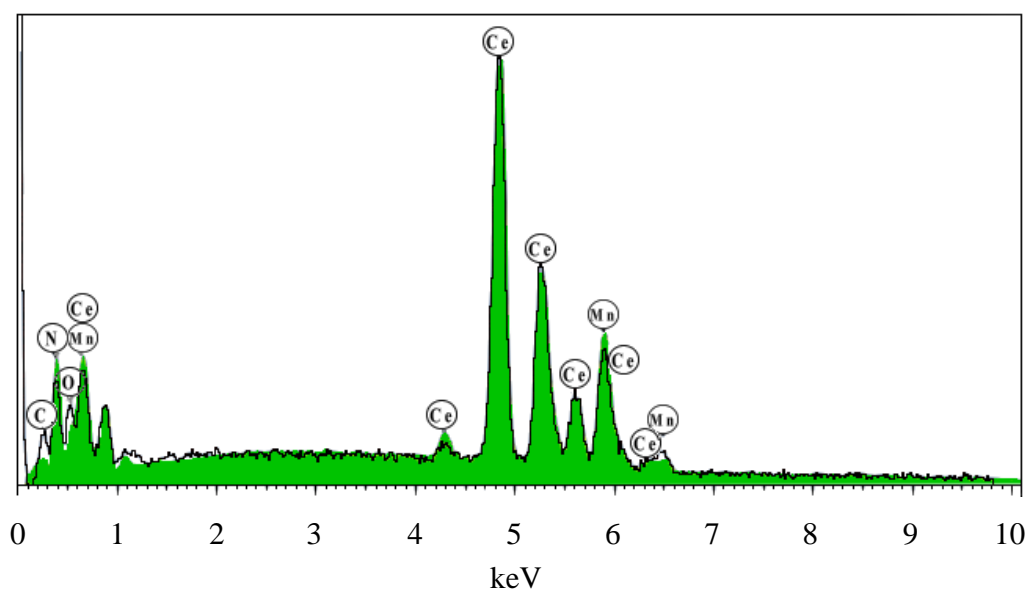


Figure 4-8. EDX pattern for Ce_2MnN_3 . The green pattern represents the theoretical 2:1:3 ratio of Ce:Mn:N and the black line the experimental data.

EDX gave the following atomic percentages: cerium 27.87%, manganese 12.44%, nitrogen 37.21%, oxygen 6.92% and carbon 15.55%. The carbon content results from the organic glue used on sample holders. Theoretical atomic percentages for the content of cerium, manganese and nitrogen in Ce_2MnN_3 were calculated and compared with the experimental ones (Table 4-7). The experimental cerium content has been adjusted to accommodate either Ce_2O_3 or CeO_2 content as the source of the oxygen. The source of the oxide was thought to be the starting Ce metal and/or a result of surface oxidation, occurring upon transfer of the sample from the glove box to the instrument. In general, PXRD suggested that the primary oxide impurity present, from initial cerium reagents used was Ce_2O_3 (section 4.1.2.2.1), however, in the presence of oxygen CeO_2 will form preferentially. Theoretical atomic percentages have been normalised to manganese and show a close correlation to the experimental data. The agreement between theoretical and experimental data, together with PXRD data, confirms that the product of the reaction of the elements is indeed Ce_2MnN_3 .

Element	Atomic %		
	Experimental		Theoretical
	$\text{Ce}_2\text{MnN}_3 + \text{CeO}_2$	$\text{Ce}_2\text{MnN}_3 + \text{Ce}_2\text{O}_3$	Ce_2MnN_3
Cerium	24.41	23.26	24.88
Manganese	12.44	12.44	12.44
Nitrogen	37.21	37.21	37.32

Table 4-7. Comparison between the experimental and theoretical EDX data. Assuming the oxygen present is a result of cerium oxide, the cerium percentage can be split into two parts.

4.1.2.2.3 Powder Neutron Diffraction (PND)

Rietveld refinement using PND was performed based on the model derived from PXRD data. Additional phases were also included, such as CeN and $\text{MnN}_{0.457}$. The model for CeN was taken from Olcese and the model for $\text{MnN}_{0.457}$ was taken from Leineweber *et al.*^{247, 259} The background was modelled by a Cosine Fourier series with sixteen terms. The peak shape was modelled by a multi-term Simpson's rule integration of the pseudo-Voigt.^{241, 242} The parameters refined were: the cell parameters (*a*, *b*, *c*) for the

three phases, one zero point, two scale factors, six isotropic thermal parameters, twelve profile parameters. The refinement parameters are summarised in Table 4-8 and the refinement profile is shown in Figure 4-9.

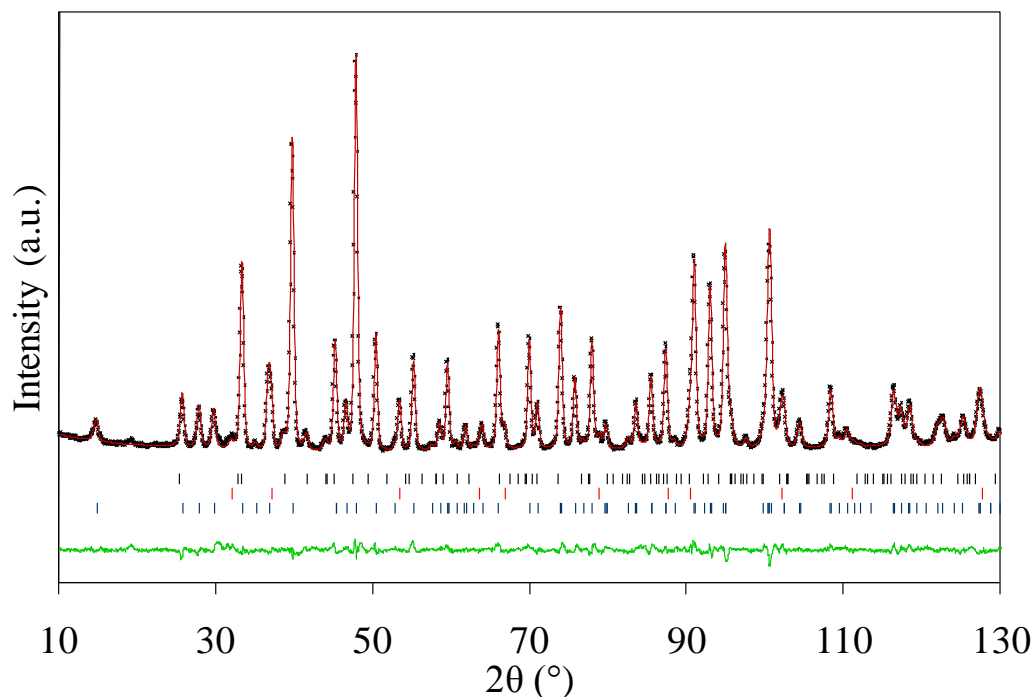


Figure 4-9. PND profiles for Ce_2MnN_3 at room temperature, showing observed (+), calculated (red line) and difference pattern (green line). Tick marks indicate reflection positions for $\text{MnN}_{0.457}$ (upper), CeN (middle) and Ce_2MnN_3 (lower) phases.

Formula	Ce_2MnN_3	
Space Group	<i>Immm</i> (no. 71)	
	PND data	PXRD data
a (Å)	3.7541(1)	3.7549(2)
b (Å)	3.4484(1)	3.4487(1)
c (Å)	12.4718(4)	12.4734(6)
V (Å ³)	161.46(2)	161.52(2)
Z	2	
Calculated density (g cm ⁻³)	7.759	
Profile function	Pseudo-Voigt	
No. of profile points	2459	
No. of parameters refined	48	
R_{wp}	0.0437	
R_{p}	0.0340	
χ_{red}^2	3.297	

Table 4-8. Summary of refinement data and lattice parameters for Ce_2MnN_3 at room temperature, derived from PND data.

The cell parameters, obtained from PND, are consistent with those obtained by PXRD. The structural parameters are given in Table 4-9. Selected bond lengths are given in Table 4-10. Quantitative determination of the CeN and MnN_{0.457} content indicated 6.6(9)% and 3.9(9)%, weight percentage, of these secondary phases respectively. These secondary phases correspond with unreacted starting reagents. It should be noted that these secondary phases were not observed in the PXRD data. A possible explanation for the detection of these phases in PND is that the grains in the polycrystalline sample analysed may contain an inner core of unreacted starting material. The increased penetration depth of neutrons compared to X-rays (section 2.3.2.3) reveals the unreacted nature of the polycrystallites. This highlights the importance of thorough mixing and reduced particle size in ensuring the reaction goes to completion.

Atom	Site	x	y	z	100 × U _{iso}	Occ.
Ce	4i	0	0	0.3533(1)	0.02(3)	1.0
Mn	2a	0	0	0	0.15(6)	1.0
N(1)	2b	0	½	½	0.20(3)	1.0
N(2)	4i	0	0	0.1636(1)	0.34(2)	1.0

Table 4-9. Structural parameters for Ce₂MnN₃ derived from PND collected at room temperature.

Distances (Å)			
Ce-N(1)	2.5142(10) × 2	Mn-N(1)	1.87707(7) × 2
Ce-N(2)	2.365(2) 2.5575(2) × 4	Mn-N(2)	2.0307(9) × 2
Ce-Mn	3.1376(8) × 4	Mn-Ce	3.1376(8) × 8
Ce-Ce	≥ 3.4484(1)	Mn-Mn (intrachain)	3.7541(1) × 2
		Mn-Mn (interchain)	3.4484(1) × 2
N(1)-Mn	1.87707(7) × 2	N(2)-Mn	2.0407(9)
N(1)-Ce	2.5142(10) × 2	N(2)-Ce	2.3653(16) 2.5575(2) × 4
Angles (°)			
N(1)-Mn-N(1)	180	N(2)-Mn-N(2)	180
N(1)-Mn-N(2)	90	Mn-N(1)-Mn	180

Table 4-10. Selected bond lengths and angles in Ce₂MnN₃ from PND collected at room temperature.

4.1.2.2.4 Magnetic Susceptibility

The magnetic susceptibility data of Ce_2MnN_3 are shown in Figure 4-10, a diamagnetic correction has been applied.¹⁹⁸ The susceptibility, χ (emu g^{-1}), was modelled to the Curie-Weiss equation $\chi = \chi_0 + C/T - \theta$, with a temperature independent term, χ_0 , as used by Niewa *et al.*⁶⁸

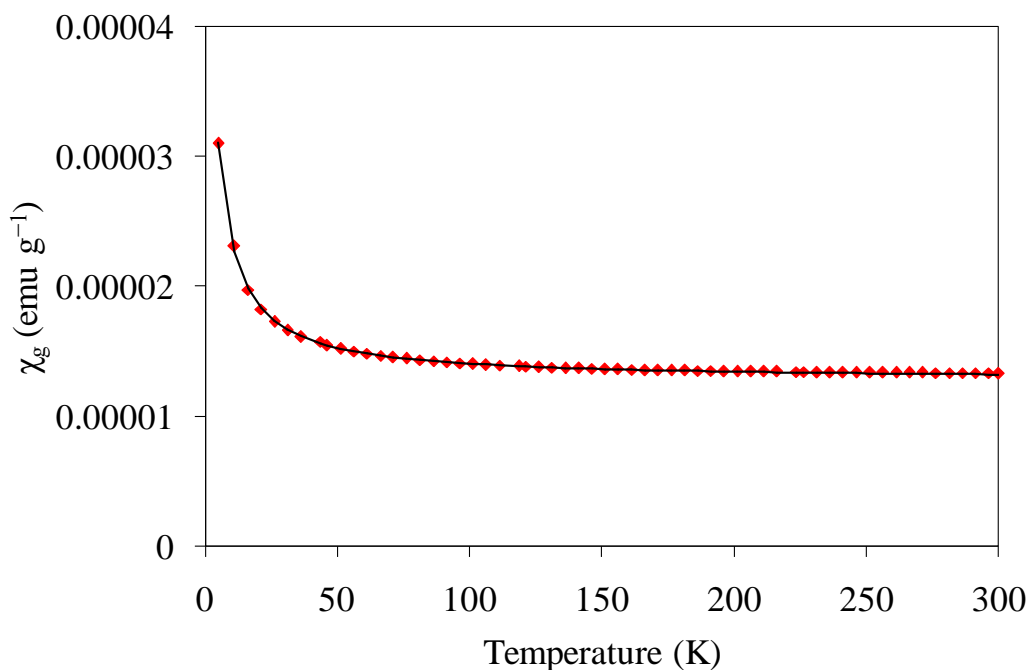


Figure 4-10. Magnetic susceptibility (χ) versus temperature data for Ce_2MnN_3 (red) with fitting based on a Curie-Weiss equation with a temperature independent component (black).

The fit to the susceptibility data demonstrated a temperature independent term, $\chi_0 = 1.280(2) \times 10^{-5} \text{ emu g}^{-1}$, $C = 1.29(1) \times 10^{-4} \text{ emu K g}^{-1}$ and $\theta = -2.1(1) \text{ K}$, giving $\mu_{\text{eff}} = 0.62 \mu_{\text{B}}$ per Mn. This value is similar to that derived by Niewa *et al.*, $\mu_{\text{eff}} = 0.53 \mu_{\text{B}}$.⁶⁸ This small moment is attributed to impurities and/or defects.

4.1.3 Conclusions

Ce_2MnN_3 was successfully prepared through two routes. The first route was reported by Niewa *et al.* and involves a two step reaction; the preparation of CeN via reaction of

cerium metal with ammonia gas and the reaction of CeN with manganese in nitrogen gas. The second route was started in this work and involves a one step reaction between elemental cerium and manganese metals and nitrogen gas. This modified synthetic route is reproducible and offers many advantages compared to the route previously reported. The main advantage is the simplicity of the experimental set-up and procedures. This route only requires a tubular furnace, silica tubes and nitrogen cylinders, which are all common in most solid-state synthetic laboratories. The second advantage is that this synthetic route is relatively quick and does not require any intermediate step or preparation of starting reagents prior to the reaction. In particular, the step of the formation of CeN is avoided. CeN is highly air sensitive, reacts violently with moisture, and can therefore be quite difficult to handle. The third advantage is that nitrogen gas is cheaper, safer and easier to handle than ammonia gas.

Moreover, there are strong indications that this reaction may be extended to the preparation of other nitrides. Other lanthanides, like lanthanum, praseodymium and neodymium, form binary nitrides of general formula LnN, when reacted with nitrogen gas.^{247, 252, 260}

4.2 Cationic Substitution in Ce₂MnN₃

Cationic substitution in Ce₂MnN₃ to prepare ternary nitrides of the Ce_{2-x}A_xMnN₃ or Ce₂Mn_{1-x}M_xN₃ family has not been extensively reported. Substitution on the Ce⁴⁺ and Mn⁺ sites were attempted to gain information into the solubility of ions within the structure, the structural stability and modification of the physical properties, such as conductivity or magnetism. Preliminary results show that only the substitution of La³⁺ for Ce⁴⁺ can be carried out successfully.

4.2.1 Substitution on the Cerium Site of Ce₂MnN₃

Substitution on the Ce⁴⁺ site would lead to the Ce_{2-x}A_xMnN₃ family of nitrides. Isovalent substitutions were carried out with the Tb⁴⁺, Dy⁴⁺, Pr⁴⁺ and Zr⁴⁺ cations. Although there is no literature detailing the solubility of these cations on the cerium site in other nitrides, there is some evidence of substitution occurring in CeO₂.²⁶¹⁻²⁶³

Aliovalent substitutions were also investigated. Substitution of Ce^{4+} with La^{3+} and Y^{3+} was performed with the goal of oxidising the manganese and, potentially, modifying the properties of the material. Cerium substitution by lanthanum and yttrium has also been observed in CeO_2 .^{264, 265} In both cases of $\text{Ce}_{1-x}\text{A}_x\text{O}_{2-\delta}$ ($\text{A} = \text{Y}, \text{La}$), A^{3+} incorporation is compensated by the formation of anion vacancies, to maintain charge neutrality. Attempts to substitute cerium for lanthanum in Ce_2MnN_3 have previously been made, by Niewa *et al.*⁶⁸ However, the route involved the reaction of CeN and LaN with manganese, under nitrogen, and resulted in no more than a two atomic percent substitution of cerium for lanthanum in Ce_2MnN_3 . Here we demonstrate that with the preparation of $\text{Ce}_{1-x}\text{La}_x\text{N}$, it is possible to increase the substitution of cerium with lanthanum, in Ce_2MnN_3 , to approximately twelve percent.

4.2.1.1 Experimental

4.2.1.1.1 Preparation of $\text{Ce}_{1-x}\text{A}_x\text{N}$ ($\text{A} = \text{Y}, \text{La}, \text{Pr}, \text{Dy}, \text{Tb}$)

The experimental procedures are similar to the one for CeN (section 4.1.1.1), using metal powders, in appropriate stoichiometric ratios. All preparations were carried out in an argon filled glove box.

4.2.1.1.1.1 Method 1 – Ammoniation of the Metals

Cerium powder was mixed with powders of either yttrium, lanthanum, praseodymium or dysprosium powder (40 mesh, ESPI, 99.9%), in the desired stoichiometry and then the mixture was hand pressed into pellets. These pellets were placed in a niobium crucible and inserted into a quartz reaction tube, which was then inserted into a tubular furnace. The system was heated to 1050 °C in flowing ammonia gas ($14 \text{ dm}^3 \text{ min}^{-1}$) for 12 hours then cooled to room temperature and flushed with nitrogen to remove residual ammonia, before returning the tube to the glove box.

4.2.1.1.1.2 Method 2 – Nitrogenation in Molten Zinc

The hand pressed pellets, of the desired stoichiometric mixtures between cerium and the lanthanide metal powders, were placed into stainless-steel crucibles and approximately ten molar equivalents of zinc shot (Sigma-Aldrich, 99.99%) was added. The crucible was sealed in a stainless-steel reaction vessel, which was connected to a nitrogen gas-feed line. The sample was gently heated to 750 °C over 9 hours in an electric furnace, under a stream of nitrogen. After 108 hours the furnace was cooled to room temperature. The zinc was removed via vacuum distillation (section 2.2.2.2.1). The reaction vessel was then isolated from air and transferred to a glove box to be opened.

4.2.1.1.2 Preparation of $Ce_{2-x}A_xMnN_3$ ($A = Tb, Dy, Zr, La$)

4.2.1.1.2.1 Method 1– Reaction of Metals and Nitrogen

In a glove box, a stoichiometric ratio of either cerium, zirconium, lanthanum, terbium or dysprosium (ESPI, 99.9%) and manganese (Aldrich, 99.99%) powder were mixed and placed in a niobium crucible. This was inserted into a quartz tube and then heated at 900 °C, in a tubular furnace, for 36 hours, under nitrogen, before cooling to room temperature. The cool quartz tube was then returned to the glove box. The resulting mixture was ground re-pelletised and the heating step was repeated to ensure complete conversion to $Ce_{2-x}A_xMnN_3$.

4.2.1.1.2.2 Method 2– Reaction of Cerium Lanthanum Nitride, Manganese and Nitrogen

In an argon filled glove box, previously prepared $La_xCe_{1-x}N$ and manganese metal powder (Aldrich, 99.99%) were ground separately to fine powders before being mixed in the required stoichiometric ratio. The mixture was hand pressed into pellets, placed into a niobium crucible and inserted into a quartz tube. The quartz tube was inserted into a furnace. The pellets were heated to 900 °C, under flowing nitrogen (purified). After 36 hours the resulting mixture was ground re-pelletised in a glove box, and the heating step was repeated to ensure complete conversion to $Ce_{2-x}A_xMnN_3$.

4.2.1.1.3 Characterisation

Powder X-ray diffraction (PXRD) was carried out on all samples using a Siemens D5000 powder diffractometer with Cu K α radiation.

High-resolution powder neutron diffraction (PND) data were collected, for the Ce_{2-x}A_xMnN₃ series, on the D2B diffractometer at the Institut Laue-Langevin (ILL), Grenoble, using a wavelength $\lambda = 1.59432 \text{ \AA}$ and covering the angular range $10 \leq 2\theta/^\circ \leq 157$ with $\Delta 2\theta = 0.05^\circ$. The sample was contained in a vanadium can of internal diameter 6.8 mm.

Magnetic susceptibility measurements were collected at the University of Birmingham, in collaboration with Prof. Colin Greaves and co-workers, on a Quantum Design MPMS SQUID magnetometer with a field of 2 T.

4.2.1.1 Results and Discussion

4.2.1.1.1 Structural Characterisation of Ce_{1-x}A_xN (A = Y, La, Pr, Tb, Dy)

4.2.1.1.1.1 Powder X-ray Diffraction (PXRD)

Both reaction of the cerium-lanthanum mixture in ammonia and with nitrogen, in a zinc flux, resulted in the successful preparation of the Ce_{1-x}La_xN solid solution in the range of $0 \leq x \leq 0.125$.

Rietveld refinement was performed using data from PXRD performed on each of the samples. The model used for Ce_{1-x}La_xN was based on that derived from CeN, in section 4.1.2.1. The occupancy of the cerium site was split between the two cations, cerium and lanthanum. In all refinements the background was initially modelled manually with a Shifted Chebyshev function and was later allowed to refine freely, once an adequate representation of the peak shape had been reached. The peak shape was modelled using

a multi-term Simpson's rule integration of the pseudo-Voigt.^{241, 242} The parameters refined were; the cell parameters (a , b , c), one zero point, three thermal parameters and five profile parameters. Due to similar absorption issues to those observed in the undoped CeN, a surface roughness correction by Suortti was applied, using the values derived from CeN.²⁵⁴

The data collection was marred by what appears to be an increasing air sensitivity of the samples with increasing values of x . As x increased it became necessary to reduce the data collection times to minimise decomposition to the binary oxides, Ce₂O₃, CeO₂, La₂O₃. The resulting reduced data quality prevented accurate refinement of the lanthanum and cerium occupancies. Therefore, these values were constrained to the theoretical occupancies of the target compositions. The unit cell parameters are shown in Table 4-11 and display an increase in cell dimensions with increasing lanthanum content (Figure 4-11). This is consistent with lanthanum incorporation, as lanthanum shows a larger ionic radii than cerium, 1.12 Å and 1.01 Å respectively.⁷⁵ The increasing lanthanum incorporation is expected to yield a linear increase in a in accordance with Vegard's law.^{266, 267}

Compound	a (Å)	V (Å ³)
CeN	5.0242(1)	126.82(1)
Ce _{0.95} La _{0.05} N	5.0264(3)	126.99(2)
Ce _{0.925} La _{0.075} N	5.0378(3)	127.86(2)
Ce _{0.9} La _{0.1} N	5.0414(5)	128.13(4)
Ce _{0.875} La _{0.125} N	5.0535(8)	129.06(6)
Ce _{0.85} La _{0.15} N	5.0487(8)	128.69(6)

Table 4-11. Cell dimensions for Ce_{1-x}La_xN, derived from PXRD data.

At values of $x > 0.125$, peaks corresponding with LaN became visible in the PXRD patterns (Figure 4-12) and the increase in cell dimensions ceased (Table 4-11), indicating the limit of cerium substitution had been reached between $0.10 < x < 0.15$. The Ce_{1-x}La_xN ($0 \leq x \leq 0.125$) series was used in the preparation of Ce_{2-x}La_xMnN₃ ($0 \leq x < 0.25$).

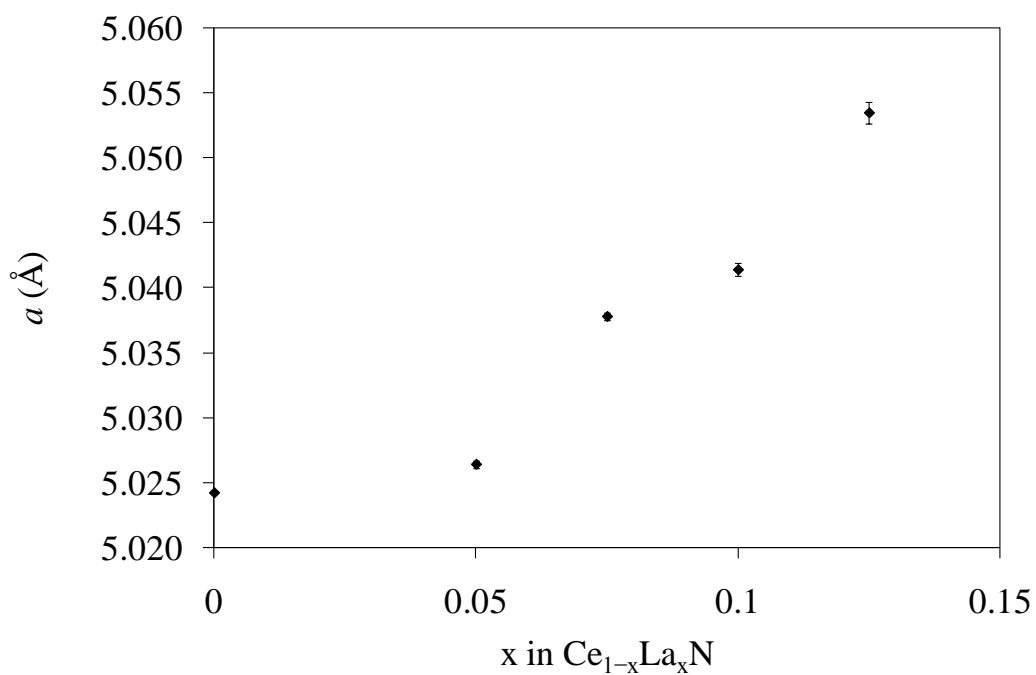


Figure 4-11. Plot showing the variation in a with lanthanum content in $\text{Ce}_{1-x}\text{La}_x\text{N}$, derived from PXRD data.

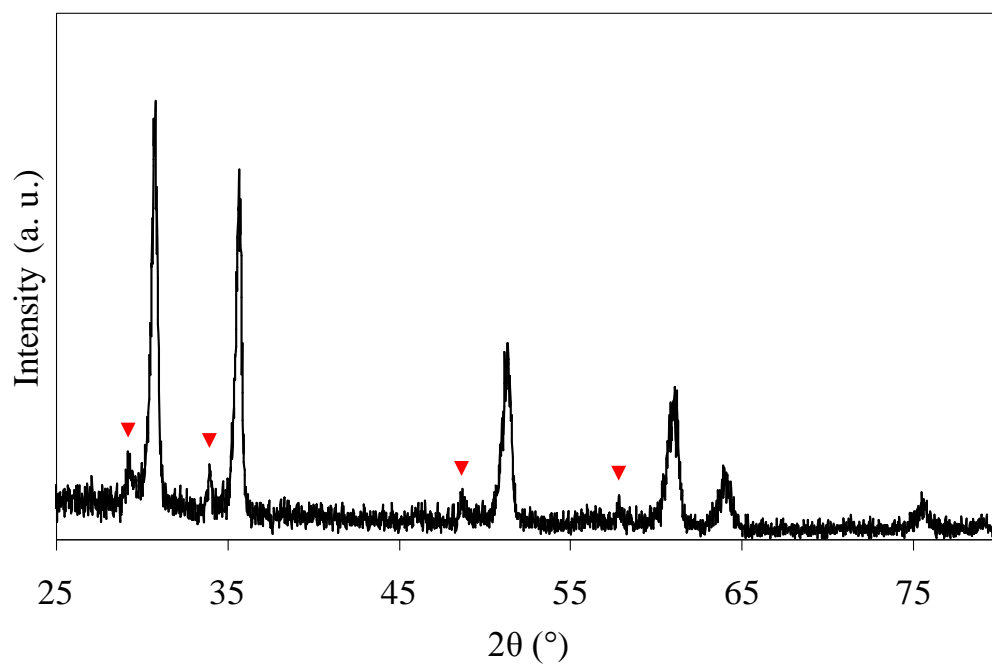


Figure 4-12. PXRD pattern for $\text{Ce}_{1-x}\text{La}_x\text{N}$ ($x = 0.15$). The peaks highlighted by the red triangles correspond with LaN . The unmarked peaks are consistent with those for $\text{Ce}_{1-x}\text{La}_x\text{N}$.

Substitutions of cerium with yttrium, praseodymium, terbium and dysprosium were also carried out. Initially $x = 0.1$ substitutions ($\text{Ce}_{0.9}\text{A}_{0.1}\text{N}$; $\text{A} = \text{Y}, \text{Pr}, \text{Tb}, \text{Dy}$) were

performed. The PXRD pattern for $\text{Ce}_{0.9}\text{Dy}_{0.1}\text{N}$ is shown in Figure 4-13 as an example of these substitution reactions. It shows diffraction peaks for both binary nitrides, DyN and CeN.

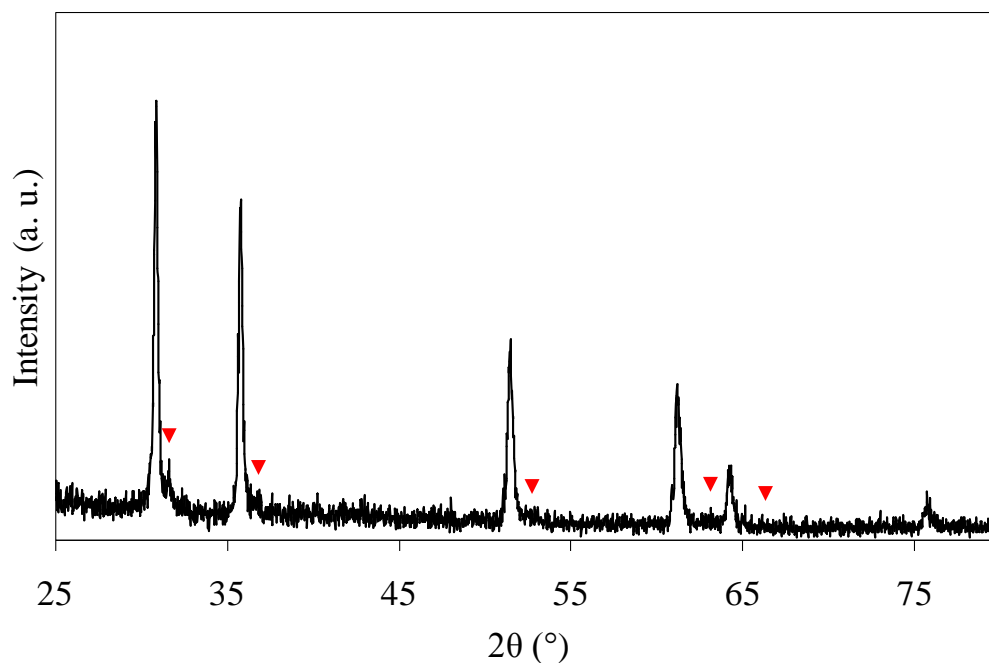


Figure 4-13. PXRD pattern for $\text{Ce}_{1-x}\text{Dy}_x\text{N}$ ($x=0.1$). The peaks highlighted by the red triangles correspond with DyN. The unmarked peaks are consistent with those for CeN.

The peaks of the major phase were indexed, to a cubic unit cell ($Fm\bar{3}m$), using the GSAS suite of programs.^{217, 240} The cell parameters obtained are shown in Table 4-12.

Target Compound	a (Å)
CeN	5.0242(1)
$\text{Ce}_{0.9}\text{Y}_{0.1}\text{N}$	5.0244(7)
$\text{Ce}_{0.9}\text{Pr}_{0.1}\text{N}$	5.0276(8)
$\text{Ce}_{0.9}\text{Tb}_{0.1}\text{N}$	5.0227(4)
$\text{Ce}_{0.9}\text{Dy}_{0.1}\text{N}$	5.0244(11)

Table 4-12. Cell dimensions for $\text{Ce}_{1-x}\text{A}_x\text{N}$ ($A = \text{Y, Pr, Tb, Dy}$), derived from PXRD.

The cell dimensions for $\text{Ce}_{1-x}\text{A}_x\text{N}$ ($A = \text{Y, Dy}; x = 0.1$) are identical to those of CeN indicating that no substitution for cerium has taken place. For $\text{Ce}_{1-x}\text{A}_x\text{N}$, with $A = \text{Pr}$

and Tb, there are small deviations in the cell dimensions, with Ce_{0.9}Pr_{0.1}N showing a minor increase in cell size and Ce_{0.9}Tb_{0.1}N a minor decrease, relative to CeN. Such deviations are consistent with substitution of cerium with cations of larger and smaller radii; 1.08 Å, 1.01 Å and 0.923 Å for Pr³⁺, Ce³⁺ and Tb³⁺ respectively.^{32, 75} The presence of peaks in the PXRD patterns, corresponding with PrN and TbN, indicate less than 10% substitution on the cerium site of CeN is taking place. Unfortunately, due to the relative low peak intensity of AN (A = Pr, Tb) and proximity to the peaks of CeN accurate phase fractions could not be determined through Rietveld refinement.

4.2.1.1.2 Structural Characterisation of Ce_{2-x}A_xMnN₃ (A = Zr, La, Tb, Dy)

4.2.1.1.2.1 Powder X-ray Diffraction (PXRD)

Two approaches were used for the preparation of Ce_{2-x}A_xMnN₃ (A = Zr, La, Tb, Dy). First, direct reactions of the metals with nitrogen were carried out. Substitutions of up to $x = 0.2$ (Ce_{1.8}A_{0.2}MnN₃, with A = Zr, La, Tb, Dy) were attempted.

Under these reaction conditions none of the lanthanide metals or zirconium successfully substitute for cerium in Ce₂MnN₃. The PXRD patterns show strong reflections for the binary nitrides, AN, together with diffraction peaks for Ce₂MnN₃, corresponding exactly with the peak positions expected for the non-substituted phase.

The lack of substitution of any of the A metals for cerium in Ce₂MnN₃ could be due to the fact that these metals react quickly with N₂ and produce very stable binary nitrides, LaN, DyN, TbN and ZrN, which do not react any further. Therefore, attempts to prepare the mixed metal binary nitrides were made.

As seen in section 4.2.1.1.1 the highest degree of cerium substitution in the binary nitride, CeN, was achieved using lanthanum metal. The Ce_{1-x}La_xN solid solution was therefore used in the preparation of the Ce_{2-x}La_xMnN₃ series. This resulted in the successful preparation of Ce_{2-x}La_xMnN₃ in the range of $0 \leq x \leq 0.2$.

Rietveld refinement was performed using data from PXRD performed on each of the $\text{Ce}_{2-x}\text{La}_x\text{MnN}_3$ samples. The model used for $\text{Ce}_{2-x}\text{La}_x\text{MnN}_3$ was based on that derived from Ce_2MnN_3 , in section 4.1.2.2. As in the refinement of Ce_2MnN_3 two additional phases were also included, Ce_2O_3 and CeN. The refinements suggested less than 3.5% of these impurities, in all cases. The occupancy of the cerium site was split between the two cations, cerium and lanthanum. The background was modelled manually with a Shifted Chebyshev function. The peak shape was modelled using a multi-term Simpson's rule integration of the pseudo-Voigt.^{241, 242} The parameters refined were; the cell parameters (a , b , c), one zero point, two phase fractions, and six profile parameters. The unit cell dimensions derived from PXRD data are shown in Table 4-13.

Compound	a (Å)	b (Å)	c (Å)	V (Å ³)
Ce_2MnN_3	3.7541(1)	3.4484(1)	12.4718(4)	161.46(2)
$\text{Ce}_{1.9}\text{La}_{0.1}\text{MnN}_3$	3.7561(5)	3.4532(5)	12.4785(20)	161.85(6)
$\text{Ce}_{1.85}\text{La}_{0.15}\text{MnN}_3$	3.7569(5)	3.4536(5)	12.4815(20)	161.93(6)
$\text{Ce}_{1.8}\text{La}_{0.2}\text{MnN}_3$	3.7579(4)	3.4570(4)	12.4855(16)	162.20(6)

Table 4-13. Cell parameters of $\text{Ce}_{2-x}\text{La}_x\text{MnN}_3$ derived from PXRD.

$\text{Ce}_{2-x}\text{La}_x\text{MnN}_3$ ($0 \leq x \leq 0.2$) show a linear increase in cell dimensions with increasing lanthanum incorporation, in accordance with Vegard's law (Figure 4-11).^{266, 267} This supports the hypothesis of successful substitution of cerium with lanthanum, in Ce_2MnN_3 .

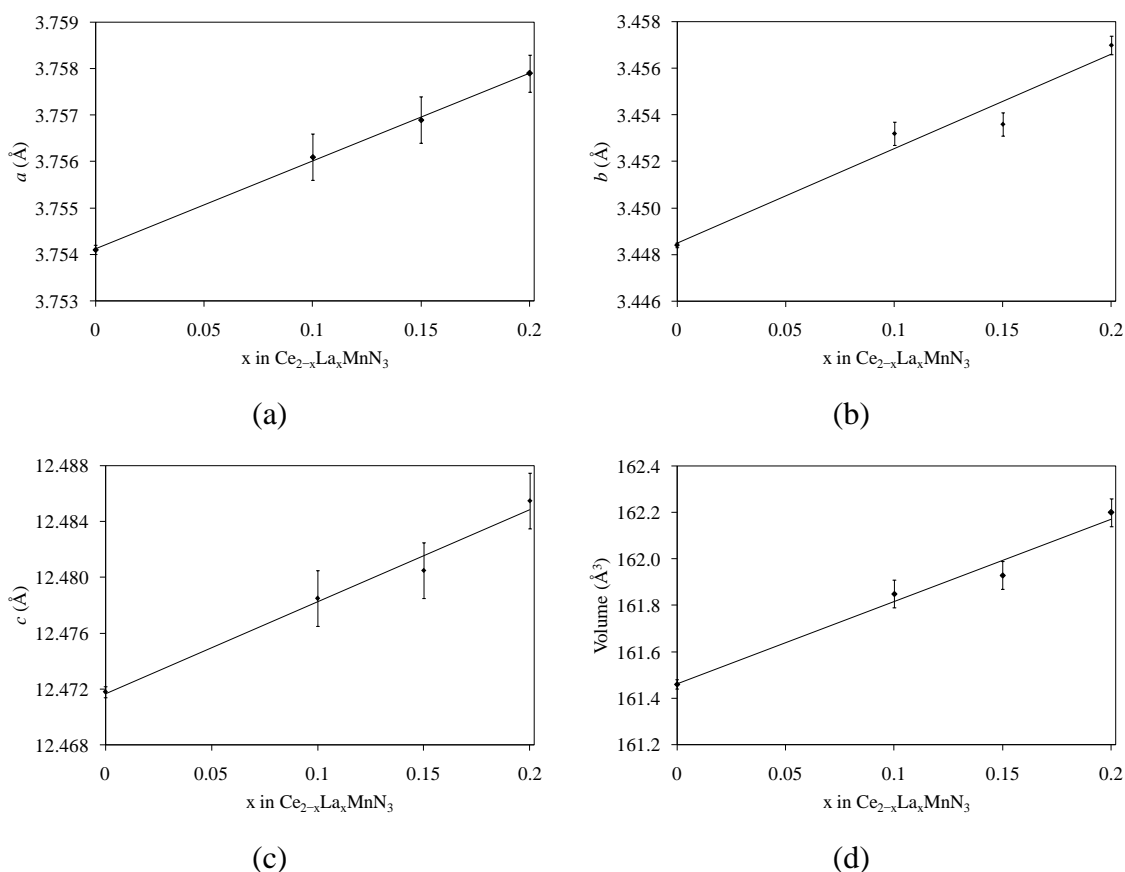


Figure 4-14. Variation in cell dimension, (a) a , (b) b , (c) c and (d) volume, for $\text{Ce}_{2-x}\text{La}_x\text{MnN}_3$ with lanthanum content.

In order to obtain accurate structural information regarding this new solid solution, neutron diffraction was performed.

4.2.1.1.2.2 Powder Neutron Diffraction (PND)

Neutron diffraction was carried out on $\text{Ce}_{2-x}\text{La}_x\text{MnN}_3$, $x = 0.1, 0.15$ and 0.2 . Rietveld refinement was performed based on the model of Ce_2MnN_3 , derived from PND data. Additional phases were also included. The model for $\text{Ce}_{1-x}\text{La}_x\text{N}$ were taken from refinement using PXRD data, the model for $\text{MnN}_{0.457}$ was taken from Leineweber *et al.* and the model for Ce_2O_3 taken from Zachariasen.^{258, 259} The background was modelled by a Cosine Fourier series with twelve terms. The peak shape was modelled by a multi-term Simpson's rule integration of the pseudo-Voigt.^{241, 242} The parameters refined were; the cell parameters (a, b, c) for the four phases, one zero point, three phase fractions and seven-eleven profile parameters. The isotropic thermal parameters were derived from the PND on Ce_2MnN_3 , and fixed to prevent refinement to negative values.

The cerium site (4i) was split between lanthanum and cerium. The occupancy of the 4i site was also constrained to give a total occupancy of one. The chemical formula for the members of the $\text{Ce}_{2-x}\text{La}_x\text{MnN}_3$ solid solution could then be deduced. The refinement parameters for $\text{Ce}_{2-x}\text{La}_x\text{MnN}_3$ are summarised in Table 4-14. An example of a refinement profile, for $\text{Ce}_{1.78(2)}\text{La}_{0.22(2)}\text{MnN}_3$, is given in Figure 4-15. Refinement profiles for $\text{Ce}_{2-x}\text{La}_x\text{MnN}_3$ ($x = 0.10(1), 0.18(2)$) are shown in Figure C-1 and C-2 of the appendices.

Formula	$\text{Ce}_{2-x}\text{La}_x\text{MnN}_3$			
Space Group	<i>Immm</i> (no. 71)			
	Ce_2MnN_3	$x = 0.10(1)$	$x = 0.18(2)$	$x = 0.22(2)$
a (Å)	3.7541(1)	3.7568(1)	3.7581(2)	3.7581(2)
b (Å)	3.4484(1)	3.4540(1)	3.4562(2)	3.4571(2)
c (Å)	12.4718(4)	12.4822(4)	12.4875(7)	12.4869(8)
V (Å ³)	161.46(2)	161.97(1)	162.20(2)	162.24(2)
Z		2	2	2
Calculated density (g cm ⁻³)		7.732	7.719	7.716
Profile function		Pseudo-Voigt	Pseudo-Voigt	Pseudo-Voigt
No. of profile points		2459	2459	2459
No. of parameters refined		33	39	37
R_{wp}		0.0473	0.0498	0.0507
R_{p}		0.0371	0.0398	0.0400
χ_{red}^2		3.261	2.863	3.388

Table 4-14. Summary of refinement data and lattice parameters for $\text{Ce}_{2-x}\text{La}_x\text{MnN}_3$ at room temperature, derived from PND data.

The cell dimensions show an increase with increasing values of x , consistent with the PXRD data. The structural parameters are given in Table 4-16-Table 4-18. Quantitative determination of the $\text{Ce}_{1-x}\text{La}_x\text{N}$, $\text{MnN}_{0.457}$ and $\text{Ce}_{2-x}\text{La}_x\text{O}_3$ contents are given in Table 4-15.

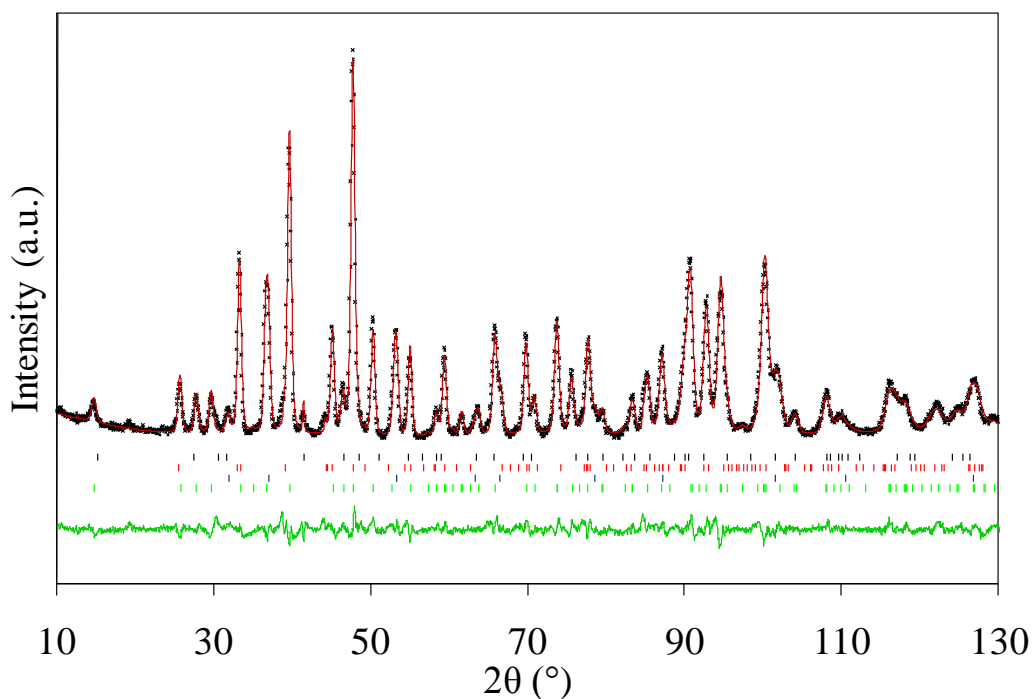


Figure 4-15. PND profiles for $\text{Ce}_{1.78(2)}\text{La}_{0.22(2)}\text{MnN}_3$ at room temperature, showing observed (+), calculated (red line) and difference pattern (green line). Tick marks indicate reflection positions for $\text{Ce}_{1.8}\text{La}_{0.2}\text{O}_3$ (black), $\text{MnN}_{0.457}$ (red), $\text{Ce}_{0.9}\text{La}_{0.1}\text{N}$ (blue) and $\text{Ce}_{1.78(2)}\text{La}_{0.22(2)}\text{MnN}_3$ (green) phases.

Compound	Weight fraction (%)		
	$\text{Ce}_{1-x}\text{La}_x\text{N}$	$\text{MnN}_{0.457}$	$\text{Ce}_{2-x}\text{La}_x\text{O}_3$
$\text{Ce}_{1.90(1)}\text{La}_{0.10(1)}\text{MnN}_3$	8.3(3)	2.6(2)	2.8(0)
$\text{Ce}_{1.82(2)}\text{La}_{0.18(2)}\text{MnN}_3$	9.9(4)	2.5(3)	8.2(0)
$\text{Ce}_{1.78(2)}\text{La}_{0.22(2)}\text{MnN}_3$	15.7(14)	1.8(3)	1.3(0)

Table 4-15. Quantitative determination of the $\text{Ce}_{1-x}\text{La}_x\text{N}$, $\text{MnN}_{0.457}$ and $\text{Ce}_{2-x}\text{La}_x\text{O}_3$ in $\text{Ce}_{2-x}\text{La}_x\text{MnN}_3$.

The presence of unreacted $\text{Ce}_{1-x}\text{La}_x\text{N}$ was not revealed by X-ray diffraction only by neutron diffraction. As in the case of undoped Ce_2MnN_3 (section 4.1.2.2.3) this may indicate that the increased penetration depth of the neutrons, over X-rays, is highlighting a core of unreacted material within the particles.

Atom	Site	x	y	z	$100 \times U_{\text{iso}}$	Occ.
Ce	4i	0	0	0.3533(1)	0.023	0.949(6)
La	4i	0	0	0.3533(1)	0.023	0.051(6)
Mn	2a	0	0	0	0.147	1.0
N(1)	2b	0	$\frac{1}{2}$	$\frac{1}{2}$	0.204	1.0
N(2)	4i	0	0	0.1632(1)	0.338	1.0

Table 4-16. Structural parameters for $\text{Ce}_{1.90(1)}\text{La}_{0.10(1)}\text{MnN}_3$ derived from PND collected at room temperature.

Atom	Site	x	y	z	$100 \times U_{\text{iso}}$	Occ.
Ce	4i	0	0	0.3535(2)	0.023	0.908(9)
La	4i	0	0	0.3535(2)	0.023	0.092(9)
Mn	2a	0	0	0	0.147	1.0
N(1)	2b	0	$\frac{1}{2}$	$\frac{1}{2}$	0.204	1.0
N(2)	4i	0	0	0.1628(1)	0.338	1.0

Table 4-17. Structural parameters for $\text{Ce}_{1.82(2)}\text{La}_{0.18(2)}\text{MnN}_3$ derived from PND collected at room temperature.

Atom	Site	x	y	z	$100 \times U_{\text{iso}}$	Occ.
Ce	4i	0	0	0.3535(2)	0.023	0.891(8)
La	4i	0	0	0.3535(2)	0.023	0.109(8)
Mn	2a	0	0	0	0.147	1.0
N(1)	2b	0	$\frac{1}{2}$	$\frac{1}{2}$	0.204	1.0
N(2)	4i	0	0	0.1631(1)	0.338	1.0

Table 4-18. Structural parameters for $\text{Ce}_{1.78(2)}\text{La}_{0.22(2)}\text{MnN}_3$ derived from PND collected at room temperature.

Incorporation of La^{3+} into Ce_2MnN_3 will result in a small amount of oxidation of manganese to ensure charge neutrality within the sample. As stated previously, Niewa *et al.* suggested that the difference in $\text{Mn-N}_{\text{bridging}}$ and $\text{Mn-N}_{\text{terminal}}$ bond lengths in Ce_2MnN_3 was a result of increased occupancy of the $\text{Mn-N}_{\text{terminal}}$ π -antibonding states over the $\text{Mn-N}_{\text{bridging}}$ π -antibonding states.⁶⁸ This difference in bond strength is believed to be optimal when manganese shows +1 oxidation state. Therefore, the difference in bond strength between $\text{Mn-N}_{\text{bridging}}$ and $\text{Mn-N}_{\text{terminal}}$ should be reduced if the oxidation state of manganese is increased with La^{3+} substitution into Ce_2MnN_3 , i.e. as x increases.

Table 4-19 shows selected Mn-N bond lengths related to increasing oxidation states of manganese devised from increased La³⁺/Ce⁴⁺ substitution in Ce₂MnN₃.

Compound	Mn Oxidation State	Mn-N _{bridging} (Å)	Mn-N _{terminal} (Å)
Ce ₂ MnN ₃	1.00+	1.87707(7)	2.0407(9)
Ce _{1.90(1)} La _{0.10(1)} MnN ₃	1.10+	1.87839(6)	2.0371(10)
Ce _{1.82(2)} La _{0.18(2)} MnN ₃	1.18+	1.87905(10)	2.0332(16)
Ce _{1.78(2)} La _{0.22(2)} MnN ₃	1.22+	1.87907(11)	2.0366(14)

Table 4-19. Selected bond lengths in Ce_{2-x}La_xMnN₃ from PND, collected at room temperature.

As predicted, the bond lengths derived show a small increase in Mn-N_{bridging} and a reduction in Mn-N_{terminal} as substitution increases. This result is consistent with the prediction by Niewa *et al.* and adds further support to the hypothesis that lanthanum has been successfully incorporated into the structure.⁶⁸

4.2.1.1.2.3 Magnetic Susceptibility

The magnetic susceptibility measurements of the Ce_{2-x}La_xMnN₃ (0 ≤ x ≤ 0.2) series show Pauli paramagnetic behaviour indicating no overall change in the magnetic behaviour compared to Ce₂MnN₃. Figure 4-16 shows the mass susceptibility plot against temperature for Ce_{1.78(2)}La_{0.22(2)}MnN₃. A diamagnetic correction has been applied.¹⁹⁸ The other compounds in the series are shown in Figure C-3 – C-5 of the appendices. As for Ce₂MnN₃, the magnetic data were modelled, independently, by Greaves at the University of Birmingham and the author at the University of Hull, to the Curie-Weiss equation; $\chi = \chi_0 + \frac{C}{T - \theta}$ and the terms derived are given in Table 4-20.

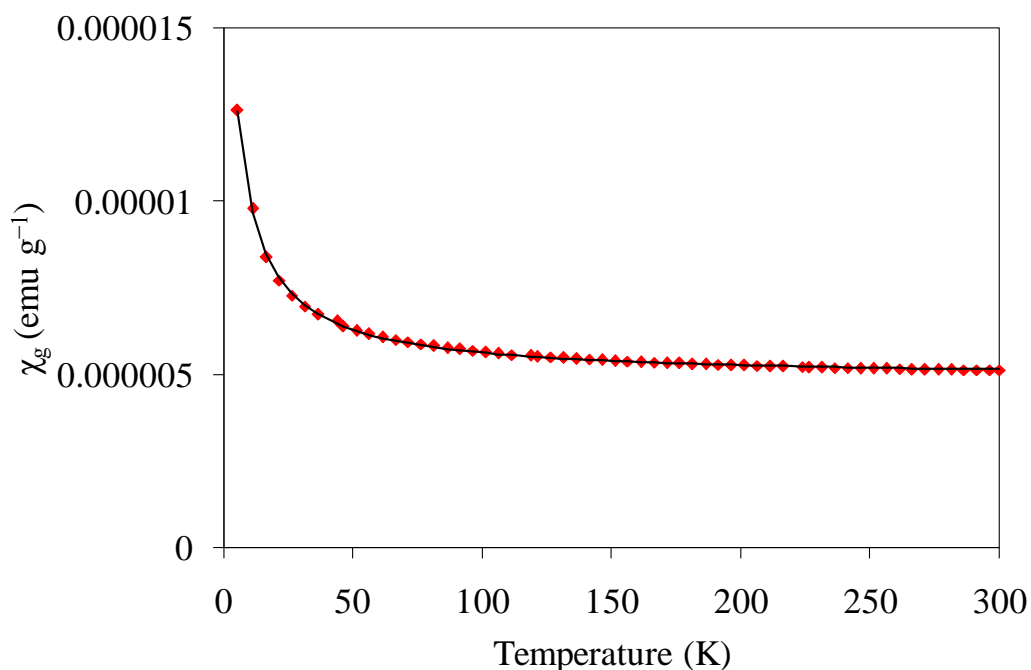


Figure 4-16. Magnetic susceptibility (χ) versus temperature data for $\text{Ce}_{1.78(2)}\text{La}_{0.22(2)}\text{MnN}_3$ (red) with fitting based on a Curie-Weiss equation with a temperature independent component (black).

Compound	χ_0 (emu g^{-1})	C (emu K g^{-1})	θ (K)	μ_{eff} (μ_B)
Ce_2MnN_3	$1.280(2) \times 10^{-5}$	$1.29(1) \times 10^{-4}$	-2.1(1)	0.62
$\text{Ce}_{1.90(1)}\text{La}_{0.10(1)}\text{MnN}_3$	$5.66(4) \times 10^{-6}$	$1.52(4) \times 10^{-4}$	-2.9(2)	0.68
$\text{Ce}_{1.82(2)}\text{La}_{0.18(2)}\text{MnN}_3$	$4.10(2) \times 10^{-6}$	$1.22(2) \times 10^{-4}$	-6.2(2)	0.61
$\text{Ce}_{1.78(2)}\text{La}_{0.22(2)}\text{MnN}_3$	$4.90(1) \times 10^{-6}$	$7.62(8) \times 10^{-5}$	-4.9(1)	0.48

Table 4-20. Curie-Weiss terms derived from modelling the magnetic susceptibility data to $\chi = \chi_0 + \frac{C}{T - \theta}$.

The calculated μ_{eff} values do not vary significantly upon lanthanum insertion, maintaining a value which approximates to 0, with the difference being associated with impurities and/or lattice defects. The drop in the value of χ_0 , from the unsubstituted Ce_2MnN_3 to lanthanum containing compounds, may indicate a decrease of the electron population at the Fermi level. This would be consistent with the oxidation of manganese induced by the $\text{La}^{3+}/\text{Ce}^{4+}$ substitution.

4.2.1.2 Conclusions

The $\text{Ce}_{2-x}\text{La}_x\text{MnN}_3$ ($0 \leq x \leq 0.22(2)$) series was successfully prepared. The increase in lanthanum intake into the material over the experiments performed by Niewa *et al.* highlight the importance of using a two step reaction in which the first step is the formation of a mixed metal binary nitride $\text{Ce}_{1-x}\text{A}_x\text{N}$. In this way intimate mixing between the metals is reached. The direct reaction of lanthanide metals with manganese in nitrogen or ammonia is not a successful route to $\text{Ce}_{2-x}\text{A}_x\text{MnN}_3$ as the formation of unreacted binary nitrides is more favourable.

The overall result of lanthanum substitution, for cerium, is an increase in cell size, in agreement with Vegard's law, and as expected from the larger ionic radii of La^{3+} over Ce^{4+} ($\sim 1.12 \text{ \AA}$ versus 1.01 \AA respectively).⁷⁵ In addition the cell increase results in a minor reduction in the difference between the $\text{Mn-N}_{\text{bridging}}$ and $\text{Mn-N}_{\text{terminal}}$ bond lengths as predicted by Niewa *et al.*⁶⁸ Magnetic susceptibility measurements indicate that the $\text{Ce}_{2-x}\text{La}_x\text{MnN}_3$ ($0 \leq x \leq 0.2$) series are Pauli paramagnetic and display a Curie-Weiss behaviour, with temperature independent component, as seen for the parent compound Ce_2MnN_3 .

Substitution of Zr^{4+} or lanthanide metals (Pr^{4+} , Tb^{4+} , Dy^{4+}) for cerium, proved unfavourable. Only a small incorporation has been obtained for $\text{Ce}_{1-x}\text{A}_x\text{N}$ ($\text{A} = \text{Pr}, \text{Tb}$; $x = 0.1$) with small variations in the cell dimensions.^{32, 75}

4.2.2 Substitution on the Manganese Site of Ce_2MnN_3

Substitution on the Mn^+ site would lead to the $\text{Ce}_2\text{Mn}_{1-x}\text{M}_x\text{N}_3$ solid solution. There are several good candidates for substitution with manganese. Transition metals that show 1+ oxidation state include Cr^+ , Co^+ , Ni^+ and Cu^+ . These show similar ionic radii of $\sim 0.645 \text{ \AA}$, 0.615 \AA , 0.545 \AA , 0.56 \AA and 0.54 \AA for Mn, Cr, Co, Ni and Cu respectively.^{‡32} Transition metals tend to show 1+ oxidation states in ternary nitrides more often than in oxides. Cobalt shows 1+ oxidation state in the nitride $\text{LiSr}_2\text{CoN}_2$.²⁶⁸

[‡] Due to the limited information of ionic radii of M^+ cations, these radii are for M^{3+} ions in octahedral coordination.

Examples of Ni^+ include BaNiN , CaNiN , $\text{Li}_{1-x}\text{Ni}_x[\text{Li}_2\text{N}]$ with $0 \leq x \leq 0.63$ and the Li-Sr-Ni-N systems.^{99, 103, 269-271} In addition, copper is known to form 1+ cations in oxygen-free compounds, including BaCuN and SrCuN .⁹⁷ Furthermore, as stated in section 1.3.3, chromium is known to form the analogous compound Ce_2CrN_3 , even though a single phase product is yet to be produced.⁹²

Here cationic substitution on the manganese site was performed with Cr, Co, Ni and Cu.

4.2.2.1 Experimental

4.2.2.1.1 Preparation of $\text{Ce}_2\text{Mn}_{1-x}\text{M}_x\text{N}_3$ ($M = \text{Cr}, \text{Co}, \text{Ni}, \text{Cu}$)

The main procedure followed used metal powders in the appropriate stoichiometric ratios as starting reagents, similarly to Method 2 employed for the preparation of Ce_2MnN_3 (section 4.1.1.2.2).

In the case of $\text{Ce}_2\text{Mn}_{1-x}\text{Cr}_x\text{N}_3$ a number of methods were employed. The preparation method for Ce_2CrN_3 reported in the literature involves the reaction of a mixture of CrN, Cr_2N and CeN, under vacuum for approximately a week, or reaction in a Li_3N flux.⁹²

Here, in addition to preparation from the elements a stoichiometric mixture of Cr_2N and CeN was heated under nitrogen at 1075 °C for four days. The formation of stable binary nitrides often results in no further reaction to ternary nitrides. CrN is very unreactive and therefore, to minimise its formation, in favour of Cr_2N production, the mixture was heated and cooled quickly under an argon atmosphere.

4.2.2.1.2 Preparation of Cr_xN_y

Commercially available chromium nitride generally consists of a mixture of CrN and Cr_2N . CrN is a highly refractory material and forms readily at temperatures below 600 °C, however, in nitrogen CrN cannot be formed without the presence of Cr_2N impurities.¹¹⁹ Reactions of the metals, cerium and manganese, in nitrogen results in the formation of CrN and manganese with no further reaction to ternary nitrides. At 600 °C

both nitrides begin to form, with a preference for CrN formation. However, at ~ 1100 °C CrN is unstable and decomposes to yield pure Cr₂N.¹¹⁹ It is then necessary to cool the material quickly to prevent CrN reformation at lower temperatures.

4.2.2.1.2.1 Method 1 – Reaction of Chromium Metal with Nitrogen

Chromium powder (Aldrich, 99.5%) was placed in a niobium crucible and inserted into a quartz reaction tube. In a tubular furnace, the powder was heated to 1075 °C in flowing nitrogen gas. After 12 hours the resulting product was cooled to room temperature, under argon (to limit CrN formation) and returned to the glove box.

4.2.2.1.2.2 Method 2 – Reduction of Cr_xN_y in Argon

The mixed phase Cr_xN_y material was reduced by heating under flowing argon at 1075 °C for 36 hours, before cooling to room temperature and placing in the glove box.

4.2.2.2 Results and Discussion

4.2.2.2.1 Structural Characterisation of Cr_xN_y

4.2.2.2.1.1 Powder X-ray Diffraction (PXRD)

Initial attempts to prepare chromium nitride from the metal resulted in a mixed phase compound of CrN and Cr₂N (Figure 4-17), despite cooling of the material being carried out in argon.

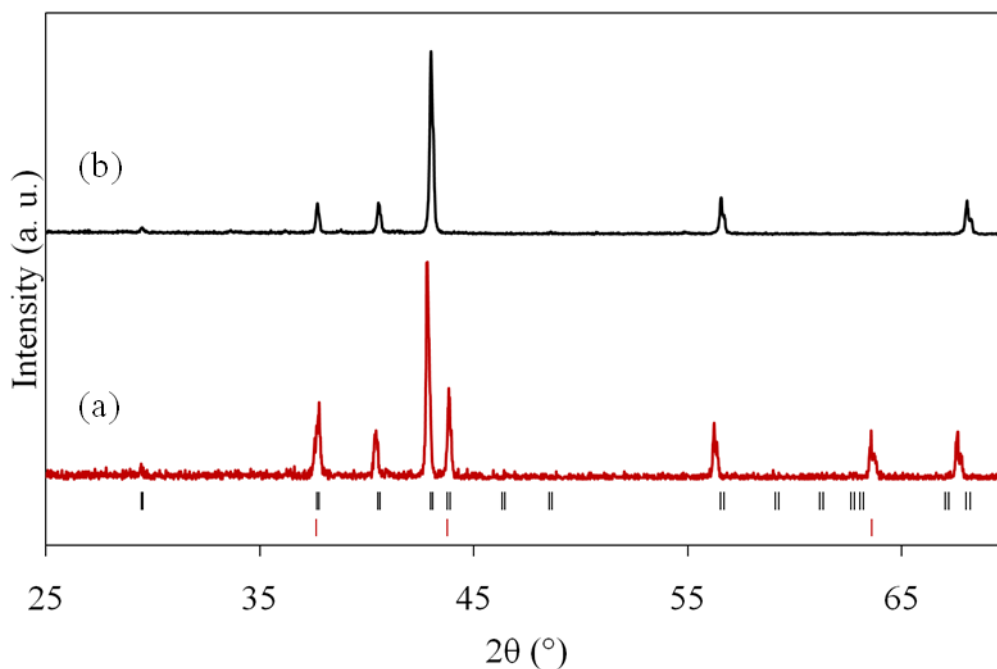


Figure 4-17. PXRD pattern for Cr_xN_y (a) prepared from the elements and (b) after reduction in argon. The tick marks correspond with Cr_2N (upper) and CrN (lower) respectively.

For this reason the mixture was subsequently heated in argon to reduce CrN and yield single phase Cr_2N . Reduction of the mixed phase resulted in successful preparation of a light grey material consistent with single phase Cr_2N , Figure 4-17.

Cr_2N has been shown by Kim *et al.* and Sundararaman *et al.* to exist in two forms, both showing a hexagonal close packed arrangements of chromium with nitrogen occupying the interstitial sites, one showing an ordered distribution of nitrogen (Kim *et al.*) and the second a random arrangement (Sundararaman *et al.*).^{120, 272} The Cr_2N model by Kim *et al.* ($P\bar{3}1m$, $a = 4.752(3) \text{ \AA}$, $c = 4.429(4) \text{ \AA}$) consists of a hexagonal close packed array of chromium atoms with half of the octahedral interstices occupied by nitrogen, in an ordered way (Figure 4-18).^{120, 273} The stacking sequence, along c , can be described as $A_M\alpha_1B_M\beta_1A_M\alpha_1B_M\beta_1A_M\dots$, where A_M and B_M correspond with the two chromium layers and α_1 and β_1 the two nitride layers.²⁷³

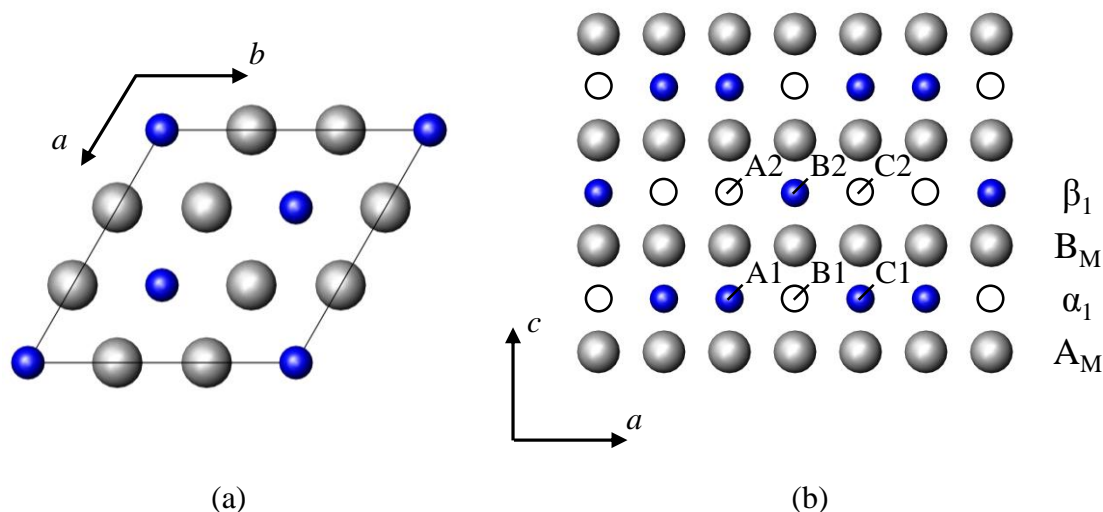


Figure 4-18. Structure of Cr_2N shown (a) along the c - and (b) b -axis. The grey and blue spheres represent chromium and nitrogen respectively. The anion vacancies are shown by the white circles. The six octahedral positions are labelled A1 to C2.²⁷³

Between the α_1 and β_1 layers the adjacent interstitial sites are approximately $0.816a_0$ ($c_0/2$) apart, while within the α_1 and β_1 layers the sites are separated by a_0 making it more favourable to occupy the A1 and C1 sites in the α_1 layers and the B2 site in the β_1 , to minimise the repulsive interactions between anions.[§]

Rietveld refinement was performed using the data obtained from a Cr_2N sample derived from reduction of the $\text{CrN}/\text{Cr}_2\text{N}$ mixture, in argon. The model for Cr_2N was taken from Kim *et al.*¹²⁰ The background was initially manually modelled by a shifted Chebyshev function with thirty-six terms and was later refined freely. The peak shape was modelled by a multi-term Simpson's rule integration of the pseudo-Voigt.^{241, 242} The parameters refined were: the cell parameters (a , b , c), one zero point, one scale factor and four profile parameters. To prevent negative values, the thermal parameters were constrained to zero. Attempts were made to refine the atomic occupancies as Cr_2N is known to exist over a compositional range of approximately 9.3% to 11.9%, by weight of nitrogen.¹¹⁹ This gave values approximating to one and, therefore, these were constrained at full occupancy. The refinement parameters are summarised in Table 4-21 and the refinement profile is shown in Figure 4-19.

[§] a_0 and c_0 correspond with the cell axis of the idealised h.c.p arrangement of the chromium atoms.

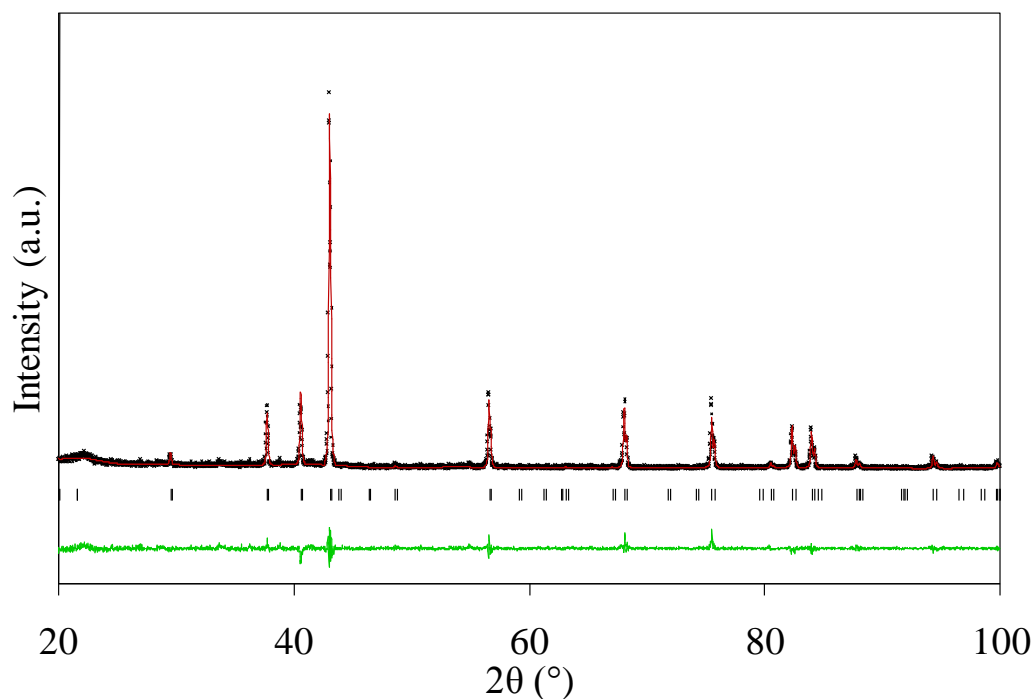


Figure 4-19. PXRD profiles for Cr₂N at room temperature, showing observed (+), calculated (red line) and difference pattern (green line). Tick marks indicate reflection positions for Cr₂N.

Formula	Cr ₂ N	
Space Group	$P\bar{3}1m$ (no. 162)	
	PXRD data	Kim <i>et al.</i> ¹²⁰
a (Å)	4.7695(1)	4.752(3)
c (Å)	4.4455(2)	4.429(4)
V (Å ³)	87.58(1)	86.6(1)
Z	3	
Calculated density (g cm ⁻³)	6.712	
Profile function	Pseudo-Voigt	
No. of profile points	4500	
No. of parameters refined	44	
R_{wp}	0.2166	
R_p	0.1535	
χ_{red}^2	1.357	

Table 4-21. Summary of refinement data and lattice parameters for Cr₂N at room temperature, derived from PXRD data.

The cell is slightly larger here than that derived by Kim *et al.* This is attributed to a higher N/Cr value of 0.5, in this work, over Kim *et al.* who demonstrated a N/Cr of 0.46.¹²⁰

Atom	Site	x	y	z	Occ.
Cr	6k	0.3333	0	0.2491	1.0
N(1)	2d	0.3333	0.6667	0.5	1.0
N(2)	1a	0	0	0	1.0

Table 4-22. Structural parameters for Cr₂N derived from PXRD collected at room temperature.

4.2.2.2.1 Structural Characterisation of Ce₂Mn_{1-x}M_xN₃ (M = Cr, Co, Ni, Cu)

4.2.2.2.1.1 Powder X-ray Diffraction (PXRD)

Ce₂Mn_{0.9}M_{0.1}N₃ synthesis was carried out. The PXRD pattern for the cobalt substituted sample is shown in Figure 4-20, and is shown as an example of the outcomes of these substitution reactions. The PXRD patterns show strong reflections for a Ce₂MnN₃-like phase and unreacted CeN. The peaks of the Ce₂MnN₃-like phase correspond exactly with the peak positions expected for the non-substituted phase. The presence of these CeN peaks could be an indication that only the unsubstituted Ce₂MnN₃ is formed. However, no peaks corresponding to Co, Ni or Cu containing phases were detected in the PXRD patterns. The absence of the peaks related to the cobalt phase could be due to the relatively low percentage of metal used and the lower scattering efficiency of the transition metals compared to the cerium containing phases.

Attempts to prepare Ce₂CrN₃ via direct reaction of the elements did not yield Ce₂CrN₃, giving only the binary nitrides CeN and CrN. However, the reaction between Cr₂N, CeN and N₂ resulted in the successful preparation of Ce₂CrN₃ (Figure 4-21). Unfortunately, this was present as a minor phase, along with unreacted starting materials. Extension of the reaction time beyond four days may result in a higher yield of Ce₂CrN₃.

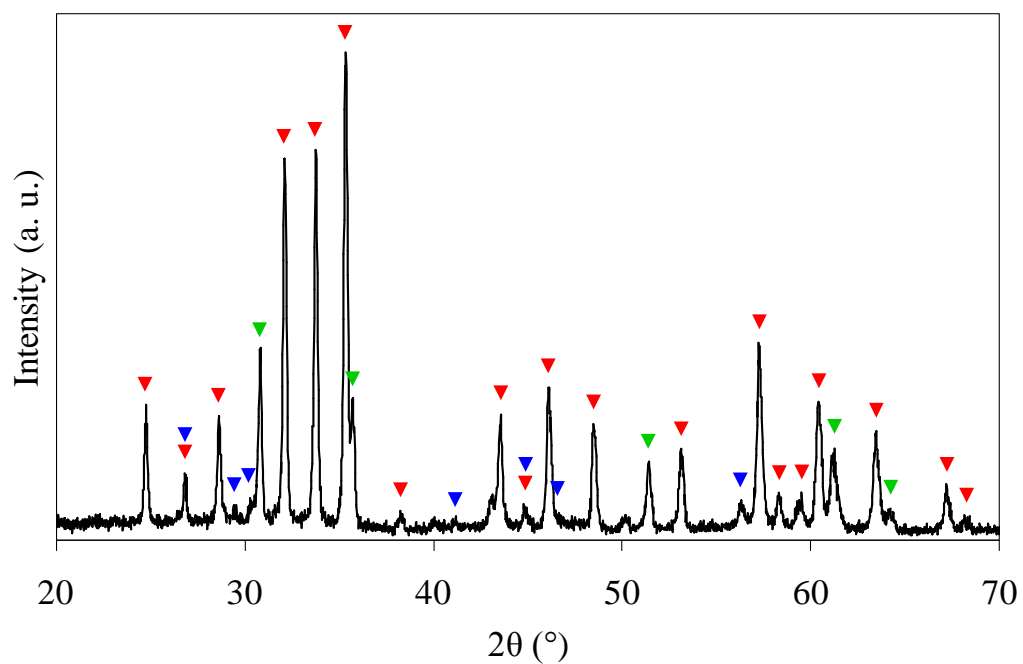


Figure 4-20. PXRD pattern for $\text{Ce}_2\text{Mn}_{0.9}\text{Co}_{0.1}\text{N}_3$. The peaks highlighted by the red, blue and green triangles correspond with Ce_2MnN_3 , Ce_2O_3 and CeN respectively.

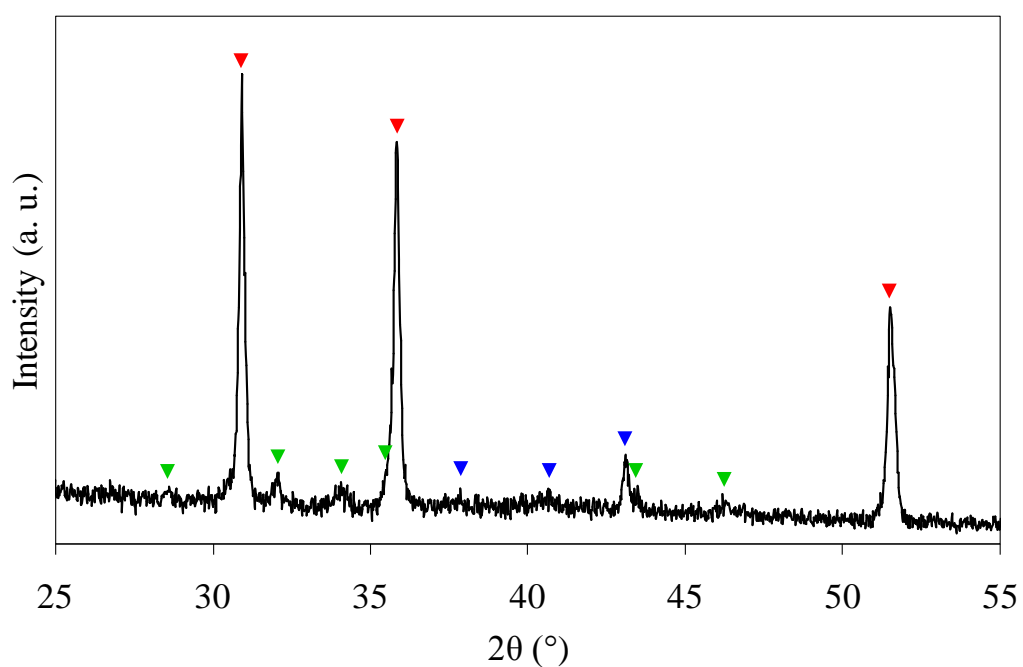


Figure 4-21. PXRD pattern for Ce_2CrN_3 . The peaks highlighted by the red, blue and green triangles correspond with CeN , Cr_2N and Ce_2CrN_3 .

4.2.3 Conclusions

Preliminary work on the synthesis of the new families of compounds, $\text{Ce}_2\text{Mn}_{1-x}\text{M}_x\text{N}_3$ ($\text{M} = \text{Cr}, \text{Co}, \text{Ni}, \text{Cu}$) was carried out, however, substitution of manganese proved unfavourable. PXRD patterns showed unreacted CeN, in all cases, indicating that only unsubstituted Ce_2MnN_3 was formed. Preparation of the known Ce_2CrN_3 was only possible in very poor yield indicating further work is required to obtain a pure material.

5 $\text{Ce}_2\text{MnN}_3\text{F}_{2-\delta}$, the First Quaternary Nitride-Fluorides

An important goal of solid-state chemists is the synthesis and characterisation of new compounds followed by chemical manipulation to induce valuable physical properties for technological exploitation. Cationic substitutions and high pressure offer two powerful ways to tune physical properties by leading to modified structures, mixed oxidation states and, in general, different coordinations and electronic configurations of metals. Anionic substitutions provide a valuable, but less utilised alternative to tailor physical properties in solids. However, chemists are now starting to understand the potential of anionic substitutions for the tuning of physical properties of materials. For example, any colour in the range from light yellow to deep red can be tailored by adjustment of the $\text{O}^{2-}/\text{N}^{3-}$ ratio in the perovskite series $\text{Ca}_{(1-x)}\text{La}_x\text{TaO}_{(2-x)}\text{N}_{(1+x)}$.²⁷⁴ As shown in section 1.1.3, in 1994 the first superconducting oxide-fluoride, $\text{Sr}_2\text{CuO}_2\text{F}_{2+\delta}$ was initially synthesised by Al-Mamouri *et al.* from the direct fluorination of Sr_2CuO_3 with fluorine gas at 210 °C.³⁰ Sr_2CuO_3 shows an anion deficient K_2NiF_4 structure, with Cu^{2+} cations coordinated by oxide anions in a square-planar fashion. The Cu-O squares join corners to form one-dimensional chains along the *b* axis. The fluorination process causes the substitution of one oxide anion with two fluoride anions and the consequent expansion of the copper coordination from square planar to octahedral and filling of the anion vacancies, giving rise to a K_2NiF_4 -structure. Extra fluoride is also inserted between the Sr-O layers of the structure, causing an imbalance in negative charge, which forces partial oxidation of the copper cation and induces superconductivity for a range of fluorine contents. This insertion occurs in a similar way to fluorination of La_2CuO_4 to give $\text{La}_2\text{CuO}_4\text{F}_\delta$.²⁷⁵

Traditionally, inorganic solid state chemistry has focused on oxides, as these compounds are relatively easy to prepare and characterise, and show a large number of structural typologies. Moreover, the chemistry of oxides has brought to attention a wealth of compounds with extraordinary properties, such as, for example, high T_c superconductivity and giant magnetoresistance.²⁷⁶⁻²⁷⁸

Aside from the oxide predominance, a significant influence in the slower development of non-oxide compounds is the challenging experimental environment often required for

the preparation and characterisation of non-oxide compounds. As we have seen in the previous chapters, the synthetic routes needed to prepare nitrides, sulfides or fluorides etc. often differ from the more conventional synthetic routes used for oxides, and, sometimes, impose the use of specialised equipment. However, more recently, progress in synthetic methods has encouraged the investigation of these materials as they represent a promising area for the discovery of new materials with original properties.

The interest of mixed anion compounds lies in the fact that anions of different nature, size, charge and electronegativity coexist in the same structural context. In some cases this results in oxide structure being adopted with the two anions occupying the oxide site, but in the majority of cases an eclectic mix of bonding types gives rise to unique structures, which have no similarities to known structural types and are often due to unusual metal oxidation states and unusual co-ordination environments to either anions (section 1.4).

Unfortunately, the scarcity of these compounds is an obstacle for understanding these solids, as general descriptions and categories based on common structural features cannot yet be drawn, to the disadvantage of a full understanding of the physical properties. If more non-oxide mixed-anion compounds are prepared and characterised, background knowledge on “interchange ability” of anions could be built to complement the already well developed background on “interchange ability” of cations.

5.1 Synthesis of $\text{Ce}_2\text{MnN}_3\text{F}_{2-\delta}$

There are very few examples of binary or ternary nitride-fluorides and no known quaternary compounds (section 1.4). Here, the first example of a quaternary nitride-fluoride is presented.²⁷⁹ The focus of this study was the fluorination of Ce_2MnN_3 to obtain $\text{Ce}_2\text{MnN}_3\text{F}_{2-\delta}$. The results described in the following section were obtained from a full collaboration involving The University of Birmingham (Prof. C. Greaves and Ms E. Sullivan) and The University of Hull. Fluorination of Ce_2MnN_3 performed at The University of Hull involved the use of solid fluorinating agents, fluorination of Ce_2MnN_3 performed at The University of Birmingham involved the use of fluorine gas. PXRD data were collected at The University of Birmingham, with

refinements based on these XRD data performed independently both at The University of Birmingham and The University of Hull. PND data were collected jointly at the Institut Laue-Langevin and these data were used by The University of Hull to determine the structure type. Analysis of the magnetic data was carried out at The University of Birmingham and showed that the composition implied by the structure was, however, not compatible with susceptibility data, and a further PND refinement that focused on the anion site occupancies was performed.

5.1.1 Experimental

As seen in section 1.1.3, fluorination of anion deficient K_2NiF_4 -type materials has resulted in oxide-fluorides with only subtle modification of the structure. The best known example of which is the ternary oxide Sr_2CuO_3 , which upon fluorination yields $Sr_2CuO_2F_{2+\delta}$.³⁰ Ce_2MnN_3 is isostructural to Sr_2CuO_3 and therefore a good candidate for fluorination to yield a quaternary nitride-fluoride material. Several methods were employed in the fluorination of Ce_2MnN_3 , using a number of the fluorinating agents. The primary goal was to insert fluoride anions into the anion-deficient structure of Ce_2MnN_3 using low temperature fluorination routes. All the reactions performed are described in the following section. Preparation of $Ce_2MnN_2F_{2-\delta}$ was also attempted via solid state reaction, using CeN_xF_{3-3x} and manganese metal as starting reagents.

There are a number of methods commonly used in the fluorination of oxide materials that may be successfully applied to non-oxide materials as well to prepare mixed-anion fluoride compounds.

An important consideration when performing fluorination reactions is the type of fluorinating agent used.³⁴

In the case of air or moisture sensitive materials, reactions are often performed under inert atmospheres reducing the efficiency of the fluorinating agent, suggesting that such processes may be aided by atmospheric oxygen. Another important characteristic of fluorination reactions is the stability of the resulting phase. Fluorinated compounds are often temperature sensitive, prone to thermal decomposition. They are commonly

metastable products (section 2.1.2). For this reason fluorination reactions are generally performed at comparatively low temperatures, between 200-400 °C.³⁴

There are currently two common methods of fluorination employed; the first is via solid-gas reactions and the second solid-solid reactions. In solid-gas reactions the fluorinating agent either takes the form of a gas, which may be passed over the sample, or alternatively from the decomposition of a suitable reagent to release F₂ gas. In the decomposition of solid fluorinating agents, to release F₂, the quantity of fluorine used can be controlled. The reagents can also be sealed separately in a reaction vessel, minimising the volume of unwanted decomposition products from the fluorinating agent. For example CuF₂, used in the fluorination of Ln_{2-x}A_{1+x}Cu₂O_{6-y} (Ln = La, Nd; A = Sr, Ca), decomposes to yield CuO, which would otherwise be left in the final reaction mixture.²⁸⁰

Although solid-gas reactions have the advantage that there are no by-products of reagent degradation, there are a number of disadvantages. Gaseous fluorinating agents are hazardous, it can be difficult to quantitatively control the extent of fluorination taking place, and can often require a secondary heating phase (post annealing). In addition, as the reaction is dependent on interaction and diffusion at the solid-gas interface, it is necessary to ensure a large surface area, which can limit the amount of sample that may be reacted at any one time.

5.1.1.1 Preparation of Ce₂MnN₃F_{2-δ}

5.1.1.1.1 Method 1 – Reaction of Ce₂MnN₃ with Polyvinylidene fluoride (PVDF)

The advantage of using organic polymers as fluorinating agents is that their thermal stability generally does not extend outside the temperature range of soft chemistry and so they decompose to volatile organic species at low temperatures, which will not be left in the final product. There are many polymers available which contain fluorine, however, it is necessary to find a polymer which is thermally unstable.

There has been some research into poly(vinylidene) fluoride, PVDF, as a fluorinating agent, as this is solid at room temperature and contains a large volume of fluorine (~ 58%).²⁸¹ P.R. Slater has shown that fluorination of oxides using PVDF is possible.²⁸²

The thermal decomposition of this material involves the formation of HF and release of volatile organic materials (Figure 5-1).

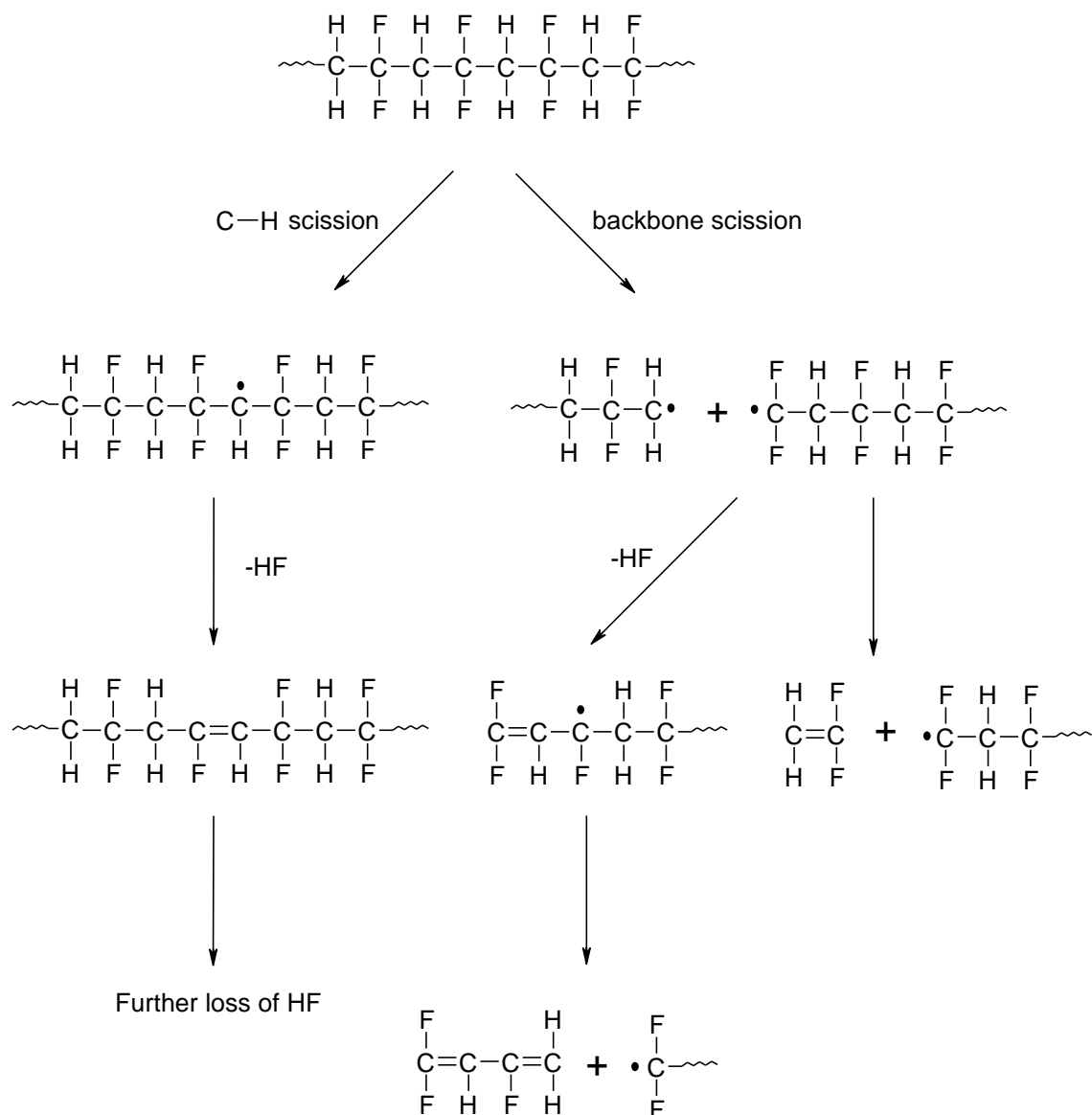


Figure 5-1. Suggested mode of thermal degradation of PVDF.²⁸¹

The temperatures involved in the use of PVDF are slightly higher than those for transition metal difluorides, to aid decomposition of the polymer. Ce_2MnN_3 and PVDF

(Aldrich, Average M_w 534,000 (GPC)) were mixed in a ratio of 2:3. The mixture was placed in an alumina boat and inserted into a quartz reaction vessel, before being removed from the glove box. In a tubular furnace, the reaction vessel was heated to 350 °C under a nitrogen atmosphere for 16 hours. The mixture was then heated for a further 16 hours at 450 °C to remove the organic residue. A similar second heating step was also employed by Slater *et al.*²⁸² As an alternative route, Ce_2MnN_3 was reacted with PVDF in 1:1 and 1:2 ratios, in one heating step, at 400 °C for 16 hours.

5.1.1.1.2 Method 2 – Reaction of Ce_2MnN_3 with XeF_2

In a glove box, Ce_2MnN_3 and XeF_2 (Aldrich, 99.99%) were placed in separate Teflon crucibles and sealed within a thermal bomb (Figure 2-5). The reagents were heated at 245 °C for 60 hours, before cooling to room temperature and returning to the glove box.

In a separate reaction, a stoichiometric ratio of Ce_2MnN_3 and XeF_2 (2:3) were mixed using a pestle and mortar at room temperature, in an inert atmosphere. The mixture was analysed via PXRD.

5.1.1.1.3 Method 3 – Reactions of Ce_2MnN_3 with MF_2 ($M = Cu, Zn$)

The most widely used solid fluorinating agents are transition metal difluorides, MF_2 ($M = Cu, Zn, Ni, Ag$). The main advantage in using MF_2 is that little metal fluoride is formed as a by-product. Unfortunately, the process of thermal decomposition of MF_2 results in metal oxides, MO in oxygen containing systems, or M in O_2 -free atmospheres. M and MO are secondary phases and must be taken into account in further analysis.²⁸³ The problem of secondary phases such as M and MO can be overcome by reacting the starting material and MF_2 in separate vessels, relying on the decomposition of MF_2 into MO (or M) and F_2 gas.

The transition metal fluorides used in the fluorination reactions were; ZnF_2 (Lancaster, 99%) and CuF_2 (Aldrich, 98%). These were used in two ways. The first was direct reaction of a mixture of Ce_2MnN_3 and transition metal fluoride and the second the

reaction of Ce_2MnN_3 and CuF_2 , placed in separate containers with Ce_2MnN_3 reacting with the gaseous decomposition products of the transition metal fluoride i.e. F_2 gas. In all cases the reagents were handled in an argon filled glove box before and after reaction.

Reactions between Ce_2MnN_3 and ZnF_2 were performed by placing a stoichiometric mixture of the reagents into a Teflon ($T < 250\text{ }^\circ\text{C}$) or nickel ($T > 250\text{ }^\circ\text{C}$) crucible. These were heated in a ratio of 5:6 at temperatures of 230, 250, 300 and 350 $^\circ\text{C}$, under argon ($T < 250\text{ }^\circ\text{C}$, in a thermal bomb) and nitrogen ($T > 250\text{ }^\circ\text{C}$, in a quartz reaction tube), for 12 hours.

For reactions between Ce_2MnN_3 and CuF_2 , a stoichiometric mixture was placed in a nickel crucible, which was placed in a quartz tube and transferred to a tubular furnace. The system was heated, under flowing nitrogen at the desired temperature. Preliminary reactions were performed at 300 $^\circ\text{C}$ for 20 hours and 230 $^\circ\text{C}$ for 16 hours. A stoichiometry of 5:6, $\text{Ce}_2\text{MnN}_3:\text{CuF}_2$ was used. Additional reactions were performed with $\text{Ce}_2\text{MnN}_3:\text{CuF}_2$ ratios of 5:6, 1:1 and 4:5. These mixtures were heated at 250 $^\circ\text{C}$ for 12, 24 and 36 hours.

Reactions between Ce_2MnN_3 and CuF_2 , in separated vessels, were also performed. The two reagents were placed separately into Teflon crucibles and heated within a thermal bomb at 230 $^\circ\text{C}$ for 65 hours, under argon.

5.1.1.1.4 Method 4 – Reactions with Fluorine Gas

Fluorination reactions using F_2 gas were performed at the University of Birmingham, on a fluorine line provided by Prof. C. Greaves. The conditions under which fluorination of Ce_2MnN_3 with F_2 were carried out were derived initially from the experiments for the synthesis of $\text{Sr}_2\text{CuO}_2\text{F}_{2+\delta}$.³⁰

A small amount of Ce_2MnN_3 ($< 0.1\text{ g}$) was placed in a nickel boat, which was placed centrally in a nickel reaction tube of a tubular furnace (Figure 2-12). The F_2 gas line was flushed with dry N_2 and attached to the reaction vessel and the system flushed with

N₂. In the initial reactions the system was heated to 230 °C, 180 °C and 100 °C. Once the temperature had stabilised, the system was switched over to a 10% F₂ in N₂ gas stream. The gas was passed over NaF pellets to remove any HF prior to entering the reaction vessel. The presence of F₂ leaving the system was verified using KI solution. Fifteen minutes after verifying that F₂ was exiting the system, N₂ gas was reintroduced, to flush out any residual F₂ gas, before the system was cooled to room temperature and the sample was returned to the glove box. Reactions were also performed in the temperature range of 95-115 °C. These reactions were heated under flowing F₂/N₂ for fifteen minutes from introduction of fluorine into the system.

Reactions were also performed in a semi-closed system. The procedure above was followed, however, once fluorine gas was detected leaving the furnace tube it was sealed at both ends. After the desired time had passed the tube was re-opened and flushed with N₂ gas, while cooling to room temperature. Reactions were performed at 40 °C and 100 °C for 15 minutes, 70 °C for 20 minutes, 80 °C for 45 minutes and 90 °C for 1 hour.

Samples reacted at temperatures below 80 °C were annealed at 150 °C in a static argon atmosphere for 5 hours. For samples fluorinated at temperatures above 80 °C, annealing was performed in the temperature range of 150-250 °C under nitrogen.

5.1.1.1.5 Method 5 - Reaction of Cerium Nitride-Fluoride, Manganese and Nitrogen

In a glove box, previously prepared CeN_xF_{3-3x} (section 5.1.1.2) and manganese metal (Aldrich, 99.99%) powder were mixed in a ratio of 2:1 and hand pressed into pellets. The pellets were placed within a nickel crucible, inserted into a quartz tube, and heated at 900 °C for 60 hours. Once cooled to room temperature the reaction vessel was returned to the glove box.

5.1.1.2 Preparation of CeN_xF_{3-3x}

Two approaches to prepare CeN_xF_{3-3x} were used. The first followed the method by Pezat *et al.*¹⁸⁰ A stoichiometric ratio of CeN, prepared as in section 4.1.1.1, and CeF₃

(Aldrich, 99.99%) were mixed and hand pressed into a pellet, in a glove box. The pellet was inserted into a nickel crucible, placed in a quartz tube and heated under a stream of nitrogen at 870 °C for 60 hours. The reaction vessel was cooled to room temperature and returned to the glove box.

The second method employed involved mixing a stoichiometric ratio of CeF₃ and Si. The mixture was hand pressed into pellets, placed into a nickel crucible, inserted in to a quartz reaction vessel and heated under flowing nitrogen at 900 °C for 60 hours. The driving force of this reaction is the formation of SiF₄, which is gaseous at the reaction temperature and leaves the system.¹¹⁵

5.1.1.3 Characterisation

Powder X-ray diffraction (PXRD) data were collected in Birmingham on a Siemens D5000 diffractometer operating in transmission mode with a Ge monochromator and a position sensitive detector. In Hull PXRD data were collected using a Siemens D5000 powder diffractometer operating in reflection mode, with Cu K α radiation and also a Stöe IPDS II single crystal diffractometer, using powder filled capillaries, with Mo K α radiation.

High-resolution powder neutron diffraction (PND) data were collected, using the sample prepared in the reaction of Ce₂MnN₃ and F₂ gas, on the D2B diffractometer at the Institut Laue-Langevin (ILL), Grenoble, using a wavelength $\lambda = 1.59432$ Å and covering the angular range $10 \leq 2\theta/^\circ \leq 157$ with $\Delta 2\theta = 0.05^\circ$. The sample was contained in a vanadium can of internal diameter 6.8 mm.

Magnetic susceptibility measurements were collected on a Quantum Design MPMS SQUID magnetometer with a field of 2 T at the University of Birmingham.

5.1.2 Results and Discussion

The most successful syntheses of Ce₂MnN₃F_{2- δ} have been performed *via* low-temperature fluorination of the ternary nitride Ce₂MnN₃ using F₂ gas and CuF₂ as

fluorinating agents. To the best of our knowledge, $\text{Ce}_2\text{MnN}_3\text{F}_{2-\delta}$ is the first quaternary nitride-fluoride to be reported. The reaction of Ce_2MnN_3 with 10% F_2/N_2 at 95-115°C yields the fluorinated phase $\text{Ce}_2\text{MnN}_3\text{F}_{2-\delta}$, with tetragonal symmetry ($P4/nmm$ $a = 3.8554(4)$ Å and $c = 13.088(4)$ Å based on powder neutron diffraction).²⁷⁹ The following section describes the results of all the methods attempted, with brief discussion of the influences the less successful reactions had on the synthetic approach. This highlights the fact that there is only a narrow range of reaction conditions in which the fluorinated phase forms. The section will start with the description of the structural characterisation of $\text{CeN}_x\text{F}_{3-3x}$, which was used in a solid state reaction with manganese metal to obtain $\text{Ce}_2\text{MnN}_3\text{F}_{2-\delta}$.

5.1.2.1 Structural Characterisation of $\text{CeN}_x\text{F}_{3-3x}$

5.1.2.1.1 Powder X-ray Diffraction (PXRD)

Powder X-ray diffraction indicated $\text{CeN}_x\text{F}_{3-3x}$ was successfully prepared through the reaction of CeN and CeF_3 under nitrogen (section 5.1.1.2) (Figure 5-2).

In addition to $\text{CeN}_x\text{F}_{3-3x}$ the mixture also contained a small fraction of CeF_3 . $\text{CeN}_x\text{F}_{3-3x}$ shows an anion-excess-fluorite structure.^{180, 181} The peaks of $\text{CeN}_x\text{F}_{3-3x}$ were indexed to a cubic unit cell ($Fm\bar{3}m$), as for the model by Vogt *et al.*, and gave $a = 5.8137(5)$ Å.¹⁸¹ The similar X-ray scattering lengths of nitrogen and fluorine prevent an accurate determination of the anion ratio and distribution.

PXRD performed on the powder resulting from the reaction between CeF_3 and Si (section 5.1.1.2) showed only peaks corresponding with CeF_3 . Therefore, although not a single phase material, $\text{CeN}_x\text{F}_{3-3x}$ formed from the reaction of CeN and CeF_3 was used in preliminary reactions with Mn.

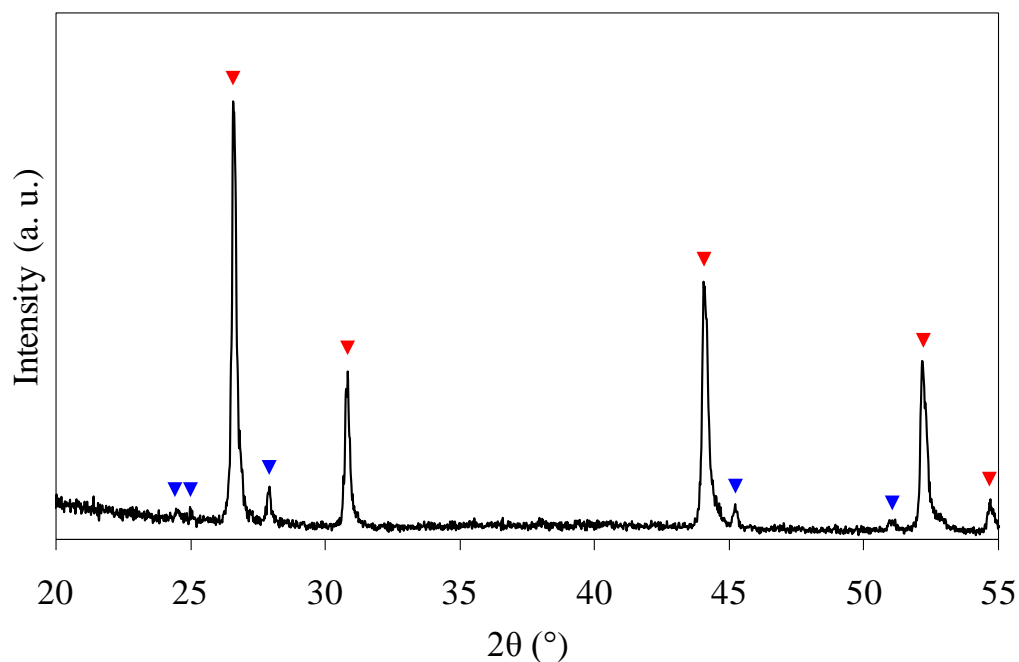


Figure 5-2. PXRD pattern of $\text{CeN}_x\text{F}_{3-3x}$. The red and blue triangles correspond with $\text{CeN}_x\text{F}_{3-3x}$ and CeF_3 respectively.

5.1.2.2 Structural Characterisation of $\text{Ce}_2\text{MnN}_3\text{F}_{2-\delta}$

5.1.2.2.1 Reaction of Cerium Nitride-Fluoride, Manganese and Nitrogen

5.1.2.2.1.1 Powder X-ray Diffraction (PXRD)

PXRD, performed on the product of the reaction of $\text{CeN}_x\text{F}_{3-3x}$ and manganese (section 5.1.1.1.5), suggested that no reaction had taken place between these reagents (Figure 5-3).

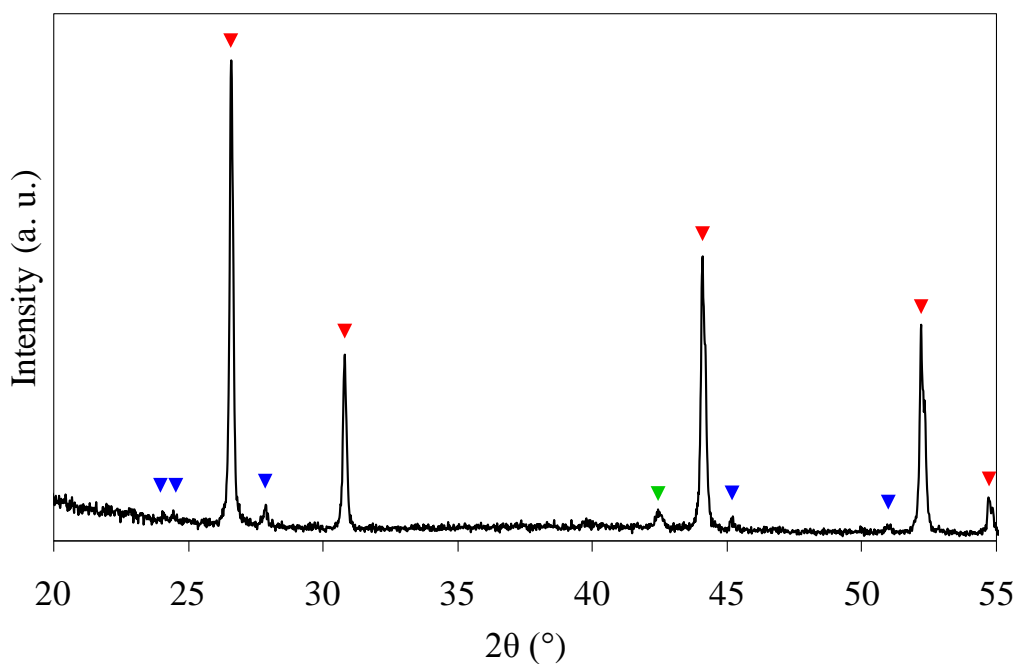


Figure 5-3. PXRD pattern on the product of the reaction between $\text{CeN}_x\text{F}_{3-3x}$ (red) and Mn (green). The peaks of CeF_3 are shown in blue.

5.1.2.2.2 Reaction of Ce_2MnN_3 with Polyvinylidene fluoride (PVDF)

5.1.2.2.2.1 Powder X-ray Diffraction (PXRD)

Preliminary reactions performed at low temperatures, $\sim 300\text{ }^\circ\text{C}$ (section 5.1.1.1.1), indicated that the polymer did not decompose to yield a powdered material. The product of reactions at these temperatures consists of a single, black, malleable pellet containing organic residue. PXRD patterns showed a large amorphous background with a number of small peaks consistent with the starting Ce_2MnN_3 only.

In fluorination of K_2NiF_4 -type oxide materials, Slater *et al.* found that at $250\text{-}350\text{ }^\circ\text{C}$ oxide-fluoride materials could be successfully prepared in the reaction with PVDF.²⁸² Degradation studies indicate that PVDF decomposes more readily in oxygen rich atmosphere.²⁸⁴ As the reactions of Ce_2MnN_3 are performed in the absence of oxygen, and owing to the large amount of residue remaining after heating at $300\text{ }^\circ\text{C}$, the resulting mixture was heated a second time at the higher temperature of $450\text{ }^\circ\text{C}$.²⁸⁴

The PXRD pattern of the reaction of Ce_2MnN_3 with PVDF, after heating at $450\text{ }^\circ\text{C}$, is shown in Figure 5-4. These reactions resulted in decomposition of Ce_2MnN_3 to yield a number of phases, most prominent of which are CeF_3 and $\text{CeN}_x\text{F}_{3-3x}$. A number of smaller, unassigned peaks are also present in the PXRD pattern, possibly the result of organic constituents still present from incomplete decomposition of PVDF.

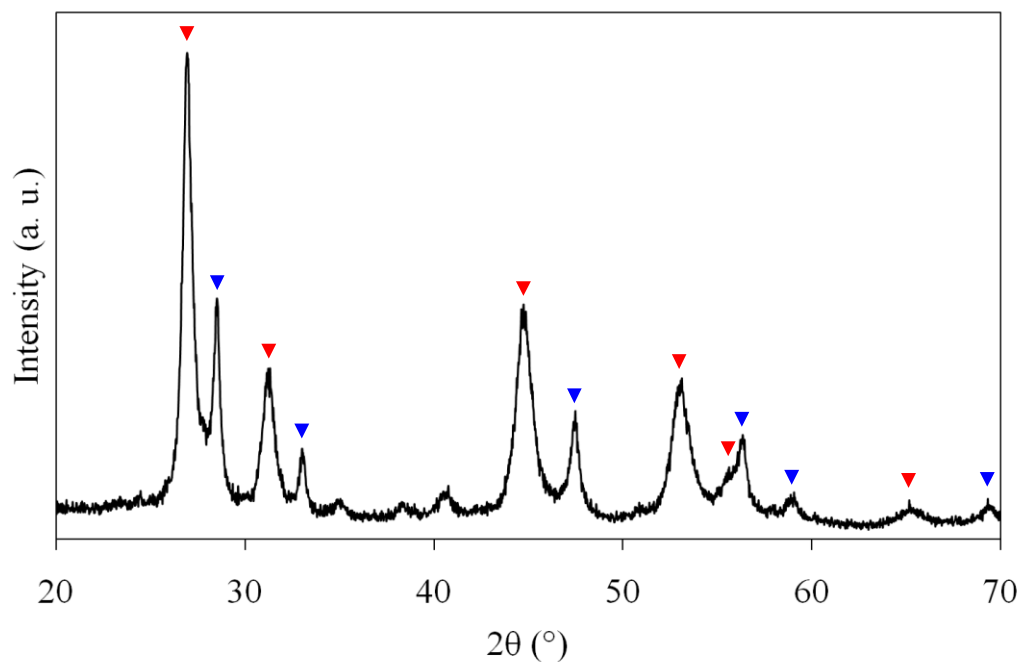


Figure 5-4. PXRD pattern from the reaction of Ce_2MnN_3 and PVDF at $450\text{ }^\circ\text{C}$. The peaks correspond with CeF_3 (blue) and $\text{CeN}_x\text{F}_{3-3x}$ (red).

PXRD from the reaction of Ce_2MnN_3 with PVDF, in a ratio of 1:1, at $400\text{ }^\circ\text{C}$ for 16 hours, showed peaks corresponding with unreacted Ce_2MnN_3 . Increasing the ratio of Ce_2MnN_3 to PVDF (1:2) resulted in partial decomposition of Ce_2MnN_3 , yielding peaks for CeF_3 and $\text{CeN}_x\text{F}_{3-3x}$.

The temperature required to ensure satisfactory decomposition of PVDF is too high for stable formation of a quaternary nitride-fluoride from Ce_2MnN_3 , favouring, instead, decomposition to $\text{CeN}_x\text{F}_{3-3x}$ and CeF_3 . This suggests PVDF is not suitable as a fluorinating agent in anaerobic environments, as it is in reactions performed in air.

5.1.2.2.3 Reaction of Ce_2MnN_3 with XeF_2

5.1.2.2.3.1 Powder X-ray Diffraction (PXRD)

Upon mixing Ce_2MnN_3 and XeF_2 in a glove box, under an argon atmosphere at room temperature, a rapid exothermic reaction occurred (section 5.1.1.1.2), with a brief flash of flames and emission of white smoke. PXRD performed on the resulting powder showed peaks of Ce_2MnN_3 alone. This may indicate the formation of a small amount of amorphous, fluorinated, material and release of gaseous decomposition products, Xe and F_2 .

PXRD indicates the reaction of Ce_2MnN_3 and XeF_2 (1:2), via the separated reagents approach at 245 °C for 60 hours (section 5.1.1.1.2) shows, in addition to Ce_2MnN_3 , a number of peaks consistent with CeN_xF_{3-3x} and peaks, which could not be identified using any of the compounds in the available structural databases (Figure 5-5). The peak intensity of this unknown phase was poor and the PXRD pattern also showed intense peaks corresponding to CeN_xF_{3-3x} . However, the peaks of the unknown phase are consistent with those observed for the $Ce_2Mn(N,F)_x$ phase obtained from the reaction of Ce_2MnN_3 with CuF_2 (section 5.1.2.2.4.1). Due to the difficulty in characterising the products of reaction between Ce_2MnN_3 and XeF_2 , other fluorinating agents were investigated.

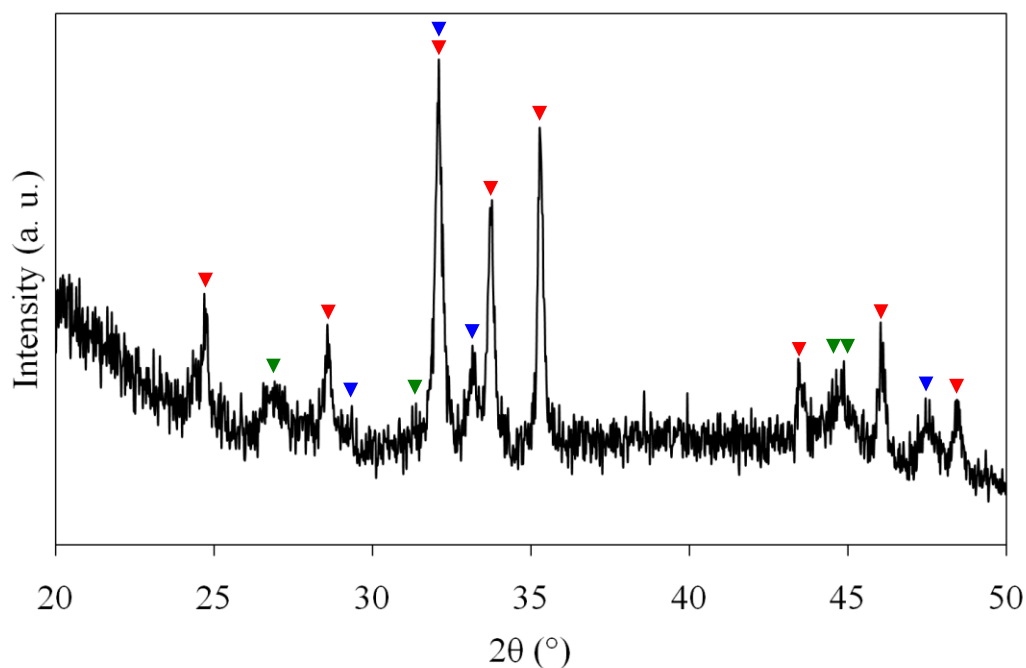


Figure 5-5. PXRD pattern from the reaction of Ce_2MnN_3 and XeF_2 at 245 °C. The peaks correspond with $\text{CeN}_x\text{F}_{3-3x}$ (green), Ce_2MnN_3 (red) and an unknown phase (blue).

5.1.2.2.4 Reactions of Ce_2MnN_3 with MF_2 ($M = \text{Cu}, \text{Zn}$)

5.1.2.2.4.1 Powder X-ray Diffraction (PXRD)

PXRD patterns showed that reactions of Ce_2MnN_3 with ZnF_2 , and CuF_2 , under suitable reaction conditions resulted with a new ternary nitride-fluoride, which was later identified as $\text{Ce}_2\text{MnN}_3\text{F}_{2-\delta}$.

In the case of reactions of Ce_2MnN_3 with ZnF_2 at temperatures up to 300 °C (section 5.1.1.1.3), PXRD indicated that ZnF_2 does not decompose readily and showed peaks for Ce_2MnN_3 and ZnF_2 only. Increasing the temperature further, to 350 °C resulted in partial decomposition of ZnF_2 to Zn (Figure 5-6). In addition the PXRD pattern showed peaks for Ce_2MnN_3 , CeF_3 and a number of unassigned peaks. The unassigned peaks are consistent with the tetragonal unit cell later identified as $\text{Ce}_2\text{MnN}_3\text{F}_{2-\delta}$. However, the unassigned peaks from the reaction of Ce_2MnN_3 and ZnF_2 are of poor intensity. In addition the PXRD pattern shows that CeF_3 is present in higher quantities. This suggests that the higher temperature conditions necessary to decompose ZnF_2 in anaerobic conditions may lead to the decomposition of either the starting Ce_2MnN_3 or

any of the nitride-fluoride which may have formed. Other fluorinating agents were then investigated.

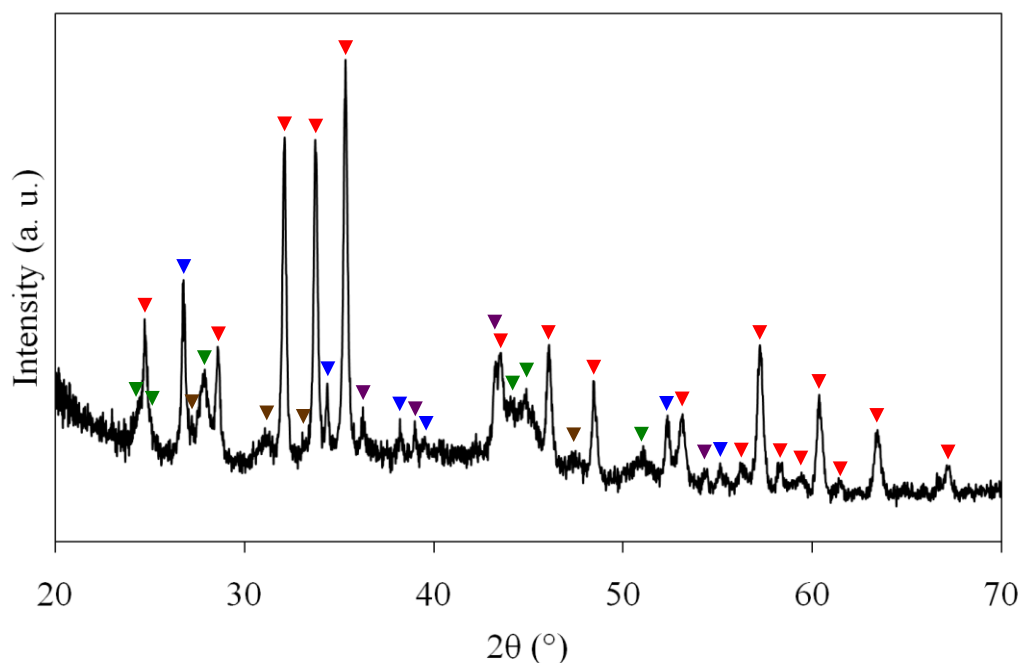


Figure 5-6. PXRD pattern from the reaction of Ce_2MnN_3 and ZnF_2 at $350\text{ }^\circ\text{C}$. The peaks correspond with Ce_2MnN_3 (red), CeF_3 (green), ZnF_2 (blue), Zn (purple) and an unknown phase (brown).

Reactions with CuF_2 proved to be a more successful solid fluorinating agent (section 5.1.1.1.3). Reactions of Ce_2MnN_3 with CuF_2 via the separated reagent approach failed to show any reaction, however, solid state reactions of a mixture of Ce_2MnN_3 and CuF_2 gave a new phase. Figure 5-7 shows the PXRD pattern after the reaction of Ce_2MnN_3 with CuF_2 (5:6), at $300\text{ }^\circ\text{C}$ for 20 hours. In this case, Ce_2MnN_3 has reacted completely to give a number of fluorination products. In addition to copper metal, from the decomposition of CuF_2 , CeF_3 and $\text{CeN}_x\text{F}_{3-3x}$, there are a number of peaks which could not be identified using any of the compounds in the available structural databases. The unknown set of peaks were indexed, using the computer program DICVOL, as a tetragonal unit cell with $a = 3.83\text{ \AA}$ and $c = 12.20\text{ \AA}$.²⁰⁹

Ce_2MnN_3 was initially selected for fluorination, due to its structural similarity to the anion deficient K_2NiF_4 -type oxides, A_2CuO_3 ($\text{A} = \text{Sr}, \text{Ca}$). These compounds have shown amenability to fluorination and oxide-fluorides, while maintaining a K_2NiF_4 -type structure. In fact, a number of oxide-fluoride materials are known which show a

K_2NiF_4 -type structure (section 1.1.3). Several of these compounds possess tetragonal unit cells with parameters similar to those of the unit cell of the new phase, e.g. $Ca_2CuO_2F_{2+\delta}$ ($a = 3.850(1) \text{ \AA}$, $c = 11.842(3) \text{ \AA}$),²⁸⁵ $Sr_2CuO_2F_2$ ($a = 3.967(1) \text{ \AA}$, $c = 12.816(2) \text{ \AA}$) and $LaSrMnO_4F$ ($a = 3.7749(1) \text{ \AA}$, $c = 14.1049(3) \text{ \AA}$).^{51, 286} All the above oxide-fluorides were obtained via low-temperature fluorination to ensure only subtle modification of the structure of the starting oxides. On the basis of these structural and synthetic considerations, the new phase was then considered a nitride-fluoride with a K_2NiF_4 -type structure.

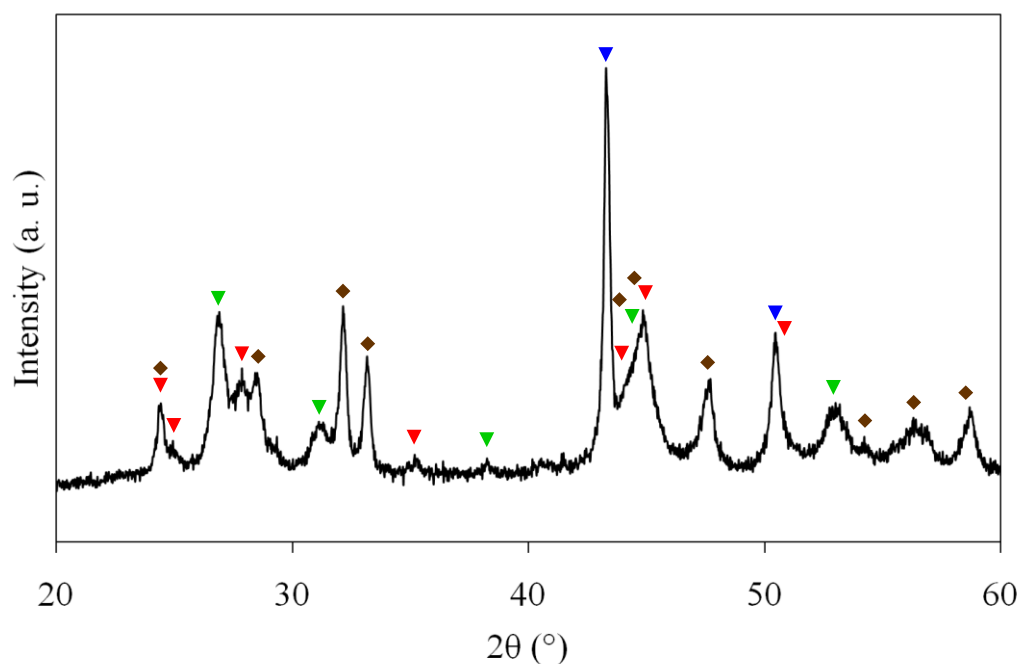


Figure 5-7. PXRD pattern from the reaction of Ce_2MnN_3 and CuF_2 at $300 \text{ }^\circ\text{C}$. The peaks correspond with CeF_3 (red), CeN_xF_{3-3x} (green), Cu (blue) and $Ce_2Mn(N,F)_x$ (brown).

Due to the presence of CeF_3 and CeN_xF_{3-3x} in the product, even though slightly less significant than in the previous reaction, temperatures lower than $300 \text{ }^\circ\text{C}$ were employed. Figure 5-8 shows the PXRD pattern from the reaction of Ce_2MnN_3 with CuF_2 (5:6), at $230 \text{ }^\circ\text{C}$ for 16 hours (section 5.1.1.1.3). Once again, the PXRD pattern of the fluorination product shows peaks associated to the new tetragonal unit cell, $Ce_2Mn(N,F)_x$.

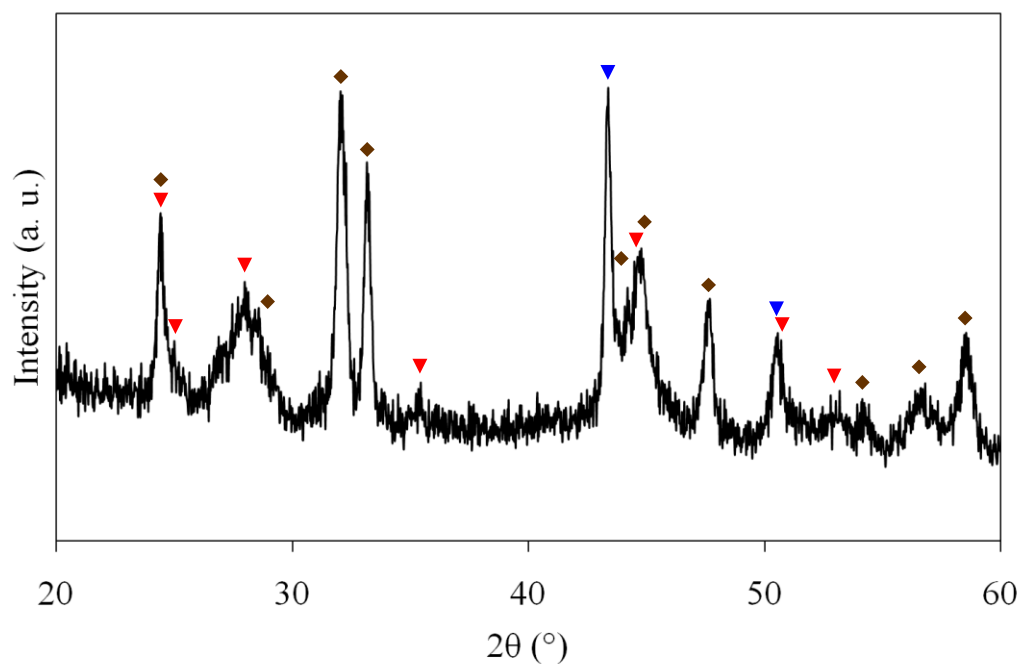


Figure 5-8. PXRD pattern from the reaction of Ce_2MnN_3 and CuF_2 at 230 °C. The peaks correspond with CeF_3 (red), Cu (blue) and $\text{Ce}_2\text{Mn}(\text{N},\text{F})_x$ (brown).

Reactions of Ce_2MnN_3 with CuF_2 , reproducibly showed peaks corresponding with $\text{Ce}_2\text{Mn}(\text{N},\text{F})_x$. CuF_2 reacts with Ce_2MnN_3 , at low temperatures ($T \leq 250$ °C), to give $\text{Ce}_2\text{Mn}(\text{N},\text{F})_x$ in sufficient yield, without high levels of $\text{CeN}_x\text{F}_{3-3x}$ or CeF_3 being formed. Therefore, further reactions were preformed, using CuF_2 , to determine the optimum reaction conditions for $\text{Ce}_2\text{Mn}(\text{N},\text{F})_x$ formation. Several reactions of Ce_2MnN_3 and CuF_2 at 230 °C showed small peaks corresponding with unreacted Ce_2MnN_3 , therefore, reactions were performed at 250 °C varying the $\text{Ce}_2\text{MnN}_3:\text{CuF}_2$ ratio and reaction time.

Figure 5-9 - Figure 5-11 shows a selection of the PXRD patterns from the reaction of Ce_2MnN_3 with various quantities of CuF_2 for 12, 24 and 36 hours. A comparison of the fluorination products suggests the peaks of $\text{Ce}_2\text{Mn}(\text{N},\text{F})_x$ are present in all samples, supporting the reproducibility of this phase. Figure 5-9 shows that for reaction times up to 36 hours, a ratio of 4:3, $\text{Ce}_2\text{MnN}_3:\text{CuF}_2$ is insufficient to remove all Ce_2MnN_3 from the final product. However, Figure 5-10 and Figure 5-11 show PXRD patterns of the products of reactions, with higher CuF_2 content, show complete reaction of Ce_2MnN_3 in as little as 12 hours. Increasing the reaction time beyond 12 hours generally results in a reduction in the $\text{Ce}_2\text{Mn}(\text{N},\text{F})_x$ peak heights and an increase in the CeF_3 content. From all experiments performed using solid fluorinating agents, the best reaction conditions

to obtain $\text{Ce}_2\text{Mn}(\text{N},\text{F})_x$ can be deduced. The highest amount of $\text{Ce}_2\text{Mn}(\text{N},\text{F})_x$, with the smallest amount of impurities, was obtained by reacting Ce_2MnN_3 with CuF_2 in a 1:1 ratio at 250 °C for 12 hours (Figure 5-10).

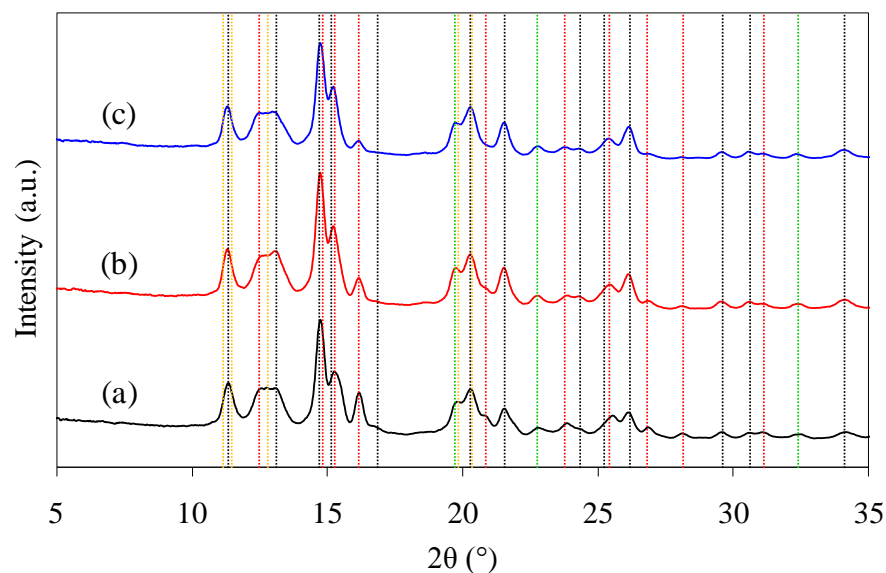


Figure 5-9. PXRD pattern from the reaction of $4\text{Ce}_2\text{MnN}_3$ and 3CuF_2 , at 250 °C for (a) 12, (b) 24 and (c) 36 hours. The dotted lines represent the peak positions of CeF_3 (yellow), Cu (green), Ce_2MnN_3 (red), and $\text{Ce}_2\text{Mn}(\text{N},\text{F})_x$ (black).^{**}

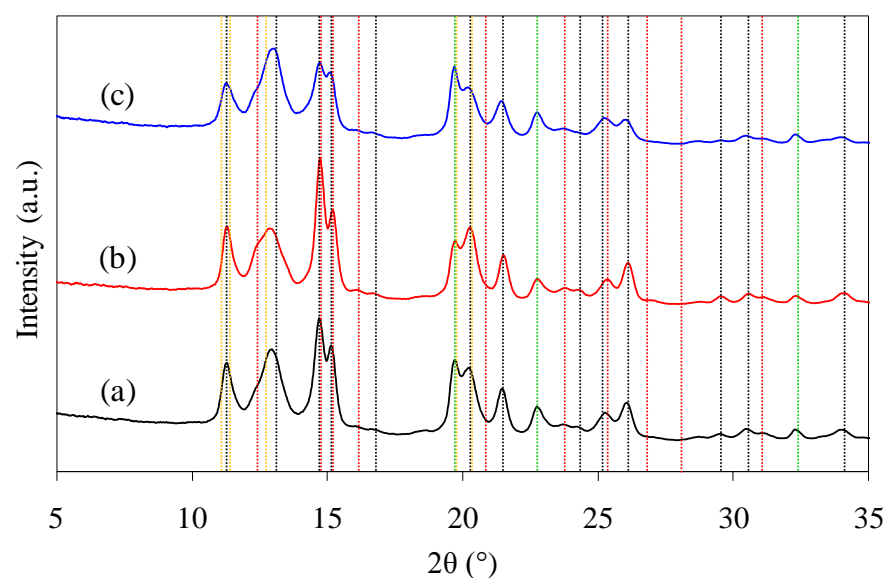


Figure 5-10. PXRD pattern from the reaction of Ce_2MnN_3 and CuF_2 , at 250 °C for (a) 12, (b) 24 and (c) 36 hours. The dotted lines represent the peak positions of CeF_3 (yellow), Cu (green), Ce_2MnN_3 (red), and $\text{Ce}_2\text{Mn}(\text{N},\text{F})_x$ (black).^{††}

^{**} The PXRD data were collected using molybdenum $K\alpha$ radiation.

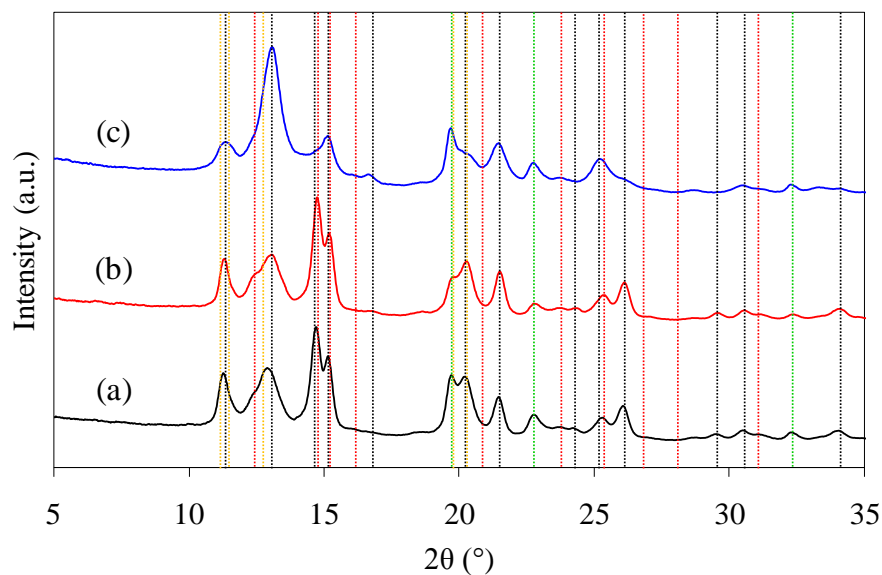


Figure 5-11. PXRD pattern from the reaction of $4\text{Ce}_2\text{MnN}_3$ and 5CuF_2 , at $250\text{ }^\circ\text{C}$ for (a) 12, (b) 24 and (c) 36 hours. The dotted lines represent the peak positions of CeF_3 (yellow), Cu (green), Ce_2MnN_3 (red), and $\text{Ce}_2\text{Mn}(\text{N},\text{F})_x$ (black).^{††}

Rietveld refinement was performed using the PXRD data obtained from the reaction of Ce_2MnN_3 with CuF_2 in a 1:1 ratio for 12 hours at $250\text{ }^\circ\text{C}$, to determine if indeed $\text{Ce}_2\text{Mn}(\text{N},\text{F})_x$ is satisfactorily described as K_2NiF_4 -type. Due to the similar X-ray scattering lengths of nitrogen and fluorine it is not possible to discriminate between these anions and the data quality limits the determination of accurate anion positions. $\text{Ce}_2\text{Mn}(\text{N},\text{F})_x$ was represented using the K_2NiF_4 model from the literature.²⁸⁷ A stoichiometry of $\text{Ce}_2\text{Mn}(\text{N},\text{F})_4$ was used and owing to the impossibility of determining the N/F distribution, O atoms were used to represent both anions in the refinement. Additional phases for CeF_3 , Cu and CeO_2 were included. $\text{Ce}_2\text{Mn}(\text{N},\text{F})_4$ is also air sensitive and CeO_2 may be present as a result of decomposition of $\text{Ce}_2\text{Mn}(\text{N},\text{F})_4$ during PXRD data acquisition. As the exact stoichiometry of $\text{Ce}_2\text{Mn}(\text{N},\text{F})_4$ was not modelled at this stage, representative phase fractions could not be calculated and the percentage weight fractions of each phase remained unknown.

^{††} The PXRD data were collected using molybdenum $\text{K}\alpha$ radiation.

Due to the presence of some amorphous materials in the powder, giving an uneven background, the background was modelled by a linear interpolation function with thirty-six terms. The peak shape was modelled by a multi-term Simpson's rule integration of the pseudo-Voigt.^{241, 242} The parameters refined were: the cell parameters (a , b , c) for the four phases, one zero point, three scale factors, five isotropic thermal parameters and nine profile parameters. To maintain the stability of the refinement, the isotropic thermal parameters of all the atoms in $\text{Ce}_2\text{Mn}(\text{N},\text{F})_4$ were constrained to be equal. The refinement parameters are summarised in Table 5-1 and compared with Ce_2MnN_3 . The refinement profile is shown in Figure 5-12. The background was subtracted after refinement.

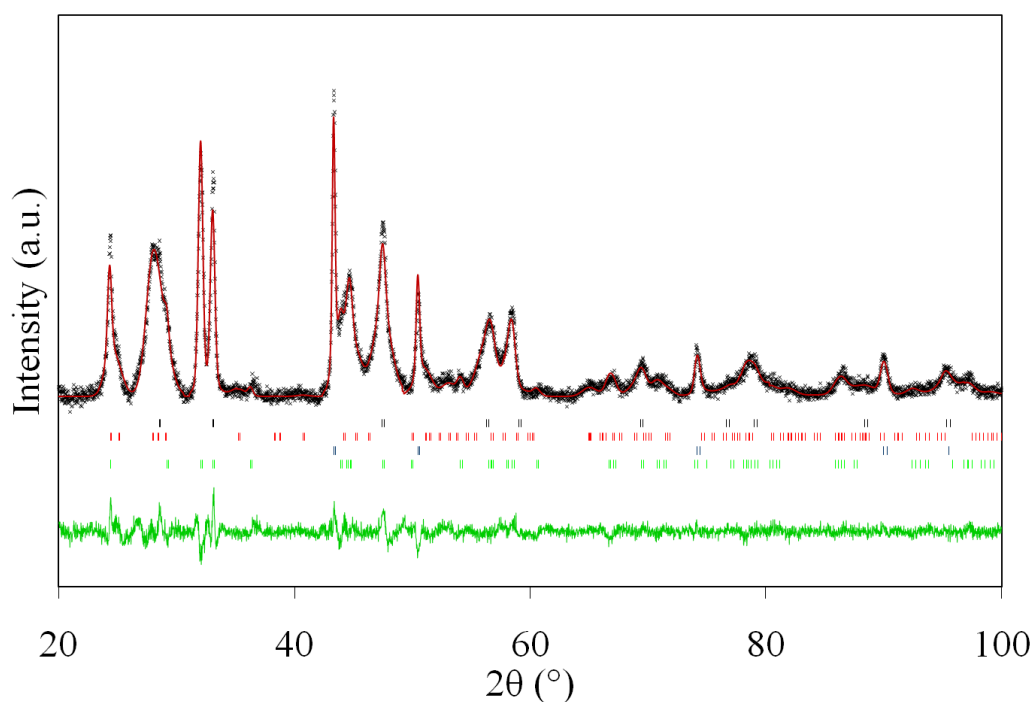


Figure 5-12. PXRD profiles for $\text{Ce}_2\text{Mn}(\text{N},\text{F})_4$, derived from the reaction of Ce_2MnN_3 and CuF_2 , showing observed (+), calculated (red line) and difference pattern (green line). Tick marks indicate reflection positions for $\text{Ce}_2\text{Mn}(\text{N},\text{F})_4$ (green), Cu (blue), CeF_3 (red) and CeO_2 (black) phases.

Formula	Ce ₂ Mn(N,F) ₄	
Space Group	<i>I4/mmm</i> (no. 139)	
	PXRD data	Ce ₂ MnN ₃
<i>a</i> (Å)	3.8285(5)	3.7549(2)
<i>b</i> (Å)	3.8285(5)	3.4487(1)
<i>c</i> (Å)	12.2312(20)	12.4724(6)
<i>V</i> (Å ³)	179.28(6)	161.52(2)
<i>Z</i>	2	
Calculated density (g cm ⁻³)	N/A	
Profile function	Pseudo-Voigt	
No. of profile points	3999	
No. of parameters refined	58	
R _{wp}	0.0449	
R _p	0.0356	
χ _{red} ²	1.724	

Table 5-1. Summary of refinement data and lattice parameters for Ce₂Mn(N,F)₄, obtained from the reaction of Ce₂MnN₃ and CuF₂, derived from PXRD data.

The refinement clearly indicated that the fluorinated material is structurally close to K₂NiF₄. The structural parameters are given in Table 5-2.

Atom	Site	x	y	z	100 × U _{iso}	Occ.
Ce	4e	0	0	0.3613(3)	1.3(2)	1.0
Mn	2a	0	0	0	1.3(2)	1.0
N/F(eq)	4c	0	½	0	1.3(2)	1.0
N/F(ap)	4e	0	0	0.2044(24)	1.3(2)	1.0

Table 5-2. Structural parameters for Ce₂Mn(N,F)₄, obtained from the reaction of Ce₂MnN₃ and CuF₂, derived from PXRD data.

The exact structural description of Ce₂Mn(N,F)_x cannot be obtained from PXRD alone, however, numerous possible structural models can be explored, based on known oxides and oxide-fluorides, which show a K₂NiF₄-type arrangement (Figure 5-13).

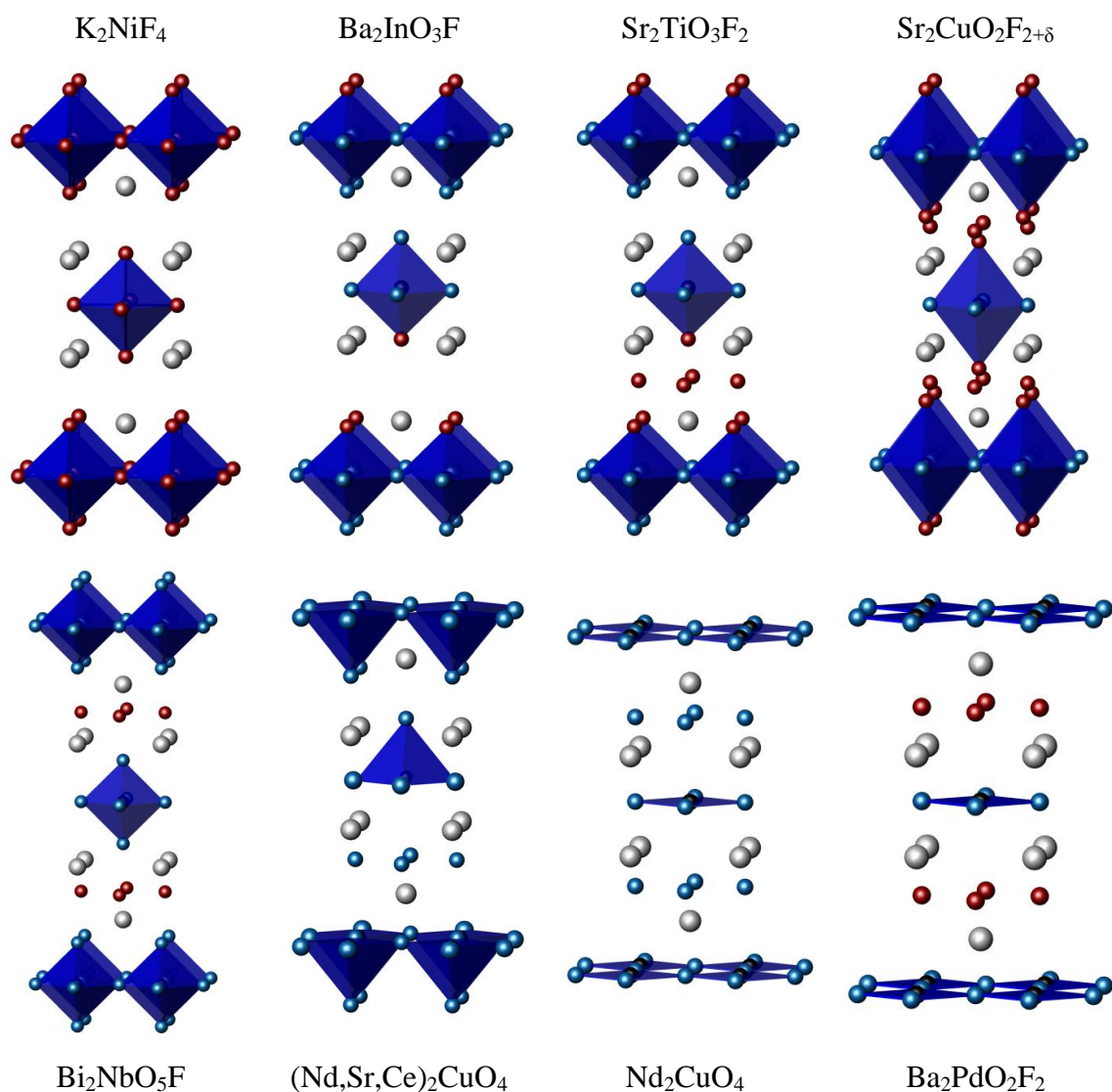


Figure 5-13. Selected structural models of structurally related oxide and oxide-fluoride materials.^{30, 38, 40, 50, 288-291}

Table 5-1 shows that upon fluorination of Ce_2MnN_3 with CuF_2 , there is an overall increase in the cell volume by approximately 11.0% from Ce_2MnN_3 to $Ce_2Mn(N,F)_4$, with a large increases in a and b and a small reduction in c . Of the models proposed, the oxide-fluorides prepared from anion deficient K_2NiF_4 -type materials isostructural to Ce_2MnN_3 are; $Sr_2CuO_2F_{2+\delta}$ and $Sr_2CuO_2F_{2,\ddagger\ddagger}$ prepared from Sr_2CuO_3 , $Ba_2PdO_2F_2$, prepared from Ba_2PdO_3 and $Ca_2CuO_2F_{2+\delta}$, prepared from Ca_2CuO_3 .^{30, 48, 50} In all cases the fluorination results in an increase in the volume of the unit cell, associated with the increase in anion content. These expansions are approximately 129.6%, 15.6%, 15.4%

^{‡‡} $Sr_2CuO_2F_2$ is formed from the reduction of $Sr_2CuO_2F_{2+\delta}$, under H_2/N_2 .

and 17.5%, for $\text{Sr}_2\text{CuO}_2\text{F}_{2+\delta}$, $\text{Sr}_2\text{CuO}_2\text{F}_2$, $\text{Ba}_2\text{PdO}_2\text{F}_2$ and $\text{Ca}_2\text{CuO}_2\text{F}_{2+\delta}$ respectively (Table 5-3). All the starting oxides listed contain one-dimensional chains of corner linked MO_4 ($\text{M} = \text{Cu}, \text{Pd}$) squares and the a/b increase is a result of the structural re-arrangement of the MO_4 units to the equatorial positions. As the cell of $\text{Ce}_2\text{Mn}(\text{N},\text{F})_x$ shows tetragonal symmetry these equatorial anion sites are equivalent. The remaining anion positions suggested by the oxide-fluoride models are the apical sites, forming transition metal centred octahedra, and/or the interstitial sites located in the rock salt layers. These models, therefore, provide a potential six anions per formula unit of fluorinated phase, i.e. $\text{Ce}_2\text{Mn}(\text{N},\text{F},\square)_6$. The oxidation states of the cations in the starting material, Ce_2MnN_3 , have been shown to be $\text{Ce}_2^{4+}\text{Mn}^+\text{N}_3$ (section 4.1).^{68, 93, 94} If it is assumed that the cerium oxidation state remains unaltered upon the oxidative treatment of fluorination, the possible stoichiometries for $\text{Ce}_2\text{Mn}(\text{N},\text{F})_x$ are; $\text{Ce}_2\text{Mn}^{4+}\text{N}_3\text{F}_3$, $\text{Ce}_2\text{Mn}^{3+}\text{N}_3\text{F}_2$, $\text{Ce}_2\text{Mn}^{2+}\text{N}_3\text{F}$, $\text{Ce}_2\text{Mn}^{2+}\text{N}_2\text{F}_4$ and $\text{Ce}_2\text{Mn}^+\text{N}_2\text{F}_3$, assuming integer values for the anion stoichiometries.

Compound	a (Å)	b (Å)	c (Å)
Sr_2CuO_3	3.5032(1)	3.9159(1)	12.7163(2)
$\text{Sr}_2\text{CuO}_2\text{F}_{2+\delta}$	5.394(1)	5.513(1)	13.468(3)
$\text{Sr}_2\text{CuO}_2\text{F}_2$	3.967(1)	3.967(1)	12.816(2)
Ba_2PdO_3	3.8362(4)	4.080(5)	13.335(2)
$\text{Ba}_2\text{PdO}_2\text{F}_2$	4.1398(3)	4.1398(3)	14.0459(13)
Ca_2CuO_3	3.249(2)	3.768(2)	12.208(6)
$\text{Ca}_2\text{CuO}_2\text{F}_{2+\delta}$	3.850(1)	3.850(1)	11.842(3)

Table 5-3. Unit cell dimension of selected oxide and oxide-fluoride materials.^{30, 48-51, 292}

Given the reduction in the c -axis, a $\text{Ba}_2\text{PdO}_2\text{F}_2$ -type structure would appear to be an encouraging choice, however, a stoichiometry of $\text{Ce}_2\text{MnN}_2\text{F}_2$ would imply unfavourable oxidation states for the cations. Only $\text{Ce}_2\text{MnN}_3\text{F}$ could potentially show the $\text{Ba}_2\text{PdO}_2\text{F}_2$ -type structure, based on the anion stoichiometry. However, such a structure would imply interstitial N^{3-} anions, which is chemically unfavourable. All other stoichiometries suggested imply at least partial occupancy of the apical anion positions.

To account for possible asymmetric manganese coordination the Mn ions were allowed to refine from the ideal 2a site, in the Rietveld refinement, and the occupancy reduced to $\frac{1}{2}$ to account for the new site multiplicity (4e). On average, the Mn cation was displaced from the 2a, by approximately 0.28 Å. This may suggest one apical F⁻ and one apical N³⁻ atom, or fluorine insertion occurring in alternate layers in the structure. Such asymmetry can be observed in Ba₂InO₃F (Ce₂MnN₃F), (Nd,Sr,Ce)₂CuO₄ (Ce₂MnN₃F), Sr₂TiO₃F₂ (Ce₂MnN₃F₂, Ce₂MnN₂F₃) and Bi₂NbO₅F (Ce₂MnN₃F₃).^{38, 40, 289, 290}

In the following section it is shown that the fluorination of Ce₂MnN₃ with F₂ gas results in a mixed nitride-fluoride phase with a tetragonal structure, $a = 3.8567(5)$ Å, $c = 13.0846(37)$ Å. PND indicated that this phase showed the Sr₂TiO₃F₂-type structure, with a stoichiometry of Ce₂MnN₃F₂. It is noticeable that, while the a axis is similar in both fluorinated phases, the c axis is larger in the phase deriving from solid-gas fluorination ($a = 3.8285(5)$ Å, $c = 12.2312(20)$ Å versus $a = 3.8567(5)$ Å, $c = 13.0846(37)$ Å for the solid-solid and solid-gas fluorinations respectively). This may indicate the two fluorination routes produce slightly different nitride-fluoride materials. The similar a -axis implies that the MnN₄ arrangement, with the four nitride anions in equatorial positions in the ab plane, is present in both structures. The Sr₂TiO₃F₂-type structure can, however, accommodate a reduction in the anion content. An alternative description of Sr₂TiO₃F₂ is a Ba₂InO₃F-type structure with staged fluorine insertion. A reduction in the occupancy of the interstitial fluorine site in Ce₂MnN₃F₂ can structurally be accommodated up to a stoichiometry of Ce₂MnN₃F, i.e. complete absence of interstitial fluorine, while maintaining feasible cation oxidation states. In addition, Ce₂MnN₃F still yields a favourable manganese oxidation state Ce₂Mn²⁺N₃F. Interestingly, based on the tolerance factor, by Chen *et al.*, the Ce₂MnN₃F stoichiometry falls within the Nd₂CuO₄-type range.²⁸ Owing to these factors, the chemical formula of Ce₂MnN₃F_{2- δ} is therefore proposed to account for the possibility of less fluorine being inserted in the lattice when Ce₂MnN₃F_{2- δ} is prepared via solid-state reaction.

5.1.2.2.5 Reactions of Ce_2MnN_3 with Fluorine Gas

5.1.2.2.5.1 Powder X-ray Diffraction (PXRD)

The focus of this study was the fluorination of Ce_2MnN_3 via direct reaction with 10% F_2/N_2 gas.³⁰ The reaction of Ce_2MnN_3 with 10% F_2/N_2 at 95-115 °C yields the highest amount of the fluorinated phase with tetragonal symmetry. Rietveld refinement using powder neutron diffraction data supports a structure related to $Sr_2TiO_3F_2$, and a stoichiometry $Ce_2MnN_3F_{2-\delta}$. However, the fluorinated phase only forms over a very narrow range of reaction conditions. In this section the development and optimisation of these reaction conditions is presented and the resulting structural characterisation processes conveyed.

Initially, the fluorination conditions were derived from the experiments for the synthesis of $Sr_2CuO_2F_{2+\delta}$. This involves a reaction in a stream of 10% F_2 in N_2 for 15 minutes at 230 °C.³⁰ However, in the fluorination of Ce_2MnN_3 , PXRD showed that under these reaction conditions only an amorphous phase results. Figure 5-14 shows the PXRD pattern of this reaction. The 2θ range of the broad peaks corresponds with the approximate range in which CeF_4 peaks are found. The narrow peaks are given by CeO_2 and are attributed to oxide impurities in Ce_2MnN_3 .

This indicates that the reaction conditions were too harsh. It was therefore decided to keep the reaction time constant, at 15 minutes, and to lower the reaction temperature. The PXRD pattern for the fluorination reaction performed at 180 °C is shown in Figure 5-14. This also showed complete decomposition of Ce_2MnN_3 . Reducing the temperature of fluorination to 100 °C gave a mixed phase product showing CeF_3 and residual Ce_2MnN_3 (Figure 5-15).

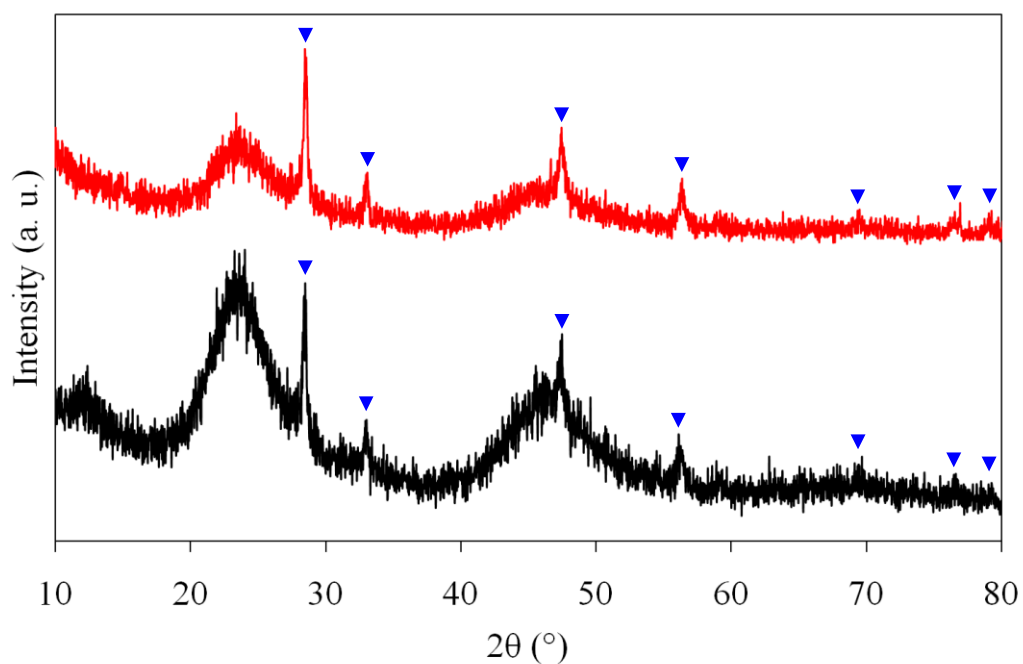


Figure 5-14. PXR D patterns from the fluorination of Ce_2MnN_3 from the reaction with F_2 gas at 230 °C (black) and 180 °C (red). The blue triangles correspond CeO_2 .

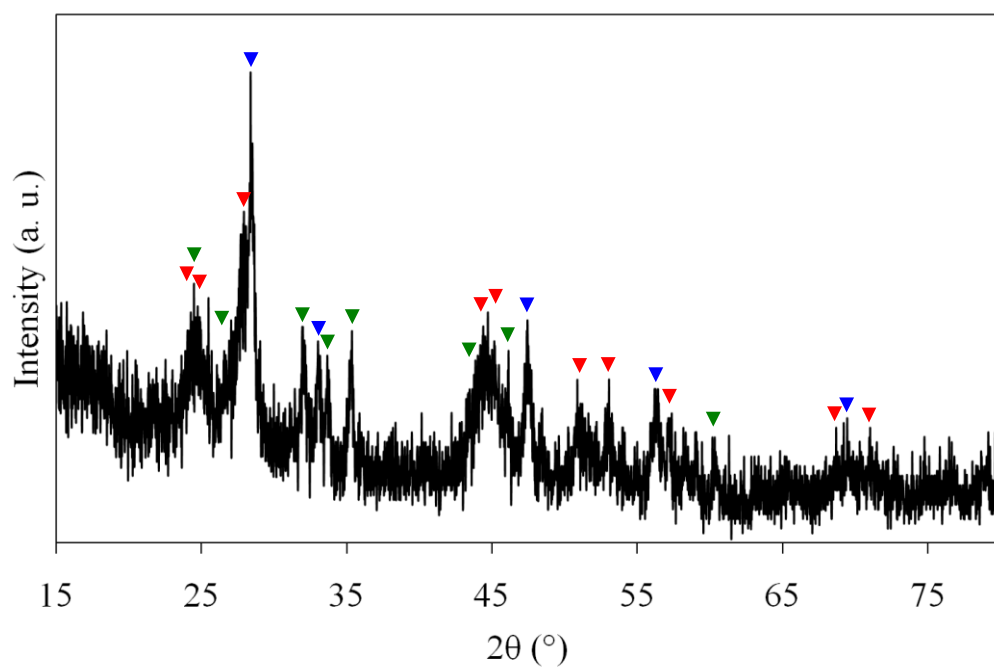


Figure 5-15. PXR D patterns from the fluorination of Ce_2MnN_3 from the reaction with F_2 gas at 100 °C. The peaks of Ce_2MnN_3 (green), CeO_2 (blue) and CeF_3 (red) are highlighted.

To reduce the severity of the reaction conditions further, a static F_2/N_2 atmosphere was used at 40 °C. PXR D of the resulting compound showed no change in the material upon fluorination, with peaks of Ce_2MnN_3 only. Several reactions were performed,

under a static atmosphere, slowly increasing the reaction temperature. Reactions at 70 °C, 80 °C and 90 °C showed only peaks consistent with Ce_2MnN_3 . For reaction of Ce_2MnN_3 and F_2 gas at 100 °C, PXRD showed a large amorphous background with no obvious diffraction peaks present.

In the all fluorinations mentioned above, reaction time began once fluorine gas was detected exiting the reaction vessel. This increases the overall contact between Ce_2MnN_3 and F_2/N_2 . For this reason, reactions were performed under flowing F_2/N_2 for 15 minutes from introduction of the F_2 gas stream into the reaction vessel. Figure 5-16 shows the product of reaction of Ce_2MnN_3 at 95 °C. PXRD showed, reproducibly, peaks identified as the starting material and a set of peaks, which was consistent with a tetragonal unit cell with $a = 3.8519(4)$ Å and $c = 13.0502(21)$ Å. As for the reaction of Ce_2MnN_3 with CuF_2 , the new tetragonal phase was attributed to a new quaternary nitride-fluoride $\text{Ce}_2\text{Mn}(\text{N},\text{F})_x$ with a structure related to K_2NiF_4 . The unit cell derived from the reaction between Ce_2MnN_3 and F_2 is larger than that obtained from the reaction with CuF_2 ($a = 3.8285(5)$ Å, $c = 12.2312(20)$ Å), as mentioned in the previous section.

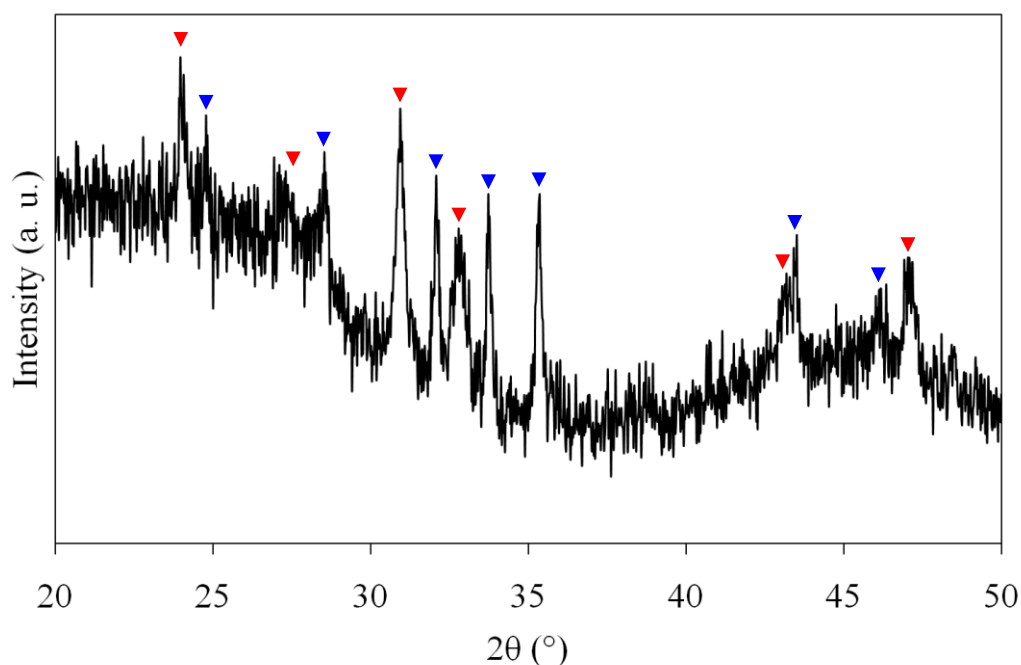


Figure 5-16. PXRD patterns from the fluorination of Ce_2MnN_3 from the reaction with F_2 gas at 95 °C. The peaks of Ce_2MnN_3 (blue) and $\text{Ce}_2\text{Mn}(\text{N},\text{F})_x$ (red) are highlighted.

In order to reduce the amount of Ce_2MnN_3 present in the fluorinated phase, the sample was re-heated under the same reaction conditions. Figure 5-17 gives a comparison between the fluorinated phases after one and two heatings with F_2/N_2 at $95\text{ }^\circ\text{C}$. The PXRD for the second fluorination treatment gives a marginal decrease in the peaks of Ce_2MnN_3 , however, an increase in the peaks attributed to $\text{Ce}_2\text{Mn}(\text{N},\text{F})_x$ is observed implying an increase in the amount of amorphous impurities present.

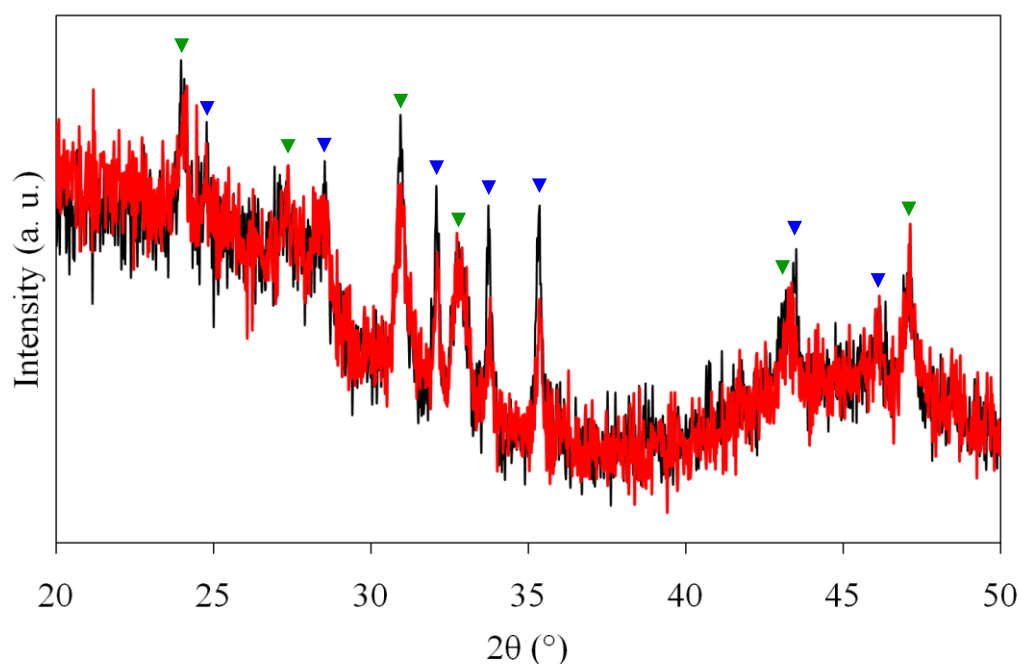


Figure 5-17. PXRD patterns from the fluorination of Ce_2MnN_3 from the reaction with F_2 gas at $95\text{ }^\circ\text{C}$ (black) and after a second treatment under the same reaction conditions (red). The peaks of Ce_2MnN_3 (blue) and $\text{Ce}_2\text{Mn}(\text{N},\text{F})_x$ (green) are highlighted.

Post annealing the samples in N_2 can act to improve the quality of fluorinated samples and allow fluorine gas, which has been absorbed on the surface of the crystallites, to react further. Samples prepared at temperature below $80\text{ }^\circ\text{C}$ were annealed at $150\text{ }^\circ\text{C}$ for five hours. This resulted in no change in the materials. PXRD of all compounds shows peaks for Ce_2MnN_3 only.

Annealing samples displaying the tetragonal phase at temperatures up to $150\text{ }^\circ\text{C}$ resulted in no overall change in the PXRD patterns. At temperatures between $150\text{-}250\text{ }^\circ\text{C}$ annealing, carried out in an attempt to improve the crystallinity of the samples, resulted in decomposition of the desired phase and the occurrence of binary fluoride, CeF_3 .

Of the temperature ranges and reaction times explored it was found that only in the narrow temperature range 95-115 °C were significant amounts of $\text{Ce}_2\text{Mn}(\text{N},\text{F})_x$ formed. Despite many attempts and many different combinations of reaction conditions a significant percentage of starting material was always found in the product, and the synthesis of a pure fluorinated phase has, to date, not been achieved.

Rietveld refinement was performed on PXRD data obtained from the reaction between Ce_2MnN_3 and F_2 gas at 115 °C for 15 minutes. A two-phase refinement was necessary to account for the presence of unreacted Ce_2MnN_3 . The model for $\text{Ce}_2\text{Mn}(\text{N},\text{F})_x$ was taken from section 5.1.2.2.4, derived from the fluorination using CuF_2 . The model for Ce_2MnN_3 was taken from section 4.1.2.2.3. The sample shows a high background, probably due to some amorphous phases present. This background was modelled using a linear interpolation function with thirty-six terms. The peak shape was modelled by a multi-term Simpson's rule integration of the pseudo-Voigt.^{241, 242} The parameters refined were: the cell parameters (a , b , c) for the two phases, one zero point, one scale factor, three atomic coordinates and fourteen profile parameters. A single isotropic thermal parameter was assigned for all atoms, but since this refined to a slightly negative number, in the final refinement U_{iso} was constrained to zero. This is quite normal for transmission PXRD data, and reflects an uncertainty in corrections for absorption. The refinement clearly indicated that the fluorinated material was structurally closely related to K_2NiF_4 . However, to account for possible asymmetric manganese coordination the Mn ions were allowed to refine from the ideal 2a site and the occupancy reduced to $\frac{1}{2}$ to account for the new site multiplicity (4e). On average, the Mn cation was displaced from the 2a, by approximately 0.4 Å (Table 5-5). This suggests an asymmetric environment for the Mn ions, e.g. by having one apical F^- and one apical N^{3-} atom, or by having fluorine insertion occurring in alternate layers in the structure. The latter was originally seen in the material $\text{LaSrMnO}_4\text{F}$ and subsequently also in $\text{Sr}_2\text{TiO}_3\text{F}_2$.^{38, 286} The results of refinement based on a stoichiometry of $\text{Ce}_2\text{Mn}(\text{N}/\text{F})_4$ are shown in Figure 5-18 and Table 5-4, the cell parameters of which are compared with Ce_2MnN_3 . Because of the presence of some amorphous material giving an uneven background, Figure 5-18 shows data for which the background was subtracted after refinement.

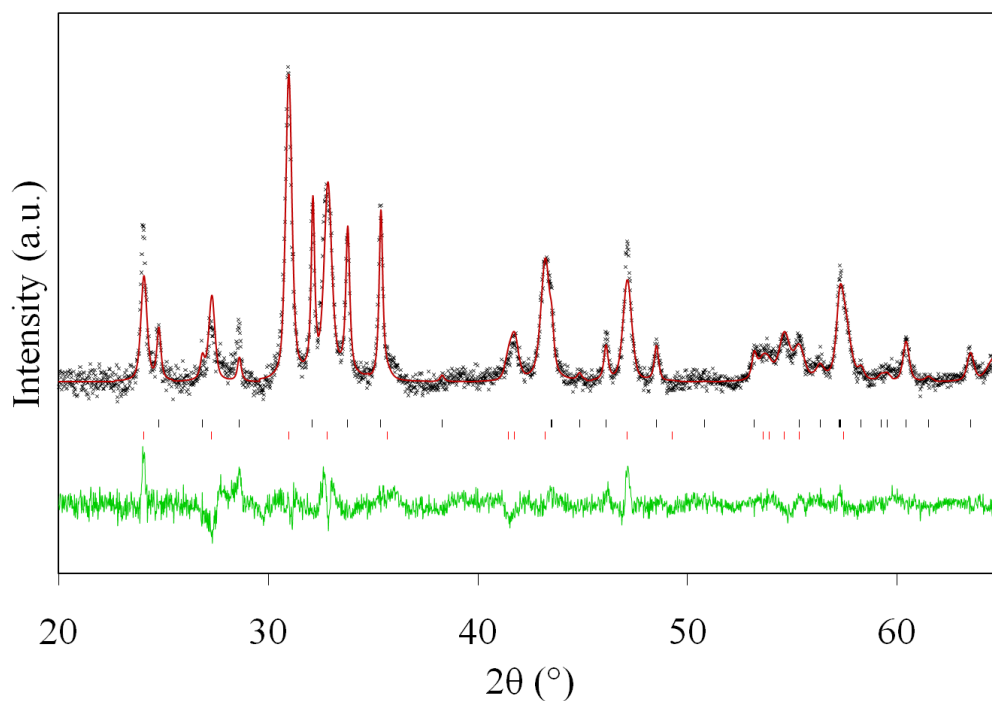


Figure 5-18. PXRD profiles of the sample obtained from the reaction of Ce_2MnN_3 with F_2 (gas) and showing observed (+), calculated (red line) and difference (green line) patterns. Tick marks indicate reflection positions for the fluorinated (upper) and Ce_2MnN_3 (lower) phases.

Formula	$\text{Ce}_2\text{Mn}(\text{N},\text{F})_4$	
Space Group	$I4/mmm$ (no. 139)	
	PXRD data	Ce_2MnN_3
a (Å)	3.8519(4)	3.7549(2)
b (Å)	3.8519(4)	3.4487(1)
c (Å)	13.0502(21)	12.4724(6)
V (Å ³)	193.63(6)	161.52(2)
Z	2	
Calculated density (g cm ⁻³)	6.846	
Profile function	Pseudo-Voigt	
No. of profile points	3939	
No. of parameters refined	61	
R_{wp}	0.0342	
R_{p}	0.0250	
χ_{red}^2	1.709	

Table 5-4. Summary of refinement data and lattice parameters for $\text{Ce}_2\text{Mn}(\text{N},\text{F})_4$, obtained from the reaction of Ce_2MnN_3 and F_2 , derived from PXRD data.

Atom	Site	x	y	z	occupancy
Ce	4e	0	0	0.3627(3)	1
Mn	4e	0	0	0.0374(9)	0.5
N/F(eq)	4c	0.5	0	0	1
N/F(ap)	4e	0	0	0.1621(21)	1

Table 5-5. Structural data for $\text{Ce}_2\text{Mn}(\text{N},\text{F})_4$ from PXRD.

As stated in the previous subsection, the reaction of Ce_2MnN_3 with CuF_2 yielded a similar K_2NiF_4 -type nitride-fluoride phase, however, the resulting phase from the reaction with F_2 shows a larger unit cell. This may indicate a different anionic content.

In order to explore fully the overall fluorine content in this phase and the N/F distribution, powder neutron diffraction (PND) data were collected, on the sample prepared in F_2 gas, since the N and F scattering lengths (0.93×10^{-14} m and 0.565×10^{-14} m, respectively) allow reasonable contrast between these species.³⁹

5.1.2.2.5.2 Powder Neutron Diffraction (PND)

Rietveld refinement performed using PXRD data suggested a nitride-fluoride phase, structurally closely related to K_2NiF_4 (or Nd_2CuO_4). Therefore, various structural models were explored which are related to K_2NiF_4 , Nd_2CuO_4 and anion excess derivatives to identify the most likely structure of $\text{Ce}_2\text{Mn}(\text{N},\text{F})_x$.

The peaks of the new nitride-fluoride phase, derived from reaction of Ce_2MnN_3 with F_2 gas, indexed to a tetragonal unit cell. In both K_2NiF_4 and Nd_2CuO_4 the transition metal is coordinated to four equatorial anions (Figure 1-3). A tetragonal unit cell implies that the anions in equatorial coordination with manganese are equivalent. PXRD demonstrated that the manganese may be in an asymmetric environment along the *c*-axis, with a distortion from the ideal 2a site. A number of models, based on known oxide-fluoride materials satisfactorily meet this description and were shown in Figure 5-13. Rietveld refinements were performed based on these models. It soon became clear that the pattern was best described by models showing the $P4/nmm$ space group.

The chemical formulae proposed, based on probable manganese oxidation states, are $\text{Ce}_2\text{MnN}_3\text{F}$ ($\text{Ba}_2\text{InO}_3\text{F}$), $\text{Ce}_2\text{MnN}_3\text{F}$ ($(\text{Nd,Sr,Ce})_2\text{CuO}_4$), $\text{Ce}_2\text{MnN}_3\text{F}_2$ ($\text{Sr}_2\text{TiO}_3\text{F}_2$), $\text{Ce}_2\text{MnN}_2\text{F}_3$ ($\text{Sr}_2\text{TiO}_3\text{F}_2$) and $\text{Ce}_2\text{MnN}_3\text{F}_3$ ($\text{Bi}_2\text{NbO}_5\text{F}$). Rietveld refinements based on $(\text{Nd,Sr,Ce})_2\text{CuO}_4$ ($\text{Ce}_2\text{MnN}_3\text{F}$) gave particularly poor fits to the data and often resulted in the refinement diverging. The remaining models are very similar, showing a K_2NiF_4 -type arrangement of MnN_5F octahedra with no interstitial fluorine, $\text{Ce}_2\text{MnN}_3\text{F}$, staged interstitial fluorine (in alternate rock salt layers), $\text{Ce}_2\text{MnN}_3\text{F}_2/\text{Ce}_2\text{MnN}_2\text{F}_3$ and full interstitial fluorine occupancy, $\text{Ce}_2\text{MnN}_3\text{F}_3$.

The model showing the best fit to the PND data was $\text{Ce}_2\text{MnN}_3\text{F}_2$, based on $\text{Sr}_2\text{TiO}_3\text{F}_2$. Comparison to the other $\text{Sr}_2\text{TiO}_3\text{F}_2$ models will be made in the description of the refinement. Rietveld refinement was performed based on a model from Slater *et al.* for $\text{Sr}_2\text{TiO}_3\text{F}_2$.³⁸ A two phase refinement was required to account for Ce_2MnN_3 . To account for a large amorphous background, the background was modelled by a linear interpolation function with thirty-six terms. The peak shape was modelled by a multi-term Simpson's rule integration of the pseudo-Voigt.^{241, 242} The parameters refined were: the cell parameters (a , b , c) for the two phases, one zero point, one scale factors, nine atomic coordinates, eleven isotropic thermal parameters and twenty-one profile parameters. Only two isotropic temperature factors were used, one for the three cation sites and one for the four anion sites. These constraints on thermal parameters were applied to stabilise the refinement and provide better sensitivity for anion site occupancies. Refinement indicates a Ce_2MnN_3 content of 49.4(9)%. The refinement parameters are summarised in Figure 5-19 and the refinement profile is shown in Table 5-6.

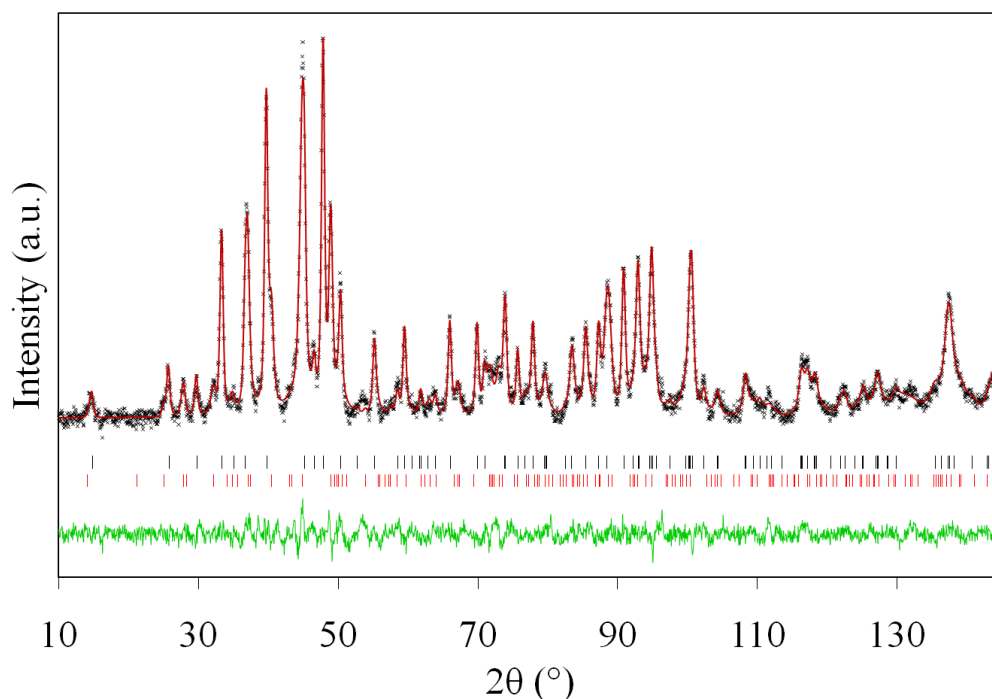


Figure 5-19. PND profiles of the sample obtained from the reaction of Ce_2MnN_3 with $\text{F}_2(\text{gas})$ and showing observed (+), calculated (red line) and difference (green line) patterns. Tick marks indicate reflection positions for the fluorinated (lower) and Ce_2MnN_3 (upper) phases.

Formula	$\text{Ce}_2\text{MnN}_3\text{F}_2$
Space Group	$P4/nmm$ (no. 129)
	PND data
a (Å)	3.8567(5)
b (Å)	3.8567(5)
c (Å)	13.0846(37)
V (Å ³)	194.62(8)
Z	2
Calculated density (g cm ⁻³)	7.092
Profile function	Pseudo-Voigt
No. of profile points	2699
No. of parameters refined	66
R_{wp}	0.0180
R_{p}	0.0143
χ_{red}^2	1.370

Table 5-6. Summary of refinement data and lattice parameters for $\text{Ce}_2\text{MnN}_3\text{F}_2$, obtained from the reaction of Ce_2MnN_3 and F_2 , derived from PND data.

The $\text{Sr}_2\text{TiO}_3\text{F}_2$ structure consists of a K_2NiF_4 -type arrangement of anions, with four equatorial oxide anions, one apical oxide anion and one apical fluoride forming the corner connected layers of TiO_5F octahedra. The additional fluoride anion inserts at an

interstitial site between these octahedra at alternate rock salt layers (section 1.1.3 and Figure 5-23). The $\text{Ce}_2\text{MnN}_3\text{F}_2$ model used for the initial refinement assumed cerium resides on the strontium site, manganese on the titanium site and nitrogen on the oxygen site in $\text{Sr}_2\text{TiO}_3\text{F}_2$. The presence of this staged anion insertion, in K_2NiF_4 -type materials, is not common. To add weight to the assignment of this structural type to $\text{Ce}_2\text{Mn}(\text{N},\text{F})_x$ a structural model free from interstitial anions was also investigated i.e. $\text{Ce}_2\text{MnN}_3\text{F}$. Such a stoichiometry would yield a manganese oxidation state of 2+, which is also feasible given the oxidative environment in F_2 gas. Rietveld refinement was performed with one apical nitride anion and one apical fluoride anion only, taken from Needs *et al.* and their model of $\text{Ba}_2\text{InO}_3\text{F}$.⁴⁰ Ce_2MnN_3 was used as the second phase. The background was modelled by a linear interpolation function with thirty-six terms. The peak shape was modelled by a multi-term Simpson's rule integration of the pseudo-Voigt.^{241, 242} The parameters refined were: the cell parameters (a , b , c) for the two phases, one zero point, one scale factors, twenty-one profile parameters. The refinement parameters are summarised in Table 5-7, compared with Ce_2MnN_3 , and the refinement profile is shown in Figure 5-20.

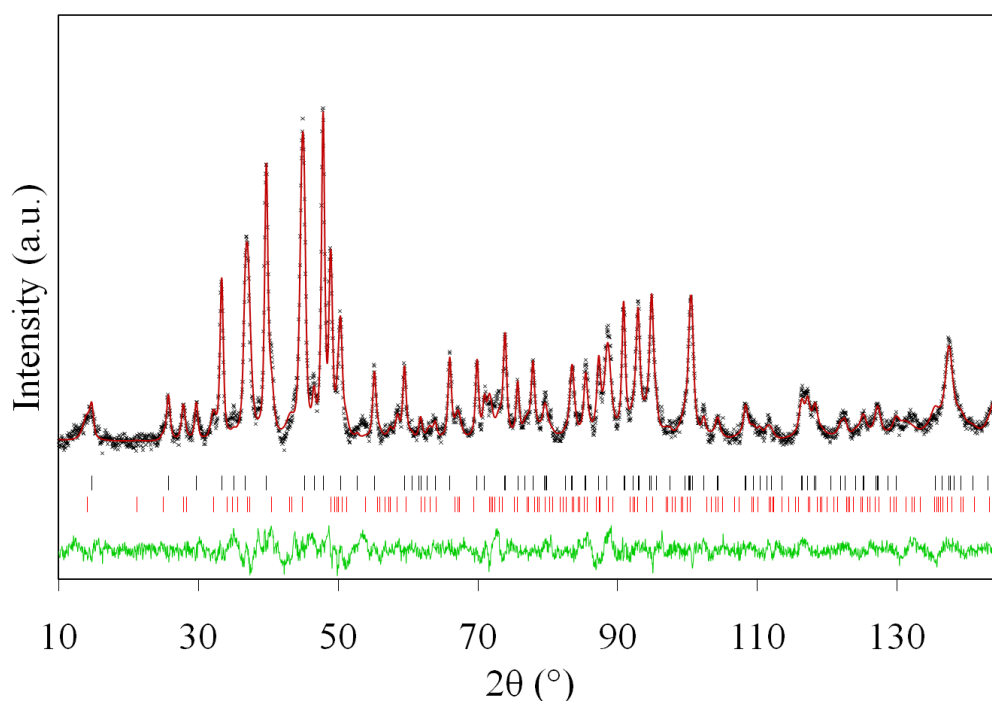


Figure 5-20. PND profiles of the sample obtained from the reaction of Ce_2MnN_3 with F_2 (gas) and showing observed (+), calculated (red line) and difference (green line) patterns. Tick marks indicate reflection positions for the fluorinated (lower) and Ce_2MnN_3 (upper) phases.

Formula	Ce ₂ MnN ₃ F	
Space Group	<i>P4/nmm</i> (no. 129)	
	PND data	Ce ₂ MnN ₃
<i>a</i> (Å)	3.8558(4)	3.7534(2)
<i>b</i> (Å)	3.8558(4)	3.4459(2)
<i>c</i> (Å)	13.0697(37)	12.4740(7)
<i>V</i> (Å ³)	194.31(6)	161.34(2)
<i>Z</i>	2	
Calculated density (g cm ⁻³)	6.772	
R _{wp}	0.0215	
R _p	0.0167	
χ _{red} ²	1.948	

Table 5-7. Summary of refinement data and lattice parameters for Ce₂MnN₃F, obtained from the reaction of Ce₂MnN₃ and F₂, derived from PND data.

The fit obtained using the Ce₂MnN₃F model is less satisfactory than that obtained using the model with staged interstitial anions. A difference Fourier map, in the *ab* plane at *z* = 0, from the Ce₂MnN₃F model is given in Figure 5-21. This gives a clear indication of, localised, insufficiently modelled electron density. This can be attributed to the interstitial anion site.

The difference Fourier map taken at *z* = 0.5 is shown in Figure 5-22. This plane corresponds with the second rock salt layer, in which interstitial anions may reside. The difference Fourier map at this height, however, does not give as strong an indication of unmodelled electron density, indicating staged anion insertion and ruling out the Ce₂MnN₃F and Ce₂MnN₃F₃ models.

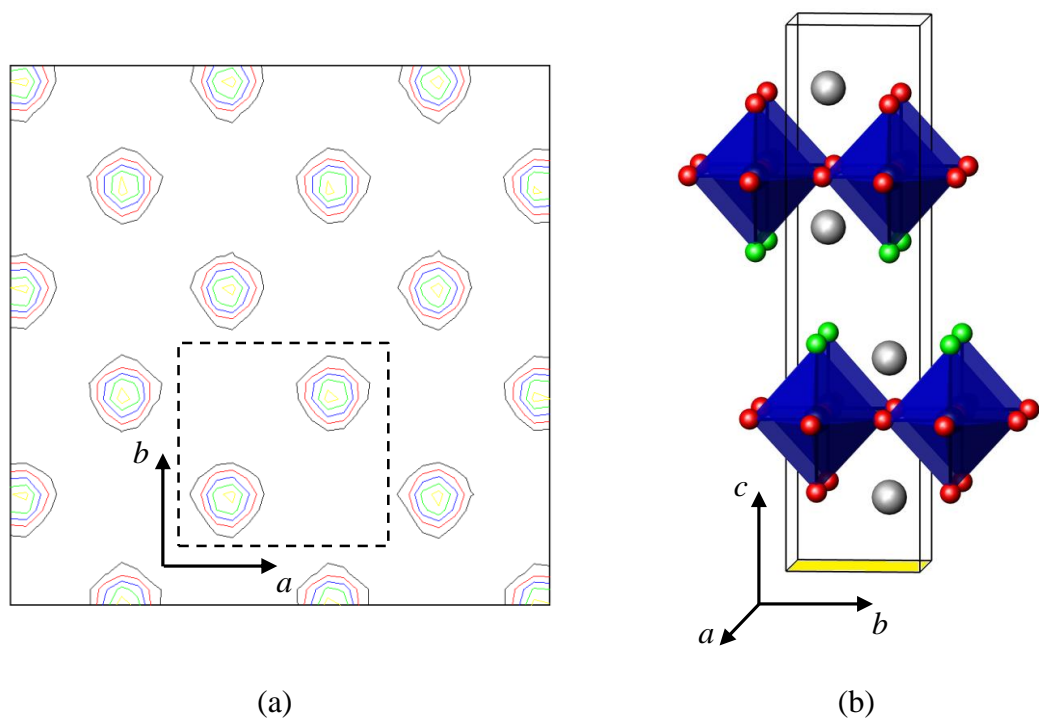


Figure 5-21. (a) Difference Fourier map, viewed along the c -axis at a height of $z = 0$. The dotted lines indicate a unit cell. (b) Structure of $\text{Ce}_2\text{MnN}_3\text{F}$ obtained from the $\text{Ba}_2\text{InO}_3\text{F}$ model. The grey, green and red spheres represent cerium, fluorine and nitrogen. The plane of the contour map is highlighted in yellow in figure (b).

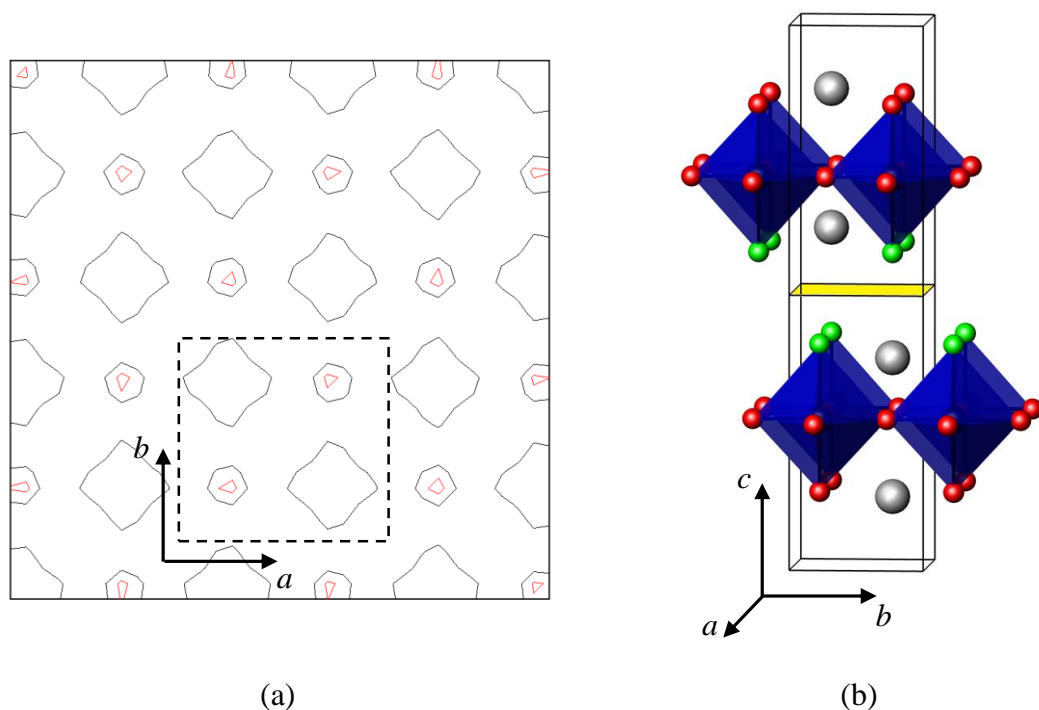


Figure 5-22. (a) Difference Fourier map, viewed along the c -axis at a height of $z = 0.5$. The dotted lines indicate a unit cell. (b) Structure of $\text{Ce}_2\text{MnN}_3\text{F}$ obtained from the $\text{Ba}_2\text{InO}_3\text{F}$ model. The grey, green and red spheres represent cerium, fluorine and nitrogen. The plane of the contour map is highlighted in yellow in figure (b).

Owing to the presence of amorphous fluorinated phases and due to the presence of a high quantity of Ce_2MnN_3 present (initial refinements indicate $\sim 50\%$, by weight) in the material, elemental analysis could not be performed. As this is the first example of a quaternary nitride-fluoride of this type it cannot be assumed that the N/F distribution will match the O/F distribution observed in $\text{Sr}_2\text{TiO}_3\text{F}_2$. To add further support for the N/F distribution over the anion sites Madelung energy calculations were performed, in addition to PND. The structural template and models examined are shown in Figure 5-23 and Table 5-8.

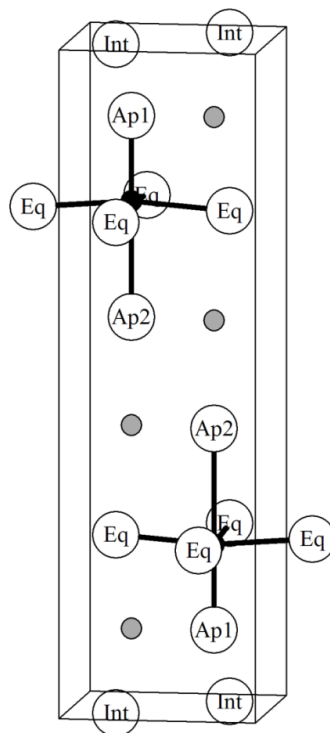


Figure 5-23. Structural template for $\text{Ce}_2\text{Mn}(\text{N},\text{F})_x / \text{Sr}_2\text{TiO}_3\text{F}_2$. The grey spheres represent strontium or cerium, the black spheres titanium or manganese and the white spheres the anions.

Model	Formula	Fractional Occupancy								Madelung Energy (Kcal/mol)
		Eq		Ap1		Ap2		Int		
		N^{3-}	F^-	N^{3-}	F^-	N^{3-}	F^-	N^{3-}	F^-	
(1)	$\text{Ce}_2\text{Mn}^{+3}\text{N}_3\text{F}_2$	1	0	0	1	1	0	0	1	-8210.4909
(2)	$\text{Ce}_2\text{Mn}^{+3}\text{N}_3\text{F}_2$	1	0	1	0	0	1	0	1	-7272.9665
(3)	$\text{Ce}_2\text{Mn}^{+3}\text{N}_3\text{F}_2$	1	0	0.5	0.5	0.5	0.5	0	1	-7922.2309
(4)	$\text{Ce}_2\text{Mn}^{+3}\text{N}_3\text{F}_2$	0	1	1	0	1	0	1	0	-7262.3282
(5)	$\text{Ce}_2\text{Mn}^+\text{N}_2\text{F}_3$	1	0	0	1	0	1	0	1	-5389.7953

Table 5-8. Models examined and corresponding Madelung energies for possible anion distribution in $\text{Ce}_2\text{MnN}_x\text{F}_y$.

Although Models (1), (2), (3) and (5) provided reasonable fits to the data (Model (1): $R_{wp} = 0.018$, $\chi^2 = 1.37$; Model (2): $R_{wp} = 0.019$, $\chi^2 = 1.50$; Model (3): $R_{wp} = 0.019$, $\chi^2 = 1.49$; Model (5): $R_{wp} = 0.090$, $\chi^2 = 1.50$). Model (1) was statistically the best and suggested that N^{3-} occupies all the equatorial sites and one apical site, with F^- occupying the other apical site and interstitial sites within alternate rock salt regions. It can be noted that a preference for the apical position, by fluorine, is also shown by the oxide-fluorides. In addition, Madelung energy calculations (Table 5-8) fully support the structure corresponding to Model (1) determined from the PND refinement. The Madelung energy for the anion distribution of Model (1) is 3.6% lower than that of the next higher energy.

The fluorination of Ce_2MnN_3 with CuF_2 gas results in a mixed nitride-fluoride phase with a smaller tetragonal structure, $a = 3.8285(5) \text{ \AA}$, $c = 12.2312(20) \text{ \AA}$ versus $a = 3.8567(5) \text{ \AA}$, $c = 13.0846(37) \text{ \AA}$ for the solid-solid and solid-gas fluorinations respectively. A possible explanation for the smaller unit cell dimensions is the removal of interstitial fluorine. The $Ce_2MnN_2F_3$ model does not support the removal of interstitial fluorine as this would result in a manganese oxidation state of less than one. $Ce_2MnN_3F_2$, however, can satisfactorily accommodate this deficiency.

To investigate anion deficiency, refinement of the occupancy was performed and indicated partial occupancy of the interstitial site (83%). The occupancy is highly correlated with U_{iso} and, due to the constraints that were necessary to describe U_{iso} , may not be totally reliable. Reduced interstitial fluoride content would imply mixed valency manganese and a non-stoichiometric chemical formula, $Ce_2MnN_3F_{2-\delta}$. It is noted that the anion temperature factors are large, which may be attributed to one or more of three factors: substitutional effects related to a small degree of N/F mixing; partial occupancy of the interstitial F site; the presence of mixed valent Mn and the consequential variation in Mn-N/F bond distances.

The refined structural data derived for $Ce_2MnN_3F_{2-\delta}$ and Ce_2MnN_3 are given in Table 5-9 and respectively. Selected bond lengths and angles for $Ce_2MnN_3F_{2-\delta}$ are given in Table 5-11. The refined structural parameters for Ce_2MnN_3 are in good agreement with those obtained by Niewa *et al.* and support the validity of the two-phase refinement.⁶⁸

Atom	Site	x	y	z	$100 \times U_{\text{iso}}$	Occ.
Ce(1)	2c	$\frac{3}{4}$	$\frac{3}{4}$	0.128(2)	0.2(3)	1.0
Ce(2)	2c	$\frac{3}{4}$	$\frac{3}{4}$	0.391(2)	0.2(3)	1.0
Mn	2c	$\frac{1}{4}$	$\frac{1}{4}$	0.284(2)	0.2(3)	1.0
N(eq.)	4f	$\frac{1}{4}$	$\frac{3}{4}$	0.272(1)	4.4(3)	1.0
F(ap.)	2c	$\frac{1}{4}$	$\frac{1}{4}$	0.118(2)	4.4(3)	1.0
N(ap.)	2c	$\frac{1}{4}$	$\frac{1}{4}$	0.422(2)	4.4(3)	1.0
F(int.)	2a	$\frac{1}{4}$	$\frac{3}{4}$	0	4.4(3)	0.83(4)

Table 5-9. Structural parameters for $\text{Ce}_2\text{MnN}_3\text{F}_{2-\delta}$ derived from PND data.

Atom	Site	x	y	z	$100 \times U_{\text{iso}}$	Occ.
Ce	4i	0	0	0.3537(3)	0.1(1)	1.0
Mn	2a	0	0	0	0.4(2)	1.0
N(1)	2b	0	$\frac{1}{2}$	$\frac{1}{2}$	0.5(1)	1.0
N(2)	4i	0	0	0.1640(2)	1.4(1)	1.0

Table 5-10. Structural parameters for Ce_2MnN_3 derived from powder neutron diffraction data.

Distances (Å)			
Ce(1)-Ce(1)	$3.8539(3) \times 4$	Ce(2)-Ce(2)	$3.8539(3) \times 4$ $3.94(3) \times 4$
Ce(1)-Mn	$3.41(2) \times 4$	Ce(2)-Mn	$3.06(1) \times 4$
Ce(1)-N(eq.)	$2.69(2) \times 4$	Ce(2)-N(eq.)	$2.48(2) \times 4$
Ce(1)-F(ap.)	$2.73(2) \times 4$ $3.21(4)$	Ce(2)-N(ap.)	$2.755(5) \times 4$ $2.44(3)$
Ce(1)-F(int.)	$2.55(1) \times 4$	Mn-F(ap.)	2.17(4)
Mn-N(eq.)	$1.934(2) \times 4$	Mn-N(ap.)	1.80(4)
Angles (°)			
N(eq.)-Mn-N(eq.)	170(2) 89.6(1)	N(eq.)-Mn-F(ap.)	85.1(8)

Table 5-11. Selected bond lengths and angles in $\text{Ce}_2\text{MnN}_3\text{F}_{2-\delta}$ from PND data.

The chosen model implies that the stoichiometry for the new fluorinated phase is $\text{Ce}_2\text{MnN}_3\text{F}_{2-\delta}$ and the structure consists of corner sharing sheets of distorted MnN_5F octahedra, stacked along the c -axis. The apical sites of the MnN_5F octahedra are occupied by N and F in an ordered fashion. This model implies that the fluorination of Ce_2MnN_3 only leads to F^- insertion and not to F^-/N^{3-} substitution, unlike fluorination reactions on the A_2CuO_3 ($\text{A} = \text{Sr}, \text{Ca}$) oxides. A comparison of Ce_2MnN_3 and $\text{Ce}_2\text{MnN}_3\text{F}_{2-\delta}$ structures is shown in Figure 5-24.

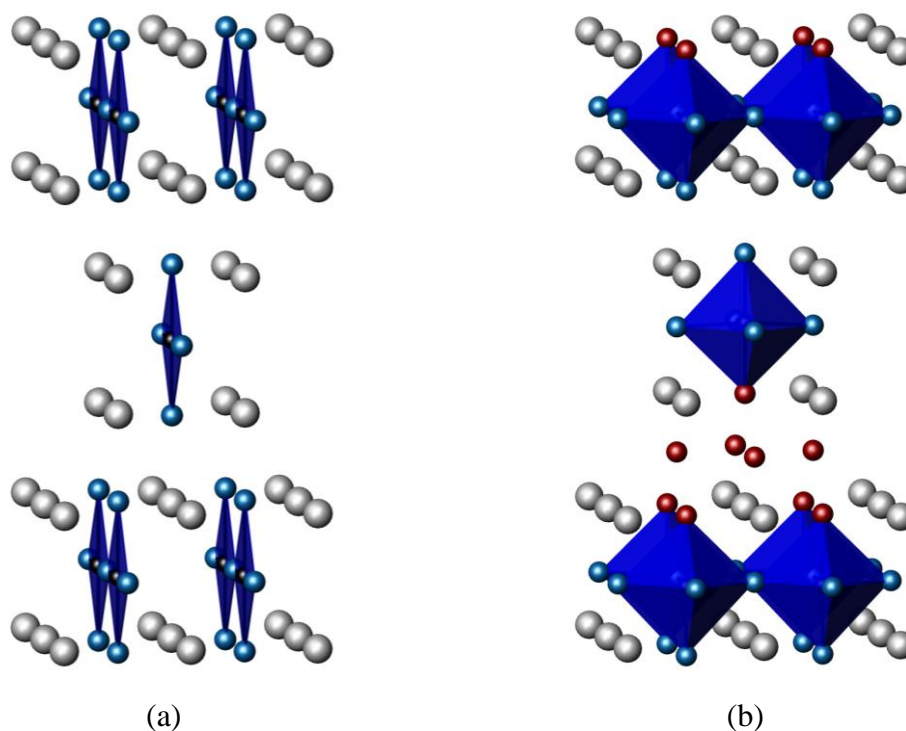


Figure 5-24. Structural representation of (a) Ce_2MnN_3 and (b) the $\text{Ce}_2\text{MnN}_3\text{F}_{2-\delta}$. The grey, black, blue and red spheres represent cerium, manganese, nitrogen and fluorine respectively.

A comparison of Ce_2MnN_3 and $\text{Ce}_2\text{MnN}_3\text{F}_{2-\delta}$ shows that upon fluorination there are several important structural rearrangements. Due to the introduction of additional anions, the cerium alters from a single site showing a roughly mon capped trigonal prism of nitrogen atoms, in Ce_2MnN_3 , to two crystallographically independent sites in $\text{Ce}_2\text{MnN}_3\text{F}_{2-\delta}$. The first site, closest to the vacant interstitial fluorine position, is coordinated to nine anions in a similar arrangement to potassium in K_2NiF_4 .²⁸⁷ The second, which is adjacent to the interstitial fluorine position, shows a coordination of eight nitride anions, at the base of a rectangular anti-prism.

The manganese coordination environment alters from the near square planar arrangement of Ce_2MnN_3 , to distorted octahedral in $\text{Ce}_2\text{MnN}_3\text{F}_{2-\delta}$. The Mn-N(eq) bond lengths of 1.934(2) Å, in $\text{Ce}_2\text{MnN}_3\text{F}_{2-\delta}$, are consistent with single bonds, appearing slightly shorter than the Mn-N single bond lengths of around 2.01 Å seen in organometallic compounds, and are longer than the Mn-N(bridging) bonds of Ce_2MnN_3 , 1.87497(3) Å.⁶⁸ The apical nitrogen lies closest to the vacant interstitial site generating a shorter Mn-N bond length of 1.80(4) Å. These bond lengths are too long to correspond with a triple bond, ~ 1.51 Å, although the Mn-N(ap) bond is similar to Mn-N double bonds, which range from around 1.74-1.80 Å.⁶⁸ The Mn-F bond length of 2.17(4) Å is similar to the Mn-F bonds in K_2MnF_4 , ~ 2.104 Å.²⁸⁸

In order to understand the transformations induced by fluorination of Ce_2MnN_3 , it is convenient to describe the fluorination processes leading to the preparation of the following oxide-fluorides: $\text{Sr}_2\text{TiO}_3\text{F}_2$,³⁸ the isostructural $\text{LaSrMnO}_4\text{F}$,²⁸⁶ $\text{Sr}_2\text{CuO}_2\text{F}_{2+\delta}$ and $\text{Ca}_2\text{CuO}_2\text{F}_{2+\delta}$.^{30, 48} $\text{Sr}_2\text{TiO}_3\text{F}_2$ is obtained via fluorination of the K_2NiF_4 -type compound Sr_2TiO_4 with NH_4F or MF_2 (M = Cu or Zn). The fluorination results in the substitution of one O^{2-} with two F^- anions, with one F^- located on the O^{2-} site and the extra F^- anions located in interstitial sites and forming alternating full and empty layers. This process does not lead to any rearrangement of the structure of the starting compound, nor does it give any hole doping. $\text{LaSrMnO}_4\text{F}$ is obtained via fluorination of the K_2NiF_4 -type compound LaSrMnO_4 , using a 10% $\text{F}_2/90\%$ N_2 gas mixture, followed by heating of the resulting phase with LaSrMnO_4 at 300 °C.²⁸⁶ The fluorination does not result in any O^{2-}/F^- substitution but only in F^- insertion. In particular, and similarly to $\text{Sr}_2\text{TiO}_3\text{F}_2$, the fluoride insertion occurs as a staged process, *i.e.* $\text{LaSrMnO}_4\text{F}$ contains layers of fully occupied interstitial sites and layers of empty interstitial sites. The fluorination process does not lead to a rearrangement of the LaSrMnO_4 structure, but causes oxidation of Mn^{3+} to Mn^{4+} . The starting materials for the preparation of $\text{Sr}_2\text{CuO}_2\text{F}_{2+\delta}$ and $\text{Ca}_2\text{CuO}_2\text{F}_{2+\delta}$, Sr_2CuO_3 and the isostructural Ca_2CuO_3 , are K_2NiF_4 -type compounds, but contain anion deficiencies, as shown by the stoichiometry of the anions. $\text{Sr}_2\text{CuO}_2\text{F}_{2+\delta}$ and $\text{Ca}_2\text{CuO}_2\text{F}_{2+\delta}$ were prepared via fluorination of Sr_2CuO_3 and Ca_2CuO_3 using either a 10% $\text{F}_2/90\%$ N_2 gas mixture,^{30, 48} solid fluorinating agents like NH_4F or MF_2 (M = Cu or Zn).^{283, 293} The fluorination of Sr_2CuO_3 and Ca_2CuO_3 is based on a combination of substitution and insertion of the F^-

anion. The two F⁻ anions substituting one O²⁻ anion complete the coordination sphere of Cu²⁺ via the transformation of the Cu-O square planes, in Sr₂CuO₃ into CuO₄F₂ octahedra, whereas in Ca₂CuO₂F_{2+δ}, the Cu remains essentially square planar and linked to oxygen, but with extra F⁻ anions inserted in interstitial sites within the CaO rock salt layer. Therefore, in these cases, the fluorination process not only provides hole doping, via the extra F⁻ anion forcing a Cu²⁺/Cu³⁺ partial oxidation, but also plays a major structural role in re-arranging the anion lattice.

Unlike in the cases of Sr₂TiO₃F₂ and LaSrMnO₄F, the starting material, Ce₂MnN₃, is a K₂NiF₄-type compound with anion deficiencies, *i.e.* it is isostructural with Sr₂CuO₃ and Ca₂CuO₃. Unlike in the case of Sr₂CuO₂F_{2+δ} and Ca₂CuO₂F_{2+δ}, in the preparation of Ce₂MnN₃F_{2-δ} two F⁻ anions are inserted in the starting Ce₂MnN₃ but no anionic substitution (N³⁻/F⁻) takes place. However, a structural rearrangement occurs, as one F⁻ anion expands the coordination of manganese from four (square-planar) to six (octahedral) occupying the apical site at ¼, ¼, 0.118(2). The second F⁻ anion inserts in the interstitial site at ¼, ¾, 0, forming layers of fully occupied interstitial sites and layers of empty interstitial sites. The fluorination process, therefore, results in a staged insertion of F⁻ anions in alternate layers of interstitial sites, similarly to the cases of Sr₂TiO₃F₂ and LaSrMnO₄F.

5.1.2.2.5.3 Magnetic Susceptibility Measurements

The magnetic susceptibility data of the Ce₂MnN₃F_{2-δ} are shown in Figure 5-25. The susceptibility, χ (emu mol⁻¹ Mn), was estimated on the molar ratio Ce₂MnN₃:Ce₂MnN₃F_{2-δ} of 1:1, as indicated by the PND data, and gives no indication of magnetic ordering. Since the sample contained un-reacted Ce₂MnN₃, the magnetic properties of this phase were also examined. The data for the mixed phase were fitted using $\chi = \chi_0 + \frac{C}{T - \theta}$, which provided a temperature independent term, $\chi_0 = 0.0023(1)$ emu mol⁻¹, $C = 1.83(1)$ emu K mol⁻¹ and $\theta = -6.1(1)$ K, giving $\mu_{eff} = 3.83(2)$ μ_B per Mn. This moment is a composite moment for Mn in the two phases, from which the effective moment for Ce₂MnN₃F_{2-δ} is derived; $\mu_{eff} = 5.38(3)$ μ_B .

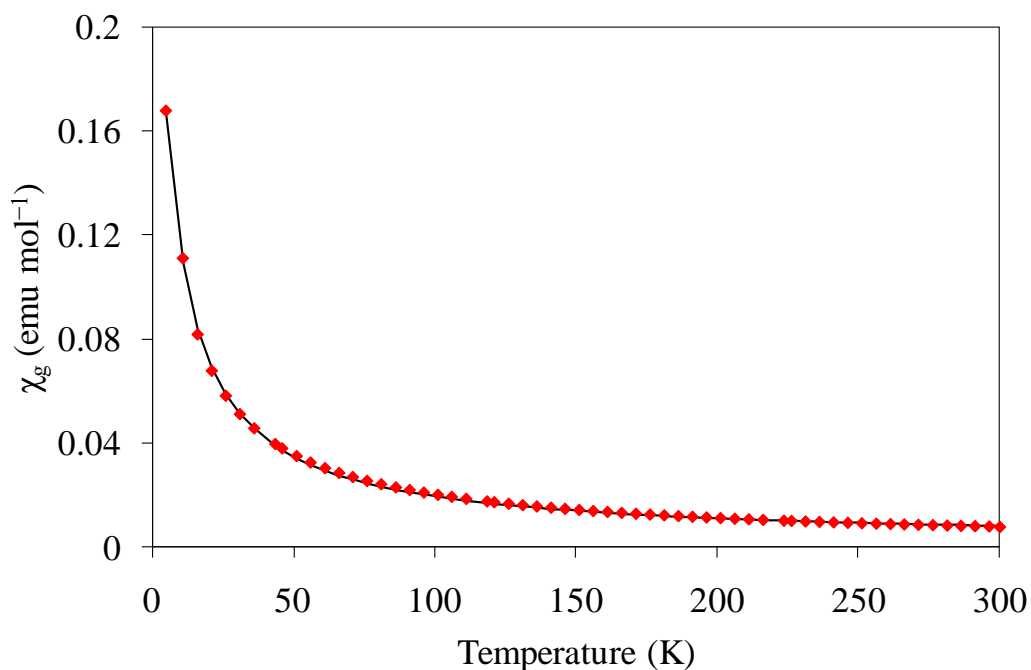


Figure 5-25. Magnetic susceptibility (χ) versus temperature data for $\text{Ce}_2\text{MnN}_3\text{F}_{2-\delta}$ (red) with fitting based on a Curie-Weiss equation with a temperature independent component (black).

Since treatment in fluorine gas will leave the oxidation state of cerium at +4, μ_{eff} corresponds to the Mn moment in $\text{Ce}_2\text{MnN}_3\text{F}_{2-\delta}$. The moment is intermediate between the spin-only values usually expected for high-spin Mn^{3+} ($4.9 \mu_{\text{B}}$) and Mn^{2+} ($5.9 \mu_{\text{B}}$) in octahedral coordination. Owing to quenching of the angular momentum, it is reasonable to expect a magnetic moment close to the spin-only value and therefore this result is consistent with the implications of the PND refinement that the material is a slightly F-deficient variant of $\text{Ce}_2\text{Mn}^{3+}\text{N}_3\text{F}_2$, and, therefore, shows mixed valance on the manganese site ($\text{Ce}_2\text{Mn}^{2+/3+}\text{N}_3\text{F}_{2-\delta}$).

5.1.3 Conclusions

A new quaternary nitride-fluoride material has been successfully prepared via the fluorination of Ce_2MnN_3 .²⁷⁹ PXRD, PND and magnetic susceptibility measurements imply a formula of $\text{Ce}_2\text{MnN}_3\text{F}_{2-\delta}$. $\text{Ce}_2\text{MnN}_3\text{F}_{2-\delta}$ has been synthesised *via* several soft-chemistry techniques, *i.e.* low-temperature fluorination of the ternary nitride Ce_2MnN_3 . $\text{Ce}_2\text{MnN}_3\text{F}_{2-\delta}$ is the first quaternary nitride-fluoride to be reported and is

therefore the first member of a new class of compounds. The mechanism of the fluorination process has also not been encountered before and it consists of the insertion of two fluoride anions, which re-arrange the structure of the starting material by expanding the coordination of manganese from four to six and creating alternate layers of fully occupied interstitial sites. The structure of $\text{Ce}_2\text{MnN}_3\text{F}_{2-\delta}$ is therefore similar to that of $\text{Sr}_2\text{TiO}_3\text{F}_2$, although some fluorine deficiency (δ) has been suggested by powder neutron diffraction data and comparison between the solid-solid and solid-gas fluorination routes. Fluorine deficiency implies a $\text{Mn}^{2+}/\text{Mn}^{3+}$ mixed valency, which is supported by the value of the magnetic moment, $\mu_{\text{eff}} = 5.38(3) \mu_{\text{B}}$.

The $\text{Ce}_2\text{MnN}_3\text{F}_{2-\delta}$ phase itself forms under a very narrow range of reaction conditions and to-date has not been prepared as a pure material. Treatment of Ce_2MnN_3 with 10% F_2/N_2 gas in the temperature range of 95-115 °C for 15 minutes yields a sample of approximately 50% purity. Reaction of Ce_2MnN_3 with the solid fluorinating agents proved to be less successful with nitrides than structurally similar oxide materials. PVDF, XeF_2 and ZnF_2 require reaction temperatures too high, or conditions too harsh for satisfactory production of the quaternary nitride-fluoride in high yield, without the formation of significant quantities of ternary nitride-fluoride or binary fluoride, CeF_3 . Only CuF_2 produced $\text{Ce}_2\text{MnN}_3\text{F}_{2-\delta}$ in high yield.

6 Ammonolysis of Apatites

Apatite-type materials are frequently investigated for their oxide ion conductivity and, hence, applicability in areas such as solid oxide fuel cells (SOFCs), as an electrolyte.²⁹⁴ Hydrogen powered SOFCs are of enormous interest as devices for production of energy with little greenhouse gas emission. However, a number of problems linked to hydrogen production, storage and transportation are slowing down the larger scale use of SOFCs. Therefore, research into alternative fuel sources, to act as intermediate during the transition to the full use of hydrogen, is of importance. Reactions of ammonia gas with $\text{La}_{9.33}\text{Si}_6\text{O}_{26}$, $\text{La}_{8+x}\text{Sr}_{2-x}\text{M}_6\text{O}_{26+x/2}$ ($\text{M} = \text{Si}, \text{Ge}; 0 \leq x \leq 2$), $\text{La}_{9.67}\text{Si}_5\text{CoO}_{26}$ and $\text{La}_{10}\text{M}_5\text{CoO}_{26.5}$ ($\text{M} = \text{Si}, \text{Ge}$) were investigated in order to determine the suitability of these apatite-type materials for use in SOFCs fuelled by ammonia.

Fuel cells operate on a similar principle to batteries, however rather than containing a fixed quantity of reagents fuel cells require a continuous input of reagents and generate a continuous output of energy.¹¹ The fuel cell consists of an anode, electrolyte and a cathode connected in a circuit. Figure 6-1 (a) gives a representation of a hydrogen fuelled cell. Hydrogen is oxidised at the anode, travels through the electrolyte to the cathode to react with oxygen, resulting in a current. The advantage of this form of power production is that the only emission of the fuel cell is water. Fuel cells can also operate on a number of fuel sources; examples include methanol, ammonia and hydrazine.

Although most work in solid oxide fuel cells is focused on using hydrogen as a fuel, other sources offer a number of advantages. Hydrogen is a potentially explosive gas, making handling and transport difficult for large scale technological applications. However, ammonia for example, is a strong alternative as a carbon free fuel source with a similar performance to hydrogen.²⁹⁵ The use of ammonia in fuel cells can potentially yield only N_2 and H_2O emissions and hence reduce greenhouse gas production, relative to burning fossil fuels.^{295, 296} Ammonia is currently produced in large quantities, with a well established fertiliser infrastructure. It can be liquefied under relatively mild conditions (10 atmospheres of pressure, or at -33°C at atmospheric pressure) for transport or alternatively dissolved in water for safe delivery.²⁹⁵⁻²⁹⁷

Fuel cells are generally categorised on the basis of the electrolyte used. The five commonly used electrolytes give rise to five different types of fuel cell. These are alkaline fuel cells (AFC), polymeric electrolyte membrane fuel cells (PEMFC), phosphoric acid fuel cells (PAFC), molten carbonate fuel cells (MCFC) and solid oxide fuel cells (SOFC).²⁹⁸ A SOFC is shown in Figure 6-1 (b) and consist of a solid electrolyte that allows oxide anion transport. One family of compounds of particular interest as solid electrolytes, in SOFCs, are the apatite-type oxides, which show high oxide ion conductivities.

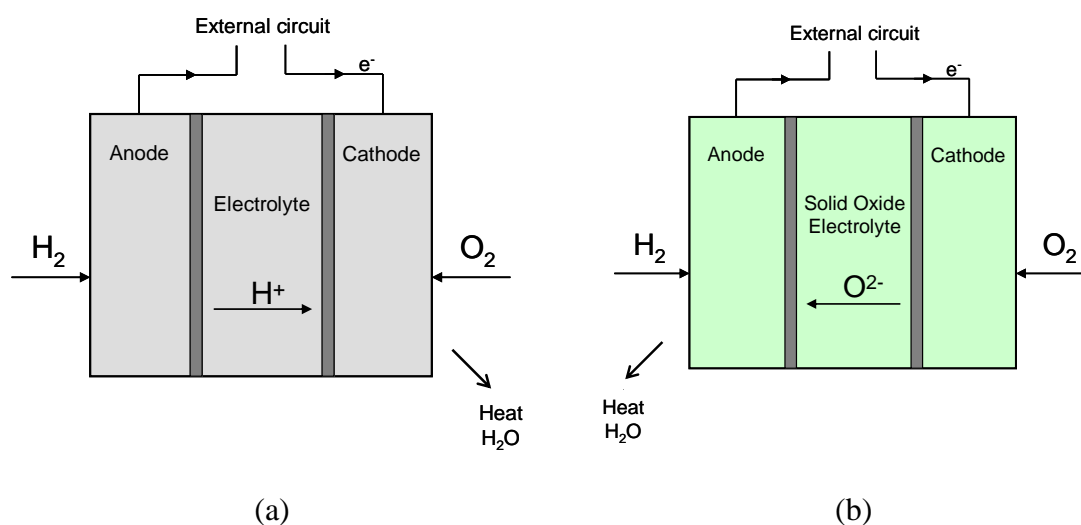


Figure 6-1. Representation of a (a) generic hydrogen fuel cell and (b) a SOFC.¹¹

Apatite materials take the general formula $A_{10}(MO_4)_6X_2$, where A is an alkali, alkaline earth, rare-earth metal, lead or bismuth, M is silicon, germanium, phosphorus or vanadium and X is oxygen, fluorine, chlorine, bromine, iodine or hydroxide. The apatite structure (Figure 6-2) consists of isolated MO_4 units with A cations in both nine and seven coordinate sites. The A cations run in linear chains along the *c*-axis and interleave the MO_4 tetrahedra. The X anions also run in linear chains along the *c*-axis located at the cell edge.

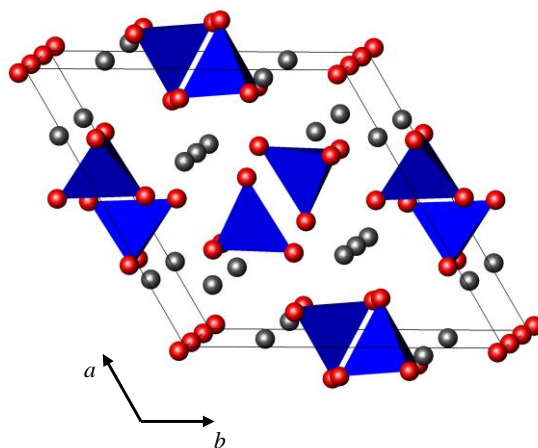


Figure 6-2. The apatite structure, $A_{10}(MO_4)_6X_2$. The grey and red spheres represent A and O/X respectively. The blue polyhedra are MO_4 tetrahedra.

Particularly high oxide ion conductivities have been observed for the $M = \text{Si/Ge}$ analogues and therefore these compounds are the focus of this work.²⁹⁴ Of particular interest has been the lanthanum silicate apatite system $\text{La}_{9.33+x}(\text{SiO}_4)_6\text{O}_{2+3x/2}$.²⁹⁴

$\text{La}_{9.33+x}(\text{SiO}_4)_6\text{O}_{2+3x/2}$ shows silicon in isolated $[\text{SiO}_4]^{4-}$ tetrahedra interleaved with lanthanum cations. In the oxygen stoichiometric material, $\text{La}_{9.33}\text{Si}_6\text{O}_{26}$, the remaining oxygen occupies the lanthanum channels running along the c -axis (Figure 6-3). This has the effect of forming linear chains of oxygen surrounded by three lanthanide cations in a triangular planar fashion. The lanthanum cations encompassing the “oxide channel” are themselves coordinated to seven anions and this lanthanum site remains fully occupied for all values of x . The remaining lanthanum sites are nine coordinate and show reduced occupancy when the stoichiometry of the apatite dictates cation vacancies i.e. $x < 2/3$. The number of vacancies is controlled by the initial stoichiometry of the metals in the synthesis.

The introduction of additional lanthanum in $\text{La}_{9.33+x}(\text{SiO}_4)_6\text{O}_{2+3x/2}$ ($x > 0$) results in incorporation of extra oxygen into the structure to maintain charge neutrality. The location of oxygen in this, and the oxygen stoichiometric ($x = 0$) apatites, has been the subject of much research and controversy. It is thought that interstitial and channel oxide anion migration plays a large role in the ionic conductivity of these materials.^{294,}

^{299, 300} In this way the apatite structure shows a fundamental difference to fluorite

(yttria-stabilised zirconia) and perovskite structures, in which ionic conductivity is due primarily to ion vacancy conduction.

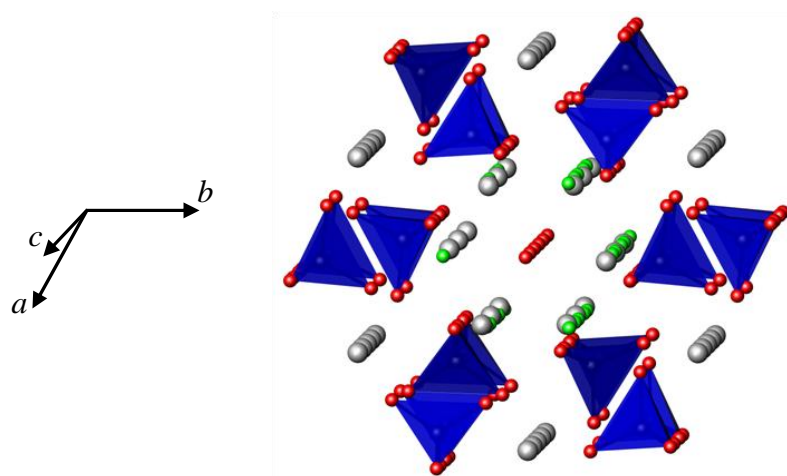


Figure 6-3. Structure of $\text{La}_{9.55}\text{Si}_6\text{O}_{26.32}$. The red and grey spheres represent oxygen and lanthanum respectively. The blue polyhedra highlight the tetrahedral coordination of silicon with four oxide anions. The green spheres show the interstitial oxide anion site, shown with full occupancy.

Powder neutron diffraction, performed by Sansom *et al.* on $\text{La}_{9.33}\text{Si}_6\text{O}_{26}$ ($P\bar{3}$, $a = 9.7248(1) \text{ \AA}$, $c = 7.1895(1) \text{ \AA}$), suggested that approximately 14% of the oxide channel anions are displaced from the ideal $(0, 0, \frac{1}{4})$ channel site to a site at $(0, 0, \approx 0.38)$.³⁰¹ Such a migration, a Frenkel-type defect, introduces anion vacancies into the oxide channel and allows for the possibility of vacancy migration along the channel and, therefore, the c -axis (Figure 6-4).^{299, 300}

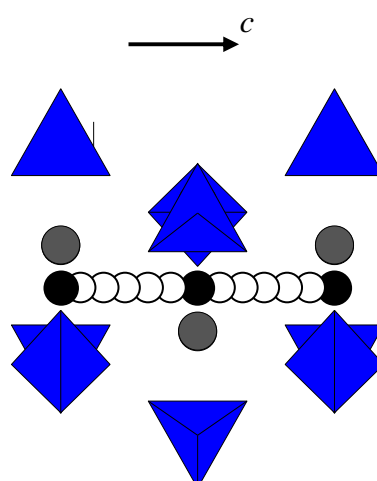


Figure 6-4. Oxygen vacancy migration along the oxide channels. O^{2-} is represented by the black spheres and its motion by the white spheres. The grey and black spheres show lanthanum and oxygen vacancies respectively. The blue polyhedra represent the MO_4 tetrahedra.

Through atomistic simulations an alternate conduction path was also suggested. Atomistic simulations by Islam *et al.* suggest that the most favourable interstitial anion site is in fact at the edge of the anion channel at (0.013, 0.233, 0.876).^{299, 300} Migration of the interstitial oxygen along the boundary of the oxide channel, in a sinusoidal-like manner (Figure 6-5) shows a lower activation energy (0.56 eV) than the vacancy mechanism (1.26 eV, calculated for $\text{La}_8\text{Sr}_2\text{Si}_6\text{O}_{26}$) and gives a good correlation to experimental values (0.65, 0.74 eV).^{299, 300}

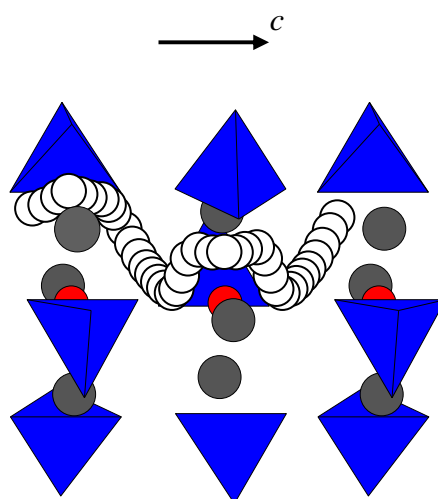


Figure 6-5. Representation of the interstitial oxygen migration (white spheres) along the oxide channels. The grey spheres show the lanthanum and the blue polyhedra represent the MO_4 tetrahedra.

As shown in Figure 6-5, the oxygen migration path runs close to the SiO_4 tetrahedra. The result is noticeable distortion away from the channel by 0.2 and 0.6-1.0 Å for silicon and adjacent oxide anions in the tetrahedra.^{299, 300} The distortion is thought to be directed towards the lanthanum sites showing cationic vacancies, highlighting the importance of such a feature.

The conduction path proposed by Islam *et al.* is also supported by conductivity measurements performed on single crystals of $\text{Ln}_{9.33}\text{Si}_6\text{O}_{26}$, suggesting anisotropic conduction.^{294, 299, 300} It is seen that, the conductivity of these materials is far higher along *c*. However, conduction in other directions is still favourable and may indicate other mechanisms may also be involved.

The conductivity of polycrystalline $\text{La}_{9.33}\text{Si}_6\text{O}_{26}$ is quite high $\sigma = 1.1 \times 10^{-4} \text{ S cm}^{-1}$ (at 500 °C), but generally improves with increasing values of x in $\text{La}_{9.33+x}(\text{SiO}_4)_6\text{O}_{2+3x/2}$. $\text{La}_{10}\text{Si}_6\text{O}_{27}$ ($x = 0.66$) for example shows a conductivity of $4.3 \times 10^{-3} \text{ S cm}^{-1}$ (at 500 °C).²⁹⁴ The result of increasing lanthanum content is an increase in oxygen stoichiometry for charge balancing reasons. Powder neutron diffraction performed on $\text{La}_{9.55}\text{Si}_6\text{O}_{26.32}$ ($P6_3/m$, $a = 9.7256(1) \text{ \AA}$, $c = 7.1863(1) \text{ \AA}$) by León-Reina *et al.*, implied that the additional oxygen anions reside at the same interstitial anion position as in $\text{La}_{9.33}\text{Si}_6\text{O}_{26}$, close to the oxide channel periphery (Figure 6-3).³⁰²

Hence, an increase in x with $\text{La}_{9.33+x}(\text{SiO}_4)_6\text{O}_{2+3x/2}$ generally results in an increasing number of anions at the interstitial site, enhancing the anion migration along this channel and, therefore, improving conductivity.

Aliovalent substitution on the lanthanum site of the silicates, with alkaline earth metals is possible. Substituting strontium on to the lanthanum site, for example, demonstrates that, firstly, reducing the number of cation vacancies acts to reduce the conductivity of the system and secondly oxygen excess and interstitial oxide anions act to counter this reduction in conductivity. This is seen with the stoichiometric apatite $\text{La}_8\text{Sr}_2\text{Si}_6\text{O}_{26}$, which shows a low conductivity of $5.6 \times 10^{-7} \text{ S cm}^{-1}$ (800 °C) and $\text{La}_9\text{SrSi}_6\text{O}_{26.5}$, showing a conductivity of $1.2 \times 10^{-3} \text{ S cm}^{-1}$.^{294, 303} Powder neutron diffraction by Sansom *et al.*, on $\text{La}_8\text{Sr}_2\text{Si}_6\text{O}_{26}$, indicated that unlike $\text{La}_{9.33}\text{Si}_6\text{O}_{26}$ the doped material does not show any Frenkel-type defects.³⁰¹

Transition metal doping can take place on both La^{3+} and Si^{4+} cation sites. In the case of cobalt Tolchard *et al.* showed that when doped onto the lanthanum site the cobalt adopts a 2+ oxidation state and partially substitutes onto the nine coordinate lanthanum position. When on the silicon site, however, cobalt shows 3+ oxidation state.³⁰⁴ The choice of cation site is dependent simply on the choice of composition/stoichiometry of the starting reagents.³⁰⁴

An alternative system to the silicates, which is also of particular interest in terms of anionic conduction, is the germanate system $\text{La}_{9.33+x}(\text{GeO}_4)_6\text{O}_{2+3x/2}$. Initial reports of conductivity of the germanates indicated higher values than those seen in the silicates,²⁹⁴ however, further reports have shown inconsistencies attributed to problems

with unwanted secondary phases (La_2GeO_5) and GeO_2 volatility issues at temperatures in excess of 1250 °C, giving rise to higher La:Ge ratios than intended.²⁹⁴

The $\text{La}_{9.33+x}(\text{GeO}_4)_6\text{O}_{2+3x/2}$ system has been shown by León-Reina *et al.* to exist in the range $0.19 \leq x \leq 0.42$,³⁰⁵ germanates within the $0.19 \leq x \leq 0.27$ range show hexagonal symmetry, with the space group $P6_3/m$. Germanates in the $0.33 \leq x \leq 0.42$ range show triclinic symmetry, $P\bar{1}$.^{306, 307} This transition to triclinic symmetry is attributed to the displacement of interstitial oxide anions resulting in greater structural distortion of the GeO_4 tetrahedra than is observed in the silicate counterparts.³⁰⁵ In fact, the silicate systems generally do not show a hexagonal to triclinic transition. The transition to a triclinic structure may be detrimental to the use of these materials as ionic conductors as, unlike in the silicate examples, increasing values of x has been shown to yield a decrease in conductivity for the germanates.³⁰⁵ However, Abram *et al.* have suggested that at higher temperatures ($\sim 500\text{-}830$ °C) the triclinic phases undergo a transition to hexagonal symmetry with an improvement in conductivity.³⁰⁷

Neutron diffraction, performed by León-Reina *et al.*, on $\text{La}_{9.60}(\text{GeO}_4)_6\text{O}_{2.4}$, indicated the same interstitial oxide anion position at the oxide channel periphery as that found in the silicates.³⁰² However, atomistic simulations by Kendrick *et al.*, on $\text{La}_{9.33}(\text{GeO}_4)_6\text{O}_2$, demonstrated a different ion migration pathway for these interstitial anions.³⁰⁸ This migration pathway is down the c -axis, between the GeO_4 tetrahedra in a “fan-like” manner.³⁰⁸ Figure 6-6 shows the proposed migration pathway. The germanium coordination is essentially extended to five, with significant local distortion of the GeO_4 tetrahedra. The formation and breaking of “ GeO_9 ” units, connecting two tetrahedra via interstitial oxygen, between adjacent channels, may also provide a migration path in the ab plane.³⁰⁸

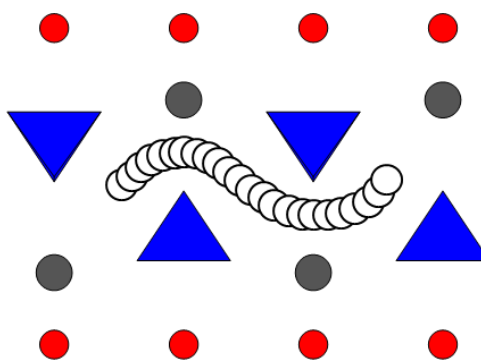


Figure 6-6. Representation of the oxide anion migration (white spheres) along c in $\text{La}_{9.33}\text{Ge}_6\text{O}_{26}$. The grey and red spheres represent lanthanum and oxygen respectively. The blue polyhedra represent GeO_4 tetrahedra.

In order to investigate further the influence of cationic vacancies, interstitial oxygen content and structural symmetry on these materials and to attempt to improve their conductive properties, a large number of investigations have been undertaken.²⁹⁴ These include cationic substitution on both the lanthanum and silicon/germanium sites, exploiting the huge diversity of the structure and wide range of possible substitutional possibilities.

In general, fewer doping studies have been carried out in the germanate apatite materials, principally due to the difficulties experienced with unwanted secondary phases and GeO_2 volatility. However, as synthetic routes have improved, a range of studies on doping in germanates have been published. In general it has been found that doping onto the lanthanum site, with alkaline earth metals, can stabilise the hexagonal symmetry.^{294, 306} Substitution of cobalt onto the germanium site is also possible, although in this case there is currently no evidence of substitution onto the lanthanum site.

An aspect of ammonia use in SOFCs, which has not had considerable attention, is the reaction of ammonia with the electrolyte under normal operating conditions. Such a reaction could result in the formation of oxynitride materials and have a negative effect on the operating efficiency of the fuel cell. This type of oxynitride preparation has been seen with the incorporation of 4.5 mol% nitrogen into CeO_2 at temperatures between 500-900 °C.³⁰⁹ Therefore, the influence of these reactions is considered here, in the case of silicate and germanates apatite-type oxide ion conductors.

Here, in collaboration with Slater and co-workers at Birmingham University, we attempt to investigate the effect of ammonia action on a number of apatite materials to determine if indeed these compounds will react with ammonia under fuel cell operating temperatures (600-1000 °C), to yield oxynitrides, and to speculate as to the likely effect such a reaction would have on the operational effectiveness of these materials.

A number of apatite materials were considered, $\text{La}_{9.33}\text{Si}_6\text{O}_{26}$, $\text{La}_{8+x}\text{Sr}_{2-x}\text{M}_6\text{O}_{26+x/2}$ ($\text{M} = \text{Si}, \text{Ge}; 0 \leq x \leq 2$), $\text{La}_{9.67}\text{Si}_5\text{CoO}_{26}$ and $\text{La}_{10}\text{M}_5\text{CoO}_{26.5}$ ($\text{M} = \text{Si}, \text{Ge}$). These apatite materials cover a wide range of important structural features and allow the investigation of a number of characteristics. Investigation of $\text{La}_{9.33}\text{Si}_6\text{O}_{26}$ allows us to examine the likely effect of ammonia treatment on the occurrence of Frenkel-type defects, shown by this material. The strontium doped materials show no cationic vacancies, but cover a range of stoichiometries and occupancies of interstitial anion sites and the influence of ammonolysis of anion excess apatites may be addressed. Finally, $\text{La}_{9.67}\text{Si}_5\text{CoO}_{26}$, $\text{La}_{10}\text{M}_5\text{CoO}_{26.5}$ ($\text{M} = \text{Si}, \text{Ge}$) samples show a cation centre, which may support a deviation in oxidation state upon treatment in a reducing atmosphere. It has been seen that cobalt in particular has the ability to show both 2+ and 3+ oxidation states in apatite materials, with a choice of lanthanum and silicon/germanium sites respectively. Therefore, through the use of XAFS, investigations of both cobalt coordination and oxidation state were investigated.

6.1 Ammonolysis of $\text{La}_{9.33}\text{Si}_6\text{O}_{26}$

6.1.1 Experimental

6.1.1.1 Preparation

Samples of $\text{La}_{9.33}\text{Si}_6\text{O}_{26}$ were provided by Slater and co-workers.^{§§} These were prepared via the solid state reaction of a stoichiometric mixture of La_2O_3 and SiO_2 at 1350 °C. The mixture was heated twice for 12 hours with intermittent re-grinding.

^{§§}P. R. Slater, A. Orera and E. Kendrick, School of Chemistry, University of Birmingham, Birmingham, England.

$\text{La}_{9.33}\text{Si}_6\text{O}_{26}$ samples were heated in flowing ammonia ($14 \text{ dm}^3\text{hr}^{-1}$) at $600 \text{ }^\circ\text{C}$, $800 \text{ }^\circ\text{C}$ and $1000 \text{ }^\circ\text{C}$ for 20 hours, using the apparatus described in section 2.2.2.

6.1.1.2 Characterisation

PXRD was performed, in Hull, using a Siemens D5000 powder diffractometer and $\text{Cu K}\alpha$ radiation. The nitrogen content was determined, by Slater and co-workers, through thermogravimetric analysis with a TA instrument SDT 600 thermal analyser. The samples, previously reacted in ammonia, were heated in air at $20 \text{ }^\circ\text{C min}^{-1}$ to $1100 \text{ }^\circ\text{C}$. This analysis, for N^{3-} content, was limited to single phase samples.

One example of a TGA pattern, collected upon heating an oxynitride in air, is given in Figure 6-7. Results specific to the ammoniation of $\text{La}_{9.33}\text{Si}_6\text{O}_{26}$, $\text{La}_{8+x}\text{Sr}_{2-x}\text{M}_6\text{O}_{26+x/2}$ ($\text{M} = \text{Si}, \text{Ge}; 0 \leq x \leq 2$), $\text{La}_{9.67}\text{Si}_5\text{CoO}_{26}$ and $\text{La}_{10}\text{M}_5\text{CoO}_{26.5}$ ($\text{M} = \text{Si}, \text{Ge}$) are given in sections 6.1.2.2, 6.2.2.2 and 6.3.2.2.5 respectively.

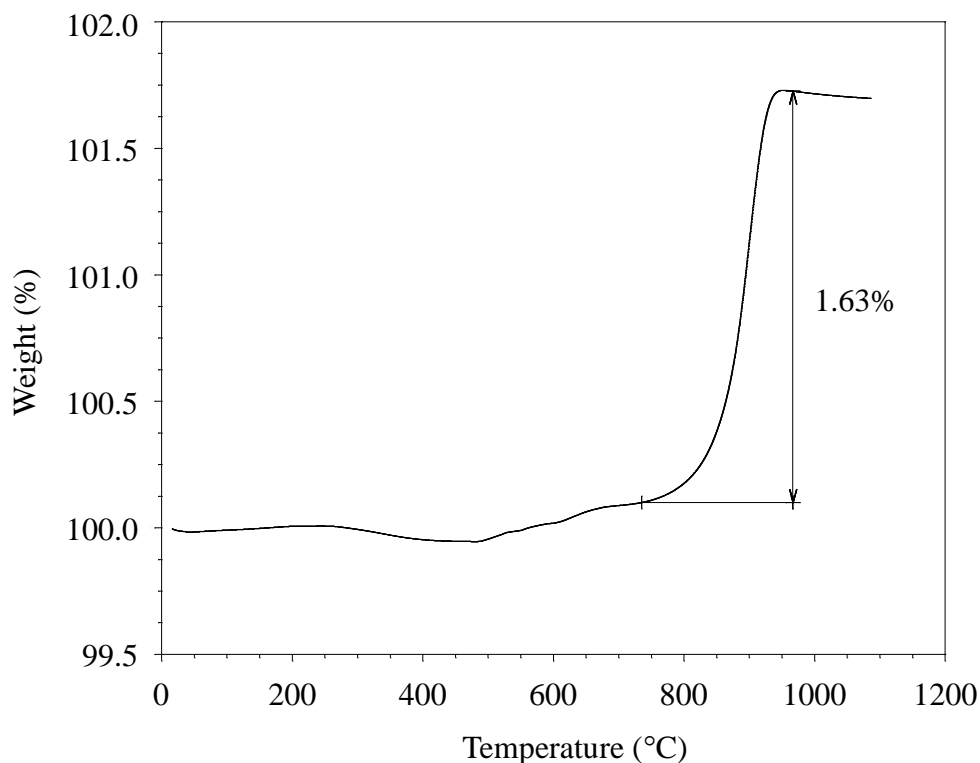


Figure 6-7. TGA pattern for $\text{La}_{9.33}\text{Si}_6\text{O}_{26}$ after reaction with NH_3 at $950 \text{ }^\circ\text{C}$.

The TGA pattern shows an increase in weight above 700 °C. This weight increase is attributed to an increase in anion content i.e. the substitution of three O²⁻ anions for two N³⁻ anions in order to maintain charge balance within the compound. If N³⁻ enters the oxide lattice during the reaction with ammonia, at high temperature, then upon heating in air the oxynitride materials will undergo complete conversion back to the starting oxide. PXRD, performed on the oxynitride before and after TGA, indicating that the apatite structure is maintained throughout. Therefore, the nitrogen content in the oxynitrides can be calculated from the weight increase.

The ratio of starting mass to final mass is equal to the ratio between the two molecular formulae; the RMM of the oxynitride and RMM of the oxide, as shown in equation (6-1).

$$\frac{\text{starting mass}}{\text{final mass}} = \frac{\text{RMM}_{\text{oxynitride}}}{\text{RMM}_{\text{oxide}}} \quad (6-1)$$

The formula of the oxynitride, formed from heating La_{9.33}Si₆O₂₆ in ammonia, can be written as La_{9.33}Si₆O_{26-3x}N_{2x}, reflecting the substitution of three O²⁻ by two N³⁻, and the RMM taken as:

$$\text{RMM}_{\text{La}_{9.33}\text{Si}_6\text{O}_{26}} + (2\text{RAM}_{\text{N}} - 3\text{RAM}_{\text{O}})x = \text{RMM}_{\text{La}_{9.33}\text{Si}_6\text{O}_{26-3x}\text{N}_{2x}} \quad (6-2)$$

Thus, a 1.63% mass increase, observed in Figure 6-7, gives a value of $x = 1.5$:

$$\frac{\text{starting mass} \times \text{RMM}_{\text{La}_{9.33}\text{Si}_6\text{O}_{26}}}{\text{final mass}} = \text{RMM}_{\text{La}_{9.33}\text{Si}_6\text{O}_{26}} + (2\text{RAM}_{\text{N}} - 3\text{RAM}_{\text{O}})x$$

$$\frac{100 \times 1880.4854}{101.63} - 880.4854 = -19.9848x$$

$$x = 1.5$$

The resulting formula for the oxynitride is La_{9.33}Si₆O_{21.5}N₃.

Time-of-flight neutron diffraction data were collected by Slater and co-workers at the POLARIS diffractometer at the ISIS pulsed spallation source, Rutherford Appleton Laboratory, UK. Approximately 1g of the $\text{La}_{9.33}\text{Si}_6\text{O}_{26}$ sample, reacted in ammonia at 950 °C, was placed into a vanadium can and diffraction data collected at room temperature.

^{29}Si NMR data were obtained from the Solid-State NMR Service at Durham University. A Varian Unity Inova spectrometer operating at 59.56 MHz was used with a direct-polarisation experiment with a 120 s recycle delay. The chemical shifts are taken relative to tetramethylsilane.

6.1.2 Results and Discussion

6.1.2.1 Powder X-ray Diffraction (PXRD)

Rietveld refinement was performed on $\text{La}_{9.33}\text{Si}_6\text{O}_{26}$ based on a model by Iwata *et al.* in the space group $P6_3/m$.³¹⁰ The background was modelled using the shifted Chebyshev function with 26 terms and the peak shape by a multi-term Simpson's rule integration of the pseudo-Voigt.^{241, 242} No absorption correction was applied. The parameters refined were: the cell parameters (a , b , c), one zero point, one scale factor, twelve atomic coordinates, seven isotropic thermal parameters, five profile parameters. The refinement parameters are summarised in Table 6-1 and the refinement profile is shown in Figure 6-8.

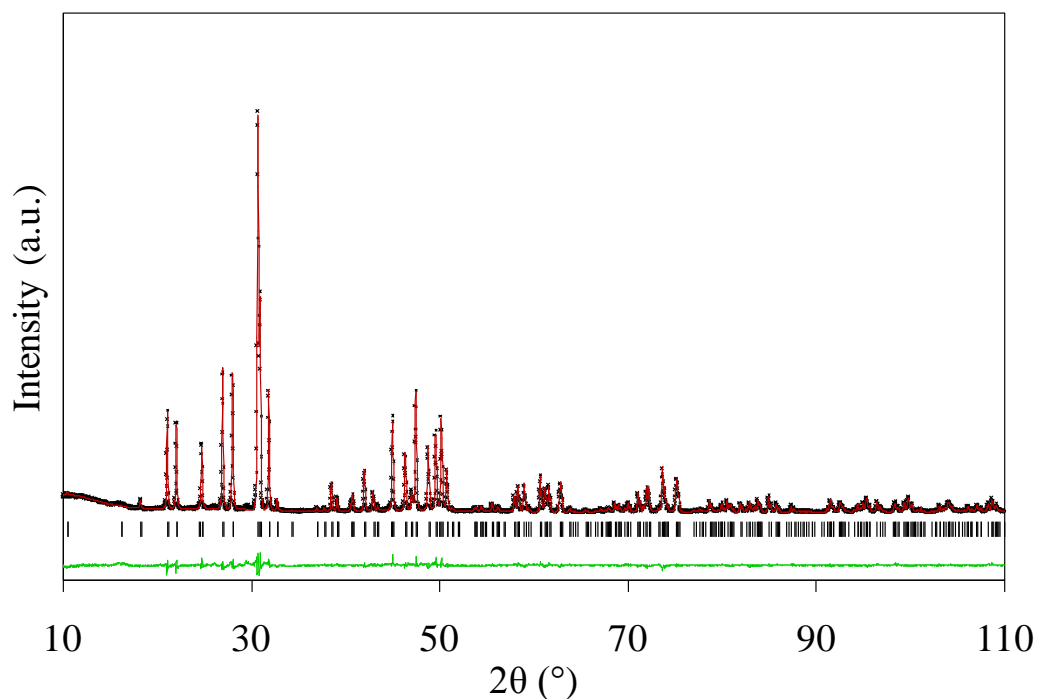


Figure 6-8. PXRD profiles for $\text{La}_{9.33}\text{Si}_6\text{O}_{26}$ at room temperature, showing observed (+), calculated (red line) and difference pattern (green line). Tick marks indicate reflection positions for $\text{La}_{9.33}\text{Si}_6\text{O}_{26}$.

Formula	$\text{La}_{9.33}\text{Si}_6\text{O}_{26}$	
Space Group	$P6_3/m$ (no. 176)	
	PXRD data	Iwata <i>et al.</i> ³¹⁰
a (Å)	9.7256(1)	9.71872(6)
b (Å)	9.7256(1)	9.71872(6)
c (Å)	7.1922(1)	7.18733(3)
V (Å ³)	589.15(2)	587.91
Z	1	
Calculated density (g cm ⁻³)	5.300	
Profile function	Pseudo-Voigt	
No. of profile points	3366	
No. of parameters refined	30	
R_{wp}	0.0764	
R_{p}	0.0560	
χ_{red}^2	3.039	

Table 6-1. Summary of refinement data and lattice parameters for $\text{La}_{9.33}\text{Si}_6\text{O}_{26}$ at room temperature.

The cell parameters are consistent with those from the literature and the sample is free from secondary phases.³¹⁰ Samples of $\text{La}_{9.33}\text{Si}_6\text{O}_{26}$ were heated in ammonia at 600 °C, 800 °C and 950 °C. Comparisons between $\text{La}_{9.33}\text{Si}_6\text{O}_{26}$ and the samples ammoniated at 600 °C, 800 °C and 950 °C are shown in Figure 6-9.

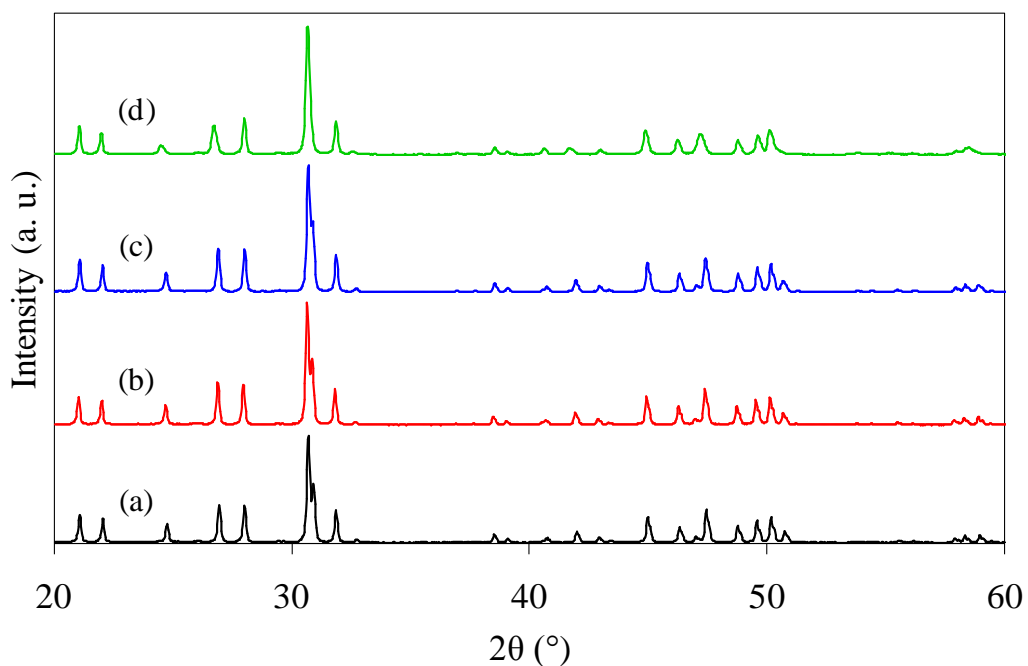


Figure 6-9. PXRD patterns for (a) $\text{La}_{9.33}\text{Si}_6\text{O}_{26}$, (b) $\text{La}_{9.33}\text{Si}_6\text{O}_{26}$ after reaction with NH_3 at 600 °C, (c) 800 °C and (d) 950 °C.

Figure 6-9 suggests that the overall apatite structure is maintained in all cases of ammonolysis, although there is evidence of increased peak broadening at higher temperatures and minor changes in peak position. In addition, the high temperature ammonolysis reactions, in particular the reaction of $\text{La}_{9.33}\text{Si}_6\text{O}_{26}$ with ammonia at 950 °C, show anisotropic peak broadening. Peaks of index $(hk0)$ appear sharp, whilst peaks of index $l > \text{one}$ are broader (Figure 6-10). The anisotropic peak broadening is discussed later in the section.

Due to the similar X-ray scattering power of nitrogen and oxygen it is not possible to determine the exact structure and the extent of nitrogen incorporation through X-ray diffraction alone. However, Le Bail fitting was performed using the PXRD data to determine the lattice dimensions. These are shown in Table 6-2.

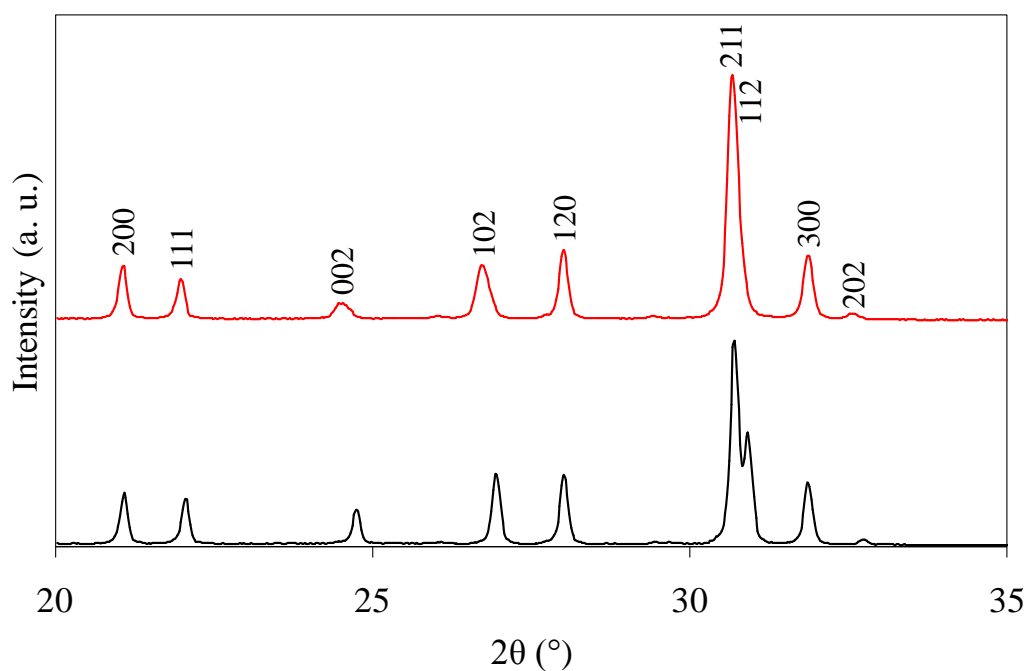


Figure 6-10. PXRD patterns of $\text{La}_{9.33}\text{Si}_6\text{O}_{26}$ (black) before and after reaction with NH_3 at 950 °C (red). The Miller indices are indicated on the peaks.

Reaction conditions	Proposed formula ^{***}	a (Å)	c (Å)
$\text{La}_{9.33}\text{Si}_6\text{O}_{26}$	$\text{La}_{9.33}\text{Si}_6\text{O}_{26}$	9.7260(1)	7.1929(1)
$\text{La}_{9.33}\text{Si}_6\text{O}_{26} + \text{NH}_3$ 600 °C	$\text{La}_{9.33}\text{Si}_6\text{O}_{26}$	9.7231(1)	7.1942(1)
$\text{La}_{9.33}\text{Si}_6\text{O}_{26} + \text{NH}_3$ 800 °C	$\text{La}_{9.33}\text{Si}_6\text{O}_{25.2}\text{N}_{0.5}$	9.7218(1)	7.2030(1)
$\text{La}_{9.33}\text{Si}_6\text{O}_{26} + \text{NH}_3$ 950 °C	$\text{La}_{9.33}\text{Si}_6\text{O}_{21.5}\text{N}_3$	9.7067(3)	7.2456(3)

Table 6-2. Lattice parameters for $\text{La}_{9.33}\text{Si}_6\text{O}_{26}$ before and after reaction with NH_3 , derived from Le Bail extraction performed using PXRD data.

The small differences in the cell dimensions may be the result of varying anion content due to nitrogen/oxygen substitution, with a reduction in a and increase in c as N^{3-} is incorporated into the apatite.

TGA was used to identify the extent of nitrogen assimilation into these materials.

^{***} Calculated from TGA (Table 6-3).

6.1.2.2 Thermogravimetric Analysis (TGA)

Figure 6-11 shows the TGA patterns for the reactions of $\text{La}_{9.33}\text{Si}_6\text{O}_{26}$ with ammonia at 600 °C (black), 800 °C (red) and 950 °C (green).

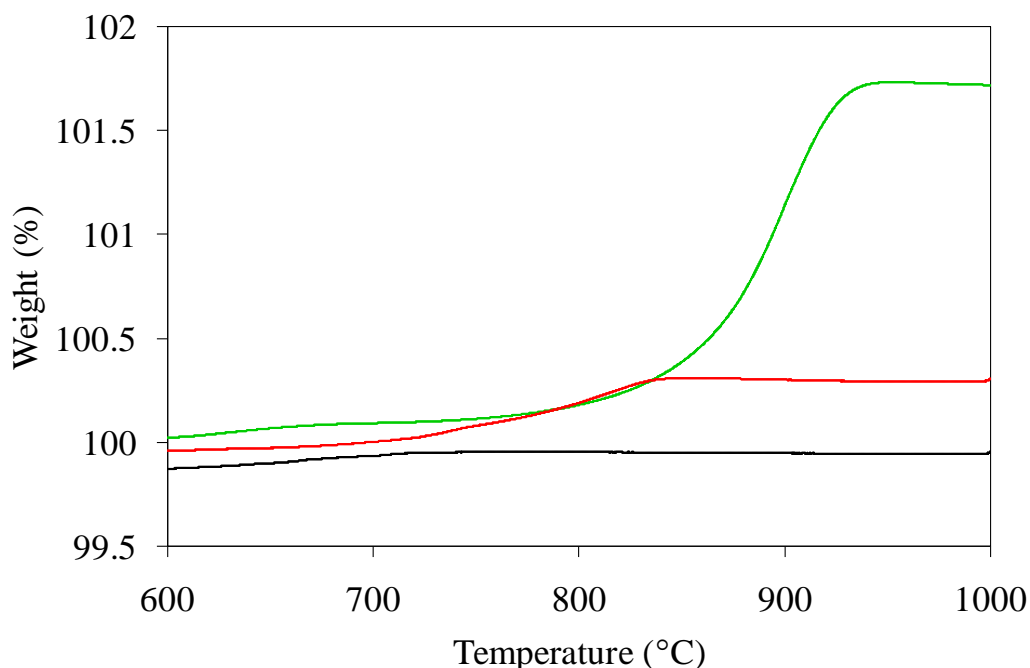


Figure 6-11. TGA patterns for $\text{La}_{9.33}\text{Si}_6\text{O}_{26}$ after reaction with NH_3 at 600 °C (black), 800 °C (red) and 950 °C (green).

The TGA patterns of the samples ammoniated at 800 and 950 °C show an increase in weight above 700 °C. This weight increase is attributed to an increase in anion content, i.e. the substitution of three O^{2-} anions for two N^{3-} anions, and confirms nitrogen incorporation into the apatite. Under this assumption, the nitrogen content in the oxynitrides can be calculated (Table 6-3). An example of the calculation is shown in section 6.1.1. It can be seen that increasing the temperature of ammonolysis acts to increase the extent of $\text{O}^{2-}/\text{N}^{3-}$ substitution.

Reaction conditions	Weight increase (%)	Chemical formula
$\text{La}_{9.33}\text{Si}_6\text{O}_{26} + \text{NH}_3$ 600 °C	0.00	$\text{La}_{9.33}\text{Si}_6\text{O}_{26}$
$\text{La}_{9.33}\text{Si}_6\text{O}_{26} + \text{NH}_3$ 800 °C	0.28	$\text{La}_{9.33}\text{Si}_6\text{O}_{25.2}\text{N}_{0.5}$
$\text{La}_{9.33}\text{Si}_6\text{O}_{26} + \text{NH}_3$ 950 °C	1.63	$\text{La}_{9.33}\text{Si}_6\text{O}_{21.5}\text{N}_3$

Table 6-3. Proposed chemical formula for the reactions of $\text{La}_{9.33}\text{Si}_6\text{O}_{26}$ with NH_3 derived from TGA.

The TGA patterns show a number of additional features, which are attributed to absorption and desorption of other simple molecules. Figure 6-7 illustrates a small mass loss (< 0.1%) occurring above 250 °C. Such a mass loss is thought to be the result of a small amount of water absorbed by the sample. The emission of water from oxynitride materials, upon heating, has been previously observed in the temperature range of 200 - 400 °C.^{311, 312} The TGA patterns of all the ammoniated apatite samples also show a small weight increase (~ 0.1 %) between 500-700 °C and a small reduction above 800 °C. This may be the result of CO₂ absorption at temperatures between 500 - 700 °C and elimination upon further heating.

6.1.2.3 Powder Neutron Diffraction (PND)

PND and structural characterisation was performed by Kendrick *et al.*³¹³ The results obtained in that study are outlined in this section. As in the previous examples of neutron diffraction performed on apatite materials two space groups were considered, $P6_3$ and $P6_3/m$. Of these space groups $P6_3$ gave the most satisfactory fit to the data ($\chi^2 = 2.283$ and 2.574 for $P6_3$ and $P6_3/m$ respectively). Rietveld refinement on $\text{La}_{9.33}\text{Si}_6(\text{O,N})_x$ was modelled based on $\text{La}_{9.67}\text{Si}_6\text{O}_{26.5}$,³¹⁴ with suitably modified site occupancies. Upon refinement, it became apparent that there was unfitted nuclear density located at the La(1)/(2) sites. The occupancies of the lanthanum sites were, therefore, allowed to refine. The occupancies of the lanthanum sites (Table 6-4) imply a higher La:Si ratio of 9.7:6 than would be expected (9.33:6). This increased ratio is likely to be the result of silicon loss. As no crystalline impurities were evident in the PXRD patterns after treatment in ammonia, the silicon may be present as an amorphous silicon rich impurity. Alternatively, silicon may be lost through silicon oxide volatilisation as observed by Shaula *et al.* when treating $\text{La}_{9.83}\text{Si}_{6-x}\text{Al}_x\text{O}_{27-y}$ under reducing atmospheres, with consequent segregation of La_2O_3 observed by SEM and XRD analysis.³¹⁵ There was, however, no evidence of La_2O_3 in the XRD and ND performed on $\text{La}_{9.33}\text{Si}_6(\text{O,N})_x$.

All the anion sites were initially modelled as oxygen sites. This model failed to satisfactorily account for intensity of all the peaks. Refinement of the occupancies on

these anion sites indicated an increase in occupancy above 1.0 for the O(1), O(2) and O(4). The neutron scattering length of nitrogen is larger than oxygen, 9.36×10^{-15} m and 5.803×10^{-15} m respectively, indicating that N was also present on these anion sites, giving rise to increased peak intensity. The formula suggested from TGA was $\text{La}_{9.33}\text{Si}_6\text{O}_{21.5}\text{N}_3$. This implies a total anion content of 24.5, a reduction in anion content compared to the stoichiometric apatite, which shows a total nominal anion content of 26. A likely location of the anion vacancies would be the channel anion site O(5), leaving the SiO_4 tetrahedra intact. The occupancy of this site refined to a value of 1.01(1), however if this site is modelled as N (site N5) anion vacancies are introduced. It is hypothesised that the 38% vacancies within the anion channel and distortions associated with local ordering of vacancies may be the cause of the anisotropic peak broadening observed in the PXRD patterns of the ammoniated sample. This hypothesis is supported by the absence of “1 > one” peak broadening when these vacancies are not present (sections 6.2 and 6.3). The residual fit parameters were $R_{\text{wp}} = 0.0248$, $R_p = 0.0434$, $\chi^2 = 2.283$ and the final atomic coordinates are shown in Table 6-4. The data suggests a final composition of $\text{La}_{9.7(1)}\text{Si}_6\text{O}_{22.6(2)}\text{N}_{2.7(2)}$. This stoichiometry is consistent with the values obtained through TGA, within experimental error.

Atom	Site	x	y	z	$100 \times U_{\text{iso}}$	Occ.
La(1)	2b	1/3	2/3	-0.001(2)	0.7(1)	0.94(4)
La(2)	2b	2/3	1/3	0.000(2)	0.6(1)	0.91(4)
La(3)	6c	0.2325(1)	-0.0123(1)	0.247(2)	0.57(2)	1.0
Si	6c	0.4019(2)	0.3719(2)	0.25	0.32(3)	1.0
O(1)/N(1)	6c	0.3227(2)	0.4859(2)	0.250(2)	0.89(4)	0.92(1)/0.08(1)
O(2)/N(2)	6c	0.5963(2)	0.4701(2)	0.250(2)	0.71(4)	0.95(1)/0.05(1)
O3	6c	0.3582(4)	0.2581(4)	0.434(1)	0.80(6)	1.0
O(4)/N(4)	6c	0.3323(3)	0.2504(4)	0.074(1)	0.98(6)	0.89(3)/0.11(3)
O(5)/N5	2a	0	0	0.250(3)	^a	0/0.62(1)

^a Anisotropic thermal displacement parameters, N5 ($100 \times U_{ij}/\text{\AA}^2$); U_{11} 0.88(7), U_{22} 0.88(7), U_{33} 1.7(2), U_{12} 0.44(4).

Table 6-4. Structural parameters for $\text{La}_{9.7(1)}\text{Si}_6\text{O}_{22.6(2)}\text{N}_{2.7(2)}$ derived from PND collected at room temperature.

Upon ammonolysis of $\text{La}_{9.33}\text{Si}_6\text{O}_{26}$ nitrogen is incorporated into the silicate tetrahedra and the anion channels, which run along the *c*-axis. The result of this is a tilting/distortion of the tetrahedra in $\text{La}_{9.7(1)}\text{Si}_6\text{O}_{22.6(2)}\text{N}_{2.7(2)}$, highlighted in Figure 6-12, with a modification of the lanthanum coordination sphere.

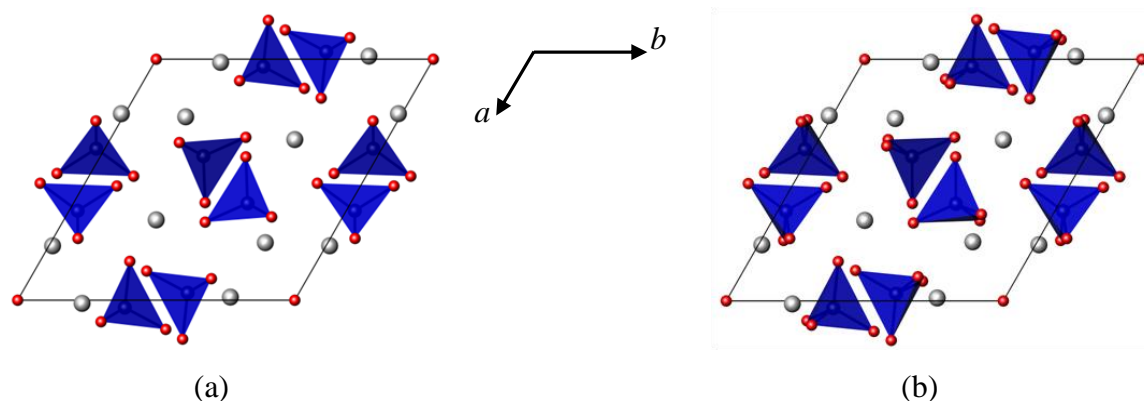


Figure 6-12. Structures of (a) $\text{La}_{9.33}\text{Si}_6\text{O}_{26}$ and (b) $\text{La}_{9.7(1)}\text{Si}_6\text{O}_{22.6(2)}\text{N}_{2.7(2)}$. The grey and red spheres represent lanthanum and oxygen/nitrogen respectively. The blue polyhedra are centred on silicon.

The La(1)-O(1)/N(1) and La(1)-O(2)/N(2) bond lengths of $\text{La}_{9.7(1)}\text{Si}_6\text{O}_{22.6(2)}\text{N}_{2.7(2)}$ are similar to La(2)-O(1)/N(1) and La(2)-O(2)/N(2), however, the result of the tilting of the $\text{Si}(\text{O},\text{N})_4$ tetrahedra is a lengthening of the La(2)-O(4)/N(4) bond lengths compared to La(1)-O(3) (Table 6-5). Consequently, while La(1) shows a coordination of nine, La(2) shows a reduced coordination of six (Figure 6-13).

Bond lengths (Å)			
La(1)-O(1)/N(1)	$3 \times 2.49(1)$	La(2)-O(1)/N(1)	$3 \times 2.48(1)$
La(1)-O(2)/N(2)	$3 \times 2.53(1)$	La(2)-O(2)/N(2)	$3 \times 2.53(1)$
La(1)-O(3)	$3 \times 2.743(3)$	La(2)-O(4)/N(4)	$3 \times 2.975(3)$
La(3)-O(1)/N(1)	2.739(2)	Si-O(1)/N(1)	1.632(2)
La(3)-O(2)/N(2)	2.502(2)	Si-O(2)/N(2)	1.634(2)
La(3)-O(3)	2.647(4)	Si-O(3)	1.644(8)
La(3)-O(4)/N(4)	2.556(4)	Si-O(4)/N(4)	1.636(8)
	2.492(5)		
La(3)-O(5)/N(5)	2.318(1)		

Table 6-5. Selected bond lengths for $\text{La}_{9.7(1)}\text{Si}_6\text{O}_{22.6(2)}\text{N}_{2.7(2)}$.

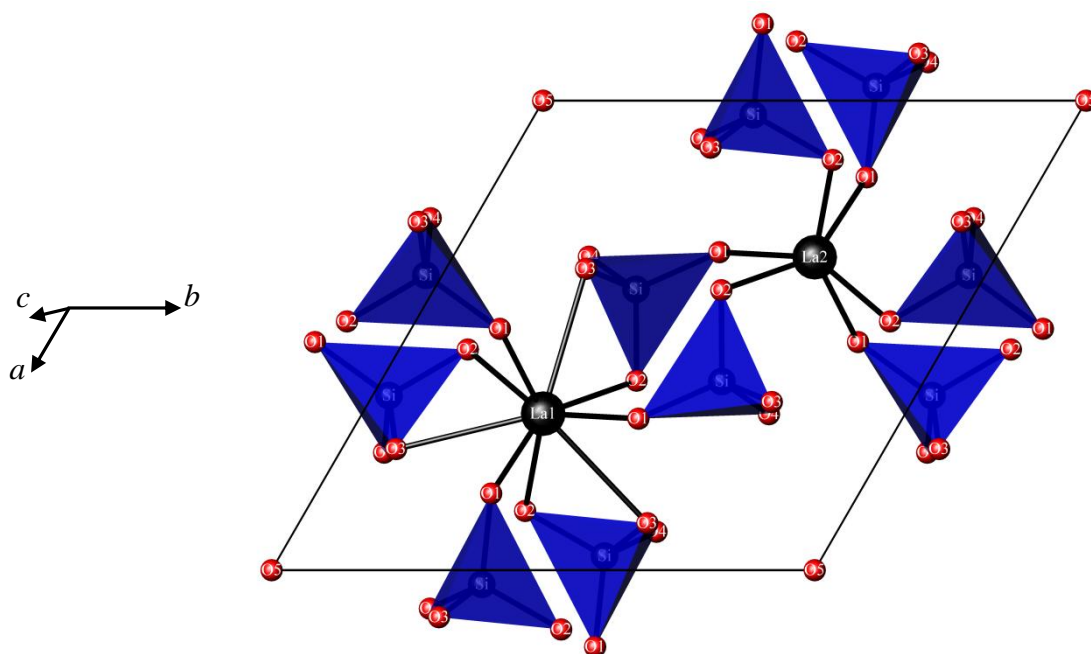


Figure 6-13. Structure of $\text{La}_{9.7(1)}\text{Si}_6\text{O}_{22.6(2)}\text{N}_{2.7(2)}$ highlighting the La(1)/La(2) coordination. The grey, black and red spheres represent La(2), La(1) and oxygen/nitrogen respectively. The blue polyhedra are centred on silicon.

6.1.2.4 ^{29}Si Nuclear Magnetic Resonance (NMR)

The ^{29}Si NMR data for $\text{La}_{9.33}\text{Si}_6\text{O}_{26}$ and $\text{La}_{9.7(1)}\text{Si}_6\text{O}_{22.6(2)}\text{N}_{2.7(2)}$ are shown in Figure 6-14.

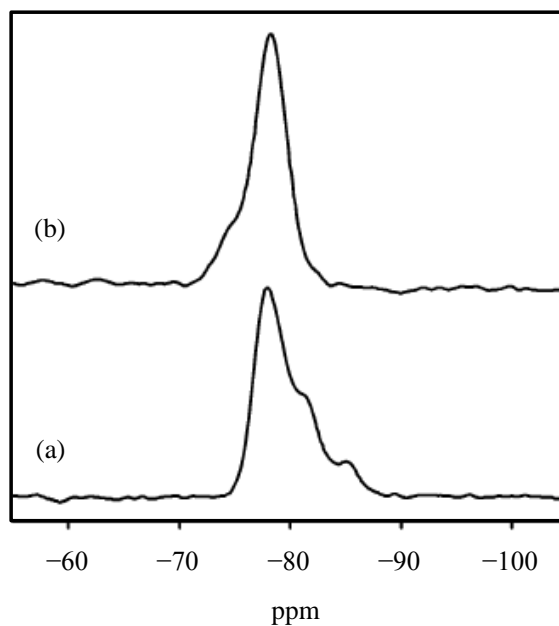


Figure 6-14. ^{29}Si NMR spectra for (a) $\text{La}_{9.33}\text{Si}_6\text{O}_{26}$ and (b) $\text{La}_{9.7(1)}\text{Si}_6\text{O}_{22.6(2)}\text{N}_{2.7(2)}$

The ^{29}Si NMR data for $\text{La}_{9.33}\text{Si}_6\text{O}_{26}$ matches those seen previously in the literature, with three peaks, -77.8 ppm, -81.0 ppm and -85.3 ppm.³¹⁶ These peaks are a result of regular $[\text{SiO}_4]^{4-}$ tetrahedra (-77.8 ppm), distorted $[\text{SiO}_4]^{4-}$ tetrahedra due to local distortions arising from cationic vacancies or anion interstitials (-81.0 ppm) and $[\text{Si}_2\text{O}_7]^{6-}$ units (-85.3 ppm).³¹⁶ The Frenkel defects of $\text{La}_{9.33}\text{Si}_6\text{O}_{26}$ implies oxide anions at the interstitial positions, resulting in changes for the $[\text{SiO}_4]^{4-}$ environments present.³¹⁶ In addition the presence of $[\text{Si}_2\text{O}_7]^{6-}$ units, due to the condensation of two $[\text{SiO}_4]^{4-}$ units, possibly from high levels of structural distortion associated with cationic vacancies, has also been suggested by Sansom *et al.* as a source of additional interstitial oxide anion defects ($2 [\text{SiO}_4]^{4-} \rightarrow [\text{Si}_2\text{O}_7]^{6-} + \text{O}_{\text{int}}^{2-}$).³¹⁶ A number of differences can, however, be seen in the spectrum of ammoniated samples. The $\text{La}_{9.7(1)}\text{Si}_6\text{O}_{22.6(2)}\text{N}_{2.7(2)}$ data shows two main peaks at chemical shifts of -78.3 ppm and -74.8 ppm. The peak at -78.3 ppm corresponds with $[\text{SiO}_4]^{4-}$ tetrahedra, while the peak at -74.8 ppm is attributed to $[\text{SiO}_3\text{N}]^{5-}$. Spectral deconvolution estimates the intensities of these peaks at 88(2) and 12(2)% respectively. The intensity of the peak at -74.8 ppm is lower than what is expected from neutron diffraction. Neutron diffraction indicates 1.4(2) $[\text{SiO}_3\text{N}]^{5-}$ units per formula, while ^{29}Si NMR suggests around half this with 0.7(1) $[\text{SiO}_3\text{N}]^{5-}$ units.

The absence of a peak at -81 ppm indicates that all the $[\text{SiO}_4]^{4-}$ units are equivalent. This may be a result of a reduction in the number of cationic vacancies or alternatively the absence of the -81 ppm signal supports assignments of this peak to SiO_4 tetrahedra adjacent to interstitial oxide anions. This hypothesis is supported by reduced anion thermal displacement parameters in the oxynitride, compared to starting oxide, suggesting far less anionic defects i.e. no Frenkel defects.^{301, 313} The peak at -85 ppm, due to dimerised $[\text{Si}_2\text{O}_7]^{6-}$ units, is also absent in $\text{La}_{9.7(1)}\text{Si}_6\text{O}_{22.6(2)}\text{N}_{2.7(2)}$. However, spectral convolution may indicate the presence of an additional peak at -80 ppm, which is tentatively ascribed to $[\text{Si}_2\text{O}_6\text{N}]^{7-}$. However, the proximity to the larger -78.3 ppm peak prevents accurate classification of this peak. The presence of $[\text{Si}_2\text{O}_6\text{N}]^{7-}$ would account for the low intensity of the -74.8 ppm, $[\text{SiO}_3\text{N}]^{5-}$ peak, compared to what would be expected from the structural information derived from neutron diffraction data. Another possibility is the presence of unreacted $\text{La}_{9.33}\text{Si}_6\text{O}_{26}$ enhancing the -78.3 ppm peak and giving a reduced $[\text{SiO}_3\text{N}]^{5-}$ peak intensity.

6.2 Ammonolysis of $\text{La}_{8+x}\text{Sr}_{2-x}\text{M}_6\text{O}_{26+x/2}$ ($\text{M} = \text{Si}, \text{Ge}; 0 \leq x \leq 2$)

6.2.1 Experimental

6.2.1.1 Preparation

$\text{La}_{8+x}\text{Sr}_{2-x}\text{M}_6\text{O}_{26+x/2}$ ($\text{M} = \text{Si}, \text{Ge}; 0 \leq x \leq 2$) were prepared, by Slater *et al.*, from La_2O_3 , SrCO_3 , SiO_2 and GeO_2 . These reagents were mixed in the correct stoichiometries and heated at 1400 °C (silicates) and 1100°C (germanates) for 14 hours. The samples were then reground and heated at 1400 °C (silicates) and 1100 °C (germanates) for a further 14 hours. In the case of the germanates an additional heating at 1300 °C for two hours was also employed.

The silicate samples were heated in flowing ammonia ($14 \text{ dm}^3\text{hr}^{-1}$) at temperatures between 600 - 1000 °C for 12 hours, using the apparatus described in section 2.2.2.2, while the germanates were heated at the lower temperatures of 600 °C and 800 °C.

6.2.1.2 Characterisation

PXRD was performed, in Hull, using a Siemens D5000 powder diffractometer and $\text{Cu K}\alpha$ radiation. The nitrogen content of the samples reacted in ammonia was determined through thermogravimetric analysis with a TA instrument SDT 600/Netzsch STA 449 thermal analyser. The samples were heated in oxygen at 10 °C/min to 1000 °C.

^{29}Si NMR data for $\text{La}_{8+x}\text{Sr}_{2-x}\text{Si}_6\text{O}_{26+x/2}$ samples heated in ammonia at 800 °C were recorded by the Solid-State NMR Service at Durham University using a Varian Unity Inova spectrometer operating at 59.56 MHz. A direct polarisation experiment was used with recycle delays of 5s ($x = 1$), 10s ($x = 0.5$) and 60s ($x = 0$). Chemical shifts are quoted relative to tetramethylsilane.

6.2.2 Results and Discussion

6.2.2.1 Powder X-ray Diffraction (PXRD)

PXRD performed on the $\text{La}_{8+x}\text{Sr}_{2-x}\text{Si}_6\text{O}_{26+x/2}$ ($0 \leq x \leq 1$) samples, after ammonolysis, indicate that in all cases the apatite structure is maintained. Le Bail extractions were performed, using the space group $P6_3/m$ and $P6_3$ for the initial and ammoniated phases respectively, and the refined lattice parameters are given in Table 6-6. In general, it appears that upon ammonolysis there is only a small difference in the cell dimensions. The a/b parameters remain relatively unaffected, however, there is an increase in the c -axis with increasing N content. TGA, shown in the following section, gives a total anion content (N + O) in all of the silicate apatites, of around 26. In addition the overall oxygen content generally does not drop below 24. This may indicate that unlike in the $\text{La}_{9.33}\text{Si}_6\text{O}_{26}$ case (section 6.1) nitrogen insertion/substitution only occurs at the anion channel site, leaving the SiO_4 tetrahedra untouched. The result of this is reduced distortion of the tetrahedra and an increase in c , possibly due to the larger ionic radii of N^{3-} ($\sim 1.46 \text{ \AA}$) over O^{2-} ($\sim 1.38 \text{ \AA}$).³²

For germanate samples heated in ammonia above $\sim 800 \text{ }^\circ\text{C}$ all samples showed some evidence of decomposition, therefore, the temperature of ammonolysis used for the germanates in subsequent reactions did not exceed $600 \text{ }^\circ\text{C}$. The structure of the initial, unreacted, germanates, $\text{La}_{8+x}\text{Sr}_{2-x}\text{Ge}_6\text{O}_{26+x/2}$, for $x \leq 1$ show hexagonal symmetry while for $x \geq 1$ the apatites are triclinic. Table 6-7 gives the cell parameters derived by Le Bail extraction for $\text{La}_{8+x}\text{Sr}_{2-x}\text{Ge}_6\text{O}_{26+x/2}$ after ammonolysis at $600 \text{ }^\circ\text{C}$. The initial germanates, $x \leq 1$, were modelled using the space groups $P6_3/m$ and $x \geq 1$ modelled using $P\bar{1}$. The refinements for $\text{La}_{9.5}\text{Sr}_{0.5}\text{Ge}_6\text{O}_{26.75}$ and $\text{La}_{10}\text{Ge}_6\text{O}_{27}$, showing triclinic unit cells were unstable. Better results could be obtained by indexing the peaks using the analysis software Chekcell.²¹⁰ Upon treatment in ammonia all the germanates, including those with triclinic unit cells, showed unit cells with hexagonal symmetry. Therefore, the ammoniated samples were fit to the space group $P6_3$. This increase in symmetry may be a result of the removing of the interstitial oxide anions and an anion content closer to the nominal stoichiometry i.e. (N + O) ≈ 26 (see TGA data, section 6.2.2.2).

Reaction conditions	Proposed formula ^{†††}	<i>a</i> (Å)	<i>c</i> (Å)
La ₈ Sr ₂ Si ₆ O ₂₆	La ₈ Sr ₂ Si ₆ O ₂₆	9.6986(5)	7.2352(5)
La ₈ Sr ₂ Si ₆ O ₂₆ + NH ₃ 600 °C	La ₈ Sr ₂ Si ₆ O _{25.75} N _{0.17}	9.7122(5)	7.2485(4)
La ₈ Sr ₂ Si ₆ O ₂₆ + NH ₃ 800 °C	La ₈ Sr ₂ Si ₆ O _{25.72} N _{0.19}	9.7181(4)	7.2548(5)
La ₈ Sr ₂ Si ₆ O ₂₆ + NH ₃ 900 °C	La ₈ Sr ₂ Si ₆ O _{25.69} N _{0.21}	9.6985(3)	7.2462(4)
La ₈ Sr ₂ Si ₆ O ₂₆ + NH ₃ 1000 °C	La ₈ Sr ₂ Si ₆ O _{25.55} N _{0.30}	9.7040(6)	7.2557(6)
La _{8.25} Sr _{1.75} Si ₆ O _{26.125}	La _{8.25} Sr _{1.75} Si ₆ O _{26.125}	9.7004(7)	7.2367(6)
La _{8.25} Sr _{1.75} Si ₆ O _{26.125} + NH ₃ 900 °C	La _{8.25} Sr _{1.75} Si ₆ O _{25.76} N _{0.25}	9.6997(7)	7.2383(7)
La _{8.25} Sr _{1.75} Si ₆ O _{26.125} + NH ₃ 1000 °C	La _{8.25} Sr _{1.75} Si ₆ O _{25.08} N _{0.70}	9.7035(8)	7.2518(7)
La _{8.5} Sr _{1.5} Si ₆ O _{26.25}	La _{8.5} Sr _{1.5} Si ₆ O _{26.25}	9.7052(4)	7.2270(4)
La _{8.5} Sr _{1.5} Si ₆ O _{26.25} + NH ₃ 600 °C	La _{8.5} Sr _{1.5} Si ₆ O _{25.54} N _{0.47}	9.7116(4)	7.2375(4)
La _{8.5} Sr _{1.5} Si ₆ O _{26.25} + NH ₃ 800 °C	La _{8.5} Sr _{1.5} Si ₆ O _{25.62} N _{0.42}	9.7174(4)	7.2517(4)
La _{8.75} Sr _{1.25} Si ₆ O _{26.375}	La _{8.75} Sr _{1.25} Si ₆ O _{26.375}	9.6966(9)	7.2248(10)
La _{8.75} Sr _{1.25} Si ₆ O _{26.375} + NH ₃ 900 °C	La _{8.75} Sr _{1.25} Si ₆ O _{24.60} N _{1.18}	9.6902(10)	7.2395(9)
La _{8.75} Sr _{1.25} Si ₆ O _{26.375} + NH ₃ 1000 °C	La _{8.75} Sr _{1.25} Si ₆ O _{24.15} N _{1.48}	9.6916(9)	7.2437(9)
La ₉ Sr ₁ Si ₆ O _{26.5}	La ₉ Sr ₁ Si ₆ O _{26.5}	9.7063(3)	7.2161(3)
La ₉ Sr ₁ Si ₆ O _{26.5} + NH ₃ 600 °C	La ₉ Sr ₁ Si ₆ O _{25.52} N _{0.65}	9.6992(9)	7.2187(8)
La ₉ Sr ₁ Si ₆ O _{26.5} + NH ₃ 800 °C	La ₉ Sr ₁ Si ₆ O _{25.23} N _{0.85}	9.6913(6)	7.2262(6)
La ₉ Sr ₁ Si ₆ O _{26.5} + NH ₃ 900 °C	La ₉ Sr ₁ Si ₆ O _{24.60} N _{1.27}	9.7018(14)	7.2494(12)
La ₉ Sr ₁ Si ₆ O _{26.5} + NH ₃ 1000 °C	La ₉ Sr ₁ Si ₆ O _{23.35} N _{2.10}	9.6959(8)	7.2500(8)

Table 6-6. Lattice parameters for La_{8+x}Sr_{2-x}Si₆O_{26+x/2} before and after reaction with NH₃, derived from Le Bail extraction performed using PXRD data.

Reaction conditions	Proposed formula ^{†††}	<i>a</i> (Å)	<i>b</i> (Å)	<i>c</i> (Å)
La ₈ Sr ₂ Ge ₆ O ₂₆	La ₈ Sr ₂ Ge ₆ O ₂₆	9.9039(5)	9.9039(5)	7.3194(4)
La ₈ Sr ₂ Ge ₆ O ₂₆ + NH ₃ 600°C	La ₈ Sr ₂ Ge ₆ O _{25.77} N _{0.15}	9.9192(5)	9.9192(5)	7.3344(4)
La _{8.5} Sr _{1.5} Ge ₆ O _{26.25}	La _{8.5} Sr _{1.5} Ge ₆ O _{26.25}	9.9116(4)	9.9116(4)	7.3224(3)
La _{8.5} Sr _{1.5} Ge ₆ O _{26.25} + NH ₃ 600°C	La _{8.5} Sr _{1.5} Ge ₆ O _{25.08} N _{0.78}	9.9112(4)	9.9112(4)	7.3311(4)
La ₉ SrGe ₆ O _{26.5}	La ₉ SrGe ₆ O _{26.5}	9.9021(8)	9.9021(8)	7.2948(7)
La ₉ SrGe ₆ O _{26.5} + NH ₃ 600°C	La ₉ SrGe ₆ O _{24.05} N _{1.63}	9.8571(8)	9.8571(8)	7.2730(7)
La _{9.5} Sr _{0.5} Ge ₆ O _{26.75}	La _{9.5} Sr _{0.5} Ge ₆ O _{26.75}	9.961(2)	9.906(2)	7.2758(8)
La _{9.5} Sr _{0.5} Ge ₆ O _{26.75} + NH ₃ 600°C	La _{9.5} Sr _{0.5} Ge ₆ O _{24.09} N _{1.77}	9.8996(3)	9.8996(3)	7.2947(3)
La ₁₀ Ge ₆ O ₂₇	La ₁₀ Ge ₆ O ₂₇	9.9377(4)	9.8955(4)	7.2600(3)
La ₁₀ Ge ₆ O ₂₇ + NH ₃ 600°C	La ₁₀ Ge ₆ O _{24.04} N _{1.97}	9.9889(9)	9.9889(9)	7.3661(8)

Table 6-7. Lattice parameters for La_{8+x}Sr_{2-x}Ge₆O_{26+x/2} before and after reaction with NH₃, derived from Le Bail extraction performed using PXRD data. La_{9.5}Sr_{0.5}Ge₆O_{26.75} ($\alpha = 90.898(5)^\circ$, $\beta = 88.775(6)^\circ$, $\gamma = 120.387(4)^\circ$) and La₁₀Ge₆O₂₇ ($\alpha = 90.805(2)^\circ$, $\beta = 88.850(2)^\circ$, $\gamma = 120.303(2)^\circ$).

^{†††}Calculated from TGA (Table 6-8)

^{†††}Calculated from TGA (Table 6-9).

In addition, the $\text{La}_{8+x}\text{Sr}_{2-x}\text{M}_6\text{O}_{26+x/2}$ ($\text{M} = \text{Si}, \text{Ge}; 0 \leq x \leq 2$) samples, unlike $\text{La}_{9.33}\text{Si}_6\text{O}_{26}$, did not show any obvious signs of anisotropic peak broadening upon reaction with ammonia, suggesting that no vacancies are present in the channels. This adds support to the previous assignment of anisotropic peak broadening to disorder arising from anion channel vacancies.

6.2.2.2 Thermogravimetric Analysis (TGA)

The stoichiometries of the ammoniated samples, suggested from TGA, are shown in Table 6-8 and Table 6-9. The TGA plots resembled those shown in Figure 6-11 and, therefore, the nitrogen content was calculated, from the percentage weight increase, as shown in section 6.1.1, assuming a mass increase above 700 °C was due to the substitution of three O^{2-} anions for two N^{3-} anions .

Reaction conditions	Weight increase (%)	Chemical formula	Final total anion content
$\text{La}_8\text{Sr}_2\text{Si}_6\text{O}_{26} + \text{NH}_3$ 600 °C	0.09	$\text{La}_8\text{Sr}_2\text{Si}_6\text{O}_{25.75}\text{N}_{0.17}$	25.92
$\text{La}_8\text{Sr}_2\text{Si}_6\text{O}_{26} + \text{NH}_3$ 800 °C	0.10	$\text{La}_8\text{Sr}_2\text{Si}_6\text{O}_{25.72}\text{N}_{0.19}$	25.91
$\text{La}_8\text{Sr}_2\text{Si}_6\text{O}_{26} + \text{NH}_3$ 900 °C	0.11	$\text{La}_8\text{Sr}_2\text{Si}_6\text{O}_{25.69}\text{N}_{0.21}$	25.90
$\text{La}_8\text{Sr}_2\text{Si}_6\text{O}_{26} + \text{NH}_3$ 1000 °C	0.16	$\text{La}_8\text{Sr}_2\text{Si}_6\text{O}_{25.55}\text{N}_{0.30}$	25.85
$\text{La}_{8.25}\text{Sr}_{1.75}\text{Si}_6\text{O}_{26.125} + \text{NH}_3$ 800 °C	0.4	$\text{La}_{8.25}\text{Sr}_{1.75}\text{Si}_6\text{O}_{25}\text{N}_{0.75}$	25.75
$\text{La}_{8.25}\text{Sr}_{1.75}\text{Si}_6\text{O}_{26.125} + \text{NH}_3$ 900 °C	0.13	$\text{La}_{8.25}\text{Sr}_{1.75}\text{Si}_6\text{O}_{25.76}\text{N}_{0.25}$	26.01
$\text{La}_{8.25}\text{Sr}_{1.75}\text{Si}_6\text{O}_{26.125} + \text{NH}_3$ 1000 °C	0.37	$\text{La}_{8.25}\text{Sr}_{1.75}\text{Si}_6\text{O}_{25.08}\text{N}_{0.70}$	25.78
$\text{La}_{8.5}\text{Sr}_{1.5}\text{Si}_6\text{O}_{26.25} + \text{NH}_3$ 600 °C	0.25	$\text{La}_{8.5}\text{Sr}_{1.5}\text{Si}_6\text{O}_{25.54}\text{N}_{0.47}$	26.01
$\text{La}_{8.5}\text{Sr}_{1.5}\text{Si}_6\text{O}_{26.25} + \text{NH}_3$ 800 °C	0.22	$\text{La}_{8.5}\text{Sr}_{1.5}\text{Si}_6\text{O}_{25.62}\text{N}_{0.42}$	26.04
$\text{La}_{8.75}\text{Sr}_{1.25}\text{Si}_6\text{O}_{26.375} + \text{NH}_3$ 800 °C	0.55	$\text{La}_{8.75}\text{Sr}_{1.25}\text{Si}_6\text{O}_{24.80}\text{N}_{1.05}$	25.85
$\text{La}_{8.75}\text{Sr}_{1.25}\text{Si}_6\text{O}_{26.375} + \text{NH}_3$ 900 °C	0.62	$\text{La}_{8.75}\text{Sr}_{1.25}\text{Si}_6\text{O}_{24.60}\text{N}_{1.18}$	25.78
$\text{La}_{8.75}\text{Sr}_{1.25}\text{Si}_6\text{O}_{26.375} + \text{NH}_3$ 1000 °C	0.78	$\text{La}_{8.75}\text{Sr}_{1.25}\text{Si}_6\text{O}_{24.15}\text{N}_{1.48}$	25.63
$\text{La}_9\text{Sr}_1\text{Si}_6\text{O}_{26.5} + \text{NH}_3$ 600 °C	0.34	$\text{La}_9\text{Sr}_1\text{Si}_6\text{O}_{25.52}\text{N}_{0.65}$	26.17
$\text{La}_9\text{Sr}_1\text{Si}_6\text{O}_{26.5} + \text{NH}_3$ 800 °C	0.44	$\text{La}_9\text{Sr}_1\text{Si}_6\text{O}_{25.23}\text{N}_{0.85}$	26.08
$\text{La}_9\text{Sr}_1\text{Si}_6\text{O}_{26.5} + \text{NH}_3$ 900 °C	0.66	$\text{La}_9\text{Sr}_1\text{Si}_6\text{O}_{24.60}\text{N}_{1.27}$	25.87
$\text{La}_9\text{Sr}_1\text{Si}_6\text{O}_{26.5} + \text{NH}_3$ 1000 °C	1.1	$\text{La}_9\text{Sr}_1\text{Si}_6\text{O}_{23.35}\text{N}_{2.10}$	25.45

Table 6-8. Compositions for $\text{La}_{8+x}\text{Sr}_{2-x}\text{Si}_6\text{O}_{26+x/2}$ samples after heating in NH_3 .

Reaction conditions	Weight increase (%)	Chemical formula	Final total anion content
$\text{La}_8\text{Sr}_2\text{Ge}_6\text{O}_{26} + \text{NH}_3$ 600°C	0.07	$\text{La}_8\text{Sr}_2\text{Ge}_6\text{O}_{25.77}\text{N}_{0.15}$	25.92
$\text{La}_{8.5}\text{Sr}_{1.5}\text{Ge}_6\text{O}_{26.25} + \text{NH}_3$ 600°C	0.36	$\text{La}_{8.5}\text{Sr}_{1.5}\text{Ge}_6\text{O}_{25.08}\text{N}_{0.78}$	25.86
$\text{La}_9\text{SrGe}_6\text{O}_{26.5} + \text{NH}_3$ 600°C	0.75	$\text{La}_9\text{SrGe}_6\text{O}_{24.05}\text{N}_{1.63}$	25.68
$\text{La}_{9.5}\text{Sr}_{0.5}\text{Ge}_6\text{O}_{26.75} + \text{NH}_3$ 600°C	0.80	$\text{La}_{9.5}\text{Sr}_{0.5}\text{Ge}_6\text{O}_{24.09}\text{N}_{1.77}$	25.86
$\text{La}_{10}\text{Ge}_6\text{O}_{27} + \text{NH}_3$ 600°C	0.88	$\text{La}_{10}\text{Ge}_6\text{O}_{24.04}\text{N}_{1.97}$	26.01

Table 6-9. Compositions for $\text{La}_{8+x}\text{Sr}_{2-x}\text{Ge}_6\text{O}_{26+x/2}$ samples after heating in NH_3 .

TGA indicated a number of trends. In general, increased reaction temperatures result in higher levels of nitridation, with the highest nitrogen content observed for reactions at 1000 °C. Furthermore, only small amounts of nitridation is observed for the stoichiometric apatites ($x = 0$), but the levels of nitrogen insertion increases with increasing quantities of interstitial anions present in the starting apatite materials (Figure 6-15 and Figure 6-16). In the case of the silicate apatites, ammonolysis shows a near linear increase in nitrogen uptake with increasing x ($\text{La}_{8+x}\text{Sr}_{2-x}\text{Si}_6\text{O}_{26+x/2}$). For the germanate apatites there is also an increase in nitrogen content with an increasing value of x ($\text{La}_{8+x}\text{Sr}_{2-x}\text{Ge}_6\text{O}_{26+x/2}$), however, this trend shows a change in slope at $x = 1$ from a sharp linear increase in nitrogen absorption, for $x \leq 1$, to a more shallow incline for $x \geq 1$ (Figure 6-16). A possible explanation of this limitation is the relative ease of nitrogen incorporation onto the two different anion positions; the anion channels or GeO_4 tetrahedra. For the $x \geq 1$ ammoniated germanates the final oxygen content is close to 24. This may indicate that the GeO_4 tetrahedra remain intact, i.e. $(\text{GeO}_4)_6$, with nitrogen only occupying the channel anion position. The instability of the germanates at temperatures in excess of 800 °C, therefore, may be attributed to nitridation of these tetrahedra and decomposition of the sample.

As in all cases (of silicates and germanates) the overall anion content (N + O) approximates to 26, suggesting that reduction of interstitial anion content may be the driving force of these reactions.

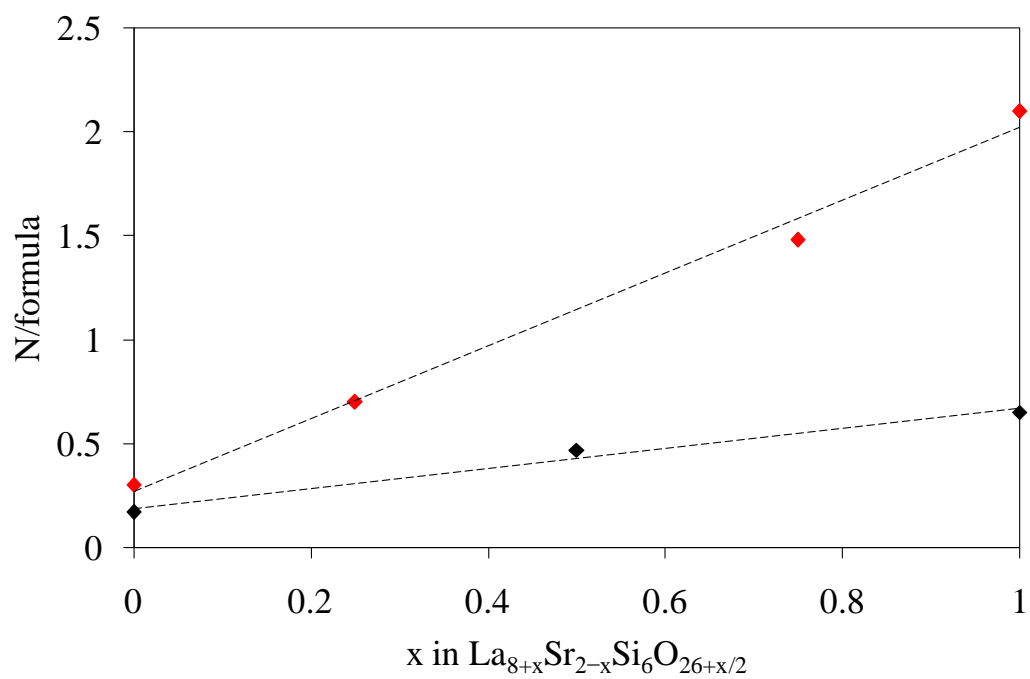


Figure 6-15. Variation of nitrogen content after heating $\text{La}_{8+x}\text{Sr}_{2-x}\text{Si}_6\text{O}_{26+x/2}$ samples in NH_3 at 600 °C (black) and 1000 °C (red).

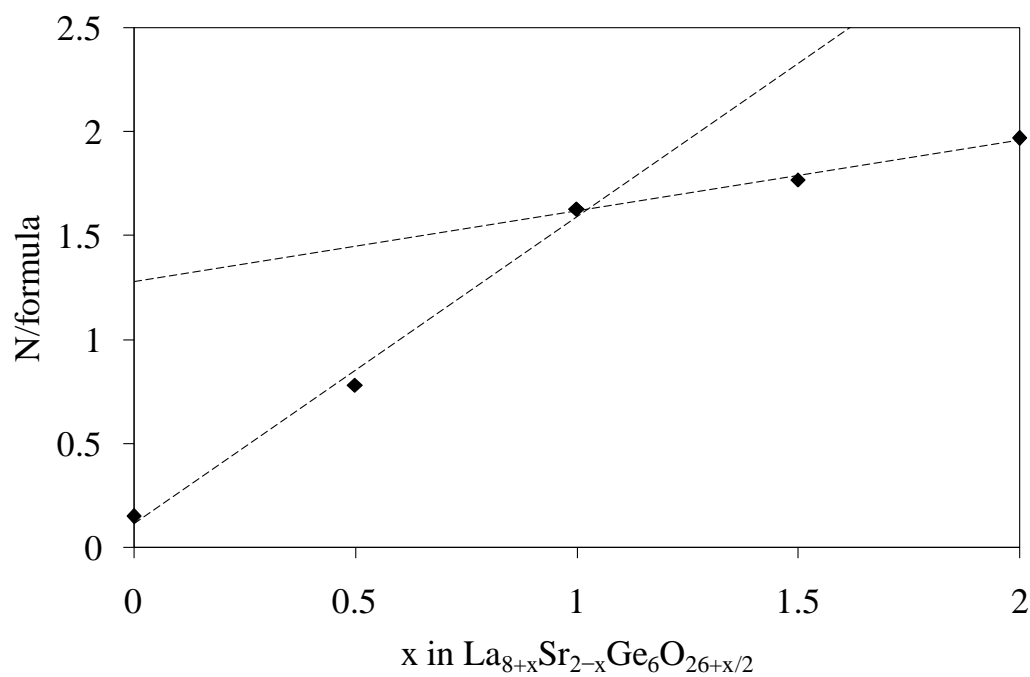


Figure 6-16. Variation of nitrogen content after heating $\text{La}_{8+x}\text{Sr}_{2-x}\text{Ge}_6\text{O}_{26+x/2}$ samples in NH_3 at 600 °C.

6.2.2.3 ^{29}Si Nuclear Magnetic Resonance (NMR)

^{29}Si NMR data for $\text{La}_{8+x}\text{Sr}_{2-x}\text{Si}_6\text{O}_{26+x/2}$ ($x \leq 1$) samples heated in ammonia at 800°C were recorded.

^{29}Si NMR studies into the unreacted silicate samples have previously been reported by Orera *et al.*³¹⁷ These showed a single peak at approximately -77 ppm for the $x = 0$ material, corresponding with $[\text{SiO}_4]^{4-}$, while the $x > 0$ samples showed an additional peak at -80 ppm attributed to $[\text{SiO}_4]^{4-}$ units adjacent to interstitial anions.

Upon ammonolysis we see a loss of this second peak in the $x = 0.5$ sample and a reduction in intensity in the $x = 1$ (Figure 6-17). Such a result is consistent with a reduction in the interstitial anion content, in agreement to TGA results. Additionally, the $x = 1$ sample also yielded a small signal at approximately -73.5 ppm. Such a signal may be due to a small amount of $[\text{SiO}_3\text{N}]^{5-}$. Due to the low intensity and proximity to the neighbouring peaks the intensity could not be determined. The general small size of this peak and its absence in the $x = 0.5$ data implies very little nitrogen incorporation in the SiO_4 tetrahedra and may suggest a preference of N at the channel anion site, in a similar way to the nitridation of $\text{La}_{9.33}\text{Si}_6\text{O}_{26}$.³¹³

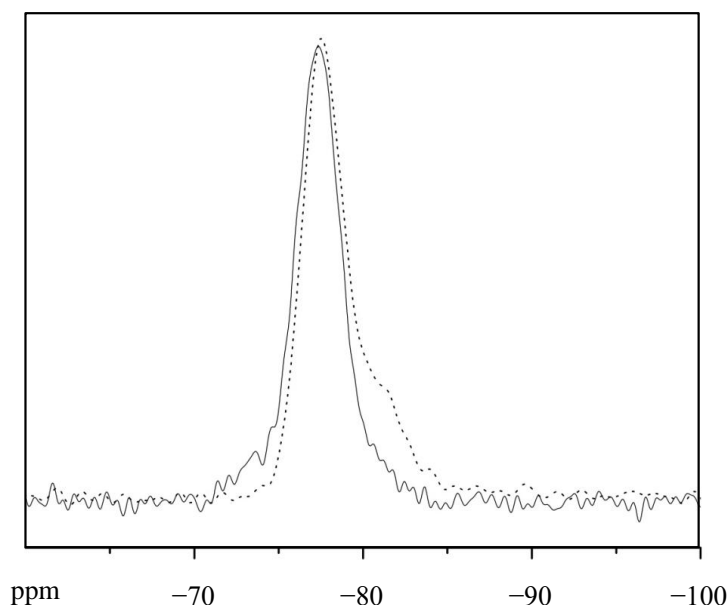


Figure 6-17. ^{29}Si NMR data for $\text{La}_9\text{SrSi}_6\text{O}_{26.5}$ (dotted line) and $\text{La}_9\text{SrSi}_6\text{O}_{24.88}\text{N}_{1.08}$ (solid line).

6.3 Ammonolysis of $\text{La}_{9.67}\text{Si}_5\text{CoO}_{26}$, $\text{La}_{10}\text{M}_5\text{CoO}_{26.5}$ ($\text{M} = \text{Si}, \text{Ge}$)

6.3.1 Experimental

6.3.1.1 Preparation

Samples of $\text{La}_{9.67}\text{Si}_5\text{CoO}_{26}$, $\text{La}_{10}\text{Si}_5\text{CoO}_{26.5}$ and $\text{La}_{10}\text{Ge}_5\text{CoO}_{26.5}$ were provided by Slater and co-workers. $\text{La}_{9.67}\text{Si}_5\text{CoO}_{26}$ and $\text{La}_{10}\text{Si}_5\text{CoO}_{26.5}$ were prepared via the solid state reaction of a stoichiometric mixture of La_2O_3 , SiO_2 and Co_3O_4 for two heat treatments at 1100 °C, with three further heatings at 1300 °C. $\text{La}_{10}\text{Ge}_5\text{CoO}_{26.5}$ was prepared via sol-gel reaction of $\text{La}(\text{NO}_3)_3 \cdot 6\text{H}_2\text{O}$, GeO_2 and $\text{Co}(\text{NO}_3)_2 \cdot 6\text{H}_2\text{O}$ with heating at 950 °C.

The silicates samples were heated in flowing ammonia ($14 \text{ dm}^3 \text{ hr}^{-1}$) at 800 °C and 1000 °C for 12 hours, using the apparatus described in section 2.2.2.2, while the germanates were heated at the lower temperatures of 600 °C and 800 °C.

6.3.1.2 Characterisation

PXRD was performed, in Hull, using a Siemens D5000 powder diffractometer and Cu $\text{K}\alpha$ radiation. The nitrogen content of the samples reacted in ammonia was determined through thermogravimetric analysis with a Netzsch STA 449 thermal analysers.

The extended X-ray absorption fine structure (EXAFS) and X-ray absorption near-edge structure (XANES) measurements were performed at Station 9.3 at the Daresbury Synchrotron radiation source (2 GeV) on cobalt containing samples, in order to identify the cobalt oxidation state and coordination environment. The Co-K-edge wavelengths were selected using a Si(111) double crystal monochromator. The samples were diluted in boron nitride and the data collected in fluorescence mode, due to the high degree of absorption from the lanthanum. The standards, LaCoO_3 , $\text{YSr}_2\text{Cu}_2\text{CoO}_7$ and CoCr_2O_4 , were collected in transmission mode as these materials showed reduced levels of absorption compared to the apatites. All spectra of both samples and standards were

collected at room temperature. Data analysis was performed in Hull, under guidance from Dr Nigel Young.

6.3.2 Results and Discussion

6.3.2.1 Powder X-ray Diffraction (PXRD)

Comparison of PXRD patterns of $\text{La}_{9.67}\text{Si}_5\text{CoO}_{26}$, $\text{La}_{10}\text{Si}_5\text{CoO}_{26.5}$, $\text{La}_{10}\text{Ge}_5\text{CoO}_{26.5}$ and the ammoniated samples are shown in Figure 6-18, Figure 6-19 and Figure 6-20. These show that the apatite structure is maintained for all reaction temperatures investigated. The only exception is $\text{La}_{10}\text{Ge}_5\text{CoO}_{26.5}$, which shows decomposition after reaction with ammonia at 800 °C with the occurrence of impurities such as La_4GeO_8 , and La_2O_3 , in addition to the starting phase (Figure 6-20).

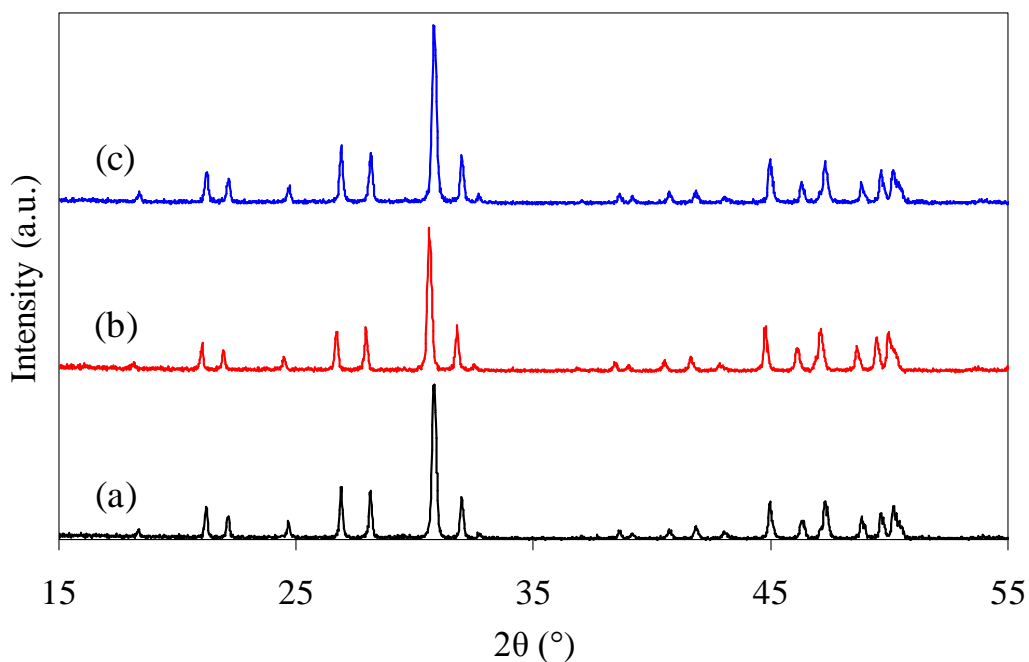


Figure 6-18. PXRD patterns for (a) $\text{La}_{9.67}\text{Si}_5\text{CoO}_{26}$, (b) $\text{La}_{9.67}\text{Si}_5\text{CoO}_{26}$ after reaction in NH_3 at 800 °C and (c) after reaction in NH_3 at 1000 °C.

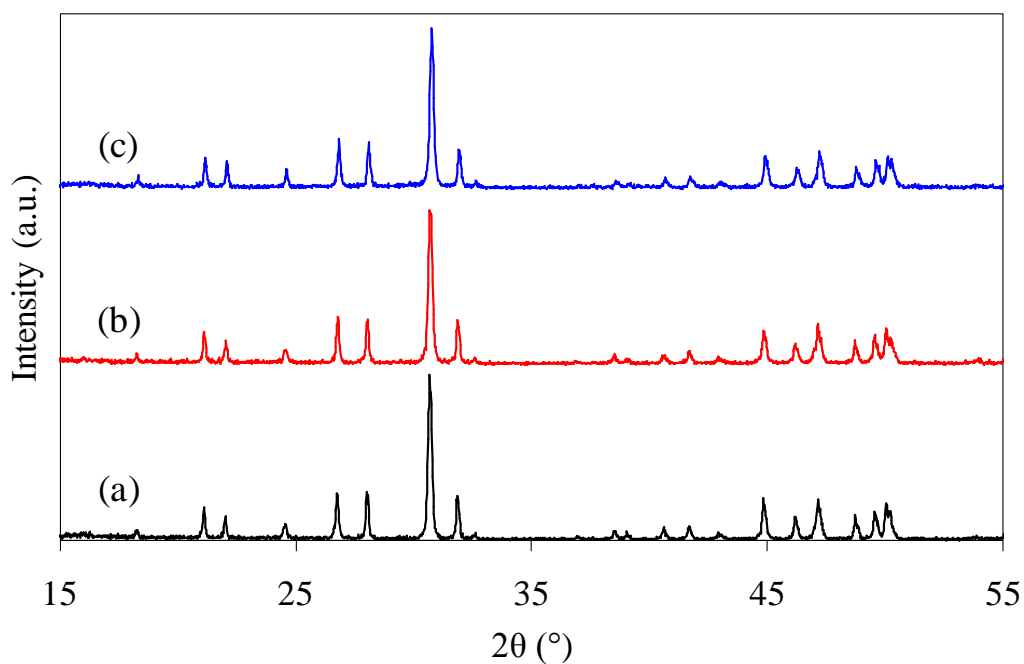


Figure 6-19. PXRD patterns for (a) $\text{La}_{10}\text{Si}_5\text{CoO}_{26.5}$, (b) $\text{La}_{10}\text{Si}_5\text{CoO}_{26.5}$ after reaction in NH_3 at 800°C and (c) after reaction in NH_3 at 1000°C .

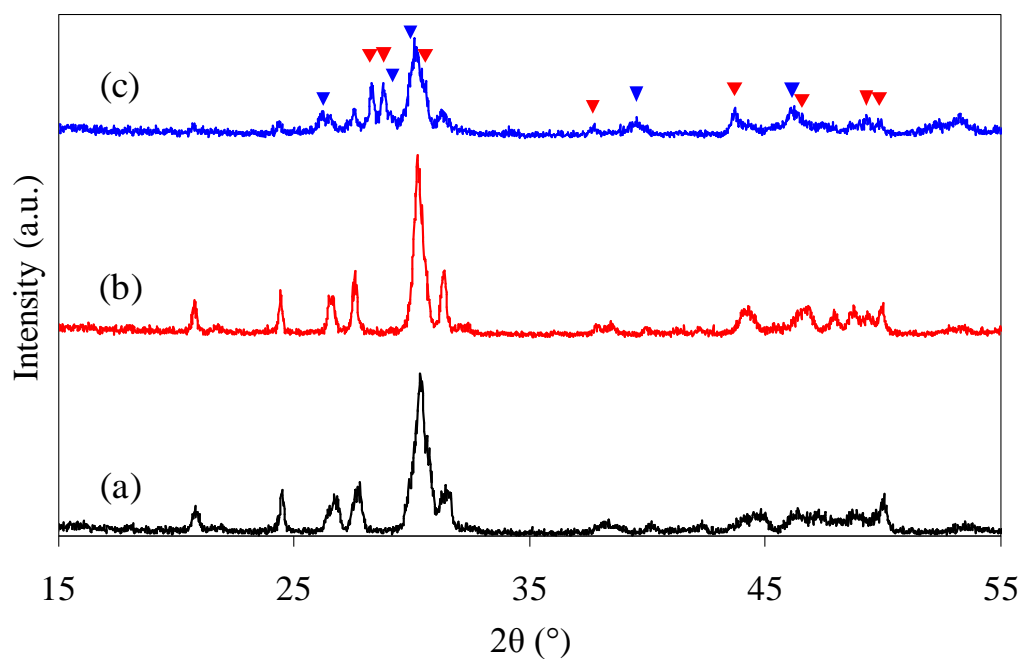


Figure 6-20. PXRD patterns for (a) $\text{La}_{10}\text{Ge}_5\text{CoO}_{26.5}$, (b) $\text{La}_{10}\text{Ge}_5\text{CoO}_{26.5}$ after reaction in NH_3 at 600°C and (c) after reaction in NH_3 at 800°C . The blue and red triangles indicate the main peaks for La_2O_3 and La_4GeO_8 respectively.

The PXRD patterns of the silicate samples were indexed to hexagonal unit cells, the lattice parameters are given in Table 6-10, using the space group $P6_3$.^{217, 240} It was not

possible to calculate the cell parameters of the germanate samples due to the broadness of the diffraction peaks, possibly arising from some triclinic distortion.

Reaction conditions	Proposed formula ^{§§§}	<i>a</i> (Å)	<i>c</i> (Å)
La _{9.67} Si ₅ CoO ₂₆	La _{9.67} Si ₅ CoO ₂₆	9.7153(7)	7.2369(6)
La _{9.67} Si ₅ CoO ₂₆ + NH ₃ 800 °C	La _{9.67} Si ₅ CoO _{25.62}	9.7359(7)	7.2611(6)
La _{9.67} Si ₅ CoO ₂₆ + NH ₃ 1000 °C	-	9.7376(10)	7.2639(9)
La ₁₀ Si ₅ CoO _{26.5}	La ₁₀ Si ₅ CoO _{26.5}	9.7304(7)	7.2555(7)
La ₁₀ Si ₅ CoO _{26.5} + NH ₃ 800 °C	La ₁₀ Si ₅ CoO _{25.87} N _{0.18}	9.7307(10)	7.2619(9)
La ₁₀ Si ₅ CoO _{26.5} + NH ₃ 1000 °C	-	9.7282(7)	7.2583(7)

Table 6-10. Cell parameters for the La_{9.67}Si₅CoO₂₆ and La₁₀Si₅CoO_{26.5} samples derived from PXRD at room temperature.

The small differences in lattice parameters between the starting compounds and the oxide-nitrides may be attributable to a modification in the anion content. The nitrogen content of the samples heated in ammonia was calculated from TGA data.

In addition, unlike La_{9.33}Si₆O₂₆, section 6.1, the reaction of La_{9.67}Si₅CoO₂₆ and La₁₀M₅CoO_{26.5} (M = Si, Ge) with ammonia yields PXRD patterns that do not appear to show significant anisotropic peak broadening. In La_{9.7(1)}Si₆O_{22.6(2)}N_{2.7(2)} the anisotropic peak broadening was attributed to displacive distortions associated with local ordering of vacancies along the oxide/nitride anion channel.³¹³ The absence of such peak broadening may therefore be an indication that such ordering is not present in the cobalt substituted apatite samples. Further structural information was obtained via XAFS analysis.

6.3.2.2 X-ray Absorption Spectroscopy

One of the main aims of this work was to investigate the stability of silicon and germanium oxide apatites while heating in ammonia and to prepare oxide-nitride materials with cobalt substituting silicon and germanium in the [Si/GeO₄]⁴⁻ tetrahedra. XAFS spectroscopy was carried out in order to determine the coordination and

^{§§§}Calculated from TGA (Table 6-22). Formulae are only suggested for single phase materials.

oxidation number of cobalt in $\text{La}_{9.67}\text{Si}_5\text{CoO}_{26}$ and $\text{La}_{10}\text{M}_5\text{CoO}_{26.5}$ ($\text{M} = \text{Si}, \text{Ge}$) oxides and corresponding oxide-nitrides, arising from reaction of these oxides with ammonia.

As indicated in section 6 there have been reports of cobalt occupying the lanthanum site in apatite materials such as $\text{La}_8\text{BaCoSi}_6\text{O}_{26}$ and the silicon site in $\text{La}_{9.67}\text{Si}_5\text{CoO}_{26}$.³⁰⁴ XAFS analysis will act to confirm the tetrahedral coordination in the initial compounds and ammoniated samples. Furthermore, unlike in the previous example outlined here, the incorporation of a transition metal into the apatite structure provides a metal centre which may have its oxidation state changed in a reducing atmosphere like ammonia.

6.3.2.2.1 Co-K-edge XANES of $\text{La}_{9.67}\text{Si}_5\text{CoO}_{26}$, $\text{La}_{10}\text{M}_5\text{CoO}_{26.5}$ ($\text{M} = \text{Si}, \text{Ge}$)

In order to provide a set of references for cobalt coordination geometries and oxidation states, the spectra of a number of known standards were collected. LaCoO_3 , $\text{YSr}_2\text{Cu}_2\text{CoO}_7$ and CoCr_2O_4 were chosen as standards containing Co^{3+} in octahedral coordination, tetrahedral coordination and Co^{2+} in tetrahedral coordination respectively.³¹⁸⁻³²⁰ Additional standards, highlighting several other possible cobalt geometries were taken, with permission, from the literature.²²⁷ These standards, Co-3,5-*t*-Bu-cysalen, $[\text{Co}(\text{salen})]_2$ and $[\text{Co}(\text{acac})_2 \cdot \text{H}_2\text{O}]_2$, show Co^{2+} in square planar, square based pyramidal and octahedral coordination respectively.²²⁷ The XAFS spectra of all standards are shown in Figure 6-21 (a-b).

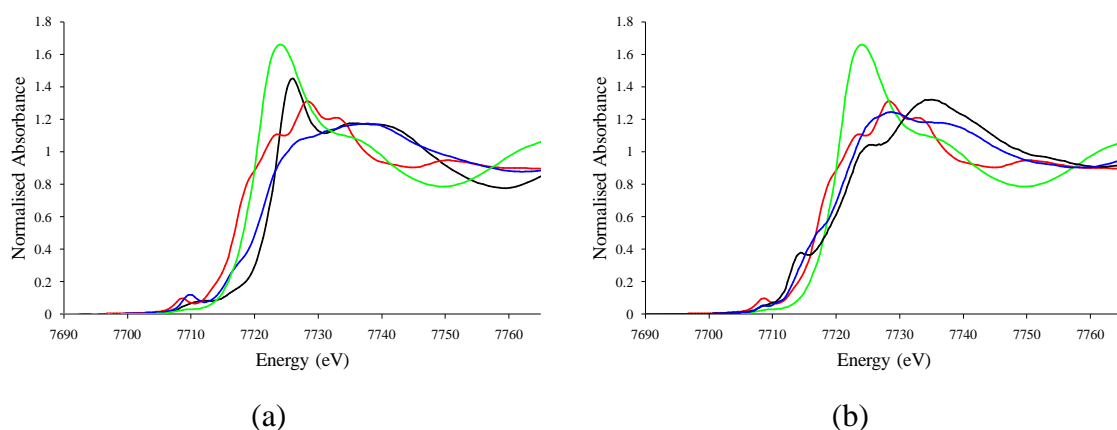


Figure 6-21. Co-K-edge XANES spectra of (a) LaCoO_3 (black), $\text{YSr}_2\text{Cu}_2\text{CoO}_7$ (blue), $[\text{Co}(\text{acac})_2 \cdot \text{H}_2\text{O}]_2$ (green) and CoCr_2O_4 (red) and (b) Co-3,5-*t*-Bu-cysalen (black), $[\text{Co}(\text{salen})]_2$ (blue), $[\text{Co}(\text{acac})_2 \cdot \text{H}_2\text{O}]_2$ (green) and CoCr_2O_4 (red).

As described in section 2.3.5, the ions of a compound can absorb X-ray radiation with the promotion of an electron from a core level out of the atom, giving the characteristic absorption edge in the XANES spectra. As each ion has its own unique absorption energy, corresponding with the energy required to excite electrons from each atomic level into the continuum, shifts in the edge position can be used as a tool to determine oxidation states within a compound. In addition, the XAFS spectra show differences in edge position when the target ions are in different coordination geometries. Figure 6-21 (a) highlights the difference in edge position between Co^{2+} (red, green) and Co^{3+} (black, blue) in tetrahedral and octahedral coordination. Figure 6-21 emphasizes this difference in XANES spectra of compounds with Co^{2+} in tetrahedral, square planar, square based pyramidal and octahedral coordination. It is therefore important to identify a compounds coordination before deriving the oxidation state.

The Co-K-edge XANES for $\text{La}_{9.66}\text{Si}_5\text{CoO}_{26}$ have been previously investigated by Tolchard *et al.* and the oxidation state and coordination of the cobalt was confirmed to be 3+ in tetrahedral coordination to four oxide anions.³⁰⁴ The same oxidation state and geometry is predicted for cobalt in $\text{La}_{10}\text{Si}_5\text{CoO}_{26.5}$ and $\text{La}_{10}\text{Ge}_5\text{CoO}_{26.5}$, from charge balancing considerations. The spectra of the silicates and germanates are compared in Figure 6-22 and in Figure 6-23 and both spectra are compared with those of the standards. The position of the edges confirms that the oxidation state in the silicates and germanates is 3+. $\text{La}_{9.67}\text{Si}_5\text{CoO}_{26}$ and $\text{La}_{10}\text{Si}_5\text{CoO}_{26.5}$ show essentially identical XANES spectra indicating the same coordination environment and an edge position consistent with Co^{3+} (Table 6-11). This is illustrated in Figure 6-22 and shows that the edges of both silicate apatite samples match the spectrum of $\text{YSr}_2\text{Cu}_2\text{CoO}_7$ standard.

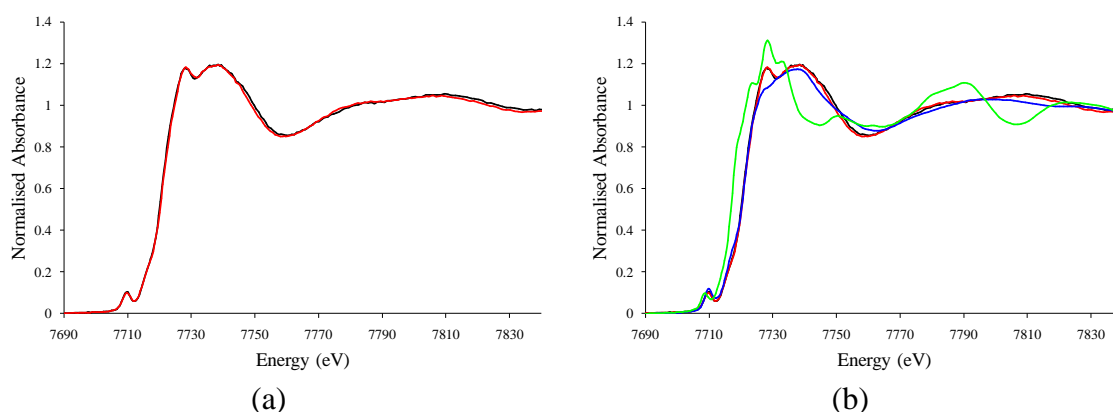


Figure 6-22. Co-K-edge XANES spectra of (a) $\text{La}_{9.67}\text{Si}_5\text{CoO}_{26}$ (black), $\text{La}_{10}\text{Si}_5\text{CoO}_{26.5}$ (red) and (b) with $\text{YSr}_2\text{Cu}_2\text{CoO}_7$ (blue) and CoCr_2O_4 (green) in addition.

The XANES spectrum of $\text{La}_{10}\text{Ge}_5\text{CoO}_{26.5}$ is shown in Figure 6-23, compared with that of the isostructural silicate $\text{La}_{10}\text{Si}_5\text{CoO}_{26.6}$. The edge positions of both are the same, consistent with Co^{3+} , see Figure 6-23 (b).

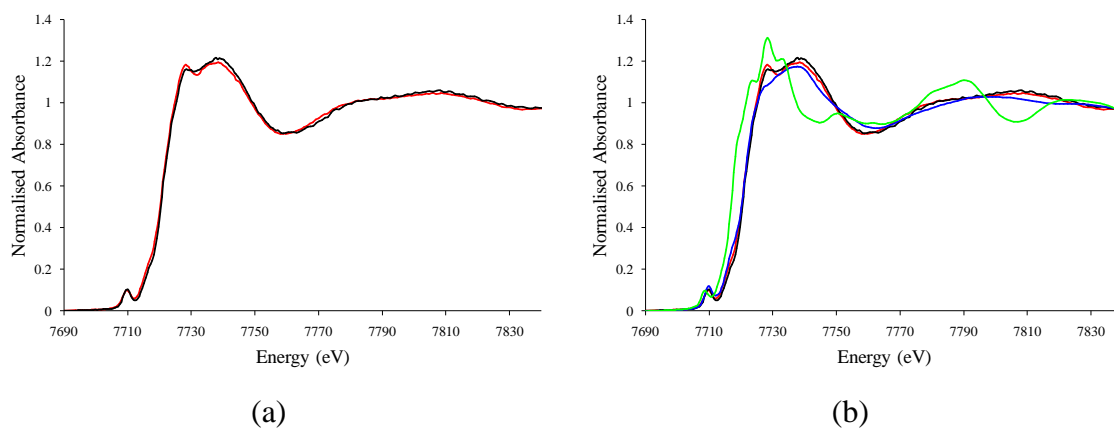


Figure 6-23. Co-K-edge XANES spectra of (a) $\text{La}_{10}\text{Ge}_5\text{CoO}_{26.5}$ (black), $\text{La}_{10}\text{Si}_5\text{CoO}_{26.6}$ (red) and (b) with $\text{YSr}_2\text{Cu}_2\text{CoO}_7$ (blue) and CoCr_2O_4 (green) in addition.

The tetrahedral coordination of cobalt in all silicates and germanates samples is confirmed in Figure 6-24 through comparison between the XANES of the samples and the standards $\text{YSr}_2\text{Cu}_2\text{CoO}_7$ and LaCoO_3 . Furthermore, the comparison between the spectra of the oxides and LaCoO_3 , containing Co^{3+} in octahedral coordination, shows that Co^{3+} in the oxides is not in octahedral coordination.³⁰⁴ The XANES spectra of $\text{La}_{10}\text{M}_5\text{CoO}_{26.5}$ ($\text{M} = \text{Ge}, \text{Si}$) show a pre-edge feature resembling that seen in the spectrum of $\text{YSr}_2\text{Cu}_2\text{CrO}_7$, confirming that Co^{3+} is tetrahedrally coordinated by O^{2-} anions. This confirms that Co^{3+} is substituting for $\text{Si}^{4+}/\text{Ge}^{4+}$ and not La^{3+} , which exhibit octahedral coordination. The pre-edge feature is associated with $1s\text{-}3d$ transitions, which are dependent on the presence of a centre of symmetry (Laporte selection rule) and/or p-d mixing of the 3d orbitals. In the symmetrical octahedral environment these transitions are Laporte forbidden and, hence, very weak.

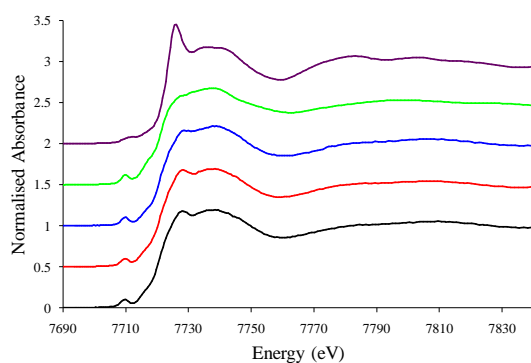


Figure 6-24. Co-K-edge XANES spectra of $\text{La}_{9.67}\text{Si}_5\text{CoO}_{26}$ (black), $\text{La}_{10}\text{Si}_5\text{CoO}_{26.5}$ (red), $\text{La}_{10}\text{Ge}_5\text{CoO}_{26.5}$ (blue), $\text{YSr}_2\text{Cu}_2\text{CoO}_7$ (green) and LaCoO_3 (purple).

6.3.2.2.2 Co-K-edge XANES of Ammoniated $\text{La}_{9.67}\text{Si}_5\text{CoO}_{26}$, $\text{La}_{10}\text{M}_5\text{CoO}_{26.5}$ ($M = \text{Si}, \text{Ge}$)

Figure 6-25 (a-c) show the XANES of $\text{La}_{9.67}\text{Si}_5\text{CoO}_{26}$, $\text{La}_{10}\text{Si}_5\text{CoO}_{26.5}$ and $\text{La}_{10}\text{Ge}_5\text{CoO}_{26.5}$ after reaction with ammonia at 800 °C (silicates) and 600 °C (germanate). After ammonolysis the edge positions appear shifted to lower energies by approximately 2.2 eV (Table 6-11).

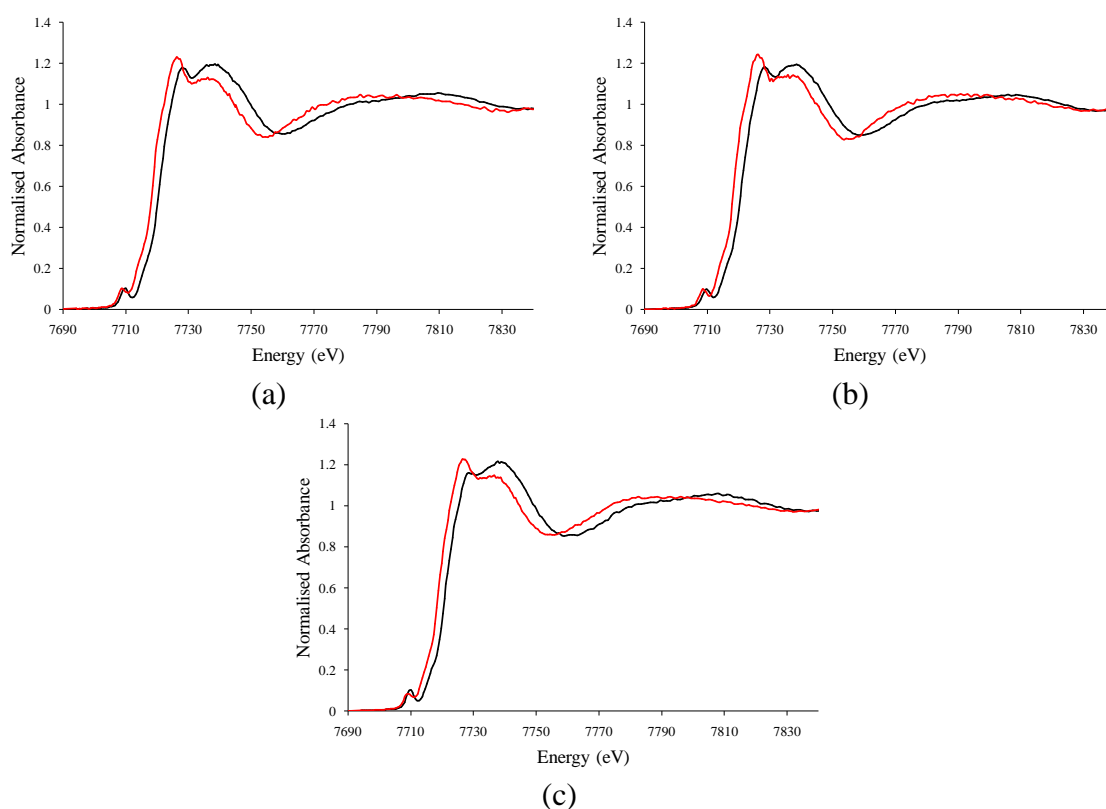


Figure 6-25. Co-K-edge XANES spectra of (a) $\text{La}_{9.67}\text{Si}_5\text{CoO}_{26}$ before (black) and after (red) reaction with ammonia at 800 °C, (b) $\text{La}_{10}\text{Si}_5\text{CoO}_{26.5}$ before (black) and after (red) reaction with ammonia at 800 °C and (c) $\text{La}_{10}\text{Ge}_5\text{CoO}_{26.5}$ before (black) and after (red) reaction with ammonia at 600 °C.

From the analysis of the XANES spectra of the silicates and germanates, reacted in ammonia at 800 °C and 600 °C, it appears that the reaction has not caused any change in the coordination of cobalt. The XANES spectra of the ammoniated $\text{La}_{9.67}\text{Si}_5\text{CoO}_{26}$, $\text{La}_{10}\text{M}_5\text{CoO}_{26.5}$ ($\text{M} = \text{Si}, \text{Ge}$) were compared with the spectra of CoCr_2O_4 , in which Co^{3+} shows tetrahedral coordination, $\text{Co-3,5-}t\text{-Bu-cysalen}$, with Co^{2+} in square planar, $[\text{Co}(\text{salen})]_2$, showing Co^{2+} in square based pyramidal coordination and $[\text{Co}(\text{acac})_2 \cdot \text{H}_2\text{O}]_2$, in which Co^{2+} is in octahedral coordination. The XANES patterns for the samples and standards are shown in Figure 6-26. The octahedral cobalt in $[\text{Co}(\text{acac})_2 \cdot \text{H}_2\text{O}]_2$ and square-planar cobalt in $\text{Co-3,5-}t\text{-Bu-cysalen}$ have only weak $1s-3d$ transitions and therefore no pre-edge features. The square based pyramidal cobalt coordination of $[\text{Co}(\text{salen})]_2$ and tetrahedral coordination of CoCr_2O_4 both give rise to this pre-edge feature, as do the apatite samples before and after treatment in ammonia. A large shoulder on the edge is common for square based pyramidal coordination ($[\text{Co}(\text{salen})]_2$) and square planar geometries ($\text{Co-3,5-}t\text{-Bu-cysalen}$), where one or more axial ligands, of an octahedron, are absent.^{321, 322} None of the apatite compounds show this feature. It can therefore be concluded that tetrahedral coordination for cobalt is maintained in the apatite compounds after reaction with ammonia.

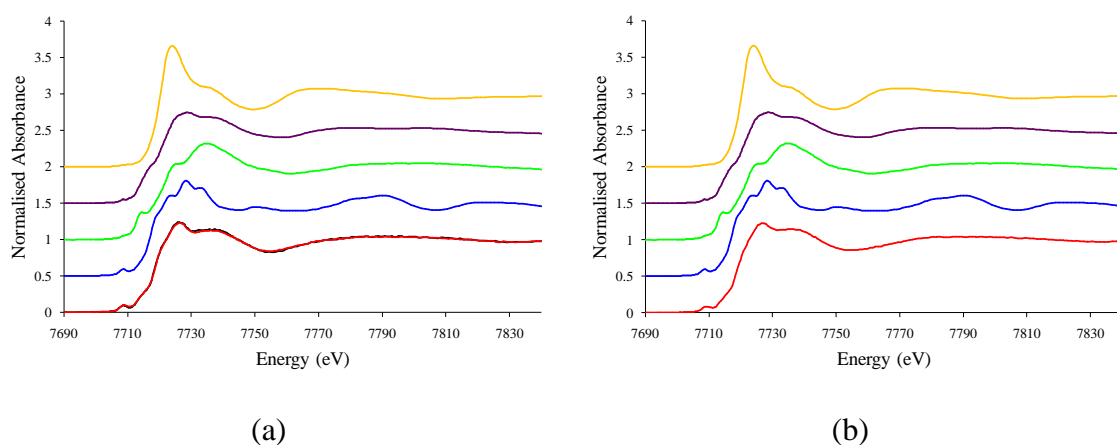


Figure 6-26. Co-K-edge XANES spectra of (a) $\text{La}_{9.67}\text{Si}_5\text{CoO}_{26}$ (red) and $\text{La}_{10}\text{Si}_5\text{CoO}_{26.5}$ (black) after reaction with ammonia at 800 °C, and (b) $\text{La}_{10}\text{Ge}_5\text{CoO}_{26.5}$ (red) after reaction with ammonia at 600 °C. CoCr_2O_4 (blue), $\text{Co-3,5-}t\text{-Bu-cysalen}$ (green), $[\text{Co}(\text{salen})]_2$ (purple) and $[\text{Co}(\text{acac})_2 \cdot \text{H}_2\text{O}]_2$ (yellow).

The comparison of XANES spectra shown in Figure 6-27 clearly shows that the edges for $\text{La}_{9.67}\text{Si}_5\text{CoO}_{26}$ and $\text{La}_{10}\text{M}_5\text{CoO}_{26.5}$ ($\text{M} = \text{Si}, \text{Ge}$) reacted with ammonia have shifted towards lower energy. This is a clear indication that the reaction in ammonia gas has

caused a reduction in the oxidation state of cobalt. The absorption edges of the silicates and germanate are between those in the $\text{YSr}_2\text{Cu}_2\text{CoO}_7$ and CoCr_2O_4 spectra. Table 6-11 indicates a $3+/2+$ mixed oxidation state for cobalt in the silicates and germanate apatites after reaction with ammonia at 800 °C and 600 °C.

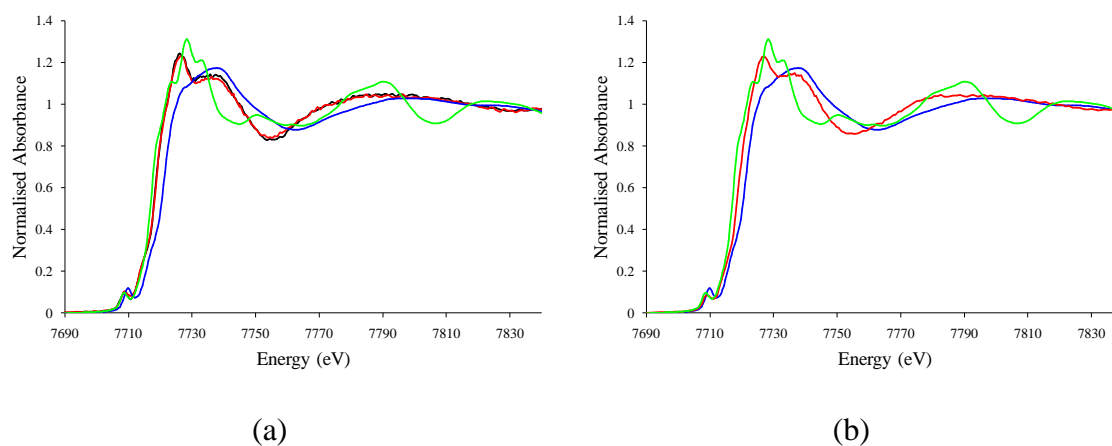


Figure 6-27. Co-K-edge XANES spectra of (a) $\text{La}_{9.67}\text{Si}_5\text{CoO}_{26}$ (red) and $\text{La}_{10}\text{Si}_5\text{CoO}_{26.5}$ (black) after ammonolysis at 800 °C, $\text{YSr}_2\text{Cu}_2\text{CoO}_7$ (blue) and CoCr_2O_4 (green) and (b) $\text{La}_{10}\text{Ge}_5\text{CoO}_{26.5}$ (red) after ammonolysis at 600 °C, $\text{YSr}_2\text{Cu}_2\text{CoO}_7$ (blue) and CoCr_2O_4 (green).

Compound/Reaction conditions	Edge position (eV)
$\text{La}_{9.67}\text{Si}_5\text{CoO}_{26}$	7720
$\text{La}_{10}\text{Si}_5\text{CoO}_{26.5}$	7720
$\text{La}_{10}\text{Ge}_5\text{CoO}_{26.5}$	7720
$\text{YSr}_2\text{Cu}_2\text{CoO}_7$ (Co^{3+})	7720
$\text{La}_{9.67}\text{Si}_5\text{CoO}_{26} + \text{NH}_3$ 800 °C	7718
$\text{La}_{10}\text{Si}_5\text{CoO}_{26.5} + \text{NH}_3$ 800 °C	7718
$\text{La}_{10}\text{Ge}_5\text{CoO}_{26.5} + \text{NH}_3$ 600 °C	7718
CoCr_2O_4 (Co^{2+})	7717
$\text{La}_{9.67}\text{Si}_5\text{CoO}_{26} + \text{NH}_3$ 1000 °C	7717
$\text{La}_{10}\text{Si}_5\text{CoO}_{26.5} + \text{NH}_3$ 1000 °C	7718
$\text{La}_{10}\text{Ge}_5\text{CoO}_{26.5} + \text{NH}_3$ 800 °C	7716
Co metal	7716

Table 6-11. Co-K-edge positions.

As the general apatite structure is maintained this may indicate that rather than the substitution of three O^{2-} by two N^{3-} there are other processes taking place. PXRD showed the apatite structure is maintained after ammonolysis and the reduction of the oxidation state of cobalt may be attributed to the reducing properties of ammonia.

Finally, the XANES for the reactions of $\text{La}_{9.67}\text{Si}_5\text{CoO}_{26}$ and $\text{La}_{10}\text{M}_5\text{CoO}_{26.5}$ ($\text{M} = \text{Si}/\text{Ge}$) with ammonia at 1000 °C (silicates) and 800 °C (germanate) are given in Figure 6-28. It can be seen that, relative to the starting materials, there are a number of differences including a shift to lower energies and an alteration in the edge features.

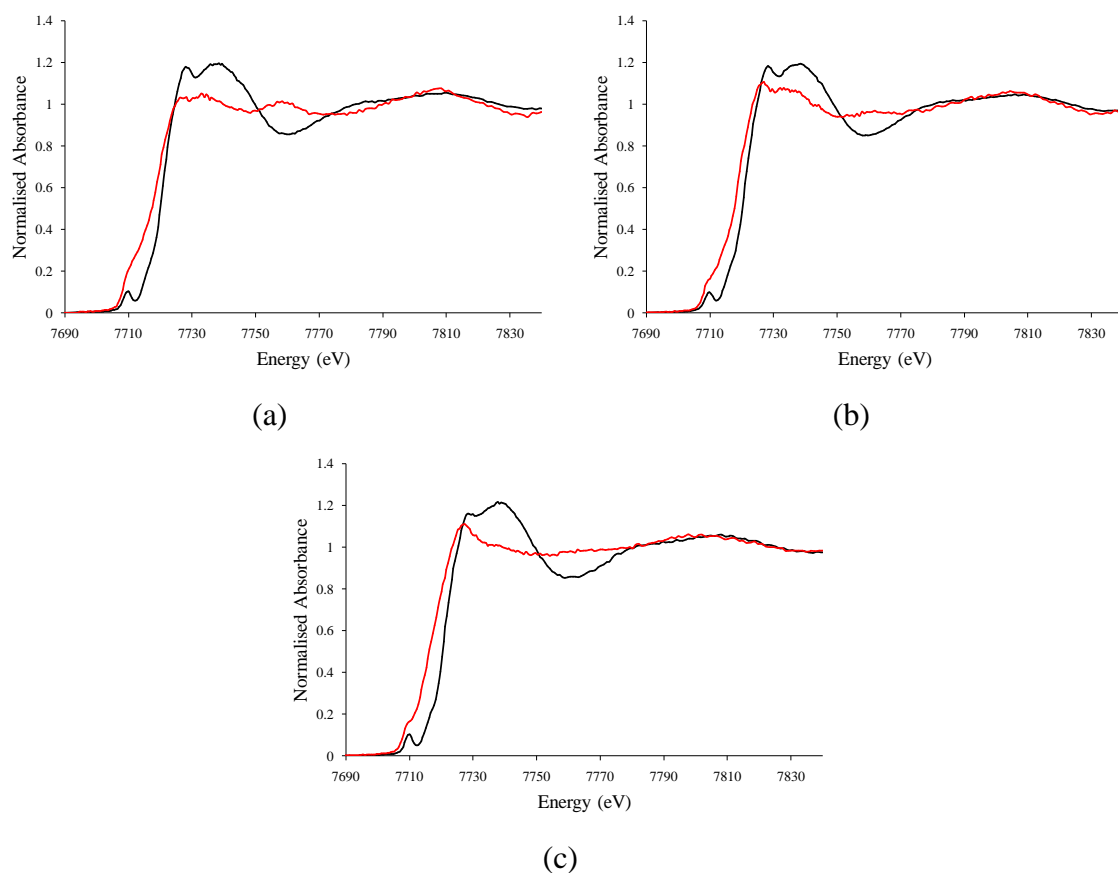


Figure 6-28. Co-K-edge XANES spectra of (a) $\text{La}_{9.67}\text{Si}_5\text{CoO}_{26}$ before (black) and after (red) reaction with NH_3 at 1000 °C, (b) $\text{La}_{10}\text{Si}_5\text{CoO}_{26.5}$ before (black) and after (red) reaction with NH_3 at 1000 °C and (c) $\text{La}_{10}\text{Ge}_5\text{CoO}_{26.5}$ before (black) and after (red) reaction with NH_3 at 800 °C.

The XANES patterns for all oxides and standards are shown in Figure 6-29. In all three cases the XANES show a complete loss of the pre-edge feature, previously attributed to $1s\text{-}3d$ transitions, and used to identify tetrahedral coordination. This implies that the cobalt is no longer in tetrahedral coordination (blue). The absence of this feature also rules out the square pyramidal coordination (purple). The ammoniated samples do, however, show a pronounced shoulder adjoining the edge. Such shoulders are seen in the square planar geometry (green) and also in the pure cobalt metal example. The best match to the XANES appears to be cobalt metal and therefore at higher temperatures ammoniation appears to cause some loss of cobalt metal from the apatite structure. A

similar loss of silicon was observed in $\text{La}_{9.33}\text{Si}_6\text{O}_{26}$ (section 6.1).³¹³ Diffraction peaks for cobalt metal are not present in the PXRD patterns (Figure 6-18, Figure 6-19 and Figure 6-20) implying an amorphous phase is present. Further evidence is shown in the EXAFS spectra in the following section.

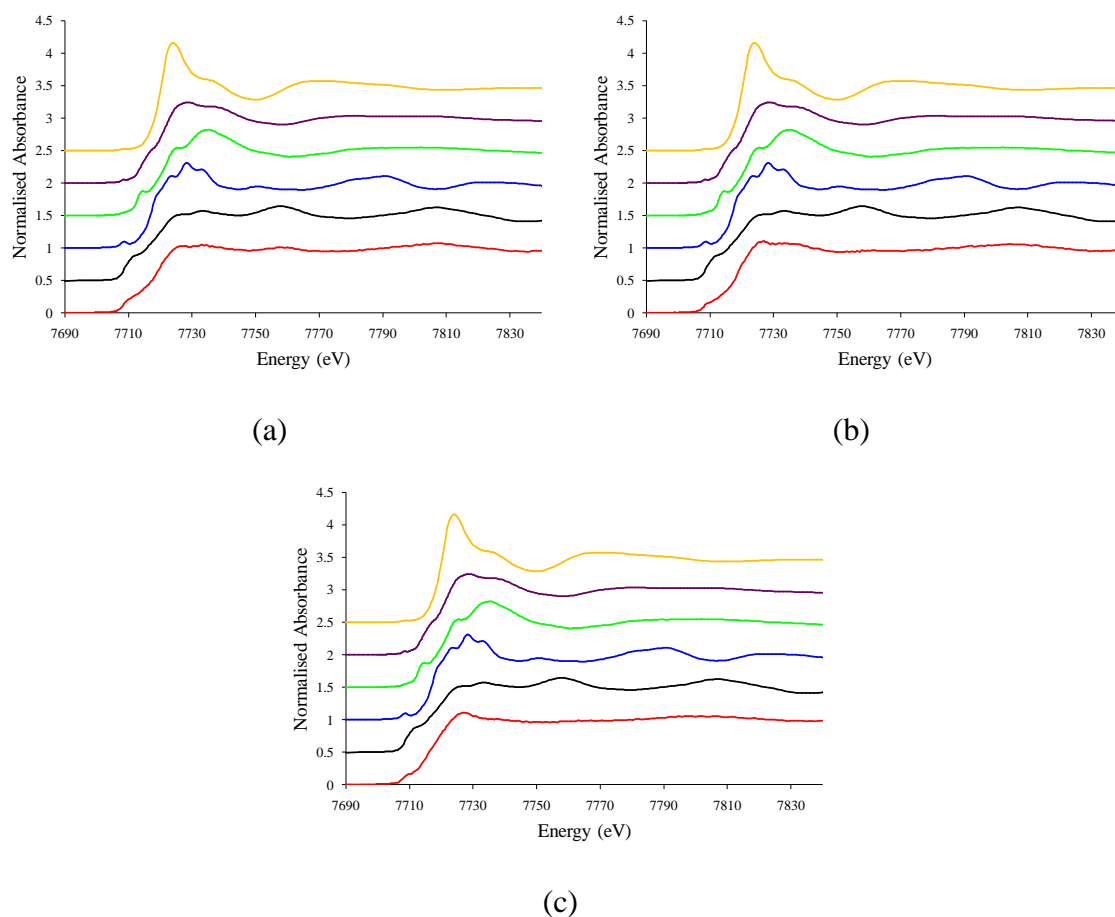


Figure 6-29. Co-K-edge XANES spectra of (a) $\text{La}_{9.67}\text{Si}_5\text{CoO}_{26}$ (red) after reaction with NH_3 at 1000 °C (b) $\text{La}_{10}\text{Si}_5\text{CoO}_{26.5}$ (red) after reaction with NH_3 at 1000 °C, and (c) $\text{La}_{10}\text{Ge}_5\text{CoO}_{26.5}$ (red) after reaction with NH_3 at 800 °C. Co metal (black), CoCr_2O_4 (blue), Co-3,5-*t*-Bu-cysalen (green), $[\text{Co}(\text{salen})]_2$ (purple) and $[\text{Co}(\text{acac})_2 \cdot \text{H}_2\text{O}]_2$ (yellow).

6.3.2.2.3 Co-K-edge EXAFS of $\text{La}_{9.67}\text{Si}_5\text{CoO}_{26}$, $\text{La}_{10}\text{M}_5\text{CoO}_{26.5}$ ($M = \text{Si}, \text{Ge}$)

As the XANES spectra indicated a tetrahedral environment of Co^{3+} for the three starting materials, $\text{La}_{9.67}\text{Si}_5\text{CoO}_{26}$, $\text{La}_{10}\text{Si}_5\text{CoO}_{26.5}$ and $\text{La}_{10}\text{Si}_5\text{GeO}_{26.5}$ a coordination of four oxide anions was assumed to model the first shell. Modelling of the data reported so far were limited to the first shell and modelling further shells proved difficult.³⁰⁴ To prevent the contributions of the other shells to the EXAFS, Fourier filtering was initially

performed. This limits the data to the first shell only ($1.1 < r < 1.9 \text{ \AA}$), removing contributions at higher r distances.

The Co-K-edge EXAFS and Fourier transformations for $\text{La}_{9.67}\text{Si}_5\text{CoO}_{26}$ are shown in Figure 6-30 (a-b). The initial Co-O bond length was set at 1.85 \AA , using the literature value for $\text{La}_{9.67}\text{Si}_5\text{CoO}_{26}$.³⁰⁴ The structural parameters obtained from the fitting of the data are shown in Table 6-12.

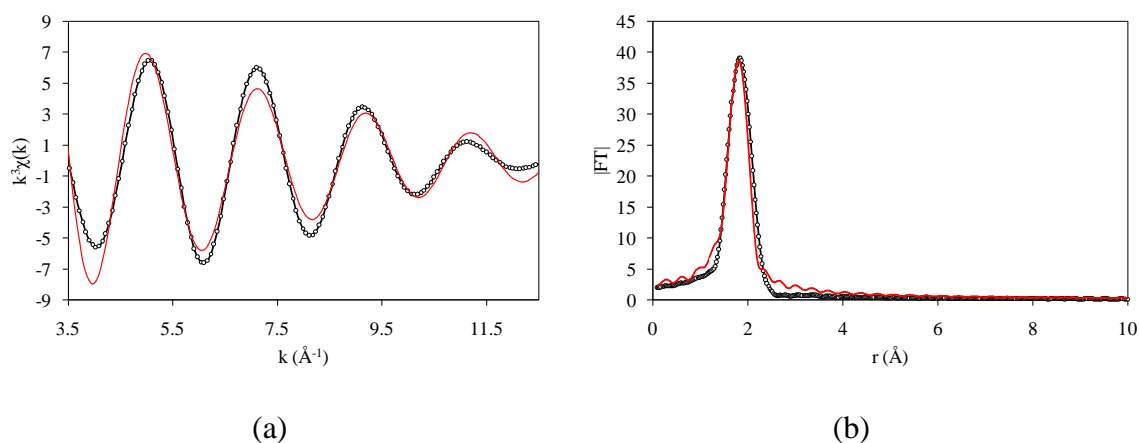


Figure 6-30. Co-K-edge (a) EXAFS and (b) Fourier transform for $\text{La}_{9.67}\text{Si}_5\text{CoO}_{26}$. The red and black lines correspond with the theoretical and experimental data respectively.

Shell	Atom type	Coordination	$r \text{ (\AA)}$	D-W factor (\AA^2)	R-fit (%)
1	O^{2-}	4	1.845(6)	0.012(1)	26.54

Table 6-12. Summary of refined Co-K-edge EXAFS parameters for $\text{La}_{9.67}\text{Si}_5\text{CoO}_{26}$.

The bond length of $1.845(6) \text{ \AA}$ is consistent with the previously obtained in the EXAFS analysis by Tolchard *et al.* and for literature values of Co-O bond lengths in tetrahedral coordination, i.e. $\sim 1.905 \text{ \AA}$ in $\text{YSr}_2\text{Cu}_2\text{CoO}_7$ and $\sim 1.986 \text{ \AA}$ in CoCr_2O_4 .^{304, 319, 320} This Co-O bond length is higher than that found by neutron diffraction performed by Tolchard *et al.* ($\sim 1.65 \text{ \AA}$) as this is based on an average (Si/Co)-O bond length,³⁰⁴ while XAS allows the cobalt site to be targeted exclusively.

Next, attempts were made to model beyond the first shell using the original, non-Fourier filtered, data. Neutron diffraction data was used as a guide to identify the likely atomic arrangements beyond the first shell.³⁰⁴

The proposed crystallographic cobalt coordination spheres, beyond the CoO_4 tetrahedra, derived from neutron diffraction are shown in Figure 6-31 and the bond lengths within 3.5 Å of the silicon/cobalt centre are given in Table 6-13.³⁰⁴

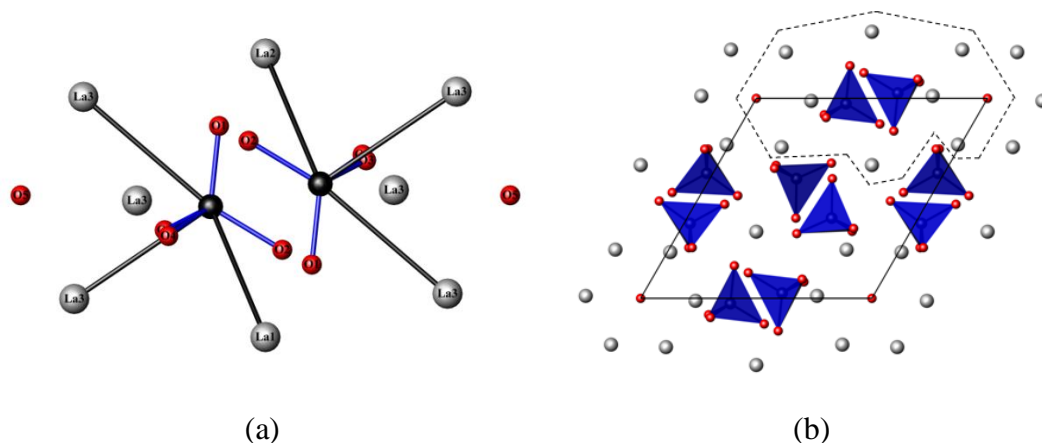


Figure 6-31. (a) The silicon/cobalt coordination (bond lengths < 3.5 Å) in $\text{La}_{9.66}\text{Si}_5\text{CoO}_{26.5}$, deduced from neutron diffraction. (b) The Si/Co coordination is highlighted, by the dotted line, in relation to the whole structure.

Bond lengths (Å)			
Si/Co – O(1)	1.607	Si/Co – La(3)	3.271
Si/Co – O(2)	1.664	Si/Co – La(2)	3.323
	3.213	Si/Co – La(3)	3.336
Si/Co – O(3)	1.590	Si/Co – La(1)	3.360
Si/Co – O(4)	1.734		

Table 6-13. Selected bond lengths in $\text{La}_{9.66}\text{Si}_5\text{CoO}_{26.5}$ derived from neutron diffraction data.³⁰⁴

The heavier atoms are more easily identified from the EXAFS (section 2.3.5) and, therefore, lanthanum cations were used to model the remaining absorption intensity in the EXAFS spectra. The neutron diffraction data shows four lanthanum atoms within 3.5 Å of Si/Co.³⁰⁴ These consist of two La(3) atoms, which are adjacent to the oxide anion channel and are part of the same $[\text{O}(5)\text{La}(3)_3]^{7+}$ triangular planar polyhedron (section 6), and two La atoms which lie between the (Si/Co) O_4 tetrahedra, La(1) and La(2). It can be said that, La(1) and La(2) alternate in linear chains running parallel to the *c*-axis. The lanthanum cations can be separated into two shells, one lanthanum at 3.271 Å (La(3)) and three lanthanum atoms at 3.340 Å, from cobalt.³⁰⁴ Refinement of

these parameters demonstrated a marked improvement in χ^2 from 3.817×10^{-6} to 2.432×10^{-6} , for the models using one and three shells respectively. The EXAFS and Fourier transformations for $\text{La}_{9.67}\text{Si}_5\text{CoO}_{26}$ are shown in Figure 6-32 and the structural parameters obtained from the fitting of the data are shown in Table 6-14.

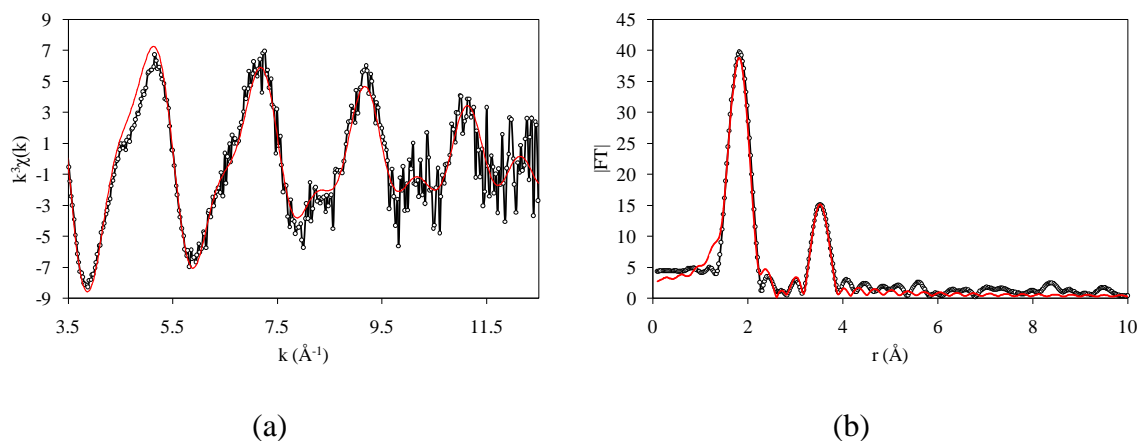


Figure 6-32. Co-K-edge (a) EXAFS and (b) Fourier transform for $\text{La}_{9.67}\text{Si}_5\text{CoO}_{26}$. The red and black lines correspond with the theoretical and experimental data respectively.

Shell	Atom type	Coordination	r (Å)	D-W factor (Å ²)	R-fit (%)
1	O^{2-}	4	1.854(5)	0.011(1)	
2	La^{3+}	1	3.113(18)	0.010(3)	28.87
3	La^{3+}	3	3.277(11)	0.014(2)	

Table 6-14. Summary of refined Co-K-edge EXAFS parameters for $\text{La}_{9.67}\text{Si}_5\text{CoO}_{26}$.

The bond lengths derived from EXAFS indicate a small reduction in all values compared to those found by neutron diffraction, but remain consistent with the apatite structure (Table 6-14 and Table 6-13).

The same data analysis procedure was applied to the EXAFS data for $\text{La}_{10}\text{Si}_5\text{CoO}_{26.5}$ and $\text{La}_{10}\text{Ge}_5\text{CoO}_{26.5}$. The fitting to the Fourier filtered EXAFS data, limited to the first shell, is presented in Appendix D.

The EXAFS and Fourier transformations for $\text{La}_{10}\text{Si}_5\text{CoO}_{26.5}$ are shown in Figure 6-33 and the structural parameters obtained from the fitting of the data are shown in Table 6-15.

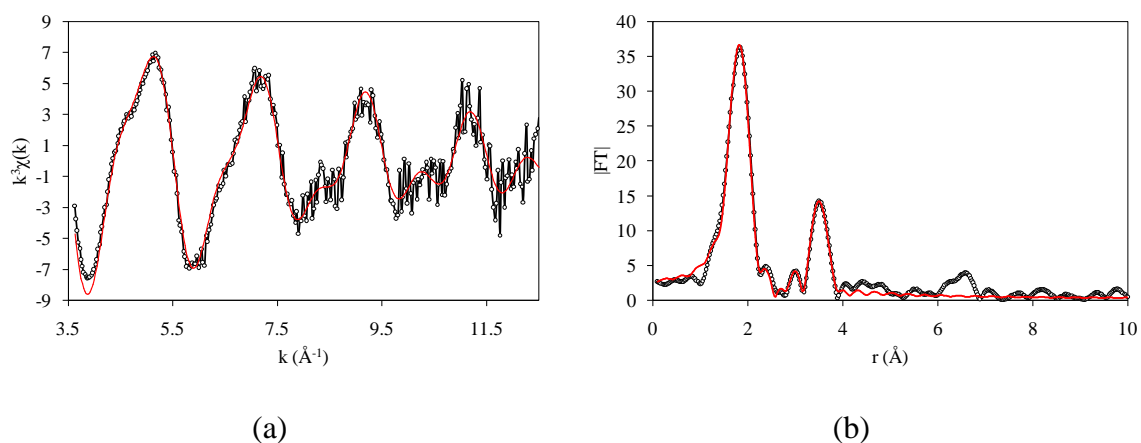


Figure 6-33. Co-K-edge (a) EXAFS and (b) Fourier transform for $\text{La}_{10}\text{Si}_5\text{CoO}_{26.5}$. The red and black lines correspond with the theoretical and experimental data respectively.

Shell	Atom type	Coordination	r (Å)	D-W factor (Å ²)	R-fit (%)
1	O^{2-}	4	1.857(5)	0.012(1)	
2	La^{3+}	1	3.096(22)	0.015(5)	24.89
3	La^{3+}	3	3.264(10)	0.016(2)	

Table 6-15. Summary of refined Co-K-edge EXAFS parameters for $\text{La}_{10}\text{Si}_5\text{CoO}_{26.5}$.

The bond distances for $\text{La}_{10}\text{Si}_5\text{CoO}_{26.5}$ are the same as those derived from the EXAFS of $\text{La}_{9.67}\text{Si}_5\text{CoO}_{26}$, within experimental error, as it may be expected due to the similar structure.

The EXAFS and Fourier transformations for $\text{La}_{10}\text{Ge}_5\text{CoO}_{26.5}$ are shown in Figure 6-34 and the structural parameters obtained from the fitting of the data are shown in Table 6-16. It was only possible to model two shells due to the poor quality of the data, with the single Co-La(3) shell omitted. The poor quality of this data set is not easy to explain as the EXAFS pattern was collected in the same conditions as the other patterns here examined.

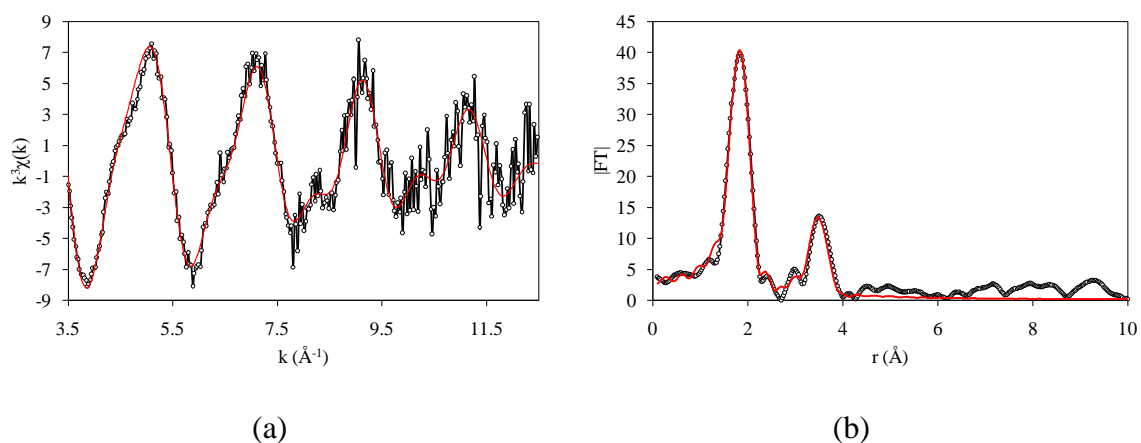


Figure 6-34. Co-K-edge (a) EXAFS and (b) Fourier transform for $\text{La}_{10}\text{Ge}_5\text{CoO}_{26.5}$. The red and black lines correspond with the theoretical and experimental data respectively.

Shell	Atom type	Coordination	r (Å)	D-W factor (Å ²)	R-fit (%)
1	O^{2-}	4	1.866(5)	0.010(1)	
2	La^{3+}	3	3.282(9)	0.020(2)	24.89

Table 6-16. Summary of refined Co-K-edge EXAFS parameters for $\text{La}_{10}\text{Ge}_5\text{CoO}_{26.5}$.

In general, the EXAFS analysis indicates that $\text{La}_{10}\text{Ge}_5\text{CoO}_{26.5}$ demonstrates similar structural features as the silicate counterparts. It does, however, appear that in the case of $\text{La}_{10}\text{Ge}_5\text{CoO}_{26.5}$, there is a slightly larger Co-O bond length than those observed in $\text{La}_{9.67}\text{Si}_5\text{CoO}_{26}$ and $\text{La}_{10}\text{Si}_5\text{CoO}_{26.5}$. The Debye-Waller factors of all samples are similar, so the difference in bond length is not attributed to increased tetrahedral distortion.

6.3.2.2.4 Co-K-edge EXAFS of Ammoniated $\text{La}_{9.67}\text{Si}_5\text{CoO}_{26}$, $\text{La}_{10}\text{M}_5\text{CoO}_{26.5}$ ($M = \text{Si}$, Ge)

Ammonolysis of the apatite materials, $\text{La}_{9.67}\text{Si}_5\text{CoO}_{26}$ and $\text{La}_{10}\text{Si}_5\text{CoO}_{26.5}$ at 800 °C and $\text{La}_{10}\text{Ge}_5\text{CoO}_{26.5}$ at 600 °C, has been confirmed through XANES and PXRD to cause no overall deterioration in the apatite structure. TGA, shown in the following section (6.3.2.2.5) indicates that nitrogen has been incorporated into the $\text{La}_{10}\text{M}_5\text{CoO}_{26.5}$ ($M = \text{Si}$, Ge) samples only and all samples also show a reduction in oxygen content. The three proposed stoichiometries are $\text{La}_{9.67}\text{Si}_5\text{CoO}_{25.62}$, $\text{La}_{10}\text{Si}_5\text{CoO}_{25.87}\text{N}_{0.18}$ and $\text{La}_{10}\text{Ge}_5\text{CoO}_{26.08}\text{N}_{0.13}$.

In the case of $\text{La}_{9.67}\text{Si}_5\text{CoO}_{25.62}$, derived from the reaction of $\text{La}_{9.67}\text{Si}_5\text{CoO}_{26}$ in ammonia at 800 °C, there appears to be only a small reduction in the oxygen stoichiometry and TGA does not indicate any N^{3-} incorporation. The most likely site for the oxide removal is the oxide anion channel. The ability of this site to incorporate anion vacancies was demonstrated in the ammoniation of $\text{La}_{9.33}\text{Si}_6\text{O}_{26}$.³¹³ This implies the CoO_4 tetrahedra would remain relatively unaltered in $\text{La}_{9.67}\text{Si}_5\text{CoO}_{26}$ ammonolysis. Due to relatively poor data quality only the first shell was modelled. The EXAFS and Fourier transformation for $\text{La}_{9.67}\text{Si}_5\text{CoO}_{25.62}$ are shown in Figure 6-35 and the structural parameters obtained from the fitting of the data are shown in Table 6-17.

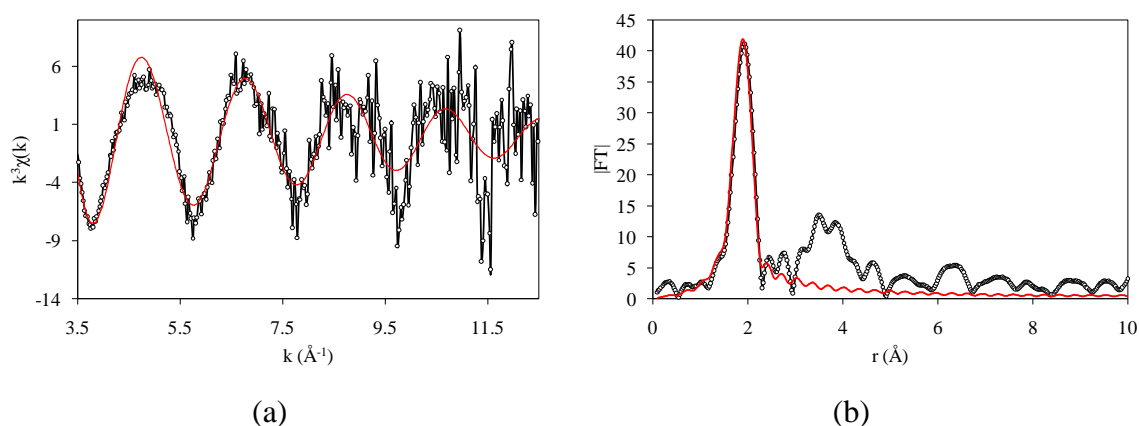


Figure 6-35. Co-K-edge (a) EXAFS and (b) Fourier transform for $\text{La}_{9.67}\text{Si}_5\text{CoO}_{26}$, after reaction in NH_3 at 800 °C. The red and black lines correspond with the theoretical and experimental data respectively.

Shell	Atom type	Coordination	r (Å)	D-W factor (Å ²)	R-fit (%)
1	O^{2-}	4	1.922(10)	0.010(2)	53.10

Table 6-17. Summary of refined Co-K-edge EXAFS parameters for $\text{La}_{9.67}\text{Si}_5\text{CoO}_{26}$ after reaction with NH_3 at 800 °C.

The Co-O bond lengths show a slight increase from 1.854(5) Å, in $\text{La}_{9.67}\text{Si}_5\text{CoO}_{26}$, to 1.922(10) Å, in $\text{La}_{9.67}\text{Si}_5\text{CoO}_{25.62}$, possibly as a result of the larger cobalt cation radii arising upon reduction in cobalt oxidation state, after ammonolysis.

Both the $\text{La}_{10}\text{M}_5\text{CoO}_{26.5}$ ($\text{M} = \text{Si}, \text{Ge}$) samples show only a small N^{3-} incorporation. The total oxygen stoichiometry does not fall below 24, as in $\text{La}_{10}\text{Si}_5\text{CoO}_{25.87}\text{N}_{0.18}$ and $\text{La}_{10}\text{Ge}_5\text{CoO}_{26.08}\text{N}_{0.13}$, so it is likely that the MO_4 tetrahedra remain free from nitrogen.

The $\text{La}_{10}\text{Si}_5\text{CoO}_{26.5}$ sample, heated in ammonia at 800 °C ($\text{La}_{10}\text{Si}_5\text{CoO}_{25.87}\text{N}_{0.18}$), was modelled using parameters derived from the initial apatite (Table 6-15). The EXAFS and Fourier transformations for $\text{La}_{10}\text{Si}_5\text{CoO}_{25.87}\text{N}_{0.18}$ are shown in Figure 6-36 and the structural parameters obtained from the fitting of the data are shown in Table 6-18.

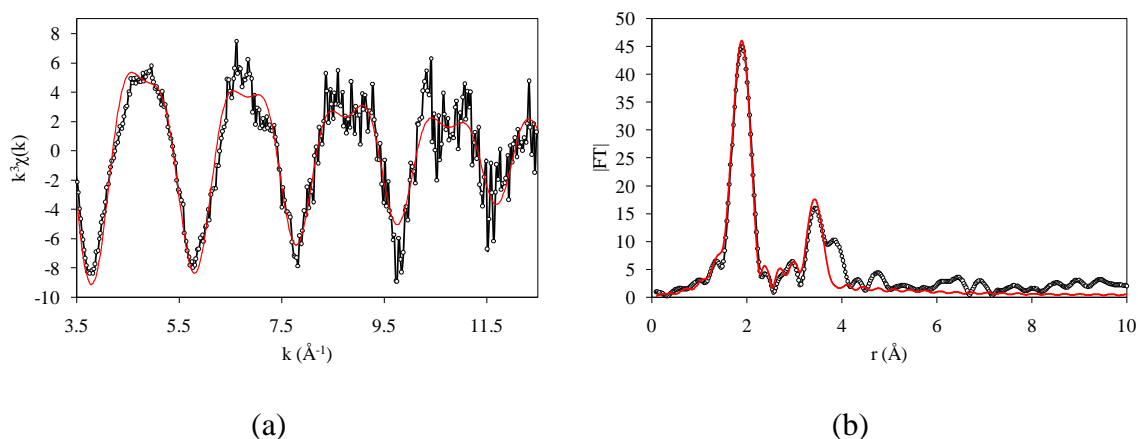


Figure 6-36. Co-K-edge (a) EXAFS and (b) Fourier transform for $\text{La}_{10}\text{Si}_5\text{CoO}_{26.5}$ after reaction with NH_3 at 800 °C. The red and black lines correspond with the theoretical and experimental data respectively.

Shell	Atom type	Coordination	r (Å)	D-W factor (Å ²)	R-fit (%)
1	O^{2-}	4	1.916(5)	0.008(1)	
2	La^{3+}	1	3.108(19)	0.009(4)	33.06
3	La^{3+}	3	3.261(11)	0.013(11)	

Table 6-18. Summary of refined Co-K-edge EXAFS parameters for $\text{La}_{10}\text{Si}_5\text{CoO}_{26.5}$ after reaction with NH_3 at 800 °C.

The structural parameters show only a small increase in Co-O bond length, from cobalt reduction. The Co-La parameters remain unaltered, relative to the initial apatite, indicating that the incorporation of such a small amount of nitrogen and the removal of the interstitial oxygen anions did not significantly modify the local Co environment. The Fourier transform does, however, show an addition unmodelled peak just below 4 Å. Figure 6-37 shows the EXAFS and Fourier transformations for $\text{La}_{10}\text{Si}_5\text{CoO}_{25.87}\text{N}_{0.18}$

and Table 6-19 shows the structural parameters from fitting the data with an additional shell of two lanthanum cations at 3.67 Å. These two cation distances were initially taken from the neutron diffraction data of $\text{La}_{9.66}\text{Si}_5\text{CoO}_{26}$.³⁰⁴

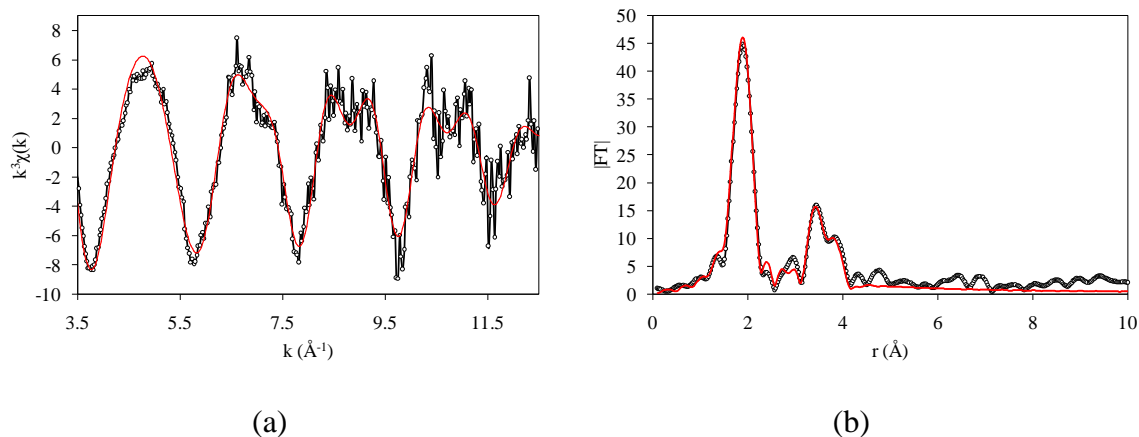


Figure 6-37. Co-K-edge (a) EXAFS and (b) Fourier transform for $\text{La}_{10}\text{Si}_5\text{CoO}_{26.5}$ after reaction with NH_3 at 800 °C. The red and black lines correspond with the theoretical and experimental data respectively.

Shell	Atom type	Coordination	r (Å)	D-W factor (Å ²)	R-fit (%)
1	O^{2-}	4	1.918(4)	0.008(1)	
2	La^{3+}	1	3.159(54)	0.016(9)	29.67
3	La^{3+}	3	3.288(23)	0.024(12)	
4	La^{3+}	2	3.577(16)	0.013(3)	

Table 6-19. Summary of refined Co-K-edge EXAFS parameters for $\text{La}_{10}\text{Si}_5\text{CoO}_{26.5}$ after reaction with NH_3 at 800 °C.

The EXAFS and Fourier transformation for $\text{La}_{10}\text{Ge}_5\text{CoO}_{26.5}$, after reaction with ammonia at 600 °C ($\text{La}_{10}\text{Ge}_5\text{CoO}_{26.08}\text{N}_{0.13}$), and the refined structural parameters are shown in Figure 6-38 and Table 6-20 respectively.

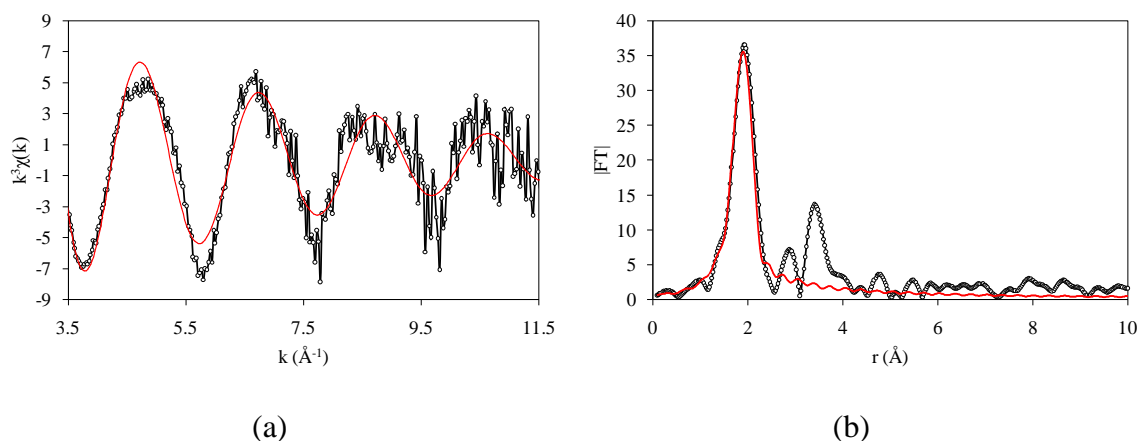


Figure 6-38. Co-K-edge (a) EXAFS and (b) Fourier transform for $\text{La}_{10}\text{Ge}_5\text{CoO}_{26.5}$ after reaction with NH_3 at 600 °C. The red and black lines correspond with the theoretical and experimental data respectively.

Shell	Atom type	Coordination	r (Å)	D-W factor (Å ²)	R-fit (%)
1	O^{2-}	4	1.930(7)	0.013(1)	42.52

Table 6-20. Summary of refined Co-K-edge EXAFS parameters for $\text{La}_{10}\text{Ge}_5\text{CoO}_{26.5}$ after reaction with NH_3 at 600 °C.

In a similar way to the ammonolysis of $\text{La}_{10}\text{Si}_5\text{CoO}_{26.5}$, $\text{La}_{10}\text{Ge}_5\text{CoO}_{26.5}$ shows only a small nitrogen absorption ($\text{La}_{10}\text{Ge}_5\text{CoO}_{26.08}\text{N}_{0.13}$) upon ammonolysis and removal of interstitial oxygen. Owing to the data quality only the first shell was modelled, but this was consistent with the other previous ammoniated, cobalt containing, apatites.

Finally are the results yielding from the high temperature ammonolysis reactions at temperature over 800 °C. The XANES analysis performed on the apatites at these temperatures showed the presence of cobalt metal in all samples. The absence of cobalt metal peaks in the PXRD patterns indicates that the cobalt is amorphous. The EXAFS for each of the samples showed the same general pattern. $\text{La}_{9.67}\text{Si}_5\text{CoO}_{26}$, after reaction with ammonia at 1000 °C, is used as an example. Figure 6-39 shows the EXAFS and Fourier transformation for $\text{La}_{9.67}\text{Si}_5\text{CoO}_{26}$, after reaction with ammonia at 1000 °C, based on a cobalt metal model.

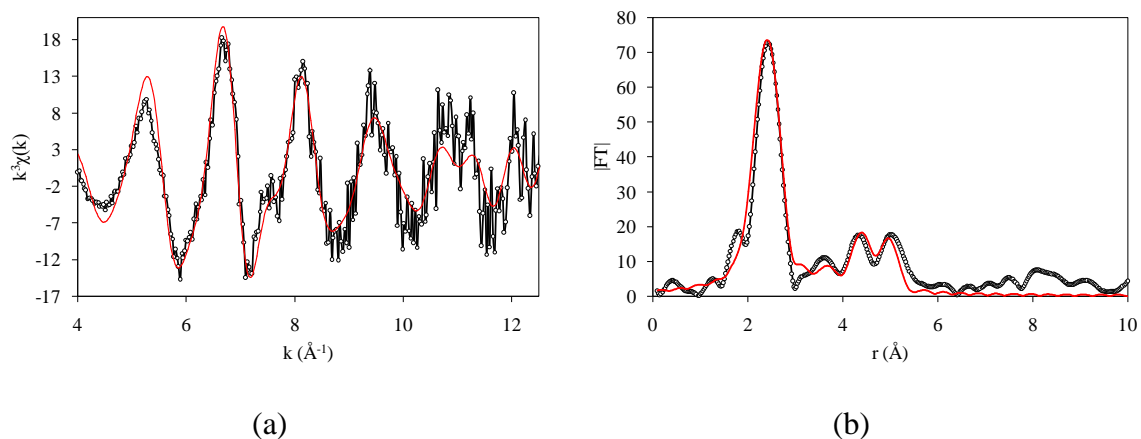


Figure 6-39. Co-K-edge (a) EXAFS and (b) Fourier transform for $\text{La}_{9.67}\text{Si}_5\text{CoO}_{26}$, after reaction in NH_3 at 1000°C . The red and black lines correspond with the theoretical and experimental data respectively.

Cobalt metal shows a hexagonal close packed structure.³²³ The theoretical model shows a strong resemblance to the experimental data, however, the derived parameters show unsatisfactory bond lengths with high errors and Debye-Waller factors. These may be the result of the amorphous nature of the cobalt or the presence of additional amorphous phases, implied by the unfitted peaks in the Fourier transform. For this reason only the first shell of the cobalt was modelled for all the samples. Figure 6-40 shows the EXAFS and Fourier transform for $\text{La}_{9.67}\text{Si}_5\text{CoO}_{26}$, after reaction in ammonia at 1000°C , modelled based on a single shell of twelve cobalt atoms at a distance of 2.5 \AA . The refined structural parameters obtained from the fitting of the data are shown in Table 6-21.

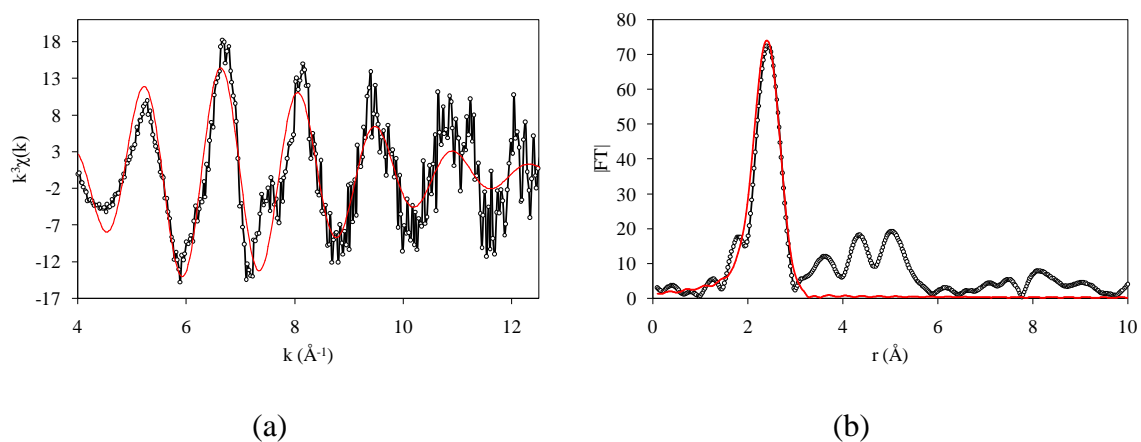


Figure 6-40. Co-K-edge (a) EXAFS and (b) Fourier transform for $\text{La}_{9.67}\text{Si}_5\text{CoO}_{26}$, after reaction in NH_3 at 1000°C . The red and black lines correspond with the theoretical and experimental data respectively.

Sample	Atom type	Coordination	r (Å)	D-W factor (Å ²)	R-fit (%)
La _{9.67} Si ₅ CoO ₂₆ + NH ₃ 1000 °C	Co	12	2.481(12)	0.026(13)	54.15
La ₁₀ Si ₅ CoO _{26.5} + NH ₃ 1000 °C	Co	12	2.482(11)	0.026(13)	57.30
La ₁₀ Ge ₅ CoO _{26.5} + NH ₃ 800 °C	Co	12	2.480(14)	0.034(2)	58.74

Table 6-21. Summary of refined Co-K-edge EXAFS parameters for La_{9.67}Si₅CoO₂₆, La₁₀Si₅CoO_{26.5}, La₁₀Ge₅CoO_{26.5} after reaction with NH₃ at 1000 °C, 1000 °C and 800 °C respectively.

The Co-Co distances in all the apatite samples reacted in ammonia at high temperature show strong correlation to the literature value,³²³ supporting the hypothesis that the original apatites have undergone partial decomposition with the loss of cobalt metal.

6.3.2.2.5 Thermogravimetric Analysis of Ammoniated La_{9.67}Si₅CoO₂₆, La₁₀M₅CoO_{26.5} (M = Si, Ge)

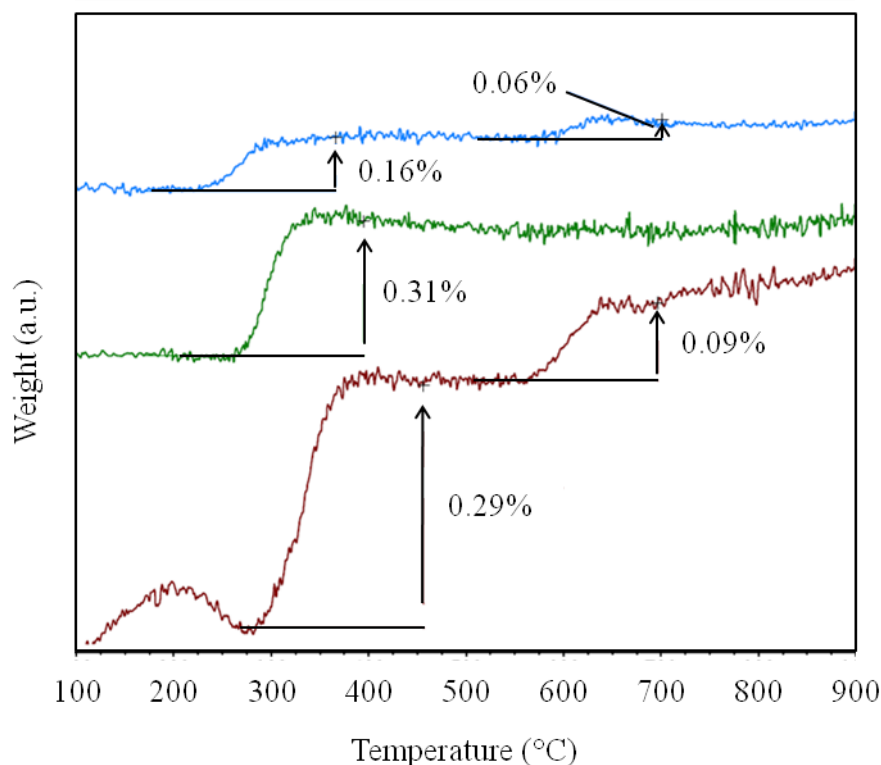


Figure 6-41. TGA plots of La_{9.67}Si₅CoO₂₆ (green), La₁₀Si₅CoO_{26.5} (brown) and La₁₀Ge₅CoO_{26.5} (blue) after reaction with NH₃ at 800 °C, 800 °C and 600 °C respectively.

As in the previous ammonolysis reactions, thermogravimetric analysis was performed to determine the extent of nitrogen incorporation into the materials. Figure 6-41 shows the

TGA trace for $\text{La}_{9.67}\text{Si}_5\text{CoO}_{26}$, $\text{La}_{10}\text{Si}_5\text{CoO}_{26.5}$ and $\text{La}_{10}\text{Ge}_5\text{CoO}_{26.5}$ after reaction with ammonia at 800, 800 and 600 °C respectively. In addition to the mass increase at ~ 600 °C there is a mass increase at ~ 300 °C. Given the apparent reduction in cobalt oxidation state, displayed in the XANES spectra, this mass increase is tentatively attributed to reincorporating of O^{2-} , lost in the reduction of cobalt. The weight increase at ~ 600 °C is attributed to the substitution of two N^{3-} by three O^{2-} . The resulting chemical formulae, calculated from TGA, are shown in Table 6-22.

The TGA of $\text{La}_{9.67}\text{Si}_5\text{CoO}_{26}$ shows no evidence of a weight increase at ~ 600 °C suggested that there has been no N^{3-} incorporation upon ammonolysis. This may be related to the fact that this sample is normally oxygen stoichiometric, while the previous work on the $\text{La}_{8+x}\text{Sr}_{2-x}\text{Si}_6\text{O}_{26+x/2}$ systems suggested that the presence of oxygen excess was the driving force for the nitridation. The weight increase at ~ 300 °C does, however, imply O^{2-} absorption to accommodate an O^{2-} deficiency in the ammoniated sample. Assuming the 0.31% weight change is due to an anion deficiency, a stoichiometry of $\text{La}_{9.67}\text{Si}_5\text{CoO}_{25.62}$ is proposed for the ammoniated sample. It should also be noted that such a stoichiometry would imply a Co oxidation state of ~ 2.23+. This is consistent with the XANES data presented earlier, which showed a Co oxidation state close to 2+, but intermediate between 2+ and 3+.

Both the $\text{La}_{10}\text{Si}_5\text{CoO}_{26.5}$ and $\text{La}_{10}\text{Ge}_5\text{CoO}_{26.5}$ ammoniated samples show weight increases at approximately 300 °C and 600 °C. These increases are attributed to $\text{O}^{2-}/\text{N}^{3-}$ substitution and an O^{2-} deficiency in the ammoniated apatites. A 0.09% mass increase in the TGA pattern of the ammoniated $\text{La}_{10}\text{Si}_5\text{CoO}_{26.5}$ sample suggests that, in the 375-550 °C range of the TGA, the stoichiometry of the sample is $\text{La}_{10}\text{Si}_5\text{CoO}_{26.23}\text{N}_{0.18}$. The 0.29% increase, associated with O^{2-} incorporation alone, implies a final stoichiometry of $\text{La}_{10}\text{Si}_5\text{CoO}_{25.87}\text{N}_{0.18}$ for the reaction of $\text{La}_{10}\text{Si}_5\text{CoO}_{26.5}$ with ammonia at 800 °C. The Co oxidation state of ~ 2.28+, this implies, is consistent with the XANES analysis. In addition, the oxidation states of ~ 2.23+ and ~ 2.28+, for $\text{La}_{9.67}\text{Si}_5\text{CoO}_{26}$ and $\text{La}_{10}\text{Si}_5\text{CoO}_{26.5}$ respectively, supports the similarity in edge position observed in the XANES.

Similarly, the mass increase of 0.06%, at 600 °C, and 0.16%, at 300 °C, for the $\text{La}_{10}\text{Ge}_5\text{CoO}_{26.5}$ ammoniated samples yields an intermediate (~ 375-550 °C)

stoichiometry of $\text{La}_{10}\text{Ge}_5\text{CoO}_{26.30}\text{N}_{0.13}$ and a final formula of $\text{La}_{10}\text{Ge}_5\text{CoO}_{26.08}\text{N}_{0.13}$. This formula implies an oxidation state of $\sim 2.55+$. This is supported by XANES analysis and is consistent with the difference in edge position seen between the isostructural $\text{La}_{10}\text{Si}_5\text{CoO}_{26.5}$ and $\text{La}_{10}\text{Ge}_5\text{CoO}_{26.5}$ upon reaction with ammonia at 800 and 600 °C respectively, Figure 6-27.

Reaction conditions	Weight increase (%)	Chemical formula (~ 375-550 °C)****	Weight increase (%)	Chemical formula (after ammonolysis)
$\text{La}_{9.67}\text{Si}_5\text{CoO}_{26} + \text{NH}_3$ 800 °C	-	-	0.31	$\text{La}_{9.67}\text{Si}_5\text{CoO}_{25.62}$
$\text{La}_{10}\text{Si}_5\text{CoO}_{26.5} + \text{NH}_3$ 800 °C	0.09	$\text{La}_{10}\text{Si}_5\text{CoO}_{26.23}\text{N}_{0.18}$	0.29	$\text{La}_{10}\text{Si}_5\text{CoO}_{25.87}\text{N}_{0.18}$
$\text{La}_{10}\text{Ge}_5\text{CoO}_{26.5} + \text{NH}_3$ 600 °C	0.06	$\text{La}_{10}\text{Ge}_5\text{CoO}_{26.30}\text{N}_{0.13}$	0.16	$\text{La}_{10}\text{Ge}_5\text{CoO}_{26.08}\text{N}_{0.13}$

Table 6-22. Compositions for $\text{La}_{9.67}\text{Si}_5\text{CoO}_{26}$, $\text{La}_{10}\text{M}_5\text{CoO}_{26.5}$ (M = Si, Ge) samples after heating in NH_3 .

The Co substituted apatites, therefore, show far less N^{3-} uptake upon ammonolysis than the unsubstituted sample, $\text{La}_{9.7(1)}\text{Si}_6\text{O}_{22.6(2)}\text{N}_{2.7(2)}$, instead favouring reduction of the cobalt metal through loss of interstitial O^{2-} anions. The result of such low N^{3-} uptake is that overall anion content does not reach values significantly below 26 in the three samples, $\text{La}_{9.67}\text{Si}_5\text{CoO}_{25.62}$, $\text{La}_{10}\text{Si}_5\text{CoO}_{25.87}\text{N}_{0.18}$ and $\text{La}_{10}\text{Ge}_5\text{CoO}_{26.08}\text{N}_{0.13}$. Once again, this may offer an explanation to the lack of anisotropic peak broadening in the PXRD ($l > 1$ peaks) when compared to $\text{La}_{9.7(1)}\text{Si}_6\text{O}_{22.6(2)}\text{N}_{2.7(2)}$, as the cobalt containing phases are free from anion vacancies along the channel anion sites.

Further data, such as neutron diffraction and/or elemental analysis, is required to support these suggestions further.

**** Chemical formula proposed for the intermediate ~ 300 -550 °C range of the TGA patterns

6.4 Conclusions

In this study it has been shown that in all cases of ammonolysis of the apatites, $\text{La}_{9.33}\text{Si}_6\text{O}_{26}$, $\text{La}_{8+x}\text{Sr}_{2-x}\text{M}_6\text{O}_{26+x/2}$ ($\text{M} = \text{Si}, \text{Ge}; 0 \leq x \leq 2$), $\text{La}_{9.67}\text{Si}_5\text{CoO}_{26}$ and $\text{La}_{10}\text{M}_5\text{CoO}_{26.5}$ ($\text{M} = \text{Si}, \text{Ge}$), at the high temperatures currently required for application in SOFCs, reaction with the fuel source (ammonia) occurs.

Results suggest that the apatites can accommodate nitride anions into the oxide anion channel, which runs along the c -axis of these materials, with the displacement of oxygen. These channels are also a suitable place for the resulting oxide anion vacancies arising from ammonolysis of apatites which are initially oxygen stoichiometric, i.e. those containing 26 oxide anions per formula unit. Additionally, structural investigations at high temperatures (> 950 °C) indicated that the silicate apatite, $\text{La}_{9.33}\text{Si}_6\text{O}_{26}$, shows the ability to accommodate some nitrogen in the SiO_4 tetrahedra, however, the stoichiometries suggested by the other apatites investigated suggest that this process is not a favourable one, with the overall oxygen content not dropping below 24, the minimum required to maintain the SiO_4 tetrahedra.

Investigation into the strontium doped samples, containing additional interstitial oxygen ($\text{La}_{8+x}\text{Sr}_{2-x}\text{M}_6\text{O}_{26+x/2}$ ($\text{M} = \text{Si}, \text{Ge}; x > 0$)), implies that the process of nitridation is driven by the removal of these interstitial anions to yield an overall anion content ($\text{N} + \text{O}$) of 26. This result was reflected in the cobalt doped apatites, however, in these cases the ability of the cobalt to reduce in oxidation state resulted primarily in elimination of interstitial oxide anions with very little nitrogen uptake.

The question of the effect of ammonolysis on the apatites is a difficult one. Conductivity measurements, performed on $\text{La}_{9.33}\text{Si}_6\text{O}_{26}$, before and after ammonolysis, showed only a small decrease from $1.1 \times 10^{-4} \text{ S cm}^{-1}$ to $4.8 \times 10^{-5} \text{ S cm}^{-1}$, at 500 °C. TGA revealed that the ammoniated sample showed only a small incorporation on nitrogen (mass increase of $< 0.1\%$). The cause of the reduced nitrogen uptake stems from the necessity to ammoniate the sample in pellet form, rather than powder, so as to produce a dense, solid, sample for conductivity measurements. The pellets show reduced surface area and slower rate of diffusion of the gaseous reagents into the

sample. It is for this reason that it is common to use powders of particularly small particle size when carrying out ammonolysis, to accelerate the reaction with ammonia. The reduction in conductivity is therefore a consequence of only surface nitridation. However, the use of this apatite-type material, as an electrolyte operating at high temperatures of 950 °C, would be likely to result in surface nitridation and the formation of a poorly conducting layer between the electrolyte and electrodes (the anode). Such a process would be detrimental to performance. Indications, therefore are that lower temperatures are required (< 600 °C), at which nitrogen uptake is negligible, to prevent adverse effects of fuel on the performance of the fuel cell.

Furthermore, in the cases of cationic substituted apatites, used for their improved conductivities, it has been shown that the effect of nitridation is a removal of the interstitial oxide anions, a fundamental requirement for the high conductivity shown by these materials. It can, therefore, be proposed to be unfavourable in terms of efficiency of these materials in SOFCs, even at temperatures as low as 600 °C.

These studies highlight the importance of further studies on the influence of ammonia on SOFC electrolytes for use with ammonia fuel cells.

7 Overall Conclusions

Historically, research in solid-state chemistry has focused largely on oxides and the chemical modification of their structure and properties. This has been achieved mainly by means of isovalent or aliovalent cationic substitutions. The relative simplicity of the preparation of oxides played a role in this general trend but it must also be said that oxides provided the scientific and technological world with a number of materials with unprecedented physical properties, such as superconductivity and colossal magnetoresistance.

Consequentially, the chemistry of non-oxide compounds has been overlooked by the majority of research groups. Recently, through progress made in synthetic methods, non-oxide compounds have enjoyed more attention, mainly due to the diversity of their chemistry. In fact, metals showing uncommon oxidation states and coordination geometries are often found in non-oxide compounds. Non-oxide compounds can be classified as single-anion and mixed-anion compounds, with one and two anion species per chemical formula respectively. Research work on examples of compounds belonging to both classes has been reported in this thesis.

The examples of single-anion non-oxide compounds reported in this thesis are: Ba_2MS_3 ($\text{M} = \text{Co}, \text{Mn}$) and Ce_2MnN_3 .

Ba_2CoS_3 shows a one-dimensional structure, with chains of corner-linked CoS_4 tetrahedra running along the [001] direction and interleaved by Ba^{2+} cations. Previous studies reported one-dimensional antiferromagnetic interactions between Co^{2+} cations mediated by the S^{2-} anions, a metallic-like conductivity and a small negative magnetoresistance.^{56, 227} Susceptibility and heat capacity data reported by Barnes *et al.* hinted at the presence of a three-dimensional magnetic order at temperatures below 46 K.²²⁷ In this work, the three-dimensional magnetic structure was confirmed and investigated via powder neutron diffraction. Each Co^{2+} cation shows a moment of $1.97(4) \mu_{\text{B}}$ aligned along [001] and is ferromagnetically coupled with four Co^{2+} cations from neighbouring chains and antiferromagnetically aligned with two others.²³⁸

Ba₂MnS₃ also shows a one-dimensional antiferromagnetic structure, with chains of corner-linked MnS₄ tetrahedra running along the [010] direction and interleaved by Ba²⁺. The structure differs slightly from the structure of Ba₂CoS₃ in the connectivity of the Ba-S polyhedra. Previous investigations indicated the presence of a three-dimensional magnetic structure at temperatures below 4 K. This magnetic structure was investigated in this work via powder neutron diffraction. Peak convolution and the relatively low peak intensity, arising from the poor scattering power of the constituent ions, a conclusive description of the magnetic structure of Ba₂MnS₃ could not be reached. However, two possible models have been proposed.

Ce₂MnN₃ is a one-dimensional nitride, isostructural with Sr₂CuO₃ showing an anion-deficient K₂NiF₄-type structure. Ce₂MnN₃ was reported by Niewa *et al.* and it is one of a small group of nitrides in which manganese shows the uncommon oxidation state +1.^{68, 93, 94} In this thesis, an alternative one-step preparative method together with cationic and anionic substitutions/insertions, performed on Ce₂MnN₃, are reported.

Of all the solid solutions prepared via isovalent and aliovalent cationic substitutions on the Ce⁴⁺ and Mn⁺ sites, only the Ce_{2-x}La_xMnN₃ ($0 \leq x \leq 0.22(2)$) was successfully prepared. A two-step reaction including the formation of Ce_{1-x}La_xN and its subsequent reaction with manganese in nitrogen or ammonia is the only route leading to Ce_{2-x}La_xMnN₃ ($0 \leq x \leq 0.22(2)$). One-step reactions, similar to the one employed to prepare the undoped Ce₂MnN₃ only favoured the formation of the stable CeN and LaN. Ce_{2-x}La_xMnN₃ showed an increase in cell size with increased substitution of cerium with lanthanum, as expected from the difference in size of the ionic radii (1.12 Å and 1.01 Å for La³⁺ and Ce⁴⁺ respectively).³² In addition, the increase in the cell size results in a minor reduction in the difference between the Mn-N_{bridging} and Mn-N_{terminal} bond lengths as predicted by Niewa *et al.*⁶⁸

The examples of mixed-anion non-oxide compounds reported in this thesis are: Ce₂MnN₃F_{2-δ} and a number of mixed-metal lanthanum oxide-nitrides.

Sr_2CuO_3 is isostructural to Ce_2MnN_3 , and therefore shows an anion-deficient K_2NiF_4 -type structure. Fluorination of Sr_2CuO_3 led to the preparation of the mixed-anion compound $\text{Sr}_2\text{CuO}_2\text{F}_{2+\delta}$ via the substitution of two fluoride anions for one oxide anion and the insertion of extra fluoride anions (δ).³⁰ This anionic substitution/insertion inspired the fluorination work on Ce_2MnN_3 , reported in this thesis. Via low-temperature fluorination techniques, $\text{Ce}_2\text{MnN}_3\text{F}_{2-\delta}$ was prepared.²⁷⁹ To the best of the student's and supervisor's knowledge, $\text{Ce}_2\text{MnN}_3\text{F}_{2-\delta}$ is the first example of quaternary nitride fluoride reported. Powder and neutron diffraction data presented show that $\text{Ce}_2\text{MnN}_3\text{F}_{2-\delta}$ shows a two-dimensional structure with corner-linked MnN_3F distorted octahedra, interleaved by cerium cations in two different coordination environments. A model for the fluorination mechanism is also presented, showing the novelty of this fluorination process compared to others previously reported. As suggested by the chemical formula, the fluorination mechanism for Ce_2MnN_3 consists of the insertion of two fluoride anions, one of which re-arrange the structure by expanding the coordination of the manganese cation from four to six and the other one creates alternate layers of fully occupied and empty interstitial sites.

Reactions of ammonia gas with $\text{La}_{9.33}\text{Si}_6\text{O}_{26}$, $\text{La}_{8+x}\text{Sr}_{2-x}\text{M}_6\text{O}_{26+x/2}$ ($\text{M} = \text{Si}, \text{Ge}; 0 \leq x \leq 2$), $\text{La}_{9.67}\text{Si}_5\text{CoO}_{26}$ and $\text{La}_{10}\text{M}_5\text{CoO}_{26.5}$ ($\text{M} = \text{Si}, \text{Ge}$) were investigated in order to determine the suitability of these apatite-type materials for use in SOFCs fuelled by ammonia. Hydrogen powered SOFCs are of enormous interest as devices for production of energy with little greenhouse gas emission. However, a number of problems linked to hydrogen production storage and transportation are slowing down the larger scale use of SOFCs. Therefore, research into alternative fuel sources, to act as intermediate during the transition to the full use of hydrogen, is of importance. Ammonia is an excellent candidate as it is already produced in large scale, it is relatively cheap and the infrastructure for storage and transportation is already in place. However, considering that SOFCs operate at temperatures higher than 600 °C, a potential problem is the potential interaction of gaseous ammonia with the materials of the fuel cell components. In this work, potential candidates for SOFCs electrolytes, $\text{La}_{9.33}\text{Si}_6\text{O}_{26}$, $\text{La}_{8+x}\text{Sr}_{2-x}\text{M}_6\text{O}_{26+x/2}$ ($\text{M} = \text{Si}, \text{Ge}; 0 \leq x \leq 2$), $\text{La}_{9.67}\text{Si}_5\text{CoO}_{26}$ and $\text{La}_{10}\text{M}_5\text{CoO}_{26.5}$ ($\text{M} = \text{Si}, \text{Ge}$), were reacted with gaseous ammonia at temperatures between 700 °C and 1000 °C to investigate the stability of the structures. It was found

that, reactions with ammonia may lead to structural modifications depending on the starting oxide, but, in general, ammoniation tends to remove the interstitial oxide anions present in the starting oxides. As the ionic conductivity of these apatite oxides is influenced by the presence of interstitial oxides their removal is detrimental to applications in SOFCs. Therefore, the interactions between ammonia and materials forming SOFC components have to be taken into account for applications and require further studies. However, the ammonolysis of $\text{La}_{9.33}\text{Si}_6\text{O}_{26}$, $\text{La}_{8+x}\text{Sr}_{2-x}\text{M}_6\text{O}_{26+x/2}$ ($\text{M} = \text{Si}, \text{Ge}; 0 \leq x \leq 2$), $\text{La}_{9.67}\text{Si}_5\text{CoO}_{26}$ and $\text{La}_{10}\text{M}_5\text{CoO}_{26.5}$ ($\text{M} = \text{Si}, \text{Ge}$) produced a range of novel oxide-nitride materials.

Overall this work demonstrates the diversity of the chemistry of non-oxide and mixed-anion compounds. An interesting aspect is the chemical tailoring via cationic and anionic substitution/insertion, which is not very common in the non-oxide chemistry, usually relying more on “ab-initio” synthesis to obtain novel compounds. Furthermore, it was shown that novel compounds can be achieved via anionic substitutions as well as the more traditional cationic substitutions. If more studies similar to this one are encouraged, anionic substitution could soon be an alternative route for the preparation of new solids.

8 References

- ¹ D. A. Fletcher, R. F. McMeeking and D. Parkin, *J. Chem. Inf. Comput. Sci.*, 1996, **36**, 746.
- ² R. M. Hazen, *Scientific American*, 1988, **258**, 74.
- ³ J. S. Zhou and J. B. Goodenough, *Phys. Rev. Lett.*, 2005, **94**, 065501.
- ⁴ V. M. Goldschmidt, *Naturwissenschaften*, 1926, **14**, 14.
- ⁵ H. Zhang, N. Li, K. Li and D. F. Xue, *Acta Crystallogr., Sect. B*, 2007, **63**, 812.
- ⁶ F. S. Galasso, 'Perovskites and High T_c Superconductors', Gordon and Breach, New York, 1990.
- ⁷ D. R. Lide, 'Handbook of Chemistry and Physics', CRC Press, Boca Raton, FL, 1999.
- ⁸ J. Emsley, 'The Elements', Clarendon Press, Oxford, 1998.
- ⁹ C. Li, K. C. K. Soh and P. Wu, *J. Alloys Compd.*, 2004, **372**, 40.
- ¹⁰ L. M. Feng, L. Q. Jiang, M. Zhu, H. B. Liu, X. Zhou and C. H. Li, *J. Phys. Chem. Solids*, 2008, **69**, 967.
- ¹¹ L. Smart and E. Moore, 'Solid State Chemistry: An Introduction', Chapman & Hall, London, 1992.
- ¹² M. B. Smith, K. Page, T. Siegrist, P. L. Redmond, E. C. Walter, R. Seshadri, L. E. Brus and M. L. Steigerwald, *J. Am. Chem. Soc.*, 2008, **130**, 6955.
- ¹³ A. De Paoli and A. A. Barresi, *Ind. Eng. Chem. Res.*, 2001, **40**, 1460.
- ¹⁴ M. S. Wrighton, A. B. Ellis, P. T. Wolczanski, D. L. Morse, H. B. Abrahamson and D. S. Ginley, *J. Am. Chem. Soc.*, 1976, **98**, 2774.
- ¹⁵ K. Domen, A. Kudo, T. Onishi, N. Kosugi and H. Kuroda, *J. Phys. Chem.*, 1986, **90**, 292.
- ¹⁶ M. Kajitani, M. Matsuda, A. Hoshikawa, S. Harjo, T. Kamiyama, T. Ishigaki, F. Izumi and M. Miyake, *Chem. Mater.*, 2005, **17**, 4235.
- ¹⁷ D. F. Xue and S. Y. Zhang, *J. Phys.: Condens. Matter*, 1997, **9**, 7515.
- ¹⁸ D. F. Xue, S. X. Wu, Y. C. Zhu, K. Terabe, K. Kitamura and J. Y. Wang, *Chem. Phys. Lett.*, 2003, **377**, 475.
- ¹⁹ R. M. Scanlan, A. P. Malozemoff and D. C. Larbalestier, *Proc. IEEE*, 2004, **92**, 1639.
- ²⁰ M. Ardit, M. Dondi, G. Cruciani and F. Matteucci, *Mater. Res. Bull.*, 2009, **44**, 666.
- ²¹ M. V. Lobanov, A. M. Balagurov, V. J. Pomjakushin, P. Fischer, M. Gutmann, A. M. Abakumov, O. G. D'Yachenko, E. V. Antipov, O. I. Lebedev and G. Van Tendeloo, *Phys. Rev. B*, 2000, **61**, 8941.
- ²² M. T. Weller and C. S. Knee, *J. Mater. Chem.*, 2001, **11**, 701.
- ²³ S. N. Ruddlesden and P. Popper, *Acta Crystallogr.*, 1957, **10**, 538.
- ²⁴ S. N. Ruddlesden and P. Popper, *Acta Crystallogr.*, 1958, **11**, 54.
- ²⁵ I. B. Sharma and D. Singh, *Bull. Mater. Sci.*, 1998, **21**, 363.
- ²⁶ J. F. Bringley, S. S. Trail and B. A. Scott, *J. Solid State Chem.*, 1990, **86**, 310.
- ²⁷ H. Shaked, P. M. Keane, J. C. Rodriguez, F. F. Owen, R. L. Hitterman and J. D. Jorgensen, 'Crystal Structures of the High-T_c Superconducting Copper-Oxides', Elsevier Science B.V., Illinois, 1994.
- ²⁸ B. H. Chen, *J. Solid State Chem.*, 1996, **125**, 63.
- ²⁹ R. D. Shannon and C. T. Prewitt, *Acta Crystallogr., Sect. B*, 1969, **25**, 925.
- ³⁰ M. Al-mamouri, P. P. Edwards, C. Greaves and M. Slaski, *Nature*, 1994, **369**, 382.

- 31 'Nobel Lectures, Physics 1901-1921', Elsevier Publishing Company, Amsterdam, 1967.
- 32 R. D. Shannon, *Acta Crystallogr., Sect. A*, 1976, **32**, 751.
- 33 'Perspectives in solid state chemistry', ed. K. J. Rao, John Wiley & Sons Ltd, New Delhi, 1997.
- 34 C. Greaves and M. G. Francesconi, *Curr. Opin. Solid State Mater. Sci.*, 1998, **3**, 132.
- 35 S. T. Lees, I. Gameson, M. O. Jones, P. P. Edwards and M. Slaski, *Chem. Mater.*, 1998, **10**, 3146.
- 36 M. H. Delville, D. Barbut, A. Wattiaux, J. M. Bassat, M. Ménétrier, C. Labrugère, J. C. Grenier and J. Etourneau, *Inorg. Chem.*, 2009, **48**, 7962.
- 37 L. D. Aikens, L. J. Gillie, R. K. Li and C. Greaves, *J. Mater. Chem.*, 2002, **12**, 264.
- 38 P. R. Slater and R. K. B. Gover, *J. Mater. Chem.*, 2002, **12**, 291.
- 39 V. F. Sears, *Neutron News*, 1992, **3**, 26.
- 40 R. L. Needs, M. T. Weller, U. Scheler and R. K. Harris, *J. Mater. Chem.*, 1996, **6**, 1219.
- 41 J. Hadermann, G. Van Tendeloo, A. M. Abakumov, M. G. Rozova and E. V. Antipov, *J. Solid State Chem.*, 2001, **157**, 56.
- 42 J. H. Kim and C. E. Lee, *Phys. Rev. B*, 1996, **53**, 2265.
- 43 F. C. Fritschij, H. B. Brom, L. J. de Jongh, A. Tighezza, J. L. Rehspringer and M. Drillon, *Physica C*, 1996, 220.
- 44 A. C. W. P. James, S. M. Zahurak and D. W. Murphy, *Nature*, 1989, **338**, 240.
- 45 E. Z. Kurmaev, V. R. Galakhov, V. V. Fedorenko, L. V. Elokhina, S. Bartkowski, M. Neumann, C. Greaves, P. P. Edwards, M. Almamouri and D. L. Novikov, *Phys. Rev. B*, 1995, **52**, 2390.
- 46 E. Z. Kurmaev, L. V. Elokhina, V. V. Fedorenko, S. Bartkowski, M. Neumann, C. Greaves, P. P. Edwards, P. R. Slater and M. G. Francesconi, *J. Phys.: Condens. Matter*, 1996, **8**, 4847.
- 47 S. D'Arco and M. S. Islam, *Phys. Rev. B*, 1997, **55**, 1.
- 48 M. Al-Mamouri, P. P. Edwards, C. Greaves, P. R. Slater and M. Slaski, *J. Mater. Chem.*, 1995, **5**, 913.
- 49 T. Baikie, E. L. Dixon, J. F. Rooms, N. A. Young and M. G. Francesconi, *Chem. Commun.*, 2003, 1580.
- 50 T. Baikie, M. S. Islam and M. G. Francesconi, *J. Mater. Chem.*, 2005, **15**, 119.
- 51 J. L. Kissick, C. Greaves, P. P. Edwards, V. M. Cherkashenko, E. Z. Kurmaev, S. Bartkowski and M. Neumann, *Phys. Rev. B*, 1997, **56**, 2831.
- 52 N. Kijima, M. Takahashi, N. Matsumoto and S. Nagata, *J. Solid State Chem.*, 1998, **135**, 325.
- 53 K. W. Boer, *J. Cryst. Growth*, 1982, **59**, 111.
- 54 T. Baikie, V. Hardy, A. Maignan and M. G. Francesconi, *Chem. Commun.*, 2005, 5077.
- 55 K. Matsuura, T. Wada, T. Nakamizo, H. Yamauchi and S. Tanaka, *Phys. Rev. B*, 1991, **43**, 13118.
- 56 T. Baikie, A. Maignan and M. G. Francesconi, *Chem. Commun.*, 2004, 836.
- 57 R. R. Chianelli, M. H. Siadati, M. P. De la Rosa, G. Berhault, J. P. Wilcoxon, R. Bearden and B. L. Abrams, *Catal. Rev.-Sci. Eng.*, 2006, **48**, 1.
- 58 I. E. Grey and H. Steinfink, *Inorg. Chem.*, 1971, **10**, 691.
- 59 L. J. De Jongh and A. R. Miedema, *Adv. Phys.*, 1974, **23**, 1.
- 60 M. A. Greaney, K. V. Ramanujachary, Z. Teweldemedhin and M. Greenblatt, *J. Solid State Chem.*, 1993, **107**, 554.

- 61 H. Y. Hong and H. Steinfink, *J. Solid State Chem.*, 1972, **5**, 93.
62 D. M. Nicholas, R. A. M. Scott and M. R. Shropshall, *J. Appl. Crystallogr.*, 1977,
10, 356.
63 J. E. Iglesias, K. E. Pachali and H. Steinfink, *J. Solid State Chem.*, 1974, **9**, 6.
64 H. D. Rad and R. Hoppe, *Z. Anorg. Allg. Chem.*, 1981, **483**, 7.
65 C. B. Shoemaker, *Z. Kristallogr.*, 1973, **137**, 225.
66 F. J. DiSalvo and S. J. Clarke, *Curr. Opin. Solid State Mater. Sci.*, 1996, **1**, 241.
67 J. Etourneau, J. Portier and F. Ménil, *J. Alloys Compd.*, 1992, **188**, 1.
68 R. Niewa, G. V. Vajenine, F. J. DiSalvo, H. H. Luo and W. B. Yelon, *Z.
Naturforsch., B*, 1998, **53**, 63.
69 R. Niewa and F. J. DiSalvo, *Chem. Mater.*, 1998, **10**, 2733.
70 P. E. Rauch and A. Simon, *Angew. Chem., Int. Ed. Engl.*, 1992, **31**, 1519.
71 G. J. Snyder and A. Simon, *J. Am. Chem. Soc.*, 1995, **117**, 1996.
72 A. Simon, *Coord. Chem. Rev.*, 1997, **163**, 253.
73 A. Gudat, R. Kniep, A. Rabenau, W. Bronger and U. Ruschewitz, *J. Less-Common
Met.*, 1990, **161**, 31.
74 G. Cordier, A. Gudat, R. Kniep and A. Rabenau, *Angew. Chem., Int. Ed. Engl.*,
1989, **28**, 1702.
75 W. H. Baur, *Cryst. Rev.*, 1987, **1**, 59.
76 J. Peters and B. Krebs, *Acta Crystallogr., Sect. B*, 1982, **38**, 1270.
77 E. Makovicky, *Rev. Mineral. Geochem.*, 2006, **61**, 7.
78 H. Yamane and F. J. DiSalvo, *Acta Crystallogr., Sect. C*, 1996, **52**, 760.
79 W. Blasé, G. Cordier, M. Ludwig and R. Kniep, *Z. Naturforsch., B*, 1994, **49**, 501.
80 S. J. Clarke and F. J. DiSalvo, *Inorg. Chem.*, 1997, **36**, 1143.
81 M. Ludwig, R. Niewa and R. Kniep, *Z. Naturforsch., B*, 1999, **54**, 461.
82 R. Niewa, D. A. Zhrebtsov, H. Borrmann and R. Kniep, *Z. Anorg. Allg. Chem.*,
2002, **628**, 2505.
83 T. Brokamp and H. Jacobs, *J. Alloys Compd.*, 1992, **183**, 325.
84 H. Jacobs and R. Niewa, *Eur. J. Solid State Inorg. Chem.*, 1994, **31**, 105.
85 P. E. Rauch, F. J. DiSalvo, N. E. Brese, D. E. Partin and M. Okeefe, *J. Solid State
Chem.*, 1994, **110**, 162.
86 R. Niewa and H. Jacobs, *J. Alloys Compd.*, 1996, **234**, 171.
87 R. Niewa and H. Jacobs, *J. Alloys Compd.*, 1996, **233**, 61.
88 A. Bowman and D. H. Gregory, *J. Alloys Compd.*, 2003, **348**, 80.
89 D. A. Zhrebtsov, L. G. Akselrud and R. Niewa, *Z. Kristallogr.*, 2002, **217**, 469.
90 O. Seeger, M. Hofmann, J. Strahle, J. P. Laval and B. Frit, *Z. Anorg. Allg. Chem.*,
1994, **620**, 2008.
91 R. Benz and Zacharia. Wh, *J. Nucl. Mater.*, 1970, **37**, 109.
92 S. Broll and W. Jeitschko, *Z. Naturforsch., B*, 1995, **50**, 905.
93 G. A. Landrum, R. Dronskowski, R. Niewa and F. J. DiSalvo, *Chem. Eur. J.*, 1999,
5, 515.
94 R. Niewa, Z. Hu, C. Grazioli, U. Rossler, M. S. Golden, M. Knupfer, J. Fink, H.
Giefers, G. Wortmann, F. M. F. de Groot and F. J. DiSalvo, *J. Alloys Compd.*,
2002, **346**, 129.
95 D. H. Gregory, *Coord. Chem. Rev.*, 2001, **215**, 301.
96 P. Höhn, S. Haag, W. Milius and R. Kniep, *Angew. Chem., Int. Ed. Engl.*, 1991, **30**,
831.
97 R. Niewa and F. J. DiSalvo, *J. Alloys Compd.*, 1998, **279**, 153.
98 A. Gudat, R. Kniep and J. Maier, *J. Alloys Compd.*, 1992, **186**, 339.
99 M. Y. Chern and F. J. DiSalvo, *J. Solid State Chem.*, 1990, **88**, 459.

- 100 T. Yamamoto, S. Kikkawa and F. Kanamaru, *Solid State Ionics*, 1993, **63-5**, 148.
101 T. Yamamoto, S. Kikkawa and F. Kanamaru, *J. Solid State Chem.*, 1995, **115**, 353.
102 G. Cordier, A. Gudat, R. Kniep and A. Rabenau, *Angew. Chem., Int. Ed. Engl.*,
1989, **28**, 201.
103 A. Gudat, S. Haag, R. Kniep and A. Rabenau, *J. Less-Common Met.*, 1990, **159**,
L29.
104 F. J. DiSalvo, S. S. Trail, H. Yamane and N. E. Brese, *J. Alloys Compd.*, 1997, **255**,
122.
105 A. Tennstedt and R. Kniep, *Z. Anorg. Allg. Chem.*, 1994, **620**, 1781.
106 A. Gudat, W. Milius, S. Haag, R. Kniep and A. Rabenau, *J. Less-Common Met.*,
1991, **168**, 305.
107 'Encyclopedia of Chemical Technology', ed. J. I. Kroschwitz and M. Howe Grant,
John Wiley & Sons, Chichester, 1991-1998.
108 D. H. Gregory, *J. Chem. Soc., Dalton Trans.*, 1999, 259.
109 H.-C. zur Loye, J. D. Houmes and D. S. Bem, 'The Chemistry of Transition Metal
Carbides and Nitrides', ed. O. S. T., Blackie Academic & Professional, Glasgow,
1996.
110 N. E. Brese and M. Okeeffe, *Struct. Bond.*, 1992, **79**, 307.
111 R. Niewa and H. Jacobs, *Chem. Rev.*, 1996, **96**, 2053.
112 'Advances in Inorganic Chemistry and Radiochemistry', ed. H. J. Emeléus and A.
G. Sharpe, Academic Press, London, 1996.
113 B. Mazumder and A. L. Hector, *J. Mater. Chem.*, 2009, **19**, 4673.
114 R. Juza, K. Langer and K. von Benda, *Angew. Chem. Int. Ed. Engl.*, 1968, **7**, 360.
115 'Handbook of Chemistry and Physics 51st edition', ed. R. C. Weast, The Chemical
Rubber Company, Cleveland, Ohio, 1970.
116 C. C. Addison, R. J. Pulham and E. A. Trevillion, *J. Chem. Soc., Dalton Trans.*,
1975, 2082.
117 N. E. Brese and M. Okeeffe, *J. Solid State Chem.*, 1990, **87**, 134.
118 G. V. Vajenine, A. Grzechnik, K. Syassen, I. Loa, M. Hanfland and A. Simon,
Comptes Rendus Chimie, 2005, **8**, 1897.
119 M. D. Lyutaya and O. P. Kulik, *Sov. Powder Metall. Met. Ceram.*, **13**, 792.
120 S.-J. Kim, T. Marquart and H. F. Franzen, *J. Less-Common Met.*, 1990, **158**, L9.
121 G. T. Beilby and G. G. Henderson, *J. Chem. Soc. Trans.*, 1901, **79**, 1245.
122 K. S. Weil and P. N. Kumta, *Mater. Sci. Eng., B*, 1996, **38**, 109.
123 P. S. Herle, M. S. Hegde, K. Sooryanarayana, T. N. G. Row and G. N. Subbanna,
Inorg. Chem., 1998, **37**, 4128.
124 A. Gomathi, *Mater. Res. Bull.*, 2007, **42**, 870.
125 H. Z. Zhao, M. Lei, X. L. Chen and W. H. Tang, *J. Mater. Chem.*, 2006, **16**, 4407.
126 D. S. Bem, C. P. Gibson and H. C. Z. Loye, *Chem. Mater.*, 1993, **5**, 397.
127 T. J. Prior and P. D. Battle, *J. Solid State Chem.*, 2003, **172**, 138.
128 T. J. Prior, S. E. Oldham, V. J. Couper and P. D. Battle, *Chem. Mater.*, 2005, **17**,
1867.
129 T. J. Prior and P. D. Battle, *J. Mater. Chem.*, 2004, **14**, 3001.
130 J. D. Houmes and H. C. zur Loye, *Chem. Mater.*, 1996, **8**, 2551.
131 E. Kroke, *Angew. Chem., Int. Ed. Engl.*, 2002, **41**, 77.
132 'IUPAC Nomenclature of Inorganic Chemistry', ed. G. J. Leigh, Blackwell
Scientific Publications, Oxford, 1990.
133 S. Yamanaka, *Annu. Rev. Mater. Sci.*, 2000, **30**, 53.
134 S. J. Hwu and J. D. Corbett, *J. Solid State Chem.*, 1986, **64**, 331.

- 135 S. J. Hwu, R. P. Ziebarth, S. Vonwinbush, J. E. Ford and J. D. Corbett, *Inorg. Chem.*, 1986, **25**, 283.
- 136 K. R. Poeppelmeier and J. D. Corbett, *Inorg. Chem.*, 1977, **16**, 294.
- 137 G. Meyer, S. J. Hwu, S. Wijeyesekera and J. D. Corbett, *Inorg. Chem.*, 1986, **25**, 4811.
- 138 K. R. Poeppelmeier and J. D. Corbett, *J. Am. Chem. Soc.*, 1978, **100**, 5039.
- 139 S. J. Hwu, D. S. Dudis and J. D. Corbett, *Inorg. Chem.*, 1987, **26**, 469.
- 140 C. C. Torardi and R. E. McCarley, *J. Am. Chem. Soc.*, 1979, **101**, 3963.
- 141 H. J. Meyer, N. L. Jones and J. D. Corbett, *Inorg. Chem.*, 1989, **28**, 2635.
- 142 U. Schwanitz-Schuller and A. Simon, *Z. Naturforsch., B*, 1985, **40**, 705.
- 143 H. J. Mattausch, J. B. Hendricks, R. Eger, J. D. Corbett and A. Simon, *Inorg. Chem.*, 1980, **19**, 2128.
- 144 C. Wüstefeld, T. Vogt, U. Löchner, J. Strähle and H. Fuess, *Angew. Chem., Int. Ed. Engl.*, 1988, **27**, 929.
- 145 K. Nukumizu, J. Nunoshige, T. Takata, J. N. Kondo, M. Hara, H. Kobayashi and K. Domen, *Chem. Lett.*, 2003, **32**, 196.
- 146 W. Jung and R. Juza, *Z. Anorg. Allg. Chem.*, 1973, **399**, 129.
- 147 R. Schlichenmaier, E. Schweda, J. Strähle and T. Vogt, *Z. Anorg. Allg. Chem.*, 1993, **619**, 367.
- 148 D. K. Smith and W. Newkirk, *Acta Crystallogr.*, 1965, **18**, 983.
- 149 L. P. Zhu, X. A. Chen and S. Yamanaka, *Solid State Commun.*, 2004, **130**, 227.
- 150 R. P. Ziebarth and J. D. Corbett, *J. Less-Common Met.*, 1988, **137**, 21.
- 151 S. Yamanaka and H. Tou, *Curr. Opin. Solid State Mater. Sci.*, 2001, **5**, 545.
- 152 X. A. Chen, H. Fukuoka and S. Yamanaka, *J. Solid State Chem.*, 2002, **163**, 77.
- 153 S. Yamanaka, K. Itoh, H. Fukuoka and M. Yasukawa, *Inorg. Chem.*, 2000, **39**, 806.
- 154 S. M. Kauzlarich, J. L. Stanton, J. Faber and B. A. Averill, *J. Am. Chem. Soc.*, 1986, **108**, 7946.
- 155 J. Oro-Sole, M. Vlassov, D. Beltran-Porter, M. T. Caldes, V. Primo and A. Fuertes, *Solid State Sci.*, 2002, **4**, 475.
- 156 R. Juza and J. Heners, *Z. Anorg. Allg. Chem.*, 1964, **332**, 159.
- 157 R. Juza and I. L. Friedrichsen, *Z. Anorg. Allg. Chem.*, 1964, **332**, 173.
- 158 M. Ohashi, S. Yamanaka, M. Sumihara and M. Hattori, *J. Solid State Chem.*, 1988, **75**, 99.
- 159 M. Ohashi, S. Yamanaka and M. Hattori, *J. Solid State Chem.*, 1988, **77**, 342.
- 160 S. Shamoto, T. Kato, Y. Ono, Y. Miyazaki, K. Ohoyama, M. Ohashi, Y. Yamaguchi and T. Kajitani, *Physica C*, 1998, **306**, 7.
- 161 S. Y. Istomin, J. Kohler and A. Simon, *Physica C*, 1999, **319**, 219.
- 162 A. M. Fogg, J. S. O. Evans and D. O'Hare, *Chem. Commun.*, 1998, 2269.
- 163 A. M. Fogg, V. M. Green and D. O'Hare, *Chem. Mater.*, 1999, **11**, 216.
- 164 A. Fuertes, M. Vlassov, D. Beltran-Porter, P. Alemany, E. Canadell, N. Casan-Pastor and M. R. Palacin, *Chem. Mater.*, 1999, **11**, 203.
- 165 D. G. Adolphson and J. D. Corbett, *Inorg. Chem.*, 1976, **15**, 1820.
- 166 H. P. Beck and C. Strobel, *Z. Anorg. Allg. Chem.*, 1986, **535**, 229.
- 167 A. W. Mann and D. J. M. Bevan, *Acta Crystallogr., Sect. B*, 1970, **B 26**, 2129.
- 168 J. Strähle and H. Bärnighausen, *Z. Anorg. Allg. Chem.*, 1968, **357**, 325.
- 169 K. Dehnicke and J. Strähle, *Z. Anorg. Allg. Chem.*, 1965, **339**, 171.
- 170 M. R. Close and R. E. McCarley, *Inorg. Chem.*, 1994, **33**, 4198.
- 171 J. Strähle, *Z. Anorg. Allg. Chem.*, 1970, **375**, 238.
- 172 J. Strähle, *Angew. Chem. Int. Ed. Engl.*, 1969, **8**, 925.

- 173 Q. T. Dinh, M. Richter, E. Niquet and J. Strahle, *Z. Anorg. Allg. Chem.*, 2002, **628**, 1255.
- 174 Q. T. Dinh, M. Richter, E. Niquet and J. Strahle, *Z. Anorg. Allg. Chem.*, 2002, **628**, 1921.
- 175 M. Weisser, S. Tragl and H. J. Meyer, *Z. Anorg. Allg. Chem.*, 2007, **633**, 802.
- 176 A. Binder, C. Maichle-Mossmer, E. Niquet and J. Strahle, *Z. Anorg. Allg. Chem.*, 2008, **634**, 1326.
- 177 J. Fawcett, R. D. Peacock and D. R. Russell, *J. Chem. Soc., Chem. Commun.*, 1982, 958.
- 178 J. Fawcett, R. D. Peacock and D. R. Russell, *J. Chem. Soc., Dalton Trans.*, 1987, 567.
- 179 B. Tanguy, M. Pezat, J. Portier and P. Hagenmuller, *Mater. Res. Bull.*, 1971, **6**, 57.
- 180 M. Pezat, B. Tanguy, M. Vlasse, J. Portier and P. Hagenmuller, *J. Solid State Chem.*, 1976, **18**, 381.
- 181 T. Vogt, E. Schweda, J. P. Laval and B. Frit, *J. Solid State Chem.*, 1986, **83**, 324.
- 182 R. Marchand, 'Handbook on the Physics and Chemistry of Rare Earths', ed. K. A. Gschneidner Jr. and L. Eyring, Elsevier Science B.V., 1998.
- 183 S. Yamanaka, K. Hotehama and H. Kawaji, *Nature*, 1998, **392**, 580.
- 184 M. G. Francesconi, M. G. Barker and C. Wilson, *Chem. Commun.*, 2002, 1358.
- 185 C. Wachsmann and H. Jacobs, *Z. Anorg. Allg. Chem.*, 1996, **622**, 885.
- 186 A. Gudat, R. Kniep and J. Maier, *Z. Naturforsch., B*, 1992, **47**, 1363.
- 187 A. J. D. Barnes, T. J. Prior and M. G. Francesconi, *Chem. Commun.*, 2007, 4638.
- 188 D. Bright and J. A. Ibers, *Inorg. Chem.*, 1969, **8**, 709.
- 189 M. G. Francesconi, M. G. Barker, P. A. Cooke and A. J. Blake, *J. Chem. Soc., Dalton Trans.*, 2000, **11**, 1709.
- 190 D. A. Vennos and F. J. DiSalvo, *Acta Crystallogr., Sect. C*, 1992, **48**, 610.
- 191 X. Z. Chen and H. A. Eick, *J. Solid State Chem.*, 1994, **113**, 362.
- 192 C. Wachsmann and H. Jacobs, *Z. Kristallogr.*, 1996, **211**, 477.
- 193 S. J. Clarke and F. J. DiSalvo, *Z. Kristallogr.*, 1997, **212**, 309.
- 194 F. K. J. Helmlinger, P. Hohn and R. Kniep, *Z. Naturforsch., B*, 1993, **48**, 1015.
- 195 A. Gudat, S. Haag, R. Kniep and A. Rabenau, *Z. Naturforsch., B*, 1990, **45**, 111.
- 196 P. Höhn, Dissertation, Technische Hochschule Darmstadt, 1992.
- 197 A. F. Clifford and C. S. Kobayashi, *Inorg. Synth.*, 1960, **6**, 204.
- 198 G. A. Bain and J. F. Berry, *J. Chem. Educ.*, 2008, **85**, 532.
- 199 A. F. Orchard, 'Magnetochemistry', ed. R. G. Compton, Oxford University Press, New York, 2003.
- 200 R. L. Carlin, *J. Chem. Educ.*, 1991, **68**, 361.
- 201 J. C. Bonner and M. E. Fisher, *Phys. Rev. A*, 1964, **135**, 640.
- 202 A. Manthiram and J. Kim, *Chem. Mater.*, 1998, **10**, 2895.
- 203 R. Tilley, 'Crystals and Crystal Structures', John Wiley & Sons, Ltd, Chichester, 2006.
- 204 M. T. Weller, 'Inorganic Materials Chemistry', ed. J. Evans, Oxford University Press, Avon, 1994.
- 205 W. Clegg, 'Crystal Structure Determination', ed. J. Evans, Oxford University Press, Avon, 1998.
- 206 R. Tilley, 'Understanding Solids: The Science of Materials', John Wiley & Sons, Ltd, Chippingham, 2008.
- 207 G. Calestani, *Adv. Imaging Electron Phys.*, 2002, **123**.
- 208 W. L. Bragg, *Proc. Cambridge Philos. Soc.*, 1913, **17**, 43.
- 209 A. Boulfif and D. Louer, *J. Appl. Crystallogr.*, 1991, **24**, 987.

- 210 J. Laugier and B. Bochu, 'Chekcell', Laboratoire des Matériaux et du Génie
Physique Ecole Nationale Supérieure de Physique de Grenoble (INPG) Domaine
Universitaire, France.
- 211 'Powder Diffraction: Theory and Practice', ed. R. E. Dinnebier and S. J. L. Billinge,
RSC Publishing, Cambridge, 2009.
- 212 C. E. Housecroft and A. G. Sharpe, 'Inorganic Chemistry', Pearson Education
Limited, Harlow, 2001.
- 213 'Characterization of Materials', ed. E. N. Kaufmann, Wiley and Sons, Inc.,
Hoboken, Jersey, 2003.
- 214 G. G. Low, *Nature*, 1968, **31**, 895.
- 215 [http://www.ill.eu/reactor-environment-safety/high-flux-reactor/technical-
characteristics/](http://www.ill.eu/reactor-environment-safety/high-flux-reactor/technical-characteristics/).
- 216 <http://www.ill.eu/instruments-support/instruments-groups/instruments/d2b/>.
- 217 A. C. Larson and R. B. Von Dreele, 'General structure analysis system (GSAS)',
Los Alamos National Laboratory Report LAUR, 2004.
- 218 'The Rietveld Method', ed. R. A. Young, Oxford University Press, New York,
2002.
- 219 L. B. McCusker, R. B. Von Dreele, D. E. Cox, D. Louër and P. Scardi, *J. Appl.*
Crystallogr., 1999, **32**, 36.
- 220 A. Le Bail, *Powder Diffr.*, 2005, **20**, 316.
- 221 J. J. Rehr and R. C. Albers, *Rev. Mod. Phys.*, 2000, **72**, 621.
- 222 [http://www.xafs.org/Tutorials?action=AttachFile&do=get&target=Newville_xas
_fundamentals.pdf](http://www.xafs.org/Tutorials?action=AttachFile&do=get&target=Newville_xas_fundamentals.pdf).
- 223 J. J. Rehr, R. C. Albers, C. R. Natoli and E. A. Stern, *Phys. Rev. B*, 1986, **34**, 4350.
- 224 N. Binsted, 'PAXAS: EXAFS Analysis Program', 1988.
- 225 A. Tenderholt, B. Hedman and K. O. Hodgson, 'PySpline: A Modern, Cross-
Platform Program for the Processing of Raw Averaged XAS Edge Data:X-ray
Absorption Fine Structure - XAFS 13', ed. B. Hedman and P. Paianetta, AIP
Conference Proceedings 2007.
- 226 S. J. Gurman, N. Binsted and I. Ross, *J. Phys. C*, 1984, **17**, 143.
- 227 A. D. J. Barnes, T. Baikie, V. Hardy, M. B. Lepetit, A. Maignan, N. A. Young and
M. G. Francesconi, *J. Mater. Chem.*, 2006, **16**, 3489.
- 228 J. Crangle, 'Solid State Magnetism', Edward Arnold, London, 1991.
- 229 R. L. Fagaly, *Rev. Sci. Instrum.*, 2006, **77**, 101101.
- 230 'Solid-State Chemistry Techniques', ed. A. K. Cheetham and P. Day, Oxford
University Press, Bury St Edmunds, 1987.
- 231 T. Baikie, M. R. Harrison, D. A. Headspith, V. Hardy, A. Maignan and M. G.
Francesconi, *in preparation*, 2009.
- 232 T. Baikie, 'PhD Thesis', The University of Hull, 2005.
- 233 N. Nakayama, K. Kosuge, S. Kachi, T. Shinjo and T. Takada, *J. Solid State Chem.*,
1980, **33**, 351.
- 234 W. Thomson, *Proc. R. Soc.*, 1957, **8**, 546.
- 235 J. Checkelsky, in 'www2.hmc.edu/~eckert/research/JCHECKELSKY.pdf'.
- 236 M. R. Harrison, V. Hardy, A. Maignan and M. G. Francesconi, *Chem. Commun.*,
2009, 2214.
- 237 L. J. Dejongh and A. R. Miedema, *Adv. Phys.*, 1974, **23**, 1.
- 238 D. A. Headspith, P. D. Battle and M. G. Francesconi, *J. Solid State Chem.*, 2007,
180, 2859.
- 239 H. M. Rietveld, *J. Appl. Crystallogr.*, 1969, **2**, 65.
- 240 B. H. Toby, *J. Appl. Crystallogr.*, 2001, **34**, 210.

- 241 C. J. Howard, *J. Appl. Crystallogr.*, 1982, **15**, 615.
- 242 P. Thompson, D. E. Cox and J. B. Hastings, *J. Appl. Crystallogr.*, 1987, **20**, 79.
- 243 C. E. Infante, 'D. Phil. Thesis', Oxford, 1975.
- 244 G. B. Jensen and O. V. Nielsen, *J. Phys. C*, 1974, **7**, 409.
- 245 J. Klatyk and R. Kniep, *Z. Kristallogr.*, 1999, **214**, 445.
- 246 J. Klatyk, R. Niewa and R. Kniep, *Z. Naturforsch., B*, 2000, **55**, 988.
- 247 G. L. Olcese, *J. Phys. F*, 1979, **9**, 569.
- 248 C.-G. Duan, R. F. Sabirianov, W. N. Mei, P. A. Dowben, S. S. Jaswal and E. Y. Tsymbal, *J. Phys.: Condens. Matter*, 2007, **19**, 315220.
- 249 A. Delin, P. M. Oppeneer, M. S. S. Brooks, T. Kraft, J. M. Wills, B. Johansson and O. Eriksson, *Phys. Rev. B*, 1997, **55**, 10173.
- 250 F. Tessier, M. R. Ranade, A. Navrotsky, R. Niewa, F. J. DiSalvo, A. Leineweber and H. Jacobs, *Z. Anorg. Allg. Chem.*, 2001, **627**, 194.
- 251 T. Nakagawa, H. Matsuoka, M. Sawa, M. Hirota, M. Miyake and M. Katsura, *J. Nucl. Mater.*, 1997, **247**, 127.
- 252 W. Muthmann and K. Kraft, *J. Chem. Soc. Abstr.*, 1903, **84**, B202.
- 253 'Handbook of Chemistry and Physics', ed. D. R. Lide, CRS Press, Inc., USA, 1991-1992.
- 254 P. Suortti, *J. Appl. Crystallogr.*, 1972, **50**, 325.
- 255 Y. Hashimoto, M. Takahashi, S. Kikkawa and F. Kanamaru, *J. Solid State Chem.*, 1996, **125**, 37.
- 256 Y. Hashimoto, M. Takahashi, S. Kikkawa and F. Kanamaru, *J. Solid State Chem.*, 1995, **114**, 592.
- 257 Y. Hashimoto, M. Takahashi, S. Kikkawa and F. Kanamaru, *Chem. Lett.*, 1994, 1963.
- 258 W. H. Zachariasen, *Z. Phys. Chem.*, 1926, **123**, 134.
- 259 A. Leineweber, H. Jacobs and W. Kockelmann, *J. Alloys Compd.*, 2004, **368**, 229.
- 260 R. A. Young and W. T. Ziegler, *J. Am. Ceram. Soc.*, 1952, **74**, 5251.
- 261 J. D. McCullough, *J. Am. Chem. Soc.*, 1950, **72**, 1386.
- 262 C. K. Narula, L. P. Haack, W. Chun, H. W. Jen and G. W. Graham, *J. Phys. Chem. B*, 1999, **103**, 3634.
- 263 P. Shuk, M. Greenblatt and M. Croft, *Chem. Mater.*, 1999, **11**, 473.
- 264 S. Y. Hao and T. X. Lue, *J. Rare Earths*, 2007, **25**, 247.
- 265 N. Gabbitas, J. G. Thompson, R. L. Withers and A. D. Rae, *J. Solid State Chem.*, 1995, **115**, 23.
- 266 L. Vegard, *Z. Phys.*, 1921, **17**, 5.
- 267 L. Vegard, *Z. Kristallogr.*, 1928, **67**, 239.
- 268 P. Höhn and R. Kniep, *Z. Naturforsch., B*, 1992, **47**, 434.
- 269 W. Sachsze and R. Juza, *Z. Anorg. Allg. Chem.*, 1949, **259**, 278.
- 270 E. Zintl and G. Brauer, *Z. Elektrochem.*, 1935, **41**, 102.
- 271 A. Gudat, R. Kniep and A. Rabenau, *Thermochim. Acta*, 1990, **160**, 49.
- 272 D. Sundararaman, P. Shankar and V. S. Raghunathan, *Metall. Mater. Trans. A*, 1996, **27**, 1175.
- 273 T.-H. Lee, C.-S. Oh, H. N. Han, C. G. Lee, S.-J. Kim and S. Takaki, *Acta Crystallogr., Sect. B*, 2005, **61**, 137.
- 274 M. Jansen and H. P. Letschert, *Nature*, 2000, **404**, 980.
- 275 B. Chevalier, A. Tressaud, B. Lepine, K. Amine, J. M. Dance, L. Lozano, E. Hickey and J. Etourneau, *Physica C*, 1990, **167**, 97.
- 276 C. N. R. Rao, A. K. Cheetham and R. Mahesh, *Chem. Mater.*, 1996, **8**, 2421.
- 277 C. N. R. Rao and A. K. Cheetham, *Adv. Mater.*, 1997, **9**, 1009.

- 278 J. G. Bednorz and K. A. Muller, *Z. Phys. B: Condens. Matter*, 1986, **64**, 189.
- 279 D. A. Headspith, E. Sullivan, C. Greaves and M. G. Francesconi, *Dalton Trans.*,
2009, 9273.
- 280 P. R. Slater, J. P. Hodges, M. G. Francesconi, C. Greaves and M. Slaski, *J. Mater.*
Chem., 1997, **7**, 2077.
- 281 S. Zulfiqar, M. Zulfiqar, M. Rizvi, A. Munir and I. C. McNeill, *Polym. Degrad.*
Stab., 1994, **43**, 423.
- 282 P. R. Slater, *J. Fluorine Chem.*, 2002, **117**, 43.
- 283 P. R. Slater, J. P. Hodges, M. G. Francesconi, P. P. Edwards, C. Greaves, I.
Gameson and M. Slaski, *Physica C*, 1995, **253**, 16.
- 284 W. W. Wright, 'High Temperature Resistance and Thermal Degradation of
Polymers', Society of Chemical Industry, London, 1961.
- 285 M. Almamouri, P. P. Edwards, C. Greaves, P. R. Slater and M. Slaski, *J. Mater.*
Chem., 1995, **5**, 913.
- 286 L. D. Aikens, R. K. Li and C. Greaves, *Chem. Commun.*, 2000, 2129.
- 287 S. Yeh, S. Y. Wu, C.-S. Lee and Y. Wang, *Acta Crystallogr., Sect. B*, 1993, **49**,
806.
- 288 D. Babel and E. Herdtweck, *Z. Anorg. Allg. Chem.*, 1982, **487**, 75.
- 289 R. L. Needs, S. E. Dann, M. T. Weller, J. C. Cherryman and R. K. Harris, *J. Mater.*
Chem., 2005, **15**, 2399.
- 290 F. Izumi, E. Takayama-Muromachi, A. Fujimori, T. Kamiyama, H. Asano, J.
Akimitsu and H. Sawa, *Physica C*, 1989, **158**, 440.
- 291 H. Wilhelm, C. Cros, E. Reny, G. Demazeau and M. Hanfland, *J. Mater. Chem.*,
1998, **8**, 2729.
- 292 Y. Laligant, A. Le Bail, G. Ferey, M. Hervieu, B. Raveau, A. Wilkinson and A. K.
Cheetham, *Eur. J. Solid State Inorg. Chem.*, 1988, **25**, 237.
- 293 P. R. Slater, P. P. Edwards, C. Greaves, I. Gameson, M. G. Francesconi, J. P.
Hodges, M. Almamouri and M. Slaski, *Physica C*, 1995, **241**, 151.
- 294 P. R. Slater, J. E. H. Sansom and J. R. Tolchard, *Chem. Rec.*, 2004, **4**, 373.
- 295 A. Klerke, C. H. Christensen, J. K. Nørskov and T. Vegge, *J. Mater. Chem.*, 2008,
18, 2304.
- 296 A. Wojcik, H. Middleton, I. Damopoulos and J. Van Herle, *J. Power Sources*,
2003, **118**, 342.
- 297 L. Zhang and W. Yang, *J. Power Sources*, 2008, **179**, 92.
- 298 N. P. Brandon, S. Skinner and B. C. H. Steele, *Annu. Rev. Mater. Res.*, 2003, **33**,
183.
- 299 M. Islam, S., J. R. Tolchard and P. R. Slater, *Chem. Commun.*, 2003, 1486.
- 300 J. R. Tolchard, M. S. Islam and P. R. Slater, *J. Mater. Chem.*, 2003, **13**, 1956.
- 301 J. E. H. Sansom, D. Richings and P. R. Slater, *Solid State Ionics*, 2001, **139**, 205.
- 302 L. León-Reina, E. R. Losilla, M. Martínez-Lara, S. Bruque and M. A. G. Aranda, *J.*
Mater. Chem., 2004, **14**, 1142.
- 303 Y. Masubuchi, M. Higuchi, T. Takeda and S. Kikkawa, *Solid State Ionics*, 2006,
177, 263.
- 304 J. R. Tolchard, J. E. H. Sansom, M. Saiful Islam and P. R. Slater, *Dalton Trans.*,
2005, 1273.
- 305 L. León-Reina, M. C. Martin-Sedeno, E. R. Losilla, A. Cabeza, M. Martinez-Lara,
S. Bruque, F. M. B. Marques, D. V. Sheptyakov and M. A. G. Aranda, *Chem.*
Mater., 2003, **15**, 2099.
- 306 P. Berastegui, S. Hull, F. J. García García and J. Grins, *J. Solid State Chem.*, 2002,
168, 294.

- 307 E. J. Abram, C. A. Kirk, D. C. Sinclair and A. R. West, *Solid State Ionics*, 2005,
176, 1941.
- 308 E. Kendrick, M. S. Islam and P. R. Slater, *Chem. Commun.*, 2008, 715.
- 309 A. B. Jorge, J. Fraxedas, A. Cantarero, A. J. Williams, J. Rodgers, J. P. Attfield and
A. Fuertes, *Chem. Mater.*, 2008, **20**, 1682.
- 310 T. Iwata, K. Fukuda, E. Bechade, O. Masson, I. Julien, E. Champion and P.
Thomas, *Solid State Ionics*, 2007, **178**, 1523.
- 311 A. Rachel, S. G. Ebbinghaus, M. Güngerich, P. J. Klar, J. Hanss, A. Weidenkaff
and A. Reller, *Thermochim. Acta*, 2005, **438**, 134.
- 312 R. Aguiar, D. Logvinovich, A. Weidenkaff, A. Reller and S. G. Ebbinghaus,
Thermochim. Acta, 2008, **471**, 55.
- 313 E. Kendrick, D. A. Headspith, A. Orera, D. C. Apperley, R. I. Smith, M. G.
Francesconi and P. R. Slater, *J. Mater. Chem.*, 2009, **19**, 749.
- 314 J. R. Tolchard and P. R. Slater, *J. Phys. Chem. Solids*, 2008, **69**, 2433.
- 315 A. L. Shaula, V. V. Kharton and F. M. B. Marques, *Solid State Ionics*, 2006, **177**,
1725.
- 316 J. E. H. Sansom, J. R. Tolchard, M. S. Islam, D. Apperley and P. R. Slater, *J.*
Mater. Chem., 2006, **16**, 1410.
- 317 A. Orera, E. Kendrick, D. C. Apperley, V. M. Orera and P. R. Slater, *Dalton*
Trans., 2008, 5296.
- 318 O. Haas, R. P. W. J. Struis and J. M. McBreen, *J. Solid State Chem.*, 2004, **177**,
1000.
- 319 H. S. C. O'Neill, *Mineral. Mag.*, 2003, **67**, 547.
- 320 V. P. S. Awana, S. K. Malik, W. B. Yelon, M. Karppinen and H. Yamauchi,
Physica C, 2002, **378-381**, 155.
- 321 T. A. Smith, J. E. Penner-Hahn, M. A. Berding, S. Doniach and K. O. Hodgson, *J.*
Am. Chem. Soc., 1985, **107**, 5945.
- 322 G. J. Colpas, M. J. Maroney, C. Bagyinka, M. Kumar, W. S. Willis, S. L. Suib, N.
Baidya and P. K. Mascharak, *Inorg. Chem.*, 1991, **30**, 920.
- 323 S. H. Baker, M. Roy, S. Louch and C. Binns, *J. Phys.: Condens. Matter*, 2006, **18**,
2385.

Appendix A

Publications

“Formation of apatite oxynitrides by the reaction between apatite-type oxide ion conductors, $\text{La}_{8+x}\text{Sr}_{2-x}(\text{Si/Ge})_6\text{O}_{26+x/2}$, and ammonia” A. Orera, D. A. Headspith, D. C. Apperley, M. G. Francesconi and P. R. Slater, *J. Solid State Chem.*, 2009, **182**, 3294.

“Synthesis and Characterisation of the Quaternary Nitride-Fluoride $\text{Ce}_2\text{MnN}_3\text{F}_{2-\delta}$ ” D. A. Headspith, M. G. Francesconi, E. Sullivan and C. Greaves, *Dalton Trans.*, 2009, 9273.

“Transition metal pnictide-halides – A class of under-explored compounds” D. A. Headspith and M. G. Francesconi, *Top. Catal.*, 2009, **52**, 1611.

“An investigation of the high temperature reaction between the apatite oxide ion conductor $\text{La}_{9.33}\text{Si}_6\text{O}_{26}$ and NH_3 ” E. Kendrick, D. A. Headspith, A. Orera, D. C. Apperley, R. I. Smith, M. G. Francesconi and P. R. Slater, *J. Mater. Chem.*, 2009, **19**, 749.

“Stereostructural behaviour of N-N atropisomers: Two conglomerate crystallisations and a crystallisation-induced deracemisation” R. J. Arthur, M. P. Coogan, M. Casadesus, R. Haigh, D. A. Headspith, M. G. Francesconi and R. H. Laye, *Cryst. Eng. Comm.*, 2009, **11**, 610.

“Long-range magnetic ordering in Ba_2CoS_3 : A neutron diffraction study” D. A. Headspith, P. D. Battle and M. G. Francesconi, *J. Solid State Chem.*, 2007, **180**, 2859.

Appendix B

Atom	Site	x	y	z	100 × U _{iso}	Occ.
Ba(1)	4c	0.3269(5)	0.0187(5)	¼	1.1(2)	1.0
Ba(2)	4c	0.9866(5)	0.8266(5)	¼	1.1(2)	1.0
Co	4c	0.2463(12)	0.3071(11)	¼	2.5(5)	1.0
S(1)	4c	0.3648(9)	0.4443(8)	¼	1.6(2)	1.0
S(2)	4c	0.0612(9)	0.3622(9)	¼	1.6(2)	1.0
S(3)	4c	0.7259(8)	0.7915(9)	¼	1.6(2)	1.0

Table B-1. Structural parameters for Ba₂CoS₃ derived from PND collected at 1.5 K.

Distances (Å)			
Ba(1)-Co	3.48(1) × 2	Co-S(1)	2.32(2)
	3.72(2)		
Ba(1)-S(1)	3.24(1) × 2	Co-S(2)	2.22(2)
Ba(1)-S(2)	3.16(1) × 2	Co-S(3)	2.45(1) × 2
	3.17(1)		
Ba(1)-S(3)	3.22(1) × 2		
Ba(2)-Co	3.83(1) × 2		
Ba(2)-S(1)	3.11(1) × 2	Co-Co (intrachain)	4.1891(4)
	3.20(1)		
Ba(2)-S(2)	3.20(1) × 2		6.153(6)
Ba(2)-S(3)	3.22(1)	(interchain)	6.5653(7)
	3.15(1)		
Angles (°)			
S(1)-Co-S(2)	112.7(7)	S(2)-Co-S(3)	106.1(4)
S(1)-Co-S(3)	107.4(4)	S(3)-Co-S(3)	117.4(7)

Table B-2. Selected bond lengths and angles in Ba₂CoS₃ from neutron data collected at 1.5 K.

Appendix C

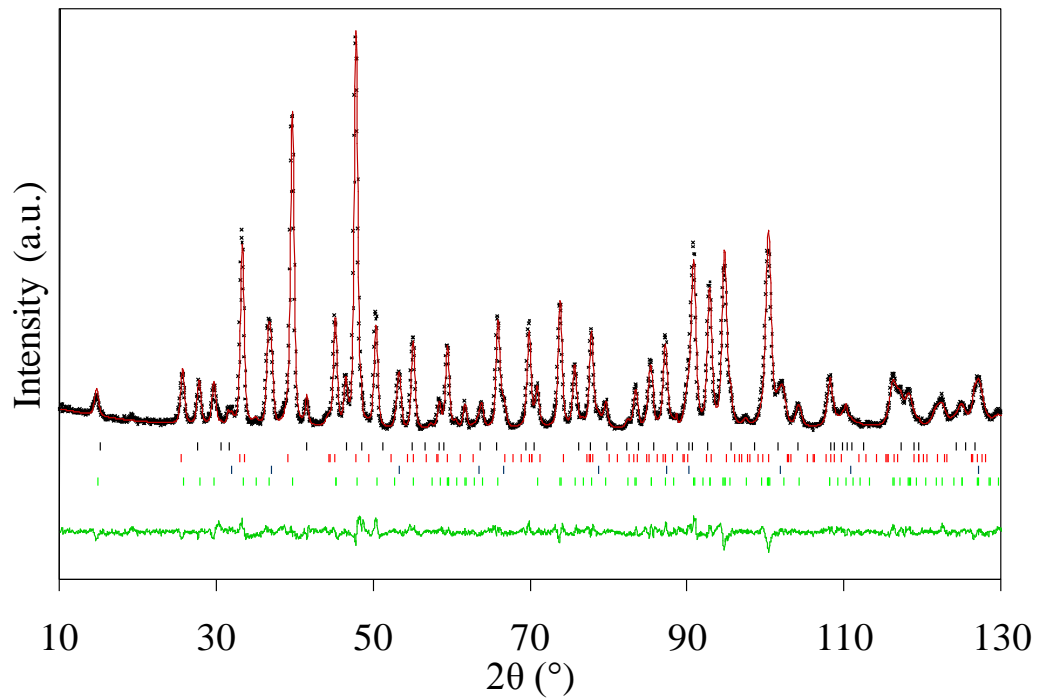


Figure C-1. NPD profiles for $\text{Ce}_{1.90(1)}\text{La}_{0.10(1)}\text{MnN}_3$ at room temperature, showing observed (+), calculated (red line) and difference pattern (green line). Tick marks indicate reflection positions for $\text{Ce}_{1.9}\text{La}_{0.1}\text{O}_3$ (black), $\text{MnN}_{0.457}$ (red), $\text{Ce}_{0.95}\text{La}_{0.05}\text{N}$ (blue) and $\text{Ce}_{1.90(1)}\text{La}_{0.10(1)}\text{MnN}_3$ (green) phases.

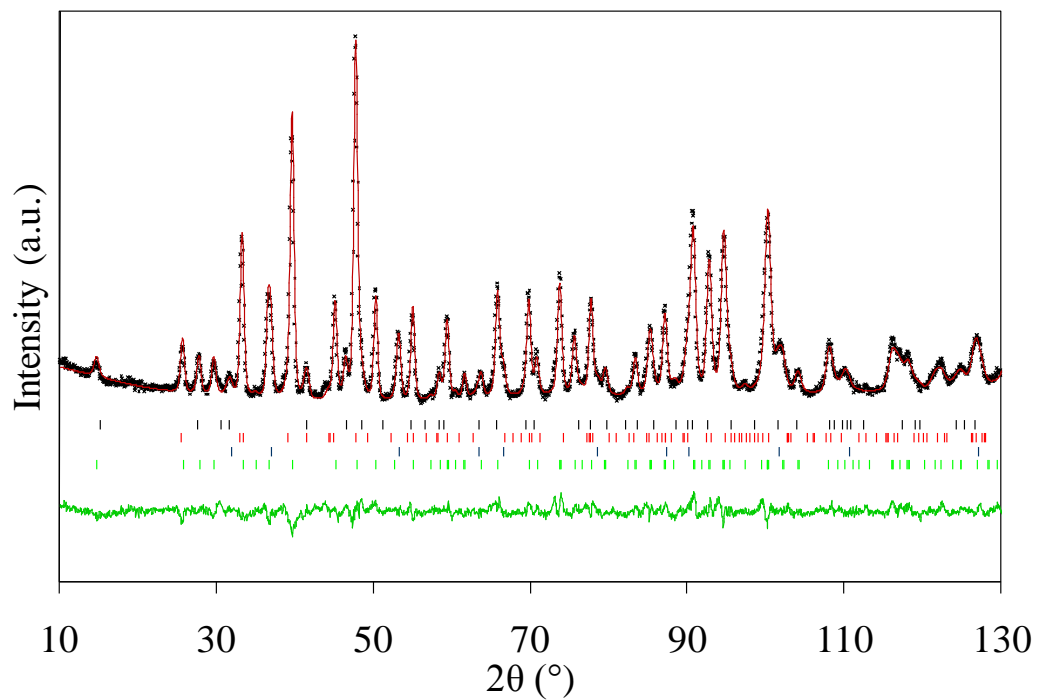


Figure C-2. NPD profiles for $\text{Ce}_{1.82(2)}\text{La}_{0.18(2)}\text{MnN}_3$ at room temperature, showing observed (+), calculated (red line) and difference pattern (green line). Tick marks indicate reflection positions for $\text{Ce}_{1.85}\text{La}_{0.15}\text{O}_3$ (black), $\text{MnN}_{0.457}$ (red), $\text{Ce}_{0.925}\text{La}_{0.075}\text{N}$ (blue) and $\text{Ce}_{1.82(2)}\text{La}_{0.18(2)}\text{MnN}_3$ (green) phases.

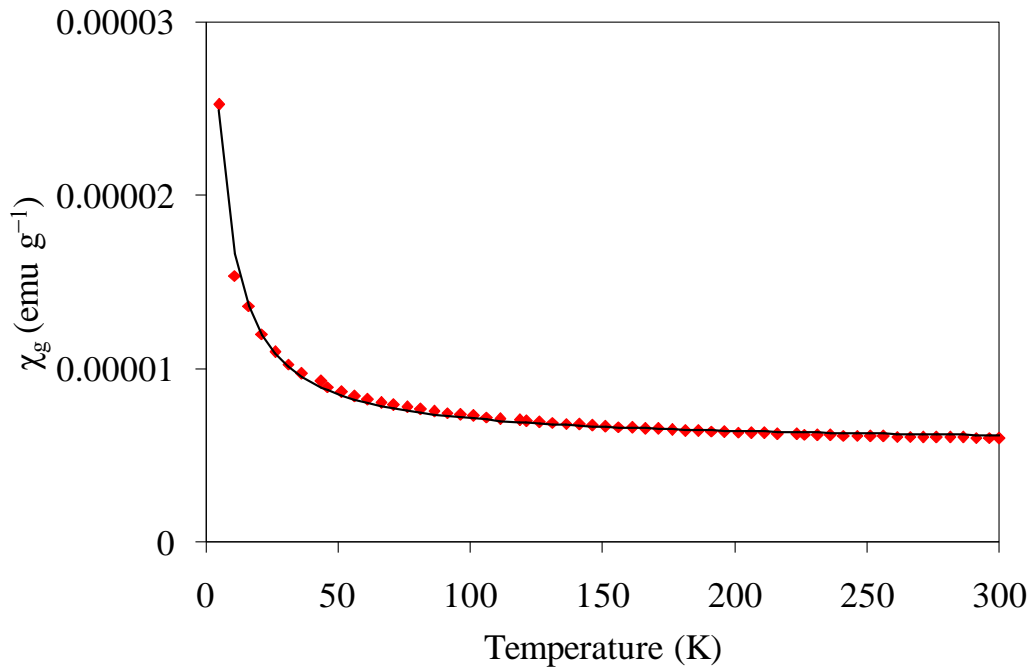


Figure C-3. Magnetic susceptibility (χ) versus temperature data for $\text{Ce}_{1.90(1)}\text{La}_{0.10(1)}\text{MnN}_3$ (red) with fitting based on a Curie-Weiss equation with a temperature independent component (black).

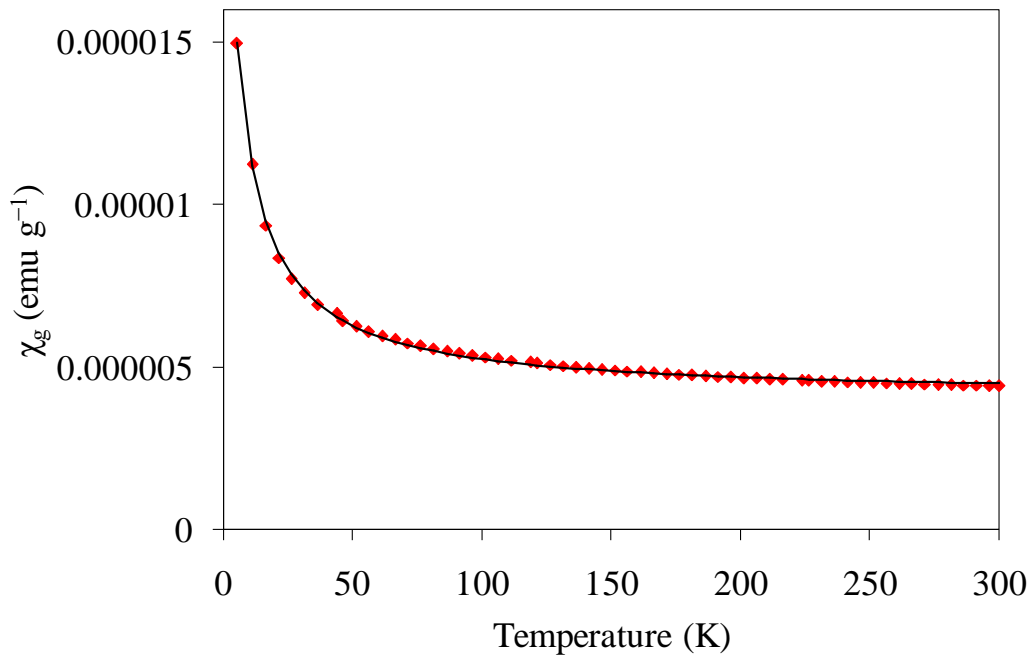


Figure C-4. Magnetic susceptibility (χ) versus temperature data for $\text{Ce}_{1.82(2)}\text{La}_{0.18(2)}\text{MnN}_3$ (red) with fitting based on a Curie-Weiss equation with a temperature independent component (black).

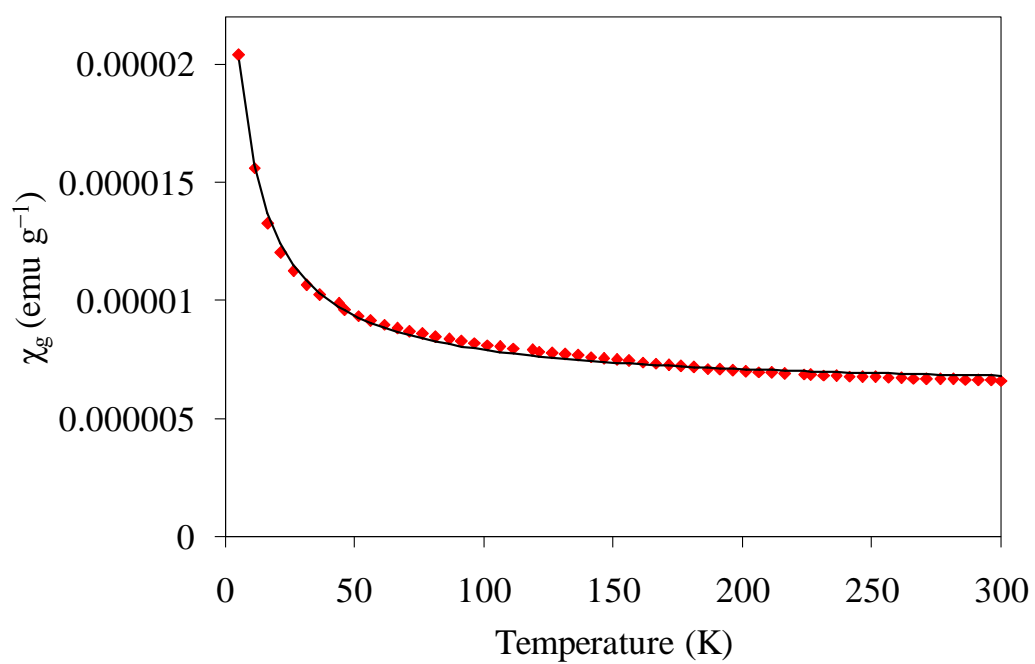


Figure C-5. Magnetic susceptibility (χ) versus temperature data for $\text{Ce}_{1.75}\text{La}_{0.25}\text{MnN}_3$ (red) with fitting based on a Curie-Weiss equation with a temperature independent component (black).

Appendix D

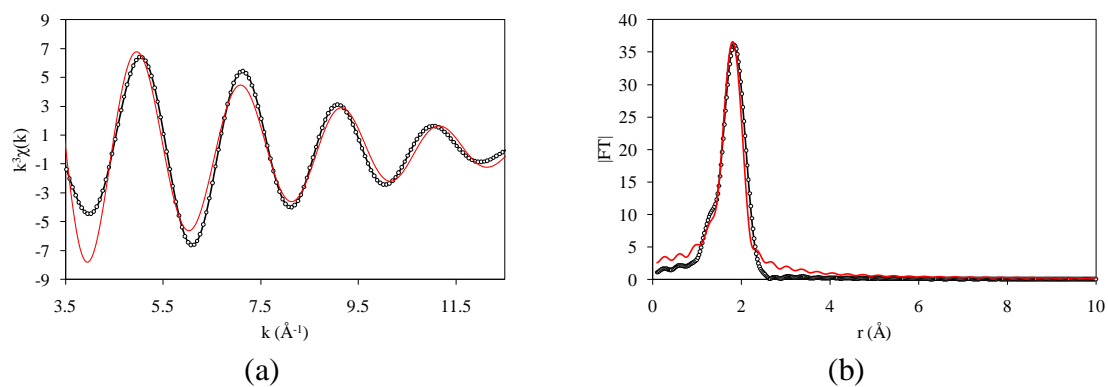


Figure D-1. Co-K-edge (a) EXAFS and (b) Fourier transform for $\text{La}_{10}\text{Si}_5\text{CoO}_{26.5}$. The red and black lines correspond with the theoretical and experimental data respectively.

Shell	Atom type	Coordination	r (\AA)	D-W factor (\AA^2)	R-fit (%)
1	O^{2-}	4	1.852(7)	0.013(1)	27.98

Table D-1. Summary of refined Co-K-edge EXAFS parameters for $\text{La}_{10}\text{Si}_5\text{CoO}_{26.5}$.

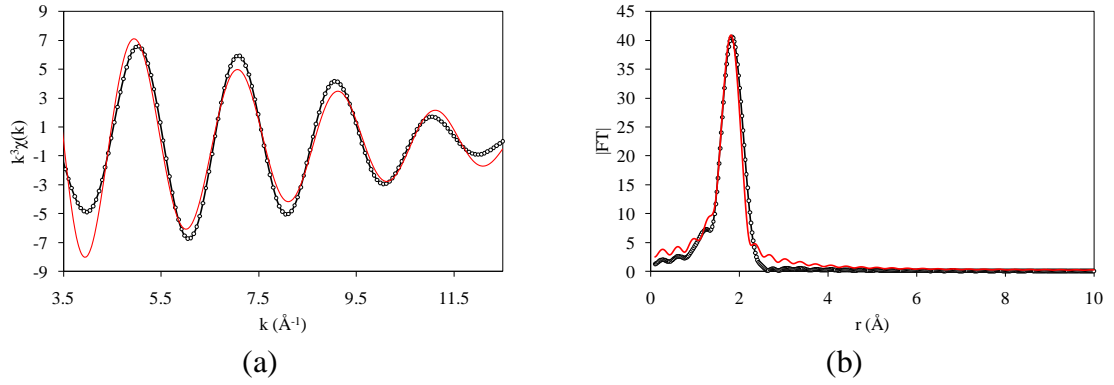


Figure D-2. Co-K-edge (a) EXAFS and (b) Fourier transform for $\text{La}_{10}\text{Ge}_5\text{CoO}_{26.5}$. The red and black lines correspond with the theoretical and experimental data respectively.

Shell	Atom type	Coordination	r (\AA)	D-W factor (\AA^2)	R-fit (%)
1	O^{2-}	4	1.854(7)	0.011(1)	31.74

Table D-2. Summary of refined Co-K-edge EXAFS parameters for $\text{La}_{10}\text{Ge}_5\text{CoO}_{26.5}$.